CRANFIELD UNIVERSITY

RICHARD HAIGH

NOVEL PIEZOELECTRIC THICK FILM ACTUATORS

SCHOOL OF INDUSTRIAL & MANUFACTURING

SCIENCE (SIMS)

PhD THESIS

CRANFIELD UNIVERSITY

SCHOOL OF INDUSTRIAL & MANUFACTURING
SCIENCE (SIMS)

PhD THESIS

ACADEMIC YEARS 2000-3

R.D. HAIGH

NOVEL PIEZOELECTRIC THICK FILM ACTUATORS

SUPERVISOR: PROF. R.W. WHATMORE

MARCH 2005

This thesis is submitted in fulfilment for the degree of Doctor of Philosophy.

Abstract

Planar-spiral piezoelectric-unimorph-actuators, that deflect out-of-their-plane, were modelled, designed and fabricated. A range of other planar piezoelectric-device designs has also been made. These include spokes, multi-arms, plates and swastikas. All these devices consisted of a mechanical support in the plane with a piezoelectric layer deposited on top. Impedance spectra demonstrated that a fabricated device was piezoelectrically active. Finite-element (FE) models of straight and spiral piezoelectric-unimorph-actuators were constructed. The mechanical stiffness of the spiral-beam was increased with the curvature of the beam; consequently, the inner coils exhibited virtually no deflection and appeared to be redundant. The advantage of the spiral-actuators is that they allow large actuator lengths to be contained compactly without the loss of mechanical stiffness.

Fabrication of the above devices necessitated the development of new fabrication technologies. The active-piezoelectric and mechanical-support were a lead zirconate titanate ($Pb(Ti_{1-x}Zr_x)O_3$ - PZT) thick-film and a platinised-silicon-wafer respectively. Vias were opened in the PZT with wet etching, and this was completed without damaging the back electrode. Powder blasting allowed any 2-dimensional-shape to be cut into the device wafer. Devices were released from the Si support with deep-reactive-ion-etching (DRIE).

The PZT thick films were fired with a Cu_2O-PbO eutectic additive. Pb and Cu were considered to dope on A and B lattice sites (of PZT) respectively, when the PZT was sintered at high oxygen-partial-pressure (po_2). The electrical conductivity of PZT thick films was increased when they were sintered at low po_2, and this was moderated by the presence of Cu^+ as an acceptor ion.

A lead-platinum intermetallic and lead silicate glass phase simultaneously formed under sintering conditions of low po_2, and this simultaneous formation, was accounted for by a six-stage mechanism. Step 1, residual C in the thick film reduces PbO to Pb followed by step 2 where Pb diffuses into the Pt back electrode. In step 3, Pt_3Pb formation occurs in the intermetallic layer followed by step 4 in which PtPb forms. Step 5 occurs with saturation of the intermetallic layer as Pb continues to diffuse from the thick film. There is additional diffusion of Pb into the underlying Si substrate. Finally step 6 occurs at some later point, when po_2 has risen, Pb is oxidised to PbO, and Si is oxidised to SiO_2. PbO and SiO_2 can flux to form $PbSiO_3$

The glass was found to undermine film/substrate adhesion.

Acknowledgement

The author wishes to gratefully acknowledge the contributions made to this work by the following: Mr. C. Matthews, Mr. A. Dyer, Mr. A. Stallard, Mr. A. Grey, Mr. A. Potter, Mr. D. Martin, Miss C. Kempton, Mrs. E. Giaracuni, Dr. S. Wilson, Dr. C.P. Shaw, Dr. Q. Zhang, Dr. S. Stringfellow, Dr. D. Corker and Prof. R. Whatmore. Mr. J. Southin was particularly helpful in the formulation of computer code for finite-element-modelling. The author also wishes to thank Dr. R. Stevens of RAL: for his help with powder blasting.

The author wishes to thank BAE systems and EPSRC for financial assistance in sponsoring this project.

Contents

Notation

Symbol	Definition
α_{PZT}	Sidewall angle of a feature etched into PZT
α_{Si}	Etching angle of anisotropically etched silicon
β	Drying Temperature
β_{ij}^{σ}	Dielectric impermittivity measured at constant stress
β_{ij}^{S}	Dielectric impermittivity measured at constant strain
χ	Crystallisation Temperature
δ	Deflection
δ_{ma}	Deflection of a multi-arm-device
δ_{s}	Out of plane deflection of a piezoelectric-unimorph-spiral-actuator. Data obtained through FE (finite element) analysis
δ_{spiral}	Deflection of a spiral actuator
$\delta_{spiral\text{-}tangential}$	Tangential deflection of a spiral unimorph actuator
δ_{spoke}	Deflection of a single spoke device
$\delta_{straight}$	Out-of-plane deflection of a straight-unimorph-actuator
Δ	Non dimensional parameter for deflection
ε_{0}	Vacuum permittivity
ε_{ij}	Permittivity
$\varepsilon_{ij}^{\sigma}$	Permittivity measured at constant stress
ε_{ij}^{S}	Permittivity measured at constant strain
ε_{r}	Dielectric constant
ϕ	Phase angle
γ	Etching efficiency
Γ	Amplification factor
$\Gamma_{out\text{-}of\text{-}plane}$	Out of the plane amplification factor
Γ_{rad}	Radial Amplification Factor corresponding to radial modes of spiral-unimorph-actuators
Γ_{s}	Out of the plane amplification factor for a unimorph-spiral-actuator calculated through FE (Finite element) analysis
ι	Edge shift
ϑ	Curvature coefficient 5
κ	Curvature
λ	Maximum mechanical energy output of a straight piezoelectric-unimorph-actuator
ν	Curvature coefficient 2
o	Curvature coefficient 3
Π	Non dimensional parameter for blocking-force
θ	Angle

Θ	Non dimensional parameter for frequency
$\theta_{elastic}$	Gun angle corresponding to maximum elastic erosion
θ_{gun}	Gun angle
θ_{max}	Maximum angle
θ_{min}	Minimum angle
θ_{table}	Table angle
ρ	Density
ρ_m	Mechanical-support density
ρ_p	Piezoelectric-plate density
ρ_v	Resistivity
σ_{ij}, σ_j	Stress
τ_{rot}	Time period of rotation
υ	Curvature coefficient 1
ϖ	Curvature coefficient 4
ω	Angular frequency
ζ_j	Eigenvalue of j^{th}, mode
(12)	Interaction between factors 1 and 2, but could also be (123) or (23) depending on experimental design.
a	Sintering temperature
A	Young's modulus ratio
^1A_r	Area number 1
^2A_r	Area number 2
a_s	Gradient of a straight line
a_{spiral}	Spiral constant
a_{spot}	Distance from table centre to the centre of r_{spot}
b	Sintering gas
B	Thickness ratio
B_{max}	Optimised thickness ratio for a unimorph actuator
C	Composite layer
c	Intercept of a straight line
C_ρ	Density ratio
C_A	Capacitance
c_{ij}, c_{ijkl}	Elastic stiffness
c_{ij}^D	Elastic stiffness measured at constant electric displacement
c_{ij}^E	Elastic stiffness measured at constant electric field
D	Set of drying conditions
D_c	Diameter of the inner circle
D_{eff}	Effective radius
D_f	Diameter of a front face feature equivalent to D_{max}
$d_{h,k,l}$	Lattice spacing
d_{ij}, d_{ijk}	Piezoelectric coefficient used when either stress or electric field are

	independent variables
D_j	Electric displacement
D_{max}	Outer diameter
D_{min}	Inner diameter
E_c	Coercive electric field
[Ex]	Matrix of experimental runs
e_{ij}, e_{ijk}	Piezoelectric coefficients used when the piezoelectric is unbounded
E_j	Electric field vector
Er	Erosion rate
Er_d	Downward etch rate
Er_l	Lateral etch rate
f	Frequency
F	Blocking force
$f_{anti-res}$	Anti-resonant frequency measured from an impedance spectrum
F_{ben}	Pure bending force
F_{ext}	Extensional force
F_{ma}	Blocking force generated by a multi-arm-device
F_s	Blocking force for a spiral actuator calculated from FE (finite element) analysis
f_s	Resonant frequency calculated from FE (finite element) analysis
f_{res}	Resonant frequency measured from an impedance spectrum
F_{shear}	Shear force
f_{spiral}	Frequency of a single spiral
F_{spiral}	Blocking force generated by a spiral-device
f_{spoke}	Frequency of a single spoke actuator
F_{spoke}	Blocking force of a single spoke device
F_{tot}	Total forces
g	Set of replicated conditions
ΔG_f^θ	Gibbs' free energy of formation under standard conditions
ΔG_f^E	Gibbs' free energy of formation at the sintering temperature
g_{ij}, g_{ijk}	Piezoelectric coefficients used when either stress or electric displacement are the independent variables
g_s	Gun speed
h	Thickness
h_E	Etch depth
h_{ij}, h_{ijk}	Piezoelectric coefficients used when either strain or electric displacement are the independent variables
h_m	Mechanical-support thickness
h_p	Piezoelectric-plate thickness
h_{wafer}	Wafer thickness
I_n	Identity
I_c	Area moment of inertia

k_{eff}	Effective electromechanical coupling coefficient
k_{ij}	Electromechanical coupling coefficient (in reduced suffix notation)
K_N	Spring constant of the spiral actuator for $N^{|}_{turns}$
K_s	Spiral spring constant
L	Length
l	Line width
$\bar{l}$	Average line width
L_b	Length across a cavity at the bottom of an etched feature
L_{bf}	Length between back face features
L_c	Length of spiral contained within the circle of radius r_c
l_c	Position of the centre of a cavity
$L_{centre\text{-}centre}$	Length from one device to the centre of an adjacent device
L_{eff}	Effective length
Lit(h,k,l)	Peak in the XRD spectrum corresponding to litharge. The litharge peak has miller indices of h,k,l
L_{max}	Maximum length
l_{max}	Maximum line width
$L_{res}1$, $L_{res}2$	Length occupied by residue on either side of the photoresist cavity
L_s	Spiral length
L_{spiral}	Spiral-device length
L_{spoke}	Length of a single spoke actuator
L_t	Length across a cavity at the top of an etched feature
L_T	Track length
m	Integer value
m_a	Mass
Mas(h,k,l)	Peak in the XRD spectrum corresponding to massicott. The massicott peak has miller indices of h,k,l
m_0	Initial mass, i.e. At time = 0
M_{ben}	Pure bending moment
M_{ext}	Extensional moment
m_{powder}	Total mass of impacting powder particles
m_t	Final mass, i.e. at time = t
M_{tot}	Total moments
n	Integer value
$N^{|}_{turns}$	Any whole number of rotations of a spiral actuator
N_{arms}	Number of spiral arms
N_c	Number of cycles
N_o	Number of experimental observations
N_{spokes}	Number of spokes
N_{turns}	Number of spiral turns
Per(h,k,l)	Peak in the XRD spectrum corresponding to Perovskite PZT. The PZT peak has miller indices of h,k,l

P_i	Polarisation vector
p_{ma}	Pressure generated by an array of multi-arm-devices
po_2	Oxygen partial pressure
P_r	Remanent polarisation
P_s	Saturation polarisation
p_{spiral}	Pressure generated by a spiral-device
p_{spoke}	Pressure generated by an array of spoke devices
Q	Electric charge
r	Radius
R	Electrical resistance
$\Re$	Resolution
r, θ, z	Polar axis
r_c	Radius of an inner circle
r_{eff}	Effective radius
revs	Revolutions
r_{max}	Outer radius
r_{min}	Inner radius
r_N	Radius of the spiral at $N^{\prime}_{turns}$
r_{spot}	Spot radius
S	Sol layer
SE	Standard error
s_{ij} s_{ijkl}	Elastic compliance
s_{ij}^{E}	Elastic compliance measured at constant electric field
s_{ij}^{D}	Elastic compliance measured at constant electric displacement
S_{ij}, S_j	Strain
t	Time
T	Temperature
[T]	Temperature matrix
tanδ	Dielectric loss
T_c	Curie Temperature
t_{run}	Run time
V	Potential difference
v	vertical displacement
w	Width
w_1	Outer width of the spoke device
w_2	Inner width of the spoke device
w_a	Actual width
w_i	Ideal width
w_{spiral}	Spiral beam width
w_{spoke}	Width of a single spoke actuator
w_{void}	Void width
x, y, z	Cartesian axis

Y	Young's modulus
y_c	Position of the centroidal axis along the y-coordinate
$Y^E{}_{ij}$	Young's modulus at constant electric field (in reduced suffix notation)
y_i	Response variable of the ith run in a statistical experiment
Y_m	Young's modulus of the mechanical-support
Y_p	Young's modulus of the piezoelectric-plate
$\lvert z \rvert$	Magnitude of displacement, along the z-coordinate, about an average line

Acronyms

Term	Definition
2D	Two dimensions
3D	Three dimensions
AC	Alternating Current
CAD	Computer assisted design
CCD	Charge Coupled device
CMF	Central Microstructure Facility
CSD	Chemical solution deposition
CTE	Coefficient of thermal expansion
DC	Direct Current
DRIE	Deep reactive ion etching
DTA	Differential thermal analysis
EB-PVD	Electron beam physical vapour deposition
EDX	Energy dispersive X-ray
FDT	Fused deposition technique
FE	Finite element
FEA	Finite element analysis
FIB	Focused ion microscope
IPA	Isopropyl alcohol
ITO	Indium tin oxide
LPCVD	Low pressures chemical vapour deposition
MOD	Metal organic deposition
Nd-YAG	Nd doped yttrium aluminium garnet
PCB	Printed circuit board
PCN	Lead cuprous niobate
PDMS	Poly(dimethyl silane)
PVDF	Poly(vinylidiene difluoride)
PZT	Lead zirconate titanate
QUB	Queens University of Belfast
RAL	Rutherford Appleton Laboratory
RF	Radio frequency
RIE	Reactive ion etching
RTA	Rapid thermal anneal
SE	Standard error
SEM	Scanning electron microscope
SFEG	Scanning field emission Gun
SPA	Sequential precursor addition
TBC	Thermal barrier coating
TEM	Transmission electron microscope
TGA	Thermo gravimetric analysis

UV	Ultraviolet
XRD	X-ray diffraction
YSZ	Yittria stabilised zirconia

Preface

Project

This project was about the fabrication and testing of a range of novel planar devices. Spiral unimorph actuators were of particular interest in the current work. These devices were piezoelectric unimorphs in which the active piezoelectric layer was a lead zirconate titanate (PZT) thick film. The thick film (~7-10 μm) was prepared on a platinised silicon substrate. These devices were designed to deflect out of the plane. The application of the thick film route to the fabrication of a range of devices was the central theme of this work. The combination of the thick film route with bulk silicon micromachining to yield a novel processing route was an integral part of this work; a set of photolithographic masks were designed and made around this processing route to facilitate device fabrication. In addition, the work also included finite element (FE) modelling of fabricated devices; the interpretation of experimental measurements was made in the light of findings from these models.

Thesis Structure

This thesis begins with an introduction and literature review leading to a statement of aims and objectives. An experimental chapter follows this statement, and the results chapters follow the experimental chapter. The results chapters, chapters 5 to 9, comprise a short introduction, an experimental section (where experimental development work was undertaken) and a results and discussion section. There was quite a lot of discussion of the experimental results in these chapters; however, this discussion was limited to the experimental results and did not include an interpretation of the results in the light of the literature. This was done in the discussion. The reason for this was to separate conclusions and findings of this work from work undertaken by other authors. This, it was thought, will make it easier for the reader to interpret the findings of this work on its own merits. The order that these chapters appear corresponds to the sequence in which they are listed: 1 introduction, 2 literature review, 3 the aims & objectives, 4 experimental, 5 design, 6 high temperature processing of PZT thick films, 7 patterning of PZT thick films, 8 process integration, 9 device fabrication & analysis, 10 discussion, 11 conclusions and 12 further work. Unwieldy mathematics, data or computer code is contained in appendices at the end of the thesis.

Chapter Content

No further mention will be made of chapters 1 to 3 and 10 to 12, as these chapters are self-explanatory. The experimental chapter is divided into a section on standard experimental techniques and a section on specific experiments undertaken in the thesis. It should be noted, that where experimental development work was undertaken the convention used in this thesis is to contain the experimental method within the results chapters.

The design chapter covers the process and mask designs, and these have to be discussed together as the process determines the sequence of masks to be used in device fabrication. It should be noted that the sequence of process steps was a strategy for device fabrication and not an experimental method. Because an experimental method refers to what has been done it is always written in past tense. However, the process design refers not to what has been done but to what is to be done; consequently, the process design text is written in present tense. The device design was based on analytical equations for straight piezoelectric unimorphs. A spiral finite-element model was not ready during the device design stage; consequently, device design was based on these analytical equations.

Chapter 6 is about the effect of temperature on film fabrication and the stability of the film-substrate interface. Stabilisation of this interface was essential before films were patterned; therefore, the chapter dealing with the patterning of thick films follows this one. Interfacial stabilisation must take place before incorporation of the thick film route into a device fabrication process; consequently, this chapter occurs before the chapters on process integration and device fabrication.

Chapter 7 is about developing methods for the patterning of PZT thick films.

Chapter 8 combines information in the two proceeding chapters into an integrated process for the fabrication of devices. In this chapter each step in the process design was tested experimentally, and at the end of this chapter a revised and final processing route is given.

A range of devices were fabricated and these are discussed in chapter 9. These devices were analysed experimentally and the results compared both with finite-element and analytical models.

1 Introduction

1.1 Material Properties

1.1.1 Ferroelectric Materials

Only a general description of ferroelectric materials is given here; however, these materials have been covered in detail elsewhere [1-6]. A ferroelectric material is one that possesses a spontaneous dielectric polarisation that can be switched with an applied field. Ferroelectrics belong to the class of polar dielectrics. These are non-centrosymmetric crystals that possess a unique axis of symmetry. An electric dipole moment will exist along this unique polar axis. The unique axis can be re-orientated between at least two stable states, by application of an electric field. In a cyclic electric field of sufficient magnitude, the polarisation will repeatedly and reversibly switch between these two states. The switching phenomenon is non-linear giving rise to ferroelectric hysteresis (see below). Ferroelectric materials can include ceramics, inorganic crystals, organic crystals and some polymers. It should be noted that the most commonly used ferroelectric materials are of the oxide single crystal type or ceramics e.g. PZT or BT ($BaTiO_3$).

Of the 32 crystal classes, 11 correspond to centrosymmetric crystals. The remaining 21 crystal classes are non-centrosymmetric (also called acentric); of these 21 non-centrosymmetric classes 20 will all exhibit piezoelectricity (see APPENDIX I). Of the 21 non-centrosymmetric crystal classes 10 are polar classes and will exhibit pyroelectricity (see APPENDIX I). Polar crystal classes are those crystals that are spontaneously polarised possessing a unique polar axis, as distinct from non-polar crystals.

1.1.2 The Piezoelectric Effect

1.1.2.1 Tensor notation

The piezoelectric effect can be described by equation (1.1) [1,8].

$$P_i = d_{ijk}\sigma_{jk} \quad (\mathrm{i, j, k} = 1,2,3) \tag{1.1}$$

Here P_i is the polarisation vector, and σ_{ij} is the second rank stress tensor. There are 9 components of σ_{ij}, see Fig 1.1, that can be reduced to 6 as $\sigma_{jk} = \sigma_{kj}$, see the tensor equation (1.2). The d_{ijk} are the piezoelectric moduli of a third rank tensor having 27 components. It is not possible to relate the components of a third rank or higher tensor to three-dimensional space, and therefore a figure such as Fig 1.1 cannot be drawn for d_{ijk}.

$$\begin{pmatrix} \sigma_{11} & \sigma_{12} & \sigma_{13} \\ \sigma_{21} & \sigma_{22} & \sigma_{23} \\ \sigma_{31} & \sigma_{32} & \sigma_{33} \end{pmatrix} = \begin{pmatrix} \sigma_{11} & \sigma_{12} & \sigma_{13} \\ (\sigma_{21} = \sigma_{12}) & \sigma_{22} & \sigma_{23} \\ (\sigma_{31} = \sigma_{13}) & (\sigma_{32} = \sigma_{23}) & \sigma_{33} \end{pmatrix} \quad (1.2)$$

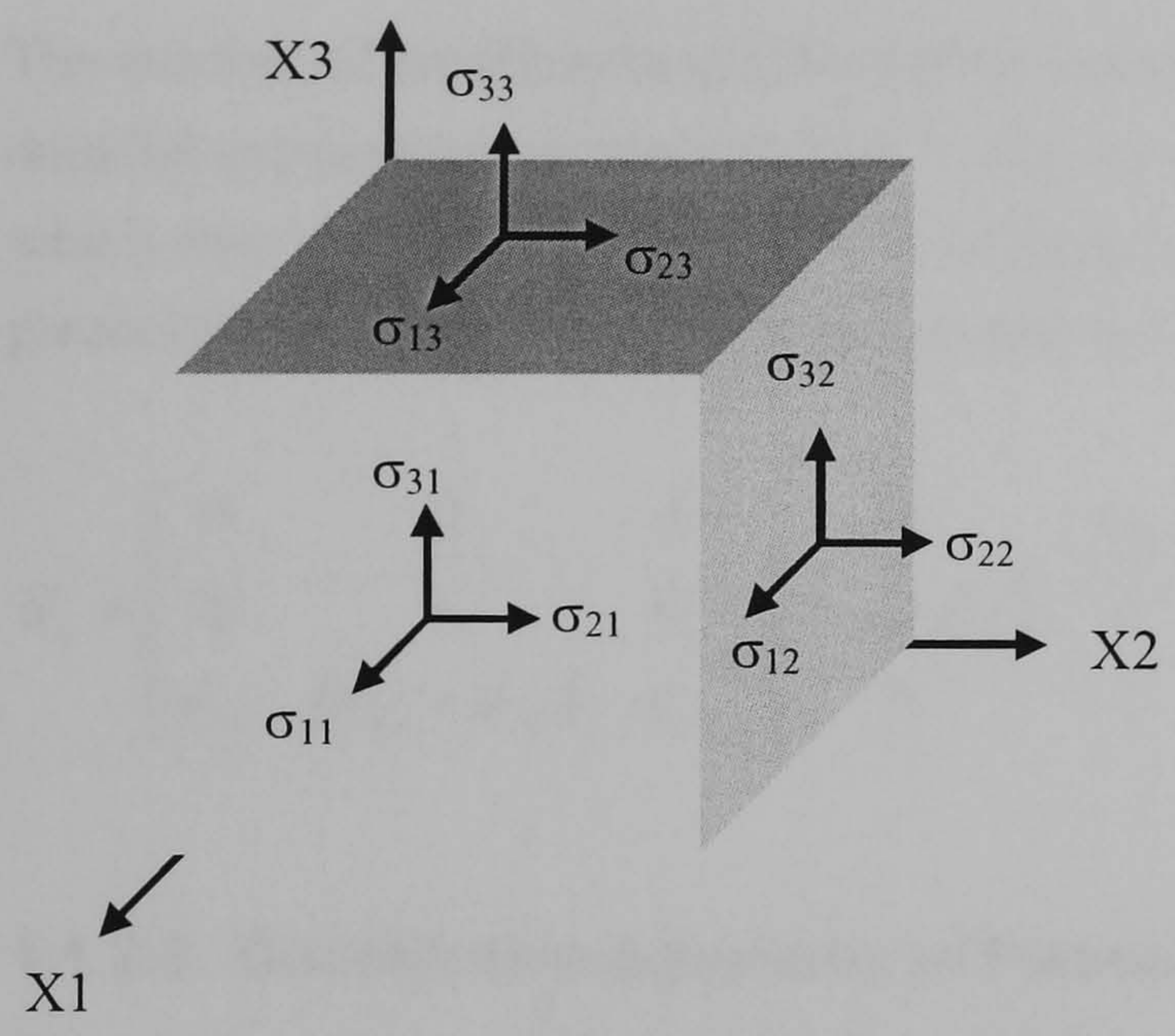

Fig 1.1 Components of the second rank stress tensor. The axis X1, X2 and X3 are equivalent to x, y, z. The axis x, y and z, will sometimes be referred to in the text as the 1, 2 and 3 directions respectively. Image taken from Nye [8].

1.1.2.2 Reduced Suffix Notation

The piezoelectric modulus is typically represented using reduced suffix notation where the first suffix i remain unchanged. The second and third suffix j and k (where j=1,2,3 and k=1,2,3) are replaced by a single suffix j (j=1,2…6). In the case of the stress tensor the suffix's i and j are reduced to j: j=1,2…6, see Table 1.1

Tensor notation (ijk)	i11	i22	i33	i23=i32	i31=i13	i12=i21
Reduced suffix notation (ij)	i1	i2	i3	i4	i5	i6

Table 1.1 Conversion between tensor and matrix notation

Therefore d_{ijk} is reduced to d_{ij} where $i = 1, 2, 3$ and j = 1, 2…6; this reduces the total number of coefficients from 27 to 18. It should be noted that for $j = k$ $d_{ijk} = d_{ij}$, but when $j \neq k$ $d_{ijk} = ½d_{ij}$. The direct piezoelectric effect is expressed in equation (1.3) using the reduced suffix notation.

$$P_i = d_{ij}\sigma_i \quad (\mathrm{i} = 1, 2,3 \text{ and } \mathrm{j}=1,2...6) \qquad (1.3)$$

There is also a converse piezoelectric effect expressed as the strain S_j caused by the product of the piezoelectric modulus and the electric field vector E_i, see equation (1.4).

$$S_j = d_{ij} E_i \quad (\mathrm{i} = 1, 2, 3 \text{ and } \mathrm{j} = 1, 2 \ldots 6) \tag{1.4}$$

The number of coefficients can be further reduced by the symmetry of the crystal; a more detailed explanation is given in Nye [8]. The average symmetry of a poled ceramic is ∞m, which has the same piezoelectric coefficients as 4mm, see equation (1.5). Tables of piezoelectric matrixes for differing symmetries have been presented elsewhere [7,8].

$$d_{ij} = \begin{bmatrix} 0 & 0 & 0 & 0 & d_{15} & 0 \\ 0 & 0 & 0 & (d_{24} = d_{15}) & 0 & 0 \\ d_{31} & (d_{32} = d_{31}) & d_{33} & 0 & 0 & 0 \end{bmatrix} \tag{1.5}$$

1.1.2.3 Constitutive equations of Piezoelectricity

Constitutive piezoelectric equations describe the relationships between mechanical and electrical variables; these equations are given in IEEE standards on piezoelectricity [7]. The mechanical variables of interest are the stress σ_j and strain S_j; the electrical variables of interest are the electric field E_j and electric displacement D_j. In the equations that follow, some symbols have the superscripts E, σ, D and S; this means that these symbols were measured under constant conditions of electric field (E), stress (σ), electric-displacement (D) and strain (S) respectively. It should be noted that s_{ij}, β_{ij} and ε_{ij} are the elastic-compliance, elastic-stiffness, dielectric-impermittivity and permittivity matrices respectively. The piezoelectric coefficients e_{ij}, h_{ij}, d_{ij} and g_{ij} represent piezoelectric coupling between the electrical and mechanical variables. The constituent equations are defined for different boundary conditions in CASE 1 to CASE 4 below.

<ins>CASE 1:</ins> An unbounded piezoelectric material.

The converse effect:

$$\sigma_j = c_{ij}^E S_j - e_{ij} E_i \tag{1.6}$$

The direct effect:

$$D_j = e_{ij} S_j - \varepsilon_{ij}^S E_i \tag{1.7}$$

<ins>CASE 2:</ins> When S_j and D_j are the independent variables.

The converse effect:

$$\sigma_j = c_{ij}^D \mathrm{S}_j - h_{ij} D_j \tag{1.8}$$

The direct effect:

$$E_i = -h_{ij} S_j - \beta_{ij}^S D_j \tag{1.9}$$

<u>CASE 3:</u> When $\mathrm{E_j}$ and σ_j are the independent variables.

The converse effect:

$$S_j = s_{ij}^E \sigma_j + d_{ij} E_i \tag{1.10}$$

The direct effect:

$$D_j = d_{ij} \sigma_j + \varepsilon_{ij}^\sigma E_i \tag{1.11}$$

<u>CASE 4:</u> When σ_j and $\mathrm{D_j}$ are the independent variables.

The converse effect:

$$S_j = s_{ij}^D \sigma_j + g_{ij} D_j \tag{1.12}$$

The direct effect:

$$E_i = -g_{ij} \sigma_j + \beta_{ij}^\sigma D_j \tag{1.13}$$

Whilst these equations are exact relationships they are applied as approximations that are valid under certain limiting circumstances. The use of one of these pairs of equations depends on the fact that certain variables on their right hand side are equal to or approximately equal to zero. In the case of a thin-rectangular-block of piezoelectric material subject to $\mathrm{E_j}$, where it can be assumed that $\sigma_{\mathrm{ij}}=0$, and $\mathrm{d_{ij}}$ is known then $\mathrm{S_j}$ may be determined from equation (1.11); in this example equation (1.11) is the same as equation (1.3)

In chapter 9 of this thesis, a finite element (FE) model of a piezoelectric unimorph actuator was constructed; however, this model uses the e_{ij} coefficient and not the d_{ij} coefficient. The application of boundary conditions to any FE model is part of the modelling process. Materials properties are entered as data at a stage before the modelling process can begin. In order to prevent extraneous boundary conditions from being applied, the piezoelectric data is un-bounded on entry. For this reason the piezoelectric coefficients are selected for the un-bounded state, i.e. e_{ij}.

1.1.2.4 Operational Piezoelectric Modes

There are three modes of operation for a piezoelectric device: thickness, longitudinal and shear. In the case of the thickness mode, a force F acts parallel to the axis of polarisation of a piezoelectric ceramic, see Fig 1.2. The force is applied through the action of a mechanical stress. The surface areas of the electrode and non-electroded surfaces are denoted ${}^1A_r$ and ${}^2A_r$ respectively. The electrical output is expressed as charge, Q, and is defined in equation (1.14)[1].

$$Q = d_{33}F \tag{1.14}$$

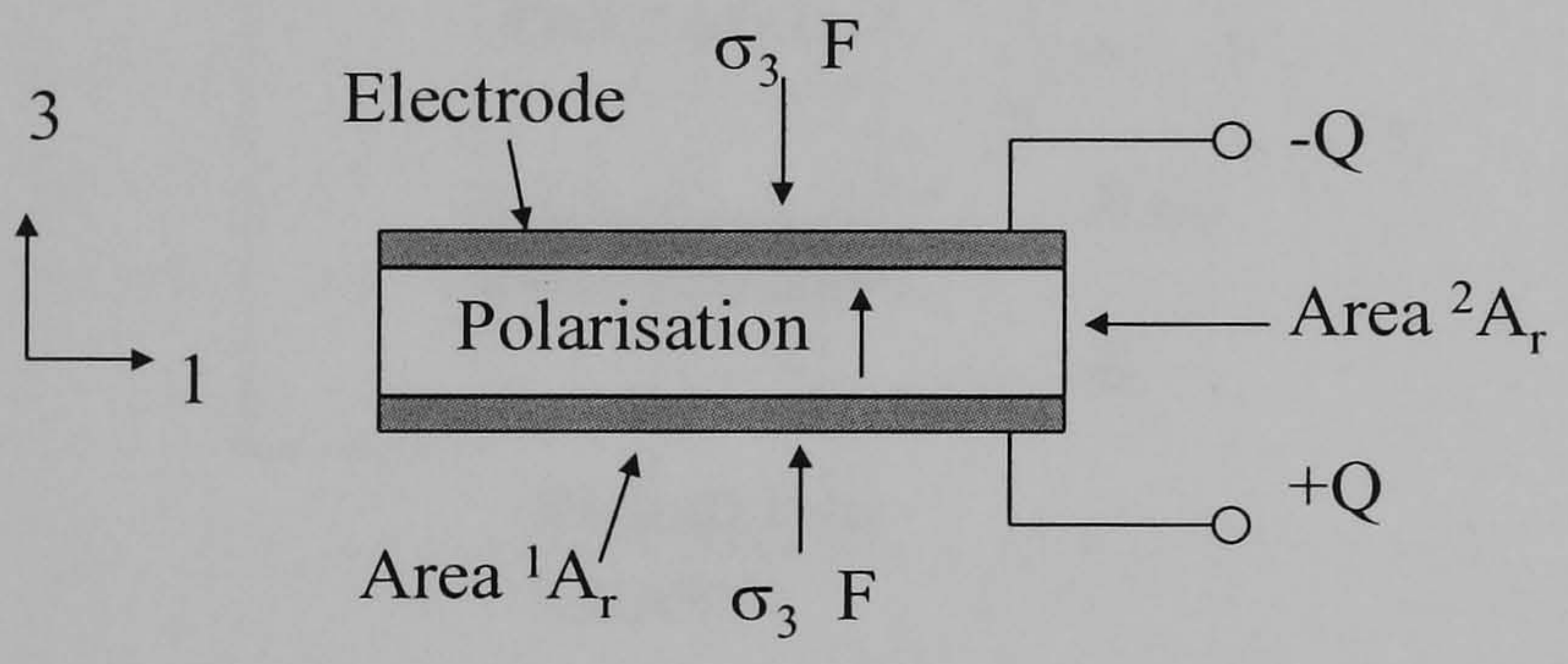

Fig 1.2 Operation of piezoelectric device in thickness mode. Taken from Whatmore[1]

In the case of the longitudinal mode, a force acts perpendicular to the axis of polarisation of a piezoelectric ceramic, see Fig 1.3 and equation (1.15)[1].

$$Q = \frac{d_{31}\,{}^1A_r F}{{}^2A_r} \tag{1.15}$$

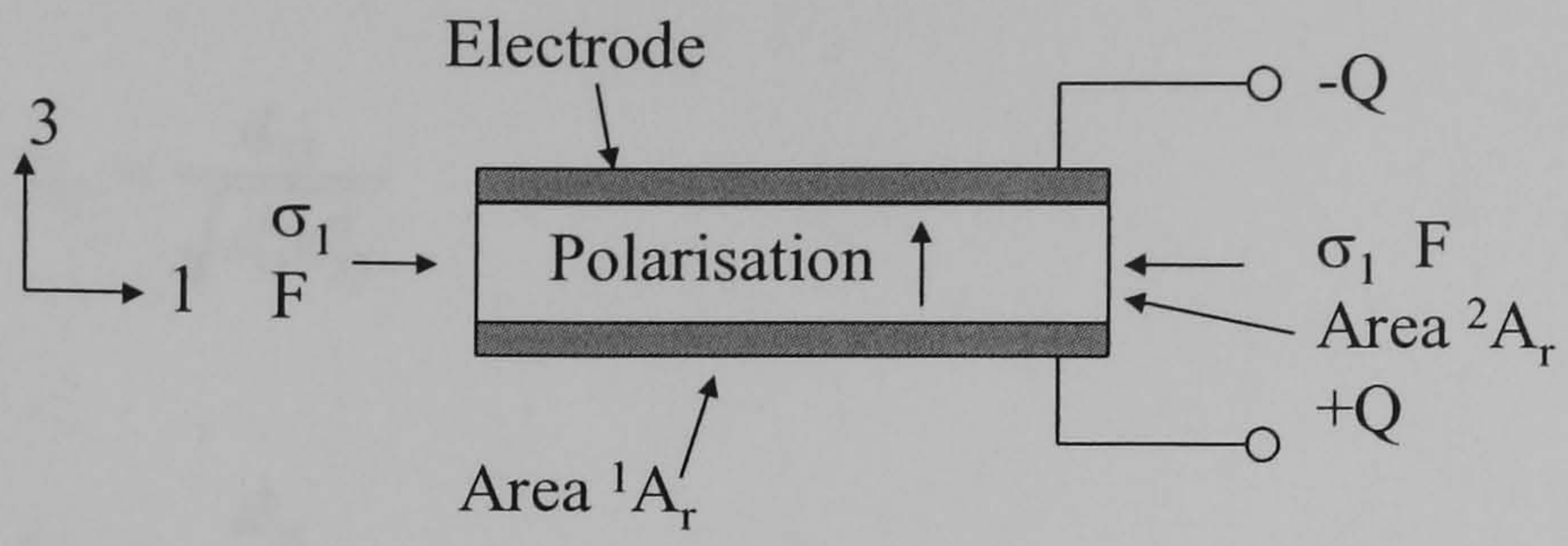

Fig 1.3 Operation of piezoelectric device in longitudinal mode. Taken from Whatmore [1]

In the case of the shear mode, a shear force F_{shear} is applied to a piezoelectric device fixed to a static support, see Fig 1.4 and equation (1.16) [1].

$$Q = \frac{d_{15}F_{shear}}{^1A_r} \tag{1.16}$$

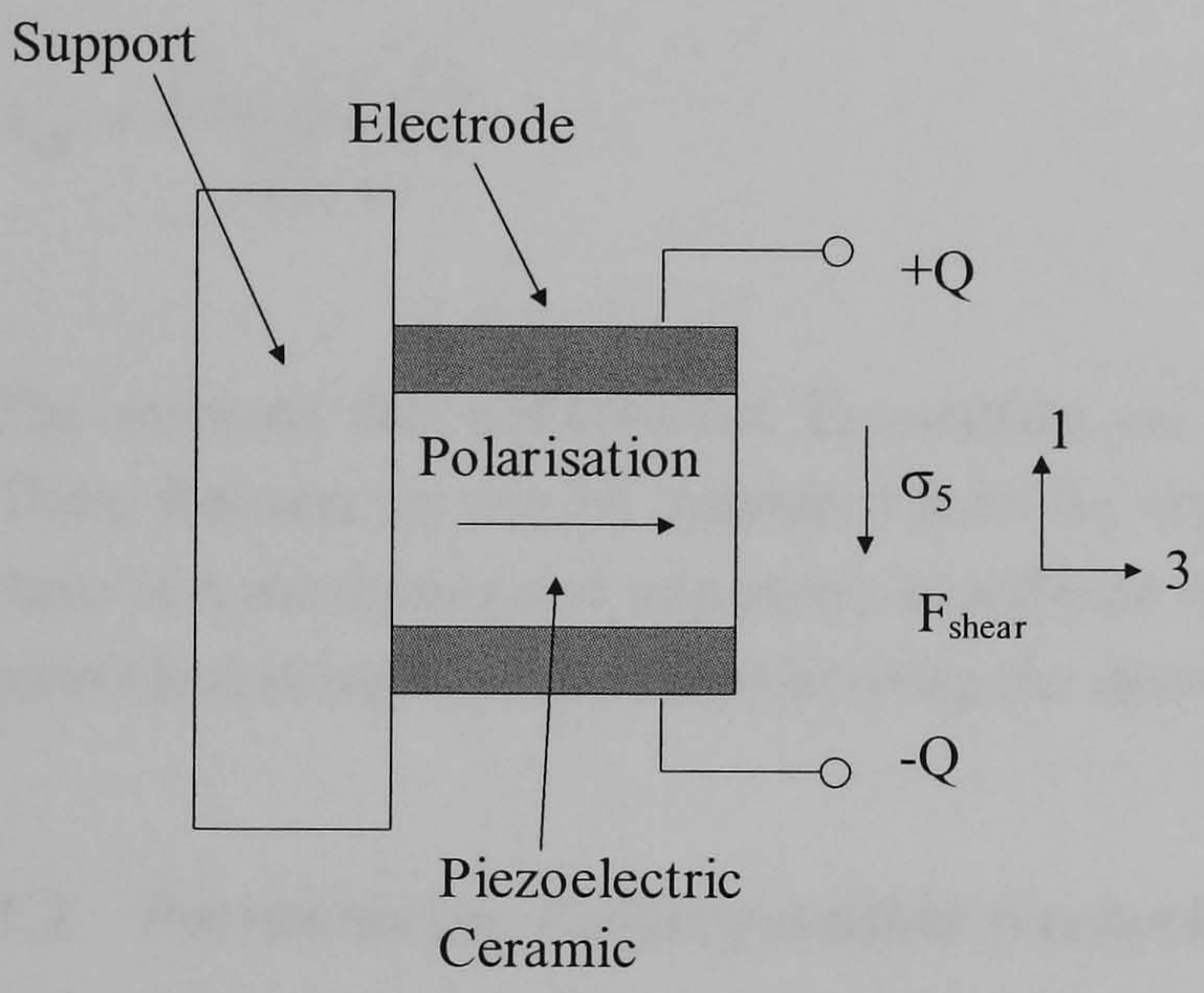

Fig 1.4 Operation of piezoelectric device in shear mode. Taken from Whatmore [1]

1.1.2.5 Electromechanical coupling

The efficiency that a piezoelectric material converts electrical into mechanical energy is given by the electromechanical coupling coefficient k_{ij} [1,7], see equation (1.17).

$$k_{ij}^2 = \frac{\text{Ourput mechanical energy}}{\text{Input electrical energy}} \tag{1.17}$$

In the case of a thin-rectangular-block of piezoelectric material, the equations (1.18) to (1.20) apply; these equations represent coupling in the thickness, longitudinal, and shear modes respectively

$$k_{33} = \frac{d_{33}}{\sqrt{s_{33}^{E}\varepsilon_{33}^{\sigma}}} \tag{1.18}$$

$$k_{31} = \frac{d_{31}}{\sqrt{s_{11}^{E}\varepsilon_{33}^{\sigma}}} \tag{1.19}$$

$$k_{15} = \frac{d_{15}}{\sqrt{s_{44}^{E}\varepsilon_{11}^{\sigma}}} \tag{1.20}$$

If the shape of the piezoelectric is more complicated than a simple block then k_{eff}, the effective electromechanical coupling coefficient can be used, see equation (1.21).

$$k_{eff}^{2} \approx \frac{f_{anti-res}^{2} - f_{res}^{2}}{f_{anti-res}^{2}} \tag{1.21}$$

The resonant and antiresonant frequencies are denoted as $f_{anti-res}$ and f_{res} respectively. These frequencies can be measured from an impedance scan as the frequency at which there is a maximum and minimum impedance respectively. This indicates how well the piezoelectric material is used in exciting the structure of interest.

1.2 Ferroelectric Polycrystalline Ceramics

A ferroelectric material is one that possesses a spontaneous dielectric polarisation that can be switched between two stable states with an applied-electric-field. Ferroelectrics have a domain structure, where the domain consists of dipoles of individual atoms aligned in the same direction (Fig 1.5). The domains are aligned randomly but can be aligned with an applied DC (direct current) field; this process is called poling.

Given that the spontaneous polarisation of a ferroelectric material can be reoriented by an external field then in a cyclic field, ferroelectric hysteresis is possible; this can be shown by plotting polarisation P vs. applied field E (see Fig 1.6). Ferroelectric hysteresis describes non-linear switching behaviour. In Fig 1.6 E_c, P_s and P_r are the coercive field, saturation polarisation and remanent polarisation respectively. P_r is the polarisation when $E = 0$; there is also a remanent polarisation in the material after poling (see Fig 1.5 right). E_c is the electric field when $P = 0$. P_s is the polarisation when all the domains are aligned in the same direction, the direction of the field.

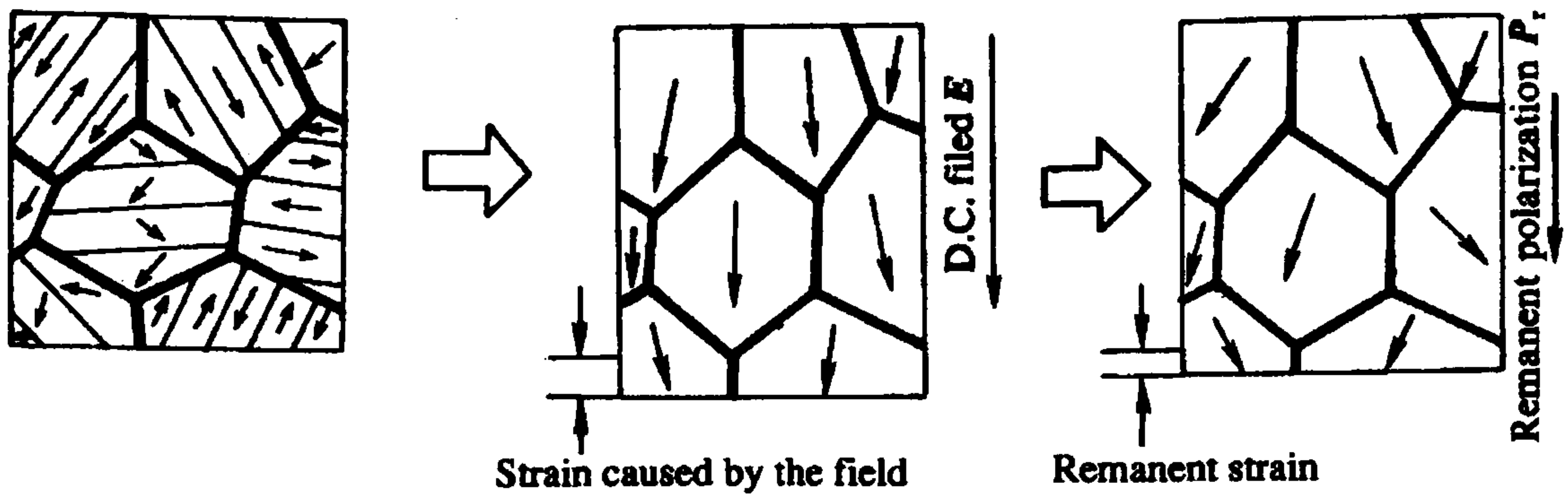

Fig 1.5 The domain structure of a Ferroelectric material, arrows within domains show the direction of polarisation, Left domains randomly orientated, Centre alignment of domains with DC field, and Right domain structure of remanent polarisation. The image was taken from Xu [5].

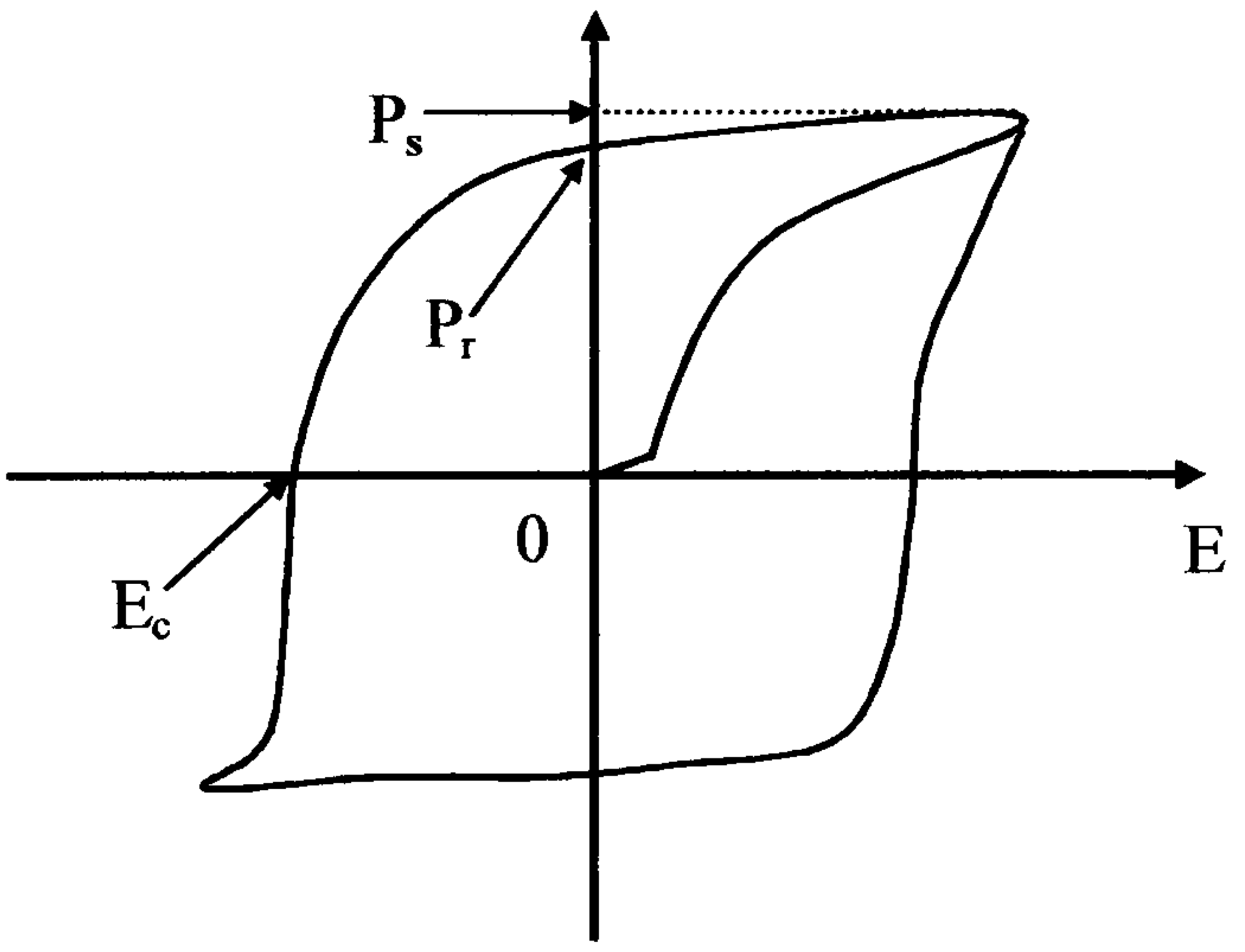

Fig 1.6 Ferroelectric hysteresis curve with polarisation P plotted against applied field E, where E is a cyclic field.

Because a ceramic is a polycrystalline material it is composed of a large number of randomly orientated crystallites, and hence ceramics are normally expected to be isotropic in their properties. Poled ferroelectric ceramics, however, exhibit anisotropic properties. It is impossible to align the direction of the crystallites of a ferroelectric ceramic; rather, it is the direction of the domains that are aligned by poling.

The polarisation is the result of dipole moments in each unit cell of a crystalline aggregate. In an un-poled ceramic, opposing dipole moments cancel, but in a poled ceramic there is a remanent polarisation, P_r. Therefore hysteresis in ferroelectric ceramics is only possible after the ceramic has been poled.

1.2.1 Lead Zirconate Titanate (PZT)

Lead zirconate titanate (often denoted by the abbreviation "PZT") is a solid solution of $PbTiO_3$ and $PbZrO_3$ ($Pb(Zr_{1-x}Ti_x)O_3$). These phases are ferroelectric and antiferroelectric respectively. The phases that form with differing compositions of PZT are shown in the PZT phase diagram in Fig 1.7. In the case of PZT, the ferroelectric-phases can be divided further into rhombohedral (high and low temperature) and the tetragonal phases. In addition, there are orthorhombic and tetragonal phases that are anti-ferroelectric. In most cases PZT-compositions are prepared near the morphotropic phase boundary as there is a sharp increase in relative permittivity and k_{ij} at this composition[1,4].

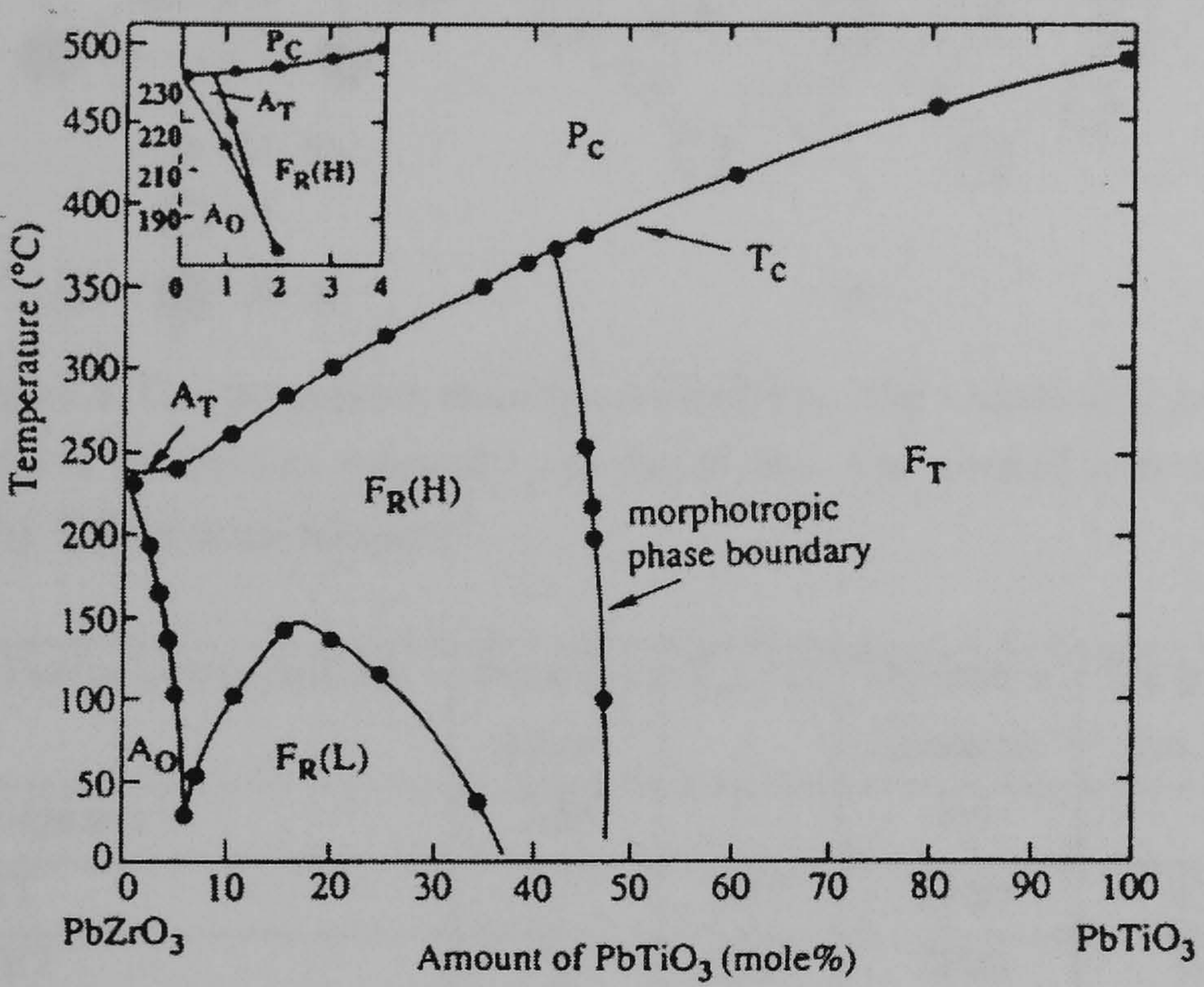

Fig 1.7 Phase diagram for the $PbTiO_3$-$PbZrO_3$ system. In the figure P_C, F_T, A_T and A_O are the paraelectric-cubic, ferroelectric-tetragonal, antiferroelectric-tetragonal and antiferroelectric-orthorhombic phases respectively. Further, $F_R(L)$ and $F_R(H)$ denote the ferroelectric rhombohedral phases of high and low temperature respectively. The Curie temperature is denoted as T_c. The Figure was taken from Xu[5]

Both PZT and BT are perovskite structured materials and have the idealised formula ABO_3, where the A-cation represents Pb, and Ba respectively, and the B-cation represents either Ti and Zr or just Ti for PZT and BT respectively. In the perovskite structure the central A-cation is 12 fold coordinated by oxygen ions (Fig 1.8 b), and the B-cations are each octahedrally coordinated (Fig 1.8 a). The structure shown is cubic; however, ferroelectric BT is tetragonal below 130 °C.

Different compositions in this series can possess high permittivities, high electro-optical properties and many other properties of interest to applications. PZT, when doped or mixed with other complex perovskite oxides, has the highest piezoelectric constants and electromechanical coupling coefficients of any ferroelectric ceramic. Some data comparing the dielectric and piezoelectric properties of selected ceramic materials are presented in Table 1.2.

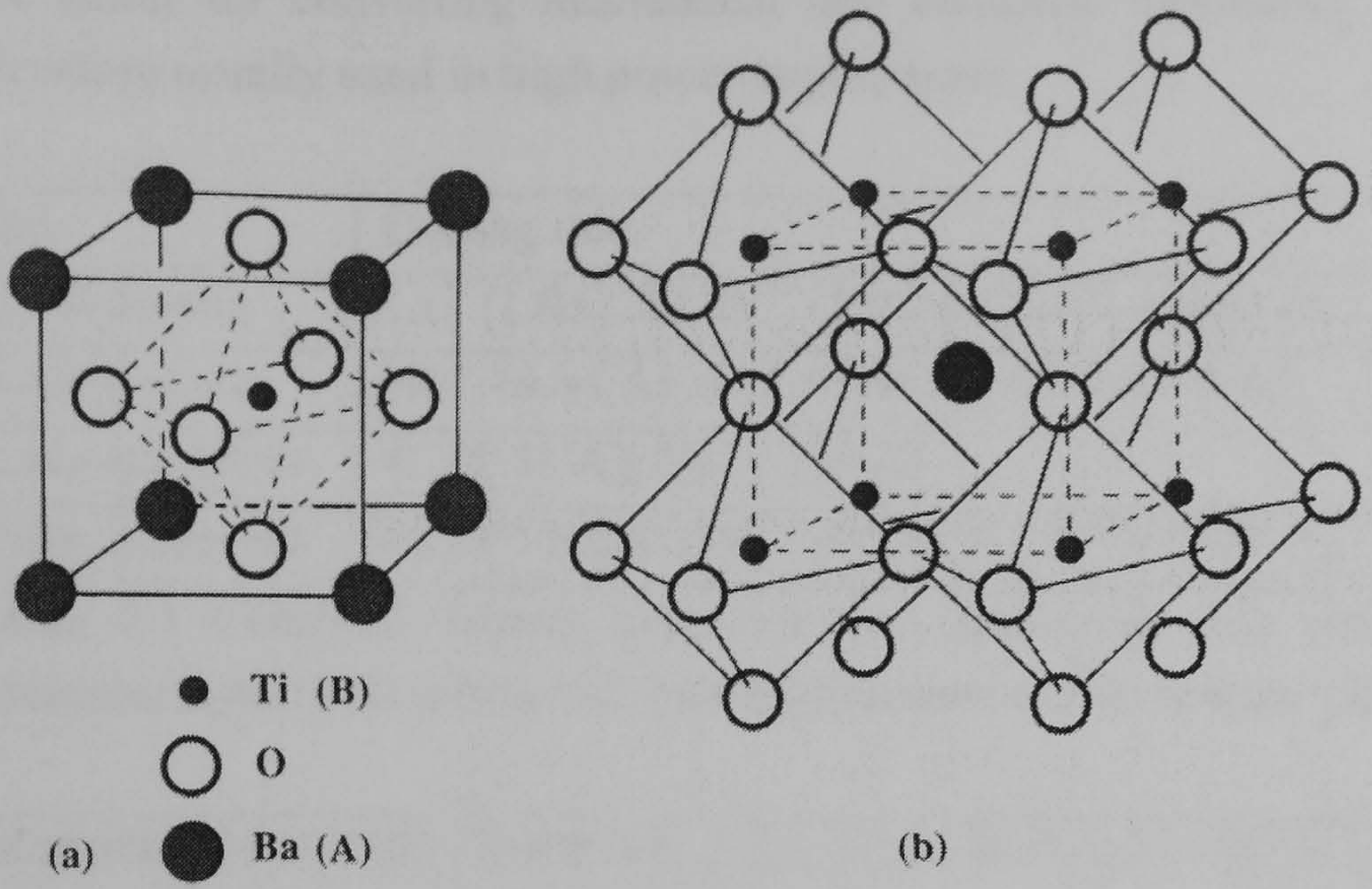

Fig 1.8 The perovskite structure of $BaTiO_3$. The Octahedral oxygen cage is shown in (a) this is sometimes referred to as the B-site. The overall perovskite structure is shown in (b). Taken from Kingery[6].

Ferroelectric ceramic	Density / g/cm^3	T_c / °C	Dielectric constant	Dielectric loss / %	d_{31} / pC/N	d_{33} / pC/N
α-Quartz	2.65	-	4.6	-	-	-
BT	5.7	130	1900	0.7	-79	190
PZT	7.7	220	2800	1.6	-234	480
$PbNb_2O_6$	5.9	560	225	1.0	-11	80
$Na_{0.5}K_{0.5}NbO_3$	4.5	420	400	1.0	-50	160
$LiNbO_3$	4.64	1210	29	-	-0.85	6
$LiTaO_3$	7.46	665	43	-	-3	5.7

Table 1.2 Electrical and piezoelectric properties of a range of selected ferroelectric ceramics. This data was taken from Moulson & Herbert[4]

There is a wide range of doping ions that can be used to substitute at either the A or the B lattice sites. Some examples of doping ions are given in Table 1.3; charge balance and the ionic radius determines the doping site. Doping ions are characterised as either acceptors (hard) or donors (soft) according to whether they accept or donate electrons to the host material. Donors and acceptors generate cation and oxygen vacancies respectively; the latter are more mobile within the host material. Consequently, hard ceramics have a lower resistivity than soft ceramics.

Donor doped PZT materials exhibit an increase in k_{ij}, permittivity, dielectric loss and mechanical loss relative to acceptor-doped PZT, see Table 1.4. Because hard doped PZT have a low mechanical loss and a low dielectric loss such materials are suited to operating under high drive fields and high mechanical stresses; therefore acceptor doped materials are better for converting mechanical into electrical vibrations, and hard-ceramics are therefore usually used in high power applications.

Site	Doping ion
A site donors	La^{3+} (1.032 Å), Bi^{3+} (1.03 Å), Nd^{3+} (0.983 Å)
B site donors	Nb^{5+} (0.64 Å), Ta^{5+} (0.64 Å), Sb^{5+} (0.60 Å)
A site acceptors	K^{+} (1.38 Å), Na^{+} (1.02 Å)
B site acceptors	Fe^{3+} (0.645 Å), Sc^{3+} (0.745 Å), In^{3+} (0.800 Å)

Table 1.3 Common doping ions and site associated with doping in the perovskite structure. Ionic radii follow the ions in parenthesis. Taken from Moulson & Herbert[4]

Material	Hard / Soft	Dielectric constant	k_{33}	d_{33} / pC/N	d_{31} / pC/N	Mechanical loss / %
PZT-5	Soft	3400	0.75	593	-274	1.54
PZT-4	Hard	1300	0.70	289	-123	0.13
PZT-8	Very Hard	1000	0.60	215	-95	0.10

Table 1.4 The properties of hard and soft PZT materials. Taken from Whatmore[1].

In addition there are two other categories of doping ions: isovalent doping ions and stabilisers. Isovalent-doping-ions reduce T_c and increase permittivity, and in the case of PZT examples include Sn^{4+}, Sr^{2+} or Ba^{2+}. Isovalent-doping-ions have the same valence as the ions on the sites that they are replacing. Like hard ceramics isovalent substitutions improve linearity at high drive fields. Stabilisers are used to stabilise the lattice against ageing, and these are usually multi valent ions e.g. Mn or U.

PZT compositions employed in this project were based on a commercially available ceramic material: PZ26 supplied by Ferroperm SA. This composition was selected because it had a 2:1 ratio of donor to acceptor doping ions. The exact composition will be discussed in the experimental chapter. The advantage being the combination of relatively high piezoelectric constants with low dielectric and mechanical losses. This, it is anticipated, will yield piezoelectric actuators with high mechanical outputs and minimum internal heat generation when operated under high cyclic-fields.

1.3 Thin And Thick Films

There has recently been considerable interest in making thin and thick films of piezoelectric materials, such as PZT, in a variety of applications in microsystems. Sol-gel derived PZT thin films, prepared by spin coating, have been prepared for a range of microsystems applications, these include acoustic microphones[9], mass balances[10] and pass-band filters[11]. PZT thick films prepared through screen-printing have also found applications in microsystems, and these include resonant humidity sensors[12], micropumps[13] and servo-valves[14].

1.3.1 Thick Film Fabrication (Screen-Printing)

A thick film is a film between 0.5 to 100 μm in thickness. Screen-printing is the most commonly employed route for the fabrication of PZT thick films and thick film devices. The screen-printing process is shown in Fig 1.9. The substrate, to be coated, is placed in a holder, and a screen is held in a frame, supported above the substrate. A quantity of ink is introduced to the screen; subsequently, a squeegee is pulled across the screen so that it traverses the substrate. Note that sufficient pressure must be applied to the squeegee to bring the screen into contact with the substrate.

The screen, a finely woven porous gauze, can be made from steel, nylon or polyester. Before printing, the screen is sealed with an ultraviolet photosensitive emulsion, and the emulsion is patterned photographically. Development yields openings for the ink to pass through, and in this way, the device shape is controlled. The screen is used to control the thickness and shape of the layer printed onto the substrate. Heating steps are often used intermittently, between printing steps, to dry and sinter printed layers. Ceramic films, made in this way, are sintered at around 850 °C as a final stage of processing.

The ink, or screen-printing paste, has three basic constituents: organic vehicle, an active material and a mineral binder. The organic vehicle is required to provide a homogeneous suspension of particles of the functional material. The organic vehicle is typically a mixture of polymers, resins, volatile solvents and surfactants. The mineral binder is included to aid densification of the active material during sintering. The mineral binders are either glass fritts or mixed oxides.

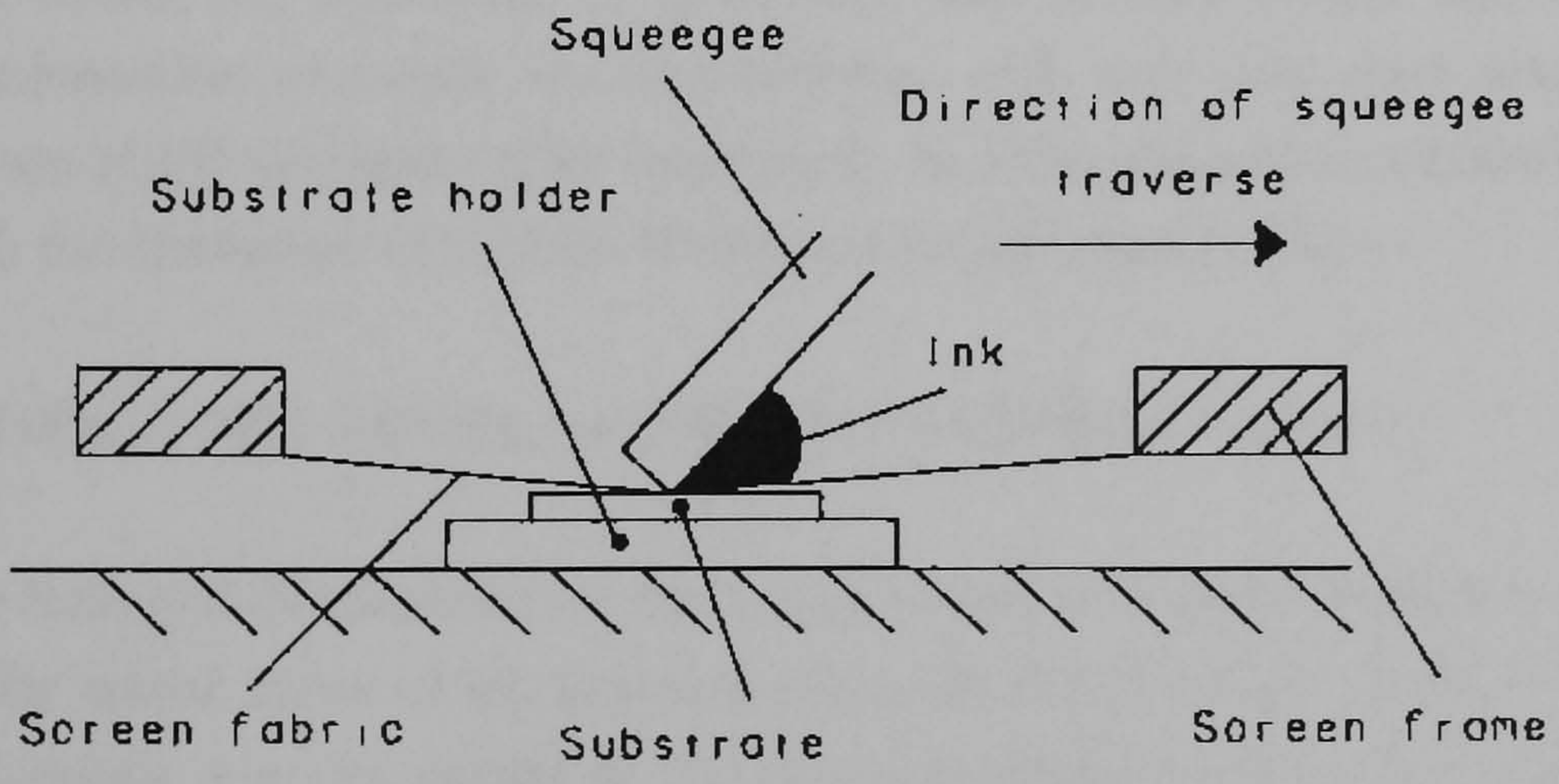

Fig 1.9 The process of Screen-printing where a ceramic ink is printed onto a substrate. The desired image is printed through a photo-patterned screen. Taken from Prudenziati [15]

1.3.2 Thin Film Fabrication

1.3.2.1 Sol Gel Chemistry

Chemical solution deposition (CSD) requires the preparation of a solution of reactive precursors. There are, in essence, two CSD processes: metal organic deposition (MOD) and sol-gel. In MOD, there is no reaction of the precursor solution before deposition: instead, gelation proceeds during the evaporation stage (see section 1.3.2.2 below and also Stage IV in Fig 1.10). The particles in the sol are formed by a partial pre-hydrolysis of the precursor molecules. Further, full hydrolysis will yield a gel i.e. a three dimensional structure dispersed uniformly in the liquid phase.

Reactive precursors are reacted together, through hydrolysis and condensation reactions, forming an inorganic oxide network. The precursors are typically metal alkoxide (sol gel) or metal carboxylates (MOD). A hybrid of the MOD and sol gel processes allows mixing of alkoxide and carboxylate precursors with chelating agents; the addition of chelating agents moderates precursor reactivity, thereby controlling the extent of the three dimensional network.

Inorganic polymerisation reactions are initiated by hydroxylation, the hydrolysis of the alkoxide ligand in the metal-organic precursor, see equation (1.22)

$$\text{M-(OR)}_n + \text{H}_2\text{O} \leftrightarrow \text{(OR)}_{n-1}\text{-M-OH} + \text{ROH} \qquad (1.22)$$

The metal, M, hydroxide is generated with alcohol (ROH and R is an alkyl group). Condensation proceeds via alcoxolation, and will only start when there are hydroxo groups (OH) available: after hydrolysis. In alcoxolation, an alcoholic group is eliminated with the formation of a M-O-M bridge (see equation (1.23)).

$$\text{M(OR)}_{n-1}\text{(OH)} + \text{M(OR)}_n \rightarrow \text{(OR)}_{n-1}\text{M-O-M(OR)}_{n-1} + \text{ROH} \qquad (1.23)$$

The lone pair of electrons on the oxygen atom of a metal hydroxide precursor coordinates to the metal atom of an adjacent alkoxide precursor to yield an intermediate; internal prototropic transfer occurs to the alkoxide ligand yielding a metal oxo-bridge complex. Subsequent loss of alcohol yields the dimer; further reactions will yield an oxide network.

Water present acts to age the sol by initiating condensation through hydrolysis. Consequently, the sol changes over time. It is for this reason that sols are prepared and stored under an inert atmosphere.

1.3.2.2 Spin Coating

Thin or thick films, of ceramic or photoresist, may be deposited onto a planar substrate through spin coating. The viscosity and concentration of the coating fluid, spin speed and spin time are the process variables that determine the thickness of each deposited layer. The number of layers determines the film thickness. Spin coating has been divided into four stages [16] (see Fig 1.10).

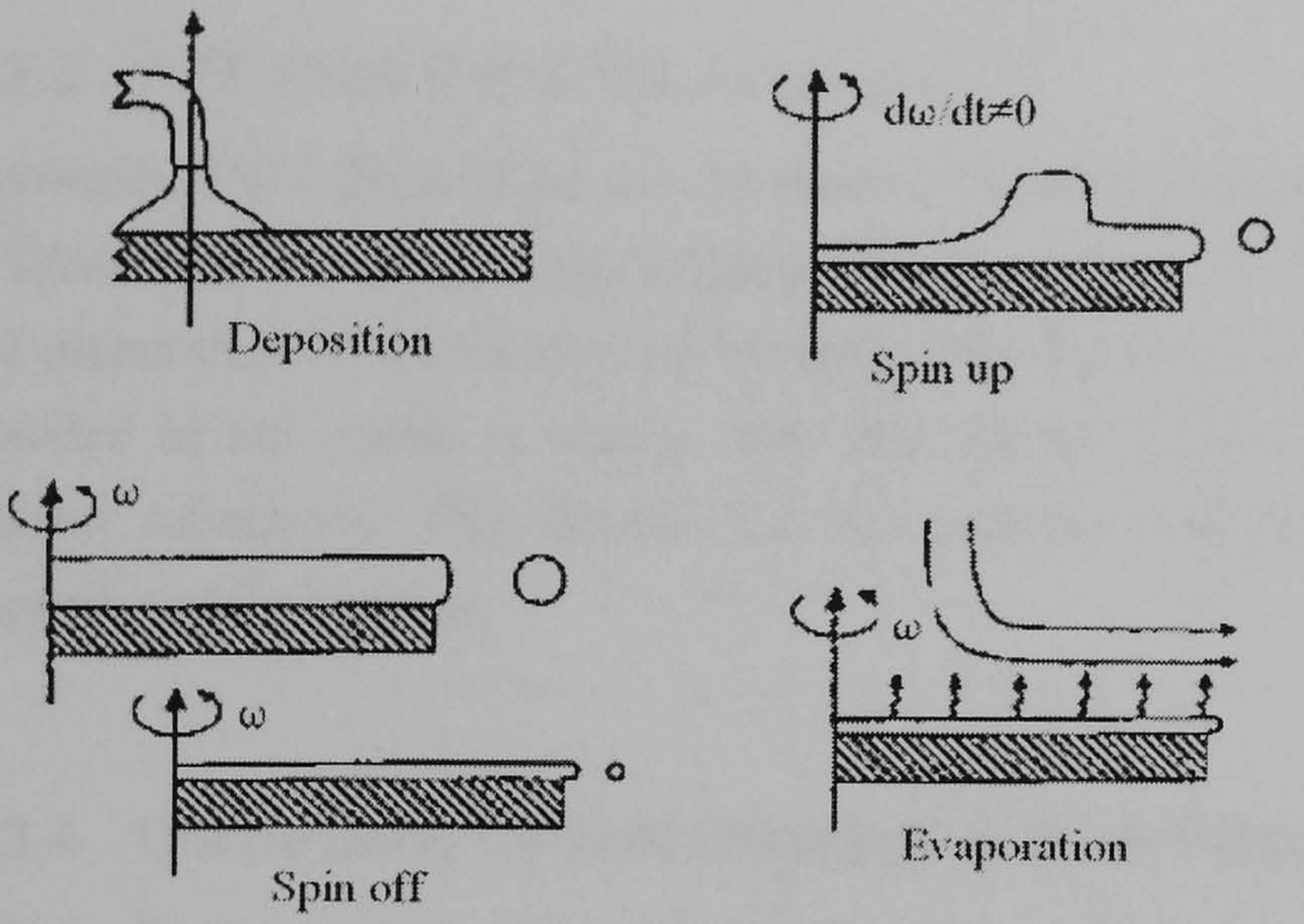

Fig 1.10 Effects on fluid flow during spin coating, (i) deposition, (ii) spin up, (iii) spin off and (iv) evaporation. It should be noted that Stages II-IV are characterised by constant substrate velocity. Taken from Birnie [16]

Stage I-deposition: an excess of the coating fluid is applied to the surface of the substrate. Stage II-Spin up: fluid is expelled from the substrate surface by rotational motion. Eventually, the fluid is thin enough to be completely co-rotating with the substrate. Fluid thickness, during stage II, is uniform across the substrate. Stage III: the spin off stage, this occurs at constant substrate velocity. Viscous forces result in the uniform and gradual thinning of the fluid. Stage IV evaporation: the fluid thickness reaches a point where the viscous forces yield only minor fluid flow. At this point, the evaporation of volatile solvent becomes the dominant process. The coating "gels", because viscosity rises with the removal of solvent.

1.3.2.3 Chemical Solution Deposition

In the case of the spin coating of a metal organic sol, of the type discussed in section 1.3.2.1 above, after stage IV of spin coating, the deposited film will require some intermittent thermal treatment between coating of each layer. The object is to either dry or pyrolyse the film. Pyrolysis and drying being the combustion of residual organics and the evaporation of solvent respectively. There will also be a crystallisation stage, at a higher temperature, at the end of deposition.

Thick films, between 0.5 to 1.0 μm, can be fabricated through repeated spin coating of metal organic sol; this approach results in the build up of internal stresses within the film. Surface damage, because of internal stresses, becomes more likely as the film thickness is increased.

1.3.3 PZT Thick Films For Actuators

Typically, PZT thick films are fabricated through screen-printing; however, this can result in films with an uneven topography. In this project, PZT thick films are prepared through the dispersion of a commercial ceramic powder in a metal organic sol. The dispersion of powder in sol yields a slurry, and this slurry is then spin cast onto planar-platinised-silicon substrates. The details for the process will be discussed in the literature and experimental chapters.

1.3.4 Connectivity Of Bulk Ceramics & Thick Films

Where there exist two intermixed phases, a cubes model [17] can be used to describe the connectivity of one phase with respect to the other (see Fig 1.11). The cubes model has, most commonly, been used for ceramic polymer composites [18]. The connectivity of one phase with respect to the other is given by two numbers: the first and second number denote the number of directions in which phase 1 and phase 2 are connected to themselves' respectively. The number of directions have values between zero to three, where a zero indicates that one of the phases is isolated from itself.

The connectivity of powder particles, in the deposited thick film, has been described by 0-3 connectivity [19] in which powder and sol correspond to phase 1 and 2 respectively. In practice, however, 0-3 connectivity is rarely seen in films from ceramic-sol slurries, as there is always some agglomeration of powder.

Closed porosity, in PZT, has also been described in this way [20] where pores and ceramic correspond to phase 1 and 2 respectively. Both d_{31} and dielectric constant showed an inverse relation to porosity [20] indicating that dense PZT thick films are desirable. It has been shown experimentally [20] that porosity has no effect on the dispersion of electrical energy in bulk PZT.

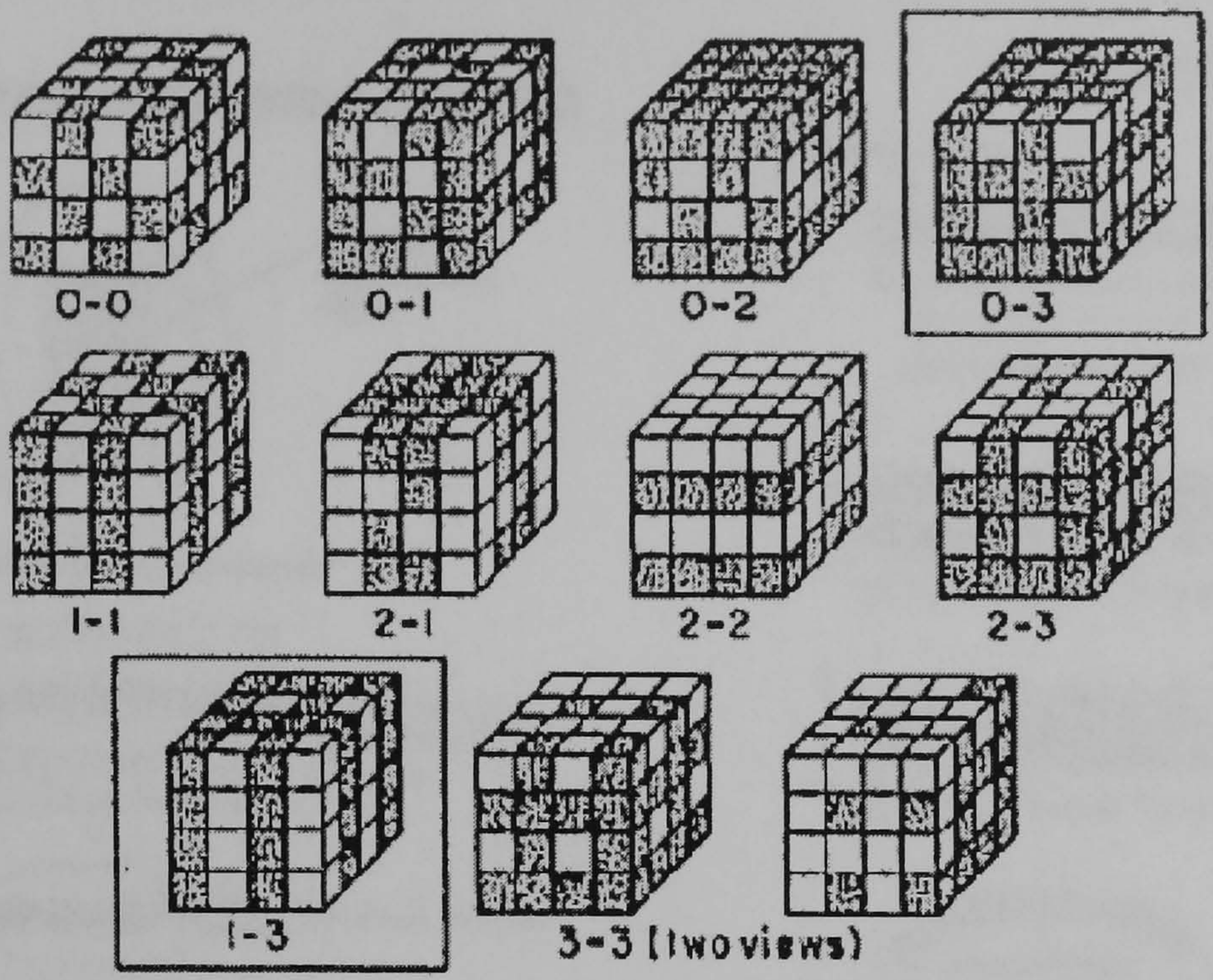

Fig 1.11 Cubes model showing the range of connectivity that can exist between two phases. The light and dark squares correspond to phase 1 and 2 respectively. Taken from Skinner et al [17]

1.4 Actuators

Piezoelectric micro-actuators are varied and include micro-speakers [21], micro-pumps [13], micro-fluidic mixers [22] and micro-valves [23]. In addition, piezoelectric ring actuators bonded to circular membranes have been used in travelling wave micro-pumps [14,24].

Piezoelectric cantilever actuators have been classified [25] into composite flextensional and bender actuators (Fig 1.12). A composite flextensional actuator is one in which the piezoelectric element is bonded to a metallic or polymeric shell structure that acts to magnify the strain of the piezoceramic mechanically.

Bender actuators maybe divided [25] into bimorphs [23,26-28] and unimorphs [26,29,30]. Bimorphs are composed of at least two piezoelectric plates bonded together or on either face of a substrate. Bimorphs are classified according to the poling direction of the piezoceramic plates, see Fig 1.12 (e and f) [25]. A unimorph is a piezoelectric layer on a non-piezoelectric support.

Piezoelectric layers can be built up through the bonding of commercial piezoelectric plates for unimorph [31] and bimorph actuators [31]. For unimorph micro-actuators, piezoelectric layers have been prepared through thin [29,30] or thick film (by screen-printing [27] or composite sol [13]) deposition routes. PZT thin films were prepared on platinised silicon through sputter [30] and sol-gel deposition [29]

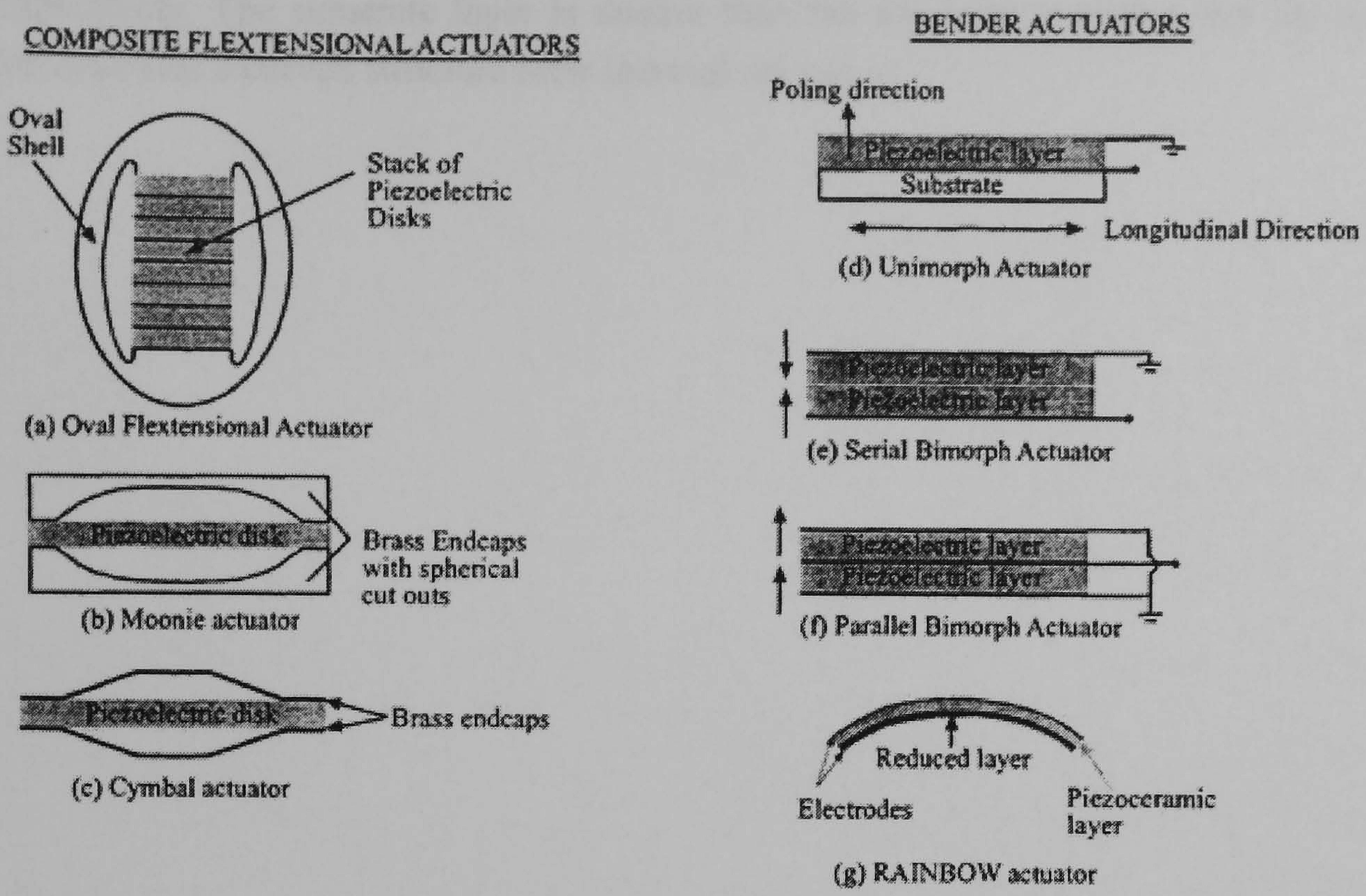

Fig 1.12 Types of piezoelectric actuator. Composite flextensional actuators are shown on the *left*. Piezoelectric bender actuators are shown on the *right*. Taken from [25]

In the case of unimorph actuators the application of a static electric field to electrodes on the top and bottom surfaces of the piezoelectric layer develops a longitudinal strain in the piezoelectric layer causing the piezoelectric to deform. The deformation in the piezoelectric layer causes a deformation in the non-piezoelectric layer resulting in a deflection in the device as a whole.

RAINBOW (reduced and internally biased wafer) actuators are a type of bending actuator related to unimorphs [25,31,32]. Rainbow actuators are produced from high lead containing piezoelectric disks or plates by a chemical reduction at high temperature. Essentially, a flat piezoelectric ceramic plate is placed on a flat graphite block and heated to a temperature ~975 °C for ~5 hours. A reduction reaction takes place at the graphite ceramic interface; formation of an electrically conducting mechanical support layer occurs. The actuator is cooled to room temperature rapidly, developing thermal stresses and hence a curved structure. The process-induced stresses result in amplified strains, and hence greater deflections than in equivalent unimorph actuators. Because of the amplification of strain due to their curved structure, Rainbow actuators have also been categorised as a type of flextensional actuator [33].

The THUNDER (thin layer ferroelectric composite unimorph driver and sensor) [34] actuator is made by bonding a piezoelectric layer between two metallic plates. The plates are then heated to 350 °C to induce thermal mismatch between the layers, and thereby pre-stress the actuator. The substrate and top layer are a steel spring and aluminium plate respectively. The substrate layer is thicker than the top layer ensuring that the actuator demonstrates a curved structure after thermal stressing.

2 Literature Review

2.1 *PZT Thick Films*

2.1.1 Thermal Processing Of PZT Thick Films

PZT thick films have been prepared from 0-3 composite slurries by a process first proposed by Barrow et al [35]. Composite slurries were prepared through the dispersion of various ceramic powders in various metal organic sols. The metal organic sol was prepared through a process called sequential precursor addition (SPA) [36]. Thick films were prepared on a variety of substrate materials through painting, spraying, and dip and spin coating. The process flow for the Barrow process is shown in Fig 2.1 below.

In SPA a solution of $PbOAc.3H_2O$ in acetic acid is prepared and dehydrated. Required quantities of $Zr(O^nPr)_4$ and $Ti(O^iPr)_4$ were then added sequentially. The Zr precursor is added first because it reacts with the acetic acid to form a compound that will not hydrolyse. Once this compound has been formed, the Ti precursor can be added. If the Ti precursor is added before the Zr precursor it will react with the acetic acid to form mono or di-acetals; consequently, condensation will occur with the formation of polyacetals[36].

A stock solution was formed through the addition of ethene glycol and water. The ethene glycol was added to reduce cracking and to improve the surface smoothness of the final film. The water was added to control the viscosity and surface tension of the sol.

Powder was added to the stock solution to yield a slurry. The stock solution/powder can be diluted with ethane glycol/H_2O to control viscosity. The dispersion was stabilised through ultrasonic mixing before chemical solution deposition of films. During CSD, the film was subjected to intermittent firing or pyrolysis. At the end of this stage, the film was sintered to achieve the desired density. It has been noted [37] that there was no advantage in pyrolysing these films above 450 °C.

PZT thick films have been fabricated on $Pt/Ti/SiO_2/Si$ substrates through an alternative 0-3 composite slurry route [38]. In this route, ceramic powder was dispersed in a xerogel to yield the slurry. The effect of heating on xerogel derived powders was analysed with DTA (differential thermal analysis) and TGA (thermo-gravimetric analysis); results are shown in Fig 2.2. The composition of the xerogel-powders was determined with XRD (X-ray diffraction). Decomposition and drying occurred at temperatures below 300 °C. Pyrochlore and perovskite phases were observed to crystallise at 350 °C and 435 °C respectively.

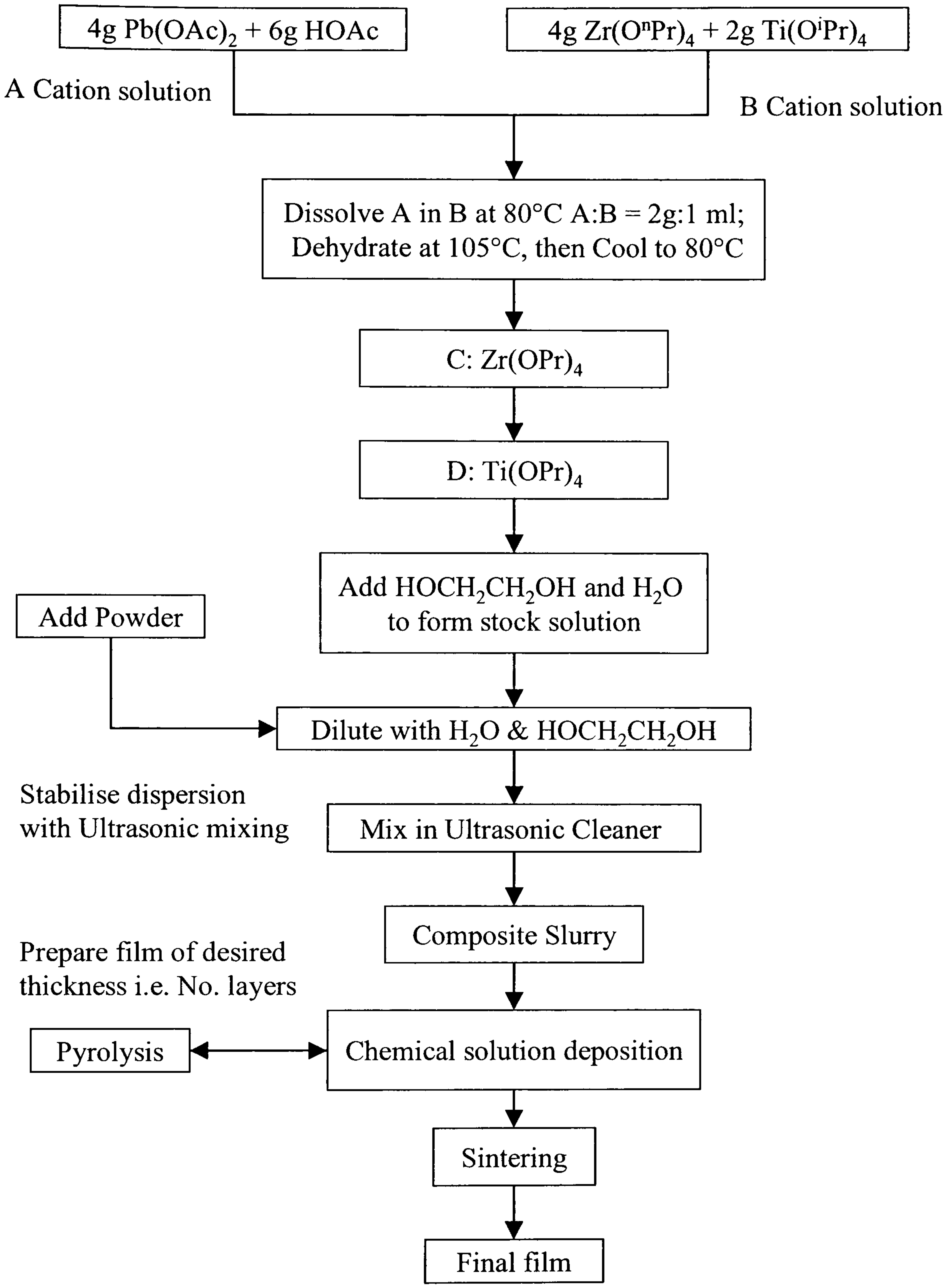

Fig 2.1 The Barrow process for the fabrication of PZT thick films. The process flow shows the fabrication from reactive precursors through sequential precursor addition. The process flow was taken from Barrow et al [35]

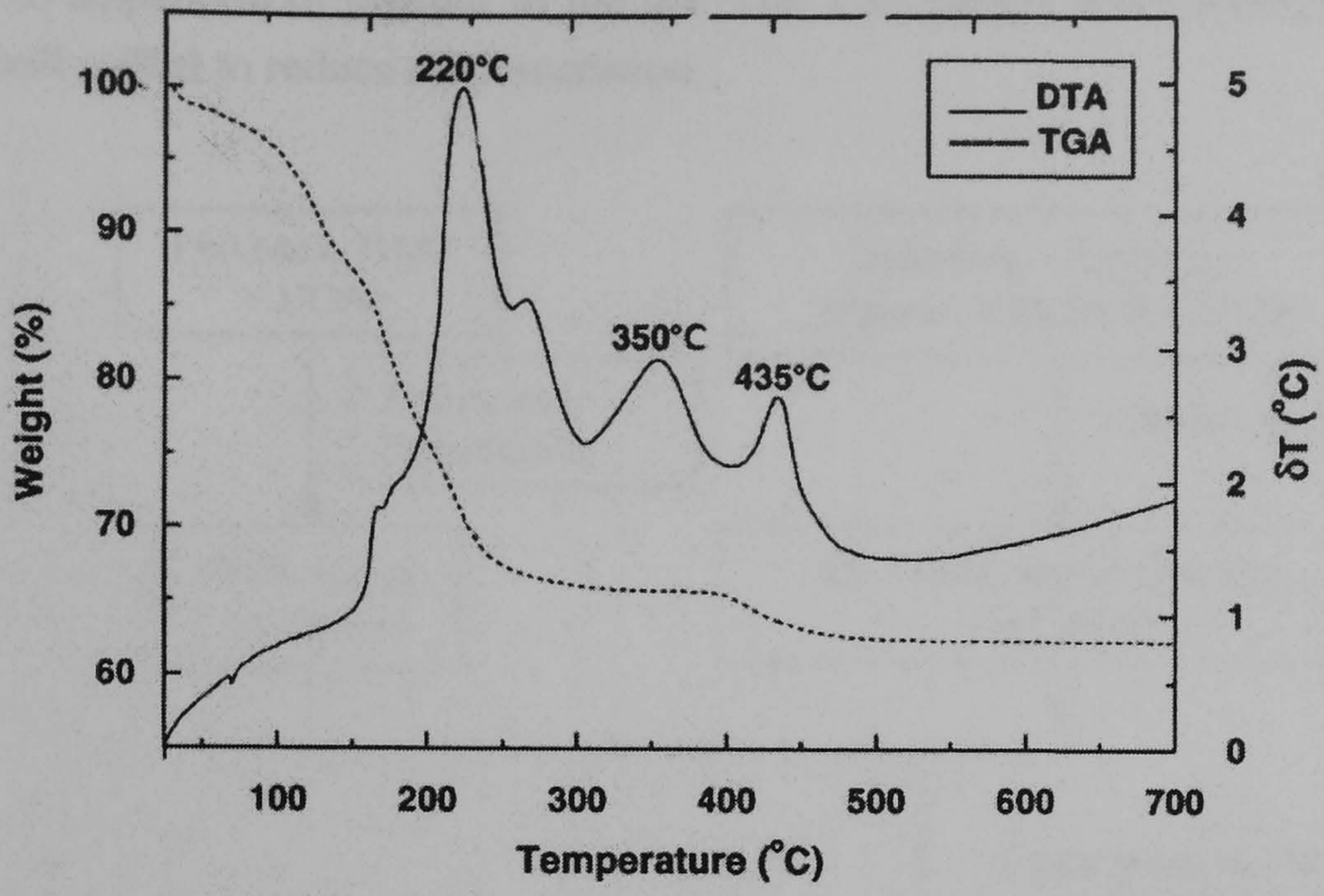

Fig 2.2 Drying, pyrolysis and crystallisation of xerogel-precursor-powders for PZT-thick-film preparation. The image is of a TGA and DTA plot against temperature. Taken from Wang et al [38]

2.1.1.1 PZT Thick Film Development At Cranfield University

The process developed at Cranfield University [39] has three stages: sol synthesis, slurry preparation and film fabrication (see Fig 2.3). The synthesis route for the fabrication of the sol was taken from the literature [40]. The sol synthesis requires the preparation of separate A and B-cation solutions. The A-cation solution involves the dehydration of lead acetate tri-hydrate through distillation in acetic acid. The components of the B-cation solution were highly sensitive to hydrolysis; therefore A and B-cation solutions were kept apart until the lead solution had been dehydrated. In order that precursors and doping ions were soluble in the 2-methoxyethanol solvent, an alcohol exchange reaction was begun through reflux.

After alcohol exchange, the A and B-cation solutions were combined and refluxed for a further three hours. Following complexation the sol was distilled to remove any remaining traces of water, and then filtered to remove any precipitates. Subsequently, ethane 1,2-diol was added to the sol to minimise the effects of ageing.

A composite-slurry was then prepared: dispersing a ceramic powder (PZ26 Ferroperm) into the sol and adding a sintering aid, dispersing agent and YSZ pellets. The sintering aid employed was the PbO-Cu_2O system: a liquid phase sintering aid. The PbO-Cu_2O system forms a eutectic solution at 680 °C when the composition is at 80 mol % of PbO (see Fig 2.4). Consequently, PZT thick films, incorporating the PbO-Cu_2O additive, could be sintered at low temperatures ~710 °C. The dispersing agent was added to help stabilise the dispersion of powder in the sol. The YSZ pellets were added so the slurry could be ball milled to reduce agglomeration.

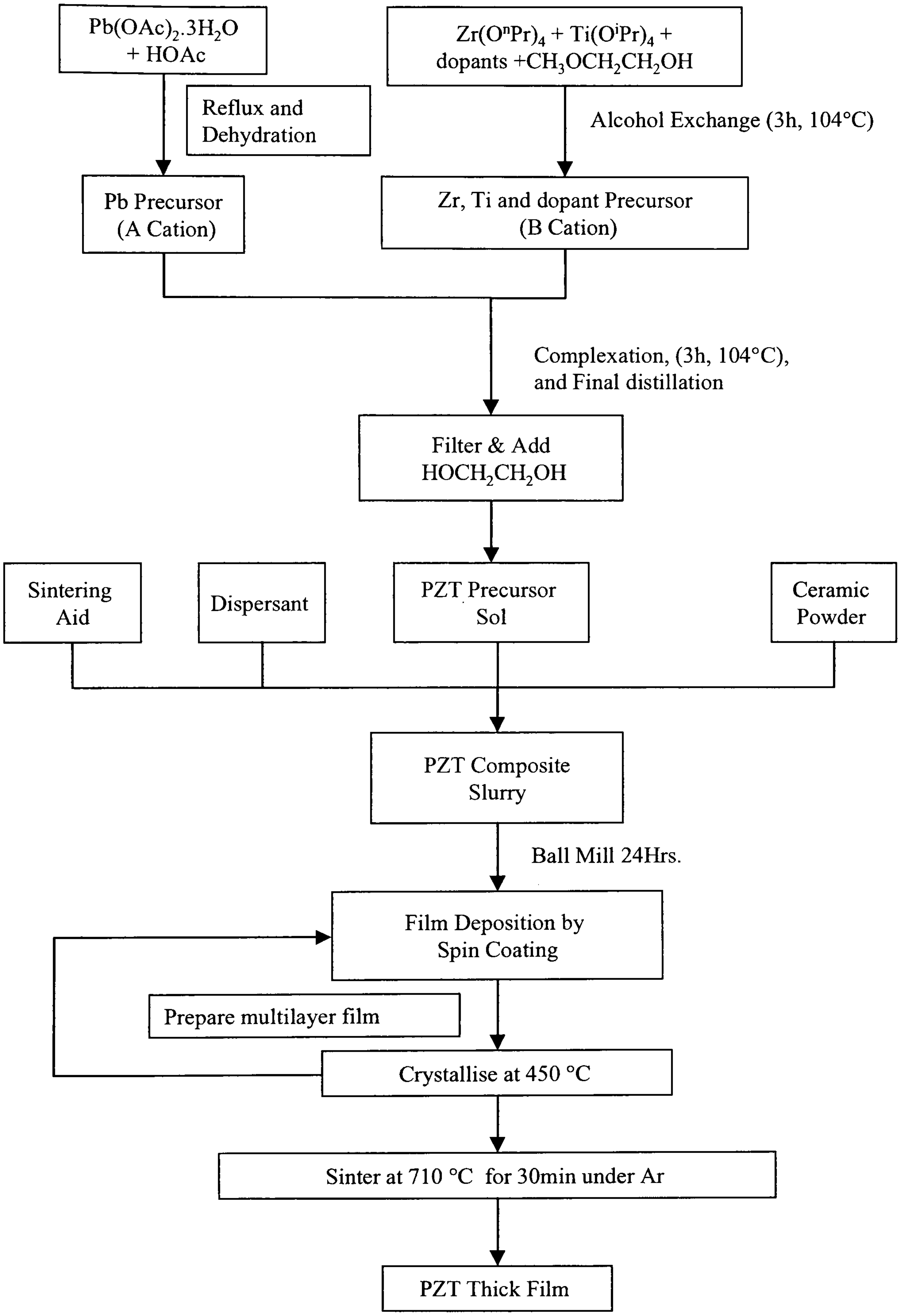

Fig 2.3 The process of thick film fabrication developed at Cranfield University. The process has three stages: sol synthesis, slurry preparation and film deposition.

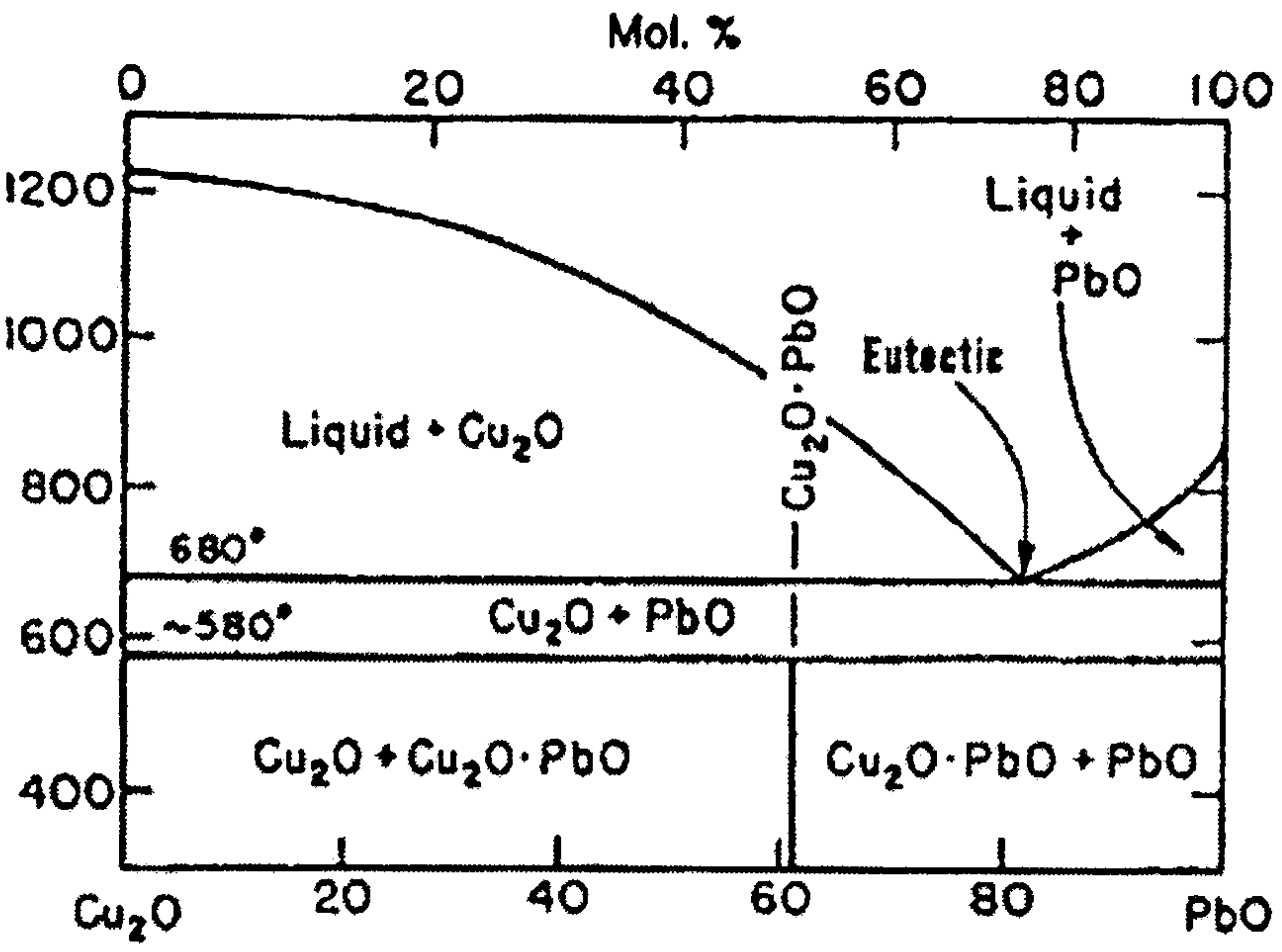

Fig 2.4 Phase diagram of the Cu_2O-PbO system. The image shows that a eutectic forms at 680 °C at ~80 mol % of PbO. Image taken from Gebhardt and Obrowski [41]

Ceramic pellets were prepared from PZ26 powder [42]; the pellets incorporated the PbO-Cu_2O additive, and they were sintered with an air atmosphere. Subsequently, the pellets were cross-sectioned for SEM (scanning electron microscopy), and composition analysis was conducted with EDX (energy dispersive X-ray). In order to resolve grain boundaries, samples were etched with 10 % HF(aq) before analysis. It should be noted that no trace of Cu was detected in samples that had been etched before analysis; however, Cu was detected in samples that had not been etched with HF(aq). The absence of Cu in etched samples indicated that Cu had been removed with the material removed during etching. As this material was removed from the grain boundary, it follows that Cu had been removed from the grain boundary by etching. The only source of Cu was the sintering aid; therefore, it may be concluded that Cu concentrates at the grain boundary during sintering.

Perin et al [39] have argued that standard films that were sintered under Ar demonstrate a split <200> peak, and this indicates that sintered thick films were highly tetragonal. Standard films were prepared by spin coating 8 layers of composite sol onto platinised silicon wafers. Between each coat the film was dried at 450 °C for 15 s. The final stage in making a standard film was to sinter at 710 °C for 30 minutes.

Films were prepared through spin casting of slurry onto 100 mm diameter Pt/Ti/SiO_2/Si wafers. After spinning, the wafer was heated on a hot plate at 450 °C for 15 s to pyrolyse the PZT thick film. The pyrolysis stage was applied to the wafer after the application of each new layer of the thick film. Most multi-layer films were composed of eight coats of slurry. Once desired film thickness had been achieved, the films were sintered under an Ar atmosphere at 710 °C for 30 minutes with a flow rate of 30 l/min.

It has been noted [39] that intermittent thermal treatment at 450 °C for 15 s was sufficient to remove residual organics from PZT thick films. Further, no pyrochlore phase was observed when PZT thick films were either heated intermittently or sintered under an Ar atmosphere.

A perovskite phase formed at 435 °C [38] in xerogel derived PZT thick films (see Fig 2.2 above), indicating that crystallisation of the perovskite phase has occurred at this temperature. As the pyrochlore phase forms in PZT thick films when intermittently treated at 350 °C (Fig 2.2), it would appear that the pyrochlore phase cannot form in films where intermittent thermal treatment is as high as 450 °C.

However, the films fabricated through the Cranfield-route exhibited a high degree of porosity [43,44] (see Fig 2.5). The film exhibited greatest density at the interface with the substrate. Porosity was found to increase toward the top of the film [43,44].

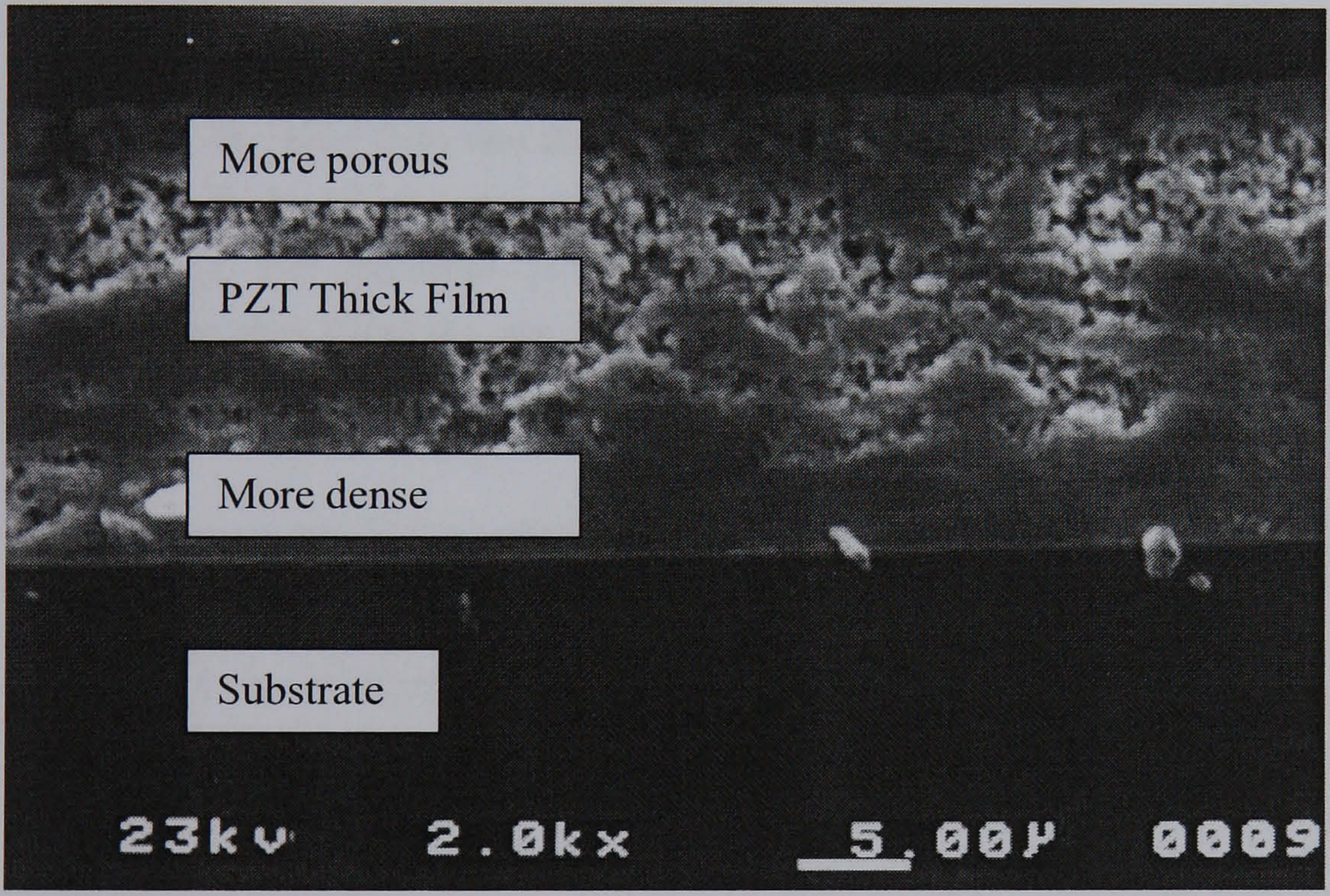

Fig 2.5 SEM micrograph of a polished cross section of a PZT thick film; the film was of the form PZT/Pt/Ti/SiO_2/Si. This film was prepared by spin coating 8 coats of slurry; after each coat the film was crystallised at 450 °C for 15 s. Finally, the film was sintered at 710 °C for 30 minutes under an Ar atmosphere. This film is an example of a standard and shows a greater densification near the interface with the substrate. Image taken from Haigh [43].

2.1.1.2 MSc. Work By The Author Preceding This Thesis

An infiltration route in which sol was used to fill the pores of the ceramic has been proposed [43]. Consecutive layers of sol and slurry were built up onto a $Pt/Ti/SiO_2/Si$ substrate surface (Fig 2.6). A drying step or crystallisation step was employed between the deposition of each layer (see Fig 2.7). As the sol and composite layers were built up consecutively, each layer was spun down before the next.

A notation has been proposed to represent the infiltration process, this notation also represents crystallisation and sintering conditions employed during thick film fabrication and has been introduced earlier [43]. In equation (2.1) the first term within the square brackets, corresponds to the first deposited layer and the last term to the last deposited layer, C and S are the composite and sol layers respectively. The superscripts β and χ denote the temperature conditions used for drying and crystallisation (for example β=200°C and χ=450°C as in equation (2.4)); n and m are integers.

$$\left[S^{\beta} + n.(C^{\chi} + m.S^{\beta}) + C^{\chi}\right]_{b}^{a} \tag{2.1}$$

There may be more than one thermal treatment applied to each layer before the next layer is deposited, in which case there are i and j thermal treatments for S and C layers respectively, see equation (2.2). It should be noted that a and b are the sintering temperature and sintering gas respectively and are taken outside the square brackets as they operate on all layers of the film.

$$\left[S^{\beta 1,\beta 2\ldots\beta i} + n.(C^{\chi 1,\chi 2\ldots\chi j} + .S^{\beta 1,\beta 2\ldots\beta i}) + C^{\chi 1,\chi 2\ldots\chi j}\right]_{b}^{a} \tag{2.2}$$

For ease of use in experiments where drying, crystallisation and sintering conditions are not investigated β, χ, a & b are assumed constant and eliminated from the notation to yield equation (2.3).

$$S + n.(C + m.S) + C \tag{2.3}$$

Significant cracking was observed in the surface of infiltrated PZT thick films when intermittent firing at 450 °C was employed [43]. In addition, single layers of sol ($[S^{450}]/Pt/Ti/SiO_2/Si$) were found to crack when heated to 450 °C on a hotplate. The cracking, of the single sol layer was attributed to poor drying of the solvent. Cracking of sol layers was eliminated through the introduction of a drying step at 200 °C for 50 s. As each intermittent thermal treatment was below 450 °C it was considered unlikely that this would result in the formation of a pyrochlore phase. It should be noted, that the preparation of sol and slurry were as shown in Fig 2.3.

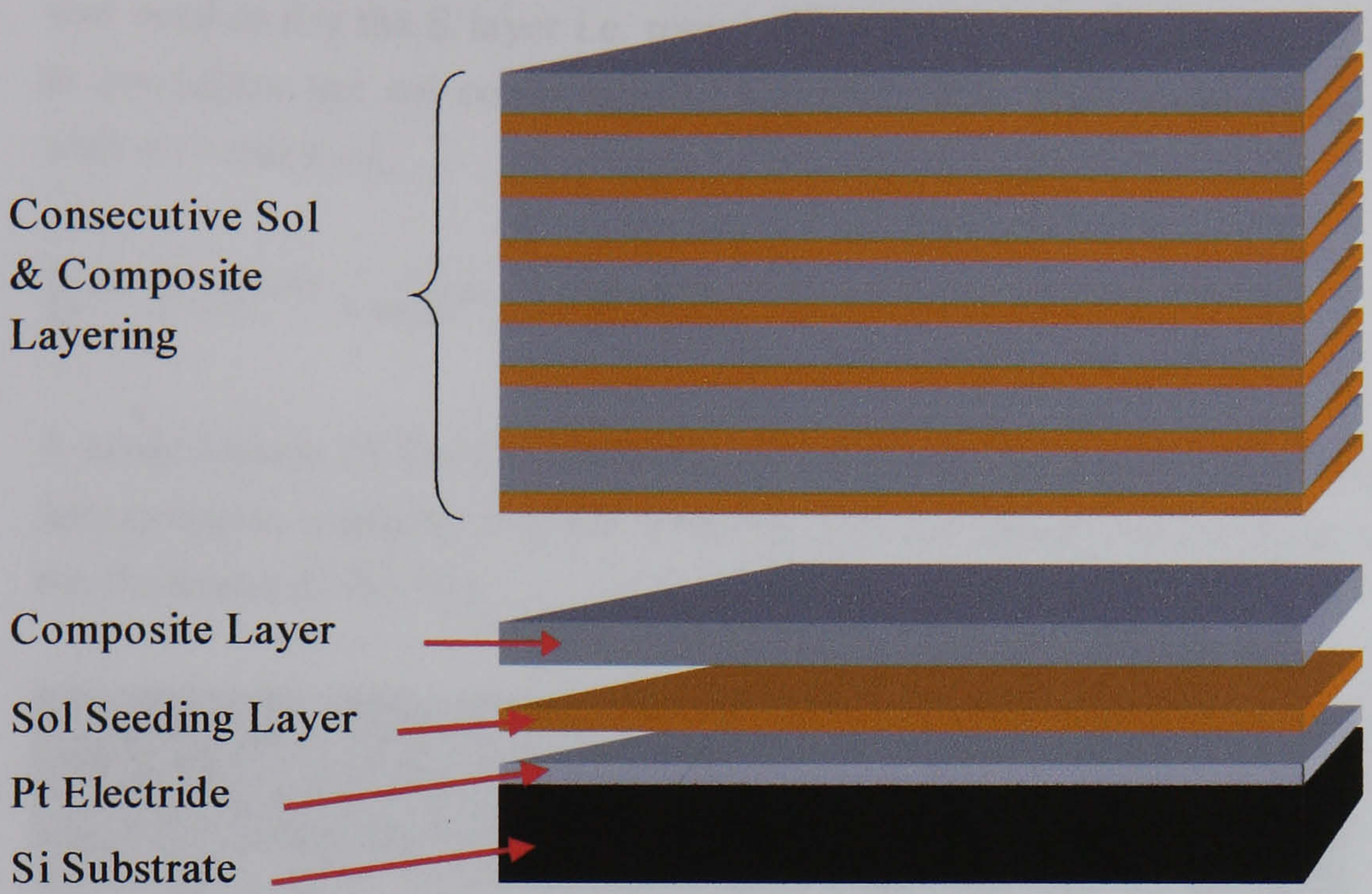

Fig 2.6 A conceptual image of the consecutive layers of sol and slurry deposited onto a platinised silicon substrate. This diagram illustrates how PZT thick films are built up. Taken from Haigh [43]

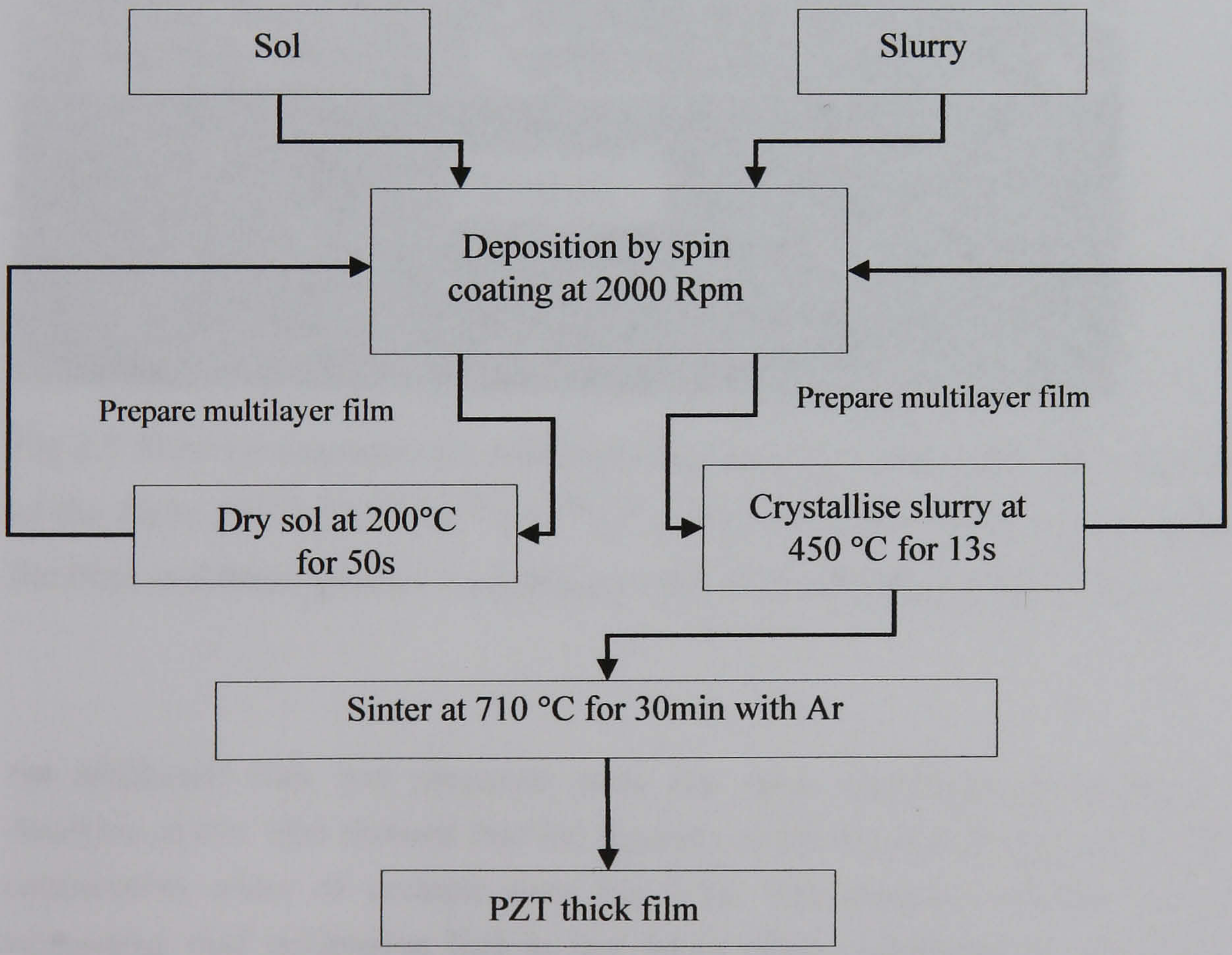

Fig 2.7 Consecutive sol and composite slurry layers. Process flow for the fabrication of layered or infiltrated PZT thick films. Taken from Haigh [43]

Optimum electrical properties, $\varepsilon_r > 800$ (dielectric constant) & $\tan\delta < 1\%$ (dielectric loss), were obtained with a film fabricated with conditions according to equation (2.4), where S and C layers were dried for 50 and 15 s respectively [43]. The thermal treatment at 200 °C was used to dry the S layer i.e. remaining solvent. Thermal treatment at 450 °C was used to crystallise the sol component of the thick film. The optimum results were achieved with n=7 and m=1.

$$\left[S^{200} + n.(C^{450} + m.S^{200}) + C^{450}\right]^{710}_{Ar} \qquad (2.4)$$

A cross section of the film, made as in the preceding paragraph is shown in Fig 2.8. It is interesting to compare Fig 2.8 with Fig 2.5: the density of the former is uniform across the thickness of the film.

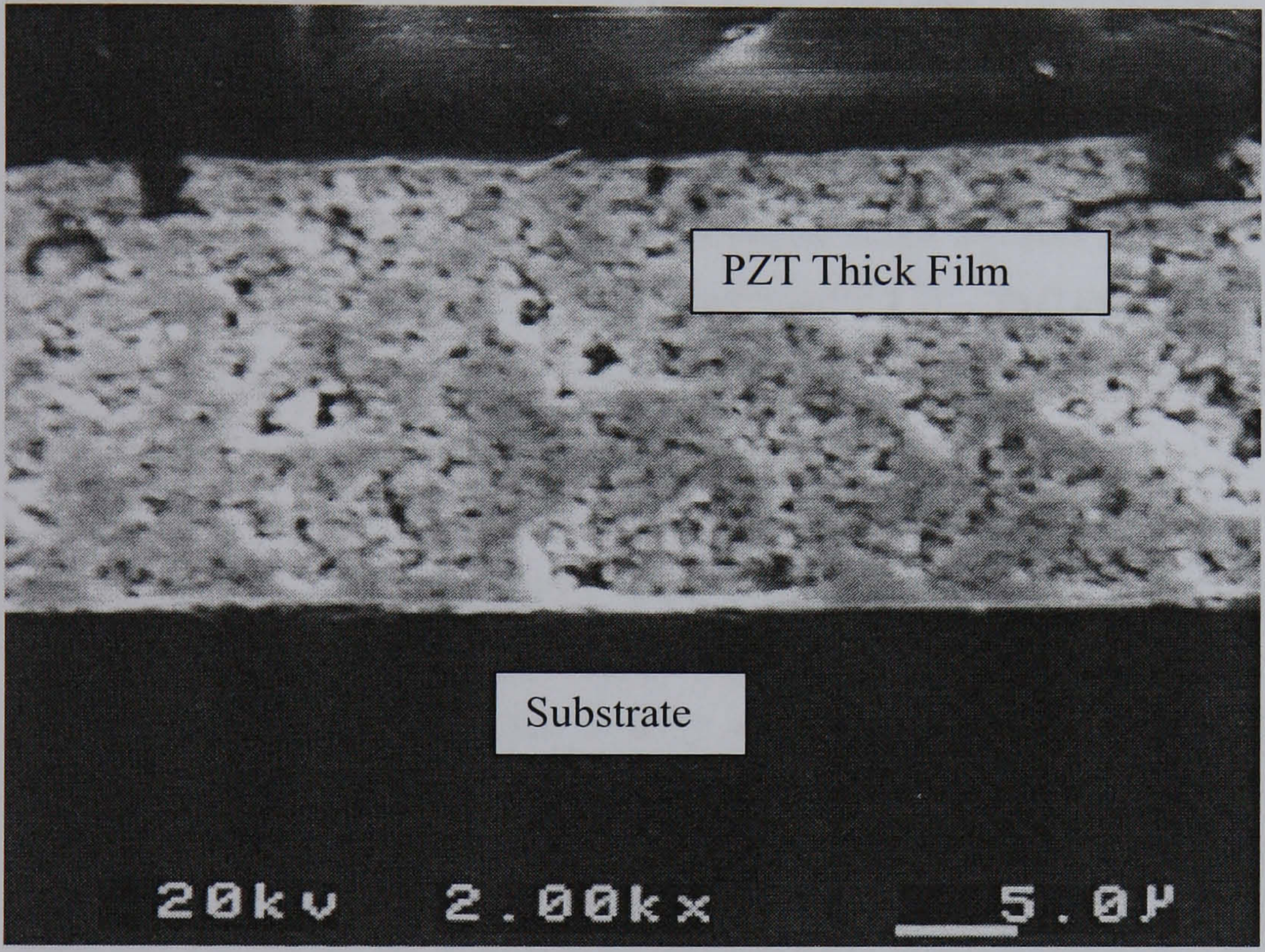

Fig 2.8 SEM micrograph of a polished cross section a PZT thick Film. The thick film was of the form: $[S^{200}+7(C^{450}+S^{200})+C^{450}]^{710}_{Ar}$ /Pt/Ti/SiO$_2$/Si. There is an even density across the film, and there appears no damage to the back electrode. Image taken from Haigh [43]

An additional film was prepared using the same conditions, but with n=7 and m=5. Analysis of this film showed that the layering of the sol had formed glassy layers between consecutive coats of ceramic (see Fig 2.9). The ceramic appears to be fully dense suggesting that infiltration had in fact taken place. Additionally, an intermetallic layer formed at the electrode-film interface [43]. Adhesion of the electrode to the substrate was very poor indeed; it was the electrode, and not the film, which had been separated from the substrate.

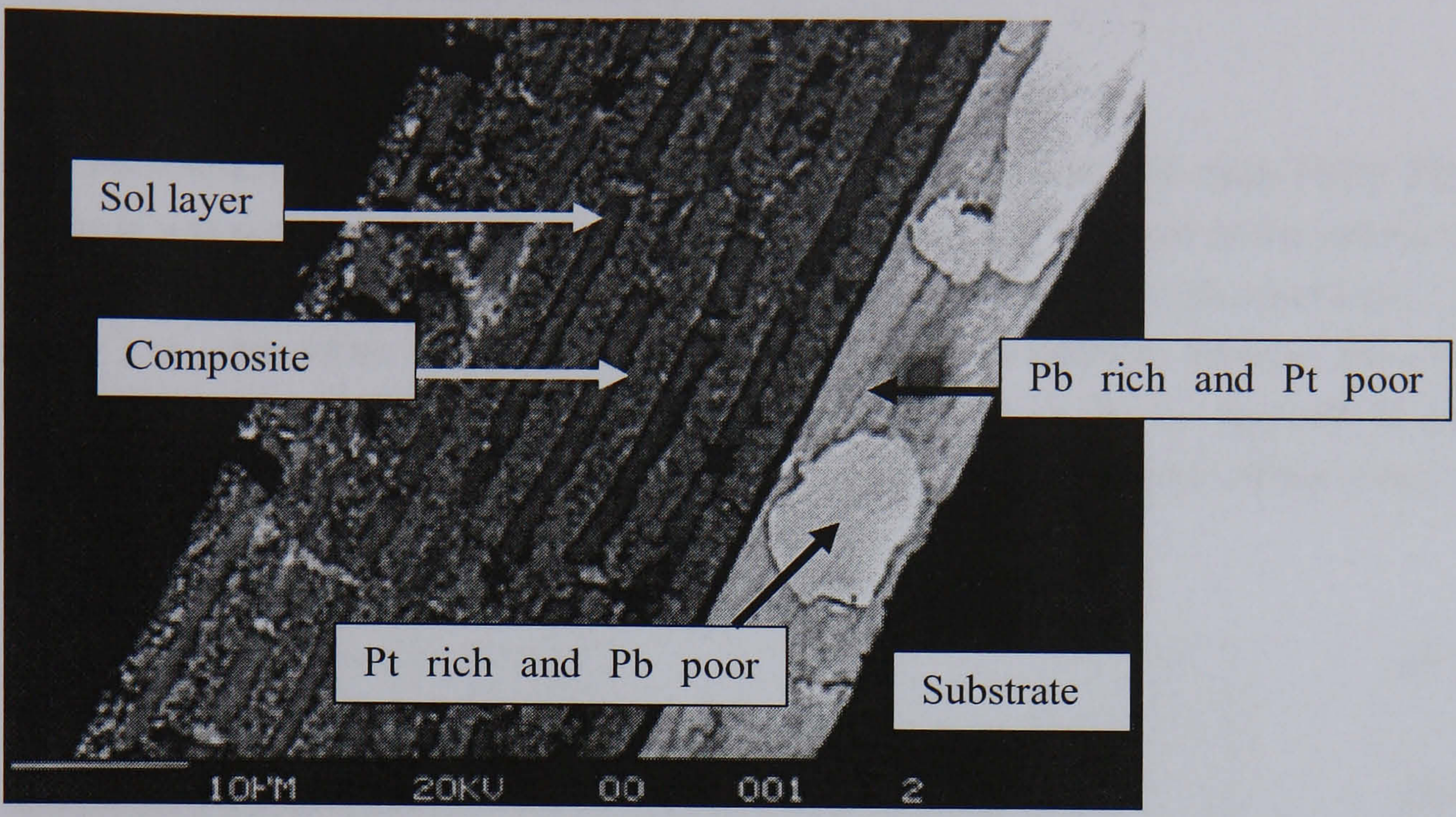

Fig 2.9 Second electron image of a polished cross section a PZT thick Film. The thick film was of the form: $[S^{200}+7(C^{450}+5S^{200})+C^{450}]^{710}{}_{Ar}$ /Pt/Ti/SiO_2/Si. The sol has formed glassy like layers between the composite layers. The back electrode has swollen with the formation Pb and Pt rich phases. Image taken from Haigh [43].

The electrical properties of PZT thick films, shown in Fig 2.5, Fig 2.8 and Fig 2.9 are reported in Table 2.1 below. Films shown in Fig 2.5 and Fig2.9 exhibited electrical properties consistent with the density of fabricated films. The dielectric constant and dielectric loss of the film in Fig 2.5 is consistent with films fabricated with the process shown in Fig 2.3. The poorer electrical properties of the film shown in Fig 2.9 , although the film of greatest density, were ascribed [43] to a discontinuous back electrode.

Form of the film	Fig No.	Thickness / μm	ε_r	Tanδ / %
8C	Fig 2.5	28	603	0.88
S+7(C+S)+C	Fig 2.8	23	701	1.14
S+7(C+5S)+C	Fig 2.9	35	26	7.41

Table 2.1 Electrical properties of consecutive layer PZT thick films. Taken from Haigh[43].

The overall density of the film in Fig 2.5 was lower than the film in Fig 2.8; nevertheless, the former was much denser at the interface with the substrate. It was proposed [43], that sol layering in film in Fig 2.9 acted to lock the sintering aid in place such that densification was more uniform across the wafer. Further, in films where no layering had been employed EDX detected relatively large signals of Cu near the substrate interface.

2.1.2 Electrode Substrate Interface

2.1.2.1 Msc. Work By The Author Continued

The intermetallic layer (as shown in Fig 2.9) was composed of PtPb with Pt_3Pb islands: analysis was conducted by EDX [43]. There was no trace of Si detected in the intermetallic layer. It was proposed [43] that the intermetallic layer had formed through equations (2.5) to (2.7). The proposition being made that pyrolysis was incomplete because the oxygen partial pressure would be lower in films sintered under an Ar as opposed to an air atmosphere. Consequently, some residual C remained in the thick films even after pyrolysis.

$$C(s) + PbO(l) \rightarrow Pb(l) + CO(g)\uparrow \tag{2.5}$$

$$C(s) + PbO(l) \rightarrow Pb(l) + CO(g)\uparrow + 3Pt(s) \rightarrow Pt_3Pb(s) \tag{2.6}$$

$$Pt_3Pb(s) + 2Pb(l) \rightarrow 3PtPb(s) \tag{2.7}$$

Intermetallics are normally re-oxidised with the reformation of the Pt electrode. In the case of PZT thin films, the Pb reforms PbO (see equations (2.8) and (2.9)).

$$Pt_3Pb(s) + \tfrac{1}{2}O_2(g) \rightarrow 3Pt(s) + PbO(s) \tag{2.8}$$

$$PtPb(s) + \tfrac{1}{2}O_2(g) \rightarrow Pt(s) + PbO(s) \tag{2.9}$$

The re-oxidised PbO is thought to diffuse back into the PZT film. In the case of PZT thin films the diffusion of PbO forms a front, and the perovskite phase is observed to grow from the electrode into the film [45].

In order for this re-oxidation to take place, O_2 must be present at the PZT electrode interface. Because the intermetallic layer shown in Fig 2.5 was present after the film had been sintered, the intermetallic layer had not been re-oxidised during sintering. Therefore, there was insufficient oxygen present at the interface when the film was sintered. The formation of glass like layers between composite layers might have sealed the film to prevent oxygen diffusion and thus the re-oxidation of Pb in the electrode.

2.1.2.2 Work By Other Authors

PZT thick films have been prepared through screen-printing onto $Pt/Ti/SiO_2/Si$ substrates [46,47]. Screen-printed thick films were fired in air at 850 °C. Bubbling was observed in the back electrode (see Fig 2.10) and reaction sites were observed in the Si beneath the back electrode. In Fig 2.10 the PZT was removed to reveal the bubbling in the electrode layer. The reaction sites were too small to be analysed by EDX, however, it was speculated that the sites had formed from Pb diffusion at sintering temperatures associated with Pb migration [47].

The damage shown in Fig 2.10 appears to have taken place beneath the back electrode, implying that the electrode material had de-laminated from the substrate and not from the PZT. It may therefore be concluded that Pb diffused through the electrode to react with the underlying Si.

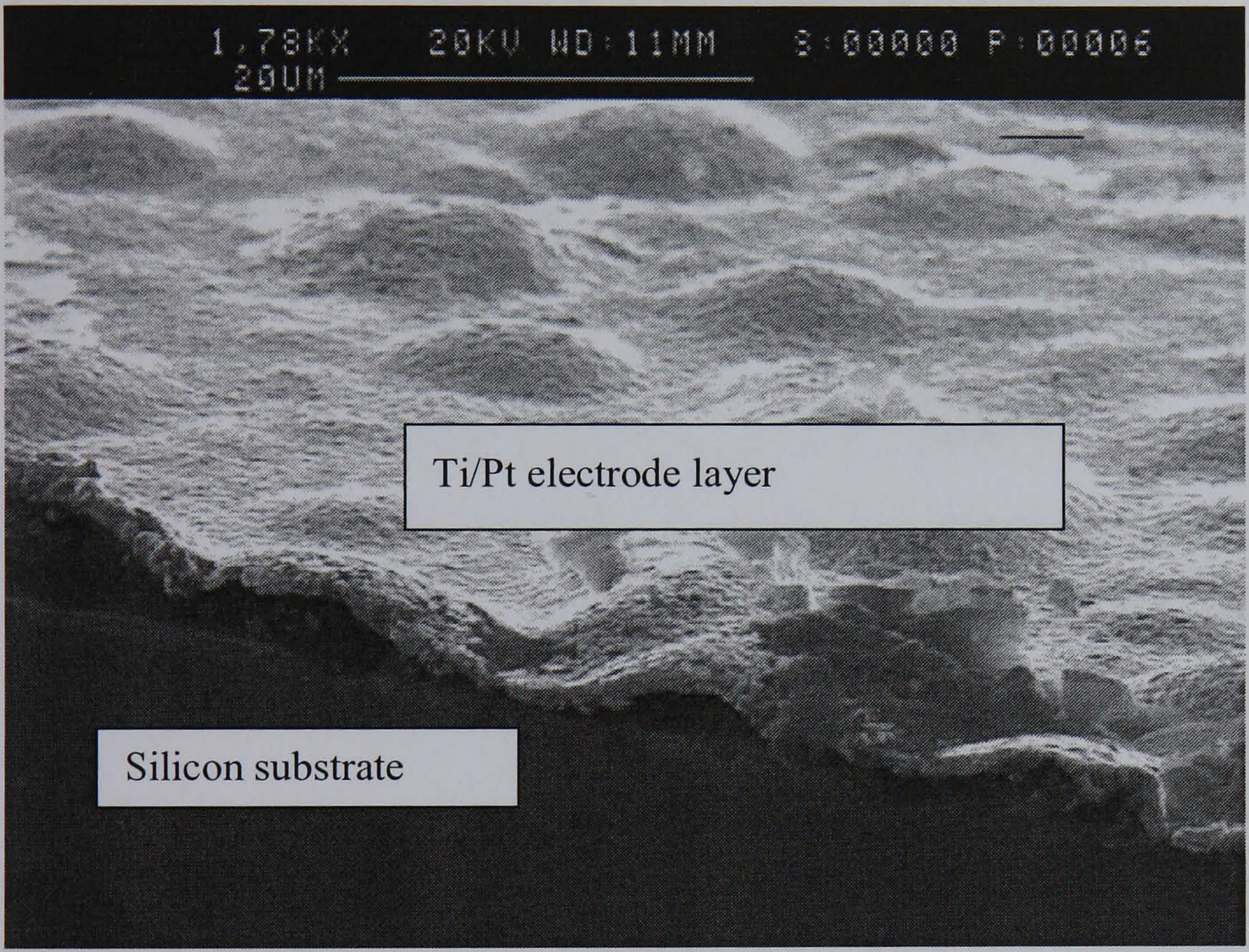

Fig 2.10 Bubbles observed in the Ti/Pt back electrode. The electrode material is seen to separate from the substrate. This damage was observed in a screen-printed PZT thick film after it had been sintered. The PZT has been removed to reveal the damaged electrode. Taken from Beeby et al [46]. The image also shows that the was electrode swollen

Wang et al [48] have analysed the PZT-Pt interface of sol-gel PZT thin films of the form PZT/Pt/Ti/SiO_2/Si (see Fig 2.11). TEM images have revealed a thin layer on the SiO_2 at the Ti/SiO_2 interface, which exhibits a mottled appearance. EDS (energy dispersive X-ray spectroscopy) has indicated that this layer is Pb rich. The implication being that this layer was a lead diffusion layer and that the Pt layer could not prevent diffusion of Pb between the PZT, the bottom electrode and substrate. This supported the view that Pt electrodes are porous and that Pb can diffuse through [48]. In a further publication [49], it was claimed that Pb migration from the PZT of a screen printed thick film into the Si had been reduced by up to ¼ through the screen-printing of a barrier layer. The barrier layer was a commercially available insulating ink, IP211 from Heraeus. An oxide layer (500 nm) was thermally grown on the ink. After firing the diffusion barrier was 10-15 μm thick. A PZT thick film was then screen-printed onto the diffusion barrier, and the PZT thick film was then sintered.

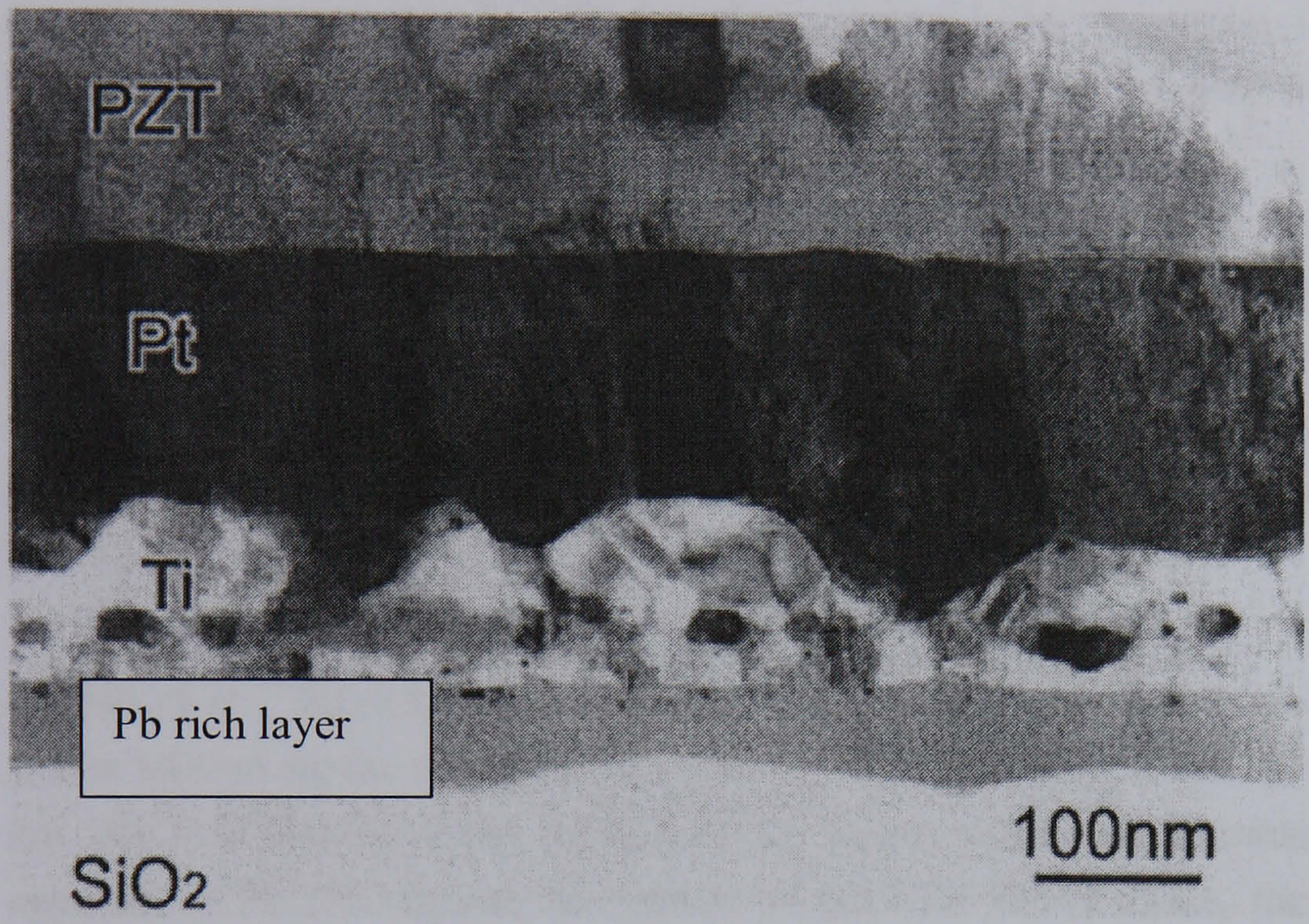

Fig 2.11 TEM Image showing a cross section through PZT/Pt/Ti/SiO_2. The image shows a layer between the Ti and SiO_2 layers. It has been proposed that this layer was lead rich. The Image was taken from Wang et al [48].

Chen and Chen [50] have claimed that a $Pt_{5\text{-}7}Pb$ phase forms at the Pt-PZT interface in MOD (metal organic deposition) PZT thin films on Pt/Ti/SiO_2/Si substrates. MOD thin films were annealed at 700 °C in Ar-O_2 (O_2=2%). $Pt_{5\text{-}7}Pb$, it was claimed [50], formed because of low oxygen partial pressure at the Pt-PZT interface; inefficient pyrolysis of organics at the interface reduced PbO to Pb^{2+} to Pb. The intermetallic phase was transient and gave rise to (111) orientated PZT thin films. At lower temperatures, it was claimed [50] that the intermetallic decomposed to pyrochlore from which (100) orientated PZT was observed to grow.

It was claimed [50], that lattice matching between PZT and the intermetallic favoured the formation of the (111) orientated texture. In a later paper [51] formation of PbO at the film electrode interface was proposed to account for the nucleation of the (100) texture. A slower heating schedule re-oxidised the intermetallic (to PbO) before the perovskite (111) PZT phase had time to nucleate. It should be noted that MOD precursors have an inherently higher carbon content than sol gel precursors, and therefore MOD films are more likely to result in the formation of the metastable phase. The presence of the intermetallic phase increased with the thickness of the PZT thin films prepared by Chen and Chen [51]. Oxygen partial pressure at the interface was reduced in thicker films, as oxygen diffusion was inhibited by the increased thickness of the PZT.

Composite PZT thick films [43] had a greater density near the Pt-PZT interface than near the top of the film. It is plausible that an increase in PZT density would reduce oxygen partial pressure at the Pt-PZT interface, and aid the formation of the intermetallic. Further, the increased density would inhibit re-oxidation yielding an intermetallic layer after sintering. However, no intermetallic layer formed in $[8C^{450}]^{710}{}_{Ar}$ films after sintering. It should be noted that packing considerations in composite thick films were anticipated to result in greater porosity compared to MOD and sol-gel thin films. Open porosity provides channels for sintering gases to diffuse along; therefore, open porosity in PZT thick films is anticipated to aid oxygen partial pressure at the film electrode interface. Porosity of the thick film, it was considered, could effect the formation of the intermetallic.

Brooks et al [52] have showed, through TEM cross section, that perovskite (111) textured grains formed on the surface of the intermetallic. Furthermore the perovskite grains grew into the thin film from the surface of the intermetallic, the intermetallic being Pt_6Pb as opposed to $Pt_{5-7}Pb$. Before nucleation of the PZT (111) phase, the film is pyrochlore; subsequently, perovskite grains start growing at the surface of the intermetallic yielding an epitaxial perovskite (111) growth into the pyrochlore film. Brooks et al did not consider sol-gel derived PZT thin films able to support the formation of the intermetallic when sintered under an oxidising atmosphere. It was considered [52], that the combination of increased oxygen partial pressure and lower carbon content, of sol-gel compared with MOD derived films, would inhibit the lifetime of the metastable phase; consequently, there would be insufficient time for PZT (111) to nucleate.

To date there have been no reports of reaction sites beneath the back electrode in composite sol PZT thick films. However, Huang et al [53] have observed, with TEM, the formation of Pt_3Pb at the Pt-PZT interface in a sol-gel derived PZT thin film. EDX analysis [53] confirmed that it was Pt_3Pb that had formed, and discounted the formation of both $Pt_{5-7}Pb$ and Pt_6Pb. The intermetallic formed within the electrode; formation occurred when annealing at 440 °C under an air atmosphere. Analysis of the relative intensities of the Pt_3Pb and PZT perovskite phases, by XRD as a function of annealing time, showed that the intermetallic was transient. The Pt_3Pb phase disappeared with the formation of a perovskite PZT phase. Haung et al [53] have not discredited Chen and Chen [54] with respect to the reduction of PbO at the Pt-PZT interface. Pt_3Pb is thus likely to form because of oxygen partial pressure at the Pt-PZT interface, indicating that residual C remains the cause of intermetallic formation, and this supports the work of Haigh [43]. Further, the intermetallic is formed at the film Pt interface and grows downward from the interface [53], and this occurs before the nucleation processes discussed above.

The damage observed by White et al [46,47] and Wang et al [48] appears to be caused by a different mechanism. This damage seems to be taking place in the substrate layer: beneath the back electrode, and not in the electrode layer, nor at its interface with the film.

2.1.3 Diffusion Barriers

Pb diffusion has been a problem for some time in PZT thin films that have been prepared on Pt/Ti/SiO_2/Si substrates. A variety of Pb diffusion barrier systems have been proposed for PZT thin films prepared through sol gel routes [55-57]. Barrier layers have included sol gel Al_2O_3 [57], sputtered YSZ [55,56] and sputtered TiO_2 [58,59]. An important variable is the effect the barrier layer has on the nucleation and crystallographic orientation of the PZT thin film; PZT is thought to nucleate at the PZT-Pt interface [53]. Seeding layers, of $PbTiO_3$, have also been included in a diffusion barrier system [57] in order to aid nucleation of the perovskite phase. However, in the case of PZT thick films it is considered most likely that nucleation (of the metal organic sol) will occur at the surface of the dispersed powder particles.

Reactive sputtering of TiO_2 thin films between 100 to 500 nm in thickness onto glass substrates has been investigated [60]. Deposited films were all amorphous with substrate temperatures less than 200 °C. However if Ti were sputtered and then thermally oxidised, at a temperature > 600 °C, it is likely that it would yield a crystalline phase. Sintering of PZT thick films, of the form: PZT/Pt/Ti/TiO_2, at 710 °C is also likely to crystallise an amorphous TiO_2 barrier. Crystallisation and the formation of grains and grain boundaries present possible diffusion paths for Pb. Consequently, there is little advantage in reactive sputtering compared with thermal oxidation as a route for the fabrication of a TiO_2 barrier layer.

Hillocks have been observed in sputtered Pt/Ti coatings on Si and have been attributed to compressive forces within the Pt layer [45]. Hillock height in sputtered Pt (300 nm)/Ti(20, 40, 55 and 70 nm)/SiO_2/Si films is a function of Ti thickness and sintering temperature (500 to 800 °C) [61]. Hillocking resulted from the build up of compressive stresses in metal layers during sintering [61] due to thermal expansion mismatch. Maximum hillock formation occurred at 700 °C with a Ti thickness of 70 nm [61]. Rémiens and Vélu [59] have grown TiO_x encapsulation layers on Ti/Pt/SiO_2/Si substrates through sputter deposition, and have observed the growth of hillocks of 10 μm diameter.

Horita et al [56] have found that a YSZ barrier layer (10 nm) was sufficient to prevent reaction between the PZT (100 nm) and the underlying silicon substrate. The YSZ barrier coating was deposited onto a <100> orientated Si substrate, through DC magnetron sputtering. The resulting PZT thin film was highly c-axis orientated with a perovskite structure. Kim et al [55] have investigated the influence of the crystallographic orientations of substrate barrier layer on the crystallographic orientation and surface morphology of the deposited PZT thin film. It was found that a YSZ and silicon crystallographic orientation of <111> yielded PZT thin films with a rough surface morphology and a high surface porosity. Surface porosity was eliminated from the PZT with a post-annealing process at 600 °C. PZT thin films that were deposited on YSZ and silicon with a <100> orientation had a good surface morphology. It should be noted that crystallographic orientation of PZT thick films is not likely to depend upon the substrate orientation.

Nicholls et al [62,63] have compared thermal barrier coatings (TBC) deposited with electron beam physical vapour deposition (EB-PVD) and plasma spraying. TBCs were fabricated from Yittria stabilised Zirconia (YSZ: ZrO_2 – 8 wt. %Y_2O_3). EB-PVD and plasma spray films had a thickness the order of 250 μm and were fabricated at 1000 °C. Thin film YSZ coatings (100 nm) have also been deposited [64] as buffer layers for superconducting thin films. EB-PVD coatings of YSZ differ from plasma sprayed coatings, in that EB-PVD coatings have a vertical columnar microstructure. Grain boundaries run vertically between the columns of the microstructure of the YSZ film [63]. The vertical microstructure allows the barrier coating to expand and contract under thermal cycling. Consequently, plasma spray coatings are less elastic than EB-PVD coatings. As thick films endure repeated thermal cycling the elasticity of an EB-PVD YSZ coating may minimise de-lamination. Screen-printed YSZ has been used, to good effect, as a diffusion barrier in powder-sol PZT thick films [65].

Chromik et al [66] have analysed 100 nm thick YSZ coatings. These coatings, deposited by EB-PVD on Si <100> substrates, were analysed with TEM. Chromik et al [66] have found the YSZ coatings to possess a nanostructure composed of rectangular blocks of 30-40 nm in diameter. Kim et al [55] have deposited YSZ coatings by reactive DC magnetron sputtering on p-type Si <111> and <100> orientated substrates. Deposition was made at 10 mtorr in a 5.8 % $O_2/(Ar+O_2)$ atmosphere (between 600 to 870 °C). All coatings processed above 700 °C demonstrated a <111> texture, in line with the spectrum obtained. This implies that YSZ forms <111> textured films irrespective of substrate and deposition process, but dependent upon processing temperature. Micro or nanostructure would appear to depend upon the substrate employed. However, ZrO_2 has been grown on Y_2O_3 buffer layers, and these films were grown with EB-PVD [64,66-69]. The crystallographic orientation of the Y_2O_3 layer was found [69] to depend upon processing temperature of the Si <100> substrate. Y_2O_3<100>/Si<100> orientated films were obtained at temperatures > 900 °C; whereas Y_2O_3<111>/Si<100> orientated films were obtained at temperatures < 900 °C.

The deposited thick film will be used in a device; it is an essential part of processing that paths be opened through the PZT to the back electrode. After sintering the thick film will be wet etched in HF(aq) back to the back electrode. Consequently, stability of the back electrode system and barrier layer to HF(aq) is an important consideration in selecting the barrier layer. Lay [70] has discussed the stability of selected ceramics to HF(aq), TiO_2 and

SnO_2 were stable but Al_2O_3 was attacked. No information could be found on the stability of YSZ to HF(aq)

2.1.4 Effect Of Sintering Gas & Aid On The Electrical Properties Of PZT

2.1.4.1 Grain Boundaries

The addition of PbO-Cu_2O sintering aid as part of the composite-slurry introduces the possibility of Cu-doping. Barranco et al [71,72] have studied the effects of MnO_2 as an additive to the $PbZrO_3$-$PbTiO_3$-$PbCu_{1/4}Nb_{3/4}O_3$ (PZT-PCN) system. The Mn doped PZT-PCN system has the same elemental composition as the PZ26 PbO-Cu_2O sintered PZT-thick-films. The PZT-PCN system did not contain any Sb^{5+} substituent: this is not considered a problem as electrical and sintering properties of Sb^{5+}-doped PZT should be similar to Nb^{5+}. For this reason the Mn-doped PZT-PCN system may be considered a good system with which to compare PZT thick films based on the PZ26 powder. In the PZT-PCN system Cu^+ and Nb^{5+} dope at the Ti^{4+} and Zr^{4+} (B-) lattice sites. It was noted that Cu^+ doping ions underwent an oxidation step i.e. Cu^+ to Cu^{2+} during air-sintering of PZT-PCN. The effect of Mn^{3+}additive, in the PZT-PCN system, was to displace Cu^{2+}, as CuO, from the B-site. Therefore, Cu^+ can displace both Ti^{+4} and Zr^{+4} from their lattice sites, but Mn^{3+} will preferentially displace Cu^{2+}. It appears that Cu^+ does not displace Nb^{5+} when it occupies the B-site. Cu^{2+} was precipitated at the grain boundary as CuO when the PZT-PCN Mn doped system was sintered with air [72].

Barranco et al [71] have compared the XRD spectra of the undoped $PbZrO_3$-$PbTiO_3$-$(Pb(Cu_{0.25}Nb_{0.75})O_3)_{0.06}$ (PZT-PCN) system with the spectra of the same system doped with 0.5 mol% MnO_2. The MnO_2 doped PZT-PCN system exhibits a powder pattern consistent with a perovskite structured material. The XRD patterns obtained were indistinguishable from those of PZT. It has been noted [71] that Mn^{4+} doping ions are reduced to $Mn^{2+ \text{ or } 3+}$ during sintering under an oxidising atmosphere [71]. Consequently sintering results in the formation of oxygen vacancies to maintain electrical neutrality.

PZT-PCN were prepared from powders; the reagents used were PbCO, ZrO_2, TiO_2, Nb_2O_5 and Cu_2O [71]. PZT-PCN samples were doped with 0.5 mol% Mn^{4+} using MnO_2. The samples were milled before firing at 800 °C under air for 1 hour at a heating rate of 50 °C/min. After firing samples were pressed at 300 MPa for another hour. After pressing the samples were sintered at 1220 °C for 2 hours in air.

2.1.4.2 Intrinsic Electrical Conduction

Gerson and Jaffe [73] have measured resistivity in PZT ceramics sintered as a function of oxygen-partial-pressure (po_2). Conductivity was higher in ceramics sintered at high po_2.

Gerson and Jaffe [73] have attributed this to the formation of cation vacancies during sintering due to Pb volatilisation: lead is lost from the host material as PbO . In order to maintain electrical neutrality positive holes are generated to balance the lead vacancies: lead vacancies act as centres of negative charge. Hole formation is the major cause of electrical conductivity in undoped-PZT.

The effect of the sintering atmosphere has been discussed for $BaTiO_3$ [74] this system is considered to be similar to PZT. In the BT system sintering with reducing atmospheres results in an increase in the electrical conductivity. This has been attributed to the reduction of Ti^{4+} to Ti^{3+} on the B-site. In turn this results in the formation of oxygen vacancies to balance the electrical charge. This process can be inhibited through doping with either variable oxidation state ions (e.g. Mn^{3+} or Co^{4+}) or ions with a lower oxidation state (e.g. Mg^{2+} or Ca^{2+}). These doping ions do not prevent oxygen vacancy formation; rather they inhibit the effect of oxygen vacancies through acting as electron traps. There are two mechanisms through which this occurs:

1. The formation of stable anion-vacancy-B-site defect pairs.
2. Isolated B-site defects acting as electron acceptors. It should be noted that holes in the valance band have a low mobility, and therefore contribute little to the electrical conductivity. Electrons from donor ions can still act to replace these holes.

2.2 Modelling & Design Of Piezoelectric Actuators

Comprehensive quasi-static models of bimorph actuators, have been derived describing generative force, tip deflection and fundamental frequency [75,76]. An analytical model of a unimorph piezoelectric actuator was proposed originally by Steel et al [77]; however, this model was limited to predicting tip deflection and elongation as functions of applied voltage. Smits and Choi [78] and, in a later paper, Weinberg [79] have derived 4 x 4 matrix descriptions of piezoelectric unimorph actuators. In these matrix equations, external excitation parameters (of applied voltage, bending moment, force and uniform load) were related to actuator responses (bending angle, tip deflection, volume displacement and electrical charge). However, this model does not represent outputs in simple terms and is therefore not considered to be well-suited to unimorph design.

The Wang & Cross [80] model (here with referred to as the Cross-model) expresses force, frequency and tip deflection, for both bimorph and unimorph actuators, using a transformed cross-section method (see APPENDIX II).

The hysteresis effect [81] results in a non-linear displacement of the actuator tip with rising and falling voltage. The source of this effect is in the plastic properties of the piezoelectric material. It has been considered [77] that the effect of hysteresis will diminish the tip deflection relative to calculated deflections. However, in a more rigorous comparison [31] tip deflections and blocking forces were greater than data calculated, using the Cross-model. As the drive-field was increased the fundamental bending frequency was observed to shift down field [31]. Therefore calculated values will, at best, approximate experimental data, but only for low drive fields.

2.2.1 Cross Model Of A Piezoelectric Unimorph Cantilever (Cross & Wang [80])

This model describes cantilever frequency, force and displacement in terms of non-dimensional parameters, and is derived under quasi-static conditions. The model is derived from first principals in APPENDIX II. The non-dimensional parameters allow comparison between substrates of different Young's modulus. In the case of a linear unimorph cantilever (see Fig 2.12) with a substrate of thickness h_m, an elastic modulus Y_m, a piezoelectric layer of thickness h_p and Young's modulus Y_p, the total thickness $h = h_m+h_p$). The densities of the cantilever substrate and piezoelectric layer are ρ_m and ρ_p respectively. For a linear unimorph cantilever of length L the first mode of frequency will be f (see equation (2.10))[80].

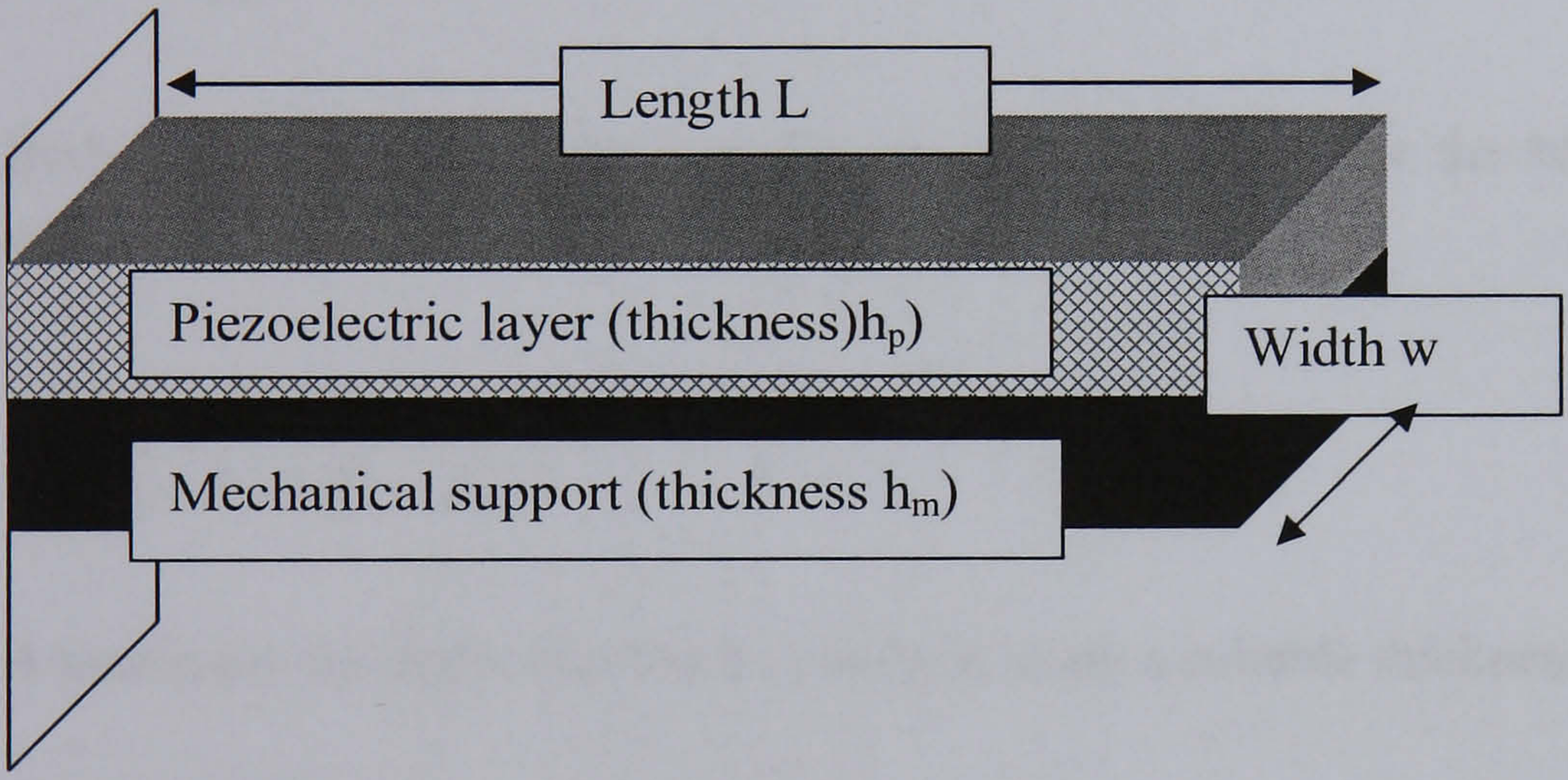

Fig 2.12 A 3D piezoelectric unimorph actuator.

$$f = \frac{3.52.h}{4.\pi.L^2}\sqrt{\frac{Y_p}{3.\rho_p}}.\Theta \tag{2.10}$$

In equation (2.10), Θ is the non-dimensional parameter for the frequency of a linear unimorph cantilever. The elastic ratio $Y_m/Y_p=A$, the thickness ratio $h_m/h_p=B$ and the density ratio $\rho_m/\rho_p=C_\rho$.

$$\Theta = \left[\frac{A^2.B^4 + 2.A.(2.B+3.B^2+2.B^3)+1}{(1+B.C_\rho)(A.B+1).(1+B)^2}\right]^{\frac{1}{2}} \tag{2.11}$$

Actuator deflection, δ, may be calculated from the longitudinal piezoelectric coefficient, d_{31}, and the applied electric field, E_3,

$$\delta = \frac{3.L^{2}}{2.h_{m}} d_{31}.E_{3}\Delta \qquad (2.12)$$

where Δ is the non-dimensional parameter for the deflection of a unimorph actuator.

$$\Delta = \frac{2.A.B.(1+B)^{2}}{A^{2}.B^{4} + 2.A.\left(2.B + 3.B^{2} + 2.B^{3}\right) + 1} \qquad (2.13)$$

When an applied electric field induces a deflection δ in an actuator the mechanical force that is required to restore the cantilever to δ = 0 is called the blocking force and is denoted F.

$$F = \frac{3.w.h^{2}.Y_{p}}{8.L}.\Pi.d_{31}.E_{3} \qquad (2.14)$$

Both Π and w denote the non-dimensional parameters for the blocking force and the width for the unimorph actuator respectively.

$$\Pi = \frac{2.A.B}{(A.B+1).(1+B)} \qquad (2.15)$$

A maximum tip deflection can be obtained using a suitable thickness ratio.

$$B_{\max} = \sqrt{\frac{1}{A}} \qquad (2.16)$$

2.2.2 Spiral Piezoelectric Models

Piezoelectric spiral actuators, of the form shown in Fig 2.13, that deflect in the plane have been modelled analytically and with finite element (FE) analysis (see Fig 2.14) [25]. The analytical models being based on an approximation where the spiral is composed of consecutive semicircles. An amplification factor Γ was defined in terms of the ratio of the tangential deflection, $\delta_{\text{spiral-tangential}}$, of the spiral actuator (see Fig 2.13) to the tip deflection of a straight unimorph actuator, δ_{straight}, (see equation (2.17)).

$$\Gamma = \frac{\delta_{\text{spiral-tangential}}}{\delta_{\text{straight}}} \qquad (2.17)$$

The amplification factor measures the how the shape of the spiral contributes to tangential deflection in spiral actuators of the type shown in Fig 2.13.

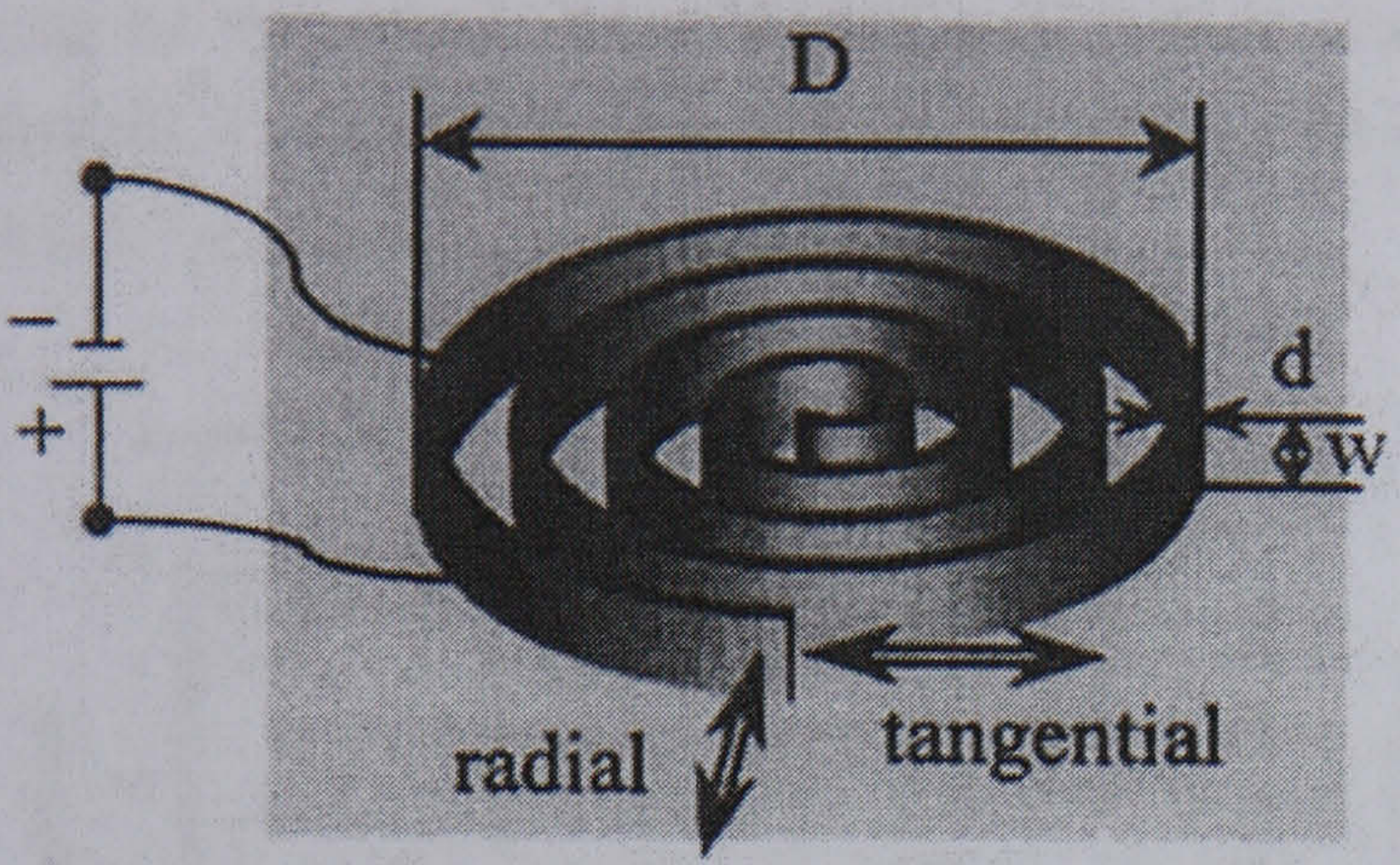

Fig 2.13 Spiral actuator produced through fused deposition technique. The image shows that the actuator deflects in the tangential and radial directions. The electrical contacts are made to the inside and outside faces of the actuator, not the top and bottom edges. Image taken from Mohammadi et al [82]

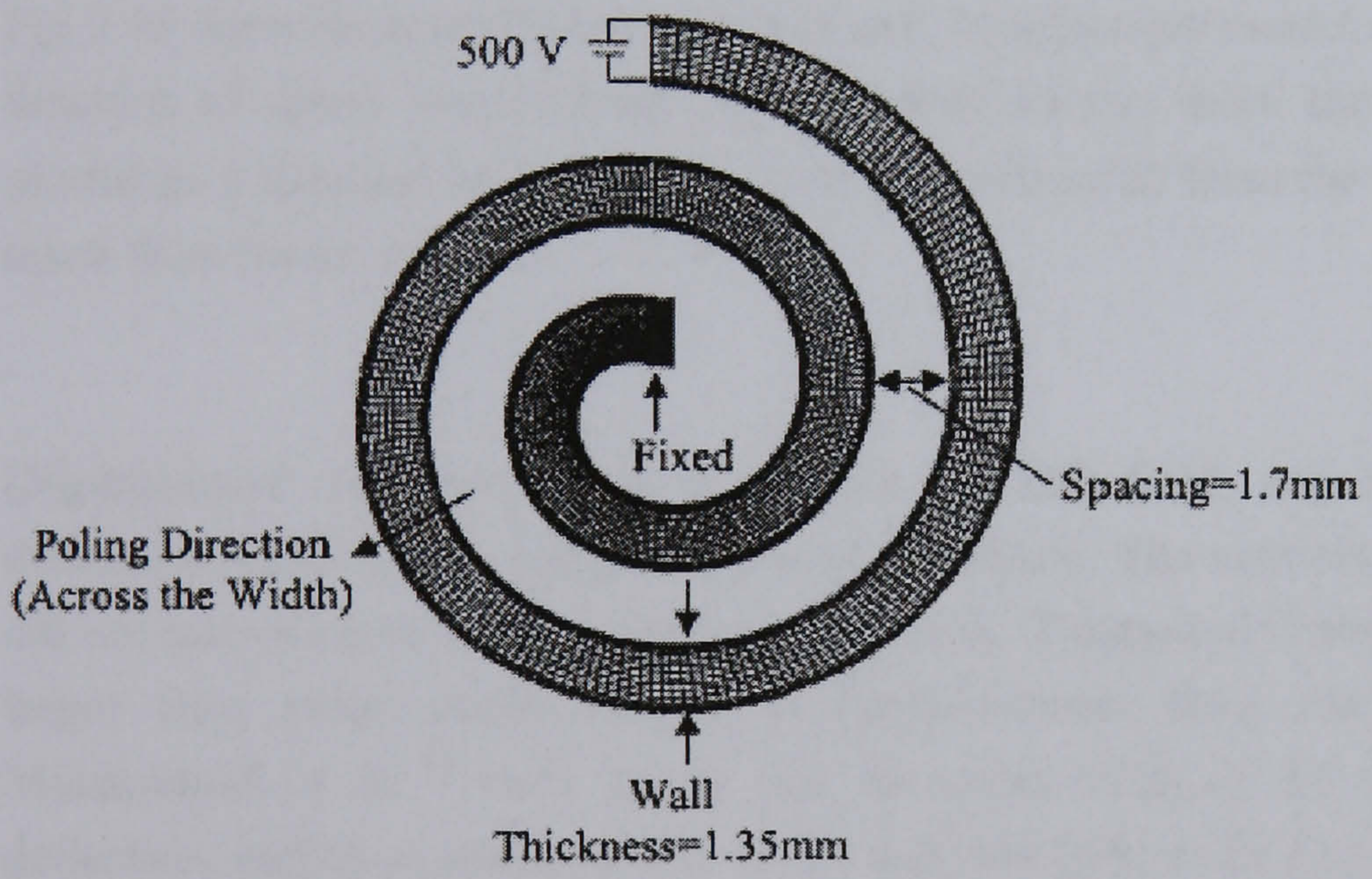

Fig 2.14 A 2D FE model of a spiral actuator designed to deflect in plane. Image taken from Safari et al [25]. Image shows the poling direction, the point that the actuator is fixed and the electrodes.

The FE model was composed of two turns with electrodes on inner and outer surfaces (see Fig 2.5). The structure was 10 elements thick and poled through its thickness. Tangential displacements were obtained through modelling plain strains driven at 500 V. The model was composed of PZT-5H and assumed a constant cross section.

Comparison between amplification factors obtained from experimental samples, FE and the analytical model were made as a function of length (see Fig 2.15 left). Both experimental devices and theoretical spiral actuators had the same dimensions, and these are given in Fig 2.14. Amplification factors, from the semicircular model, were plotted as a function of θ (see Fig 2.15 (right)). A steady state value of Γ was reached after the first turn of the spiral. This, steady state value, was predicted by both FE and analytical models, but experimental data did not appear to support this finding; suggesting, instead, that Γ increases linearly with length.

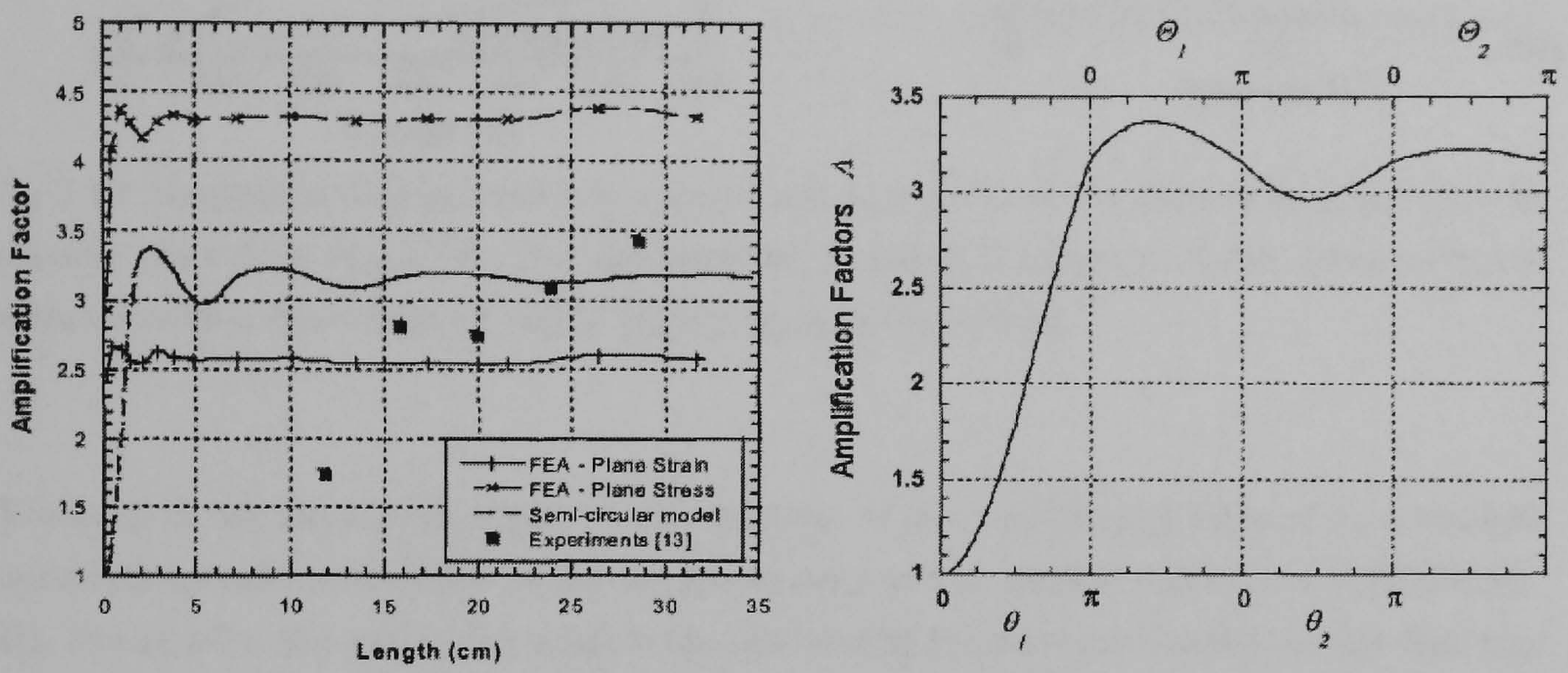

Fig 2.15 Amplification factors of FE model, semicircular model and experimental data as a function of spiral length (left). Amplification factors from the semicircular model were plotted as a function of angle θ, where θ was measured from the fixed point (right). Images taken from Safari et al [25].

Displacement was plotted as a function of DC field, see Fig 2.16 [82]. Tangential deflections gave rise to a high degree of hysteresis. The semicircular or spiral FE model did not take account of the effects of hysteresis. Tangential deflections were significantly larger than radial displacements or displacements from straight actuators. Further, Mohammadi et al [82] have found that the inner coils of the spiral produce the least deflection, and have attributed this to the fact that these coils have the largest curvature.

The resonance shown in Fig 2.16 (*right*) was attributed [82] to a bending mode similar to the coiling of a watch spring. This motion results from a change in curvature, of the actuator, and not from a change in elongation. The change in curvature and elongation arose from the thickness and longitudinal modes respectively.

It has been argued [82], for spiral actuators of the type shown in Fig 2.13, that the spring constant, arising from the spiral shape, is larger than the elastic compliance of the piezoceramic. It was speculated [82] that generated blocking forces will be lower in PZT spiral actuators than in straight actuators of equivalent length: the spring constant of the spiral being greater than the bar.

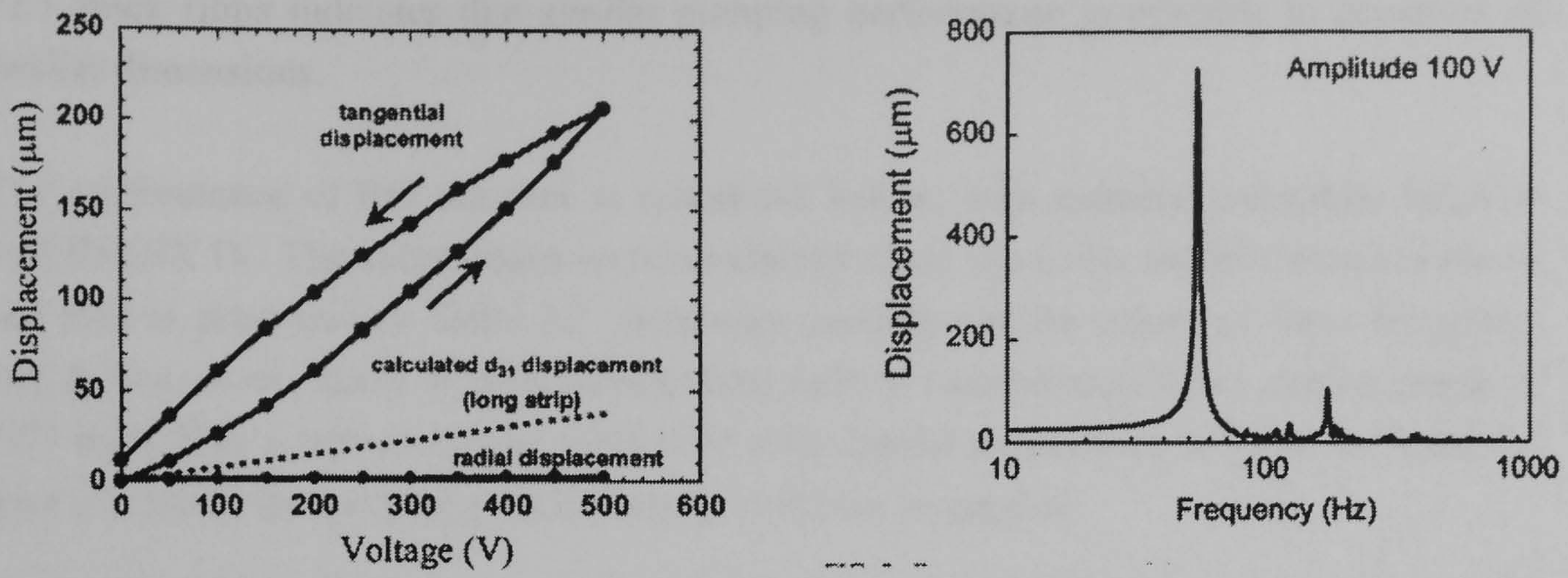

Fig 2.16 Tangential displacement of a spiral actuator (left) of the same dimensions as the actuator shown in Fig 2.14. The fundamental bending frequency of the same actuator obtained with a drive field of 100 V (right). Images taken from [82]

However, in an alternative paper [83] the stiffness of the mechanical support in a straight unimorph actuator was found to aid displacement and mechanical forces (see APPENDIX III). Essentially, the stiffer the support the greater the proportion of input energy that was converted into mechanical output energy. It should be born in mind that the spiral and linear actuators discussed above deflect in and out of the plane respectively. Another difference is the presence of the mechanical support in unimorph actuators. Amplification factors for the circular model of the spiral are proportional to $d_{33}/(-d_{31})$ where as unimorph deflection exhibits a direct proportionality to d_{31}.

There are no models available for spiral actuators that deflect out of the plane, or are fixed at the outer circumference. In addition, all analytical models for unimorphs, discussed in section 2.2 above, assume a straight beam with constant cross section. The beam is deformed out of the plane by an electric load, and the resulting forces and moments were determined (see APPENDIX II). Deformation was assumed to occur only in two dimensions x and y along the centroidal axis. The width of the straight actuator was assumed to remain constant and not subject to a bending deformation. All points along the x direction of the centroidal axis had a constant stiffness.

2.2.3 Piezoelectric Micro-Pumps

Piezoelectric actuated membrane micro-pumps have been fabricated in which the active layer was a screen-printed PZT thick film (100 μm) [13,84]. The mechanical support for the piezoelectric layer was Si (90 μm), and the actuator was of the form shown in Fig 2.12. Simulated flow rates for micro-pumps, based on this actuator, have been proposed [84]. Flow rates were the order of 300 μl/min operating the pump at a frequency of 1 kHz against a back pressure of 40 kPa. Actuator performance the order of those obtained for

PZT thick films indicates that similar pumping performance is possible in actuators of similar dimensions.

The performance of this actuator is calculated below, with material properties listed in APPENDIX IV. The calculations were conducted using the Cross model discussed above and data is presented in Table 2.2. Actuators yielding similar values of force frequency and deflection are likely to yield similar flow rates if incorporated into a similar pump. If PZT thick film actuators can be fabricated with similar dimensions to those in Table 2.2 then it is likely that pumping performances will also be similar.

Length / mm	Width / µm	Deflection / µm	Deflection / Length / %	Pressure / kPa	First Resonant Frequency / kHz
8.0	4.0	27.16	0.34%	17.35	8.1967
7.5	3.5	20.79	0.28%	22.66	10.706
7.0	3.0	15.28	0.22%	30.84	14.572
6.0	3.0	15.28	0.26%	30.84	14.572
6.5	2.5	10.61	0.16%	44.41	20.983
6.0	2.0	6.79	0.11%	69.39	32.787

Table 2.2 Performance of screen-printed PZT thick film (100 µm) on Si (90 µm) substrate with cantilever dimensions taken from White et al [84]. The table shows quasi-static values of blocking force/area, deflection and frequency. Actuators that achieve similar values are likely to achieve similar pump rates if incorporated into a similar pump.

2.3 Micromachining Of PZT Thick Films

PZT is both chemically inert and mechanically hard; consequently, it is difficult to pattern. There are in essence three approaches for the patterning of PZT materials: shaping of powders, carving and direct photo patterning. To date shaping of powders has been used for three-dimensional patterning of bulk ceramic and two-dimensional patterning of PZT thick films. Typically, the powder is incorporated into an ink with an organic binder before being shaped. Carving of PZT has been applied to bulk ceramics, thin films and thick films; carving works through either mechanical abrasion or through chemical etching.

2.3.1 Photo-Patterning Of PZT

Patterned PZT thin films (~0.3 µm) have been made with a photosensitive metal organic sol [85]; the sol incorporated acetylacetone (AcAc) as the photoactive component. Thin films were prepared on ITO (indium tin oxide) electrodes on quartz glass and silicon substrates through dip coating. The films were UV exposed through a photo mask and developed in Methanol before annealing at 680 °C in air for 30 minutes. There are to date no publications on photo patterned PZT thick films. The problem is that dispersed fine powder particles will act to scatter incident light; consequently, exposure will be non-uniform throughout the film.

2.3.2 Powder Shaping.

Ceramic powders have been dispersed in polymeric binders and solvents milled to yield a ceramic dough which could then be extruded, press formed or moulded [86]. A range of shapes has been explored through this process including rods, tubes, domes, springs, thick films and fine structures. Moulding is particularly useful for the fabrication of 3D fine structures such as rods [86-88] in which structures have been achieved down to 100 μm diameters. In the lost mould process X-ray-LIGA is typically used to fabricate a negative image of the desired pattern in the form of a mould [86,87]. The LIGA process is a specialised photolithographic process used to create high-aspect-ratio features in specific photoresists. In the lost mould process, the feature is in the form of a mould made in the photoresist. Ceramic slurry, typically consisting of a powder dispersed in a polymeric binder, a solvent and a surfactant, is poured into the mould and allowed to set and dry. The mould is then removed chemically [86] or through burn out [87] before the ceramic is sintered. Formally, the lost mould process is a process in which the mould is destroyed as part of the processing. Lost mould processes have been developed with wax moulds in which the desired shapes were fabricated through mechanical punching into the wax [88]: involving no lithography. Organic fibres have also been employed [88] as moulds. Both organic fibres and waxes were burned out before sintering of the PZT. In some cases [87] the moulded structure is refilled with polymer after sintering to support the ceramic during a grinding stage. A perturbation on this process is injection moulding [89] where a ceramic slurry is forced under pressure into a mould, dried, heat treated to remove binder and sintered after removal from the mould. However, the surface roughness of injection moulded or lost moulded structures is likely to be significantly higher than films fabricated through spin coating of sol-gel composite slurry PZT thick films.

2.3.2.1 Rapid Prototyping

Direct write processes have also been developed allowing complex 3D shapes to be patterned. In direct write processes a pen writes a ceramic ink onto a substrate, the substrate is on a computer controlled stage that moves in x-y, the stage moves according to a pattern that has been defined in a CAD instruction file, and in this way the desired device shape is printed or written onto the substrate. The ceramic is either in a liquid ink [90] or a plastic filament [91] in the latter case the filament is fed through a pen with a heated nozzle. In the case of ceramics prepared from ceramic-plastic filaments, also referred to as the fused deposition technique (FDT), wall depths have been fabricated down to 0.4 mm with heights of 6 mm [91]. It should be noted that the spiral structure discussed earlier was fabricated through this process (see Fig 2.13). The aspect ratio of the liquid ink is lower, typically 1 to 1: minimum values 10 mm x 10 mm. The drying depends only on solvent evaporation and the slurry does not set immediately on leaving the nozzle of the pen; consequently, the definition of features is poorer than in the FDT. Surface roughness of features fabricated through this route is likely to be poorer than spin coated PZT thick films. In addition, line widths of >400 µm are not sufficiently fine enough to fabricate the devices that are required for this project.

Direct patterning of crack free PZT thick films (80-130 µm) onto Si/Ti/Pt substrates has been accomplished with microstereolithography [92], in which a computer controlled stage, suspended in a photo-curable solution, was positioned below a focused Ar^+ laser beam. The laser beam was stationary but the stage could be moved in x, y and z directions. In addition, a blade was added to the apparatus to control layer thickness of the photo-curable suspension before polymerisation with the laser. The photo-curable solution consisted of commercial PZT powder (1 µm), UV curable monomer, photo-initiator, surfactant and solvent; the solution was ball milled before patterning could take place. It has been claimed that the Ar^+ laser was focused to spot sizes of 1-2 µm although there were no details of line widths achieved in films fabricated by this process. After deposition, PZT films were annealed at temperatures up to 850 °C. No details were given on the shrinkage of these films.

2.3.3 Carving Of PZT

Bulk PZT has been patterned mechanically through both diamond sawing [93] and ultrasonic cutting [94]. Ultrasonic cutting is a machining method using ultrasonic motion and pressure in which small amounts of materials are eroded at a time. For ultrasonic cutting and diamond sawing, cutting is achieved with an array of parallel steel blades and a circular saw respectively. In both processes, a block of ceramic will be cut in one direction, back filled with polymer and then rotated through 90 ° and re-cut. It should be noted that the ceramic is partially cut through leaving a base as a support. Removal of the remaining polymer results in arrays of square pillars. Minimum blade widths for ultrasonic cutting and diamond sawing are 500 and 300 µm respectively. There are two main limitations to these processes: 1, device sizes are too large and 2, cutting is limited to straight edges.

PZT has been patterned through laser ablation with excimer [95-97], copper vapour [95], and Nd doped yttrium aluminium garnet (Nd-YAG) [98] lasers. Copper vapour, excimer and Nd-YAG operate in the visible, UV and visible wavelengths respectively. Copper vapour and excimer lasers [99] have high pulse energies, sharp spot sizes, and low pulse repetition rates; Nd-YAG lasers have much lower pulse energies. High pulse energies and low pulse repetition rates can deposit energy into a material on a shorter time scale than is needed for thermal diffusion; ablation of irradiated material can occur before the heat can spread and cause local damage. Bulk PZT ceramics have been micromachined with XeCl [96] and

KrF [97] excimer lasers to minimum focal widths of 50 and 200 μm respectively. Surface damage was observed about laser cut grooves in bulk PZT [96]; grooves were cut with excimer laser radiation of 50 μm focal width and fluences of 10.8 J/cm^2. The damage was attributed to the melting of the PZT about the groove from the low fluence tail of the line of focus [96]. It should be noted that etching did not occur without surface damage. In the case of micromachined PZT thick films, cuts were achieved with aspect ratios of 5:1 with depths up to 50 μm with a KrF excimer laser [95]. Micromachining was also attempted with copper vapour lasers, but a significant heat affected zone was observed beneath the cut. The size of the heat-affected zone is important as de-poling of the PZT can occur locally. It should be noted that the base of the cut zone has not been fully resolved with this process. If the process was to be used for the removal of material to yield a bare Pt electrode for electrical contact, it is unclear how well excimer lasers would work.

In order to reduce the effects of the heat affected zone bulk PZT prepared from the conventional powder processing (PZ26 from Ferroperm) was patterned with water cooled laser ablation [100]. Etching of PZ26 was conducted with Nd-YAG laser at a wavelength, spot diameter, frequency, fluence and pulse length of 1064 nm, 50 μm, 1 kHz, 59 J/cm^2 and 180 ns respectively. However, thin inter-penetrating platelets were observed to grow on the surface of the bulk ceramic, about the etched zone. The platelets had a thickness of 50-160 nm with a lateral size up to 60 μm.

Bulk PZT has been patterned through laser assisted chemical etching [101] in which an Ar^+ laser was used to increase etch rates of PZT in acids and alkalis. The laser was operated at 1 W power output. Acids, HCl (35%) and H_2SO_4 (95%), were found to vaporise and condense on the lens of the laser. Bases were found to be more effective for the etching of PZT: KOH (10 mol/L) exhibited an etch rate of 150 μm/s. Features were patterned with line widths down to 50 μm with no surface damage. However, it will be discussed, subsequently, that KOH damages the interface between PZT and substrate; consequently, laser assisted etching of PZT was considered an inappropriate technique.

Laser micromachining can achieve good control over the dimensions of patterned features. It is unclear how effective laser micromachining is at removing PZT from the base of etched cavities. Resolution of etched cavities is essential to make electrical contact to the back electrode.

Reactive ion etching of PZT has been reported for sol gel thin films on Si/Ti/Pt substrates [102-105] and bulk ceramic [106] respectively. PZT thin films have been selectively patterned with a reactive SF_6 plasma [104]. Physical sputtering with an Ar plasma has been used to selectively pattern Ti/Pt back electrodes [19]. Patterning of bulk PZT has been carried out through a deep reactive ion etching technique [106]; however, this is not to be confused with DRIE used for the micromachining of Si. The deep reactive etching of PZT, unlike DRIE, involves no passivation step; accordingly, there is no formation of fluro-polymers. Features were etched with aspect ratios of 1:1 with line widths of 10 μm using a SF_6 plasma. This presents the possibility of patterning PZT thick films with SF_6, etching the Ti/Pt electrode with Ar and using DRIE to cut into the Si substrate.

A concern with RIE patterning of PZT thin films has been the effect of the reactive plasma on the ferroelectric properties of the final film [105]. Ar and Cl_2 plasmas selectively removed Pb^{2+} whilst CF_4 was found to selectively remove Zr^{4+} and Ti^{4+} from the sidewall of the etched thin film. There was also evidence of surface contamination of PZT with residual Cl^- and F^-. These effects become more significant as the size of feature is reduced. In the case of dense thick films and bulk PZT, 10 nm is relatively unimportant. However, in the case of PZT thick films that have been prepared through the composite slurry route there may be open porosity. Ions, reactive and otherwise, may enter the internal structure of the film depleting or doping at grain boundaries. The extent that RIE will damage a PZT thick film is unclear.

Wet chemical etching combined with standard photolithography has been used to successfully pattern PZT thin films on Pt/Ti/Si substrates [107]. The PZT was fully removed without damaging the underlying Pt. Wet chemical etching is likely to be superior to RIE in that no doping or depletion of the PZT occurred during etching. The advantages of wet etching over laser micromachining is the absence of a heat-affected zone about the etching site, and full removal of PZT from the base of the etched cavity. However, wet etching can result in an undercut of the PZT. This is important for example in thin-film-devices where precise control of the etched feature is essential. A further disadvantage of wet etching are the chemicals that are used, for example HF(aq); HF(aq) is both highly toxic and highly reactive, and can degrade photoresists and back-electrode-materials.

PZT thick films have been patterned through jet machining [87]. A green ceramic tape of thickness 1 mm, consisting of PZT powder and binder, was laminated with a photoresist. The photoresist was patterned with a standard photomask and developed. The tape was structured by repeated scanning with a solvent-air jet: yielding grooves of 140 μm width and depths of up to 650 μm. After patterning, the photoresist was stripped and the PZT was sintered (at 1250 °C). The advantage of jet machining is that round or square holes can easily be cut into PZT. However, this technique cannot be applied to pattern brittle materials.

Powder blasting is an alternative route that allows rapid erosion of brittle materials and has previously been applied to glass [108-112]. Powder blasting and jet machining are similar: a high-pressure jet erodes surface material. However, in powder blasting the jet carries a high velocity stream of abrasive solid particles. Mechanical etching results as the sum total of many single-particle-impacts at the substrate surface.

To date there has been only a small number of publications in which powder blasting has been applied to microsystems. Micro-cantilevers have been fabricated [108] with a dimension of 5 x 2 mm in glass for sensor applications. Micro-fluidic channels of (length) 7000 μm by (width) 100 μm by (depth) 20 μm have been fabricated in glass [108,111]. Micro-pores of 250 μm radius have been fabricated in glass [112]. Powder blasting has been used previously to fabricate a capillary electrophoresis device [113] in which channels of 6 cm by 85 μm with a depth of 20 μm were cut in to a glass substrate.

3 Aims & Objectives

The main objective of this project is to design and fabricate a range of high displacement piezoelectric actuators. The intended actuators are for use in a piezoelectric-actuated membrane-micro-pump. The heightened displacement will yield an increase in stroke length of the membrane, and thereby an increase in the volume of fluid that can be displaced through pumping. Spiral wound beams contain large lengths contained within compact areas, and it is anticipated will exhibit large deflections. Unfortunately, the large tangential deflections that have resulted from piezoelectric spiral actuators, of the type shown in Fig 2.13, cannot be used for membrane actuation. Blocking force and deflection are enhanced in straight unimorph actuators by the rigidity of the mechanical support (see APPENDIX III). The rigidity of a spiral beam is greater than that of a straight bar, and therefore it is likely that spiral unimorph actuators will exhibit greater blocking forces and deflections than straight unimorphs.

There have been, to date, no FE models of spiral wound piezoelectric unimorph actuators with the actuator being engineered to deflect out of the plane. In addition, there have been no such actuators fabricated. Therefore, there is no data on how such actuators will behave, and how their shape will effect performance. A requirement of this project is to devise a FE model of a piezoelectric actuator to investigate and compare performance with linear unimorph actuators. Experimental data from actuators is required to interpret the models.

The actuators were intended to be fabricated with PZT thick film technology, allowing very long and thin actuators to be made. Spin coating will yield precise control over the thickness of the conformable coating.

Inconsistencies in the fabrication, concerning the oxidising effect of the atmosphere, needed to be resolved before actuator fabrication. Why was it, when infiltrated films were sintered under a reducing atmosphere, that the intermetallic formed, yet the intermetallic did not form in non-infiltrated thick films sintered under the same atmosphere? Why did non-infiltrated films yield poorer electrical results when sintered under a higher oxygen partial pressure? If, in infiltrated films the infiltration improves density, then why should films with m=5 layers exhibit poorer electrical properties than those with m=1? How can the density and electrical properties of the films be improved without damaging the electrode-substrate interface? In short, in order to maximise electrical properties the density of thick films needs to be improved such that the back electrode is continuous, a continuous back electrode being essential to the operation of piezoelectric actuators. In order to apply the PZT thick film technology the technology needs to be developed to a state where it can be applied; therefore, the difficulties regarding the high temperature processing of PZT thick films need to be resolved.

PZT thick films will be prepared on silicon substrates. The films and support will require processing to yield actuators of the desired size and shape; therefore, PZT thick film processing must be integrated with silicon microfabrication technology. The PZT thick films require patterning, to this end, both powder blasting and wet chemical etching will require incorporation into the processing route.

4 Experimental

4.1 Generic Experimental Procedures & Equipment

This section of the experimental chapter sets out the standard procedures and standard equipment that was used throughout this project. This section is divided into two subsections: one covering synthesis and the other covering analysis. Synthesis tools and processes describe both the experimental equipment used and the method of fabrication employed in the manufacture of the actuators. The analysis subsection covers both equipment and methods used in the analysis of materials and devices.

4.1.1 Synthesis Tools & Processes

4.1.1.1 Spin Coaters

PZT thick films were deposited onto Pt/Ti/(Si or Si_3N_4/Si) or Pt/Ti/BARRIER LAYER/(Si or Si_3N_4/Si) coated substrates using a Headway Research Inc. CR315 spin coater. The deposition was made through the spin casting of a 0-3 composite slurry onto platinised silicon wafers. Photoresist deposition, mask cleaning and substrate cleaning were completed using an Electronic Micro Systems Ltd., Model 4000 spin-coater. The PZT deposition was kept separate from other spin coating steps to prevent powder contamination of the CR315 spin coater.

4.1.1.2 Wafer Cleaning

A compressed air gun was used to remove any dust particles from the wafer surface before placing the wafer into the spin coater. Substrates were squirted with acetone and IPA during spin coating (4000 rpm / 60 s). The substrate was dried on a hot plate at 115 °C for 50 s, evaporating the remaining solvent from the sample surface.

Residual organics were stripped from the surface of the sample by plasma ashing using a VG Microtech Polaron PT7160 Plasma Barrel Etcher. An O_2 plasma was used at 20 W for 3 min to remove organic residues. Reactive oxygen ions from the plasma react with organic residue on the wafer surface to yield volatile organic species. The organic species are subsequently removed from the vacuum chamber by the vacuum pump. This process is ideal for removing organic residues such as undeveloped photoresist left after patterning, grease or residual solvent (acetone or IPA) after spin cleaning.

4.1.1.3 Mask Cleaning

Masks were cleaned before and after use. An air gun was used to remove unwanted dust from a mask before placing the mask onto the mask cleaning chuck in the spin coater.

The mask was spun at 700 rpm and was squirted with acetone and isopropyl alcohol (IPA). After spin coating, the mask was dried with compressed air before storage or use.

4.1.1.4 Mask Aligner

All mask alignment in this project was completed with the Karl Süss 423000 (double side mask aligner. The exposure time was the only variable, and depended only on type of photoresist used, its thickness and the optical properties of the substrate.

4.1.1.5 Sputtering System

The Nordiko sputtering system was used to deposit thin layers of metals through either RF or DC sputtering. Metallic targets used in this project, their properties and applications are listed in Table 4.1. All sputter depositions were conducted with Ar as the inert gas with a base pressure on the Penning gauge of 5 x 10^{-7} torr and a sputtering pressure of 0.001 torr.

Target	Type	Deposition Rate / nm/s	Electrical conditions	Thickness / nm	Purpose Of Layer
Cr	RF	1.60	200 W	300	Back face protection
Cr	RF	1.60	200 W	5	Adhesion layer electrode
Au	RF	0.42	100 W	100	Surface electrode
Ti	RF	0.29	300 W	200	Diffusion barrier
Ti	RF	0.29	300 W	8	Adhesion layer electrode
Pt	DC	1.72	0.725 A at 425 V	200	Back electrode

Table 4.1 Sputtering conditions used for the Nordiko system. Also given are the applications of the layers deposited, and the thickness of sputtered layers.

4.1.1.6 Barrier Layers

It will be discussed, subsequently, that Pb diffusion results in the delamination of PZT thick films from their substrates. To eliminate detachment diffusion barriers were investigated. Two systems were of interest. The first system was YSZ and the second was TiO_2.

4.1.1.6.1 EBPVD (Electron Beam Physical Vapour Deposition) Deposition of YSZ Coatings

Yittria Stabilised Zirconia coatings were made using an Electrotec, Electron Beam- Ion Plating Vacuum System, No. CL 680. The system consisted of an upper and a lower vacuum chamber. Samples were loaded into the upper chamber into an oven fixture and supported over a shutter system. A stand was fabricated from stainless steel to support 4" wafers at a maximum chamber height of 12" above the shutter (Fig 4.1). The lower chamber consisted of an electron beam gun that was used to vaporise the melt and coat the wafer. The stand was designed to position the sample at a maximum height above the melt, such that the intensity of the cone, of the vapour, was as evenly distributed as possible. YSZ coatings were deposited at 1 μm thickness with conditions listed in Table 4.2.

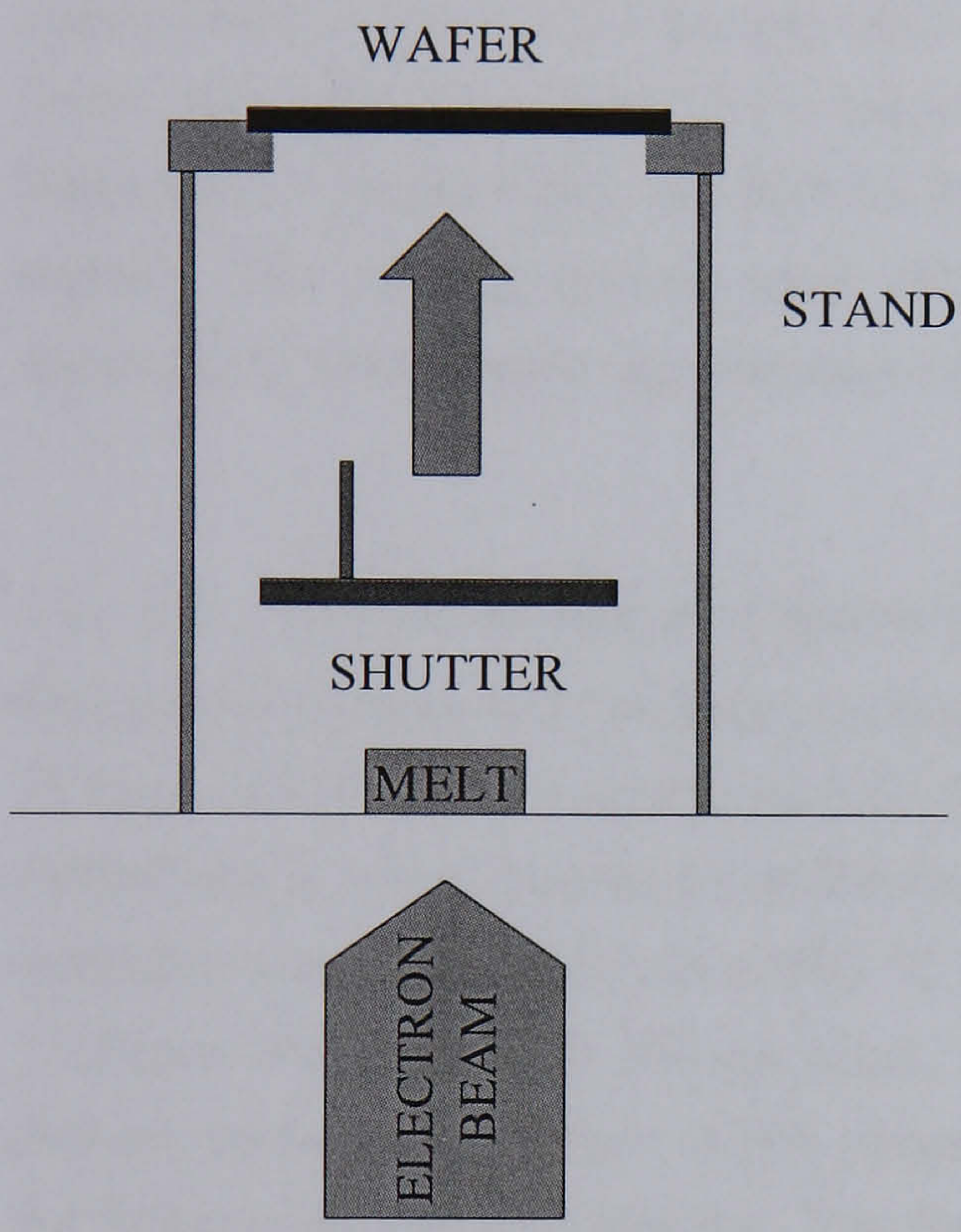

Fig 4.1 Experimental set up for the deposition of YSZ by EB-PVD. The wafer face, to be coated, is supported face down by a stand. The melt is vaporised by an e-beam. The exposure time of the experimental sample is controlled by a shutter.

Exposure time / s	Upper chamber Pressure / 10^{-3} Torr	Temperature / °C	Flow rate of $Ar+O_2$ / $cm^3.min^{-1}$	Potential difference / kV	Beam current / A	Lower chamber Pressure / 10^{-4} mbar
40	7.0	730	185	10	0.45	3.4

Table 4.2 Conditions used for the deposition of YSZ films. These conditions were employed irrespective of the substrate material.

YSZ was prepared on both substrate systems, Si and Si_3N_4, by EB-PVD deposition with a YSZ $((YO_2)_{0.18}\ (ZrO_2)_{0.82})$ melt. The experimental process was based on the literature

[64,66,114] in which 100 nm YSZ coatings were deposited by EB-PVD onto Si <100> substrates. Deposition conditions were discussed by Matthee et al [114] where YSZ was grown on Si at 700 °C at an oxygen partial pressure of 1 x 10^{-5} mbar. For YSZ to be grown, through epitaxy, on the Si substrate, the native oxide was stripped through EB-PVD deposition of Zr according to (4.1), Chromik et al [66].

$$Zr + 2.SiO_2 \rightarrow ZrO_2 + SiO \qquad (4.1)$$

Thin films were deposited at 700 °C in an air/argon atmosphere, using the conditions summarised in Table 4.2. The only difference with the literature [66] and the fabricated YSZ layers was that no sample pre-treatment other than surface cleaning was used before deposition. Consequently, the surface oxides would have remained intact on the substrate surface. The coating system used had been set up for TBC coatings of 250 μm in thickness. Consequently, the minimum attainable thickness was 1 μm.

4.1.1.6.2 Thermal Oxidation of Sputtered Ti to Yield TiO_2 Coatings

Thermal oxidation of Ti to TiO_2, on both substrates, yielded a stable diffusion barrier. A Ti layer of 200 nm was sputtered onto both substrate systems, and thermal oxidation was carried out in a box furnace (PyroTherm Box furnace No. I-Temp 16/b). Further, thermal oxidation was executed in air at 700 °C for 10 minutes; the ramp rate up and down was at 3 °C/min. The oxide was 300 nm thick. The slow ramp rate had been selected to minimise thermal stress in the barrier. Al_2O_3 supports were used to keep the samples off the base of the furnace floor during heating. The low heating rates were employed to reduce thermal stress during heating.

4.1.1.7 PZT Thick Film Fabrication

4.1.1.7.1 Sol Synthesis

The sol-gel synthesis has been discussed in chapter 2, and the reader is referred to Fig 4.2 for an overview of the process.

Two precursor stock solutions are prepared for the A and B-cation. The A-cation is the Pb precursor solution, and the B-cation is the precursor solution for the following: Ti, Zr and the doping ions. The proportions of constituents of A and B-cation solutions are given in Table 4.3 and Table 4.4 respectively.

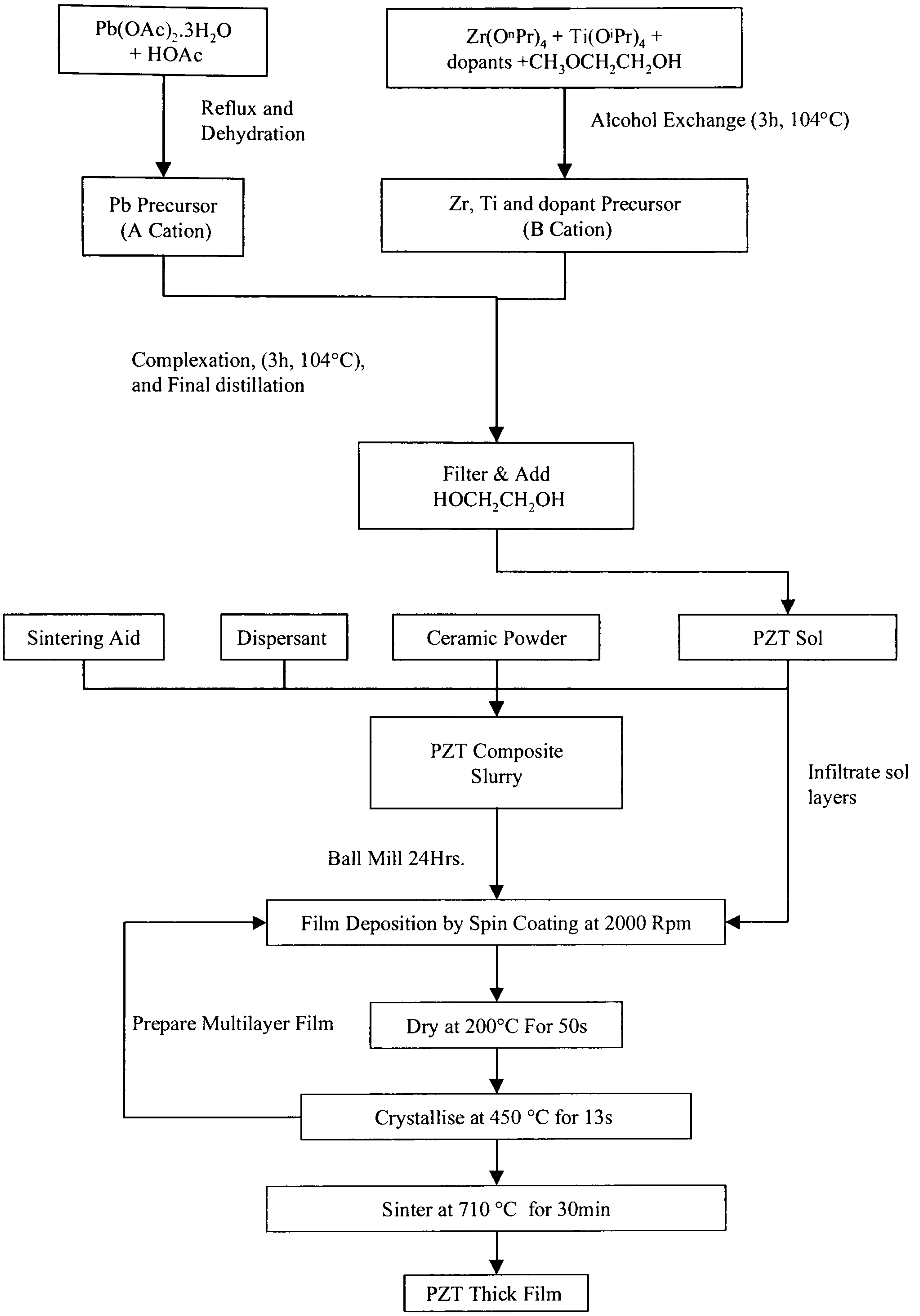

Fig 4.2 Process of PZT thick film fabrication. The process incorporates a layering or infiltration step with metal organic sol. It should be noted that that the drying or crystallisation steps may be omitted. Sintering can be done under Ar or air.

Components of A-cation	Supplier	Mass / g
$Pb(OAc).3H_2O$	Aldrich	52.5
HOAc (glacial acetic acid)	Aldrich	30 ml

Table 4.3 Components of A-cation (Pb Stock solution)

Components of B-cation	Supplier	Mass / g
$Ti(O^iPr)_4$	Aldrich	17.99
$Zr(O^nPr)_4$ (@ 76% purity)	Aldrich	26.31
$Sb(OEt)_3$	Inorgtec	0.64
$Nb(OEt)_5$	Inorgtec	0.79
$Mn(OAc)_2$	Inorgtec	0.427
$CH_3OCH_2CH_2OH$	Aldrich	50 ml

Table 4.4 Components of B-cation (Ti, Zr & Doping ions)

The sol was prepared to the same composition as the ceramic powder (PZ26 from Ferroperm), ensuring a homogeneous composition throughout the film. The PZT compositions employed in this project were prepared with a 2:1 ratio of donor to acceptor substituents in order to achieve high piezoelectric constants with low dielectric losses.

The A-cation solution was prepared with 5% excess Pb, and this was the case for all sols used in this project. Lead acetate tri-hydrate ($Pb(OAc)_2.3H_2O$) was placed into a round bottomed flask (250 ml) and glacial acetic acid (HOAc) was added, i.e. 52.5g and 30 ml respectively. The flask was incorporated in to a reflux set-up, the glassware was checked for leaks, and the system purged with dry $N_2(g)$. Refluxing was begun, and timed for 3 hours, from the point when droplets began to form on the coil of the condenser.

Following reflux, the A-cation flask was cooled to room temperature. Subsequently, the A-cation solution was distilled at 102°C to 104°C. The distillation was run until 20 ml of distillate had been removed. Following distillation, the A-cation flask was cooled to room temperature; before sealing under dry $N_2(g)$, with a screw cap lid to prevent contact with atmospheric water.

The B-cation precursors, in Table 4., were added to a clean, dry, round-bottomed flask (250ml). Mixing was conducted under dry nitrogen in a glove box, preventing contamination by atmospheric water. Following mixing the flask was sealed with a screw cap and removed from the glove box. The B-cation flask was set up for reflux.

It was important at this stage to ensure that all glassware was free from leaks, and that the flask was completely sealed from the air. Reflux was set underway and again timed for 3 hours from the point where droplets form on the base of the coil of the condenser column.

At the end of reflux, the flask was cooled to room temperature, before sealing with a screw cap under flowing $N_2(g)$. Both A and B-cation flasks were removed to the glove box.

The contents of the B-cation flask were added to the A-cation flask. The combined A and B-cation flask was then sealed with a screw cap and shaken vigorously before removal from the glove box. This flask was then incorporated into a reflux set-up, again under $N_2(g)$ with all glassware and seals being checked for leaks. Again, the reflux was run for 3 hours, from the point where droplets formed on the coil of the condenser. Ten minutes after the start of reflux, precipitation was observed; this precipitate was probably $Pb(OAc)_2$ or $Mn(OAc)_4$. This reflux corresponds to the final complexation stage shown in Fig 4.2. Following completion of the reflux, the flask was cooled to room temperature. When cool, the flask was sealed under $N_2(g)$ with a screw cap and stored in the glove box overnight.

The next day the flask was removed from the glove box before being set up for the final distillation under vacuum. In order to ensure no contamination from atmospheric water the setting up was carried out under flowing $N_2(g)$. The distillation was started and held at 84°C, before being allowed to steadily increase to a final hold temperature (102°C to 104°C). The temperature was controlled with a heating mantle (set to level 3 for 102 – 104°C and level 2.5 for 84°C). The distillation was allowed to proceed until a clear sol was formed, and the distillation was continued for another fifteen minutes thereafter. It should be noted that the final distillation usually takes between 4 – 5 hours and a full day is needed to complete it.

Following distillation, the sol was cooled to room temperature. A volume of 2-methoxyethanol equal to that of the distillate was added to the sol. Ethylene glycol ($HOCH_2CH_2OH$ Aldrich) (5g) was added to a glass bottle (500 ml) with a screw cap. The bottle was sealed, and a vacuum filtration was set up. The cold sol was vacuum filtered into the glass bottle to remove any solid precipitates; subsequently, the bottle was sealed under $N_2(g)$,and the sol was aged for 24 hours before use.

Metal organic sols were kept for a maximum duration of one month. It was thought that prolonged ageing of the sol would have a detrimental effect on the observed properties of fabricated PZT thick films.

4.1.1.7.2 Slurry Preparation

The sol was incorporated in a composite slurry, a mixture of sol and PZT powder, in the proportions given in Table 4.5. The reader is referred to Fig 4.2 for the slurry preparation.

Component	Supplier	Mass / g
Sol	N/A	30ml
PZ26 Powder	Ferroperm	45
PbO	Aldrich	1.926
Cu_2O	Aldrich	0.3105
KR55	Kenrich	0.9

Table 4.5 Components and proportions of the slurry

It should be noted that PZ26 powder is a PZT powder with the same composition and doping ions as the sol. The PZ26 powder has a particle size of 0.6 μm, and was supplied by Ferroperm S/A. PbO and Cu_2O were used as the sintering aid, where their summed weight was 5% of the powder weight. The sol-to-powder ratio was 1:1.5.

The dispersing agent used was KR55; essentially this is a titanium coupling agent. The coupling agent has a reactive head group and an a-polar tail group. The coupling agent binds to the powder via hydrolysis and condensation. The powder surface was then stabilised in the organic solvent via the large tail of the coupling agent.

The above components were weighed into a glass bottle (150 ml) in the glove box. Into the glass bottle was placed YSZ pellets (200 g), the bottle was sealed, removed from the glove box and ball milled for 24 hours. Ensuring that agglomerates were, as far as possible, dispersed in the slurry. After ball milling, the slurry was ready for use.

4.1.1.7.3 Film fabrication

A wafer substrate was placed in the CR315 spin coater, and a quantity of slurry was pipetted onto the Pt surface of the electroded substrate. The wafer was then spun at 2000 rpm for 30 s. Films of the form: $4[C^{200,450}+4S^{200,450}]$ are prepared, unless otherwise stated in the text. The substrates employed in film fabrication were Si/YSZ/Ti/Pt, unless otherwise stated. Layers are built up to achieve the desired thickness of film.

Intermittent drying steps for sol and composite layers were conducted on conventional laboratory hot plates. Unless otherwise stated all layers were dried and crystallised at 200 °C (50 s) and 450 °C (15 s) respectively.

PZT thick films were sintered through Rapid Thermal Annealing (RTA) using an AG Associates Heat Pulse 210 furnace. The RTA furnace was wired into gas supplies of compressed air, N_2 and Ar. PZT thick films sintered in this project were sintered under air or Ar atmospheres at a flow rate of 30 l/min. All films were sintered for periods of 30 minutes. Most films were sintered at 710 °C; however, some were sintered at 800 °C and

900 °C, it will be specified where other conditions were employed. The ramp rate employed, for all films, was 30 °C/s. The sol was diluted to 50 % for the infiltration of S layers; however, there was no dilution of the sol component of the composite slurry.

4.1.1.8 Poling

Corona poling was employed in this project to pole the PZT thick films. Essentially a large voltage is applied to a needle, or an array of needles, suspended at a given height above a ferroelectric sample on a grounded plate (see Fig 4.3). The brass plate is masked about the rim of the sample with PTFE: ensuring that the flux of the field passes through the sample.

The poling set-up employed in this project involved an array of 16 needles suspended at a height of 4 cm above the wafer. The voltage used was 20 kV and samples were poled for 10 minutes (at 120 °C). Only PZT thick films on 10 cm diameter device wafers were poled.

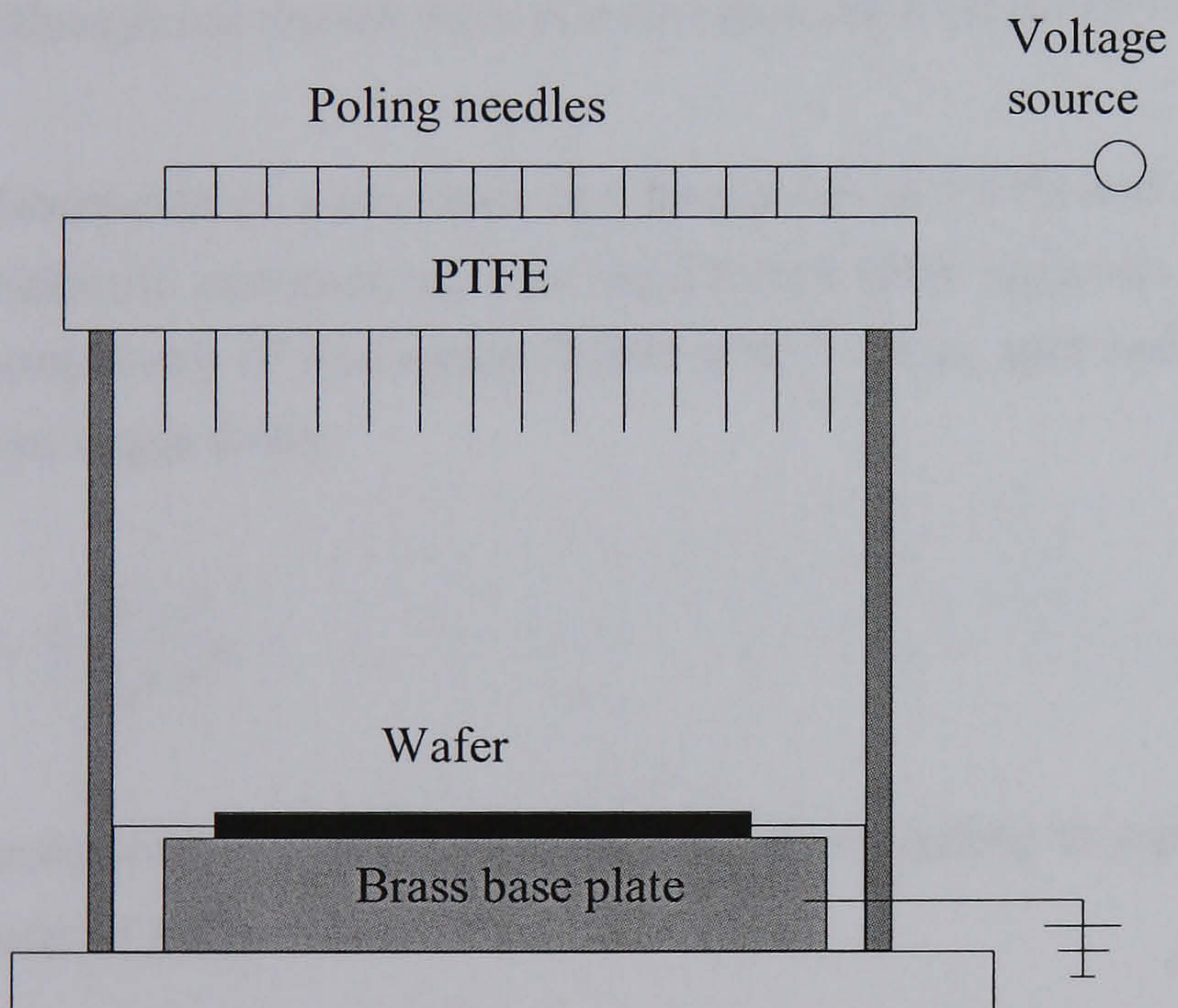

Fig 4.3 Corona discharge poling apparatus. A wafer is placed on an earthed base plate and masked by PTFE. The plate is heated and a voltage is applied to an array of needles.

4.1.2 Analytic Tools

4.1.2.1 Electrical Measurements

Electrical measurements presented in this thesis were conducted using a Research Instruments Probe Station. This consisted of two pin contacts wired to shielded BNC cables for contact to suitable measurement stations.

4.1.2.1.1 Resistivity, Dielectric Constant & Dielectric loss

After fabrication, PZT thick films were electroded with Cr and Au spots of 2 mm diameter by vacuum evaporation. Electrical properties (C_A, capacitance; R, resistance and tanδ, dielectric loss) were measured spot to spot, see Fig 4.4, using a Wayne Kerr 6425 Precision Component Analyser connected to the probe station via the BNC cables.

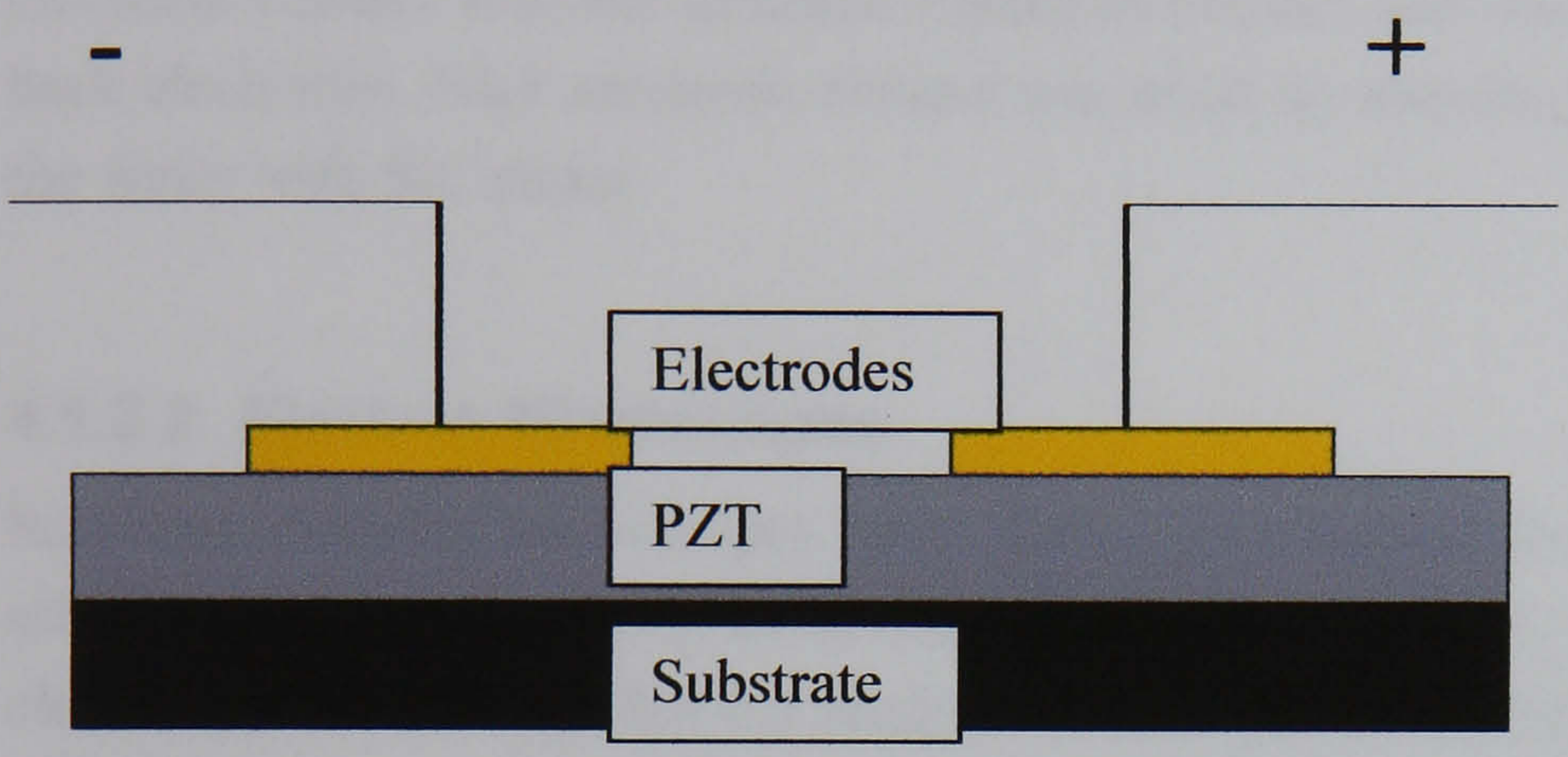

Fig 4.4 Point to point contact for dielectric measurements for PZT thick films. Although not shown there is a common back electrode at the PZT substrate interface.

Measurements were made at a frequency of 1 kHz and a potential difference of 100 mV. Dielectric constant, ε_r, was determined from equation (4.2), where ε_0, r and h are the permittivity of free space (8.834×10^{-12} F/m), spot radius and the thickness of the thick film respectively.

$$\varepsilon_r = \frac{C_A.h}{\varepsilon_0 \pi . r^2} \tag{4.2}$$

Resistivity, ρ_v, was measured from R according to equation (4.3) and was expressed in units of MΩm.

$$\rho_v = \frac{R.\pi . r^2}{2.h} \tag{4.3}$$

It should be noted that in the case of two spots on the surface of the PZT with a common back electrode the length between the two spots will be 2h, where h is the thickness of the PZT thick film.

4.1.2.1.2 Admittance Spectra

Admittance analysis was conducted with a Hewlett Packard HP4192A admittance analyser. Admittance scans were run from 1 to 100 kHz at 1V and phase angle and admittance were plotted as functions of frequency. A probe station was employed to make electrical contact with the samples. Electrical contact was made between the surface and back electrodes. Back electrode contact was made by abrading the PZT from one edge of the wafer with SiC paper.

4.1.2.2 Electron Microscopes

Scanning electron microscopes only detect information from electrically conducting surfaces. Hence, electrically insulating surfaces, such as PZT, must be coated with a thin, electrically conducting film for analysis to take place. All SEM samples were sputtered with Au/Pd (using a Polaron Equipment Ltd. SEM coating Unit E500).

Samples were secured to stubs with conductive epoxy resin, and the sample grounded to the stub (Fig 4.5). For fracture cross sections, the sample was diced before mounting. A metallic clip was used to hold the sample vertically and the sample was glued in place with conducting epoxy. Electrical contact between the sample and the base of the stub was made with conductive epoxy.

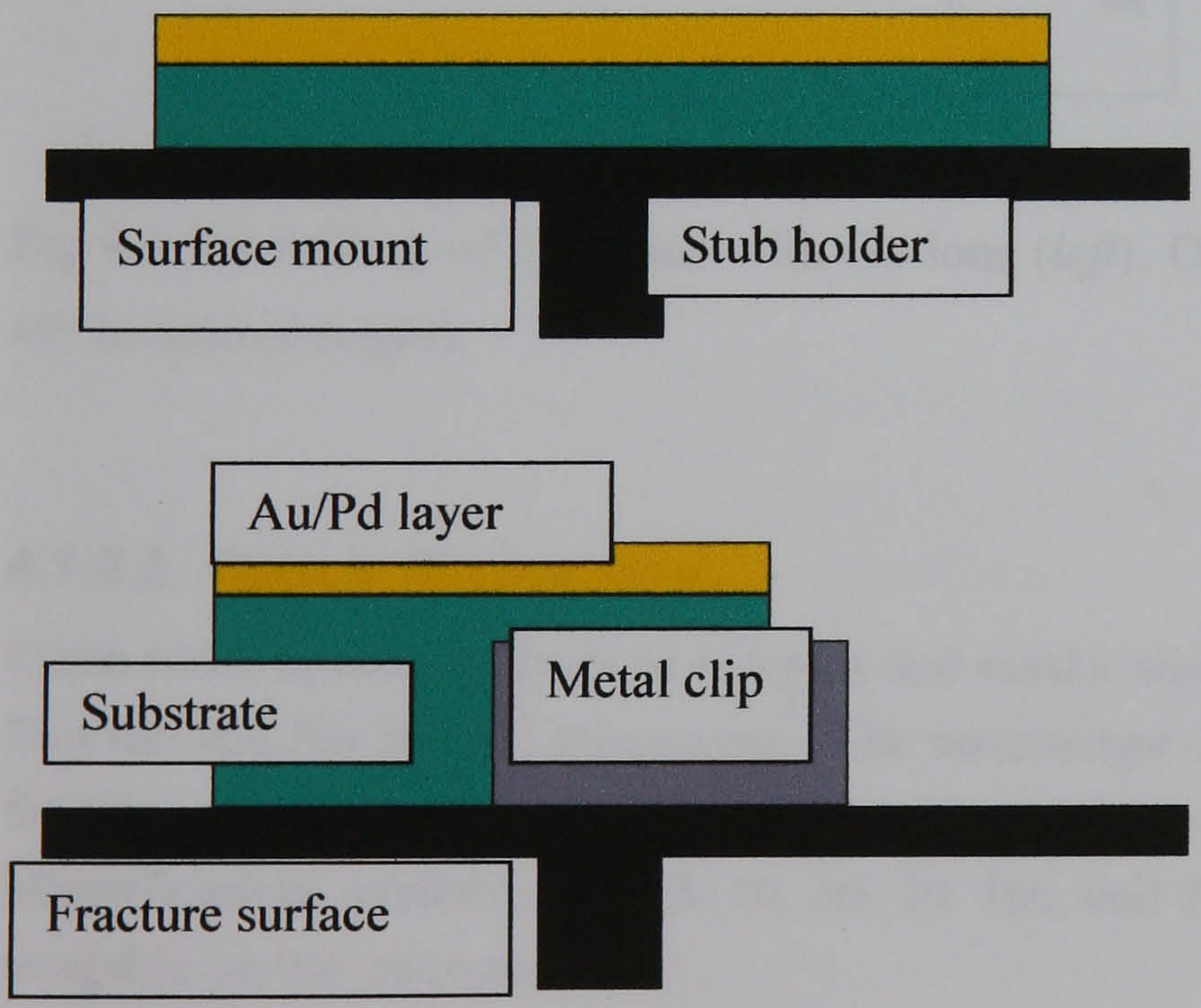

Fig 4.5 Stub mounting of SEM samples. Surface mounting is shown *top*, and fracture surface mounting is shown *below*.

Early project analysis was conducted using the Cambridge Instruments ABT 55 and Stereo Scan systems. The arrival of the Philips SL30 SFE G (scanning field emission gun) mid way through this project permitted higher resolution of micrographs. The Cambridge Stereo Scan and Phillips SFE G were both equipped with EDX for local chemical analysis. The SFE G system has an additional advantage over the Cambridge system in that it is equipped to detect carbon and oxygen.

A focused ion beam microscope (FIB) etches samples with a focused beam of Ga ions. There is a detector for scattered Ga ions. This permits visual imaging during the etching process. The FIB microscope, Phillips FIB 2000 was used mainly for interface analysis between PZT thick films and the substrate.

A trench would be cut into the sample surface to the desired depth. The sample would then be tilted to an angle of 45 ° where the etched film face could be observed (see Fig 4.6). Samples were surface mounted for FIB analysis; however, unlike SEM, no conductive coating was required.

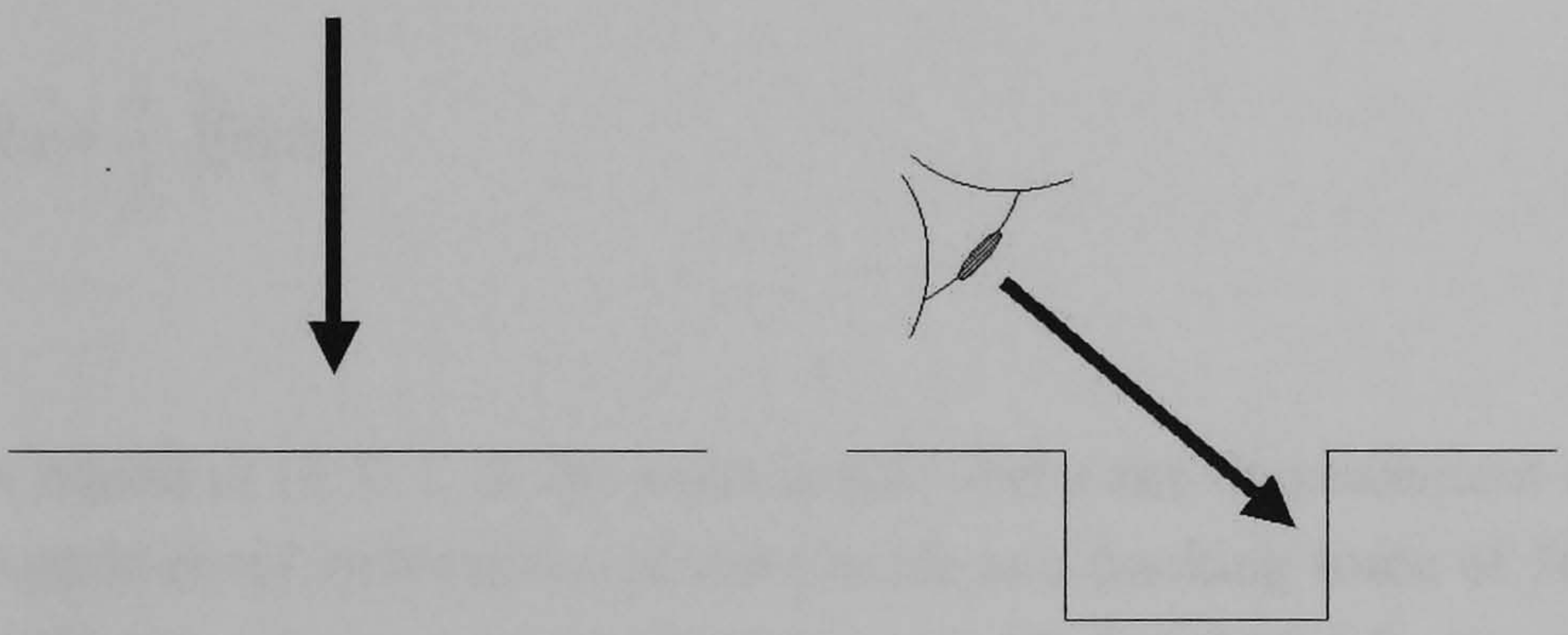

Fig 4.6 Ion milling of a surface with Ga ions (*left*). Observation of the milled surface at 45° to normal (*right*).

4.1.2.3 Optical Microscopy

Clean room optical analysis of samples and masks was conducted with a Reichert-Jung, Polyvar-Met No 300602 microscope. The microscope was equipped with a photographic facility enabling Polaroid photographs to be taken of samples during processing. Magnifications available were 5, 10, 20, 50, 100, and 150 times. No calibrated scale was available on this microscope.

For non clean-room microscopy, the image analyser was used. This consisted of a Nikon Optishot microscope, a JVC KY55 BE 3CCD camera, a standard desktop computer and AcQuis® software from Syncroscopy. This device enables pictures to be taken up to 40 times magnification and to be recorded directly on to electronic format. Software allowed calibrated measurements to be made. Magnifications available were 2.5, 5, 10,20, and 40 times

4.1.2.4 X-Ray Diffraction

X-ray diffraction measurements were conducted on a Siemens D5005 X-ray diffractometer. Measurements were made from 20°θ to 60°θ with a step size of 0.05 °; each step was held for one second. Further, all measurements were made with Cu(Kα) radiation with a slit size on the detector and source of 0.6 and 1 cm respectively.

4.1.2.5 Surface Roughness Analysis

Surface roughness and step heights were measured with a Vecco Dek-Tak 3 Surface Profiler No. 22127. Standard measurements of surface roughness have been discussed [115], in which Ra and Rt are the average and the peak to valley height roughness respectively. Rt is measured directly from the profile scan and Ra may be determined, automatically, from the scan using equation (4.4).

$$Ra = \frac{1}{L}\int^{L} |z| dx \qquad (4.4)$$

In equation (4.4) L is the scan length and z the displacement about an average line. All experimental measurements were made at a tracking force of 30 mg. The scan length was 2000 μm with a vertical resolution of 20 Å/ 1310 kÅ. In order to achieve maximum resolution scans were conducted for 50 s duration.

4.2 Experimental Procedures Non Generic

This section of the experimental chapter covers the specifics of work undertaken in the following chapters. This section is subdivided according to the corresponding chapter. It should be noted that where the work, in a particular chapter, can be defined as experimental development the experimental section for that chapter is contained within that chapter. This section contains details of how the generic processes, discussed in the preceding section, were applied. In other words, this section is about specifics as opposed to generics: what was done, how it was done and why it was done, how the generic processes of fabrication and analysis were adapted etc.

4.2.1 High Temperature Processing Of PZT Thick Films (Chapter 6)

4.2.1.1 Thermal Processing Of PZT Thick Films

PZT thick films were fabricated by spin casting of composite slurries. Infiltrated thick films were fabricated by spin coating (each layer at 2000 rpm for 30 s) the composite slurry onto platinised silicon substrates (Pt (100 nm) / Ti (Ti 8 nm) /Si: Pt/Si for short). In this study, no barrier layer system was used. Infiltrated thick films were of the form S+7(*C*+S)+*C*. Sintering was conducted at low and high oxygen partial pressures Ar and air atmospheres respectively. The experimental variables that were kept constant in this study are listed in Table 4.6.

Parameter	n	m	Spin speed / k.rpm	Drying time (at 200°C) / s	Crystallisation time (at 450°C) / s
Experimental Variable	7	5	2.0	50	13

Table 4.6 Experimental variables that were kept constant during the high temperature analysis of PZT thick films.

For each sinter gas, Ar and air, 3 sets of 3 films were prepared, with one film of each set being sintered at 710, 800 and 900°C respectively. All PZT thick films were sintered in the RTA. A drying temperature of 200 °C and a crystallisation temperature of 450 °C were applied between each coating. Within each set of three films, there were three intermittent thermal treatments; a combination of a drying and a crystallisation step, corresponding to each film in the set. The drying and crystallisation temperatures that were used are encased in the following brackets: ($\beta1=200$; $\chi2=450$), ($\beta1=200$; $\chi1=200$, $\chi2=450$) & ($\beta1=200$, $\chi2=450$; $\beta1=200$, $\chi2=450$). In the preceding sentence β and χ are as they were in equation (2.2). Using equation (2.2), the experiment may be represented by a 3 by 3 matrix to reduce complexity. The parameters **D** and **T** are the matrices of drying conditions and sintering temperature respectively. **Ex** is the matrix of experimental runs and b is the sinter gas and is taken outside the brackets.

$$\mathbf{D}\cdot[\mathbf{T}]_{\mathrm{b}}=[\mathbf{Ex}]_{b} \tag{4.5}$$

Expanding equation (4.5) and expressing for different sintering atmospheres yields equation (4.6) for Ar and equation (4.7) for air atmospheres. Thermal conditions for each fabricated film are contained within curly brackets.

$$\begin{bmatrix} 710^{\circ}C & 800^{\circ}C & 900^{\circ}C \end{bmatrix}_{Ar} \cdot \begin{bmatrix} \beta 1, \chi 1 & \beta 1, \chi 1, \chi 2 & \beta 1, \beta 2, \chi 1, \chi 2 \\ \beta 1, \chi 1, \chi 2 & \beta 1, \chi 1 & \beta 1, \chi 1, \chi 2 \\ \beta 1, \beta 2, \chi 1, \chi 2 & \beta 1, \beta 2, \chi 1, \chi 2 & \beta 1, \chi 1 \end{bmatrix} \tag{4.6}$$

$$= \begin{bmatrix} \{(\beta 1, \chi 1) \cdot 710^{\circ}C\} + \{(\beta 1, \chi 1, \chi 2) \cdot 800^{\circ}C\} + \{(\beta 1, \beta 2, \chi 1, \chi 2) \cdot 900^{\circ}C\} \\ \{(\beta 1, \chi 1, \chi 2) \cdot 710^{\circ}C\} + \{(\beta 1, \chi 1) \cdot 800^{\circ}C\} + \{(\beta 1, \chi 1, \chi 2) \cdot 900^{\circ}C\} \\ \{(\beta 1, \beta 2, \chi 1, \chi 2) \cdot 710^{\circ}C\} + \{(\beta 1, \beta 2, \chi 1, \chi 2) \cdot 800^{\circ}C\} + \{(\beta 1, \chi 1) \cdot 900^{\circ}C\} \end{bmatrix}_{Ar}$$

$$\begin{bmatrix} 710^{\circ}C & 800^{\circ}C & 900^{\circ}C \end{bmatrix}_{Air} \cdot \begin{bmatrix} \beta 1, \chi 1 & \beta 1, \chi 1, \chi 2 & \beta 1, \beta 2, \chi 1, \chi 2 \\ \beta 1, \chi 1, \chi 2 & \beta 1, \chi 1 & \beta 1, \chi 1, \chi 2 \\ \beta 1, \beta 2, \chi 1, \chi 2 & \beta 1, \beta 2, \chi 1, \chi 2 & \beta 1, \chi 1 \end{bmatrix} \tag{4.7}$$

$$= \begin{bmatrix} \{(\beta 1, \chi 1) \cdot 710^{\circ}C\} + \{(\beta 1, \chi 1, \chi 2) \cdot 800^{\circ}C\} + \{(\beta 1, \beta 2, \chi 1, \chi 2) \cdot 900^{\circ}C\} \\ \{(\beta 1, \chi 1, \chi 2) \cdot 710^{\circ}C\} + \{(\beta 1, \chi 1) \cdot 800^{\circ}C\} + \{(\beta 1, \chi 1, \chi 2) \cdot 900^{\circ}C\} \\ \{(\beta 1, \beta 2, \chi 1, \chi 2) \cdot 710^{\circ}C\} + \{(\beta 1, \beta 2, \chi 1, \chi 2) \cdot 800^{\circ}C\} + \{(\beta 1, \chi 1) \cdot 900^{\circ}C\} \end{bmatrix}_{Air}$$

Dielectric constant, dielectric loss and resistivity were determined from the fabricated PZT thick film (see section 4.1.2.1.1). SEM structural analysis of samples was performed using the ABT SEM ABT-55. SEM samples were analysed by means of fracture surfaces. XRD was used to analyse air and Ar sintered films (dried at β=200 °C,450 °C; χ=200 °C,450 °C) for sintering temperatures between 710 to 900 °C.

4.2.1.2 Electrode Substrate Interface

Two substrate systems were of interest for this investigation: Si and Si_3N_4 / Si. Si wafers p <100> were polished on a single side and supplied by Queens University Belfast (QUB). Si_3N_4 coated wafers were also supplied by QUB and the nitride layer was 200 nm thick deposited by LPCVD (low pressure chemical vapour deposition).

It will be argued below that Pb diffusion damages the interface between the PZT thick film and the substrate. Barrier layers are introduced to eliminate Pb diffusion, and maintain the integrity of the interface.

TiO_2 barriers were prepared on both substrates through the route discussed above (section 4.1.1.6.2). YSZ barrier layers were also prepared on both substrates through the route discussed above (section 4.1.1.6.2). Barrier layers were analysed through Cross section SEM on the S FEG and by XRD. The FIB microscope was used to analyse the interface between TiO_2 barrier layers on both Si and Si_3N_4 substrates.

PZT thick films (10 μm), of the form: $3[C^{200,450}+3S^{200,450}]^{710}{}_{Air}$, were prepared on TiO_2 and YSZ diffusion barrier layers on both substrate systems. The barrier layers were electroded with Ti (8 nm) / Pt (200 nm) before deposition of the PZT. The electrode was deposited by sputter deposition in the Nordiko system. Compositional, structural and interfacial analysis of PZT, TiO_2 and YSZ films was conducted by means of XRD, SEM and FIB respectively.

Adhesion of the PZT thick films at the substrate / electrode interface was determined with the FIB microscope (see also Fig 4.6 above). PZT thick films on each of the barrier systems and the experimental standards were analysed by FIB. A list of PZT thick films on differing barrier and substrate systems is presented in Table 4.7.

Sample number	Film composition
Rhsul2	PZT / Ti / Pt / YSZ (1 μm) / Si
Rhsul3	PZT / Ti / Pt / YSZ (1 μm) / Si_3N_4 / Si
Rhsul4 Experimental standard.	PZT / Ti / Pt / Si_3N_4
Rhsul7	PZT / Ti / Pt / Ti O_2 (300 nm) / Si
Rhsul8	PZT / Ti / Pt / TiO_2 (300 nm) / Si_3N_4 / Si

Table 4.7 PZT thick films, and their corresponding reference numbers: corresponding to films prepared on differing substrates.

4.2.2 Device Fabrication And Analysis (Chapter 9)

In this chapter a range of devices is fabricated using the integrated processing route that will be developed in chapter 8. The devices are characterised by admittance spectroscopy and results interpreted with FE.

4.2.2.1 Device Fabrication

Two device wafers, Rh100 and Rh200 were prepared according to the Si-DRIE process (as will be discussed in section 8.3.5 of chapter 8). PZT thick films were prepared according to the standard route (see section 4.1.1.7 above). It was decided to sinter these samples under air as this resulted in films of a greater density. The YSZ barrier layer was found to be superior for Si substrates (this statement will be qualified in chapter 6). The YSZ layer minimising damage to the substrate caused through diffusing Pb.

A 1 μm YSZ barrier layer was grown on a 10 cm diameter Si wafer. A Ti/Pt electrode was sputtered onto the YSZ. The back face of the wafer was coated with a protective Cr layer. Device wafers were not wet etched because of the possibility of pin-holing in the PZT (this will be discussed in section 8.2.3 of chapter 8 below).

A Cr/Au electrode was applied through sputtering and a lift off process was employed for patterning. Subsequently, device wafers were powder blasted to cut desired structures into the underlying Si. The process conditions for powder blasting are introduced in chapter 7 section 7.2.1, below.

The device wafers rh100 and rh200, which were of the form: Si/YSZ/Ti/Pt/PZT/Cr/Au were prepared for DRIE etching. After powder blasting, the SBX® was removed from rh100 and rh200 with the stencil remover. The Cr protection layer was removed from the device wafers with the Cr etching solution before Si etching could take place.

The wafer, Rh100, was spin coated at 2000 rpm for 40 s with AZ4562 (Clariant) photoresist. Rh100 was soft baked at 90 °C for 110 s before UV exposure (25 s) with mask 1 (the mask set will be discussed in section 5.3 of chapter 5 below). The photoresist was developed for 260 s in 20% AZ351B (Clariant) developer solution. The photo patterned sample was secured to a support wafer with vacuum grease before DRIE etching could take place (see Fig 4.7). Etching was continued until all the cantilevers were fully released. Deep reactive ion etching (DRIE) was conducted using the STS Multiplex ASE (Advanced Silicon Etcher) STS35413.

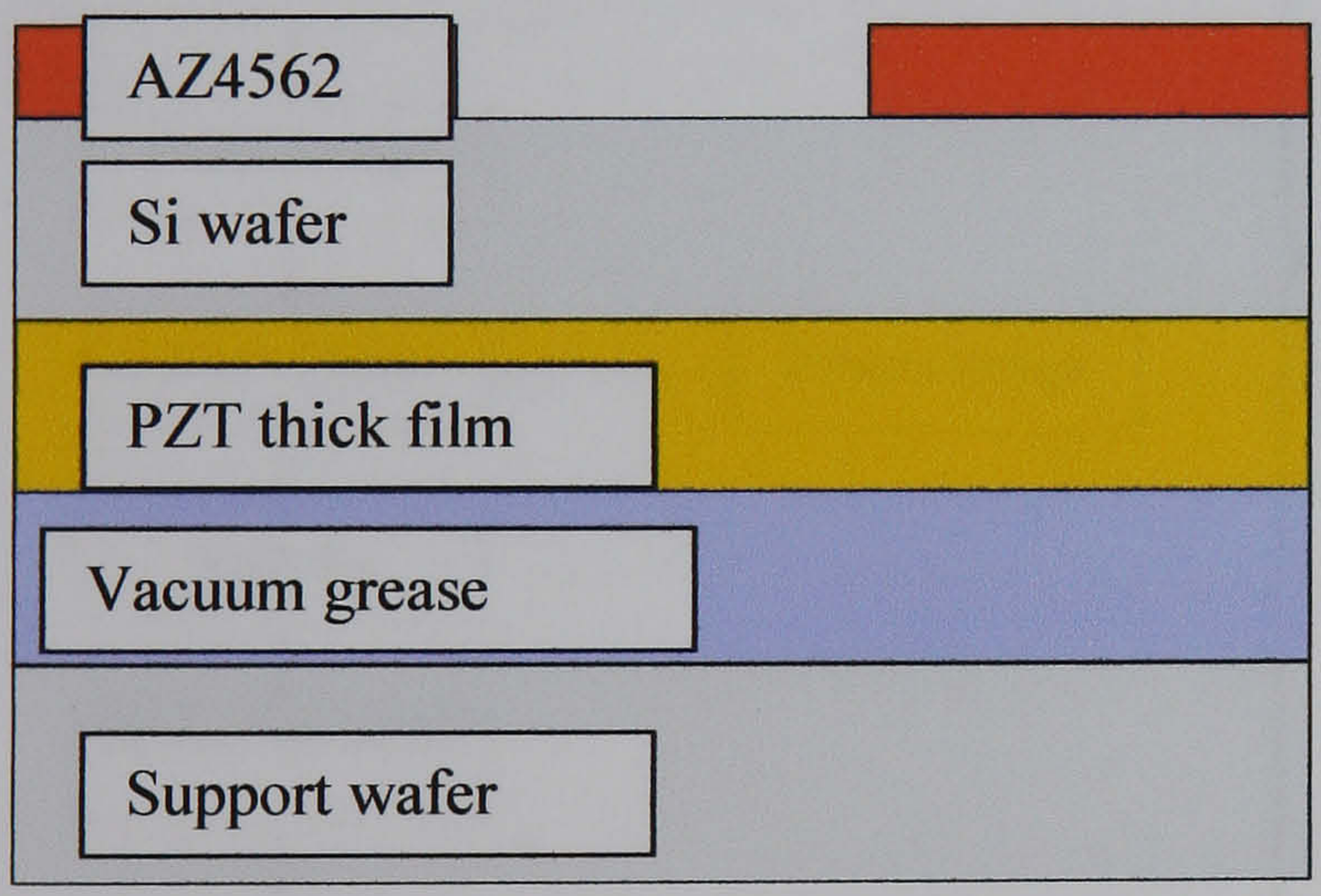

Fig 4.7 Sample mounting for DRIE patterning of Si. This step enables actuator release

4.2.2.2 Device Characterisation

Released devices were characterised by admittance scans of the type discussed in 4.1.2.1.2 above. This data was included for comparison with FE data.

5 Design

5.1 Device Design

5.1.1 Introduction

At the time of the actuator design, there was no finite element (FE) model of a spiral actuator available. Therefore there was no way of knowing what effect the spirals shape would have with respect to the frequency of the first resonant mode, blocking force or deflection. The writing of FE code took much longer than was expected; consequently, analytical models for straight unimorph actuators were used to design devices for incorporation into a mask set. The FE code was eventually finished, but only after the mask set had been fabricated.

With reference to Fig 5.1 analytical models were used to design devices (this chapter). The next stage was to devise a fabrication process (the process design is discussed in this chapter), and to combine this process into the mask design (this chapter). From the mask design, a mask set was fabricated . Devices were fabricated using the mask set (chapter 9), and these devices were tested with impedance analysis (chapter 9). Predictions made through FE were then tested against impedance data and discussed in chapter 9.

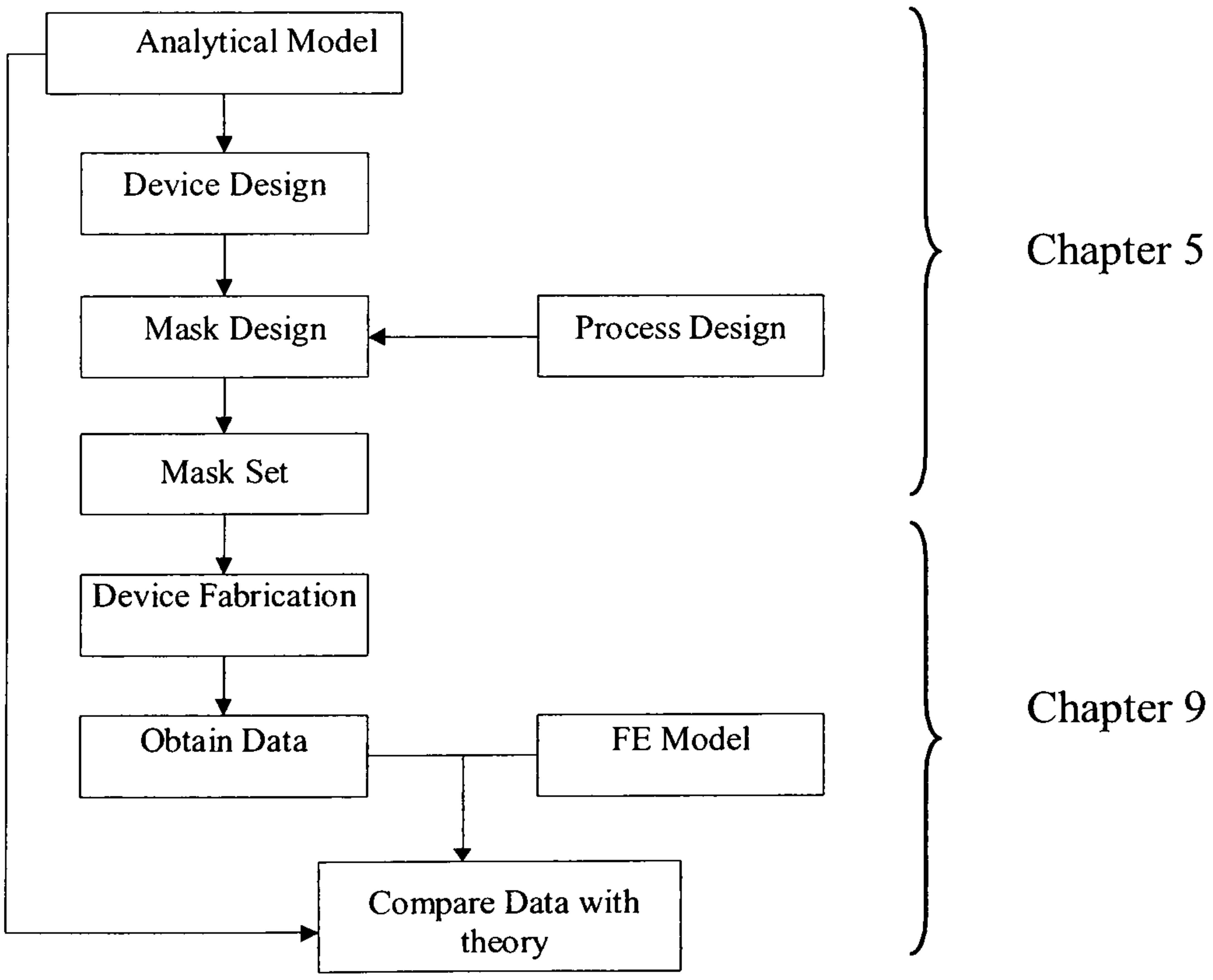

Fig 5.1 Flow diagram for the actuator design process, used in this project. The diagram also shows the stages at which device fabrication, testing, FE modelling and theory/data comparison take place.

All devices were modelled as straight actuators, i.e. straight-unimorph-type cantilevers, where changes in performance arise because of differences in length, width and thickness. The actuators were modelled using analytical-equations that had been derived for straight-piezoelectric-unimorph-cantilevers. Material properties were based on Motorola 3203HD (see APPENDIX IV). At the time of modelling, the data for Ferroperm PZ26 was incomplete; however, a complete set of data has since been published by Ferroperm on their web site and is shown in APPENDIX V. Consequently, all models, analytical or FE, were based on the Motorola HD3203 material.

Motorola HD3203 and Ferroperm PZ26 are soft and hard PZT materials respectively. Analytical models of unimorph piezoelectric actuators were introduced in the literature review (see equations (2.10), (2.12) and (2.14)) and are discussed, further, in the next subsection of this chapter. These analytical models employ only three materials properties from the piezoceramic material: Young's Modulus (Y_p), density (ρ_p) and piezoelectric coefficient (d_{31}). Motorola HD3203 has a greater ρ_p and d_{31} than Ferroperm PZ26; however, Ferroperm PZ26 has a greater Y_p than Motorola HD3203. According to equation (2.10) only ρ_p and Y_p will effect the frequency f. It is likely that Y_p has a much greater influence on f than does ρ_p as the difference between the two densities is smaller than the difference between the two Young's moduli. Blocking Force, F, and tip deflection, δ, are directly proportional to Y_p and inversely proportional to Y_p respectively; therefore actuators made from Ferroperm PZ26 will yield larger F and smaller δ than actuators with an active piezoelectric layer made from Motorola HD3203. Both the F and δ will be directly proportional to d_{31}; as Motorola HD3203 has roughly twice the value of d_{31} as Ferroperm PZ26 the effect of d_{31} on F and δ is likely to be greater than that of Y_p. Therefore, theoretical calculations, based on Motorola HD3203, will yield larger F and δ for unimorphs than measured quantities from devices where the active piezoelectric layer is Ferroperm PZ26. There is no reason to suppose that FE models will generate values any different from the analytical models.

It is likely that the differences in values between the two data sets are much smaller than the differences between the bulk material and the thick film material. The extent to which the thick film effects final actuator properties cannot be estimated.

A range of devices were designed and modelled for inclusion into a mask set. These devices included spirals, linear unimorph actuators, spokes, multi-arms and miscellaneous devices. A description of the devices is given below.

5.1.2 Devices

5.1.2.1 Linear Beam Actuators

Unimorph piezoelectric actuators of the type shown in Fig 2.12 were modelled using equations (2.10) to (2.15) (see the literature chapter). These equations are reproduced below to aid the reader as equations (5.1) to (5.3).

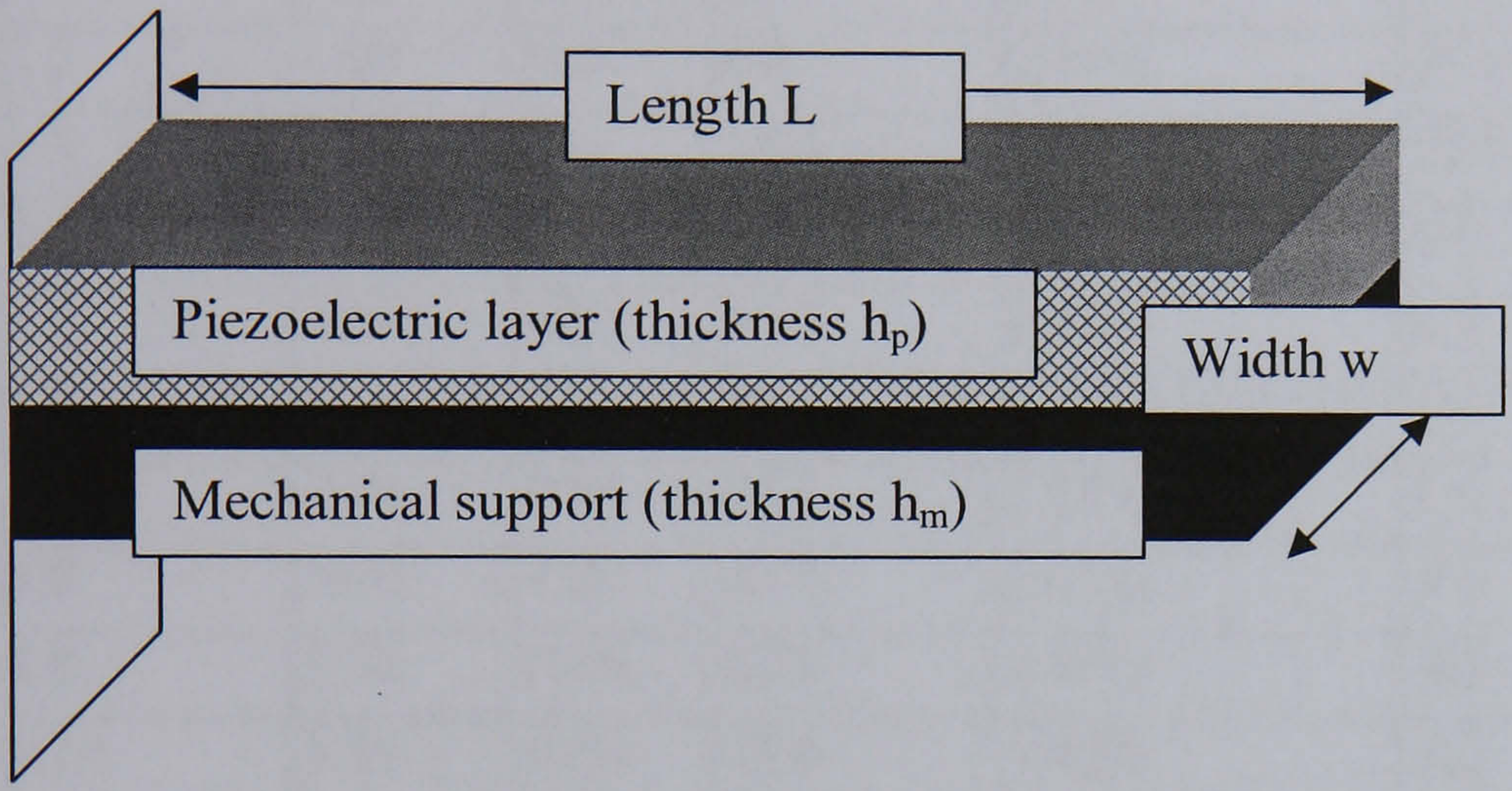

Fig 5.2 A piezoelectric unimorph actuator.

The models describe the actuators performance under a static electric field: where performance is in terms of the deflection, first resonant frequency and the blocking force.

$$f = \left(\frac{3.52.h}{4.\pi.L^2}\right) \times \sqrt{\left(\frac{Y_p}{3.\rho_p}\right) \times \left[\frac{A^2.B^4 + 2.A.\left(2.B + 3.B^2 + 2.B^3\right) + 1}{\left(1 + B.C_p\right).\left(A.B + 1\right).\left(1 + B\right)^2}\right]} \qquad (5.1)$$

$$\delta = \left(\frac{3.d_{31}.E_3 L^2}{2.h_m}\right) \times \left(\frac{2.A.B.(1 + B)^2}{A^2.B^4 + 2.A.\left(2.B + 3.B^2 + 2.B^3\right) + 1}\right) \qquad (5.2)$$

$$F = \left(\frac{3wh^2 Y_p d_{31} E_3}{8L}\right) \times \left(\frac{2.A.B}{\left(A.B + 1\right).\left(1 + B\right)}\right) \qquad (5.3)$$

A range of linear actuators of differing lengths and widths are proposed in Table 5.1; in which the thickness of the piezoelectric layer is based upon a composite slurry PZT thick film (10 µm). The performance was calculated through equations (5.1), (5.2) and (5.3). The actuator dimensions used are shown in Table 5.1, and material properties that were used are given in APPENDIX IV. Values proposed are for actuators that have been included in a mask set for fabrication.

The pressure, p, generated by one of these actuators may be determined through dividing F by the surface-area of the actuator p = F/(Lw). Pressures are quoted in preference to blocking forces in Table 5.1

Device No.	Length / mm	Width / µm	Deflection / µm	Deflection / Length / %	Pressure / kPa	First Resonant Frequency / kHz
L1	0.50	500	1.2	0.24%	108.1	130.198
L2	1.00	500	4.8	0.48%	27.0	32.549
L3	1.50	500	10.9	0.73%	12.0	14.466
L4	2.00	500	19.4	0.97%	6.8	8.137
L5	2.50	500	30.3	1.21%	4.3	5.208
L6	3.00	500	43.6	1.45%	3.0	3.617
L7	3.00	250	43.6	1.45%	3.0	3.617
L8	3.00	750	43.6	1.45%	3.0	3.617
L9	3.00	1000	43.6	1.45%	3.0	3.617
L10	3.00	1250	43.6	1.45%	3.0	3.617
L11	3.00	1500	43.6	1.45%	3.0	3.617

Table 5.1 Linear actuators selected for inclusion into the mask set. The table contains calculations for quasi-static performance from actuator-dimensions.

Deflection and pressures, for L1 to L11, are approximately the same as those proposed for linear cantilevers based on screen-printed PZT thick films: these values were discussed in the literature chapter. In the literature chapter, the same analytical equations were used to calculate values for static actuator performance. Calculated values for pump flow rates for pumps based on this type of actuator are likely to be similar to those in the literature. Therefore, linear beam actuators of the dimensions discussed are likely to produce actuators capable of generating desired pump flow rates.

5.1.2.2 Spokes

A spoke device may be considered an array of spokes situated within a circle (see Fig 5.3). The number of spokes is denoted N_{spoke}. The outer most diameter of the circle is denoted D_{max}. At the centre of the circle there is a smaller circle that has been cut out, the diameter of this smaller circle is denoted D_{min}.

The dimensions of individual spokes are shown in Fig 5.4; here, L_{spoke} and w_{spoke} are the length and width of the individual spoke respectively. The thickness of the piezoelectric and mechanical support, substrate, are denoted as h_p and h_m respectively. The total thickness of the actuator $h=h_m+h_p$.

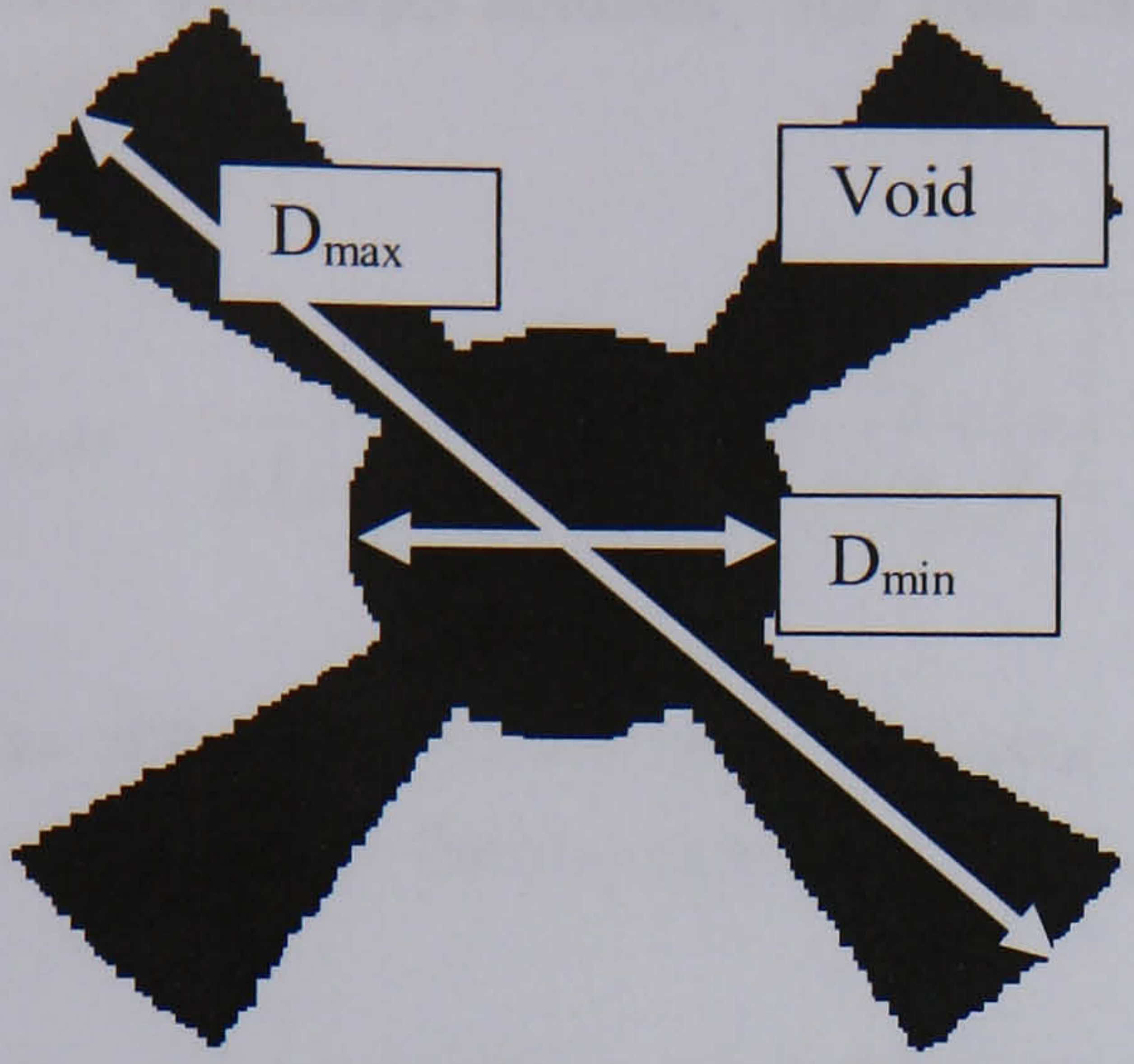

Fig 5.3 Spoke devices where D_{min} and D_{max} are the diameters of the inner and outer circles respectively. The Fig shows four spoke devices about a circular void.

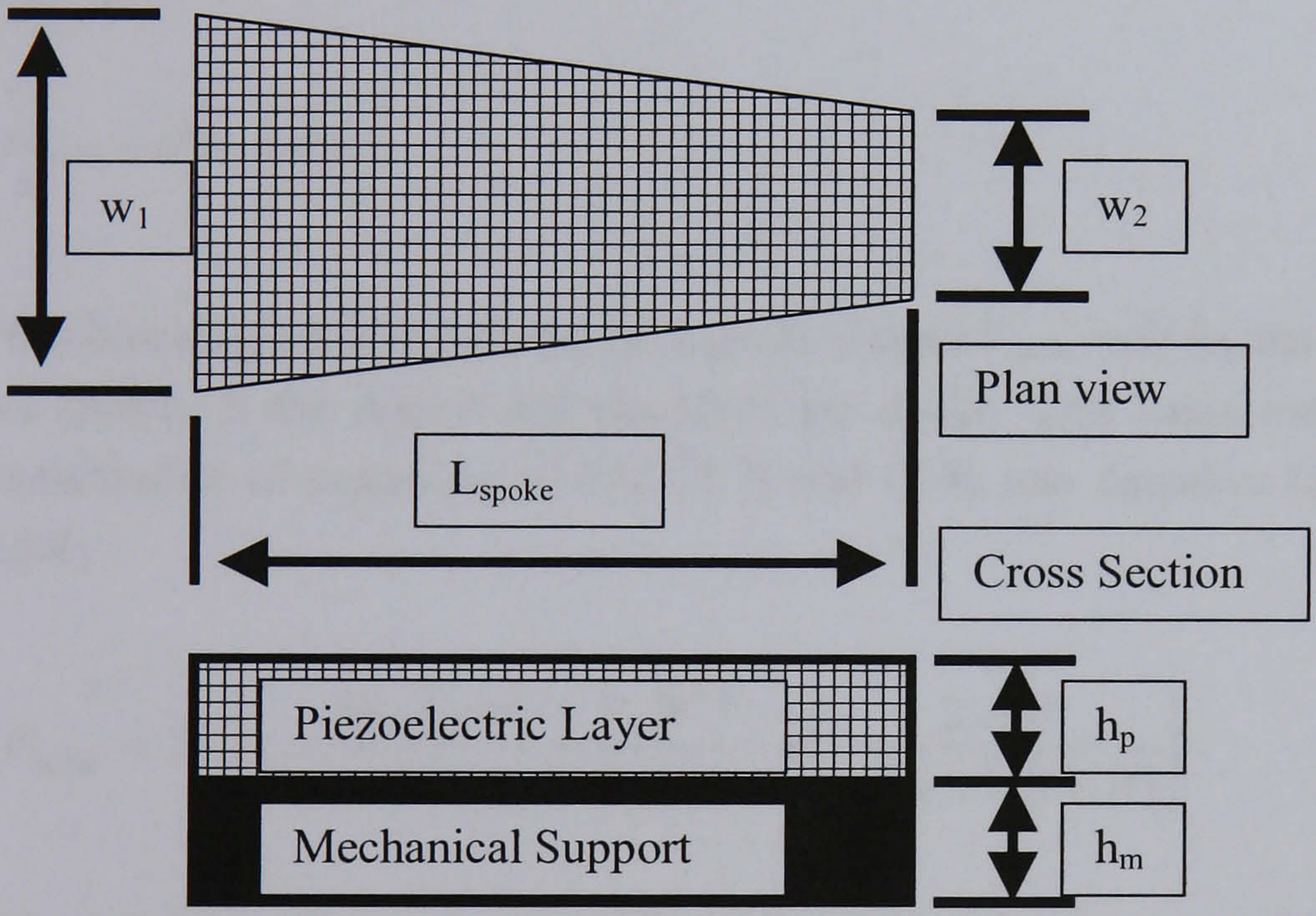

Fig 5.4 Dimensions of a single spoke actuator. The widths $w_1$and w_2 are the outer and inner widths of the actuator respectively.

The length of the spoke can be expressed in terms of the diameters of the two circles (see equation (5.4).

$$L_{spoke} = \tfrac{1}{2}\left(D_{\max} - D_{\min}\right) \tag{5.4}$$

The frequency of a single spoke can be approximated using equation (2.10). Substitution of L_{spoke} for L yields equation (5.5). It is assumed here that the spoke will behave as a linear unimorph actuator, and that the shape of spokes will not adversely change the frequency.

$$f_{spoke} = \frac{3.52.h}{\pi.(D_{\max} - D_{\min})^2}\sqrt{\left(\frac{Y_p}{3.\rho_p}\right) \times \left(\frac{A^2.B^4 + 2.A(2.B + 3.B^2 + 2.B^3) + 1}{(1 + B.C_p)(A.B + 1)(1 + B)^2}\right)} \qquad (5.5)$$

The deflection, of the spoke actuator, δ_{spoke}, defined in equation (2.12) as δ for a linear cantilever, can then be expressed in terms of the diameters of the circles.

$$\delta_{spoke} = \left(\frac{3d_{31}E_3(D_{\max} - D_{\min})^2}{8.h_m}\right) \times \left(\frac{2.A.B.(1 + B)^2}{A^2.B^4 + 2.A(2.B + 3.B^2 + 2.B^3) + 1}\right) \qquad (5.6)$$

The width of the spoke, w_{spoke}, was taken as the average of the two widths w_1 and w_2 (see Fig 5.4)

$$w_{spoke} = \tfrac{1}{2}(w_1 + w_2) \qquad (5.7)$$

The blocking force generated by a spoke device F_{spoke} will be the product of the number of spokes in the device and the force per spoke. This value may be obtained through substitution of equations (2.15), (5.7) and (5.4) into equation (2.14) to yield equation (5.8).

$$F_{spoke} = N_{spoke} \times \frac{3d_{31}E_3(w_1 + w_2)h^2Y_p}{8(D_{\max} - D_{\min})} \times \left(\frac{2.A.B}{(A.B + 1)(1 + B)}\right) \qquad (5.8)$$

The pressure, p_{spoke}, generated by an array of spoke devices will be $p = F_{spoke}/\text{area}$. In this case, the area corresponds to the area of the circle with diameter D_{max}, and this circle has a radius r_{max}. Therefore, as $r_{max} = \frac{1}{2}D_{max}$ it follows that area $= \pi.r_{max}^2 = \pi(\frac{1}{2}D_{max})^2$; consequently, if $p = F_{spoke}/$ area then $p = F_{spoke}/(\pi(\frac{1}{2}D_{max})^2$ and equation (5.9) is proposed.

$$p_{spoke} = \left(\frac{N_{spoke}}{\pi(\frac{1}{2}D_{\max})^2}\right) \times \left(\frac{3d_{31}E_3(w_1 + w_2)h^2Y_p}{8(D_{\max} - D_{\min})} \times \left(\frac{2.A.B}{(A.B + 1)(1 + B)}\right)\right) \qquad (5.9)$$

Spoke actuators have much shorter lengths than spiral actuators and will generate much higher blocking forces, higher resonant frequencies and lower tip deflections (Table 5.2). Geometrically a spoke is similar to a linear cantilever and agreement, in terms of device performance, is likely to be good between the performance of a spoke and an analytical model of a linear cantilever. Again, device pressure is calculated to decline with device diameter; however, device pressures are large enough to achieve acceptable blocking forces. Deflections and pressures are of the same order as those predicted for screen-printed PZT thick films (see the literature chapter) indicating that pump flow rates will be similar.

Device No.	Diameter / mm	No. Spokes	Width outer rim / mm	Width inner rim / mm	Deflection / μm	Pressure / kPa	First Resonant Frequency / kHz
sp1	2	4	1.27	0.42	2.2	43.7	73.236
sp2	2	8	0.49	0.16	2.2	33.4	73.236
sp3	2	12	0.22	0.07	2.2	23.1	73.236
sp4	4	4	2.54	0.42	13.5	7.7	11.718
sp5	4	8	0.97	0.16	13.5	5.8	11.718
sp6	4	12	0.45	0.07	13.5	4.0	11.718
sp7	8	4	5.08	0.42	65.1	1.6	2.421
sp8	8	4	5.08	0.42	65.1	1.6	2.421
sp9	8	8	5.08	0.42	65.1	3.2	2.421
sp10	8	12	1.94	0.16	65.1	1.9	2.421

Table 5.2 Spoke devices selected for inclusion into in the mask set. The table contains calculations for quasi-static performance from actuator-dimensions.

5.1.2.3 Spirals

The dimensions of a spiral actuator are shown in Fig 5.5; D_{max} gives the outer diameter. The thickness of the piezoelectric and substrate are denoted as h_p and h_m respectively. The total thickness of the actuator $h=h_m+h_p$.

The radius r of the spiral, within the plane of the spiral, at any angle θ from its origin is defined by equation (5.10).

$$r = a_{spiral}\theta \tag{5.10}$$

In order to convert from degrees into units of length a proportionality constant, a_{spiral}, is used. This constant is defined in equation (5.11). The radius from the centre of the spiral to the outer circle is defined as r_{max}: where $r_{\max} = \frac{1}{2} D_{\max}$. The total angle that the spiral has rotated through, from its origin to its terminus, is termed θ_{max}.

$$a_{spiral} = \frac{r_{\max}}{\theta_{\max}} \tag{5.11}$$

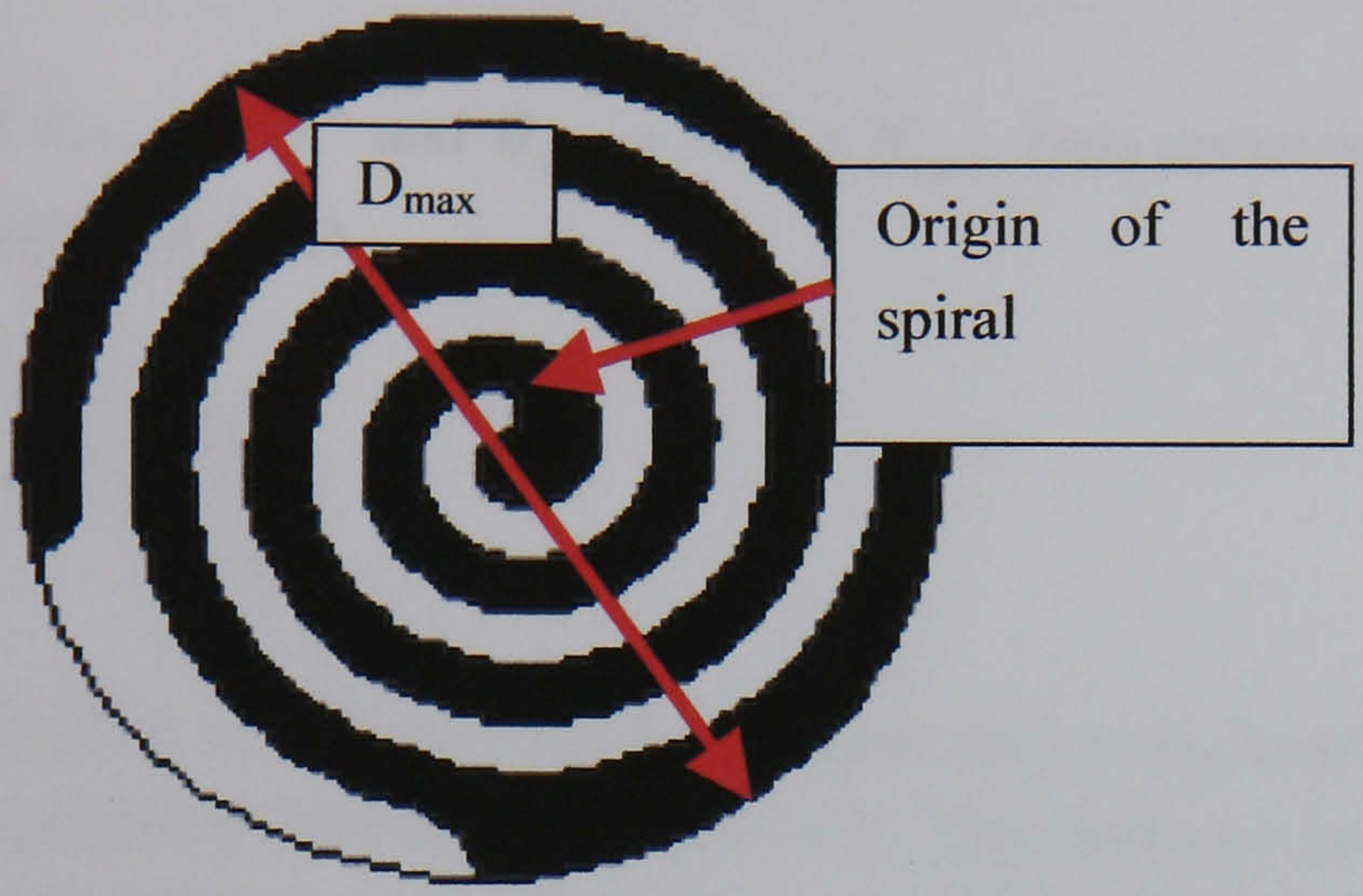

Fig 5.5 Plan view of spiral actuator device. The device has a number of turns (N_{turns}) equal to 3. The void area is shown in black and the device in white.

The number of turns, or complete rotations of the spiral, is defined in equation (5.12) as N_{turns}. This expresses the number of complete rotations, through 360 °, from the origin of the spiral to its terminus.

$$N_{turns} = \frac{\theta_{\max}}{360^{\circ}} \tag{5.12}$$

For the first rotation, subscript min, the spiral will have rotated through $\theta_{\min} = 360$ °. Therefore, the radius of the first rotation, $r_{\min}$, can be obtained from equations (5.10) and (5.11) accordingly:

$$r_{\min} = \left(\frac{r_{\max}}{\theta_{\max}}\right)\theta_{\min} \tag{5.13}$$

Given that $r_{\min} = \frac{1}{2} D_{\min}$ an equation for the minimum diameter, the diameter of the first rotation, can be obtained:

$$D_{\min} = 2 \times \left(\frac{r_{\max}}{\theta_{\max}}\right)\theta_{\min} \tag{5.14}$$

Equation (5.14) can be expressed in terms of D_{max}.

$$D_{\min} = \frac{D_{\max}\theta_{\min}}{\theta_{\max}} \tag{5.15}$$

If $\theta_{min} = 360°$ and $\theta_{\max} = 360° \times N_{turns}$ (see equation (5.12)) the following expression is obtained for D_{min}.

$$D_{\min} = \frac{D_{\max}}{N_{turns}} \tag{5.16}$$

Singh et al [116] have derived an equation for the length of a spiral beam; this equation is reproduced here as equation (5.17). The width of the spiral beam is termed w_{spiral}. The width of the void between consecutive turns of the spiral beam is termed w_{void}.

$$L_{spiral} = \tfrac{1}{2}\pi.N_{turns}\left(.D_{\min} + \tfrac{1}{2}\left((w_{spiral} + w_{void}).(N_{turns} - 1)\right)\right) \tag{5.17}$$

For practical purposes, it is better to express L_{spiral} in terms of D_{max}.

$$L_{spiral} = \tfrac{1}{2}\pi\left(.D_{\max} + \tfrac{1}{2}\left((w_{spiral} + w_{void}).(N_{turns} - 1).N_{turns}\right)\right) \tag{5.18}$$

In the case of a straight unimorph cantilever, the structural frequency depends upon its length L. Here we assume that the spiral actuator will behave as a straight unimorph actuator. In other words using the equations, introduced earlier, for the structural frequency of a straight unimorph actuator, L_{spiral} is substituted for L. The assumption being that frequency of the actuator is independent of its shape.

In determining the length of the spiral, the void width can be regarded as a dependent variable (equation (5.19)). The independent variables, that govern L_{spiral}, are D_{max}, N_{turns} and w_{spiral}.

$$w_{void} = \frac{D_{\max}}{2N_{turns}} - w_{spiral} \tag{5.19}$$

The frequency of the spiral can be determined through substitution of (5.17) and (2.11) into (2.10) to yield (5.20).

$$f_{spiral} = \frac{14.08.h}{\pi^2.\left(D_{\max} + \tfrac{1}{2}\left((w_{spiral} + w_{void}).(N_{turns} - 1).N_{turns}\right)\right)^2} \tag{5.20}$$
$$\times\sqrt{\left(\frac{Y_p}{3.\rho_p}\right)\times\left(\frac{A^2.B^4 + 2.A.\left(2.B + 3.B^2 + 2.B^3\right) + 1}{\left(1 + B.C_p\right)\left(A.B + 1\right).\left(1 + B\right)^2}\right)}$$

Using a similar approach the deflection of the spiral, δ_{spiral}, can be determined through substitution of (5.17) and (2.13) into (2.12) to yield (5.21).

$$\delta_{spiral} = \frac{3d_{31}E_3\pi^2\left(D_{\max} + \tfrac{1}{2}\left((w_{spiral} + w_{void}).(N_{turns} - 1).N_{turns}\right)\right)^2}{32h_m} \tag{5.21}$$
$$\times\left(\frac{2.A.B.(1 + B)^2}{A^2.B^4 + 2.A.\left(2.B + 3.B^2 + 2.B^3\right) + 1}\right)$$

Again, a similar approach is used to obtain the blocking force, F_{spiral}, for a spiral actuator: through substitution of equations (5.17) and (2.15) into (2.14) to yield equation (5.22).

$$F_{spiral} = \frac{3d_{31}E_3 w_{spiral} h^2 Y_p}{8\pi^2\left(D_{\max} + \tfrac{1}{2}\left((w_{spiral} + w_{void}).(N_{turns} - 1).N_{turns}\right)\right)} \tag{5.22}$$
$$\times\left(\frac{2.A.B}{\left(A.B + 1\right).\left(1 + B\right)}\right)$$

As there is only one spiral present the pressure, p_{spiral}, exerted by the spiral is given simply by dividing (5.22) by the outer circles area:

$$p_{spiral} = \left(\frac{1}{\pi\left(\tfrac{1}{2}D_{\max}\right)^2}\right) \tag{5.23}$$
$$\times\frac{3d_{31}E_3 w_{spiral} h^2 Y_p}{8\pi^2\left(D_{\max} + \tfrac{1}{2}\left((w_{spiral} + w_{void}).(N_{turns} - 1).N_{turns}\right)\right)}$$
$$\times\left(\frac{2.A.B}{\left(A.B + 1\right).\left(1 + B\right)}\right)$$

Three device diameters were considered to simplify the design: $D_{\max}$ = 2, 4 and 8 mm. Because spiral stiffness and hence blocking force is increased at smaller diameters (see chapter 2) only spiral devices of 2 and 4 mm were considered for the mask set. Data for selected spirals is shown in Table 5.3. It should be noted that FE predicts higher blocking forces, by implication pressures, and lower deflections for these devices based on comparison between spiral actuators and equivalent linear cantilevers. A range of spirals was selected in order to vary the number of turns and the beam width; the cantilever length was a function of these two parameters. Deflections are much larger than for linear actuators based on screen-printed PZT thick films: stroke lengths are likely to be larger for spiral actuators. Pressures are significantly lower than for other devices and actuators based on screen-printed PZT thick films.

Device No.	Diameter / mm	No. Turns	Width / μm	Deflection / μm	Pressure / kPa	First Resonant Frequency / kHz
s1	2	1	166.7	51	443	3.102
s2	2	1	250.0	49	679	3.241
s3	2	1	333.3	46	925	3.391
s4	2	2	83.3	201	111	0.783
s5	2	2	166.6	203	222	0.778
s6	2	3	83.3	442	75	0.357
s7	2	3	166.7	444	150	0.355
s8	2	4	83.3	778	57	0.203
s9	4	1	666.7	238	204	0.662
s10	4	2	166.7	811	28	0.194
s11	4	3	166.7	1776	19	0.089
s12	4	3	333.3	1794	37	0.088
s13	4	4	166.7	3123	14	0.050
s14	4	4	333.3	3148	28	0.050

Table 5.3 Spiral devices selected for inclusion into in the mask set. The table contains calculations for quasi-static performance from actuator-dimensions.

5.1.2.4 Multi-Arms

In the case of multi arm devices (see Fig 5.6) where there is more than one spiral arm in a device, the origin of all spirals is at the centre of the circle. Therefore, the radius of the circle is common to all spiral arms. As can be seen from Fig 5.6 the void width, w_{void}, between successive turns of the same arm is always constant; however, the void width between different arms is not always constant.

In order to reduce stresses at sharp points corners are rounded at the joints of the devices, and a central circle shape is placed about the point where the two arms converge (see Fig 5.7). As noted above, r_{max} is common to all arms and has its origin at the centre of the circle. The smaller circle has a radius r_c. The multi-arm device can only deflect along the length of the arm from the outer diameter of the large circle to the point where the arm joins the smaller circle i.e. a distance r_c from the origin. The radius that the spiral moves through to this point is the effective radius and is termed r_{eff} (see equation (5.24)). The terms D_c and D_{eff} correspond to the diameters of the effective and central circles respectively.

$$r_{\max} = r_c + r_{eff} = \tfrac{1}{2}\left(D_c + D_{eff}\right) \tag{5.24}$$

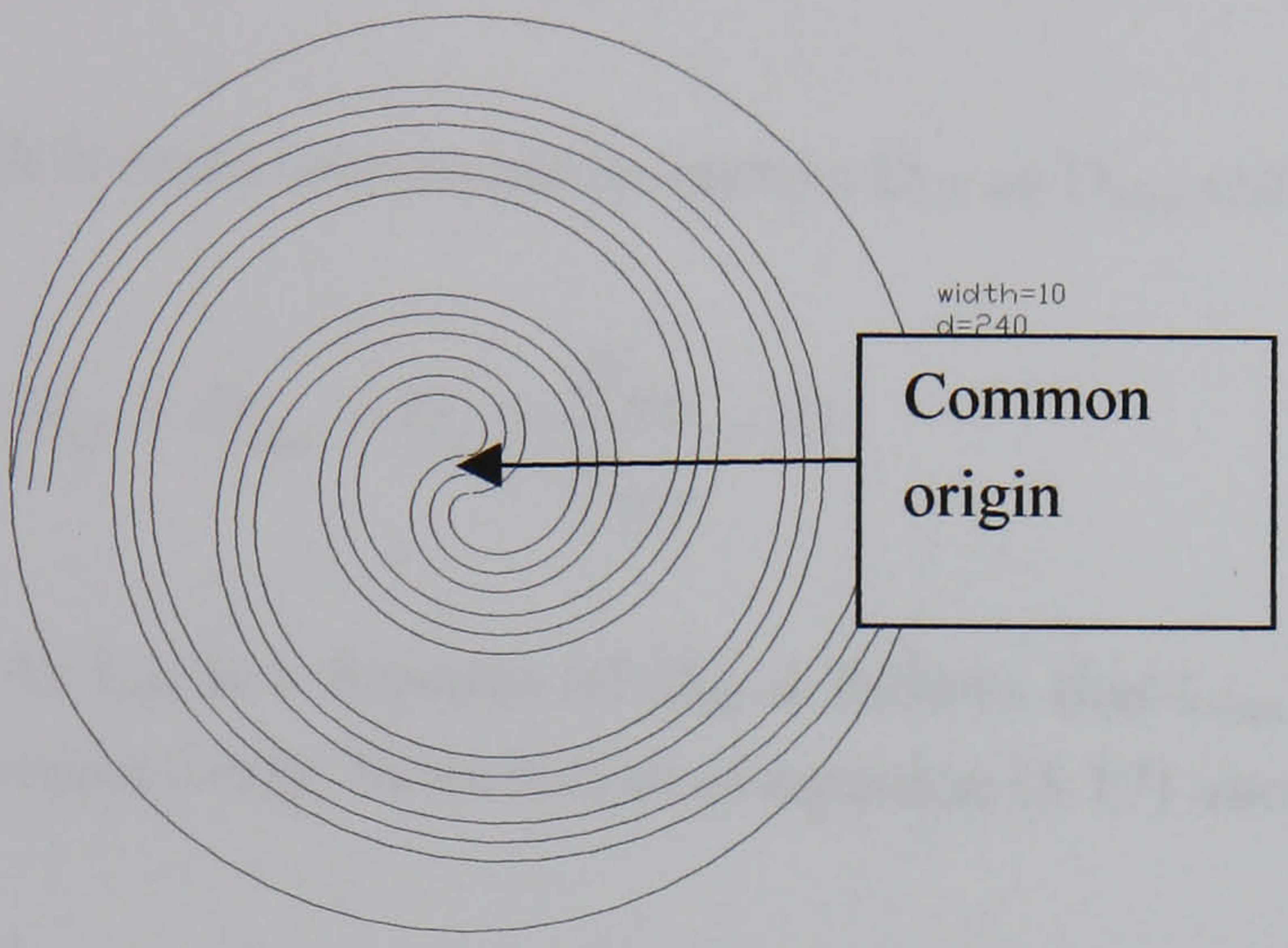

Fig 5.6 Multi-arm device with two arms. There is a common origin for both spirals located at the centre of the circle.

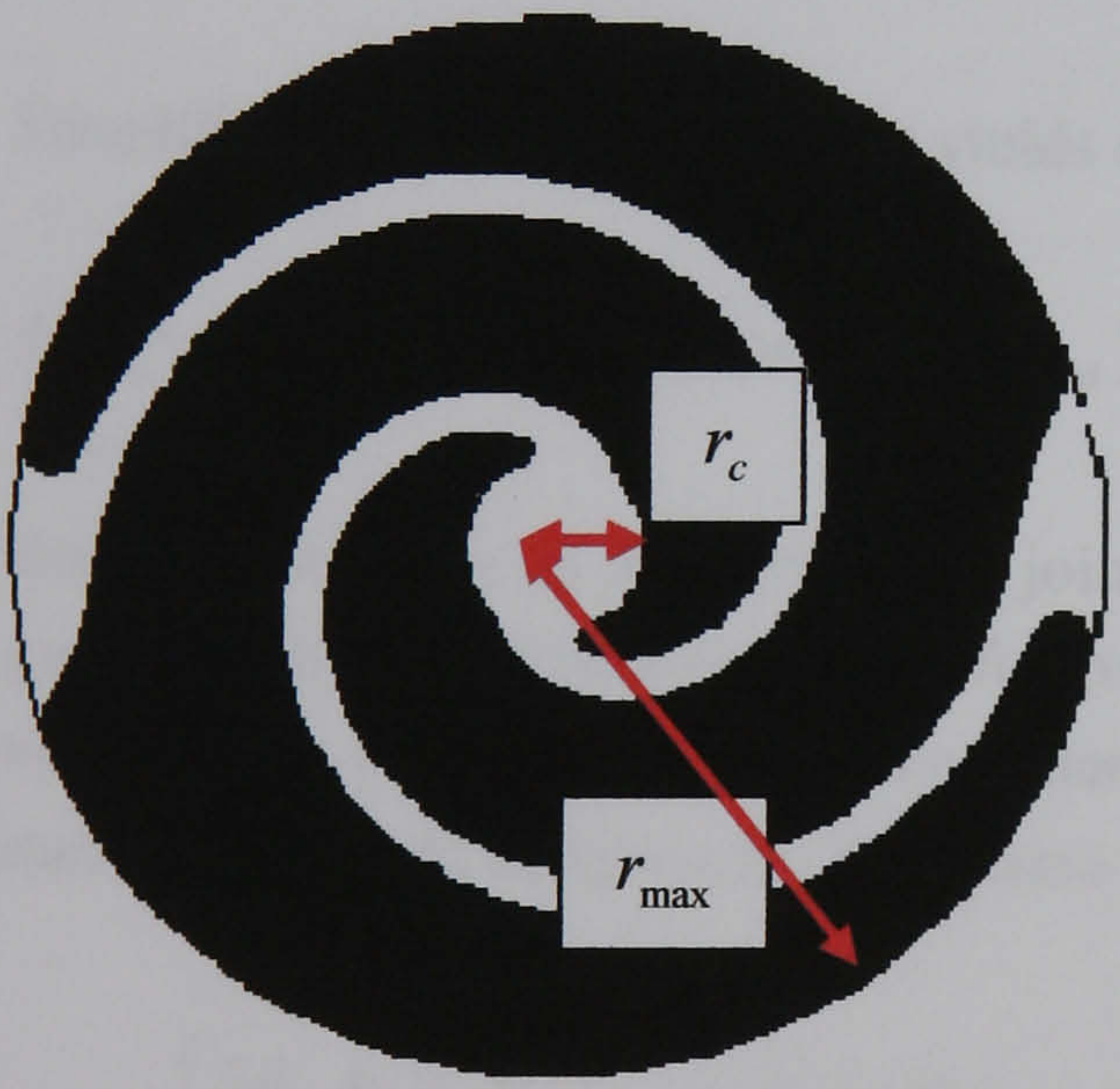

Fig 5.7 Plan view of a multi-arm spiral actuator. The actuator has two arms or $N_{arms}=2$. The parameters r_c and $r_{\max}$ denote the radius of the inner circle and outer circle respectively.

The length of the spiral arm that is involved in deflection is termed the effective length and is given the symbol L_{eff}. The total length of one spiral arm from the origin to the outer circumference, of the large circle, is denoted as L$_{max}$. The length of one spiral arm within the circle of radius r$_c$ is denoted L$_c$. The effective length of the spiral can thus be expressed:

$$L_{eff} = L_{\max} - L_c \tag{5.25}$$

It is more convenient to express D$_{eff}$ as D$_{max}$ and D$_c$

$$D_{eff} = D_{\max} - D_c = \frac{D_{\min}}{N_{turns}} - D_c \tag{5.26}$$

As L$_{eff}$ is a function of D$_{eff}$ it follows that L$_{max}$ and L$_c$ will be functions of D$_{max}$ and D$_c$ respectively. Substitution of equation (5.17) into (5.25) yields (5.27).

$$\begin{aligned} L_{eff} &= \frac{\pi}{2}\left(D_{\max} + \frac{(w_{spiral} + w_{void}).(N_{turns} - 1).N_{turns}}{2}\right) \\ &- \frac{\pi}{2}\left(D_c + \frac{(w_{spiral} + w_{void}).(N_{turns} - 1).N_{turns}}{2}\right) \end{aligned} \tag{5.27}$$

Simplification of equation (5.27) yields equation (5.28).

$$L_{eff} = \tfrac{1}{2}\pi\left(\left(D_{\max} - D_c\right) + \left((w_{spiral} + w_{void}).(N_{turns} - 1).N_{turns}\right)\right) \tag{5.28}$$

Because the arms of the device are joined at the origin, the maximum deflection is that generated by one arm along the effective length. Cantilever deflection does not increase as each arm is added to the device. Therefore, substitution of equations (5.28) and (2.11) into (2.10) yields equation (5.29), where the subscript ma denotes multi arm.

$$\begin{aligned} \delta_{ma} &= \left(\frac{3d_{31}E_3\pi^2\left(\left(D_{\max} - D_c\right) + \left((w_{spiral} + w_{void}).(N_{turns} - 1).N_{turns}\right)\right)^2}{8h_m}\right) \\ &\times \left[\frac{2.A.B.(1+B)^2}{A^2.B^4 + 2.A.\left(2.B + 3.B^2 + 2.B^3\right) + 1}\right] \end{aligned} \tag{5.29}$$

The force, F$_{ma}$, generated by a set of spirals in a multi-arm device, of number N$_{arms}$, will be as noted in equation (5.30).

$$F_{ma} = N_{arms} \times \frac{3d_{31}E_3 w_{spiral}h^2 Y_p}{4\pi\left(\left(D_{\max} - D_c\right) + \left((w_{spiral} + w_{void}).(N_{turns} - 1).N_{turns}\right)\right)} \times \left[\frac{2.A.B}{(A.B+1).(1+B)}\right] \tag{5.30}$$

The pressure generated by a set of spiral multi-arms, p_{ma}, may be calculated through division of the force by the area that the device occupies:

$$p_{ma} = \left(\frac{N_{arms}}{\pi\left(\frac{1}{2}D_{\max}\right)^2}\right) \times \left(\frac{3d_{31}E_3 w_{spiral}h^2 Y_p}{4\pi\left(\left(D_{\max} - D_c\right) + \left((w_{spiral} + w_{void}).(N_{turns} - 1).N_{turns}\right)\right)}\right) \times \left[\frac{2.A.B}{(A.B+1).(1+B)}\right] \tag{5.31}$$

Multi-arm actuators were designed to achieve intermediary force, tip deflection and resonant frequency. Multi-arm actuators exhibit ~ 2 to 4 times the pressures of spiral actuators of the same diameter (see Table 5.4). Multi-arm actuator deflections are significantly less than those calculated for spiral actuators. Deflections, for multi-arm actuators, are greater than for linear beam and screen-printed thick film actuators.

Device No.	$D_{\max}$ / mm	D_c / mm	N_{turns}	N_{arms}	w_{spiral} / µm	Deflection / µm	Pressure / kPa
ma1	4	0.67	1	2	83.3	191	45
ma2	4	0.67	1	2	166.7	183	90
ma3	4	0.67	1	4	83.3	191	179
ma4	4	0.67	1	4	166.7	183	358
ma5	4	0.67	2	2	83.3	764	45
ma6	4	0.67	2	2	166.7	770	90
ma7	4	0.67	2	4	83.3	764	179
ma8	8	1.33	1	4	166.7	766	45
ma9	8	1.33	1	4	333.3	732	90

Table 5.4 Multi-arm devices selected for inclusion into the mask set. The table contains calculations for quasi-static performance from actuator-dimensions.

Multi-arm actuators maximise pressure in two ways. Firstly, force is expressed as the product of the number of spirals and the force per spiral. Secondly, the length of the spiral actuator is reduced through containing more than one spiral in a given area; blocking force is increased through shortening the length of a given beam. Consequently, actuator deflections will be much reduced.

5.1.2.5 Devices Miscellaneous.

Swastikas, square spirals, plates and bridge structures were also included in the mask set. Swastikas, partially clamped plates and fully clamped plates have applications as accelerometers [117] and acoustic resonators [10]. Bridge structures have been fabricated as acoustic resonators with both thin [11,118] and thick [119] PZT films on silicon. Thick film bridge resonators were made with dimensions (L x w x h) of 2mm x 0.5 mm x 30 μm and a surface to volume ratio of 3.33 %. A small surface to volume ratio allows resonator operation at atmospheric pressure without appreciable interference from squeeze film damping [119]. For this reason: bridge type resonators that were designed in the mask set had a surface to volume ratio of 2.4 to 2.8 %. These structures were not modelled but were mainly included to explore the range of shapes that could be fabricated with the flowing process.

5.1.3 Reduction Of Stress Concentration

In order to maximise device lifetimes all devices, discussed in the preceding sections, have been drawn with curved corners to reduce stresses at sharp points. Joints where the spiral is attached to the main structure were made smooth to avoid sharp points to reduce stresses. An additional feature, was that joints were made as broad as possible to strengthen the attachment of the beam to the main structure.

5.2 Process Design

A Si_3N_4 mask is prepared on the wafer surface through LPCVD (low-pressure chemical vapour deposition). At the end of processing, the silicon is anisotropically etched with KOH to release the cantilevers. The process employs a Si buried oxide wafer with dimensions and properties in Table 5.5. The buried oxide layer acts as an etch stop and is included to ensure a uniform control over the cantilever thickness.

Wafer Diameter	Crystallographic orientation	Wafer thickness	Buried oxide depth	Buried oxide thickness	Polished sides
100 mm	<100>	555 μm	20 μm	2000 nm	Double

Table 5.5 Properties and dimensions of buried oxide wafer for the fabrication of micro cantilevers.

5.2.1 The Si_3N_4-KOH Standard Process

The standard process design is summarised in Fig 5.8 (on page 84-85), and the process details are given in Table 5.6 (on page 86-87). Step 2 is the deposition of Si_3N (200 nm) by LPCVD onto both faces of the wafer; this process is to be done at Queens University Belfast (QUB). The silicon nitride is incorporated as a masking material to selectively protect the Si against attack from KOH during wet etching. Step 4 is the reactive ion etching (RIE) of the back face nitride: opening apertures in the nitride for anisotropic etching later in the process. A set of alignment marks is incorporated in mask one such that back to front alignment is possible for subsequent stages.

Lead diffusion will be discussed in chapter 6; a diffusion barrier system is incorporated through the sputtering of Ti (200 nm) and subsequent thermal oxidation of this layer to TiO_2 (step 4). This is done in a box furnace at 700 °C for 10 minutes; to minimise stress in the TiO_2 the furnace is heated and cooled at a rate of 3 °C/min. A back electrode layer is applied to the surface of the TiO_2 through sputter deposition of Ti (8 nm) /Pt (200 nm)(step10).

A Cr layer is sputtered onto the back face of the wafer (Step 11) to protect against scratching and staining from subsequent processing steps. PZT thick films are to be prepared through the spin coating of a 0-3 composite slurry onto the Ti/Pt electrode. The PZT thick film is to be sintered at 710 °C for 30 minutes; the back face Cr layer would be completely oxidised at this stage; chrome oxide may be removed by commercial Cr enchants before or after sintering. It should be noted that sintered PZT is stable to the Cr etch; however, there is some attack of green PZT by the etching solution (this will be discussed in more detail in Chapter 8). For this reason, the Cr layer is left in place until later in the process. Sintering is the last of the high temperature treatments used during fabrication. After sintering the PZT can be corona poled: subsequent steps, will not destroy the ordering of the domain structure.

Step 17, is the photo patterning of S1818 (Shipley) photoresist with mask 2 for the subsequent wet etching of the PZT thick film. Step 18 is the wet etching of the PZT thick film in a dilute solution of $HF(aq)_{(aq)}$ and $HCl_{(aq)}$; this will yield a via for contact to the back electrode. Back to front alignment between masks 1 and 2 to insure correct positioning of holes for the back electrode with respect to the back face pattern.

Step 21 is the photo patterning of the PZT for the deposition of a top electrode: with S1818. A Cr/Au top electrode is deposited through sputter deposition, step 22. The wafer is left in acetone over night to remove unwanted photoresist and waste electrode from the surface of the PZT (lift off). Ultrasonic agitation is an option for the removal of unwanted material; however, ultrasound may damage the PZT thick film and a prolonged lift off process in acetone is preferred.

Process Design

Process 1: Si_3N_4-KOH

Process steps

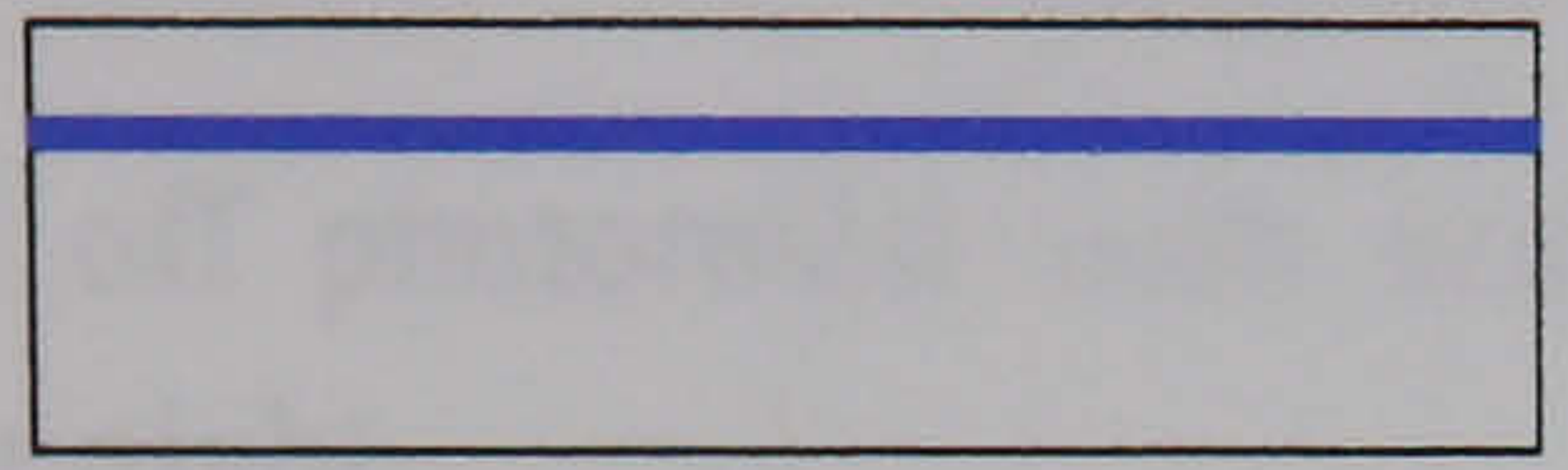

Buried Oxide wafer

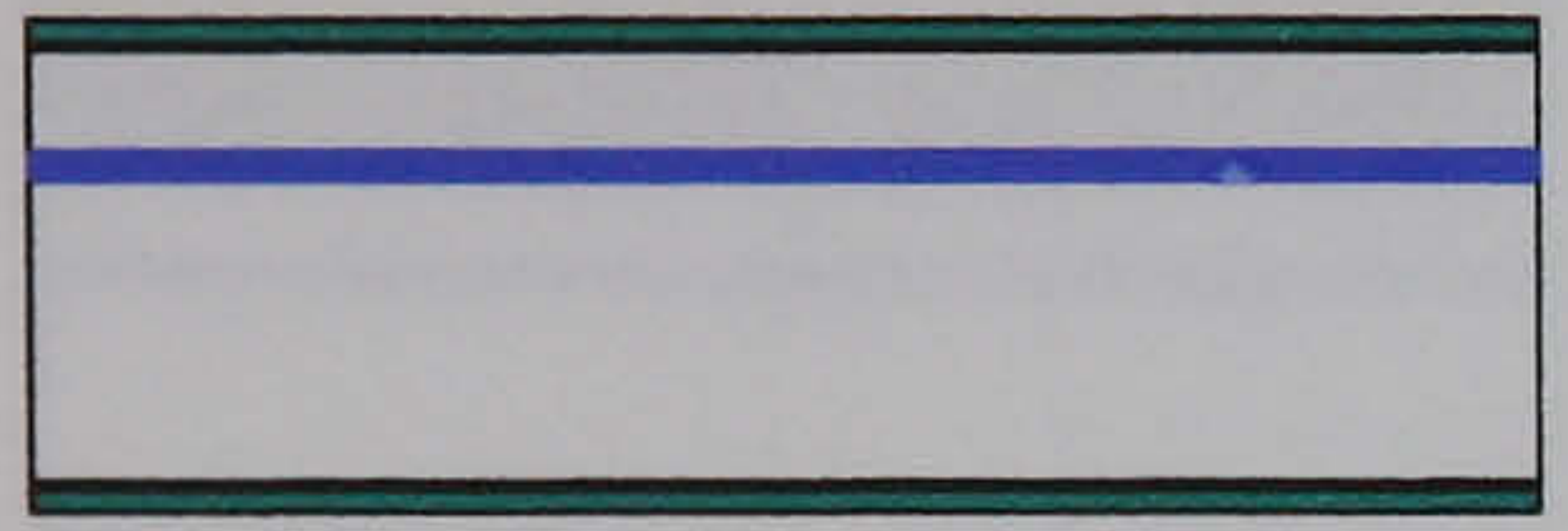

Deposition of Si_3N_4 – LPCVD at QUB

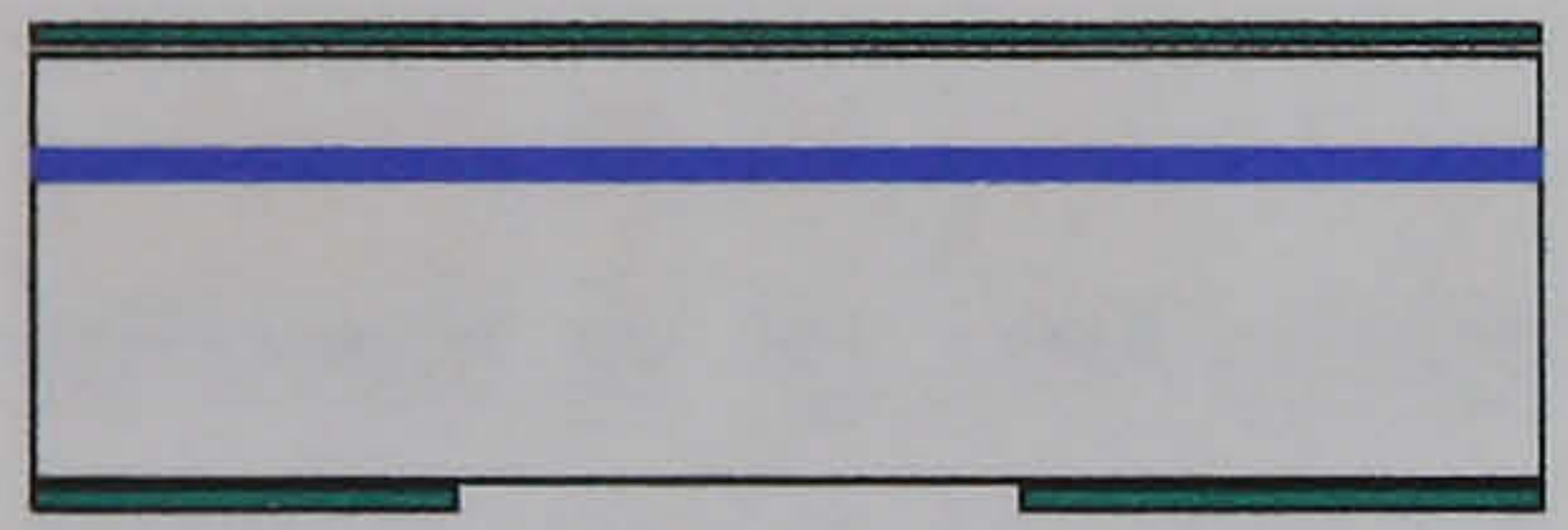

Mask 1 Patterning of nitride; the mask incorporates alignment marks. At QUB

7

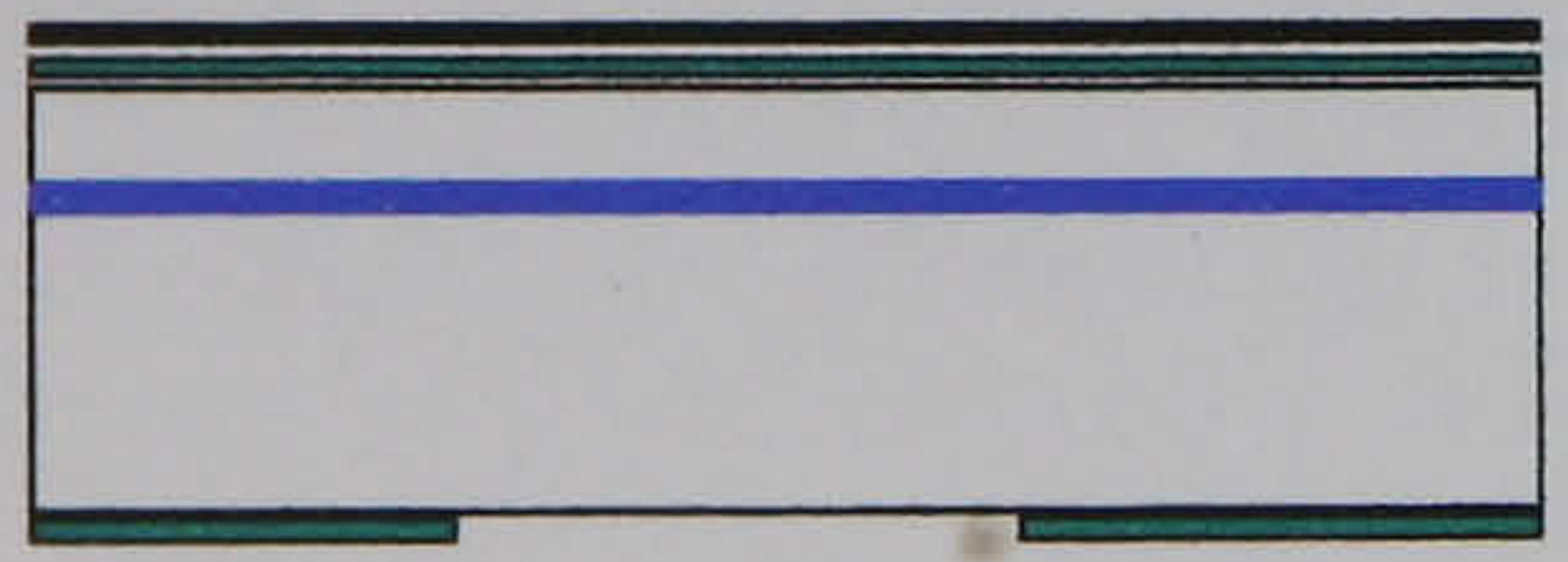

Sputtering of Ti and thermal oxidation toTiO_2

10

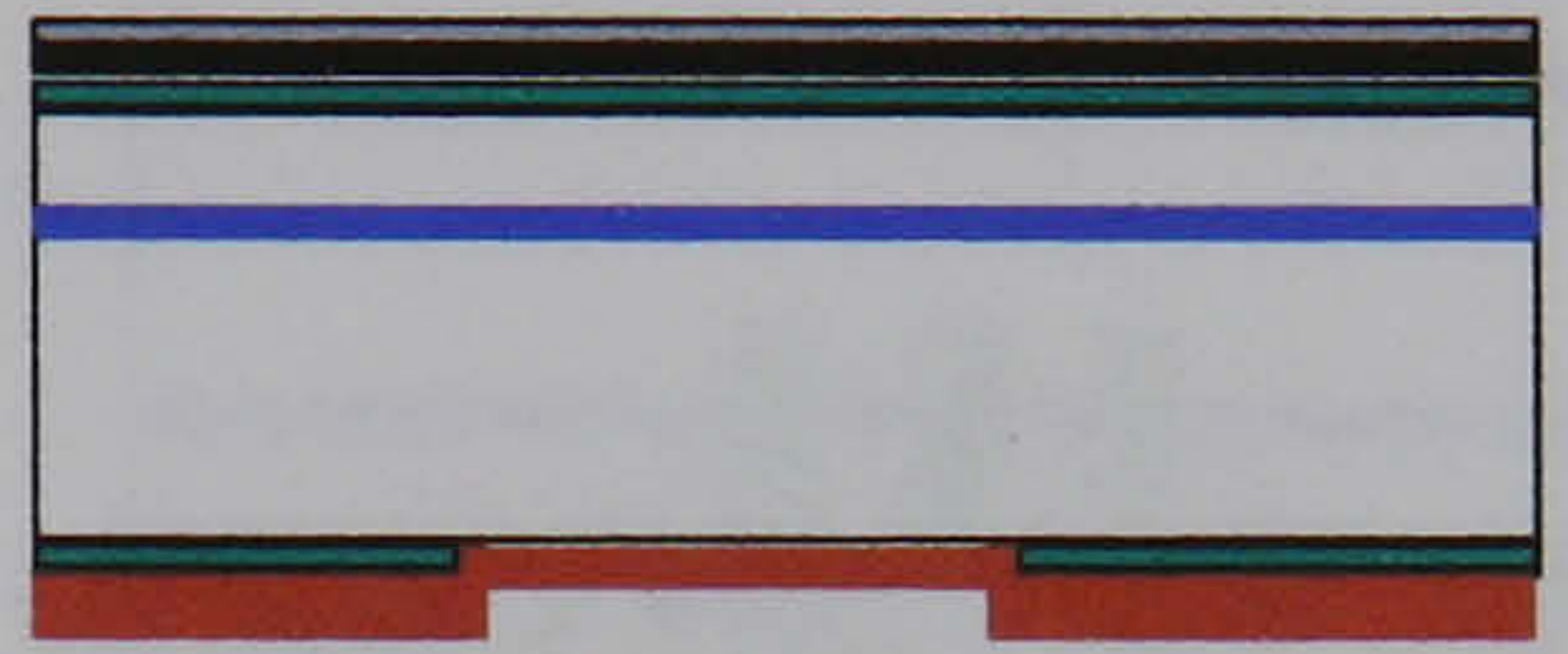

Sputtering of a Ti/Pt back electrode (for the front face), and secondly a Cr layer for back face protection.

13

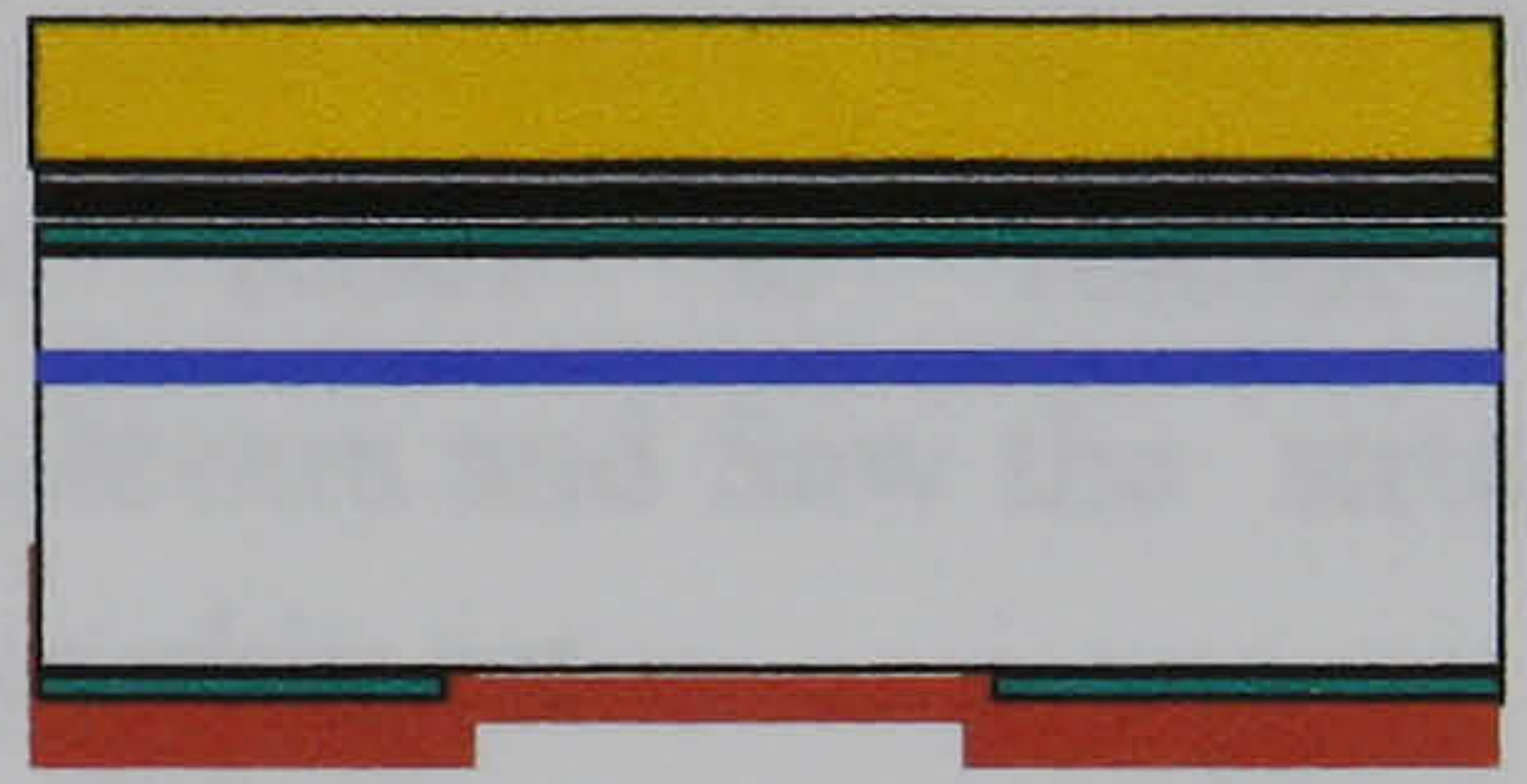

Deposit, Sinter (710 °C) and Corona pole the PZT thick film

17

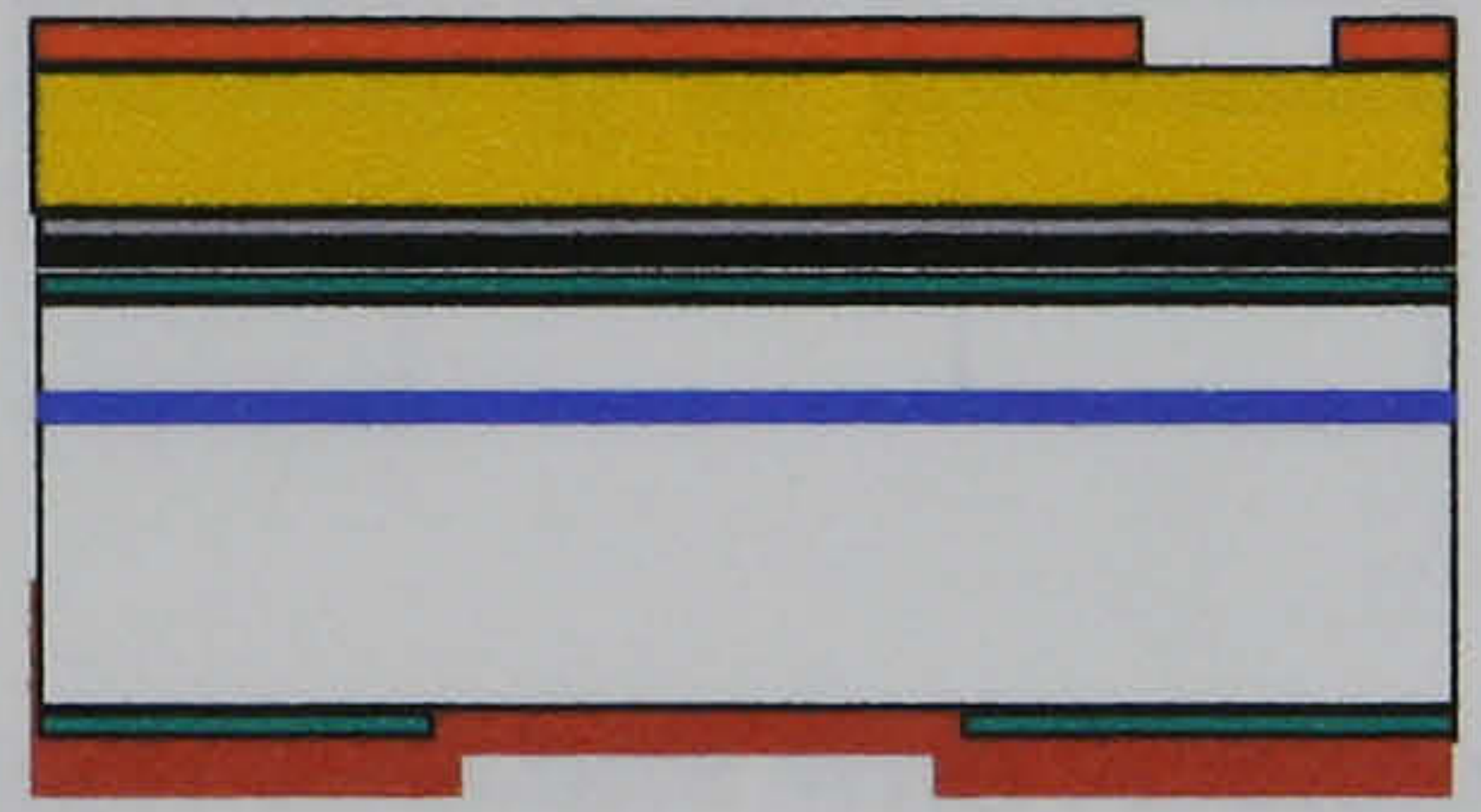

Mask 2: Photo-patterning of the PZT with S1818

18

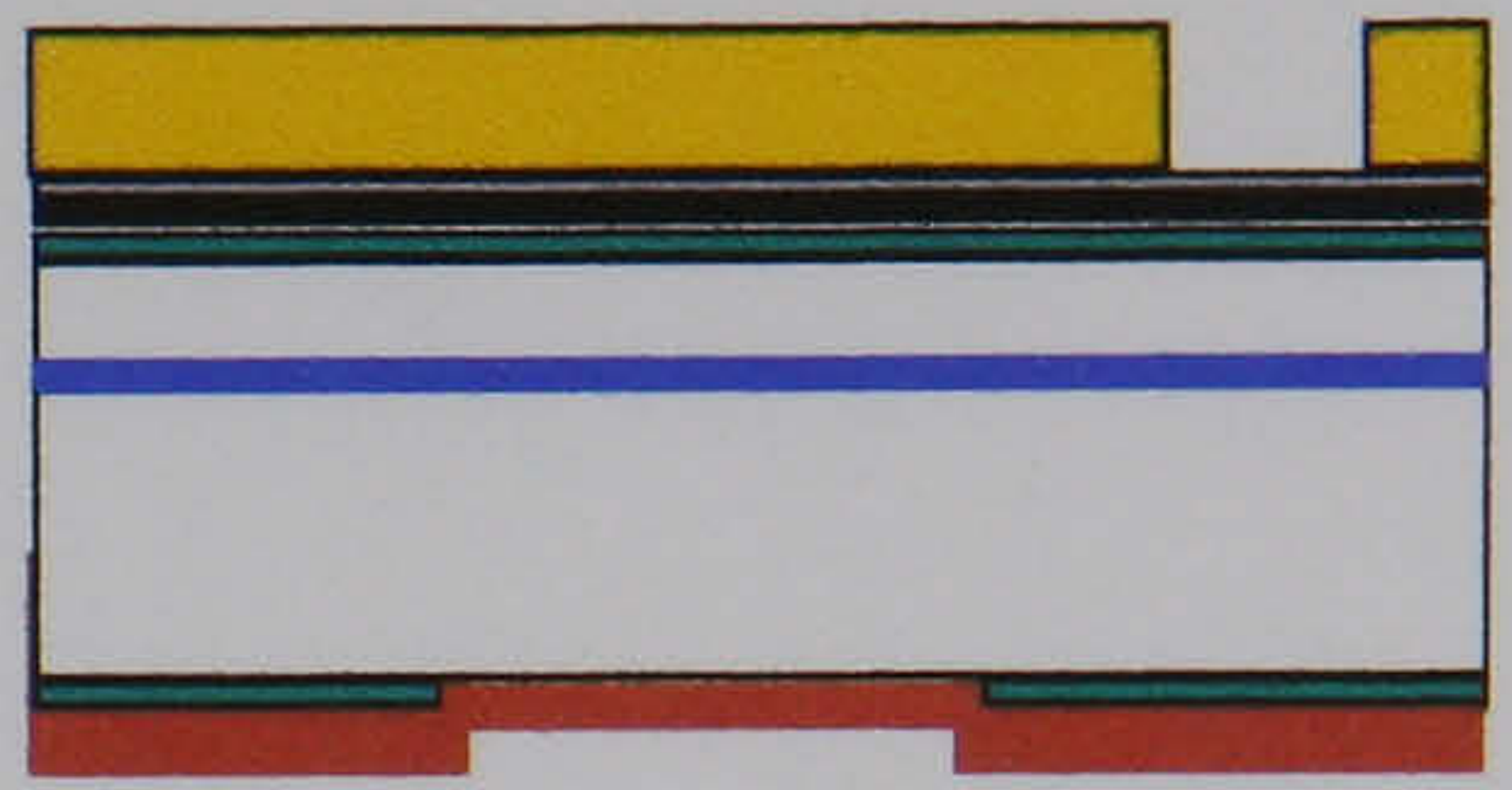

Wet etch PZT in HF(aq)/H_2O & strip S1818 with Acetone

21

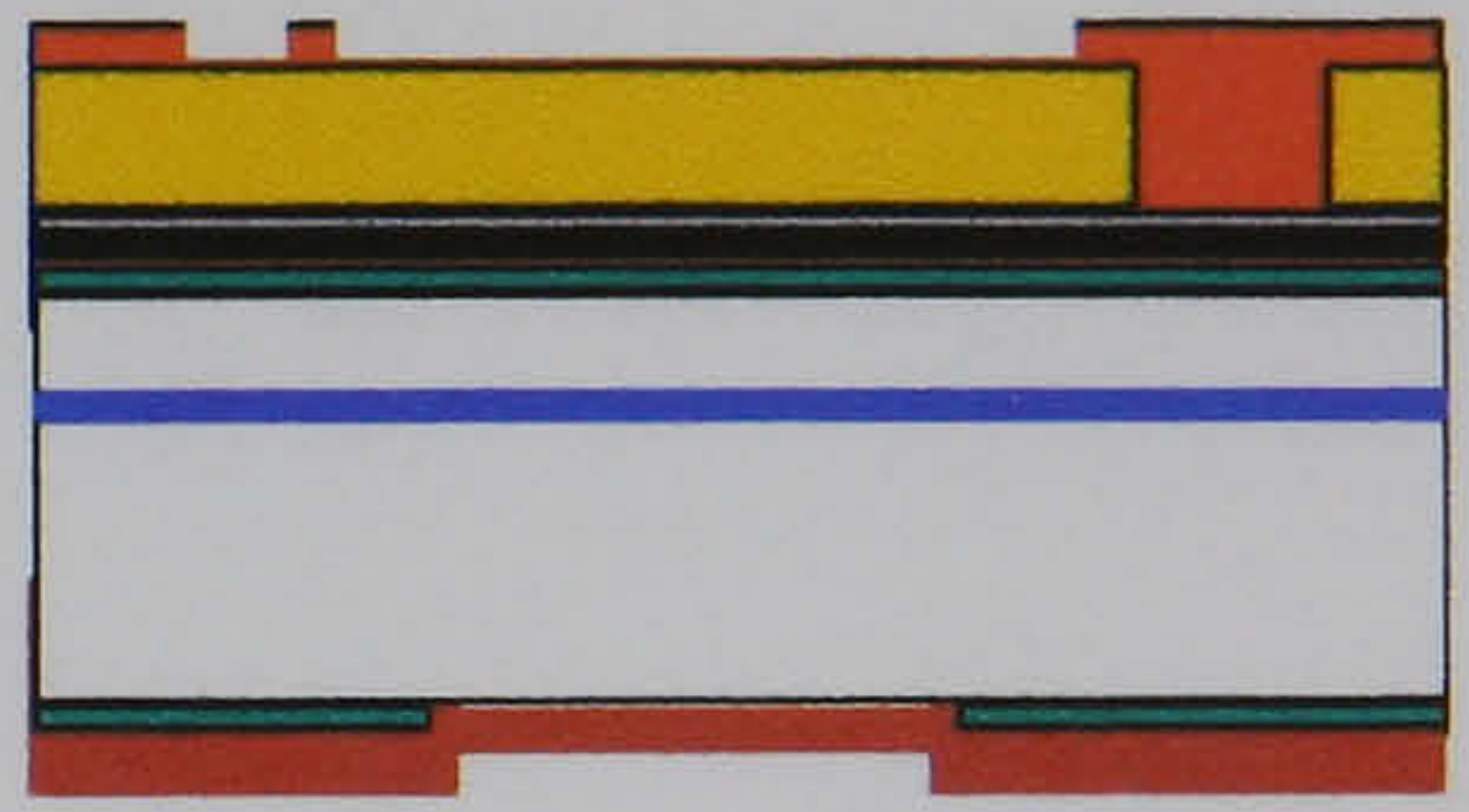

Mask 3: Photo-patterning of PZT with S1818

22

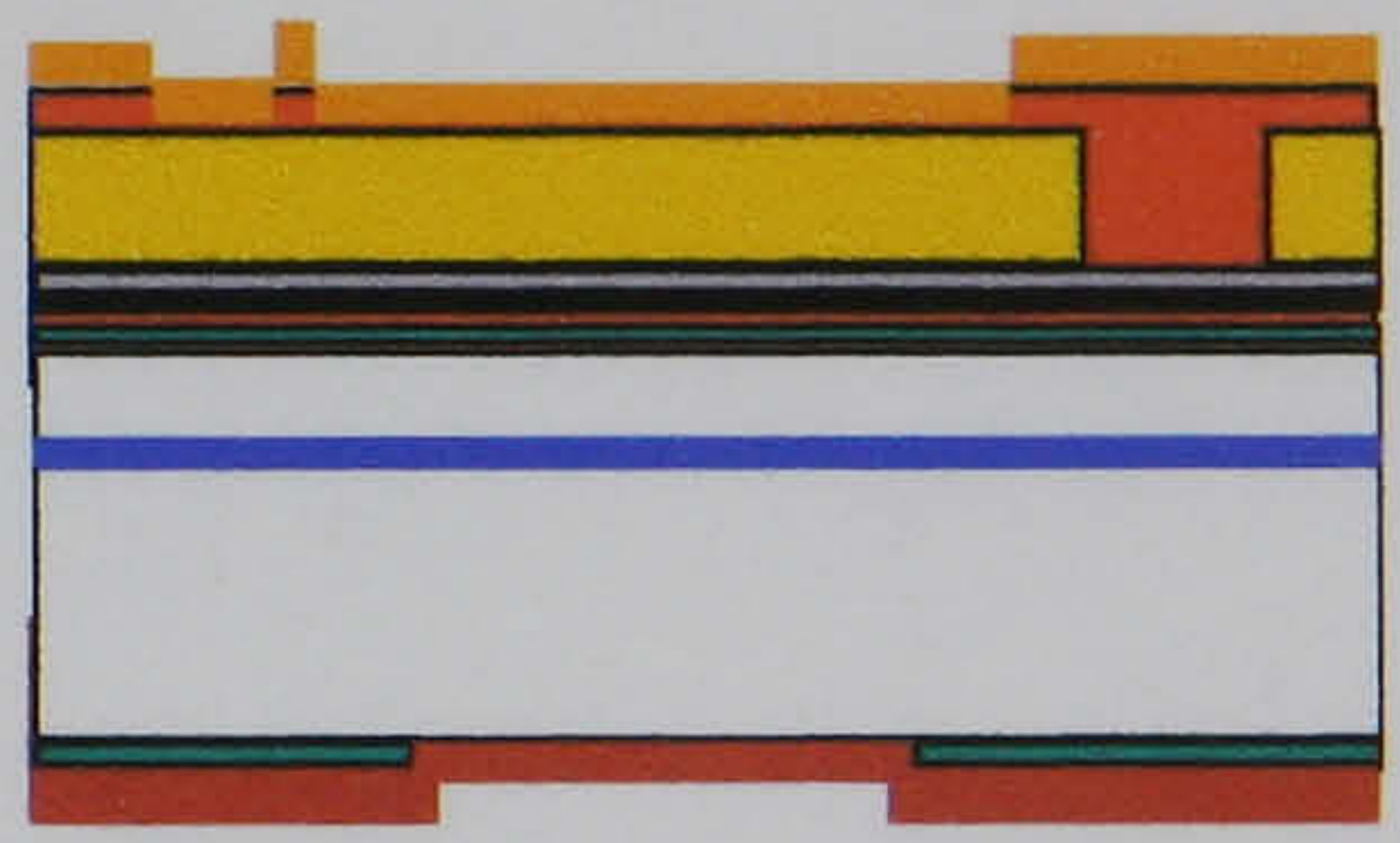

Sputter deposition of Au/Cr top electrode

23

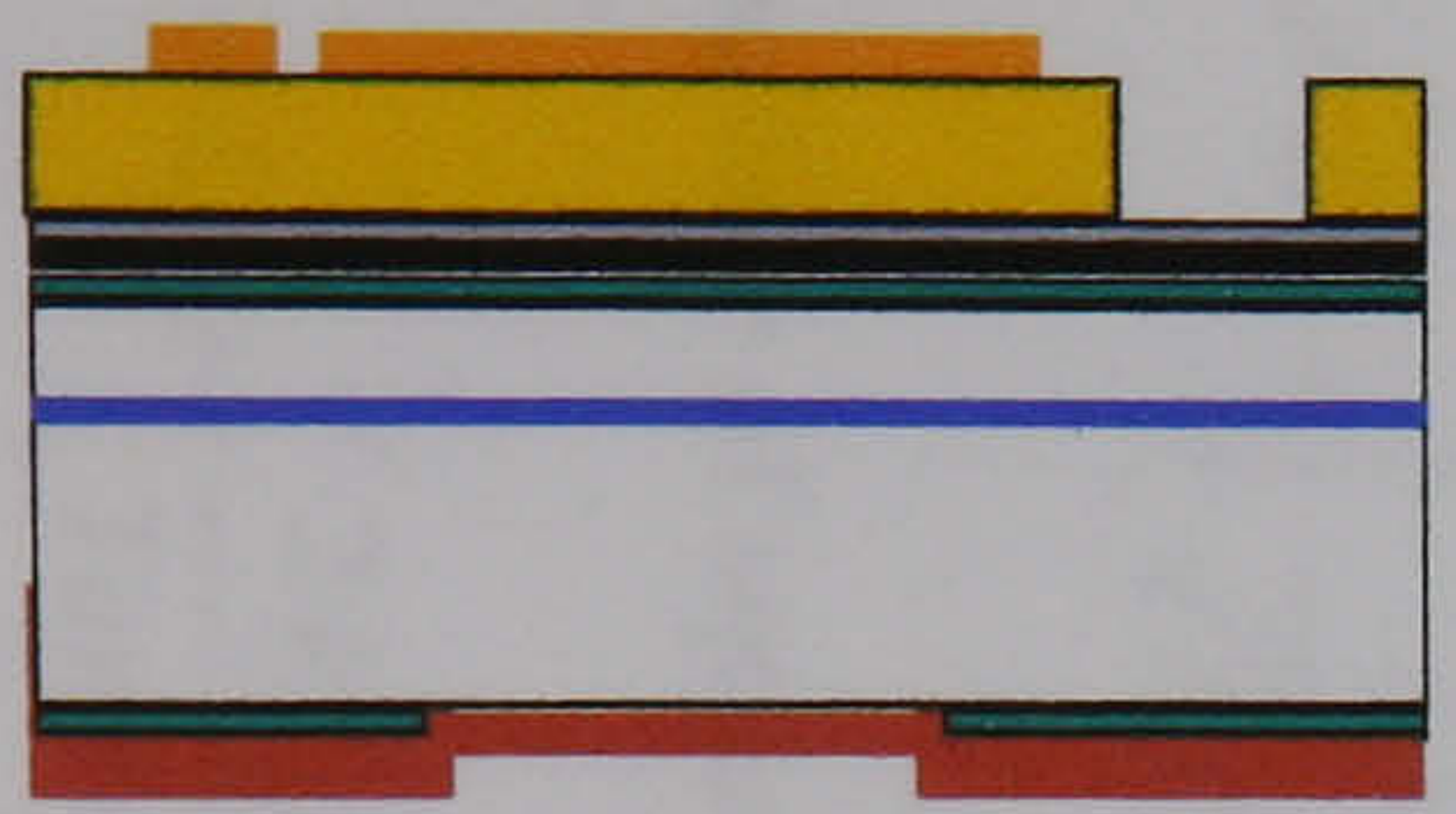

Lift off photoresist with acetone over night.

25

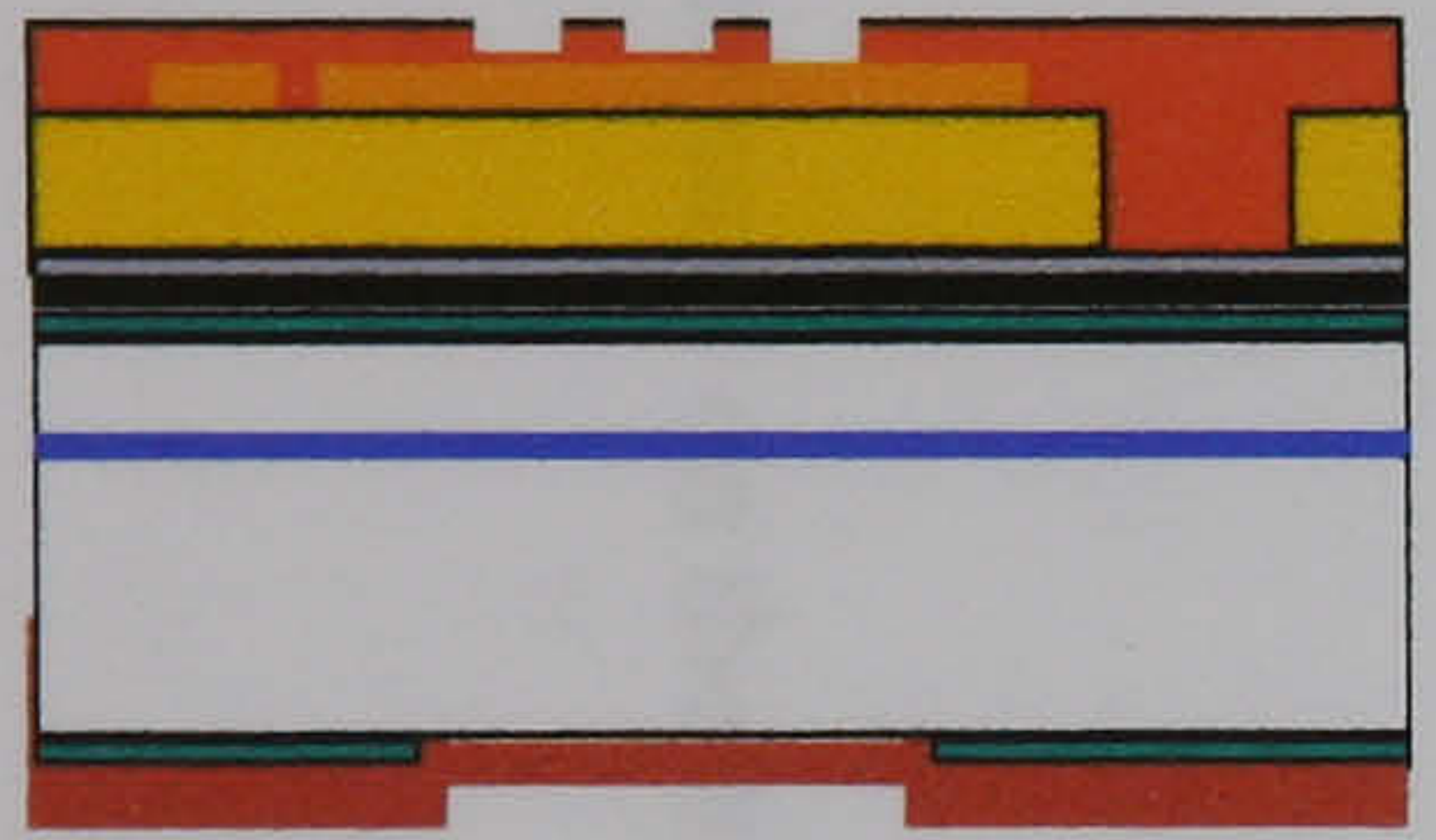

Mask 4 Photo-patterning of SBX

26

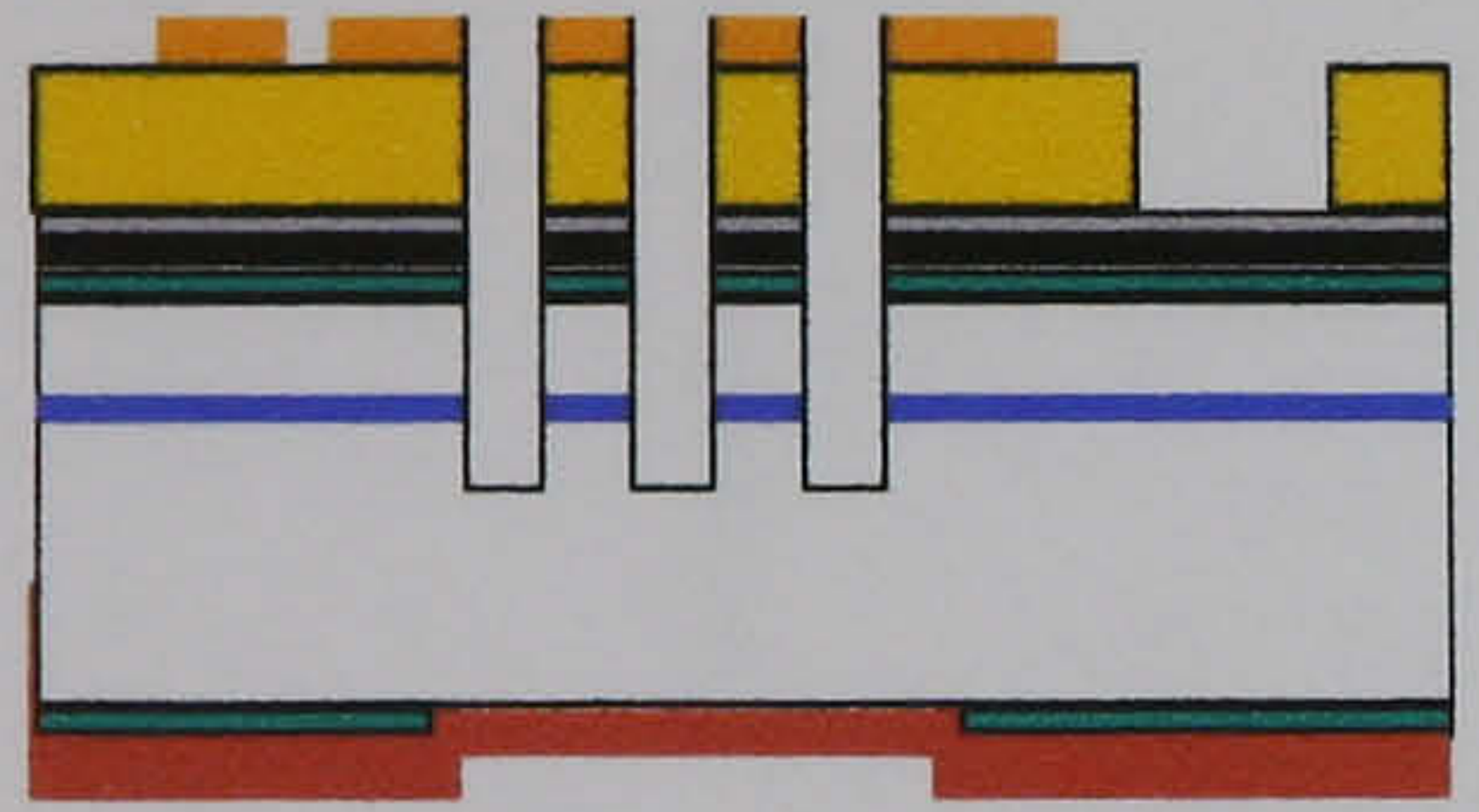

Powder blasting of device structures and stripping of SBX

33

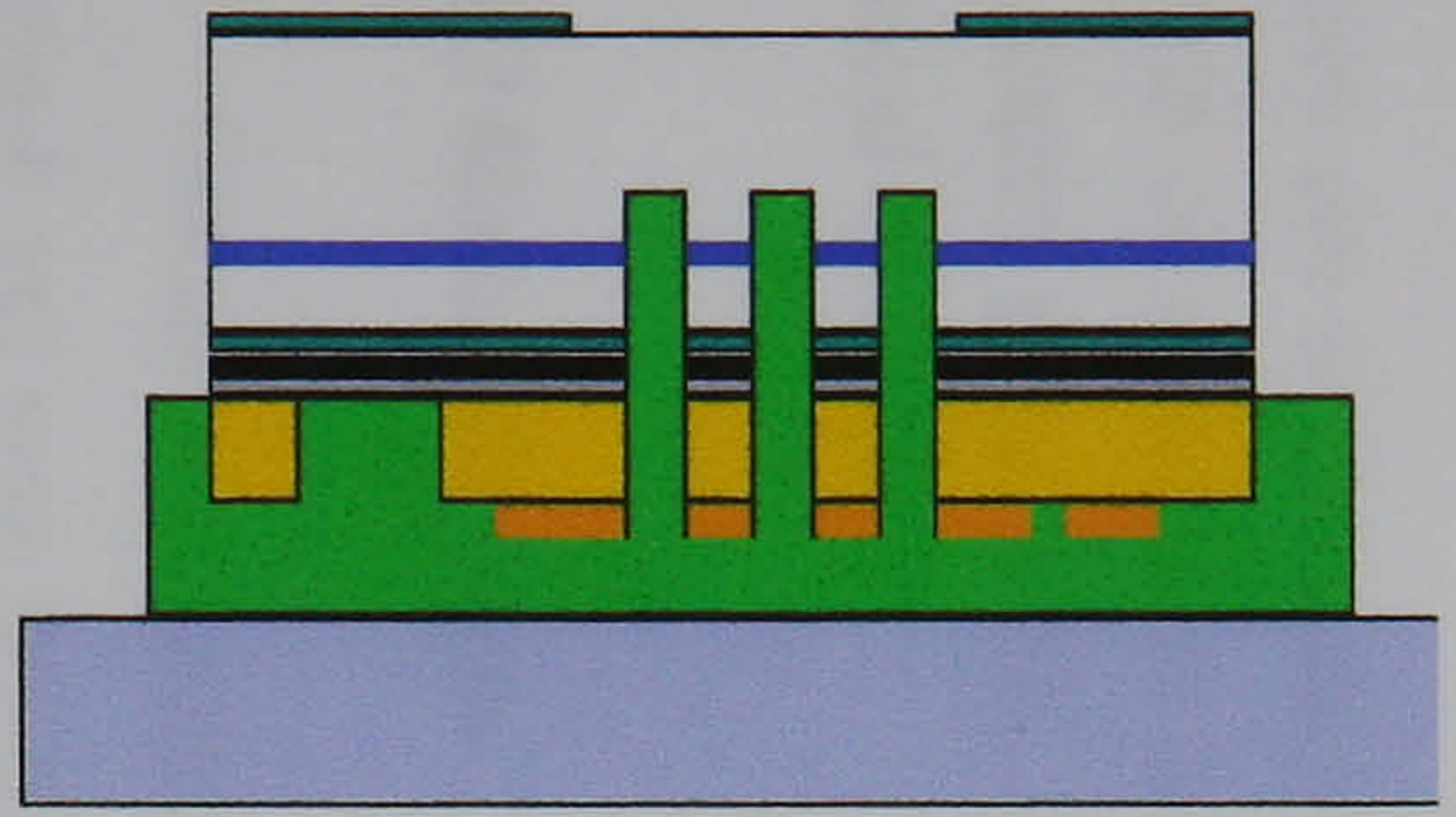

Use black wax to secure the wafer to a glass support, wet etch the Si with KOH to release the cantilevers and Saw the structure into a chip set

36

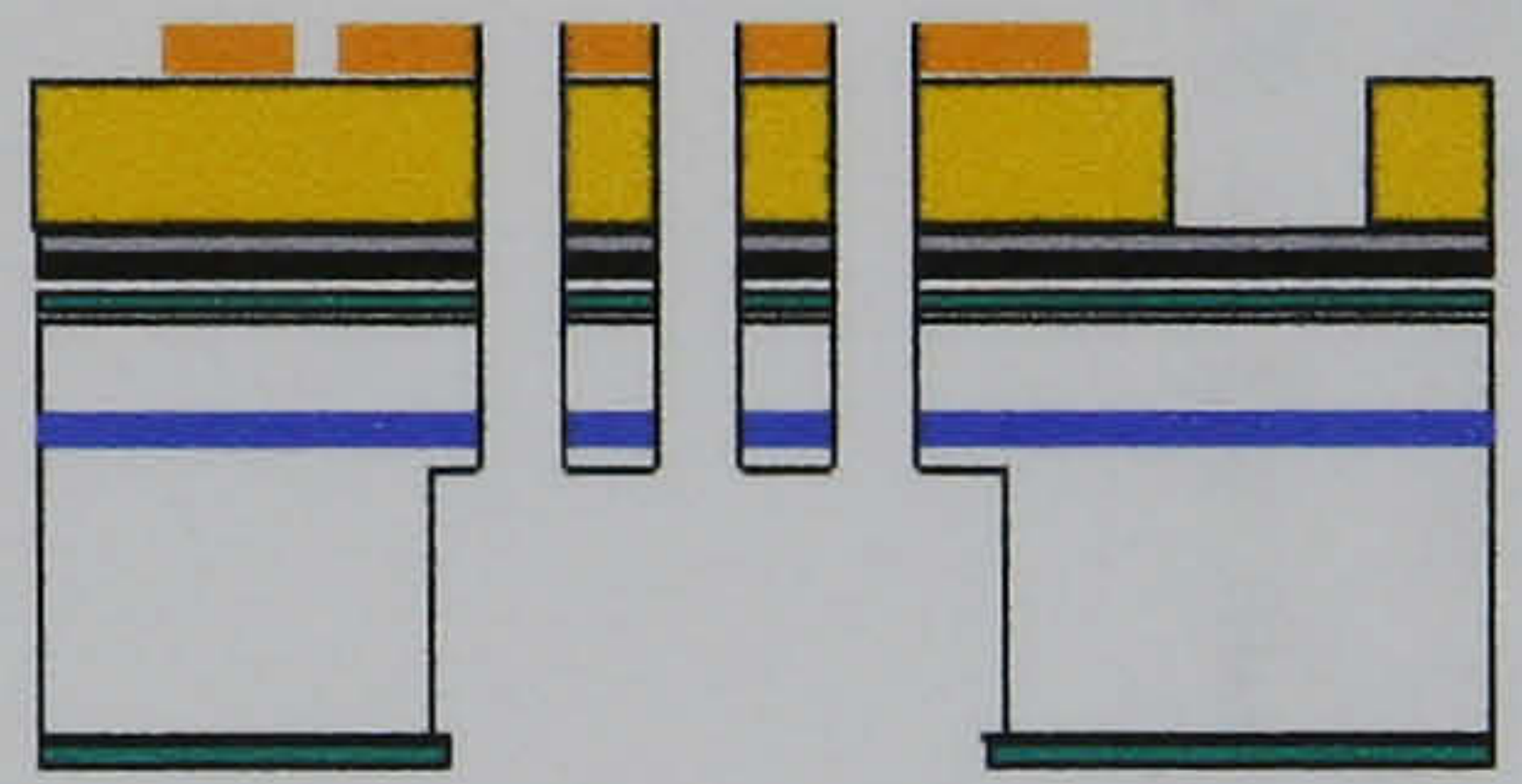

Release structure with Acetone

Fig 5.8 Process 1 – process flow.

Photo-patterning of the PZT with SBX® (PhotoBrasive Systems) with mask number four (step 25) is completed before powder blasting. Cantilever structures are cut into the PZT and into the underlying substrate to a depth below the buried oxide layer: through powder blasting (step 26). Powder blasting will be conducted with Al_2O_3 particles (15 µm diameter) at 80 psi. SBX® is an elastomeric photoresist that cannot be removed with acetone; a commercial stencil remover has to be used. Both the PZT and the Si are inert with respect to the stencil remover.

After powder blasting, the Cr on the back face is removed with a commercial Cr etch to expose the Si_3N_4 mask and Si features. Exposure of the Si features allows for etching of the Si and subsequent release of the cantilevers. The device wafer requires support during the etching stage; for this reason, the device wafer is secured to a glass support with black wax. The Black wax melts at around 80 °C, and this is sufficiently low not to de-pole the ceramic. Anisotropic wet etching of Si in KOH is used to release the cut cantilevers from the bulk silicon of the substrate.

Devices are to be sawn whilst on the glass support held in place with black wax. The removal of structures from the glass support with Toluene before mounting on a PCB with super glue. Wire bonding can then be made to the devices and to the PCB for electrical testing.

5.3 Mask Design

5.3.1 General Layout

The mask set was designed for anisotropic wet etching of <100> orientated Si: with a wall angle α_{Si} of 54.7°. The thickness of the wafer was noted as h_{wafer}. All back face features were designed to be square with side lengths of L_{bf}. The diameter of the front face feature D_f, assuming a circle shaped feature, may be related to the dimensions of the back face feature:

$$L_{bf} = D_f + \left(\frac{2.h_{wafer}}{\sqrt{2}.Tan.\alpha_{Si}} \right) \tag{5.32}$$

In the case of square shaped features on the front face of length L_f:

$$L_{bf} = L_f + \left(\frac{2.h_{wafer}}{Tan.\alpha_{Si}} \right) \tag{5.33}$$

Step	Description
Starting material	Buried Oxide wafer see Table 5.5
1. Clean	Standard clean see experimental chapter
2. Si_3N_4	Deposition of 200 nm Si_3N_4 by LPCVD at QUB
3. Photolithography	Mask 1 (back face pattern) at QUB
4. Etch	RIE of back face Si_3N_4 at QUB
5. Strip	Strip photoresist at QUB
6. Clean	
7. Metal	Sputtering of Ti (200 nm)
8. Oxide	Thermal oxidation to TiO_2 (300 nm) – Diffusion barrier
9. Clean	
10. Metal	Sputtering of Ti (8 nm) and Pt (200 nm) back electrode
11. Metal	Sputtering of Cr on to back face(300 nm)
12. Clean	
13. PZT	Deposit PZT thick film with intermittent thermal cycling up to 450 °C for 15 s
14. Sintering	Sinter the PZT at 710 °C for 30 min in air
15. Poling	Corona pole the PZT at 115 °C 10 kV for 10 min
16. Clean	
17. Photolithography	Mask 2 wet etch of PZT
18. Etch	Etch openings in the PZT with a dilute solution of $HF(aq)_{(aq)}$ and $HCl_{(aq)}$
19. Strip	Strip photoresist
20. Clean	
21. Photolithography	Mask 3 top electrode
22. Metal	Sputter deposition of Cr (8 nm) and Au (100 nm) top electrode
23. Lift off	Lift off photoresist with acetone over night.
24. Clean	
25. Photolithography	Mask 4 Device set for powder blasting. At RAL
26. Powder Blasting	Powder blasting of device structures with Al_2O_3 (15 μm) at 80 psi.
27. Strip	Remove SBX with Stencil remover
28. Clean	Remove powder with air wash before removing to the clean room for standard clean
29. Photolithography	Protect PZT
30. Etch	Remove Cr from the back face
31. Strip	Strip photoresist
32. Clean	
33. Mount	Support glass for KOH etching with black wax
34. Etch	Wet etch Si in KOH
35. Sawing	Sawing of structure into chip set

36. Release	Release chips from grease with acetone
37. Plasma ash	Clean up surface of devices
38. Mount	Mount chips on PCB
39. Wire bond	Form wire bonds to device and PCB

Table 5.6 The Si_3N_4-KOH (Standard) Process

The completed wafer set design can be seen in Fig 5.9. The device wafer has been designed to be divided into a set of chips: 12 x 12 mm. Each chip contains 1,2 or 4 devices dependent upon D_f. The minimum gap between devices, i.e. four on one chip, is 800 μm. This spacing is measured between the features for Si etching on the back face and determines the distribution of devices.

$$L_{center-center} = \frac{L_{bf1}}{2} + 800\times10^{-6}m + \frac{L_{bf2}}{2} \tag{5.34}$$

The length from device centre to centre $L_{centre-centre}$ may be defined from the diameters of device 1 and device 2: $D_{max}1$ and $D_{max}2$ respectively.

$$L_{center-center} = \tfrac{1}{2}(D_{\max}2 + D_{\max}1) + \left(\frac{2.h_{wafer}}{\sqrt{2}.Tan.\alpha_{Si}}\right) + 800\times10^{-6}m \tag{5.35}$$

The mask set is composed of four masks; each mask is drawn in AutoCAD R14 as one of four layers. Mask features are drawn as closed polylines of zero line width. The AutoCAD drawing was converted to a DXF file before conversion to GDSII file, from which the e-beam machine could write the masks. The mask set was drawn onto 2.5 mm thick glass (amorphous quartz) plates; this was done by CMF (Central Microstructure Facility) at RAL (Rutherford Appleton Laboratory). The E-beam will not read (and hence not write) open polylines of zero width, or objects that are contained within closed polylines or polygons. However, an inner object may be subtracted from an outer object by exclusive overlap.

There are two sets of alignment marks, major and minor, that have been incorporated into the design. The larger alignment marks provide a window of a few mm for alignment between the mask and the wafer, and are located at the edge of the mask. The minor alignment marks have been located between the device chips towards the centre of the mask. The minor marks provide a back up mechanism for alignment allowing alignment near the centre of the wafer. An additional alignment mark is incorporated for aligning the mask against the wafer flat.

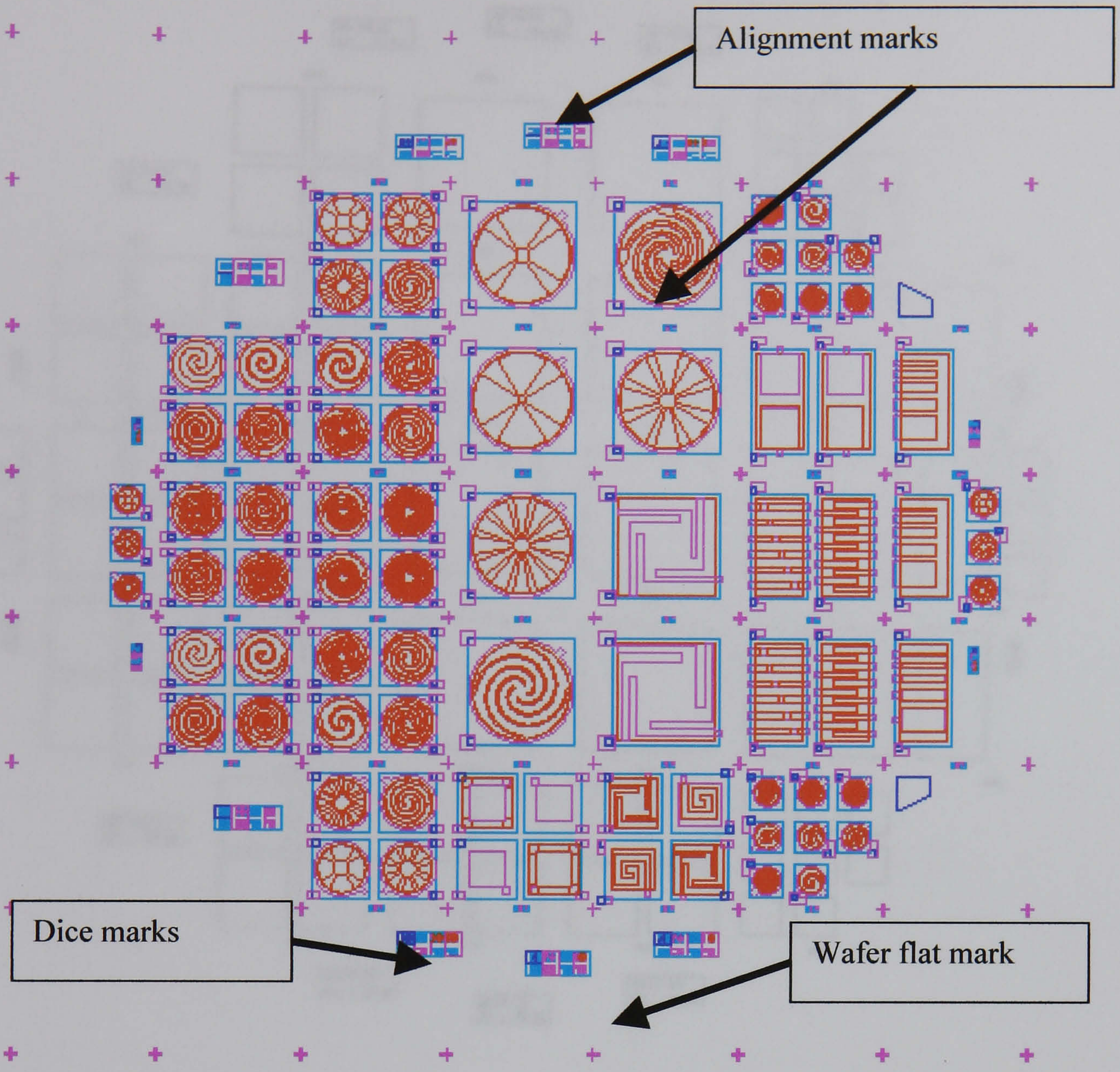

Fig 5.9 Complete mask set; a composite of the four masks: mask 1 (blue), mask 2 (dark blue), mask 3 (pink) and mask 4 (red)

5.3.2 Mask Set

5.3.2.1 MASK 1 Si Etch (Fig 5.10)

The back face mask design for the wet etching of Si is shown in Fig 5.10. It should be noted that this design has been mirrored in the mask such that cavities etched in the back face are coincident with front face devices. The mirroring operation was carried out as part of the mask fabrication process at RAL. As noted, square features were incorporated specifically for anisotropic wet etching of the Si.

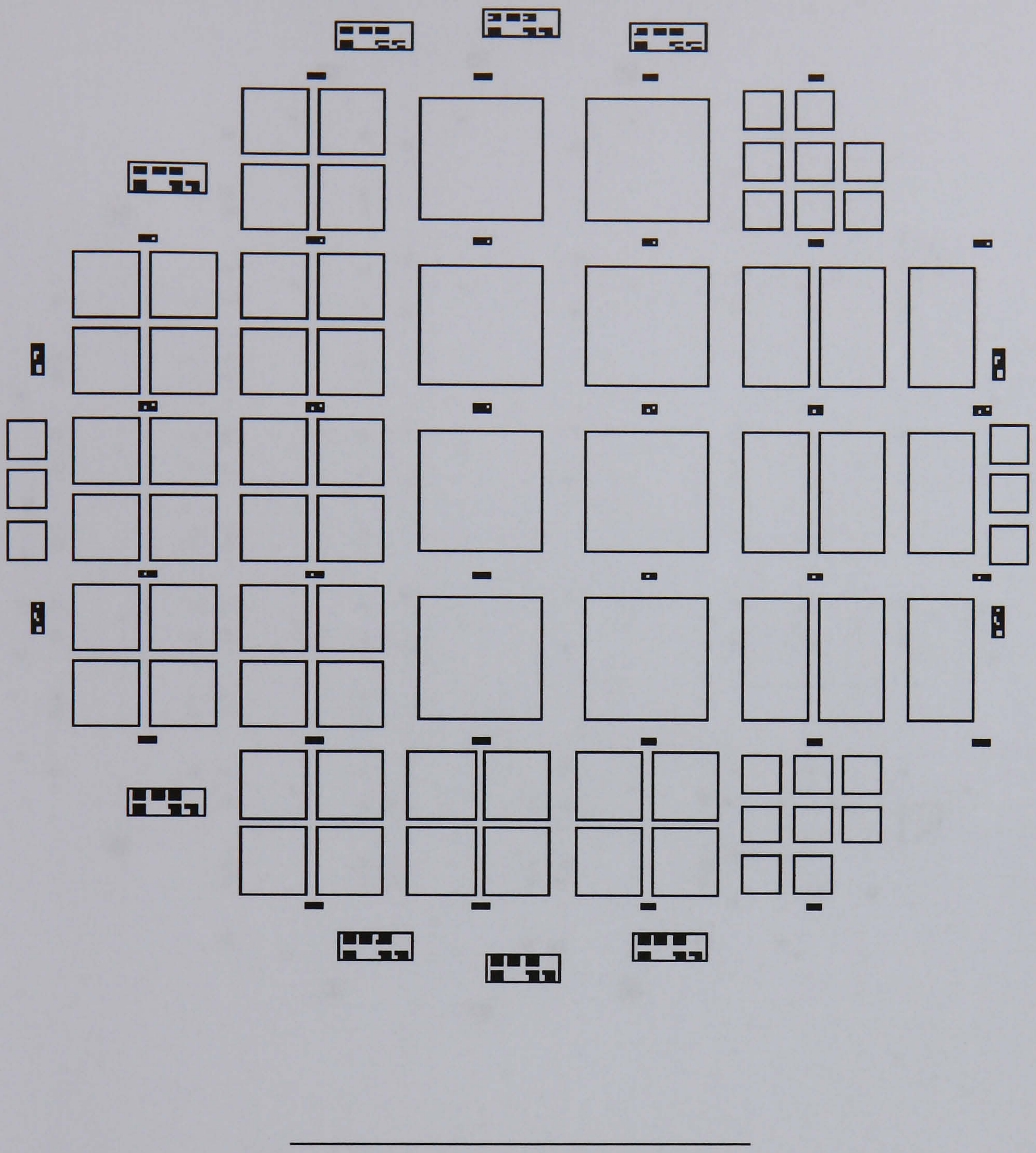

Fig 5.10 Mask1: For the wet etching of Si. Back face mask

5.3.2.2 MASK 2 PZT Etch (Fig 5.11)

This is the mask for the photolithographic patterning of the PZT for the PZT wet etching. The object was to open paths through the PZT for electrical contact to the back electrode.

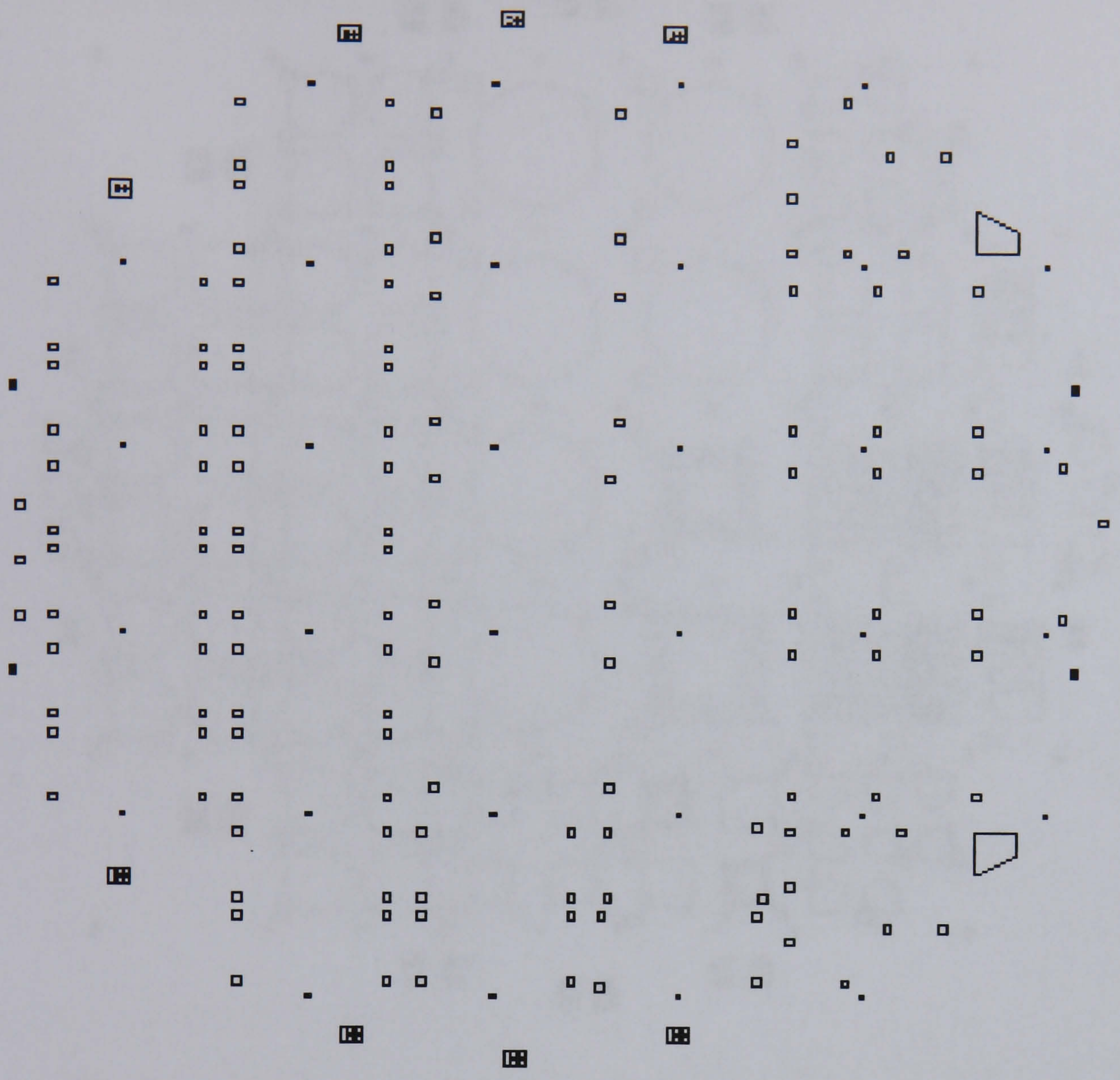

Fig 5.11 Mask 2: For the wet chemical etching of the PZT thick film

5.3.2.3 MASK 3 Top Electrode (Fig 5.12)

Electrode and dicing mask set (Fig 5.12). Circular pads are drawn to encase the entire device. This will result in electrode pads covering the area of the devices during processing. The pads will be blasted through during the powder blasting stage leaving the surface of the devices with a uniform continuous electrode.

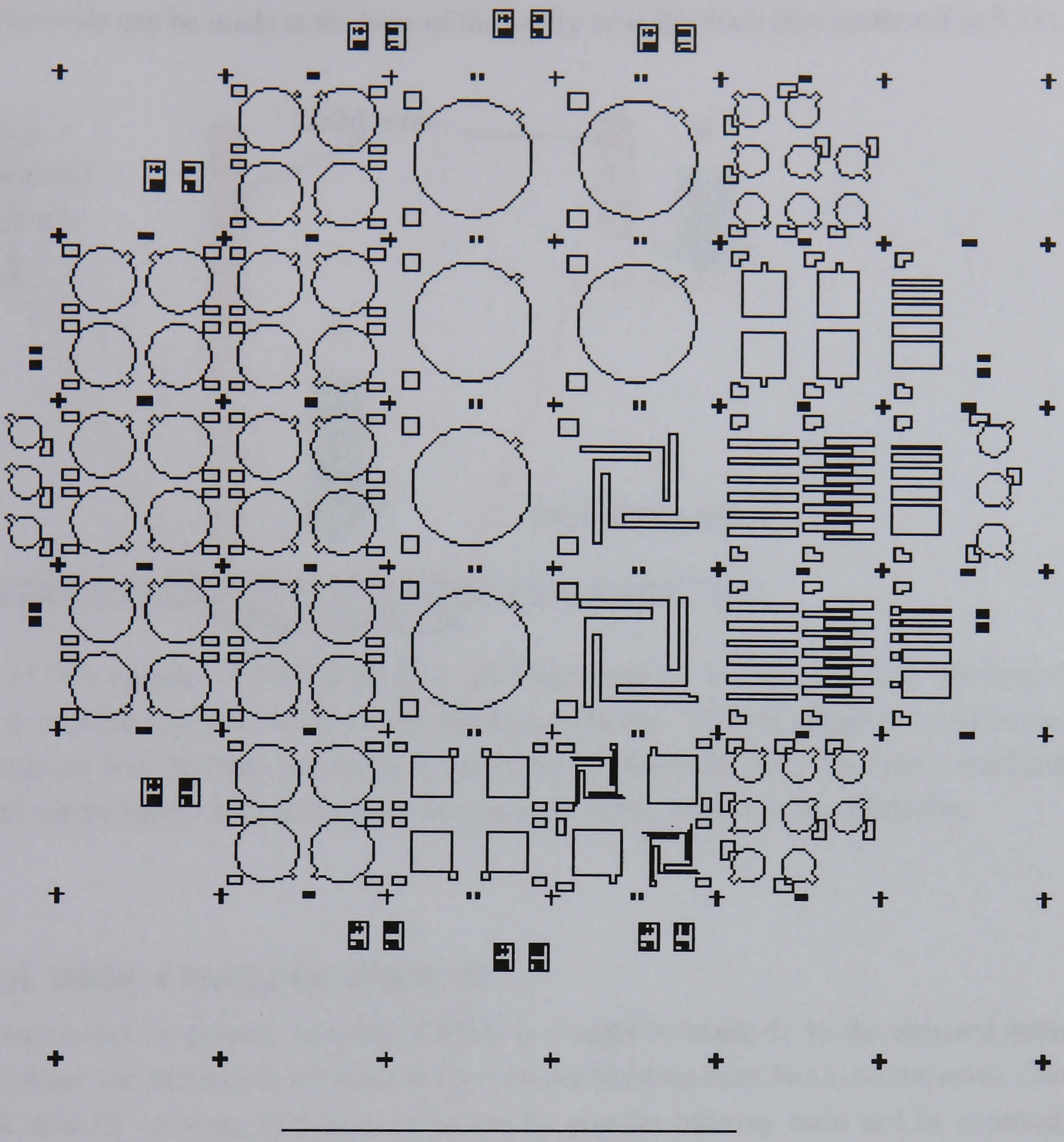

Fig 5.12 Mask 3: For the top electrode pattern

Additional pads (500 x 500 μm) were added for wire bonding contacts; these were added to both the top and back electrodes. Contact to the bottom electrode can be made through wire bonding to an Au contact pad either at the base of the etched via or at the surface (Fig 5.13). It is envisaged that wire bonding will be done at RAL, beyond the end of this project, through thermo-compression bonding.

Dice marks were incorporated in mask 1 in the initial design to divide devices into chips through sawing. However, a consideration is the support of the cantilevers during sawing: mechanical vibration could damage fragile beams. Devices will be supported faces down on support wafers during the sawing stage with black wax obscuring the dice marks. Sawing will be conducted by eye on the back face. After sawing, chips will be mounted on a PCB for testing. Electrical contact to each device will be made through wire bonding from the device to the PCB. Wire bonding will be used to make electrical contact to both the top and bottom electrodes of each device. As noted earlier electrical contact to the base electrode can be made at the base of the cavity or at the thick film surface (Fig 5.13).

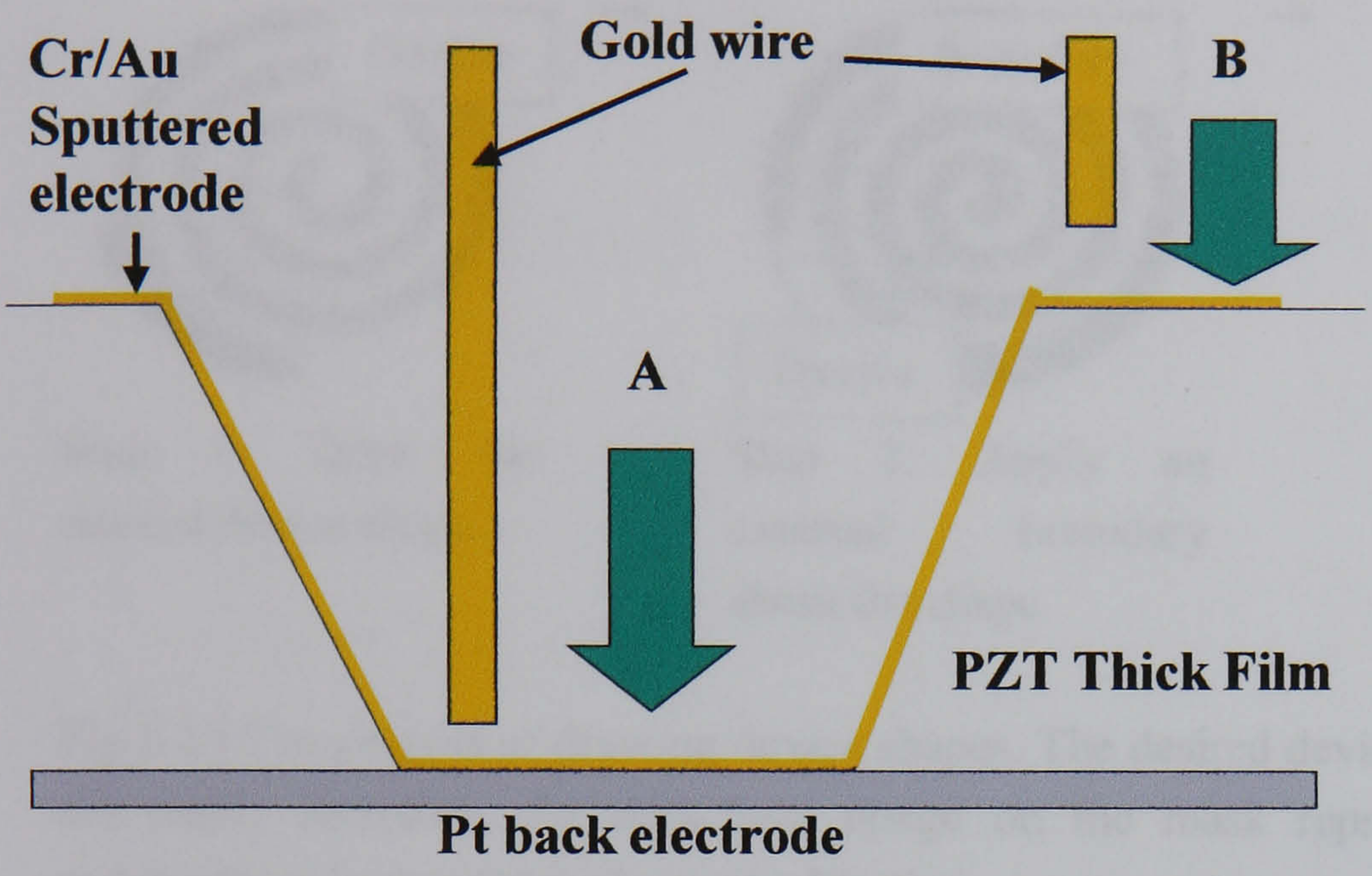

Fig 5.13 Via opened in PZT thick film, with sputtered Cr/Au film for wire bonding at point A or B for electrical contact with the base electrode. The image shows a continuous gold coating from the back electrode to the surface of the thick film. Therefore, electrical contact can be made either at the back electrode or on the surface of the thick film.

5.3.2.4 MASK 4 Device Set (Fig 5.15)

The photoresist for powder blasting, SBX®, is a negative mask 4. As the exposed areas will be kept: the sections to be removed by powder blasting must be Cr on the mask. The SBX® directly covering the areas to be cut by powder blasting must not be exposed; these areas must be dark-field on the mask. The following steps ensure that Cr covers the unwanted areas, and that areas that are to be retained on the device-wafer are clear field on the mask, see Table 5.7

Steps	Actions
1	Draw feature shape that is to be kept
2	Place a boundary about that feature shape
3	Apply exclusive overlap

Table 5.7 Summary of mask properties. This table lists the requirements that need be born in mind for the masks to be drawn

Exclusive overlap works by subtracting only the areas contained within closed features; however, if a closed feature is contained within another closed feature then the innermost feature will be subtracted from the outermost feature (see Fig 5.14). In addition, the desired feature and the area beyond its perimeter should be clear (light field). The properties of the masks are listed in Table 5.8

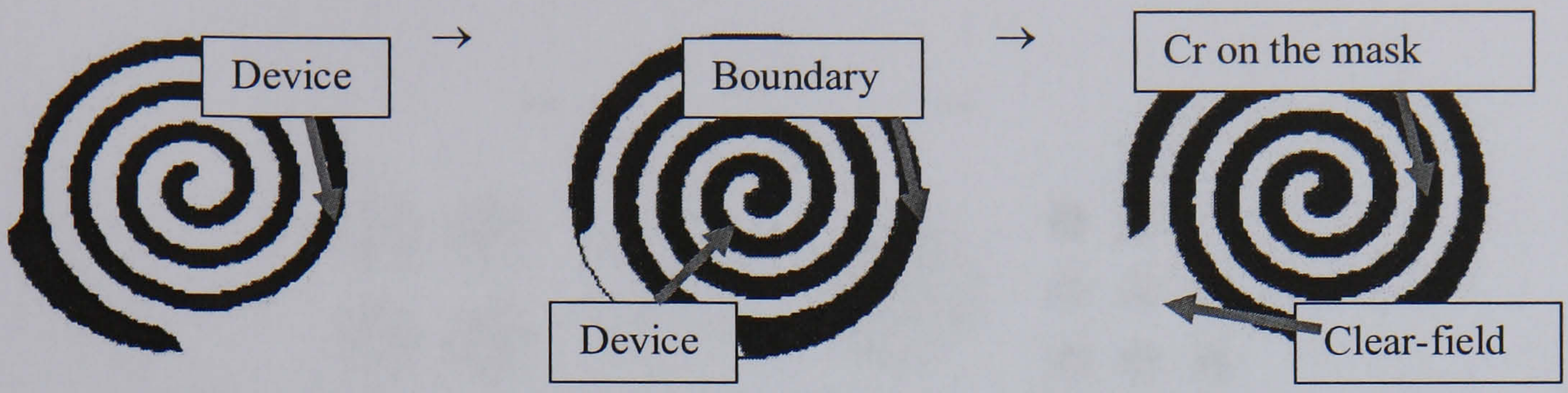

Step 1: Draw the desired device shape.

Step 2: Apply an external boundary about the shape.

Step 3: Use exclusive overlap to retain a dark field image of the unwanted area.

Fig 5.14 The process of drawing device shapes. The desired device must be clear-field on the mask; therefore, the dark-field image on the mask represents the area that is eventually to be lost through powder blasting.

Mask No.	Function	working	Field outside polygon feature	Operations	Exclusive Overlap
1	Si Etch	+ ve	Dark	Mirrored	Yes
2	PZT Etch	+ ve	Dark	Standard	Yes
3	Top Electrode	+ ve	Dark	Standard	Yes
4	Device Set	- ve	Light	Standard	Yes

Table 5.8 Summary of mask properties. This table lists the requirements that need be born in mind for the masks to be drawn.

5.3.3 Alignment Marks

The complete set of alignment marks is shown in Fig 5.16 representing the superimposition of all the alignment marks from all the masks. The Fig also shows the set of alignment marks for MASK1. In the case of positive working masks (MASKS 1-3) all alignment marks consist of a clear window in a dark field mask with opaque features (Cr alignment marks). The clear window is necessary because it creates a visible region for alignment between the marks. This has been drawn as a set of closed polygons within a closed polygon border.

The alignment mark set is divided into eight units; each unit allows alignment between two masks (or one mask and the wafer). Each unit corresponds to a specific mask and face of the wafer (see Table 5.8). Wet etching of PZT thick films results in features with rough sidewalls, see chapter 7, because alignment marks that have been wet etched into the PZT are unlikely to possess the definition necessary for precise alignment to subsequent masks in the set. The fact that only one unit has been assigned for alignment between mask two and 1, means that there are seven units remaining for further alignment of subsequent masks in the set.

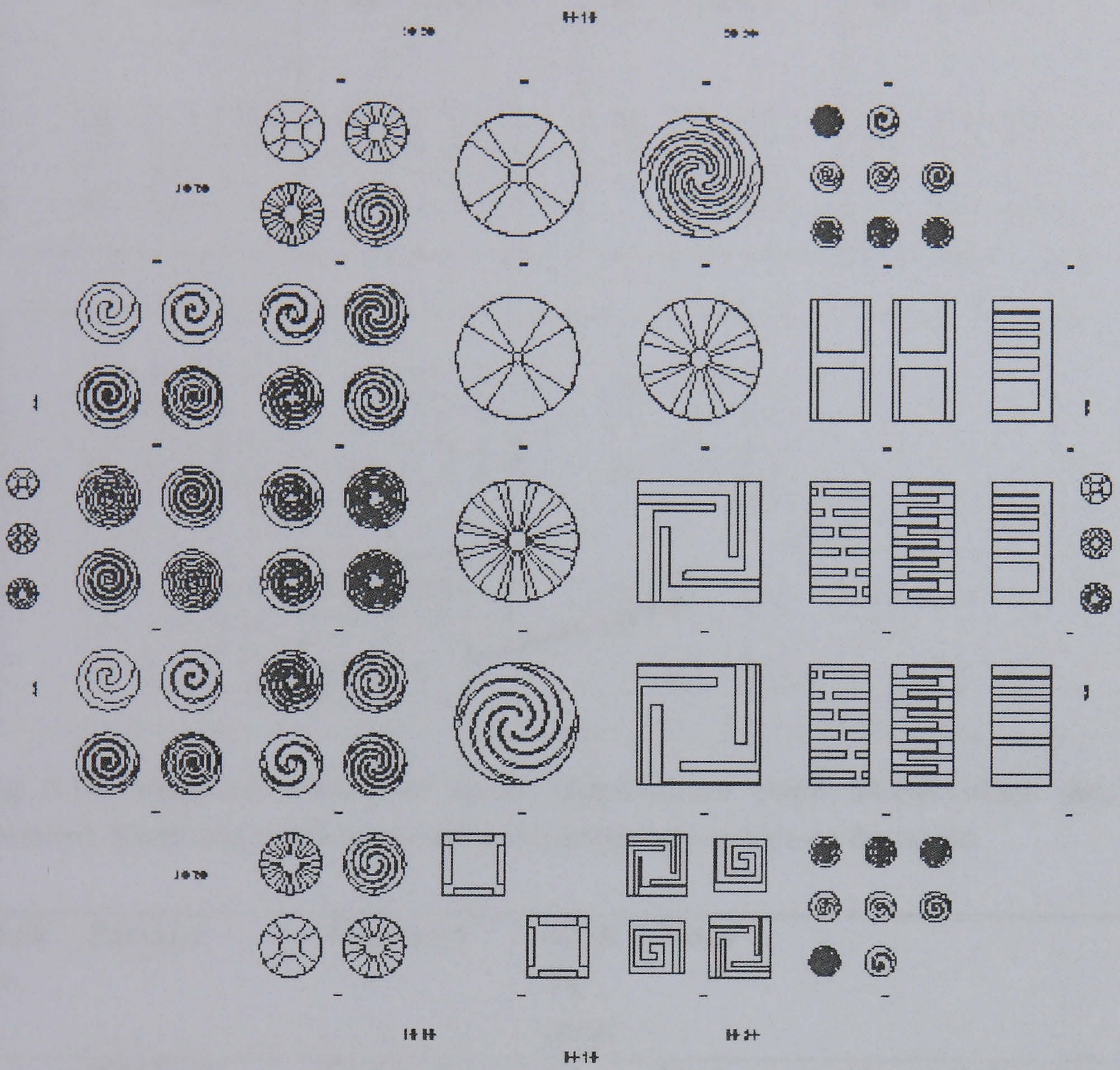

Fig 5.15 Mask 4:For the powder blasting of actuators.

The top electrode pattern has been designed so that all masks that come after mask 3 in the set can be aligned through front to front alignment with mask 3. That is to say that when the Cr/Au top electrode pattern is applied through sputtering, alignment marks will also be deposited on the surface of the PZT for subsequent alignment. Additionally, all further masks can be aligned to the back face; this is a belt and braces approach. There are two spare sets of numbers for mask X and Y; these are spare alignment marks in case additional masks were required in a later project.

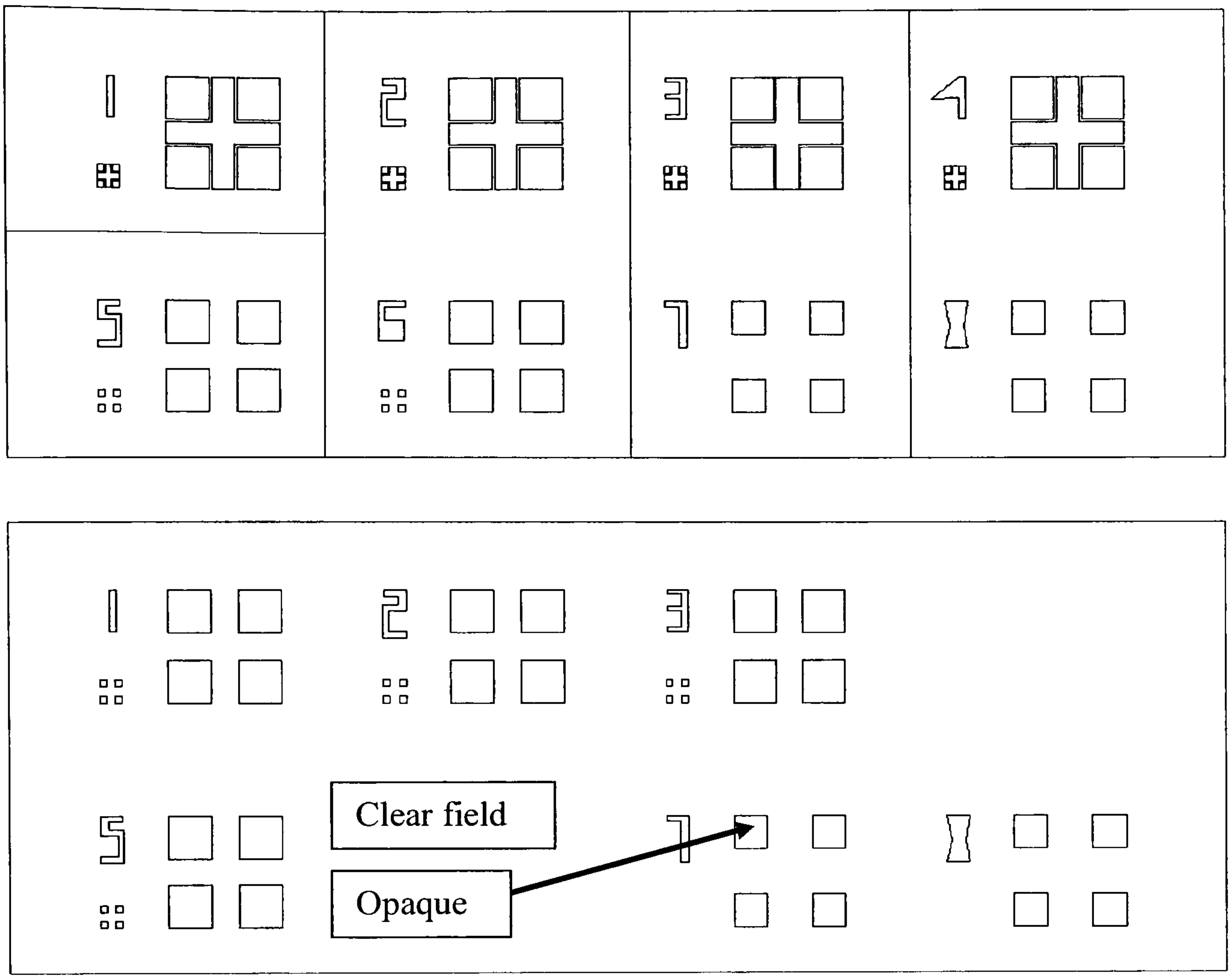

Fig 5.16 Alignment marks, all layers superimposed (top). MASK1-Back face set (bottom). Small and medium squares and numbers are opaque on the masks.

Mark No.	Function	Alignment	Mask To mask	Notes
1	PZT Etch	Back to front	2:1	Marks cannot be used for alignment after PZT wet etching
2	Top Electrode	Back to front	3:1	Marks to be used for further alignment
3	Device Set	Back to front	4:1	
4	Device Set	Front to front	4:3	
5	Spare	Back to front	X:1	
6	Spare	Front to front	X:3	
7	Spare	Back to front	Y:1	
8	Spare	Front to front	Y:3	

Table 5.8 Summary of the design of alignment marks. The letters X and Y correspond to additional masks that can be added to the mask set, if required later.

6 High Temperature Processing Of PZT Thick Films

6.1 *Introduction*

This chapter reports on the thermal processing of PZT thick films of the form PZT/electrode/substrate. Particular attention is given to the interfaces between the PZT thick film, the electrode and the substrate. The electrode and PZT thick film was found to de-laminate from the Si substrate when sintered. Pb diffuses from the PZT thick film into the substrate. The Pb is oxidised to PbO before it can flux with SiO_2 to yield a eutectic liquid at the sintering temperature. The eutectic liquid, PbO-SiO_2, forms beneath the electrode. Sintering stresses parallel to the plane of the thick film are considered the most likely cause of film delamination and blistering.

The PZT thick films are to be used as active layers in piezoelectrically actuated devices. Separation of the PZT from the substrate has to be minimised in order to fabricate effective devices. The incorporation of a diffusion barrier layer of the form PZT/electrode/barrier layer/substrate was studied. The object of the diffusion barrier was to eliminate Pb diffusion, and hence minimise electrode substrate de-lamination. Substrate systems considered were Si and Si_3N_4/Si as devices were to be fabricated on these materials. Yittria stabilised Zirconia (YSZ) and titania (TiO_2) were considered as barrier systems. YSZ/SiO_2/Si and TiO_2/Si_3N_4 were found to be most effective; PZT showed best adhesion with these combinations.

6.2 *Results*

6.2.1 Thermal Processing Of PZT Thick Films

The electrical properties of PZT thick films on Pt/Ti/SiO_2/Si substrates were measured for films sintered under Ar and air atmospheres. For each sintering gas, samples were sintered at 710 °C, 800 °C and 900 °C. For each sintering temperature, three films were prepared according to intermittent thermal treatment i.e. drying and crystallisation temperatures. Conditions 1 to 3 are given below in Table 6.1 below.

Graphs for dielectric constant, loss and resistivity are plotted against sintering temperature and are shown below in Fig 6.1, Fig 6.2 and Fig 6.3 respectively. In general, intermittent thermal treatment was shown not to have a significant effect on electrical properties of the deposited thick films. However, in films fired in an Ar atmosphere, at 710°C, a dielectric constant of 816 was achieved with a dielectric loss of 2%.

Intermittent thermal treatment	Sol Layers		Composite Layers	
	Drying	Crystallise	Drying	Crystallise
Condition 1	200 °C/50 s	-	-	450 °C/15 s
Condition 2	200 °C/50 s	-	200 °C/50 s	450 °C/15 s
Condition 3	200 °C/50 s	450 °C/15 s	200 °C/50 s	450 °C/15 s

Table 6.1 Thermal treatments applied to films for each sintering temperature. These treatments are applied intermittently between spin coating steps. These thermal treatments are applied before the sintering stage.

Fig 6.1 shows that the dielectric constant declined as the sintering temperature was increased, and this was the case for films sintered either under an air or an Ar atmosphere. The decline in dielectric constant, between 710 to 800 °C, appears more rapid in the case of Ar sintered films. This finding is unusual in that sintering temperature was expected to increase the density, of the film, and thereby the dielectric constant. Fig 6.2 shows that tanδ increases rapidly in films sintered under Ar at higher temperatures, and that it decreases in films sintered under air. This suggests that films fired under Ar become electrically conducting when sintered at higher temperatures. Fig 6.3 shows resistivity plotted against sintering temperature, confirming that films sintered under Ar become electrically conducting as the sintering temperature is increased. Further, that films sintered under air become electrically insulating as sintering temperature is increased.

SEM fracture surfaces of films fired under Ar are presented in, Fig 6.4 to Fig 6.12 for films fired at 710 to 900. These films may be subdivided according to the intermittent thermal treatment applied during film fabrication (see Table 6.1). These images show a progressive increase in the damage to the back electrode in proportion to the sintering temperature. Films that were fired both at 800 and 900 °C exhibited closed porosity. The overall thickness of these films was reduced with increasing temperature; suggesting that some evaporation has taken place during sintering..

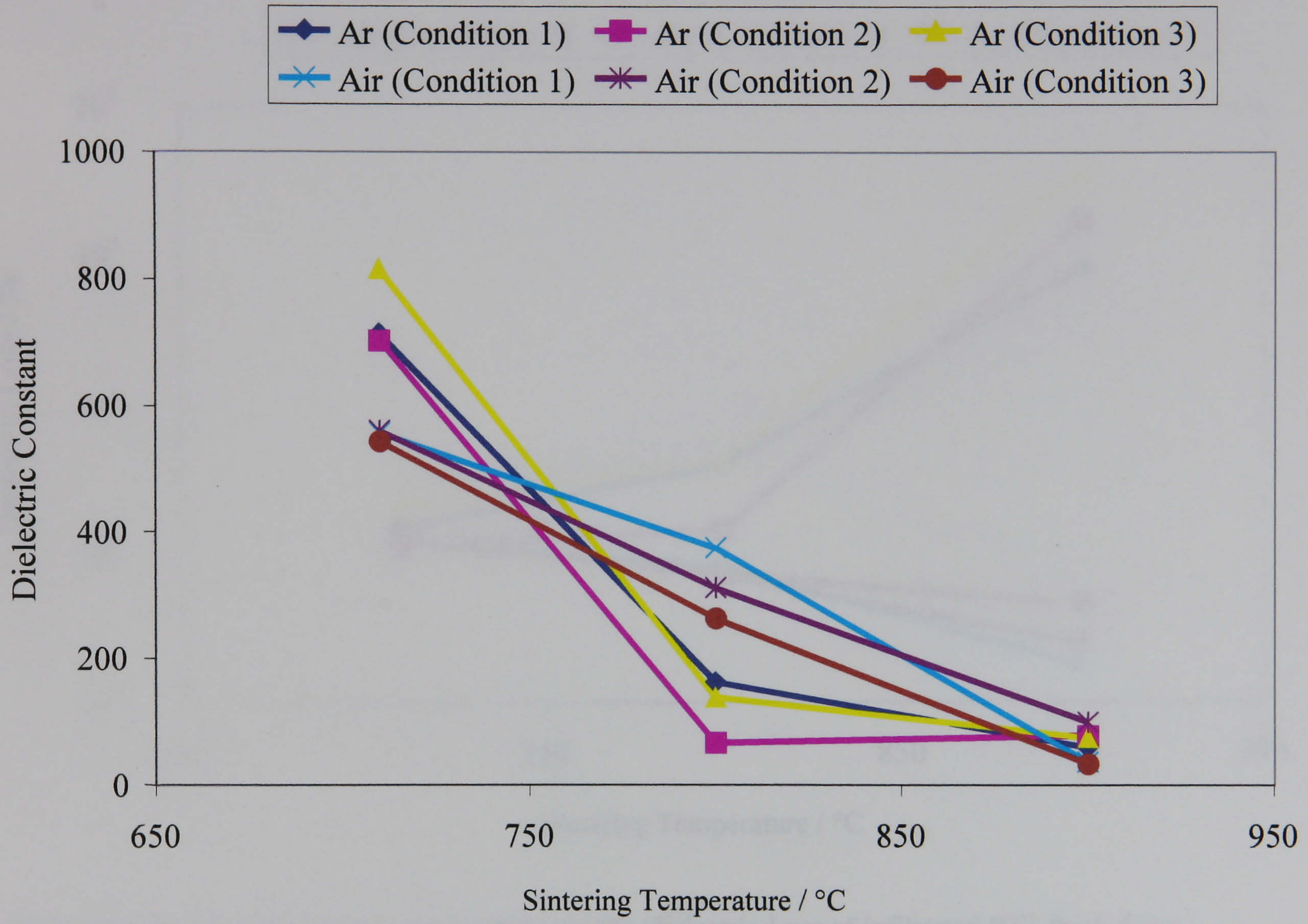

Fig 6.1 Effect of thermal treatment and sintering atmosphere on the relative permittivity of infiltrated PZT thick films.

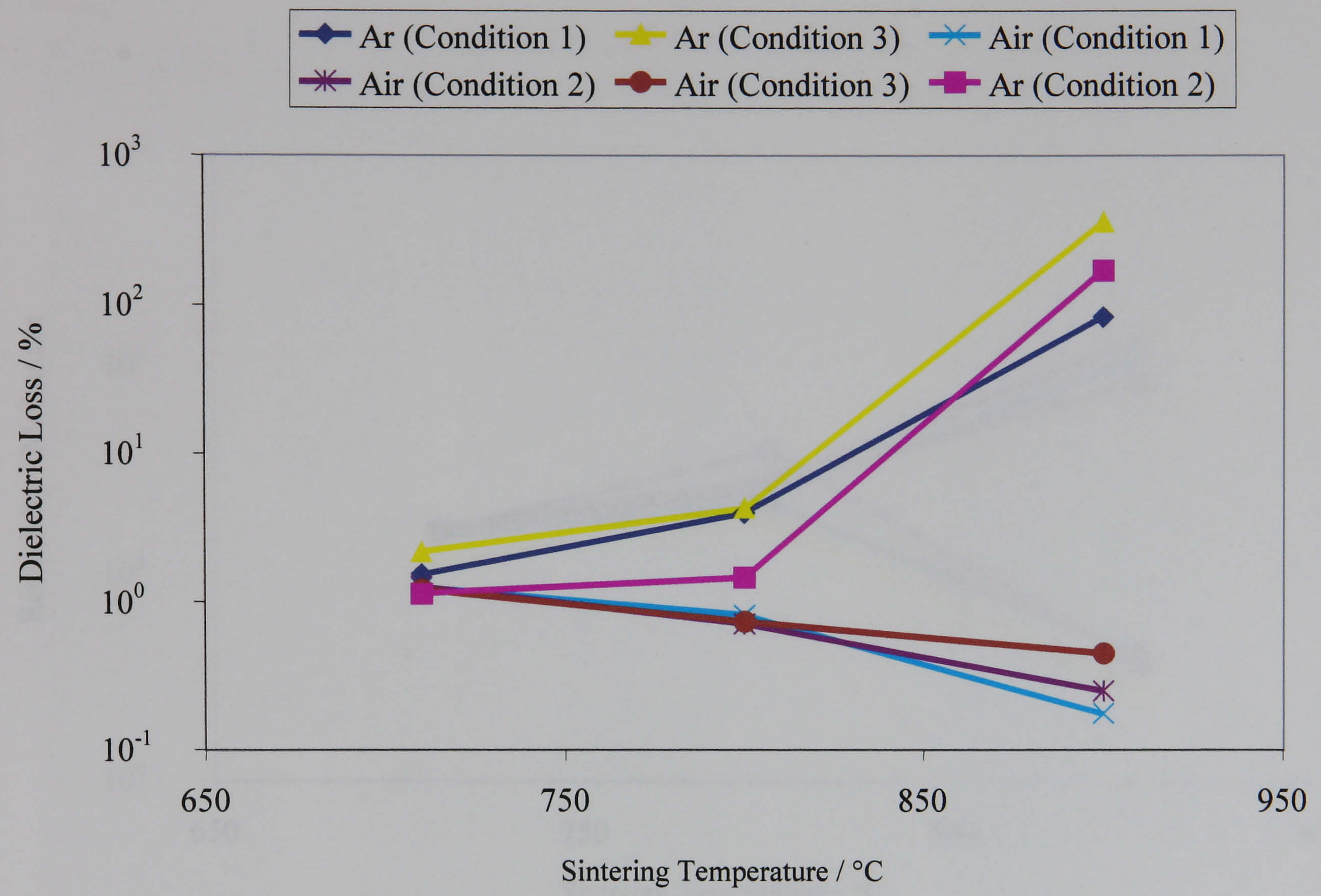

Fig 6.2 Effect of thermal treatment and sintering atmosphere on the Dielectric Loss of infiltrated PZT thick films

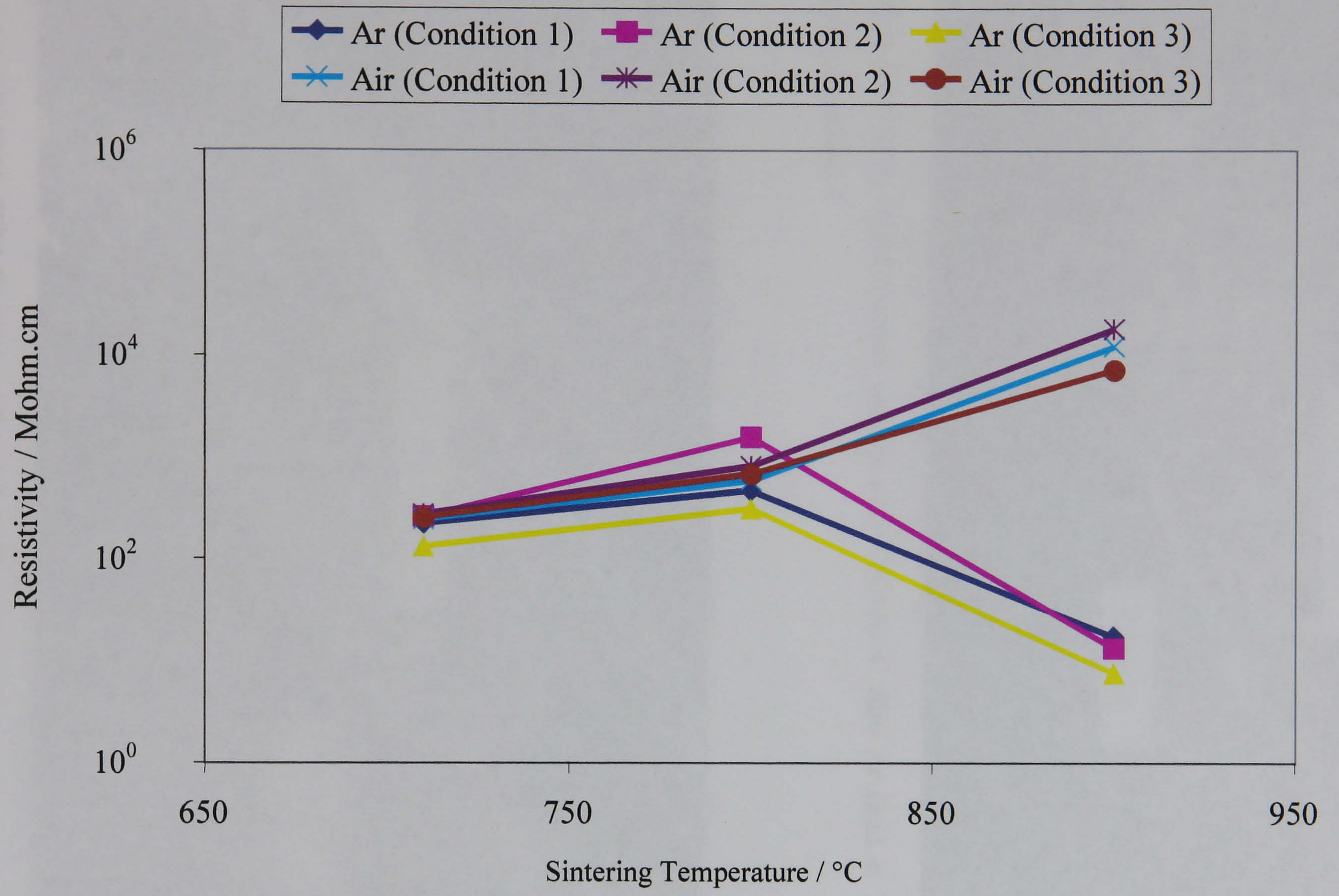

Fig 6.3 Effect of thermal treatment and sintering atmosphere on the resistivity of infiltrated PZT thick films

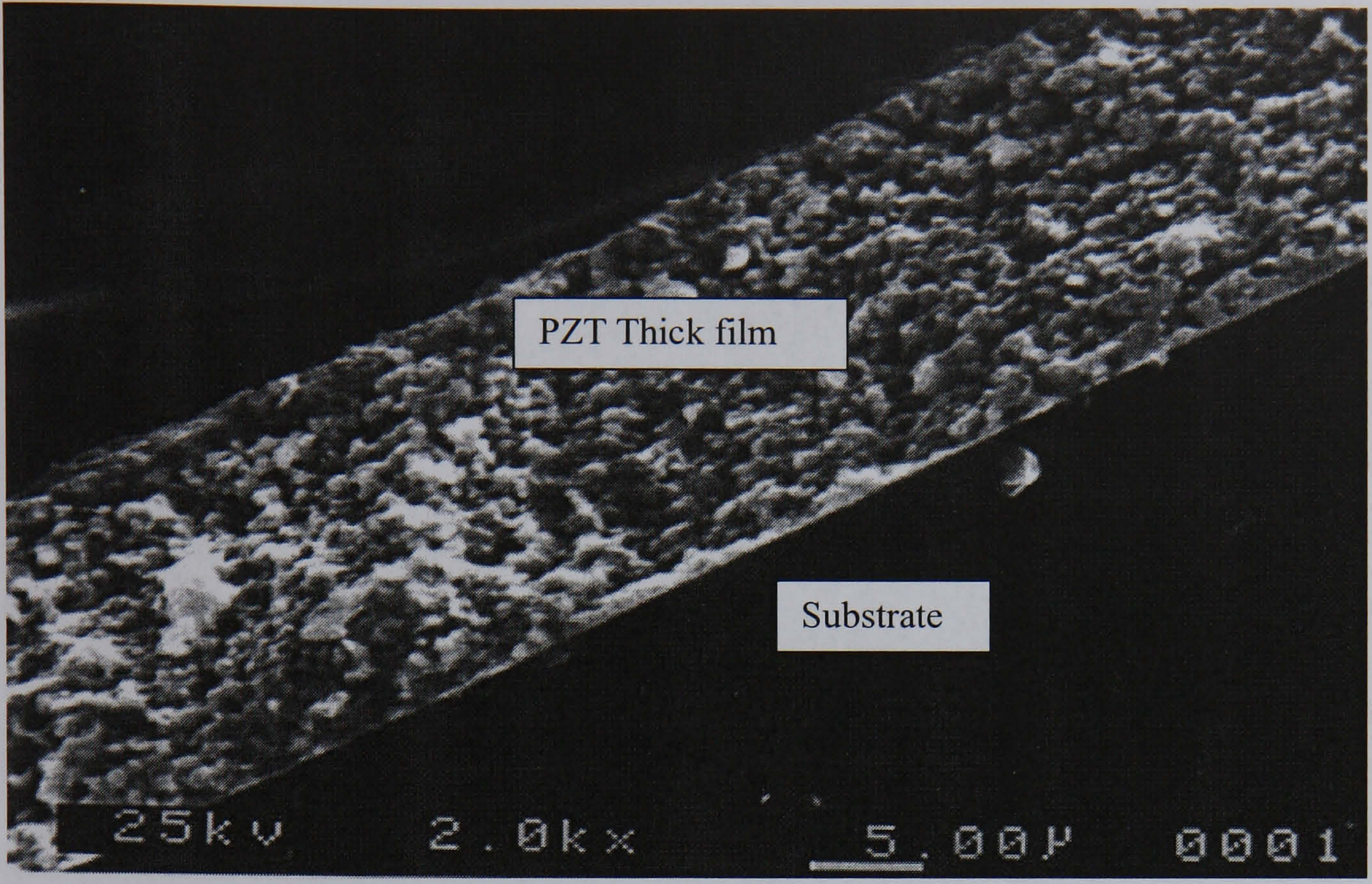

Fig 6.4 PZ42001 SEM fracture surface of S+7(C+S)+C film Ar fired at 710°C using drying condition 1

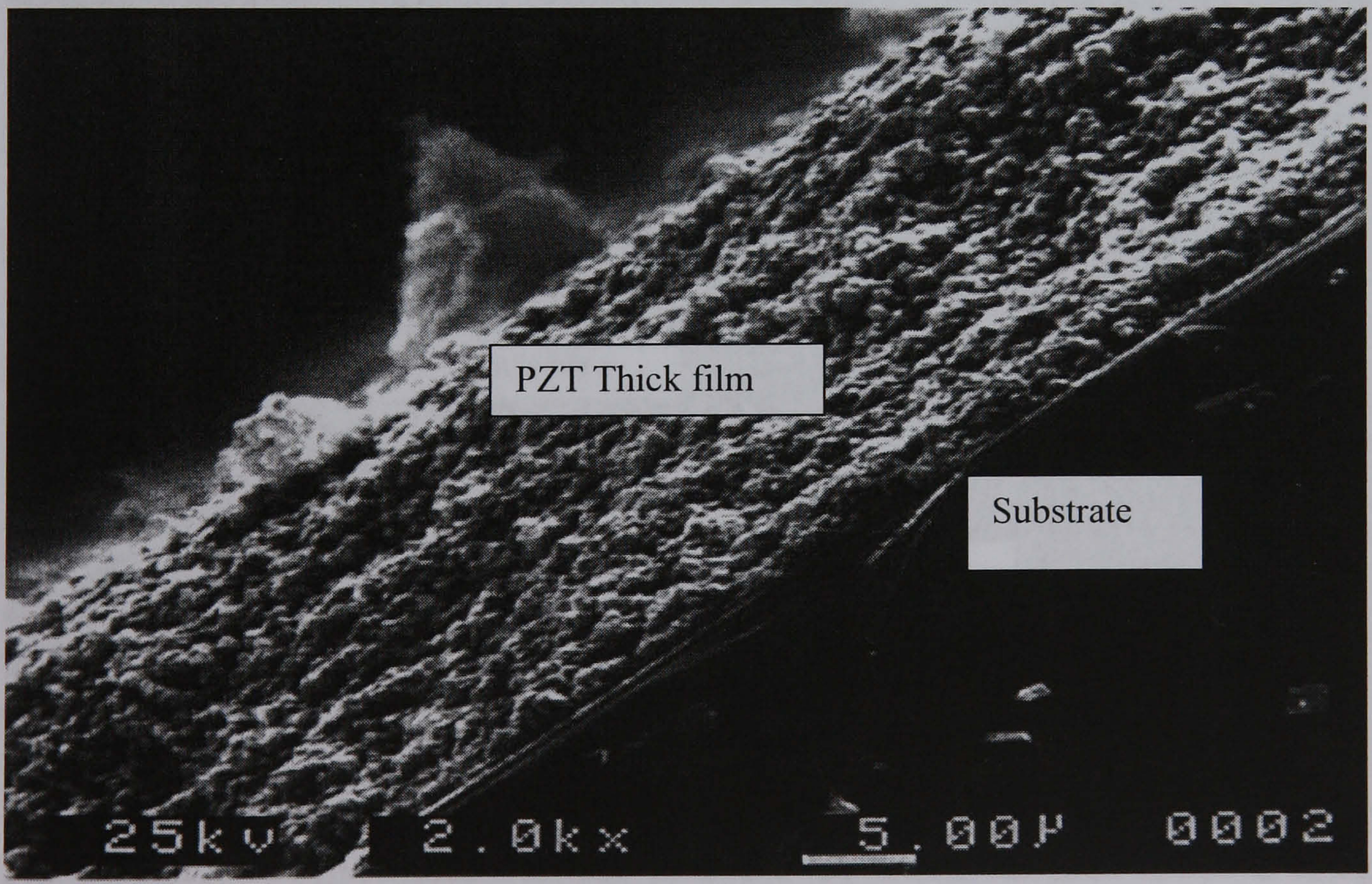

Fig 6.5 PZ42002 SEM fracture surface of S+7(C+S)+C film Ar fired at 710°C using drying condition 2

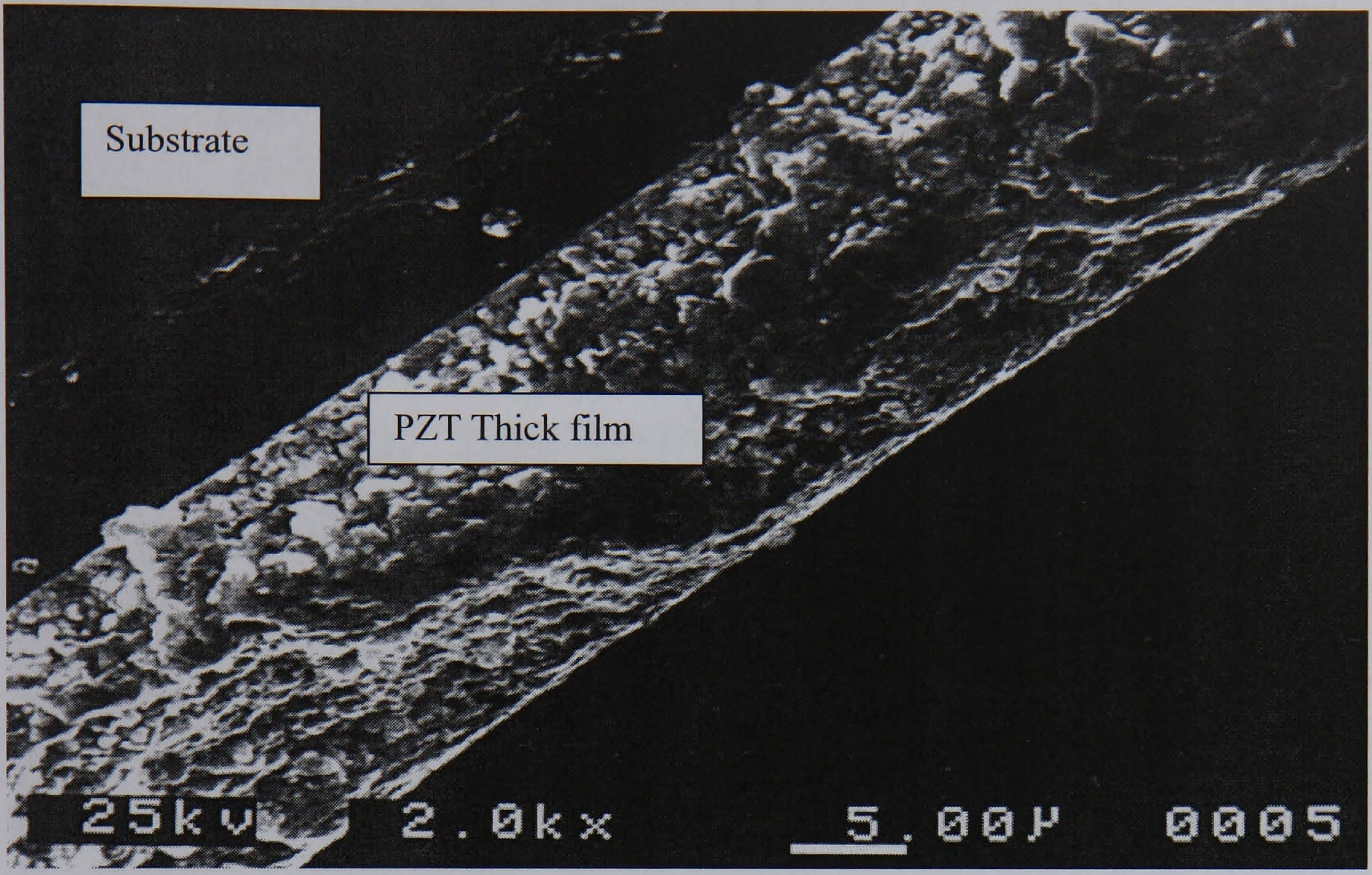

Fig 6.6 PZ42003 SEM fracture surface of S+7(C+S)+C film Ar fired at 710°C using drying condition 3

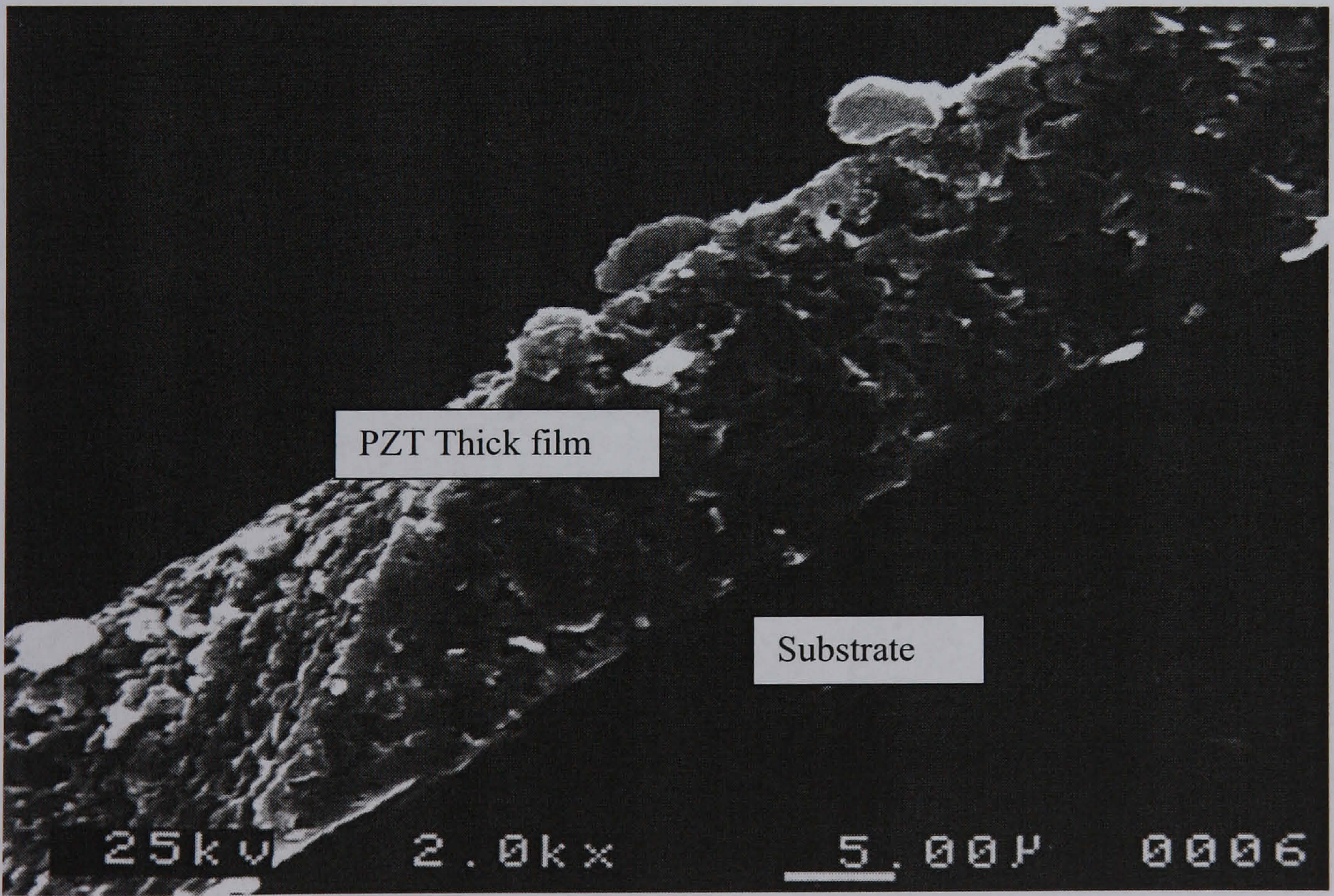

Fig 6.7 PZ42004 SEM fracture surface of S+7(C+S)+C film Ar fired at 800°C using drying condition 1

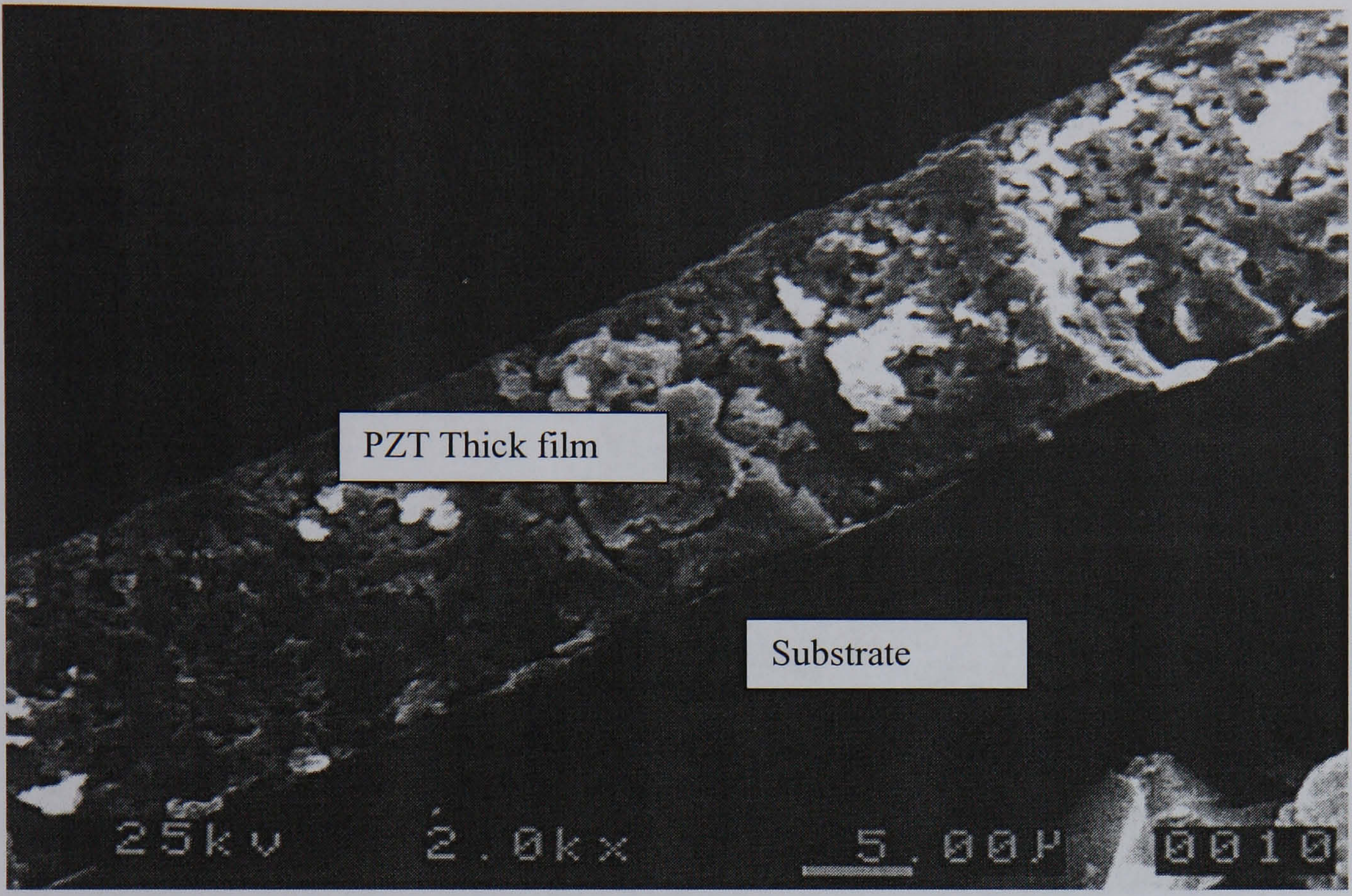

Fig 6.8 PZ42005 SEM fracture surface of S+7(C+S)+C film Ar fired at 800°C using drying condition 2

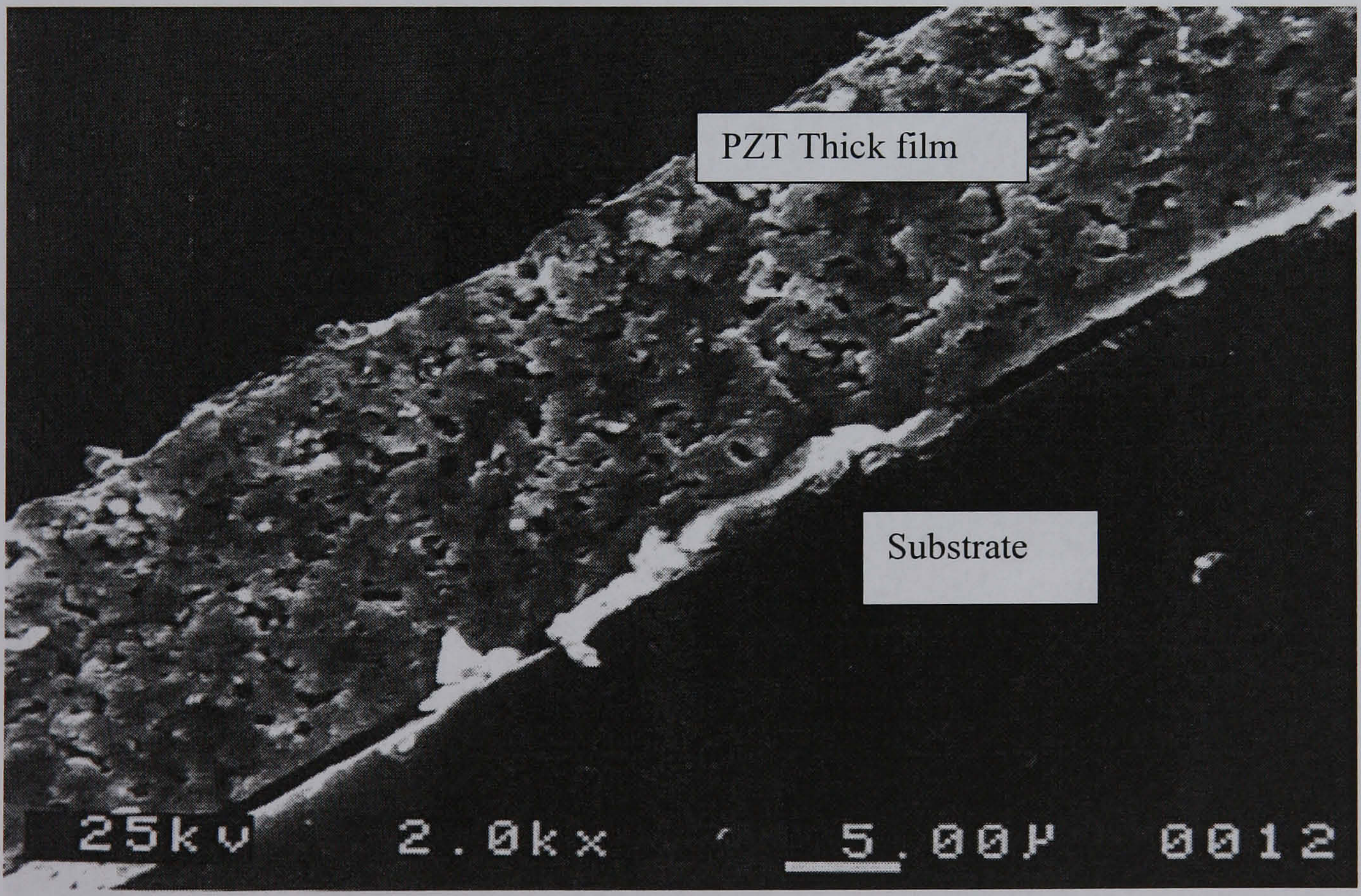

Fig 6.9 PZ42006 SEM fracture surface of S+7(C+S)+C film Ar fired at 800°C using drying condition 3

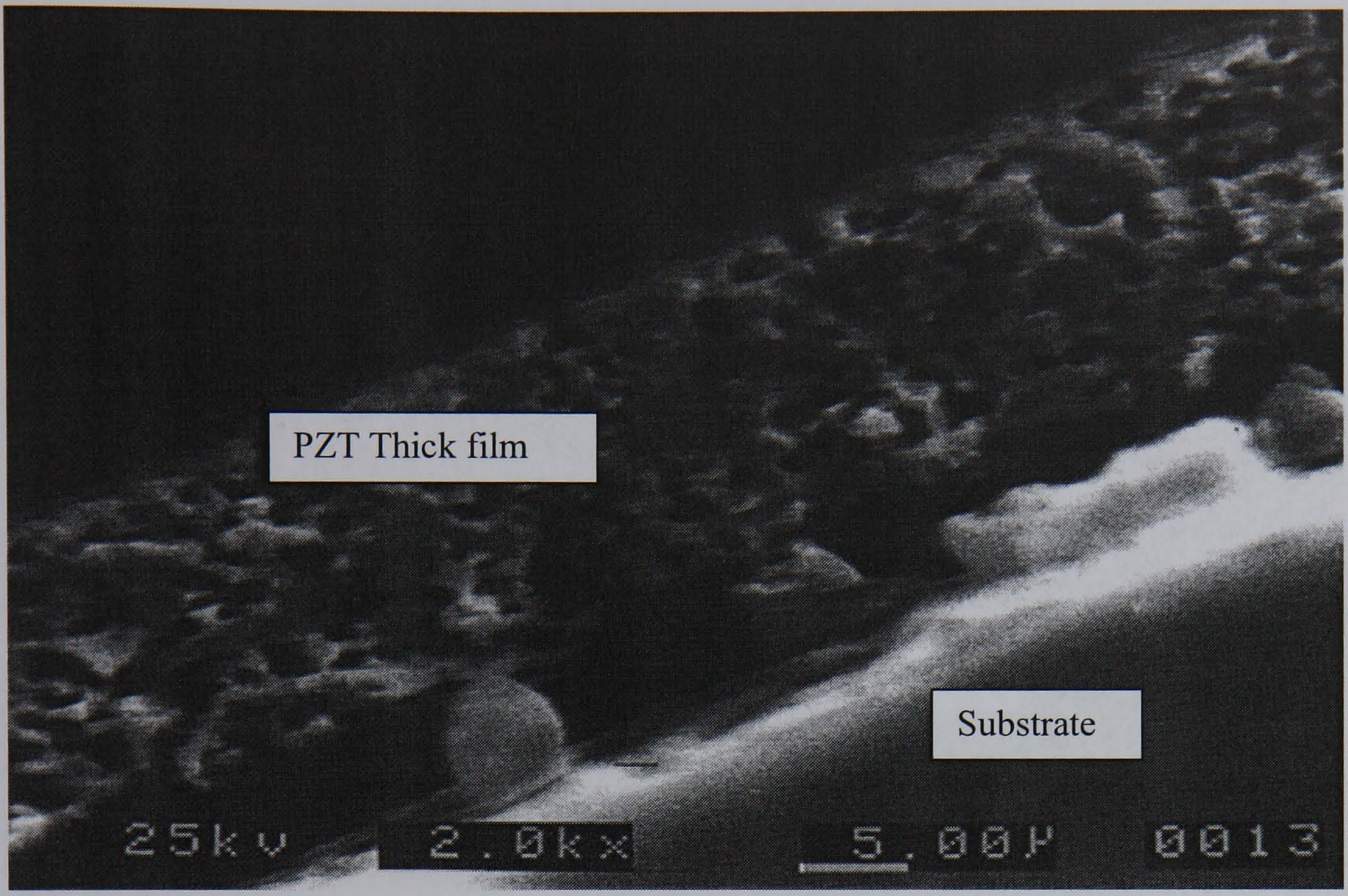

Fig 6.10 PZ42007 SEM fracture surface of S+7(C+S)+C film Ar fired at 900°C using drying condition 1

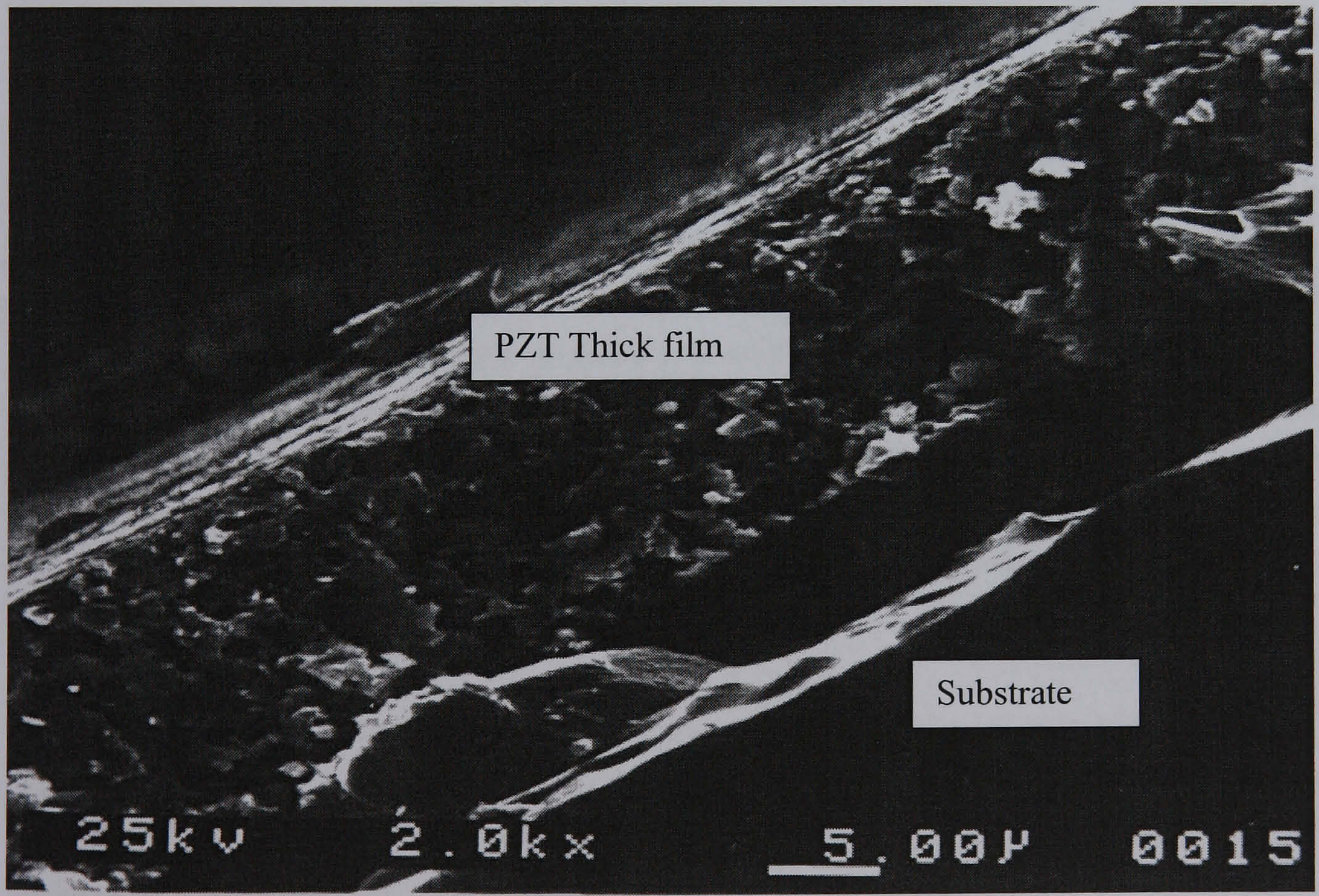

Fig 6.11 PZ42008 SEM fracture surface of S+7(C+S)+C film Ar fired at 900°C Condition 2

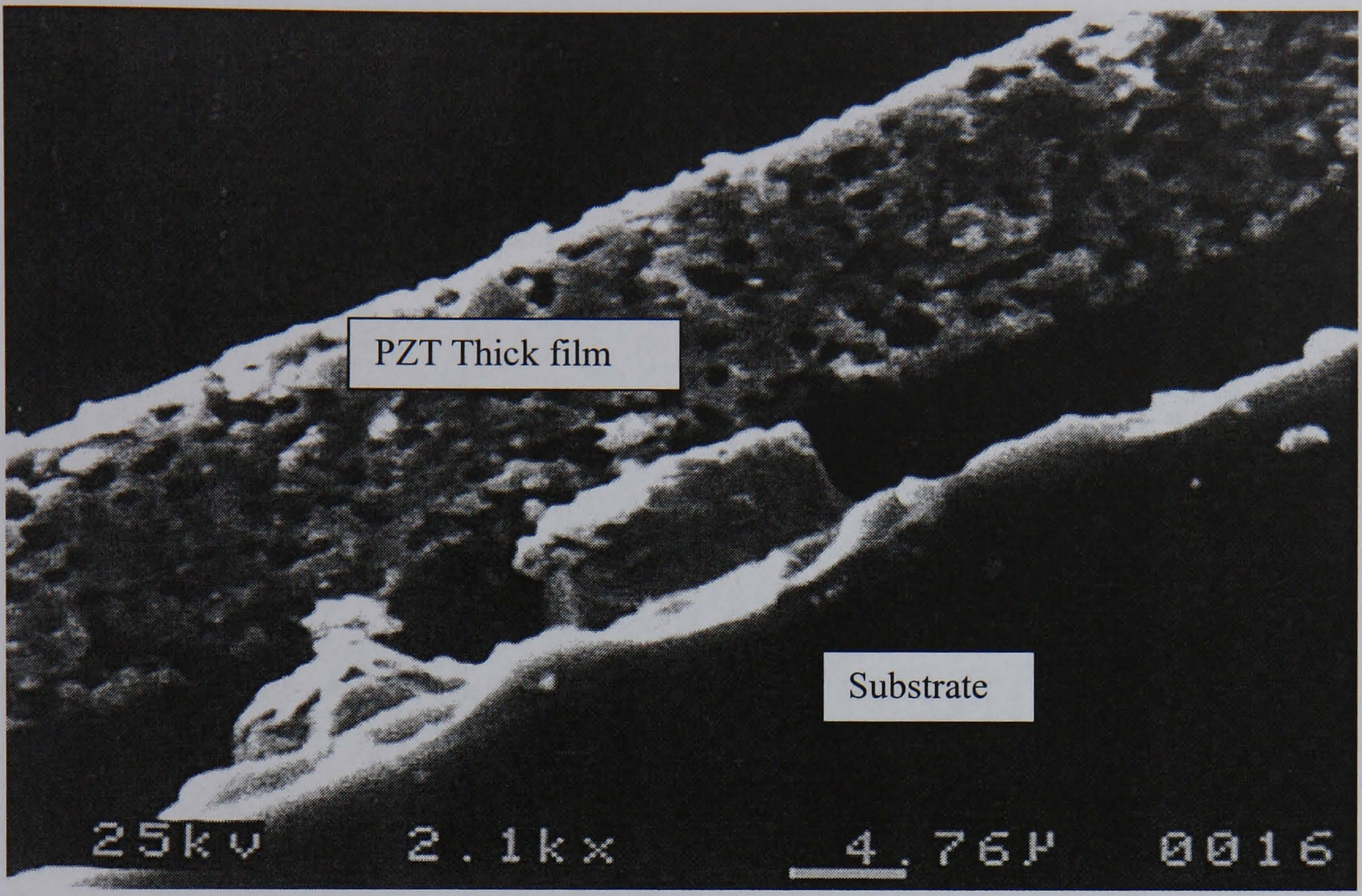

Fig 6.12 PZ42009 SEM fracture surface of S+7(C+S)+C film Ar fired at 900 °C using drying condition 3

SEM fracture surfaces for films sintered under air, at 710, 800 and 900°C are shown in Fig 6.13 to Fig 6.21. These films may be subdivided according to the intermittent thermal treatment applied during film fabrication (see Table 6.1). The 710°C films have a high micro-porosity (lots of small pores), the 800°C films appear much denser but with some closed porosity and the 900°C films are fully dense. Fig 6.1 implies that the dielectric constant is inversely proportional to sintering temperature and hence the density of the thick film. However, any increase in density would actually result in a higher dielectric constant. The SEM fracture surfaces show increasing damage to the back electrode with increasing temperature. It is proposed that the electrode damage accounts for the decline in dielectric constant with increasing sintering temperatures and this arises from a discontinuous back electrode. Further, if the electrode were stable then the dielectric constant would have increased with the density of the film.

Comparison of the films sintered at 900 °C under air (Fig 6.19 to Fig6.21) and under Ar (Fig 6.10 to Fig 6.12) shows that the Ar sintered films were porous whereas the air sintered films were dense. This suggests that densification was better under an air atmosphere, and it was not clear why this should be the case.

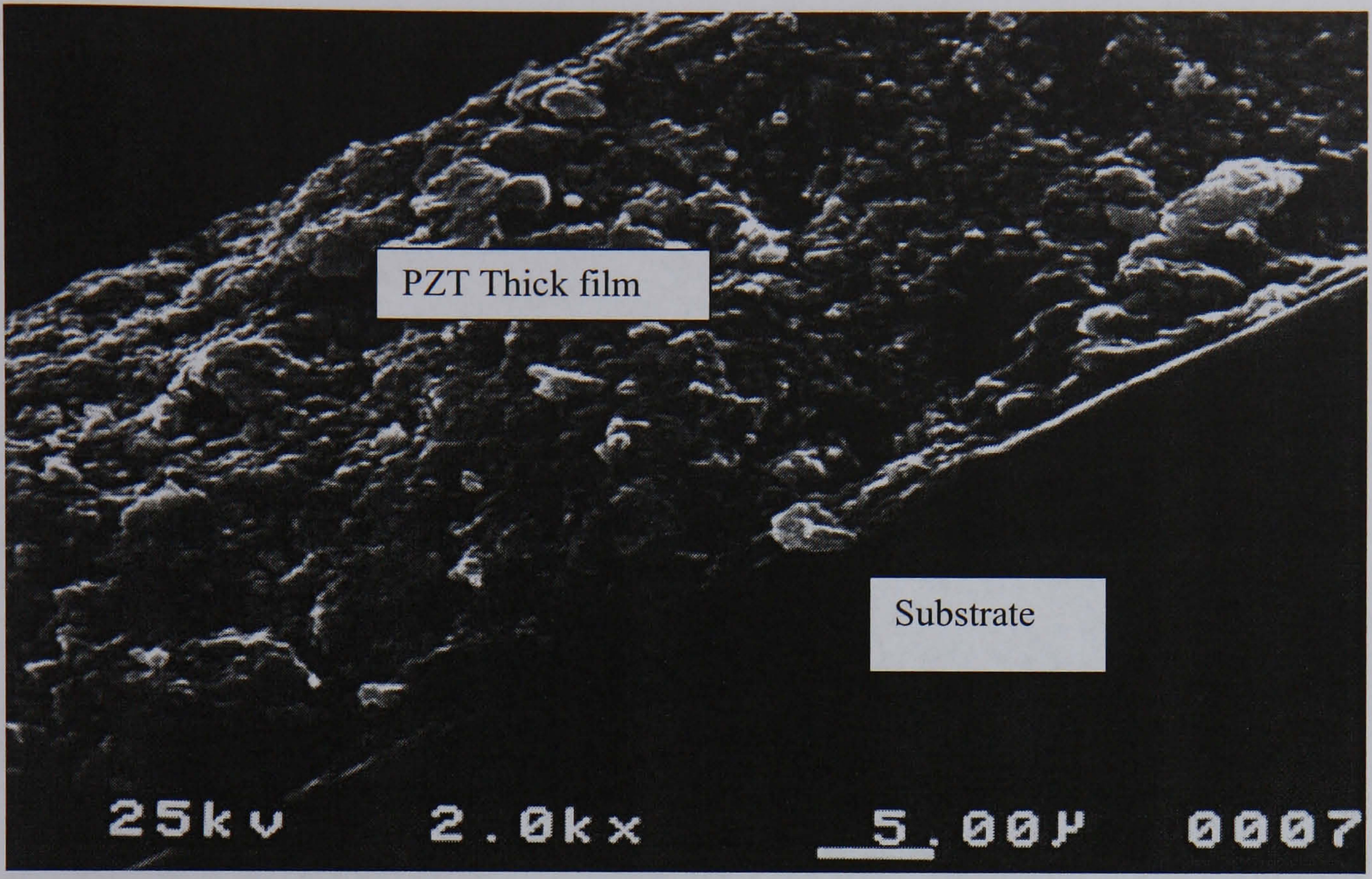

Fig 6.13 PZ420019 SEM fracture surface of S+7(C+S)+C film air fired at 710°C using drying condition 1

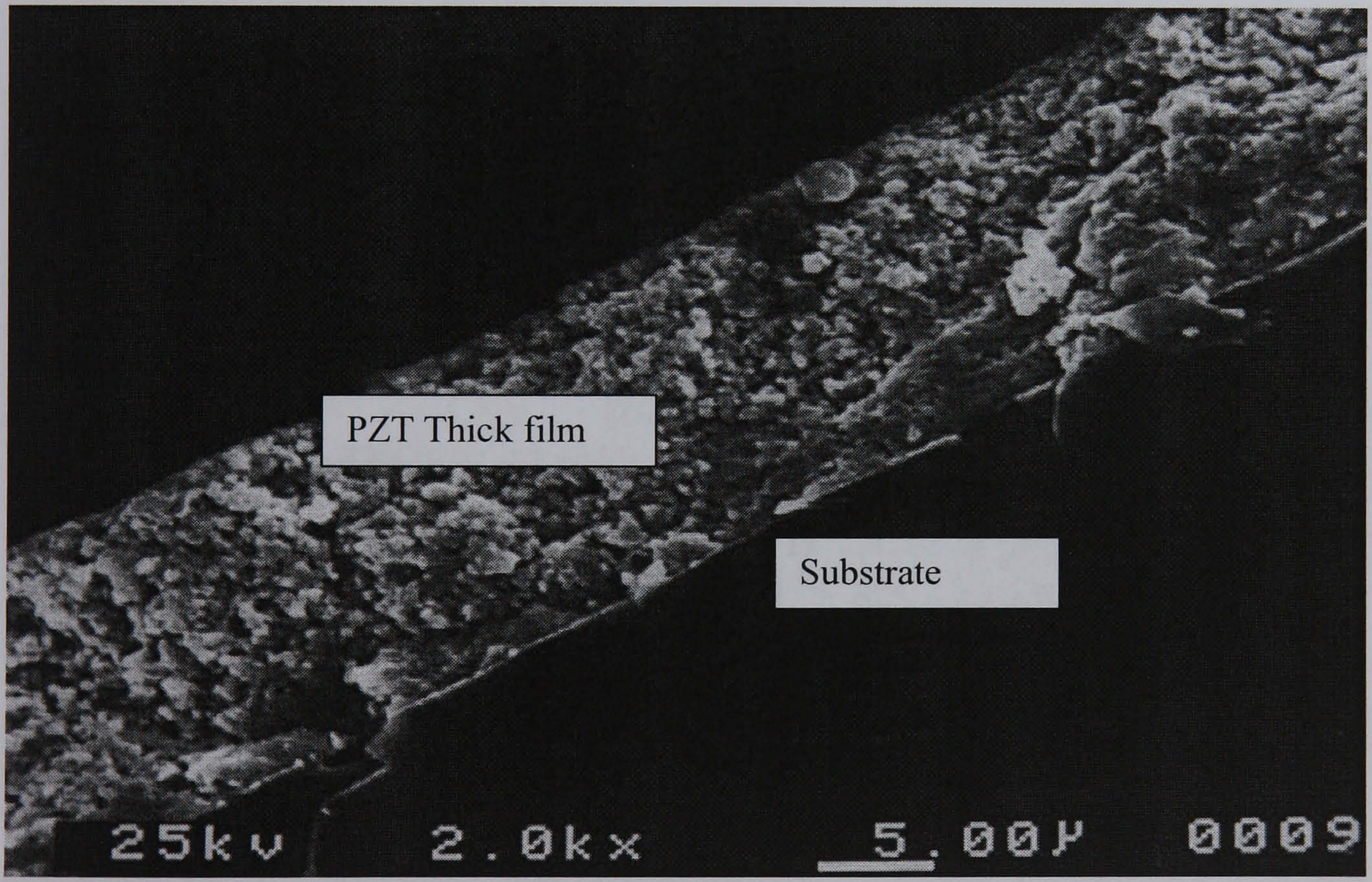

Fig 6.14 PZ42020 SEM fracture surface of S+7(C+S)+C film air fired at 710°C using drying condition 2

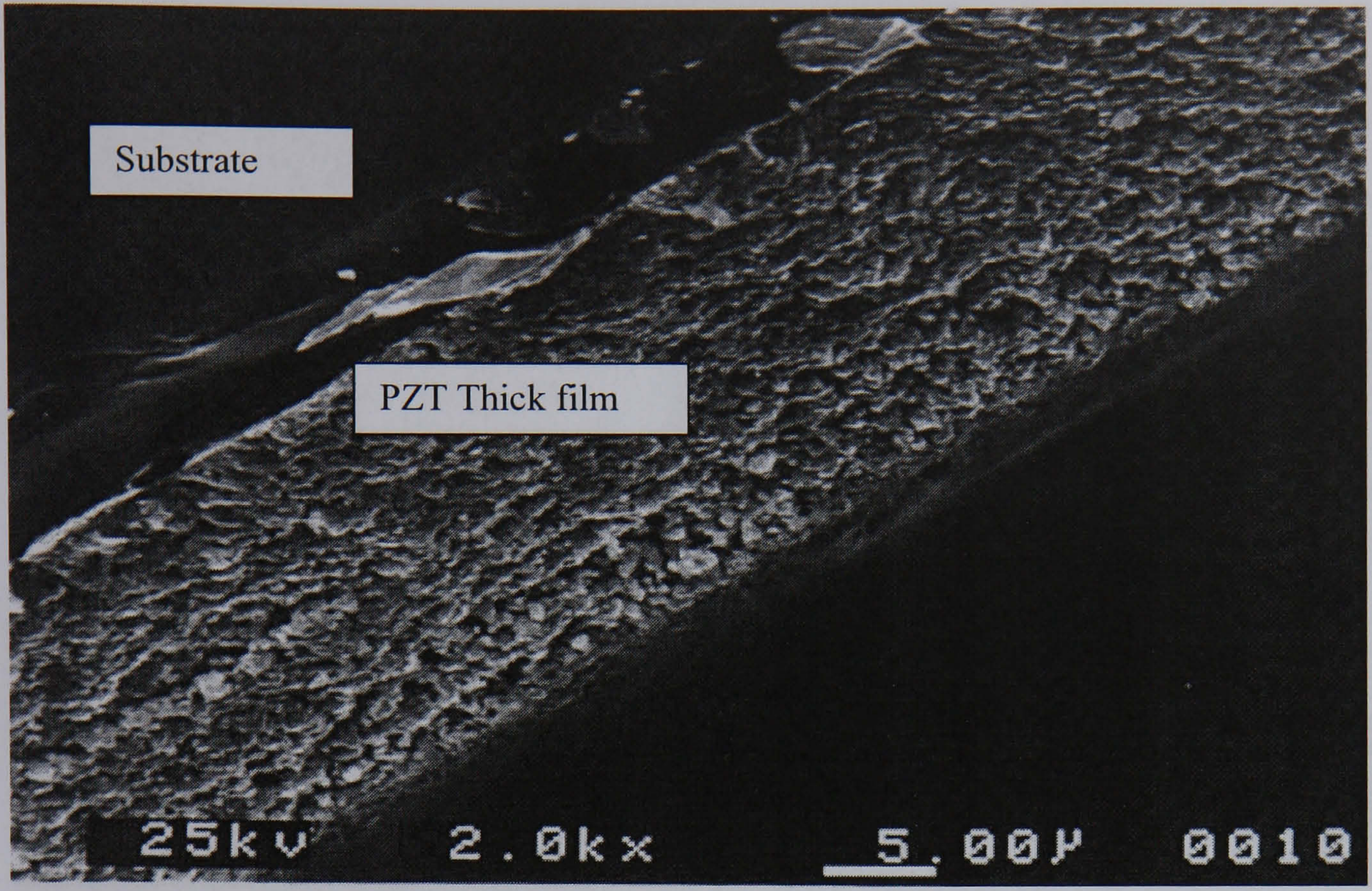

Fig 6.15 PZ42021 SEM fracture surface of S+7(C+S)+C film air fired at 710°C. Condition 3

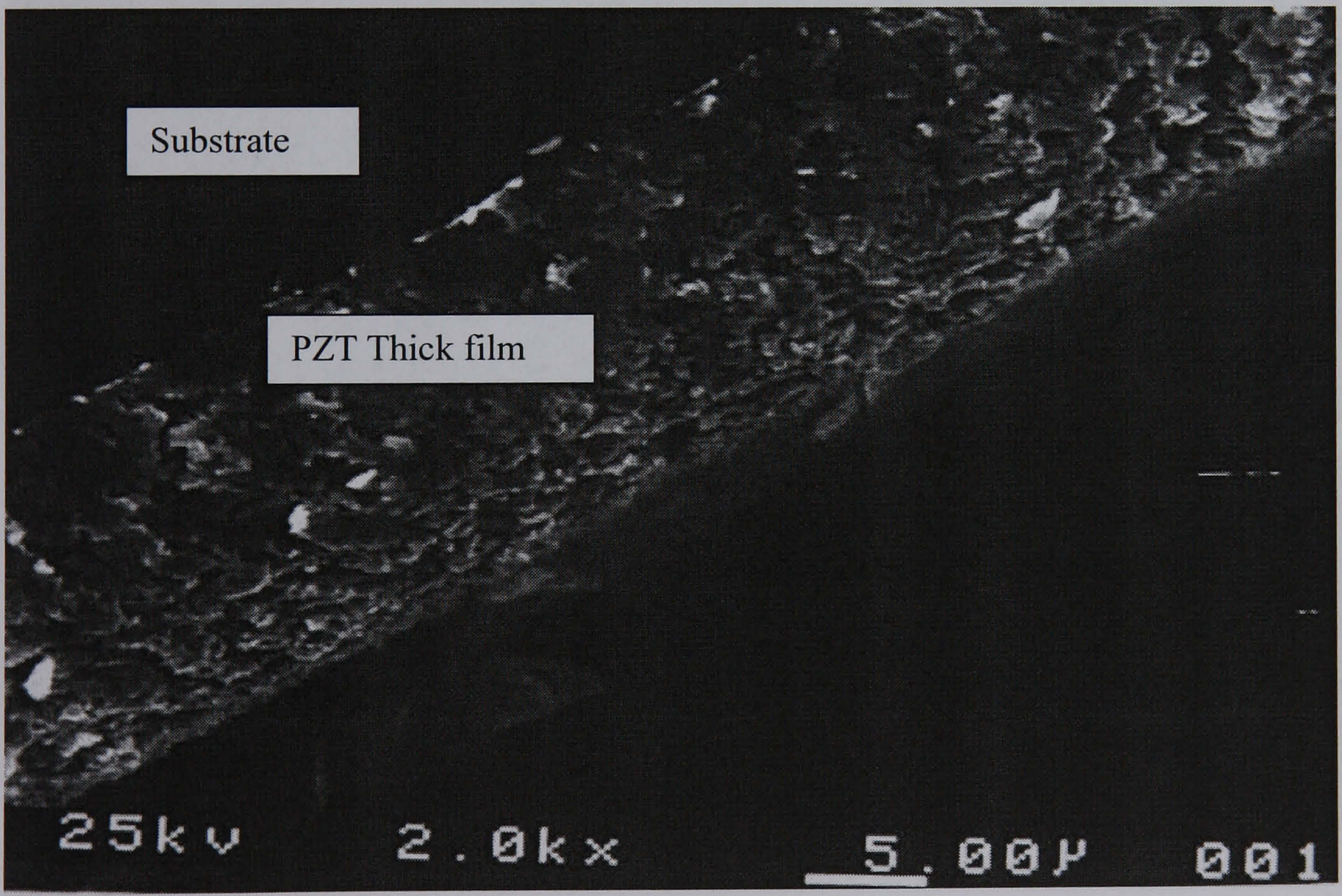

Fig 6.16 PZ42022 SEM fracture surface of S+7(C+S)+C film air fired at 800°C using drying condition 1

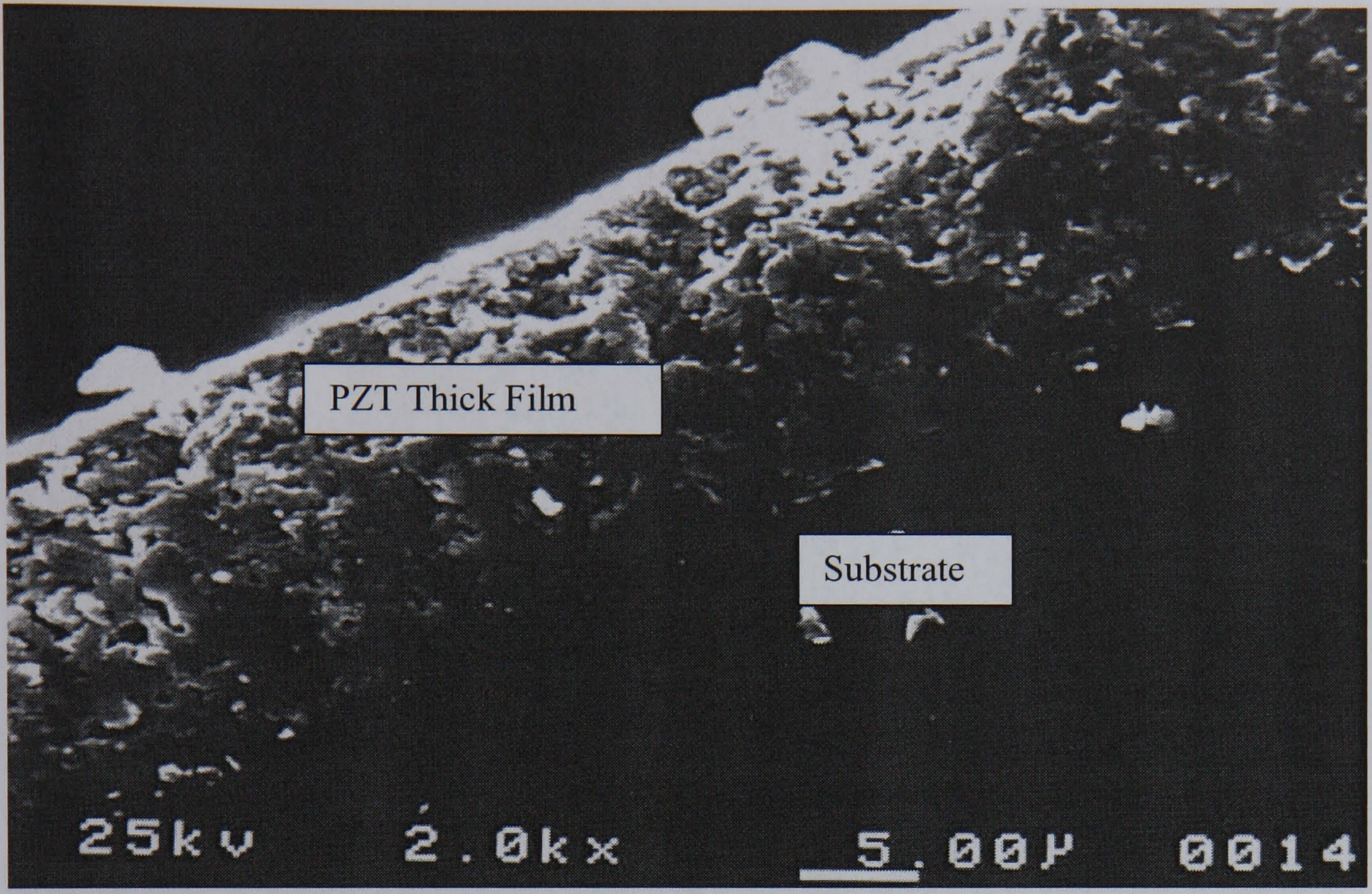

Fig 6.17 PZ42023 SEM fracture surface of S+7(C+S)+C film air fired at 800°C using drying condition 2

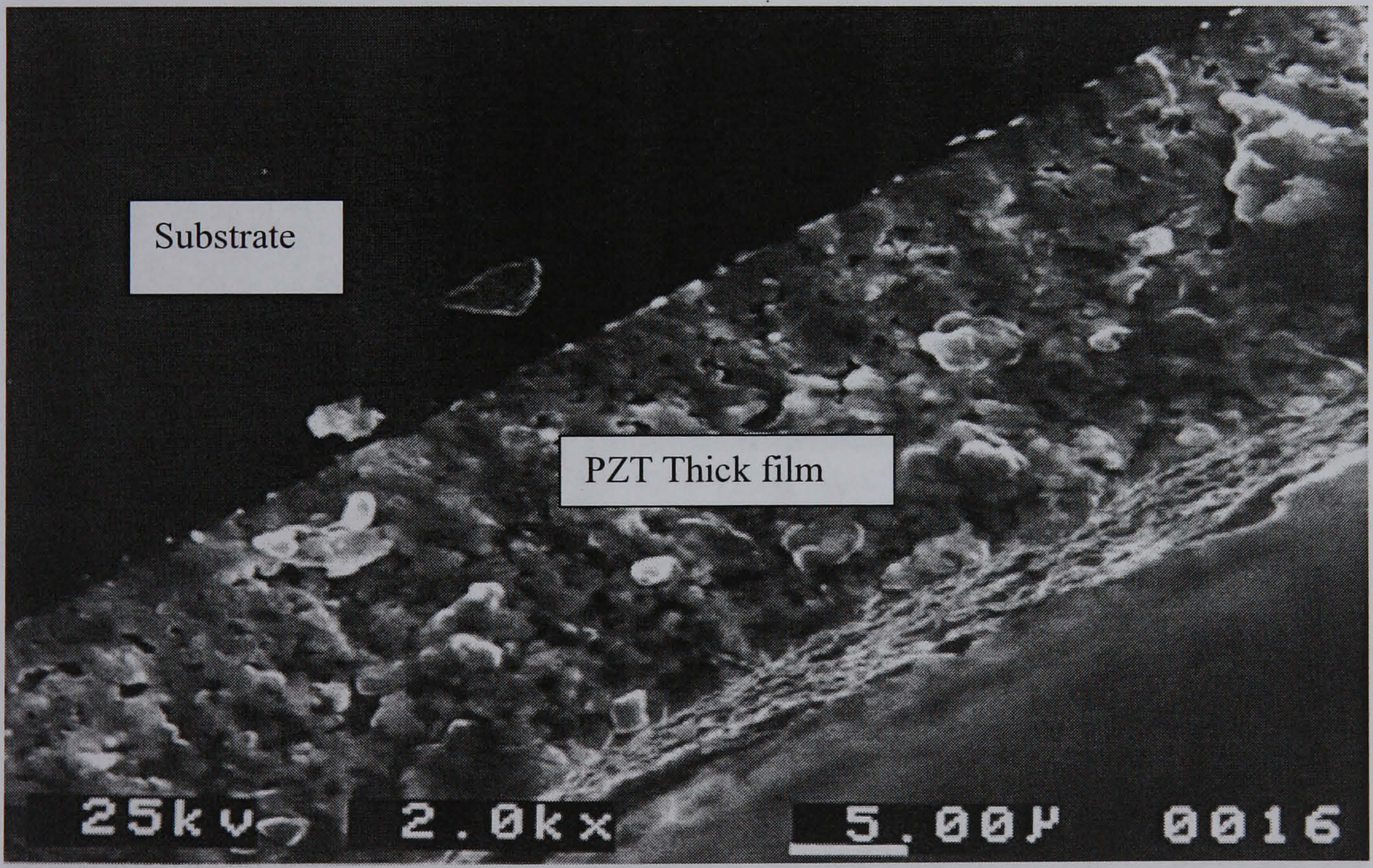

Fig 6.18 PZ420024 SEM fracture of S+7(C+S)+C film air fired at 800°C using drying condition 3

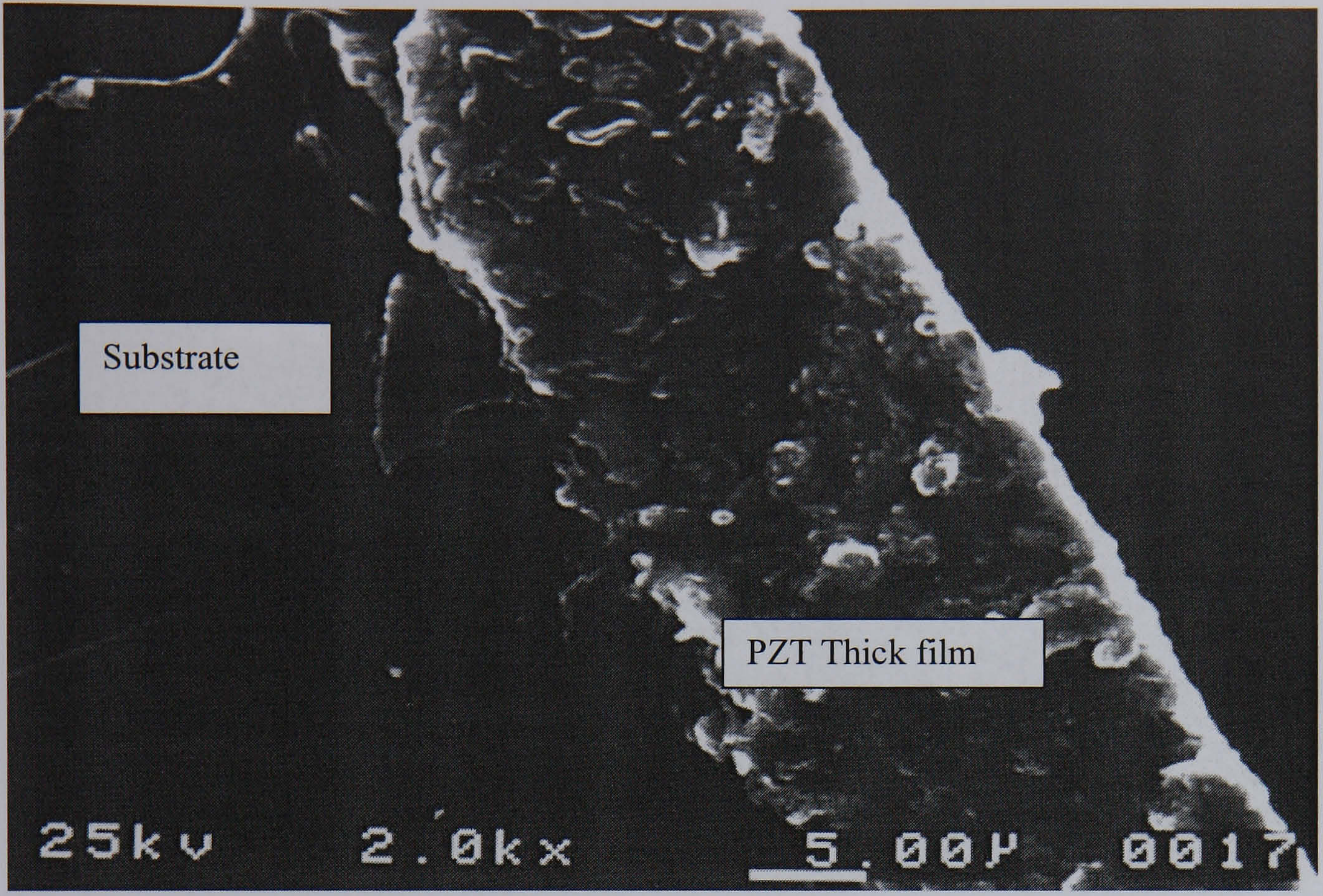

Fig 6.19 PZ420025 SEM fracture surface of S+7(C+S)+C film air fired at 900°C using drying condition 1

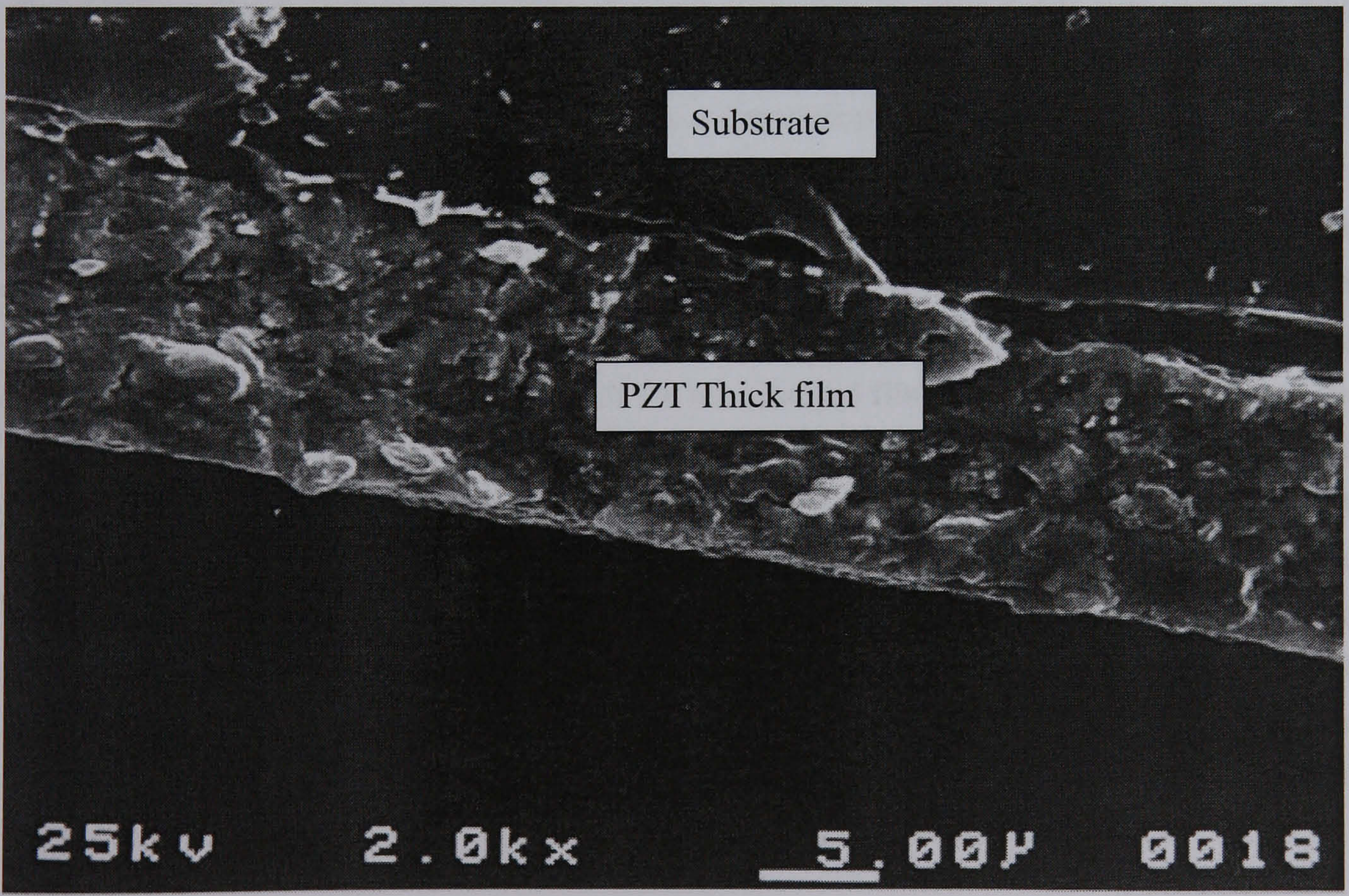

Fig 6.20 PZ420026 SEM fracture surface of S+7(C+S)+C film air fired at 900°C using drying condition 2

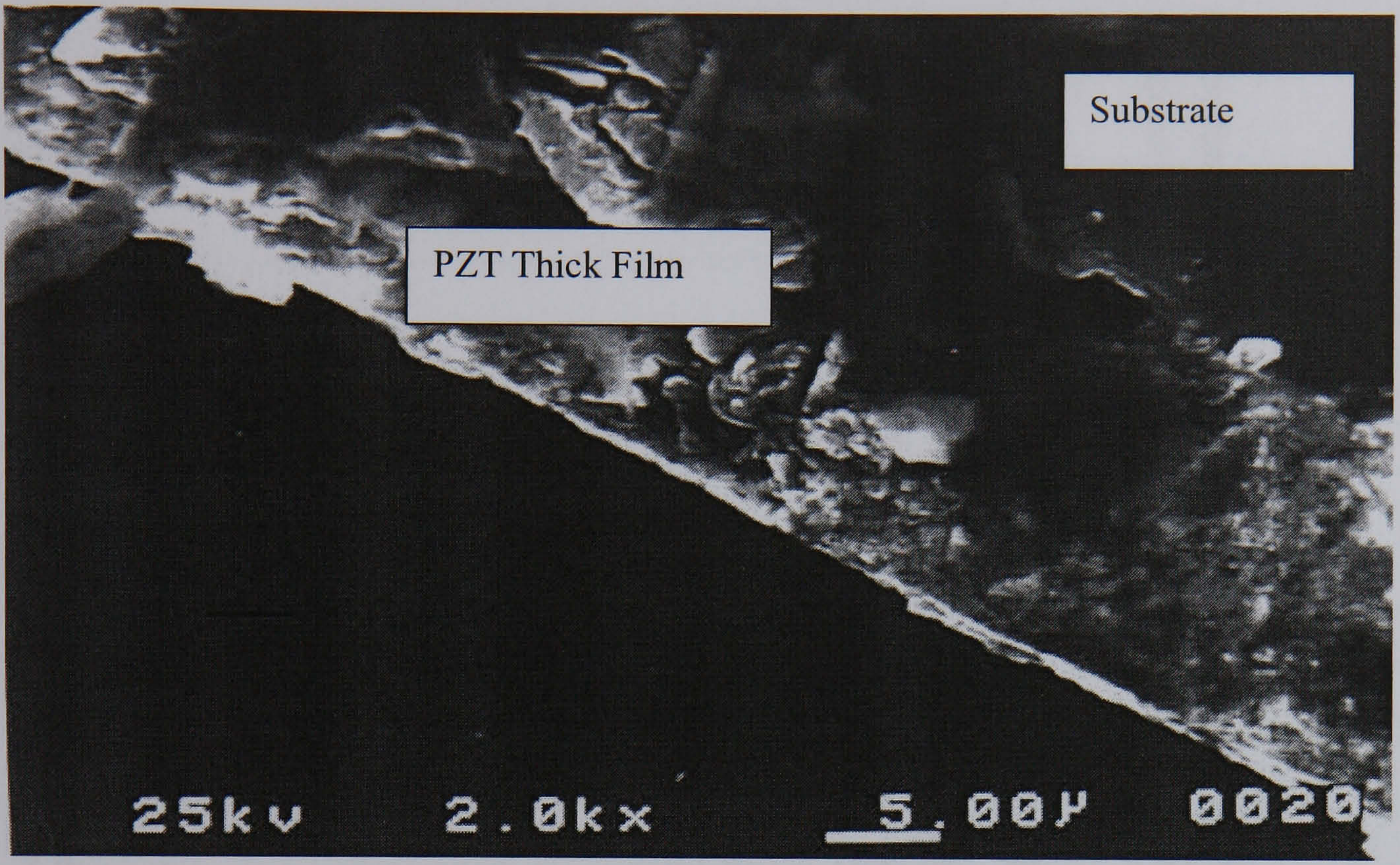

Fig 6.21 PZ420027 SEM fracture surface of S+7(C+S)+C film air fired at 900°C using drying condition 3

The XRD patterns of Ar sintered films at 710 °C to 900 °C (Fig 6.22) has shown a PZT powder pattern with an additional phase (see also Table 6.2). The powder pattern is consistent with a thick film fabricated from a dispersion of randomly orientated powder particles in a composite slurry. The additional phase is present in all films regardless of drying conditions. This phase was first observed in films sintered at 710 °C, and then disappeared at 800 °C; however, another phase formed in films sintered at higher temperatures (900 °C). This phase has been identified as PbO. As no volatilisation or unidentified phase were present in any of the air-sintered films, shrinkage is accounted for by densification. It should be noted that no trace of lead platinum inter-metallic, lead silicate glass or pyrochlore could be detected in any of the spectra. The unidentified phase forms at 2θ values associated with pyrochlore <222>. However, pyrochlore peaks are broad and pyrochlore does not usually form at temperatures as high as 710 °C and so pyrochlore formation was considered unlikely. The thickness and density of the PZT would be expected to block X-rays from reaching the back electrode, indicating that the unidentified phase is present within the bulk of the thick film. It should be noted that drying conditions did not alter the composition of the thick films see Fig 6.23.

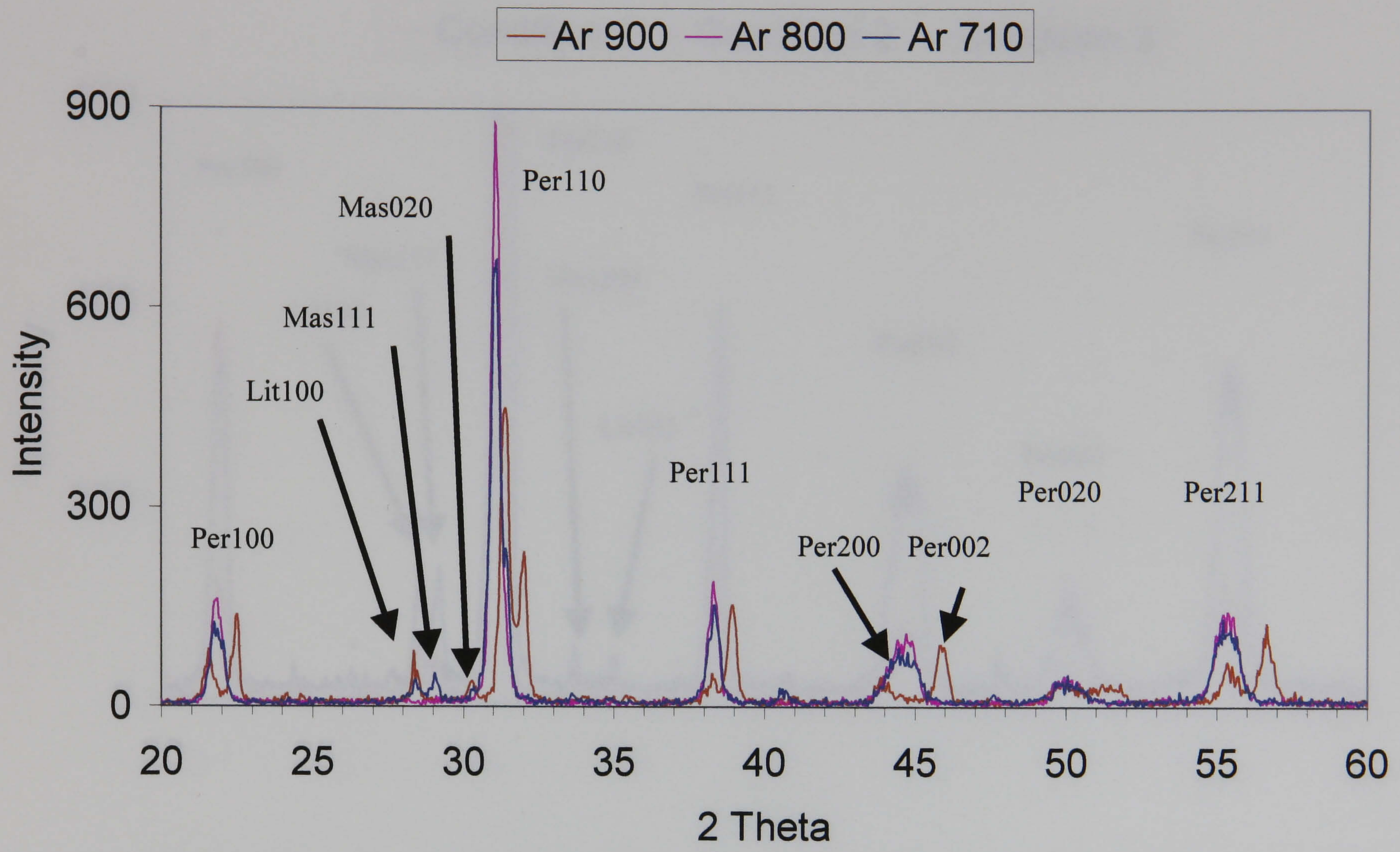

Fig 6.22 XRD spectra of Ar sintered films. The spectra show the effect of sintering temperature. All films analysed were analysed with condition 1. The pattern has all the peaks associated with a PZT powder pattern and an additional phase. In the figure Per, Mas and Lit correspond to perovskite (PZT), massicott (PbO) and litharge (PbO) respectively.

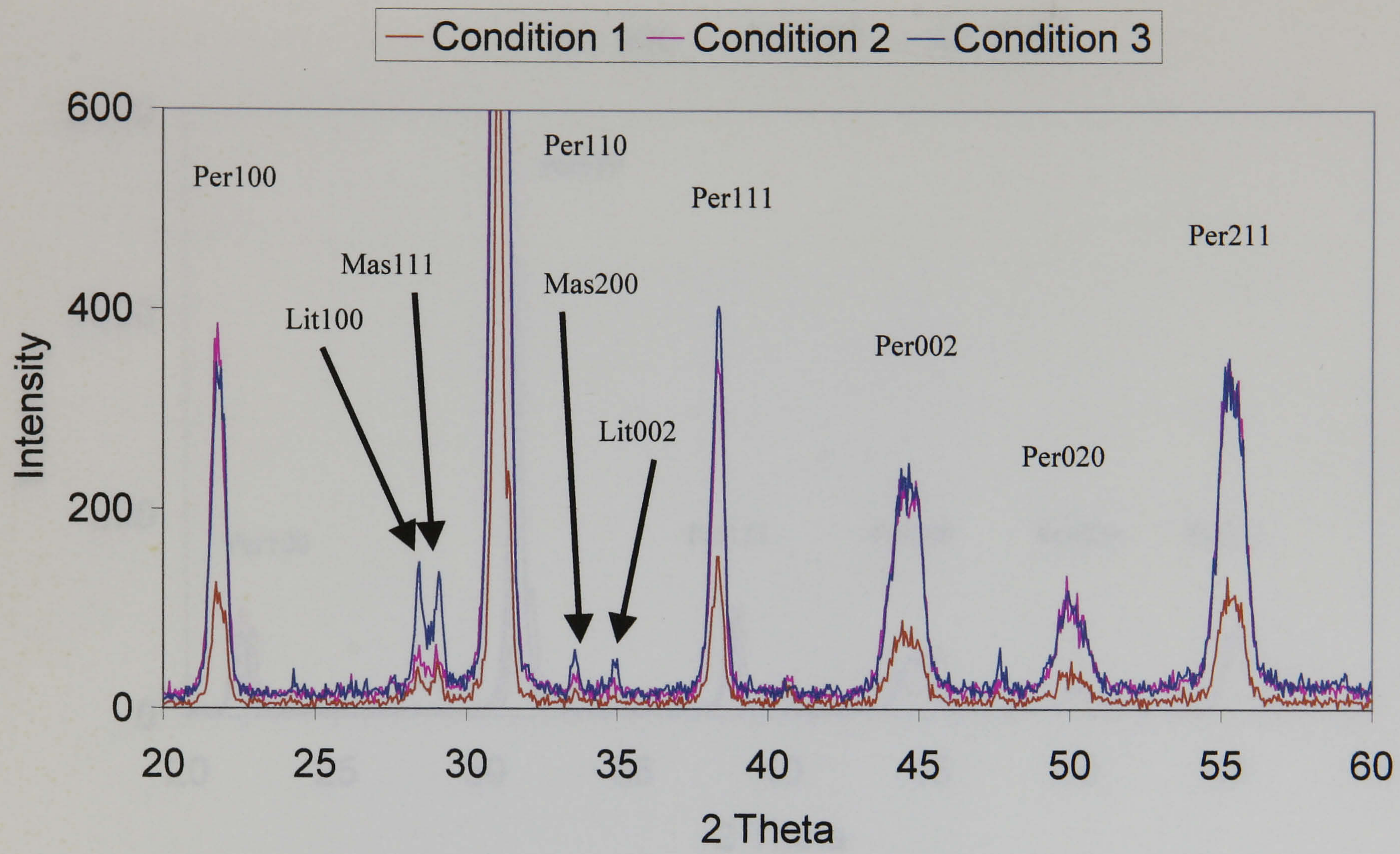

Fig 6.23 XRD spectra of films sintered at 710 with Ar and dried with conditions 1-3. The additional phase is most apparent in films that have had a condition 3 intermittent thermal treatment. In the figure Per, Mas and Lit correspond to perovskite (PZT), massicott (PbO) and litharge (PbO) respectively.

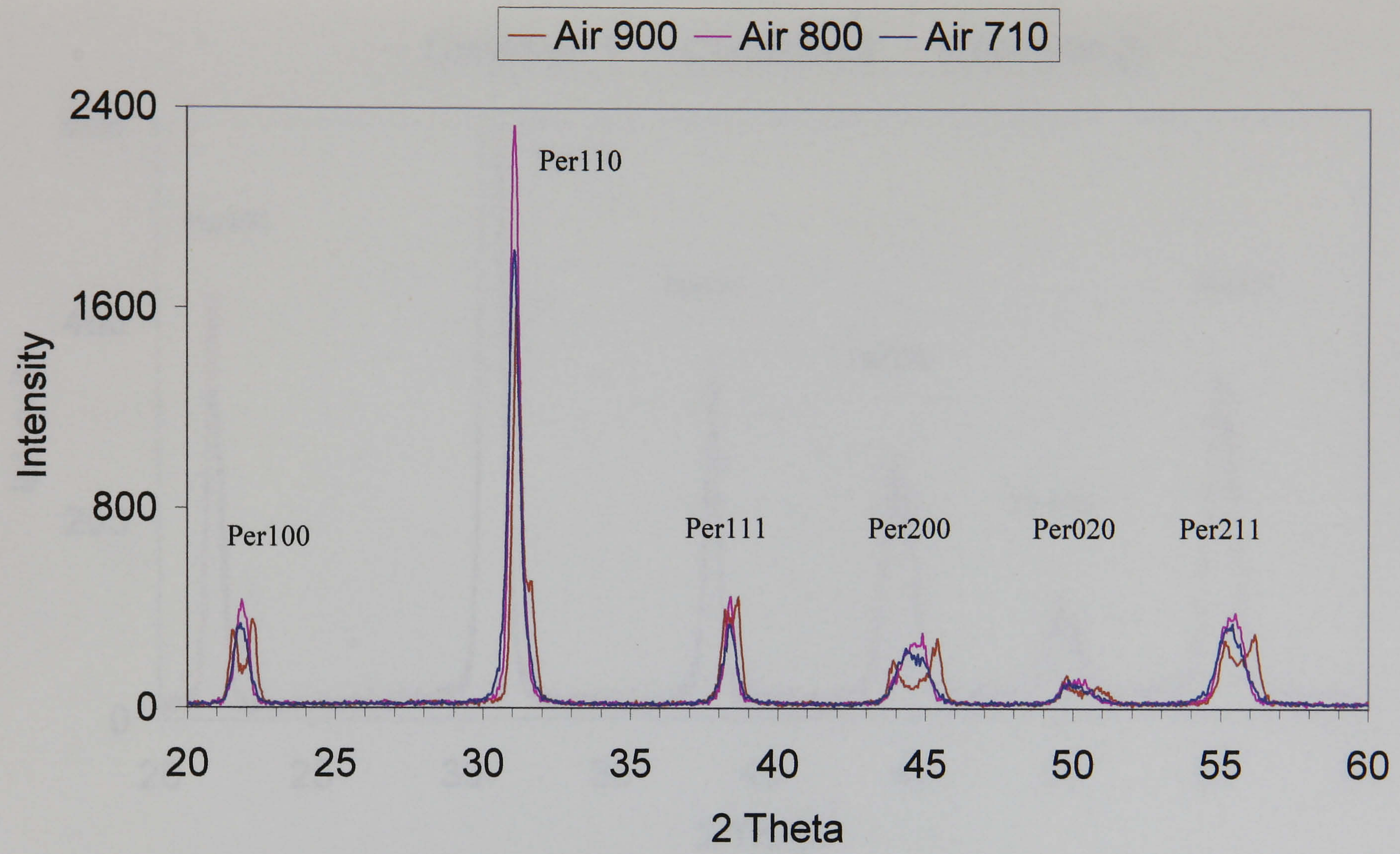

Fig 6.24 XRD spectra of air sintered films. The spectra shows the effect of sintering temperature. All films analysed were analysed with condition 1. . In the figure Per corresponds to perovskite (PZT).

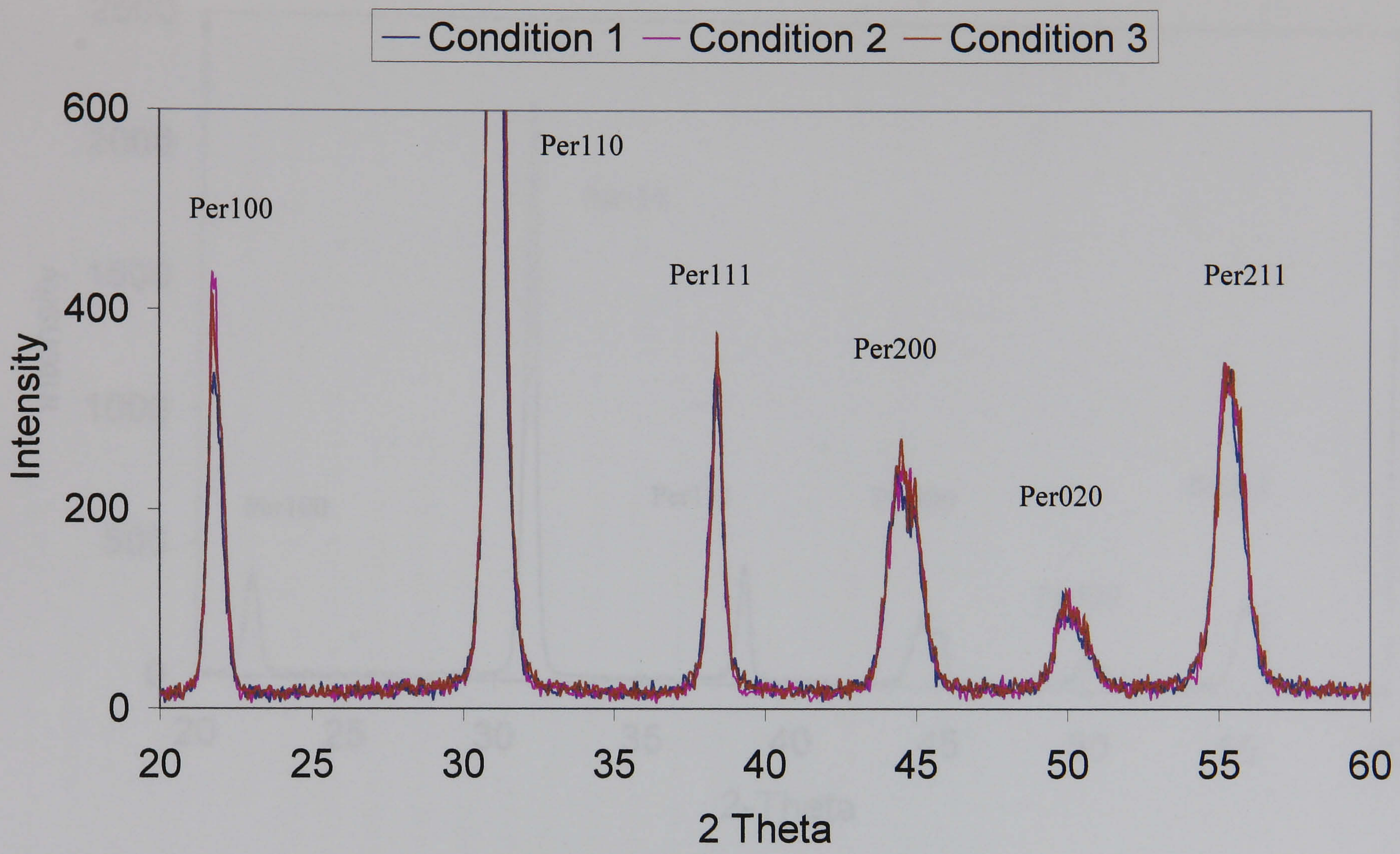

Fig 6.25 XRD spectra of films sintered at 710 °C with an air atmosphere, under drying conditions 1 to 3 - showing no effect of drying conditions on phase. The spectra is consistent with a PZT powder pattern.

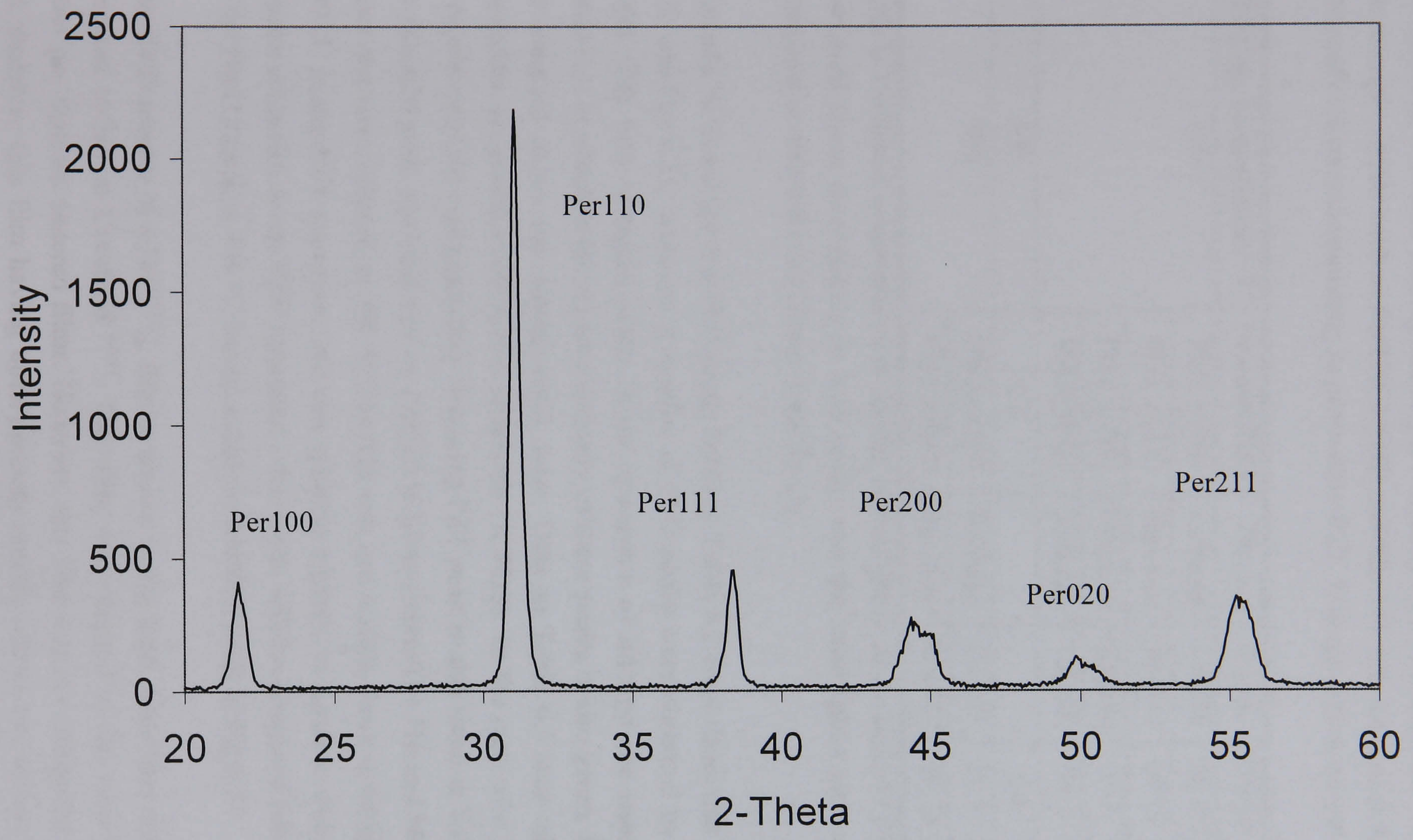

Fig 6.26 Standard PZT thick film sintered under Ar. This film involved no infiltration step and was of the form $[8C]^{710}_{Ar}$

A notation is introduced to label peaks in the XRD spectra above and in the tables below; this is Label,h,k,l where h,k,l are the miller indices of the particular peak. The labels are Per, Mas and Lit these correspond to perovskite (PZT), massicott and litharge respectively. For example, labels such as Per110, Lit100 and Mas111 may be read as the (110), (100) and (111) reflections corresponding to perovskite-PZT, litharge and massicott respectively.

Sintering Temperature / °C	Indexed Peak	Phase	Label	2 theta	d_{hkl}/ Å
710	PbO_t (100)	Litharge	Lit100	28.45	3.137
	PbO_o (111)	Massicot	Mas111	29.15	3.063
	PbO_o (200)	Massicot	Mas200	33.6	2.667
	PbO_t (002)	Litharge	Lit002	35.5	3.493
800	n.d.			n.d.	n.d.
900	PbO_t (100)	Litharge	Lit100	28.35	3.148
	PbO_o (020)	Massicot	Mas020	30.25	2.954

Table 6.2 Indexed peaks observed for the second phase in Ar sintered PZT thick films. The additional phase corresponds to lead oxide, and the subscripts t and o correspond to the tetragonal or orthorhombic forms respectively.

It should be noted that the PbO peaks listed in Table 6.2 were those that were visible in Fig 6.22 and Fig 6.23; however, a number of PbO peaks were obscured by more intense PZT peaks. The four strongest peaks in the spectrums of litharge and massicott are listed in Table 6.3; in addition the relative intensity of these peaks is also given. Weaker peaks were not detected above the experimental noise. Data in Table 6.3 was taken from the joint committee on powder diffraction standards (JCPDS). In the case of a PbO peak that has been obscured the corresponding obscuring PZT peak is also listed in Table 6.3. In Fig 6.22 the Mas020 peak was obscured by Per110 in films sintered at 710 and 800 °C; however, the films that were sintered at 900 °C Mas020 was just visible. Peak splitting seems to result at 900 °C in the PZT spectrum, and this splitting appears to result in more precisely defined (narrower) peaks in the PZT spectrum - this point will be discussed below. The narrowing of the Per110 peak at 900 °C has revealed the Mas020 peak in Fig 6.22.

The XRD pattern of a $[8C]^{710}{}_{Ar}$ film is shown in Fig 6.26. This film was identical to those prepared earlier at Cranfield [42,44]. This film was sintered in Ar, and therefore subject to lower p_{O_2} than air sintered films. However, this film was not infiltrated with metal-organic sol; therefore this film having open porosity readily allows the diffusion of oxygen, even under conditions of lower-p_{O_2}. It is interesting to compare this spectrum with that of an infiltrated PZT-thick-film, that has been sintered under Ar at 710 °C (see Fig 6.23). The thing to note is the absence of a second phase in Fig 6.26. It seems that the second phase only forms under very low p_{O_2}; this point will be discussed further in the discussion section.

Litharge (ref. JCPDS 05-0561)				Massicott (ref. JCPDS 38-1477)			
2θ	Intensity / %	Miller indices	Obscuring peak	2θ	Intensity / %	Miller indices	Obscuring peak
28.633	100	(100)		29.078	100	(111)	
31.831	62	(110)	Per110	30.315	24	(020)*	Per110*
35.743	18	(002)		32.593	23	(200)	
48.595	37	(112)	Per020	37.821	17	(201)	Per111

Table 6.3 The four most intense peaks in the XRD spectrums of Litharge and Massicott.. The table also lists where a peak will be obscured by a more intense PZT peak in the spectrum. *Denotes a PbO peak that was obscured, in the spectra of films that were sintered at 710 and 800 °C but visible in the spectrum of a film sintered at 900 °C.

The XRD patterns of the films sintered at 710 °C to 900 °C, and the films dried under conditions one to three under air atmospheres, indicate a PZT powder pattern independent of either sintering (Fig 6.24) or drying (Fig 6.25) conditions. The second phase was not present in these spectra. The peaks in the PZT spectrum were observed to split with increasing sintering temperature. All peaks have been indexed, see Table 6.4.

Peak splitting at higher temperatures seems to have resulted from a better resolution of the signal. For example at 710 and 800 °C only a broad singlet corresponding to Per 100 was observed, but sintering at 900 °C has resolved this peak into Per 001 and Per 100. In the case of tetragonal PZT the lattice spacing a = b = Per 100 ≠ c where c = Per 001. It follows that for air sintered films, the unit cell dimensions will be a=b=3.995 Å and c=4.105 Å. In the case of films sintered under Ar, the dimensions will be a=b=3.952 Å and c=4.114 Å. Undoped PZT, sintered under air, has unit cell dimensions a = b = 4.036 and c=4.146 (ref. JCPDS 33-0784); suggesting that doping of the PZT in the thick films has resulted in a contraction of the unit cell. The contraction seems most pronounced in films sintered under an air atmosphere.

Broad peaks were observed in the spectra of PZT thick films sintered under air at lower temperatures; peak splitting was not as apparent in these films. The broad <200> peak at 43 ° 2θ to 45 ° 2θ indicates that a mixture of rhombohedral and tetragonal phases were present in the infiltrated PZT thick films. It should be noted that no trace of lead platinum inter-metallic or lead silicate glass could be detected in any of the spectra. The analysis of drying conditions showed that no new phase was formed during the drying of air-sintered films.

The disappearance of the Si peak may be attributed to an increase in the density of the PZT thick film with increasing sintering temperature.

TEMPERATURE / °C		710	800	900	710	800	900
Atmosphere		air			Ar		
Indexed peak [h,k,l]	~ 2θ / °	Lattice spacing d_{hkl} / Å					
Per 001	21.8	-	-	4.105	-	-	4.114
Per 100	22.1	4.077	4.068	3.995	4.086	4.068	3.952
Per 101	31.2	2.880	2.880	2.880	2.885	2.885	2.853
Per 110	31.7	-	-	2.823	-	-	2.797
Per 111	38.2	2.344	2.338	2.350	2.353	2.353	2.353
Per 002	44.0	2.042	-	2.060	2.032	-	2.060
Per 200	45.4	-	2.025	1.998	-	2.019	1.998
Per 102	49.9	1.840	1.840	1.840	-	-	-
Per 210	51.3	-	-	-	1.819	1.819	1.819
Per 112	55.5	1.660	1.660	1.670	1.656	1.656	1.656
Per 211	56.2	-	-	1.638	-	-	1.646

Table 6.4 Indexed peaks in XRD spectra of PZT thick films sintered under different atmospheres. Two number in a cell indicates a doublet. A perovskite peak is noted as Per.

The infiltration route has since been optimised elsewhere [120], and it was found that maximum d_{33} and e_{31} were achieved with four infiltrations per composite slurry layer (see Table 6.4). Optimum conditions were achieved using a lower viscosity sol of 50 % concentration to aid filling of the pores. Prepared films were of the form: $4[C^{200,450}+4S^{200,450}]^{710}_{air}$. These films differed from earlier films through the elimination of the sol seeding layer and the use of air sintering.

Film structure	Sol Viscosity	ε_r	e_{31} / C/m^2	d_{33} / p.C/N
$[4(C^{200,450}+4S^{200,450})]^{710}_{Air}$	High	300	-1	50
$[4(C^{200,450}+4S^{200,450})]^{710}_{Air}$	Low	800	-5	80

Table 6.4 The piezoelectric and electrical properties obtained from PZT thick films; prepared by means of the infiltration technique. Table taken from Dorey et al [120]

6.2.2 Titania Barrier Layers

Fig 6.28 is an ion milled image of TiO_2 (200 nm)/Si_3N_4 (200 nm) /Si; TiO_2 was formed through thermal oxidation of Ti. The image was observed at an angle of 45 ° see Fig 6.27.

Unfortunately, there is little information about the individual layers but a hillock can be observed in the Titania.

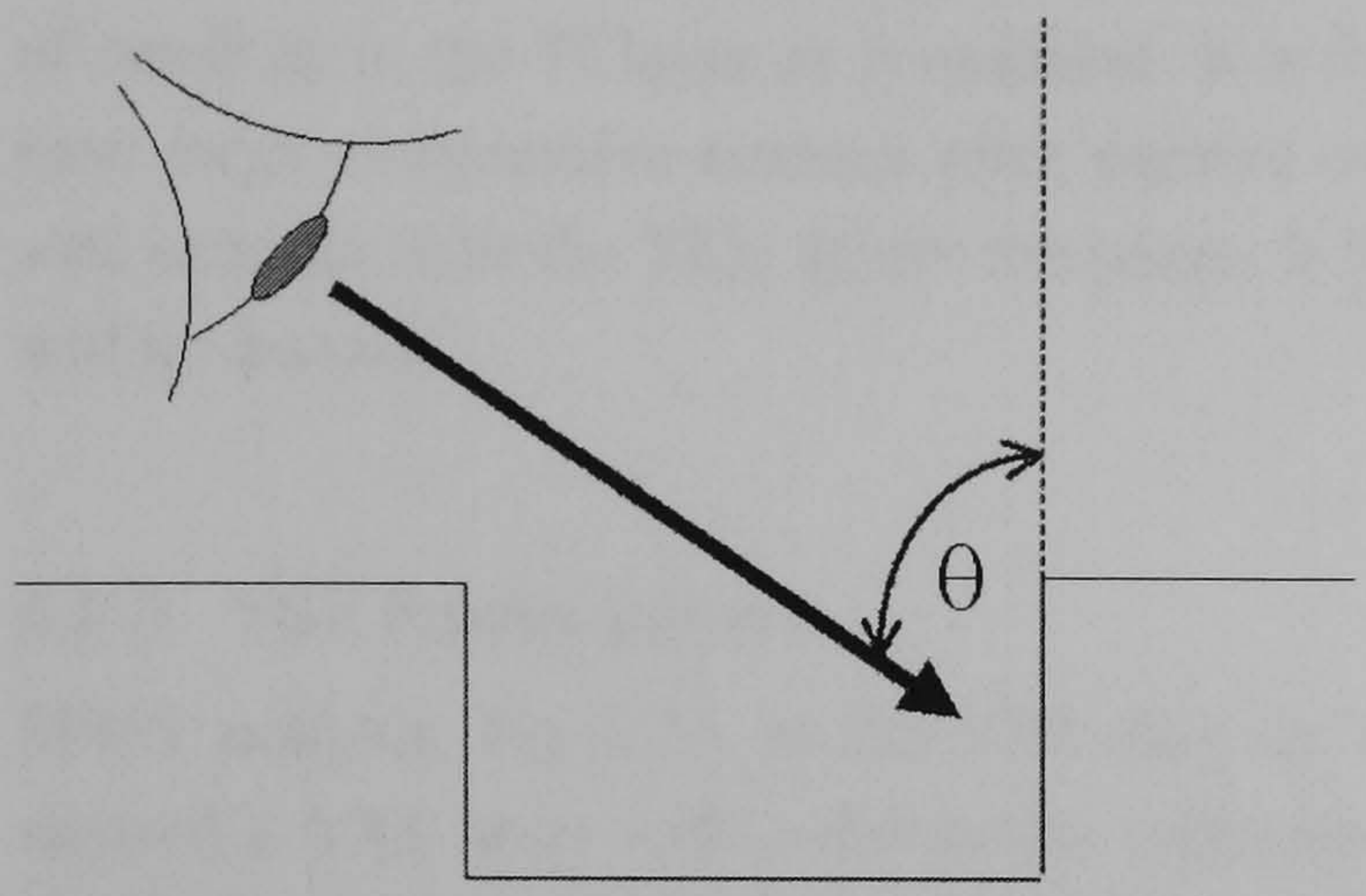

Fig 6.27 Observation angle for the FIB analysis of ion milled samples. The angle of observation θ is 45 ° for all ion milled samples.

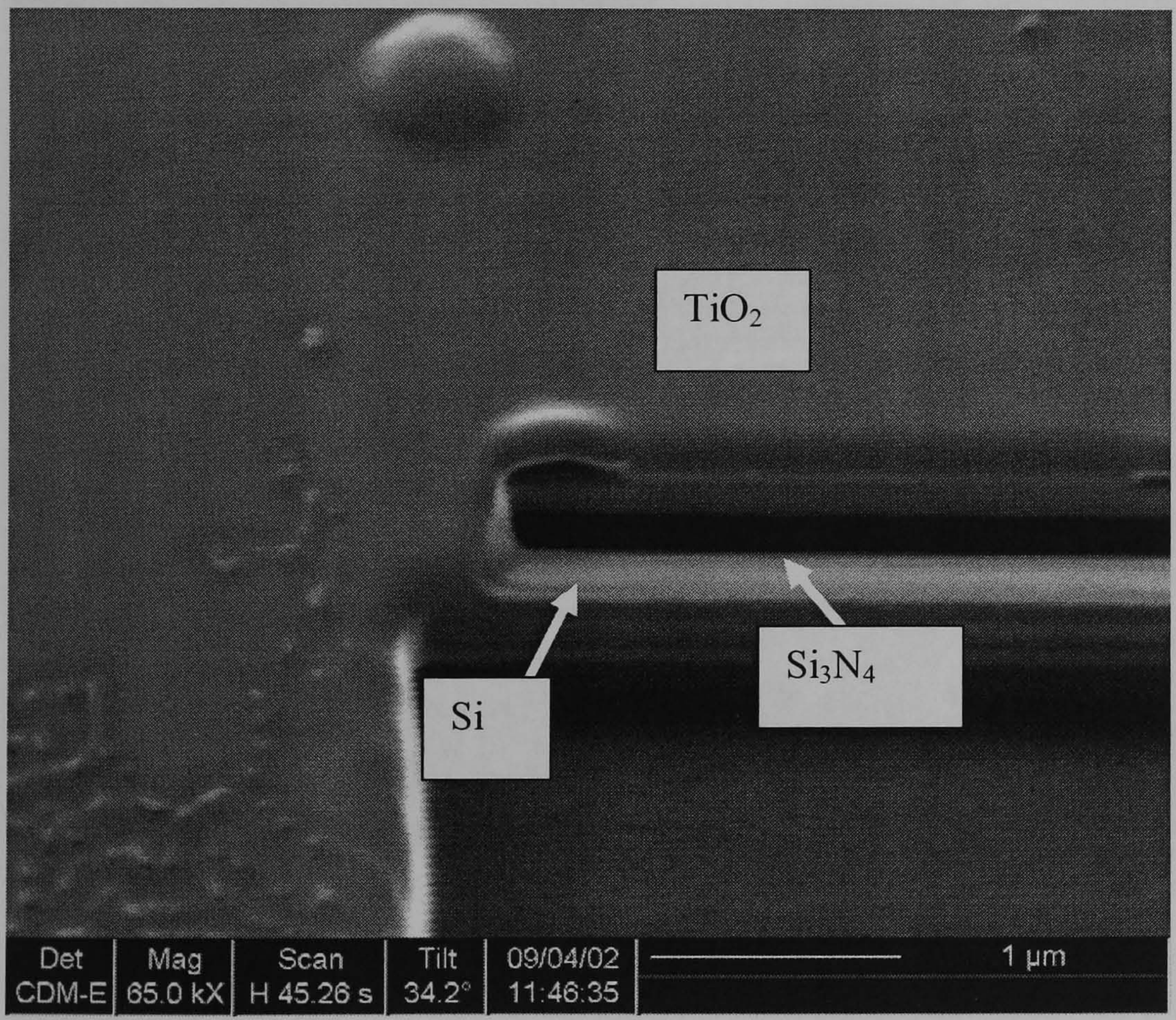

Fig 6.28 FIB image of a TiO_2 (283 nm)/Si_3N_4/Si film. The film was deposited by sputtering Ti (200 nm) onto Si_3N_4/Si and then thermal annealing in air (at 600 °C for 7 minutes). A trench has been dug in the surface of the film and the sample rotated 45 ° to view the interface. The image shows the formation of hillocks on the oxide surface.

By contrast, no hillock growth was observed in films of the form: Pt/Ti/SiO_2/Si. This would suggest that hillock formation occurs in the TiO_x layer and not in Ti or Pt layers. The hillocks observed in the TiO_2 layer, shown below, were considered to have formed because of swelling in the Ti layer as it oxidised. It is thought most likely that the TiO_2 layer will have large compressive stresses after thermal oxidation and that the compressive stresses will increase with the TiO_2 layers thickness. It follows therefore that TiO_2 layers on Si_3N_4 will be stressed.

6.2.3 YSZ Barrier Layers

SFEG analysis, Fig 6.29, of the YSZ film on the silicon nitride coated silicon substrate showed a YSZ layer with a distinctive columnar microstructure. XRD indicated that both the YSZ on nitride and YSZ on silicon films were crystalline and had a <111> texture (see Fig 6.30).

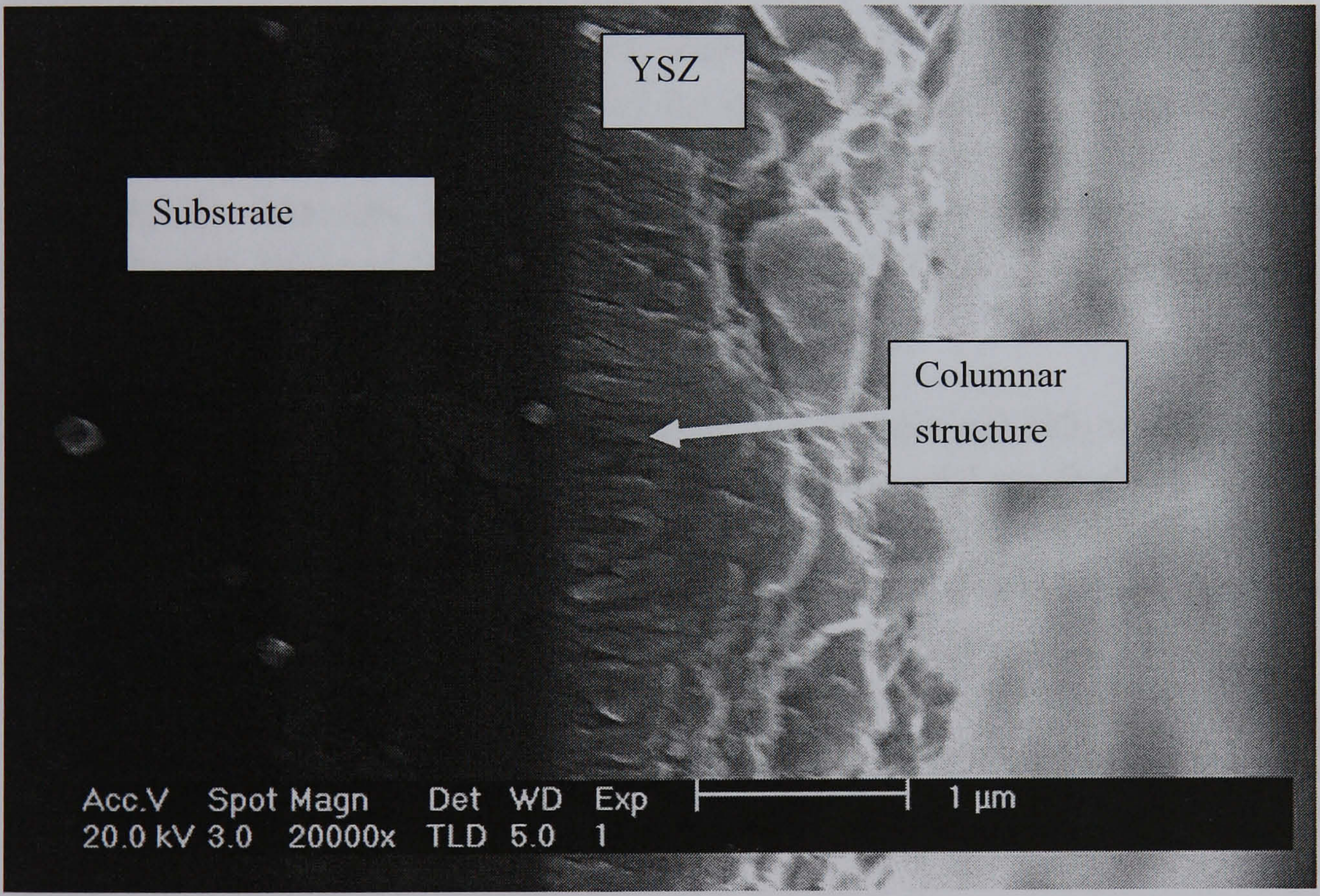

Fig 6.29 SFEG image of a YSZ film deposited by EB-PVD on to a Si_3N_4 coated Si wafer. Image shows a dense film with a columnar microstructure

Indeed as was discussed in the literature sections EB-PVD coatings of YSZ processed above 700 °C demonstrate a <111> texture. This film was prepared through sputtering. The fact that a <111> orientation of barrier layers was observed in experimental YSZ films on Si_3N_4 and Si substrates prepared in this project by EB-PVD, indicates that YSZ forms <111> textured films irrespective of substrate and deposition process, but dependent upon the processing temperature.

6.2.4 PZT On Barrier Systems

FIB analysis of the PZT/Pt/Ti/YSZ on silicon nitride film (Fig 6.31) showed that the YSZ had delaminated from the substrate. All FIB images were obtained at an angle of 45 ° to normal (see Fig 6.27 above). It is unclear, if the de-lamination of the PZT had occurred in the silicon nitride or in the silicon layers. The electrode appeared to separate from the substrate and remain in contact with the PZT. The electrode also appears swollen. However, no delamination was observed in the PZT/Pt/Ti/YSZ on silicon film (Fig 6.32). The oxidation of Pb to PbO will be discussed in the discussion section.

There were some unidentified layers in Fig 6.31, Fig 6.32 and Fig 6.33. Admittedly these layers could have been analysed by a scanning electron microscope equipped with EDX. However, as these layers were <1 μm thick and the limit of the sensitivity for EDX was ≥1 μm it was considered unlikely that EDX would have proved to be of use in the identification of these layers.

FIB analysis of PZT/Pt/Ti/TiO_2 on silicon nitride, Fig 6.33, showed a stable back electrode. There was, however, some separation of the electrode and the underlying substrate. It is unclear from the FIB image if the separation occurs between silicon of the substrate or the silicon nitride. Although, it should be noted that the titania-barrier-layer is effective in preventing the diffusion of Pb. The adhesion of the PZT/Pt/Ti/TiO_2 on silicon is much poorer (Fig 6.34)

YSZ was chosen as the stabilisation system for Si substrates and TiO_2 was selected for the stabilisation of Si_3N_4 system. FIB images of the experimental standard (Fig 6.33 and Fig 6.36) have revealed exceptionally poor adhesion between the Pt/Ti electrode and the underlying substrate. It should be noted in all films and in all systems, where de-laminations have occurred that the de-lamination occurs between the electrode and substrate: not the electrode and the PZT thick film. The blistering on the surface of the experimental standard was analysed by digging a trench and progressively eroding this back with the ion beam. Underneath the blister, a large cavity was observed (Fig 6.36); the electrode had detached from the substrate.

In a system with a stable back electrode, the stable electrode will oppose the sintering stresses and densification. However, where Pb can diffuse through the back electrode to react with the underlying substrate, a eutectic liquid will form between the substrate and the electrode (Fig 6.37). The electrode and thick film become partially mobile with respect to the substrate and de-lamination occurs at points of high stress (blisters).

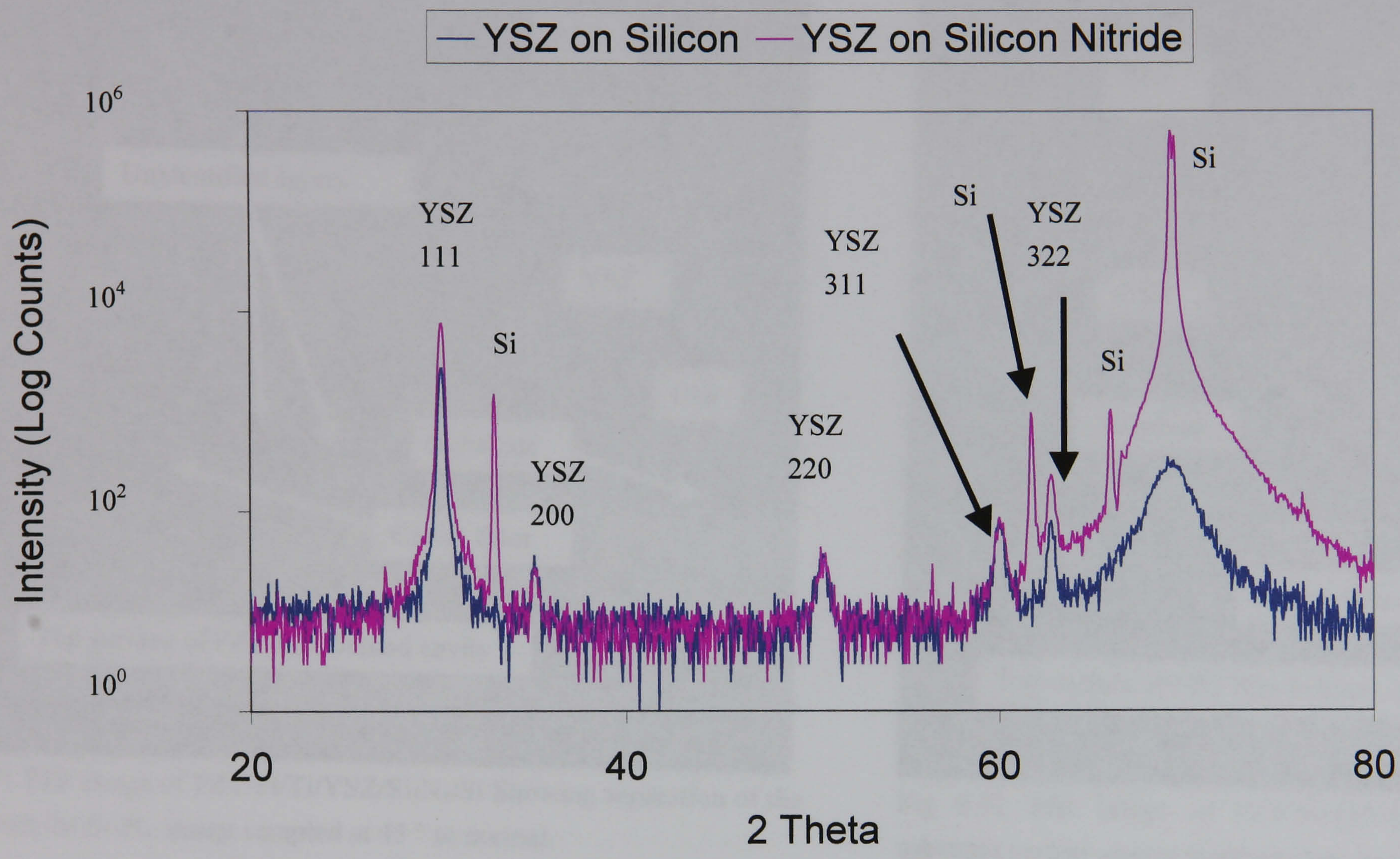

Fig 6.30 XRD pattern of YSZ films on a Si and Si_3N_4 substrates. The pattern shown a <111> texture.

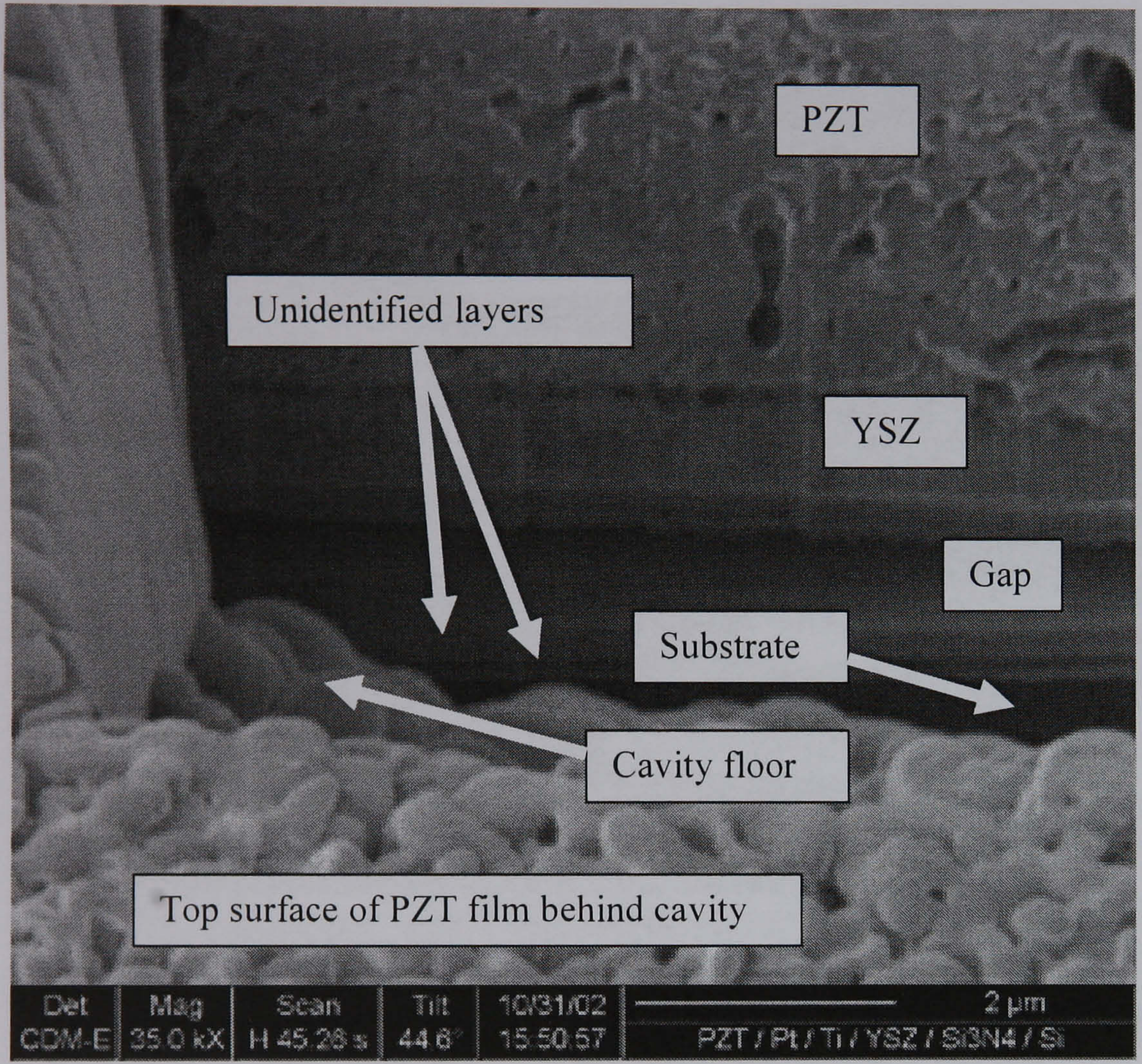

Fig 6.31 FIB image of PZT/Pt/Ti/YSZ/Si_3N_4/Si Showing separation of the YSZ from the Si_3N_4. Image sampled at 45 ° to normal.

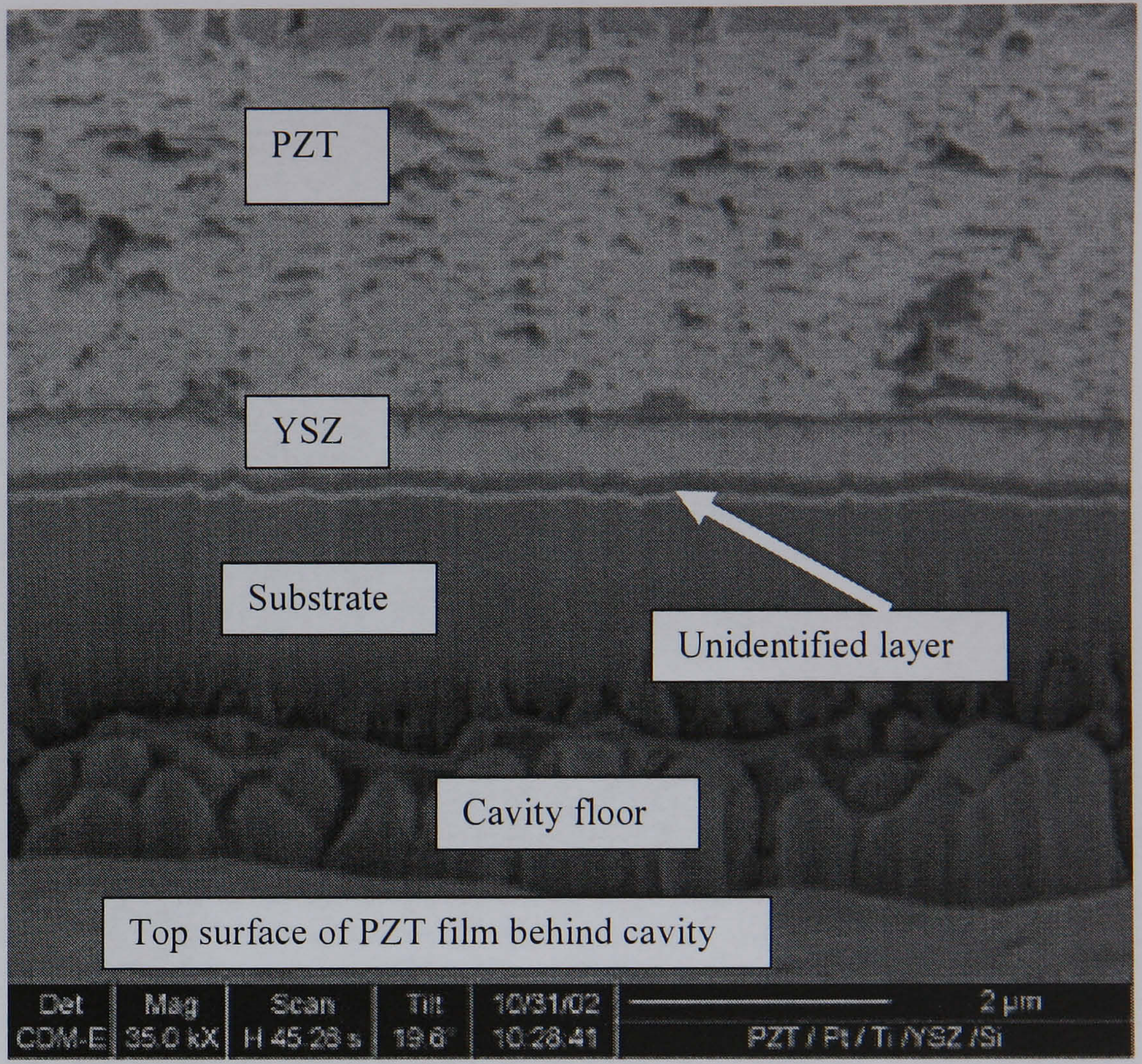

Fig 6.32 FIB image of PZT/Pt/Ti/YSZ/Si showing stabilisation of substrate system against delamination. Image sampled at 45 ° to normal.

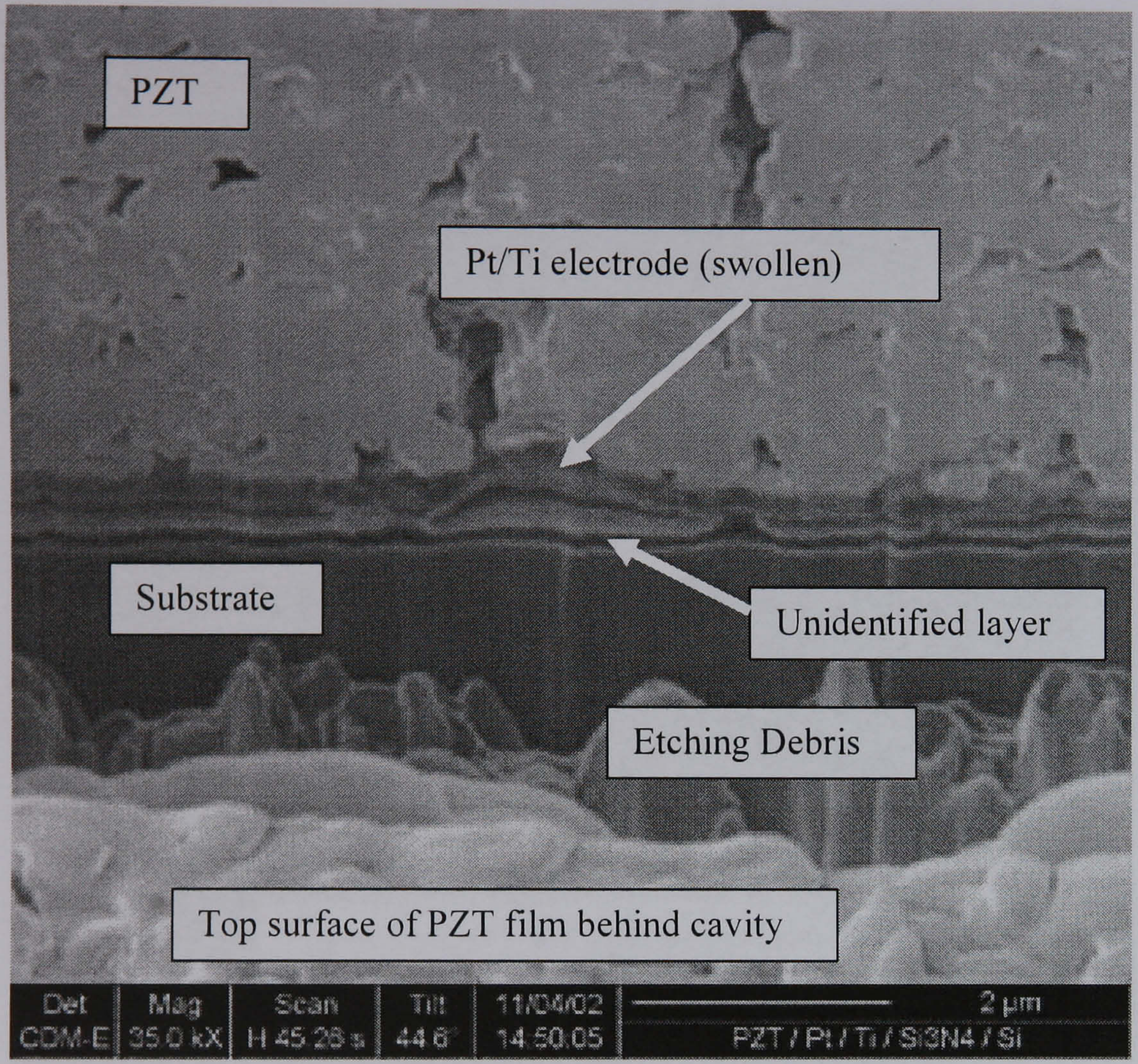

Fig 6.33 FIB Image of PZT thick film on a Ti/ Pt electrode on a Si_3N_4 coated Si wafer i.e. without a diffusion barrier. Experimental standard. Image shows significant de-lamination of the Ti/Pt electrode from the Si_3N_4 or under lying Si. Image sampled at 45 ° to normal.

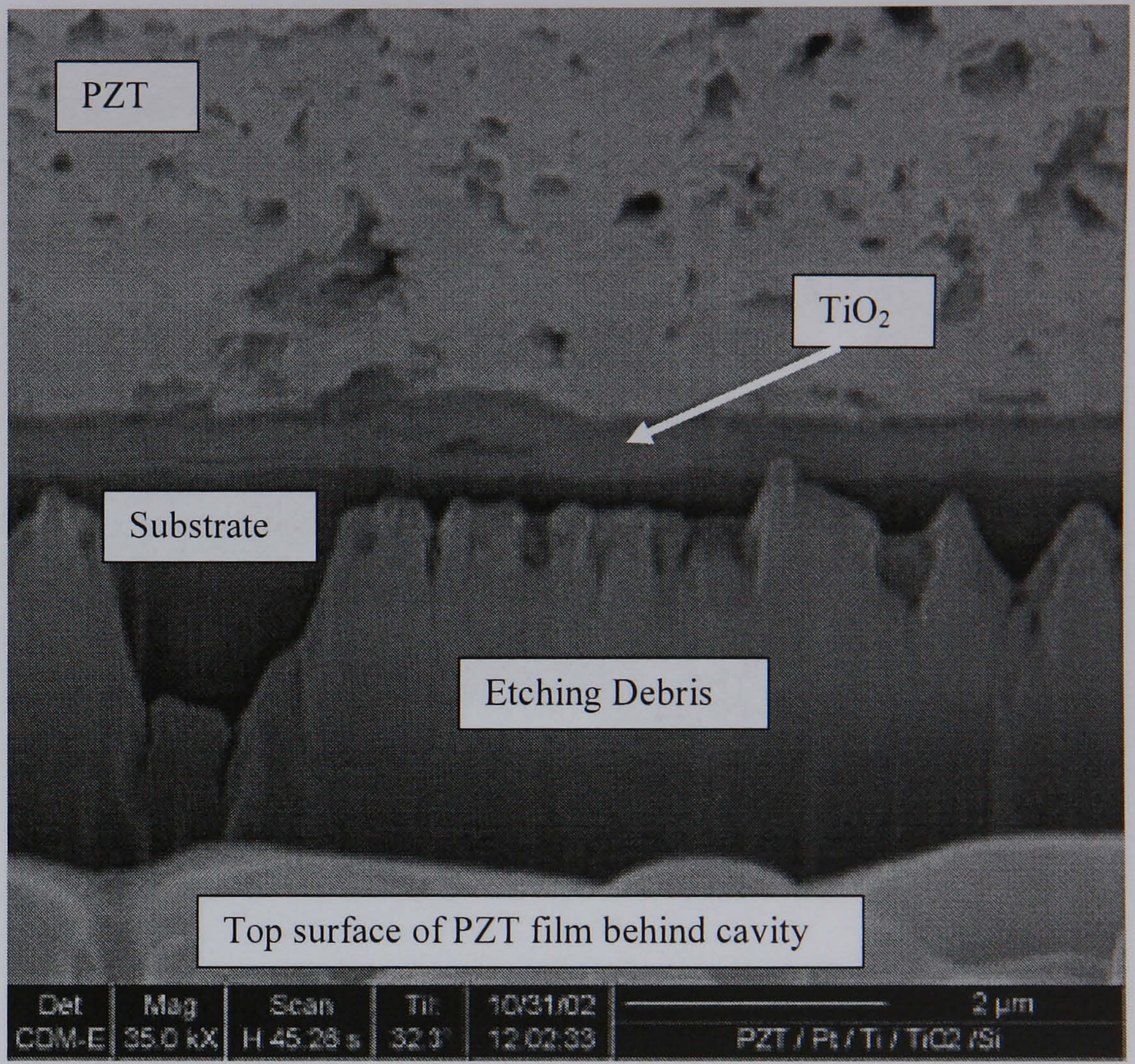

Fig 6.34 FIB Image of PZT thick film with back electrode stabilised with TiO_2 layer on Si. Image shows some separation from the substrate. Image sampled at 45 ° to normal.

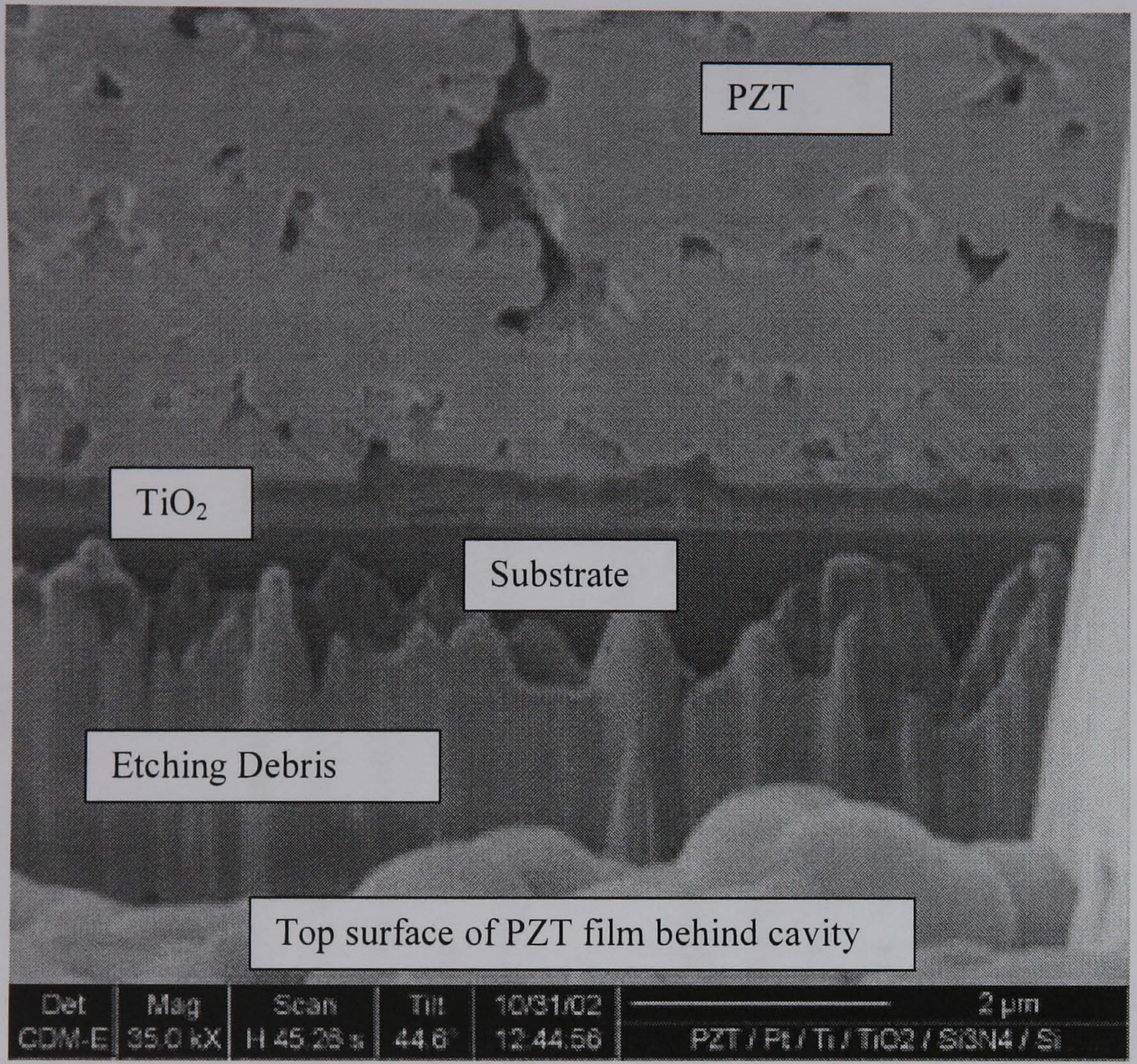

Fig 6.35 FIB image of PZT thick film with TiO_2 barrier layer on Si_3N_4. Showing some separation between the TiO_2 and the Si_3N_4. Image sampled at 45 ° to normal.

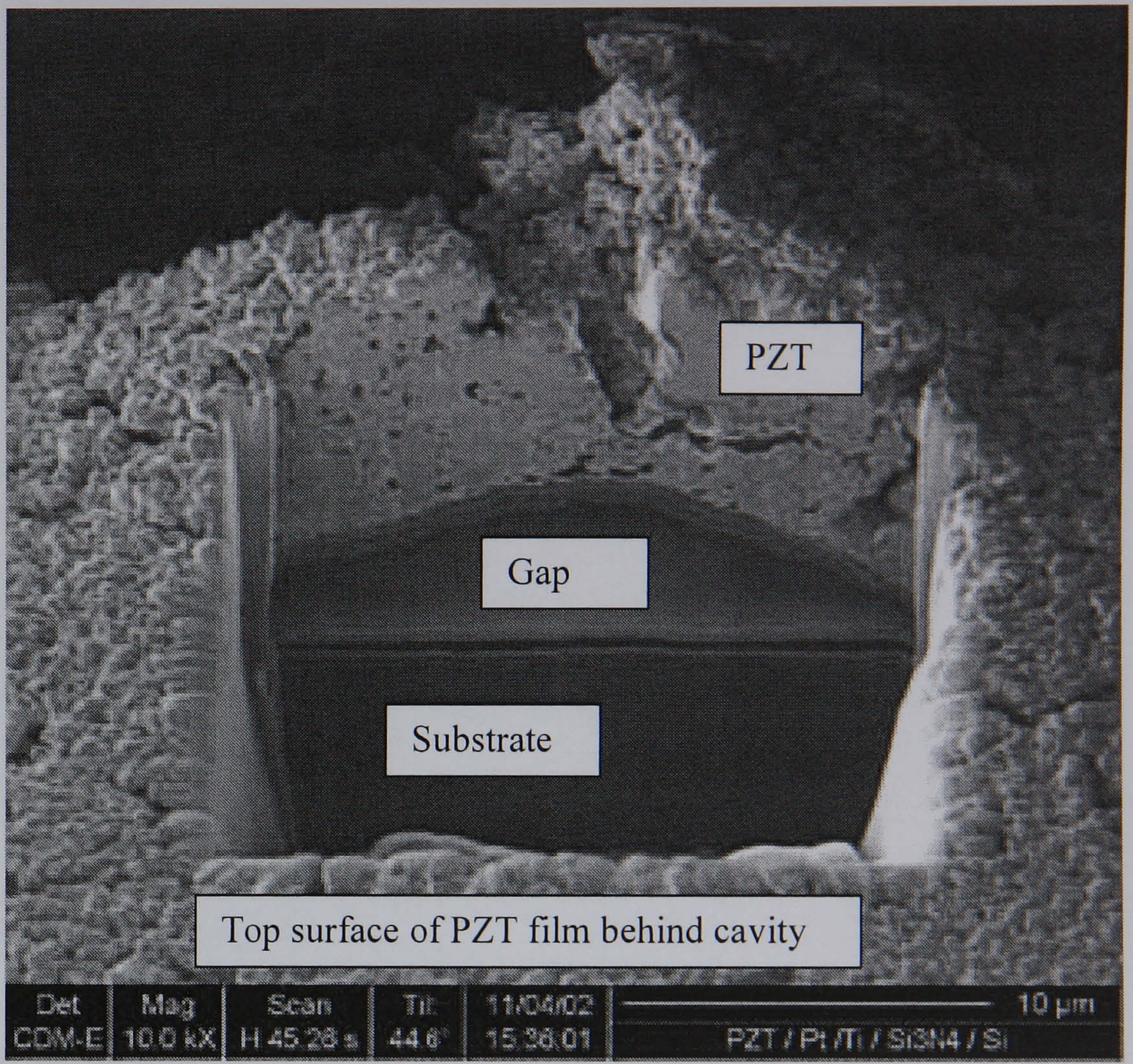

Fig 6.36 FIB Image of blister on experimental standard. Image sampled at 45 ° to normal.

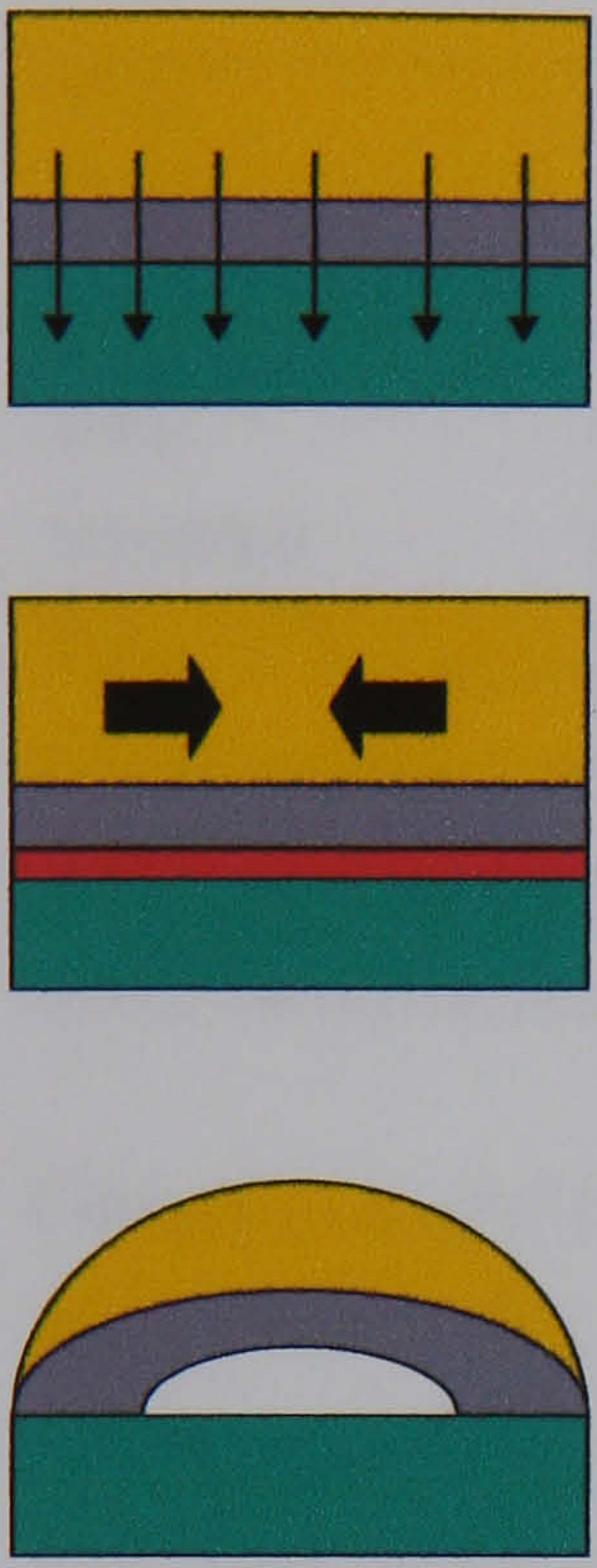

Fig 6.37 Mechanism for blister formation. Pb diffuses through the back electrode (*top*) to yield a eutectic fluid with SiO_2 (*in middle*). Under the compressive forces of sintering, the electrode de-laminates from the substrate yielding a blister (*bottom*). Si = green, Ti/Pt = grey, PZT = yellow, eutectic $PbO\text{-}SiO_2$ = red.

Table 6.5 shows roughness values for the barrier layer on the particular substrate. YSZ layers have demonstrated remarkably low roughness indicating that they are superior to their titania analogues. It should be noted that the surface roughness values were acceptable for the barrier layer systems. The PZT thick films deposited on each of the barrier layer systems was analysed for roughness variation. The analysis was conducted after sintering. The surface roughness of the PZT film with the YSZ barrier layer had the lowest Ra value indicating the surface roughness was determined by the PZT electrode interface. In other words, blistering at the substrate electrode interface determines the surface roughness of the PZT thick film.

The YSZ on Nitride barrier had the highest value of surface roughness, and this was consistent with the FIB image of the same system, where extensive de-lamination at the substrate electrode interface was observed. Surface roughness values for PZT films on titania indicated that for the silicon nitride substrate titania was a better barrier layer then YSZ. A possible explanation for this arises from the mean coefficient of linear expansion (CTE).

Barrier Layer	Substrate	Ra Barrier layer / Å	Ra Thick film / Å
YSZ	Si	54	728
YSZ	Si_3N_4	-	5936
TiO_2	Si	254	1470
TiO_2	Si_3N_4	208	708
Standard	Si_3N_4	-	10800

Table 6.5 Surface roughness data of both barrier layers and PZT thick films. Barrier layers and thick films have been prepared on differing substrates, and the PZT thick films were prepared on platinised barrier layers. The roughness values were obtained after the thick films had been sintered under Ar.

Comparison of CTE values of titania (9.1×10^{-6} $°C^{-1}$), silicon nitride (3.0×10^{-6} $°C^{-1}$) and silicon oxide (0.5×10^{-6} $°C^{-1}$) indicates that the mismatch between silicon oxide and titania is much greater than silicon nitride. It should be noted that there would be a thin SiO_2 layer on the surface of the Si substrate. Rapid thermal cycling of the PZT thick films could result in expansion variations within the different layers, and separation will probably occur where the difference in CTEs is greatest.

The tape test was applied to all samples after wet etching of the PZT. It should be noted that a positive-tape-test was where material had been removed by the tape from the sample of interest; conversely, a negative-tape-test was where no material had been removed by the tape from the sample. The tape test indicated that only PZT films prepared on a YSZ diffusion barrier on silicon were negative. In all other systems and films the tape test yielded positive results. The extent of back electrode peeling observed during the tape test increased in proportion to the extent of de-lamination between the electrode and substrate. Further, the surface roughness of the PZT in the same samples was proportional to the amount of material that was removed by the tape test. Indicating that surface roughness of the PZT is in part determined by the extent of substrate/electrode adhesion.

7 Patterning Of PZT Thick Films

7.1 Introduction

This chapter reports on the patterning of deposited PZT thick films. Two processes are used to pattern the PZT. The first process is powder blasting or abrasive micromachining. The second process discussed is wet chemical etching. The object of powder blasting is to cut a pattern into the PZT. This is employed to generate the actuator shape. Wet chemical etching is used to open paths for electrical contact to the back electrode. In both processes, PZT films are first prepared onto platinised silicon substrates.

Powder blasting has the added advantage that the underlying silicon support can be patterned. This chapter concerns itself with experimental development of the powder blasting and wet chemical etching processes; consequently, an experimental section is included in this chapter as opposed to being included in the experimental chapter (chapter 4).

7.2 Experimental

7.2.1 Powder Blasting

7.2.1.1 Photo Patterning

Au coated PZT thick films were prepared on single sided polished silicon substrates (Table 7.1) where the PZT was of the form: $4\left[C^{200,450} + 4S^{200,450}\right]_{Ar}^{710}$ prepared through the standard route. Metallised coatings were applied through sputter deposition. As the device structures were designed to be cut through the surface electrode, it was essential that the resolution of the photolithographic resist above the electrode should have the best resolution. It was for this reason that all photolithographic resist patterning was done on a gold surface.

Material	Au^a	Cr^a	PZT^b	Pt^c	Ti^a	Si
Thickness / nm	100	5	10^4	100	8	5×10^5

Table 7.1 Substrates used for Powder blasting analysis. The coatings are in order of top to bottom where Si is the substrate. Superscripts a, b, and c indicate that layers were applied through R.F. sputtering, CSD (chemical solution deposition) and DC sputtering respectively

An important consideration in powder blasting is the masking of the samples. Masking materials have been compared [121]; materials included clamped metallic (copper) masks, polyimide photoresist, negative resist foil and electroplated copper. Metallic copper masks were found to result in damage to the surface of the target material beneath the mask. This was due to particles getting between the mask and the target during blasting. Electroplated Cu resulted in the best protection of the cut substrate surface. Line widths of 10 μm were cut, 30 um deep, into Pyrex glass. In the electroplated Cu process, a thin electrode of Ti/Cu is sputtered onto the substrate's surface, a resist foil is then applied and patterned, photolithographically, before electroplating the Cu. The foil is then removed with KOH and the sample powder blasted. After powder blasting, the Cu is stripped from the substrate with concentrated HNO_3. KOH has been shown to undermine adhesion between the substrate and the PZT thick film: electroplating of Cu is unsuitable for the masking of PZT thick films. Cracks in the substrate material were observed to form beneath the resist foil making this unsuitable for use. Polyimide photoresists achieved patterned features with line widths of 10 μm. Although the erosion rate of the resist was high.

The photoresist chosen for the patterning of features was SBX® (PhotoBrasive Systems). SBX®, a negative working synthetic latex, yields an elastomeric (non-brittle) coating on development; abrasive particle impact would be absorbed by the resist preventing erosion of the resist system. SBX® deposition conditions are listed in Table 7.2. It should be noted that the developer for SBX was water.

SBX® Thickness / μm	25	50	35
Spin speed / rpm	1000	500	1000
Spin time / s	40	40	20
Ramp rate up / k.rpm/s	5	5	5
Ramp rate down / k.rpm/s	10	10	10
Drying Temperature / °C	25	25	25
Drying time / h	12	12	12
Exposure time / s	25	90	90

Table 7.2 Conditions used to coat whole wafers with SBX®. These conditions comprise: spin coating, drying and exposure time.

Initial powder blasting was conducted with 25 and 50 μm thick photoresist. All powder blasted samples were eroded with Al_2O_3 powder with a particle size of 15μm. Initially-powder-blasted-samples were cleaved, mounted in epoxy resin and polished to obtain polished cross sections for analysis by optical microscopy. Cleaved-samples were supported, vertically, with a clip in a 2.5 cm diameter by 2.5 cm high plastic-tub. Epoxy resin was poured into the tub and allowed 24 hours to set (see Fig 7.1). Upon setting, the samples were released from the tub. The samples were then ground down with 240μm and then 150μm SiC paper. Following grinding samples were polished with a 6μm polishing wheel using ethene glycol as a lubricant. Samples were then cleaned with water before analysis.

Fig 7.1 Cross-section of sample-mounting for optical microscopy. Samples are mounted in epoxy resin and the face is polished back to reveal a cross section of the sample. This process was used for the preparation of cross sections of powder-blasted PZT-thick-films on platinised-silicon-substrates

A calibration mask with a graduated set of lines was used to make a graduated set of cavities in the SBX® (Fig 7.2): to determine edge shift in the resist. Samples were powder blasted before measuring edge shift. The line widths were 50, 75, 100, 250 and 500 μm. Wafers with SBX® patterned in this way were used as a standard calibration for powder blasting. Edge shift (i.e. $\iota = w_a - w_i$) was measured with the image analyser in terms of the actual width of the feature (w_a) and the width of the mask feature (w_i), see Fig 7.3. Values of w_a were obtained for features at w_i = 50, 75, 100, 250 and 500 μm patterned in 25 and 50 μm thick SBX®. It should be noted that ι was measured according to equation (7.3) below.

Line width, l, has been defined by Rai-Choudhury [122]:

$$l = (x1 - L_{res}1) - (x2 + L_{res}2) \tag{7.1}$$

where x1 and x2 are lengths along an axis x $(= w_a)$ measured from $left \rightarrow right$ of a cavity in a photoresist. The resist length occupied by residue on either side of the cavity is given by $L_{res}1$ and $L_{res}2$. It follows that resolution, $\Re$, will be related: $\Re \propto 1/l$. If $\Re$ is determined after powder blasting the edge shift must be taken into account. A centre line l_c is defined to measure the centre of the cavity:

$$l_c = \frac{(x1 - L_{res}2) + (x2 - L_{res}2)}{2} \tag{7.2}$$

from which the edge shift ι may be defined:

$$\iota = (x1 - L_{res}2) + (x2 - L_{res}2) - w_i \qquad (7.3)$$

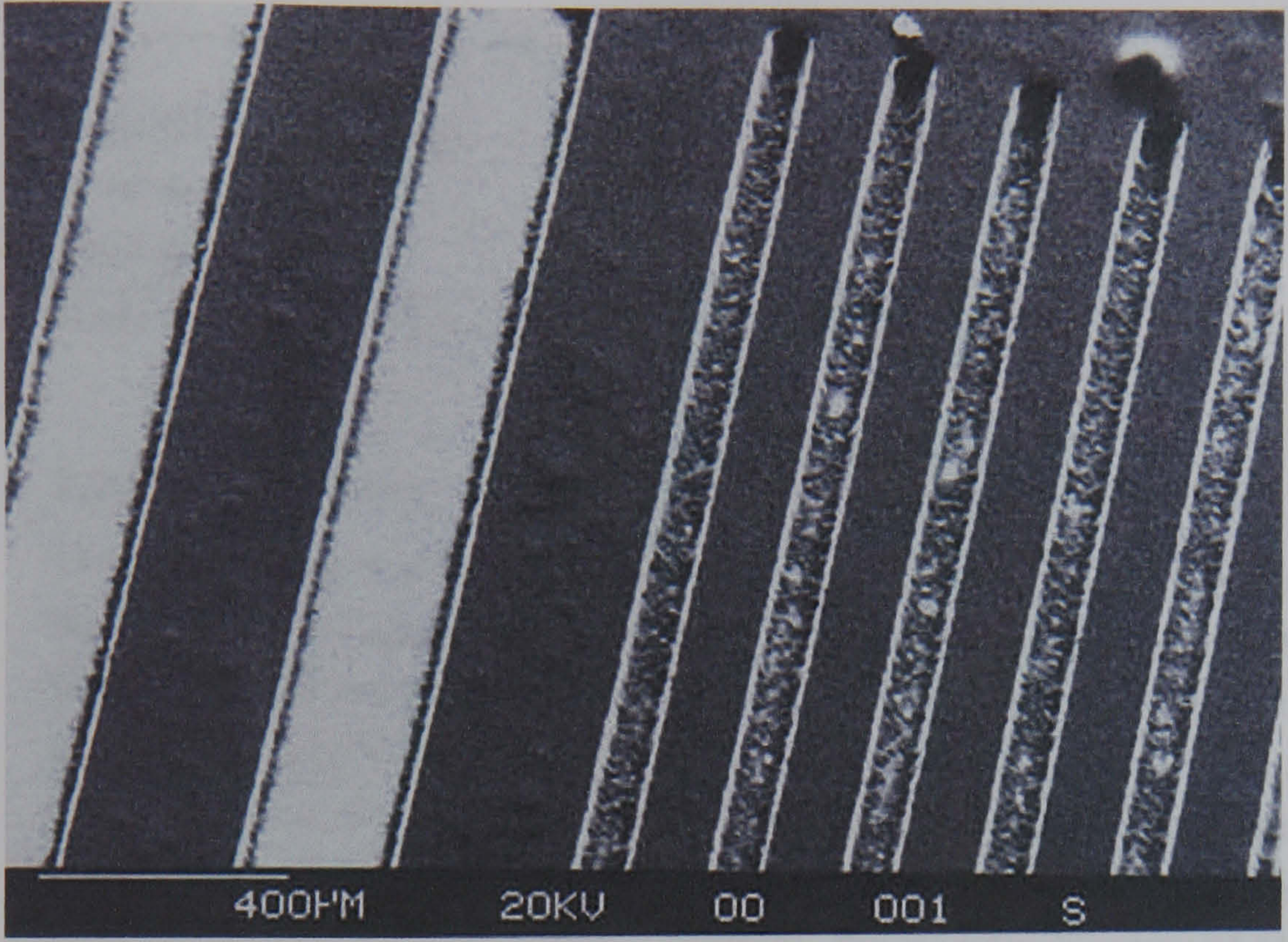

Fig 7.2 A calibration pattern of SBX® (50 µm) on a PZT thick film surface. Residue accumulates with the reduction of cavity width.

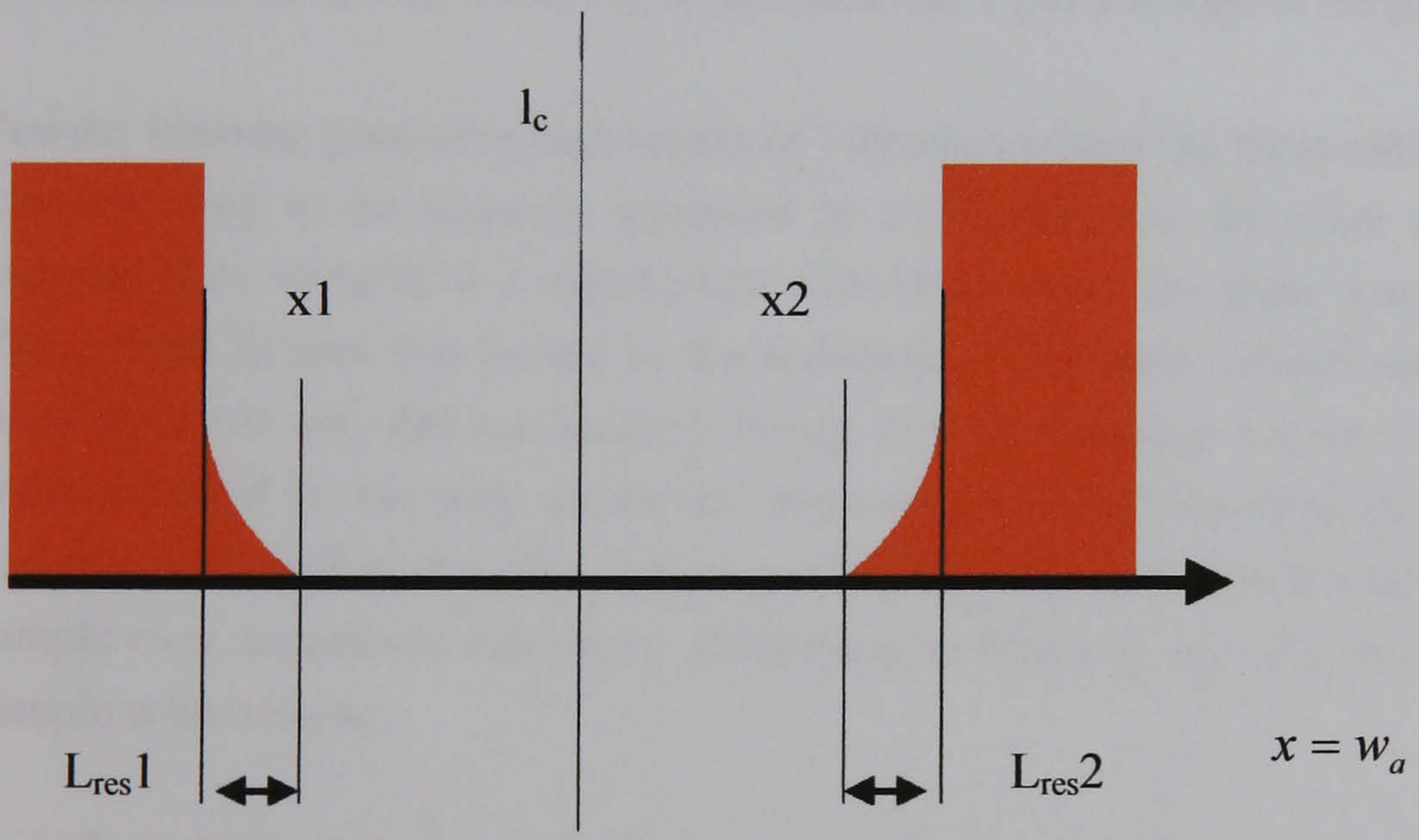

Fig 7.3 Diagram of photoresist line width resolution. Image taken from Rai-Choudhury [122].

Patterned SBX® was initially developed with tap water from the mains supply. However, the low pressure of the mains supply resulted in inefficient washing out (i.e. developing) of material in the photoresist cavities. Consequently, residue was found to accumulate in the photoresist cavities after development. A high pressure automated washing system

(SSEC Model 160 Solid State washing unit) was employed to fully resolve pattern features. Automated washing conditions are listed in Table 7.3.

Step	Step Time / s	Spin Speed / rpm
High Pressure Washing	20	1000
Blow dry in dry N_2	10	1000
Spinning	20	2000

Table 7.3 Automated development conditions for SBX®

7.2.1.2 Machining

The powder blaster consists of a blast cabinet, a cyclone and a compressor (Fig 7.4). The blast cabinet is a sealed chamber with a door; within the chamber, there is a table on which to mount samples, and a powder gun to blast samples. During powder blasting, the table rotates relative to the gun and the gun scans forward and back along a track. The compressor is a source of pressurised air. The air stream carries powder in a flow from the powder collection box (located beneath the filters) to the gun where it is ejected in the form of an aerosol. After eroding samples, the powder is returned to the cyclone. The cyclone separates particles according to size; allowing the separation of powder particles from sample debris. The powder and the debris streams are passed through a set of filters to physically remove any debris. The powder is returned to the collection box. The powder used for attrition was Al_2O_3 and this had a particle size of 15 μm.

Powder blasting generates high levels of vibration within the blast cabinet. Consequently, samples need to be securely mounted to avoid fracture. In order to prevent fracture samples were secured to a metal plate with black wax. The plate was bolted to a plastic disk, which in turn was bolted to the turntable of the blast cabinet see Fig 7.5. Samples secured in this way did not fracture during Powder Blasting. Either whole or part wafers were mounted in this way. However, there was a loss in the flow of powder with time, and this was attributed to the clogging of the powder with black wax from the mounted sample over successive run times. After powder blasting, the wax was stripped from the sample with toluene.

A cycle is defined as the time taken for the gun to scan once forward and once backward along the track. The length of the track is set by the manufacturer and cannot be varied experimentally. The number of cycles, the speed at which the gun moves along the track (gun speed) and the speed the table rotates at are experimental variables and may be controlled from the control panel of the blast cabinet. It should be noted that pressure had been set by the manufacturer at 80 psi and could not be varied.

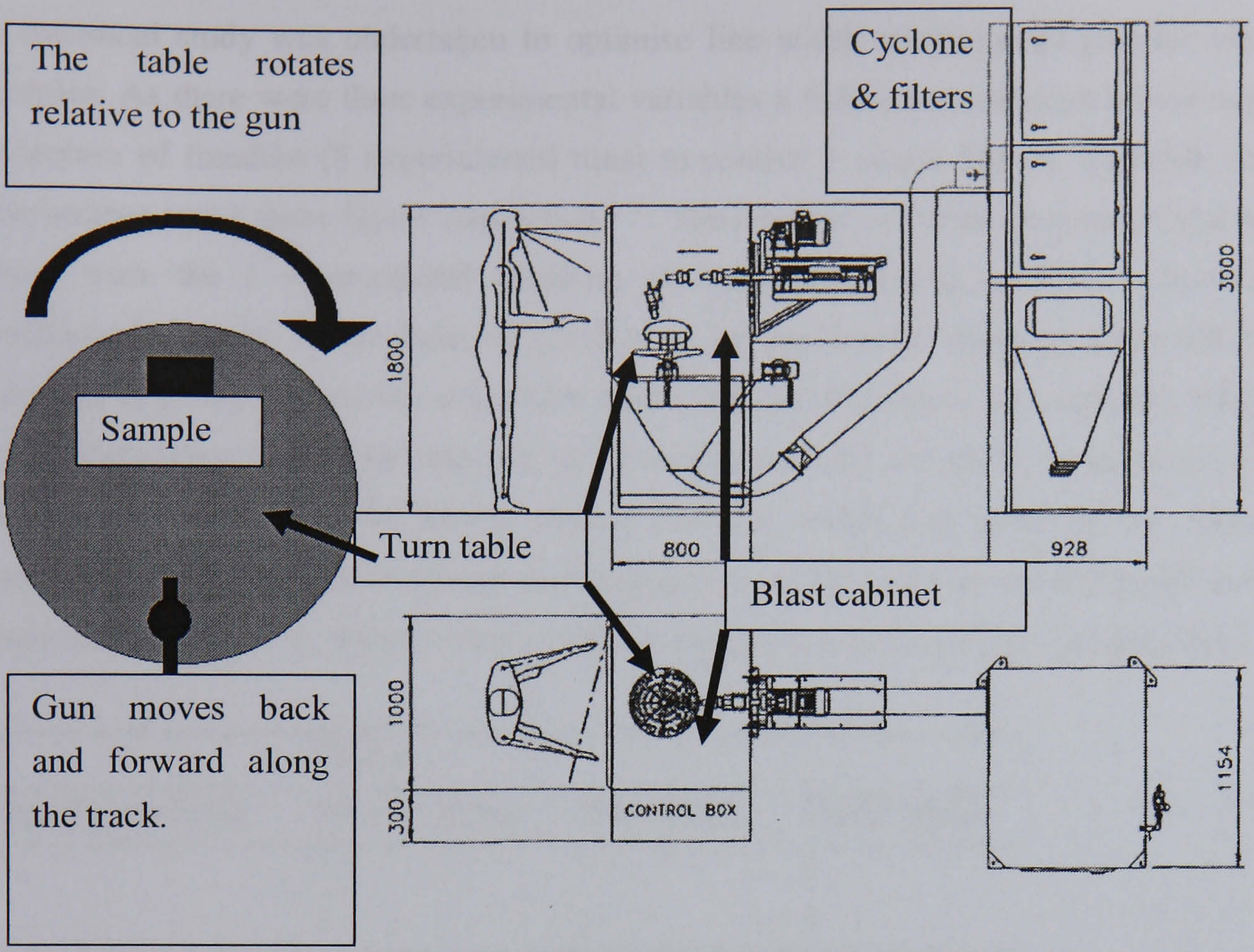

Fig 7.4 Powder blasting set up. Profile of the powder blaster *above* and a plan view of the system *below*.

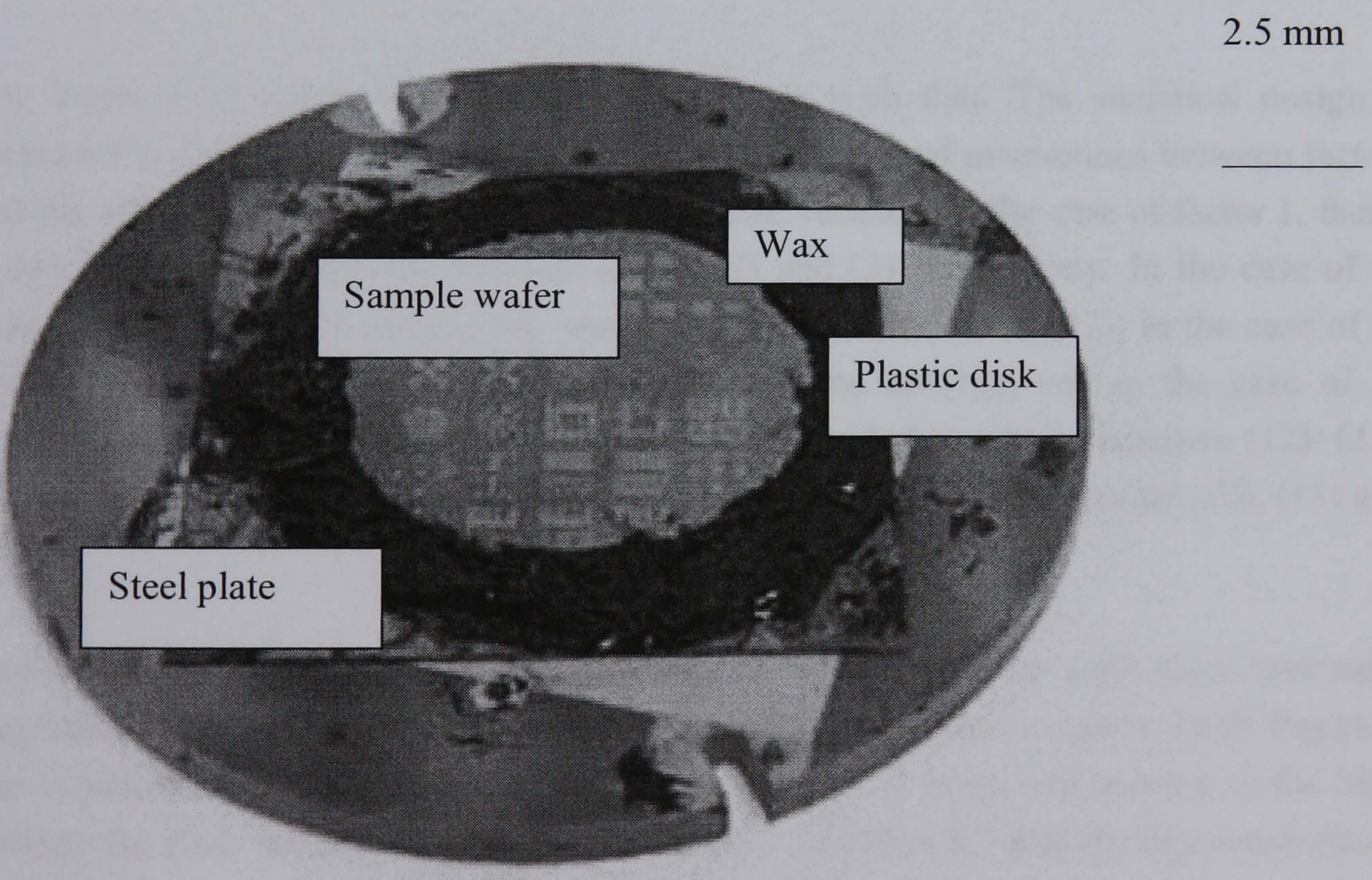

Fig 7.5 Sample preparation for powder blasting.

A statistical study was undertaken to optimise line width resolution of powder blasted samples. As there were three experimental variables a full factorial design would require 7 degrees of freedom (8 experimental runs) to resolve 3 single factors, 3 double factor interactions and 1 three factor interaction [123]. The number of cycles, gun speed and table speed were the 3 experimental variables (factors). Resolution could be effected by residual photoresist in the base of cavities or by photoresist stripping from the blast intensity. The smallest cavity size either unaffected by blasting or incompletely filled in by residual photoresist was selected for measurement of l according to equation (7.1). Formally: resolution of the lowest measurable line width was taken as the response variable. Levels were selected from dial settings on the blast cabinet control panel and are presented in Table 7.4, where + and – indicate the upper and lower levels respectively.

	Factors		
Upper/lower level	No. of Cycles	Gun Speed	Table Speed
+	3	3	3
-	2	2	4

Table 7.4 Upper and lower levels of factors in the experimental design. Values taken from the dials of the control panel of the powder blasting system.

The levels were selected about middle values on each dial. The statistical design is presented in Table 7.5. Statistical design allows resolution of interactions between factors and the effect of these interactions on the response variable. In the case of factor 1, factor 2 and factor 3 these will be denoted as (1), (2) and (3) respectively. In the case of an interaction between (1) and (2) the interaction will be denoted as (12), in the case of an interaction between (1) and (3) this will be denoted as (13), and in the case of an interaction between (1), (2) and (3) this will be denoted as (123). Because (12)=(21), (13)=(31) and (23)=(32) the convention is to only consider the interactions (12), (13) and (23).

Two wafers patterned with a calibration pattern (in SBX®) were each diced into eight fragments. The SBX® was developed with water from the mains supply. Each fragment was mounted on a separate steel plate with black wax. A plate was secured in the blast cabinet, the dials set according to the run number in Table 7.5 and the run commenced. This process was repeated run by run until all eight runs had been completed, such that there were eight samples blasted according to conditions in Table 7.5. The eight runs were repeated with the eight remaining fragments. The fragment samples were removed from the plates before measuring line widths on the image analyser.

Run No. (i)	Factors			Interactions				Response variable
	No. of Cycles (1)	Gun Speed (2)	Table Speed (3)	(12)	(123)	(13)	(23)	Mean line width $\bar{l} = \frac{1}{2}\left(l_i + l_{\left(i+\frac{1}{2}N\right)}\right)$ / µm
1	2	2	3	+	-	+	+	100
2	3	2	3	-	+	-	+	60
3	2	3	3	-	+	+	-	225
4	3	3	3	+	-	-	-	80
5	2	2	4	+	+	-	-	100
6	3	2	4	-	-	+	-	50
7	2	3	4	-	-	-	+	155
8	3	3	4	+	+	+	+	95

Table 7.5 Statistical experiment for the optimisation of powder blaster operating conditions. A full factorial design, 2^3 =8 runs with 7 degrees of freedom allowing resolution of up to three factor interactions. The values attributed to factors correspond to dial settings on the powder blasting cabinet control panel.

Measured line width values are presented as a mean of the replicated runs $\bar{l}$ in Table 7.5, where $\bar{l} = \frac{1}{2}(l_1 + l_2)$. Identities and effects were calculated from the data in Table 7.5 using equation (7.4) and presented in Table 7.6.

$$I_n = \frac{1}{4}\left(\pm y_1 \pm y_2 \pm \ldots \pm y_{\frac{1}{2}N}\right) \qquad (7.4)$$

In equation (7.4), n is the integer-value corresponding to the column-number of the respective factor or interaction in Table 7.5, and y_i is the response variable corresponding to the ith run in the design. N_o is the number of observations i.e. the number of runs multiplied by the number of replications. The sign of y_i was the product of the sign of the factor(s) or factorial interaction(s) of the ith run in the identity. As $I_n \to \infty$ it follows that $l \to \infty$, however, for maximum resolution $l \to 0$ when $I_n \to \infty$. The condition $l \to 0$ when $I_n \to \infty$ was achieved through expressing responses as $l_{\max} - \bar{l}_i$, where l_{max} was the maximum line width observed in N_o values and $\bar{l}$ was the average of the two line width measurements. Substitution into equation (7.5) yields values of y_i that were used to calculate the appropriate identities in equation (7.4), above.

$$N_o = 16 \qquad (7.5)$$

$$i = 1,2....\tfrac{1}{2}N_o$$

$$y_i = l_{\max} - \tfrac{1}{2}\left(l_i + l_{\left(i+\frac{1}{2}N_o\right)}\right)$$

The standard error SE is a measure of noise within a statistical experiment. In the case of an eight run experiment replicated twice the SE may be expressed as in equation (7.6) [123], where g is the set of replicated conditions (number of experimental runs i.e. g = 8). The value of any calculated effect was deemed significant if it was found at least twice that of the standard error.

$$SE = \sqrt{\left(\frac{4\sum\left(l_i - l_{\left(i+\frac{1}{2}N_o\right)}\right)^2}{2N_o g}\right)} \qquad (7.6)$$

7.2.1.3 Device Wafers

A jig was designed and fabricated at Cranfield University to hold entire wafers and eliminate the need for black wax (Fig 7.6). The jig consisted of a base plate bolted to two upper plates in the shape of a 4" Si wafer. The upper plates created a cavity into which a polymer (PDMS Dow Corning) was used a cushion. A washer and a ring were bolted to the upper plates with six evenly distributed hex screws. The PDMS cushion was used to damp vibrations from the blasting system. The washer secured the wafer in place. The design was such that the weight of the plate was evenly distributed across the wafer. The hex bolts were tightened along diagonals to reduce uneven loading of the wafer during clamping.

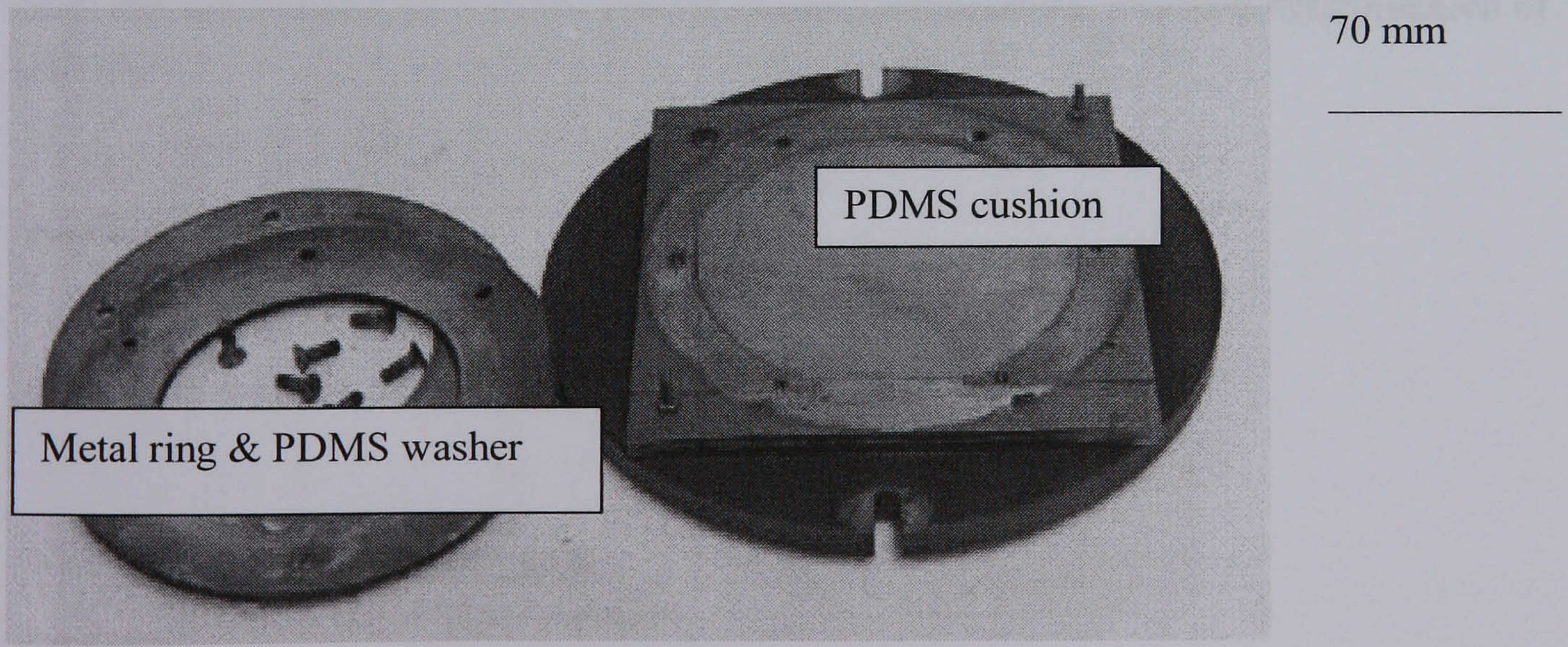

Fig 7.6 Powder blasting Jig

Two device wafers were fabricated of the form: Au/Cr/PZT/Pt/Ti/YSZ/Si/Cr these were labelled rh100 and rh200 respectively. These wafers were coated with 35 μm thick SBX®

(Table 7.2); the SBX® was developed automatically. Device wafers were mounted in the wafer jig secured in the blasting system. In order to achieve maximum resolution, gun speed and table speed dials were set to two and four respectively; in accord with run 6 of the statistical study (Table 7.5). In order to achieve an etched depth of 30 μm (10 μm for the PZT and 20 μm for the cantilever) the number of cycles was repeated until the desired depth was achieved. After powder blasting, the SBX® was removed with 25 % stencil remover (Absolute Screen Ltd.).

7.2.2 Wet Chemical Etching Of PZT

Standard photolithography was employed to pattern substrates before wet etching. The standard photolithographic technique consists of spin coating the photoresist onto the substrate, soft baking, exposure and development. The photoresist used in wet etching trials was S1818 (Shipley Europe Ltd.). S1818 was spun at 4000 rpm for 60 s, soft baked at 115 °C for 90 s, exposed for 15s and developed (75 s) in MF319 (Shipley Europe Ltd). Residual organics were removed from patterned samples through plasma ashing at 12 W for 3 minutes. At the end of etching, the resist was stripped in acetone.

A PZT thick film was prepared on a Pt/Ti/Si wafer through the standard route and sintered under an Ar atmosphere. The wafer was patterned through the standard photolithographic technique and then divided into pieces of 2cm x 2cm. Wafer pieces were supported with the PZT thick films face down in the etching solution see Fig 7.7. The samples were etched without stirring to begin with. Samples were held with a vacuum pen held in a lab clamp. A standard etching solution was prepared from HCl (37 % wt in water (Aldrich Chemicals CAS 764701-0)) and HF(aq)(48 % wt in water (Aldrich Chemicals CAS 7664-39-3)). The etching solution was prepared by mixing of HF(aq) and HCl, and diluting the solution to 0.08 M and 0.16 M respectively. Etching time was varied between 5 to 45 minutes at room temperature: enabling determination of etch rate.

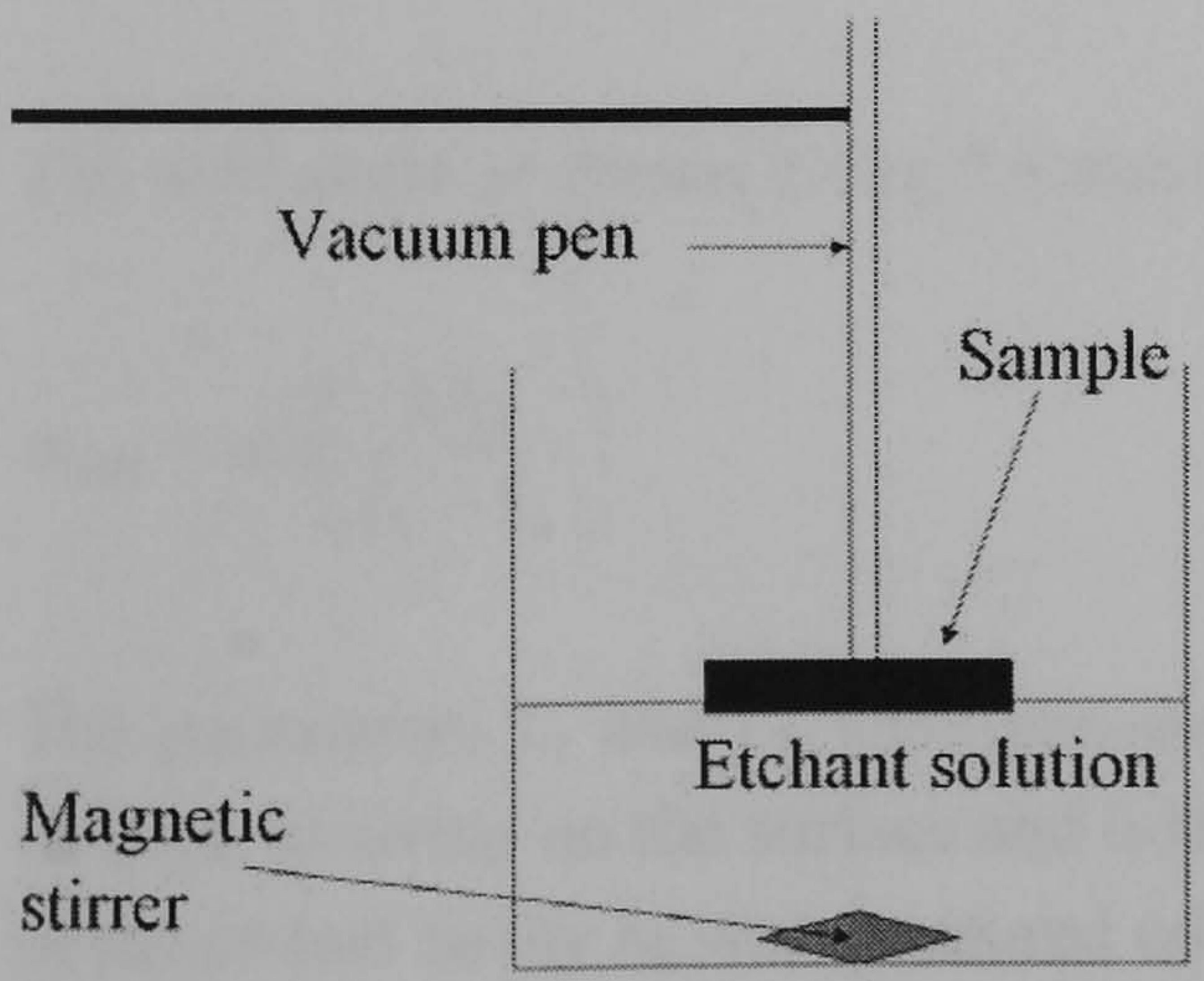

Fig 7.7 Experimental set up for the chemical etching for PZT thick films.

The etch rate, Er_d, is a function of the thickness of the thick film etched, h_E, and the time, t, the film was etched for, see Fig 7.8 and equation (7.7).

$$Er_d = \frac{h_E}{t} \tag{7.7}$$

In order to measure the under cut the lateral etch rate, Er_l, was defined in equation (7.8). L_t and L_b are the lengths of the mouth and the base of the etched cavity respectively.

$$Er_l = \frac{(L_t + L_b)}{4.t} \tag{7.8}$$

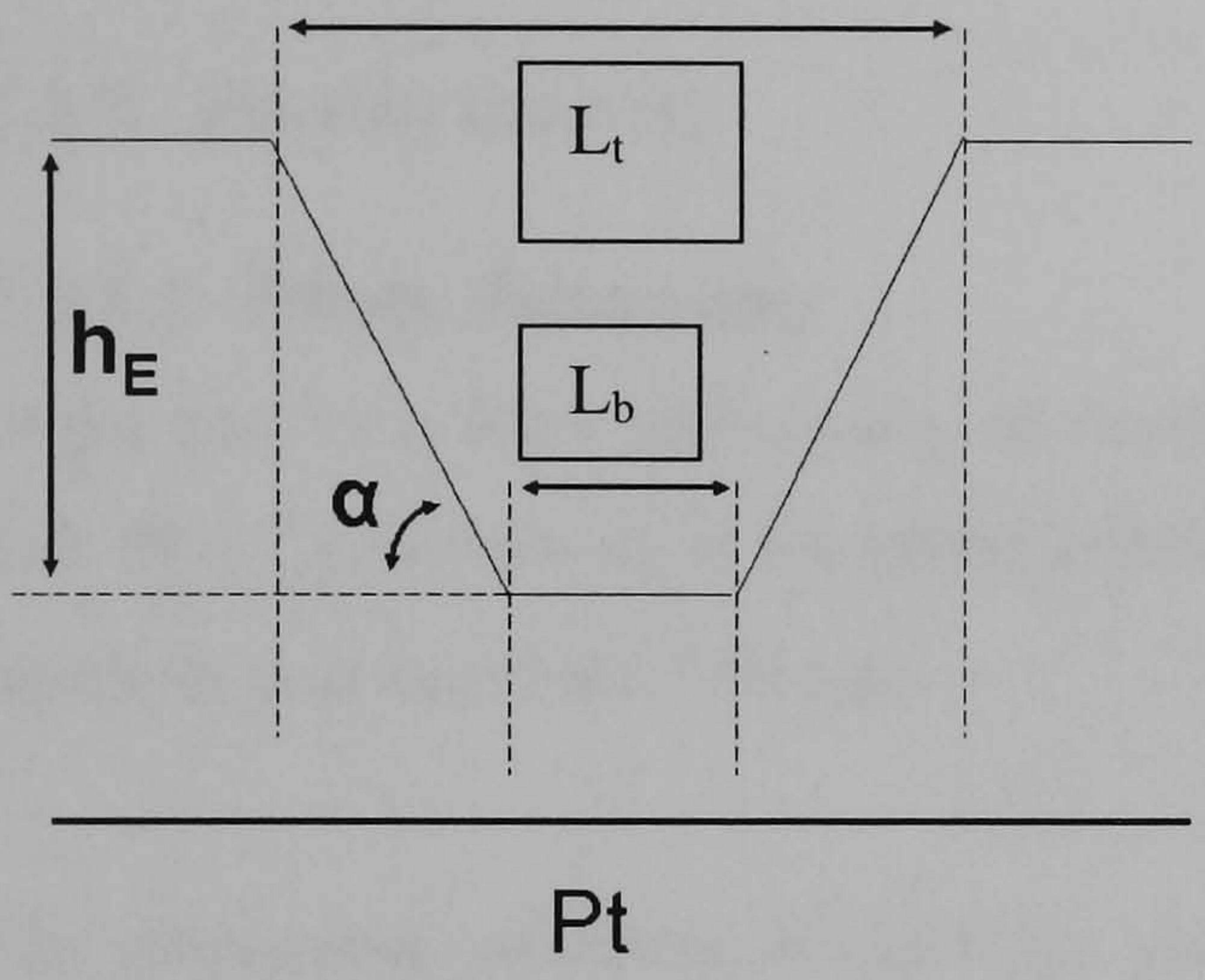

Fig 7.8 Diagram of the cross section of an etched cavity in a PZT thick film. Here α corresponds to α_{PZT}: the wall angle etched in the ceramic.

The etching efficiency γ is expressed as a percentage of the downward etch of the total etch rate:

$$\gamma = \frac{100.Er_d}{Er_d + Er_l} \tag{7.9}$$

The wall angle as shown in Fig 7.8 may be expressed as α_{PZT}:

$$\alpha_{PZT} = \cot\left(\frac{2.h_E}{L_t - L_b}\right) \tag{7.10}$$

The parameters L_t and L_b were measured with an optical microscope (Image analyser) through focusing on the surface and bottom of the etched cavities respectively. The depth of the etched cavity h_E was measured with the Dek-Tak as a step height.

In order to determine the stability of S1818 to the etching solution a pattern was prepared onto a Pt/Ti/Si wafer and placed into the etching solution for 10 minutes. The etch rate of the resist was determined as an indication of the resists stability.

The effect of stirring and concentration on the etching process were investigated. Samples were etched with stirring for 1 minute, and Er_d was determined before the etching had gone through the thick film to the bare metal. This experiment was repeated with a low concentration etching solution: 6×10^{-2} M by HF(aq) and 12×10^{-2} M by HCl.

7.3 Results

7.3.1 Powder Blasting

7.3.1.1 Photo Patterning

In the case of a thick photoresist, its resolution will be effected by its aspect ratio: such that $\Re \propto {}^{w_a}/_{h_r}$ where h_r is the photoresist-thickness. In order to achieve reasonable line widths h_r was kept below 50 μm.

The subsequent patterning of the resist yielded features of line widths as low as 100 μm and 50 μm, for the 50 μm and 25 μm thick resist samples respectively. The build up of residue in cavity widths less than 100 μm was considered too great to yield good quality patterned features in 50 μm thick SBX®. The required line width definition was determined by feature size of the mask. No gap between two lines was less than 80 μm; consequently, a resist thickness < 50 μm was required to achieve the desired value of $\Re$. Changing the exposure time for the SBX® had no effect in reducing the residue. A side wall of a cavity in the 50 μm thick SBX® resist is shown in Fig 7.9; and the build up of residue with the change in cavity width in Fig 7.2.

The presence of the residue prevented the Al_2O_3 powder from efficiently cutting the desired feature in the substrate surface. Line width resolution of the 'cut feature' was reduced by the presence of the residue.

Polished-cross-sections of powder blasted PZT thick films on Si are shown in Fig 7.10 and Fig 7.11 for the 25 and 50 μm thick SBX® respectively. There appears to be no damage to the PZT beneath the SBX®: indicating that there has been no under cut of the resist during powder blasting.

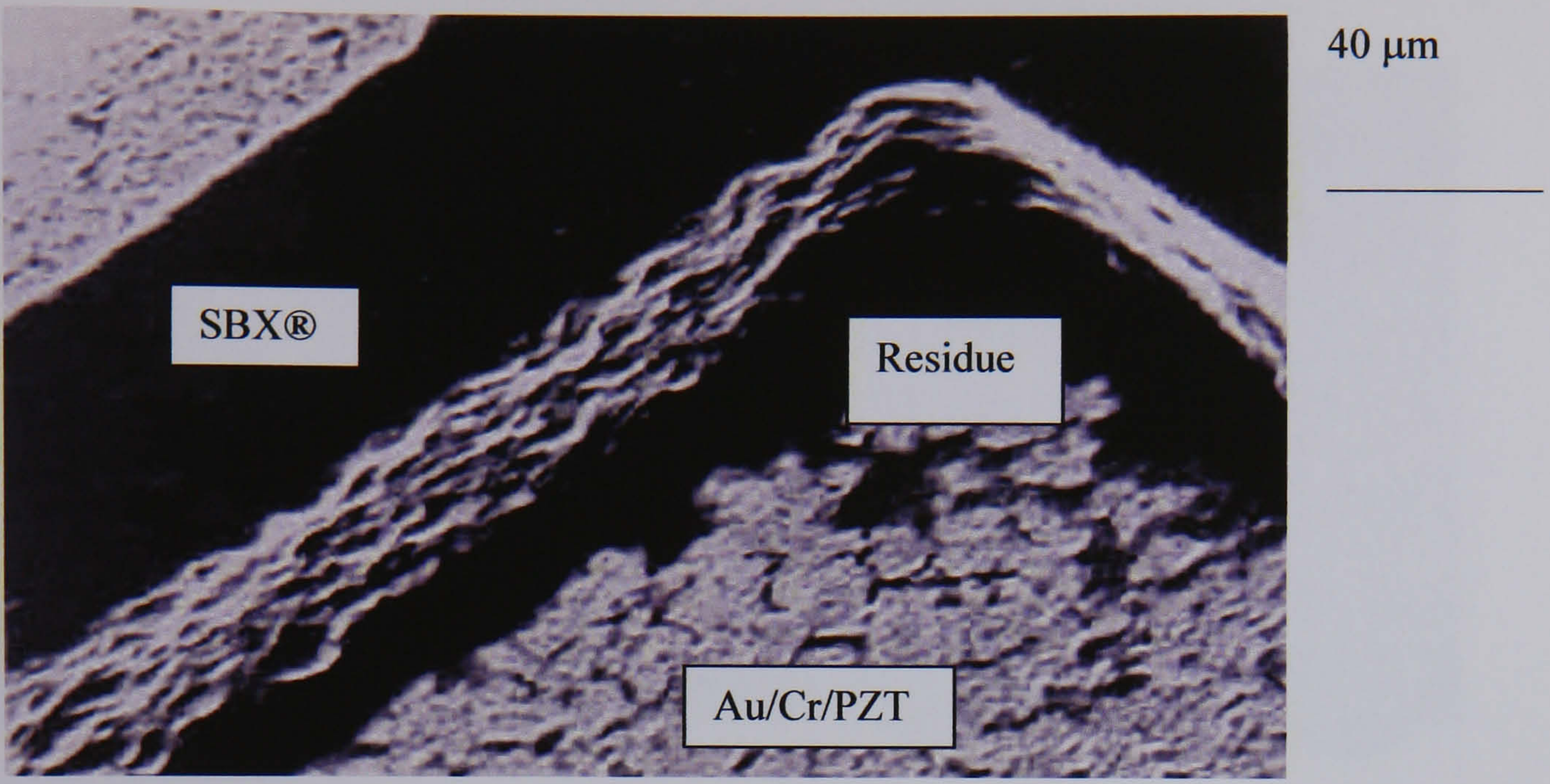

Fig 7.9 SEM micrograph of a SBX® resist feature on a PZT thick film. Residue can be seen at the base of the feature..

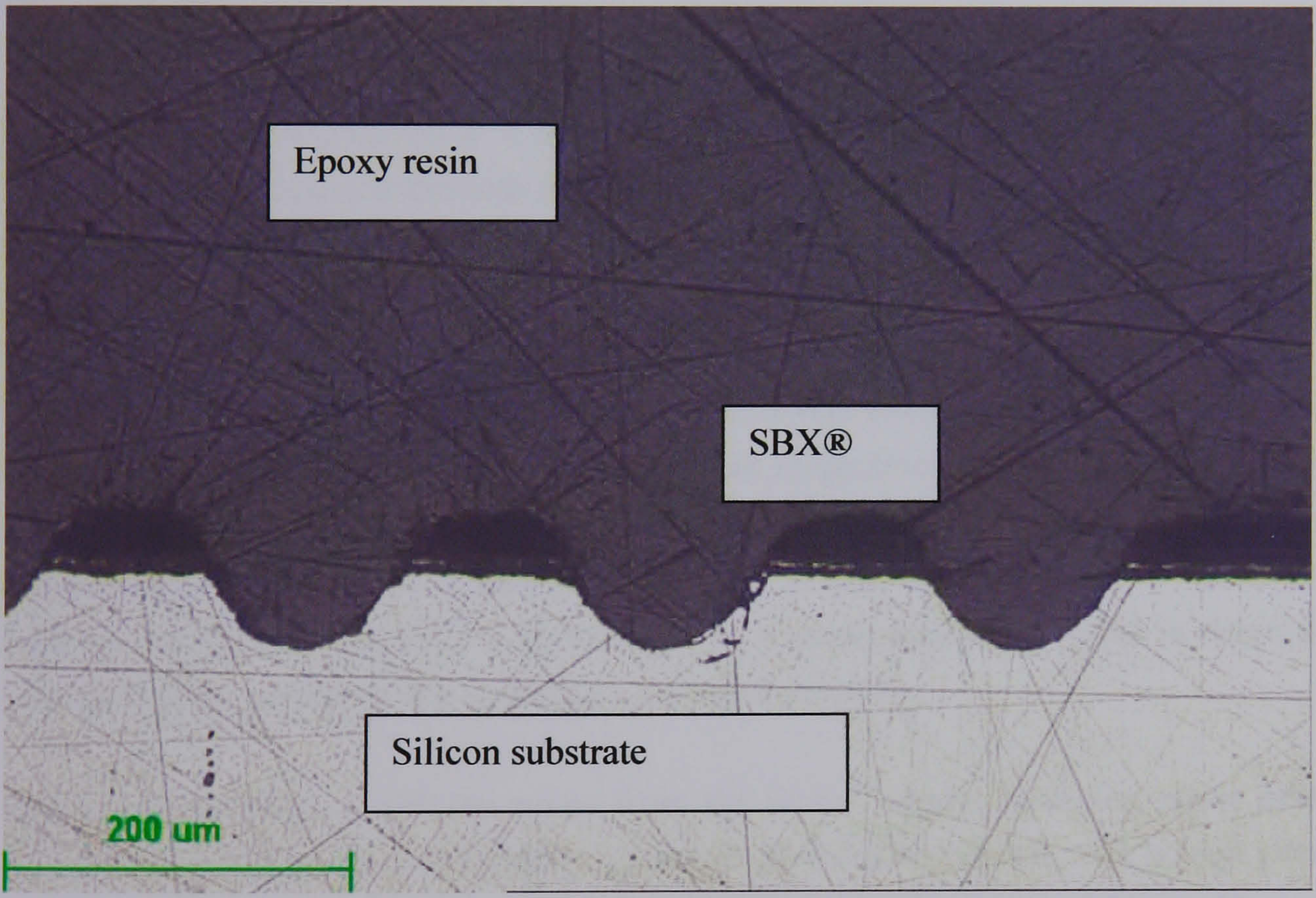

Fig 7.10 Optical micrograph of a polished cross section of (100 μm) cavities cut into a PZT-thick-film on silicon through powder blasting. The film has a photoresist coating of 25 μm thick SBX®.

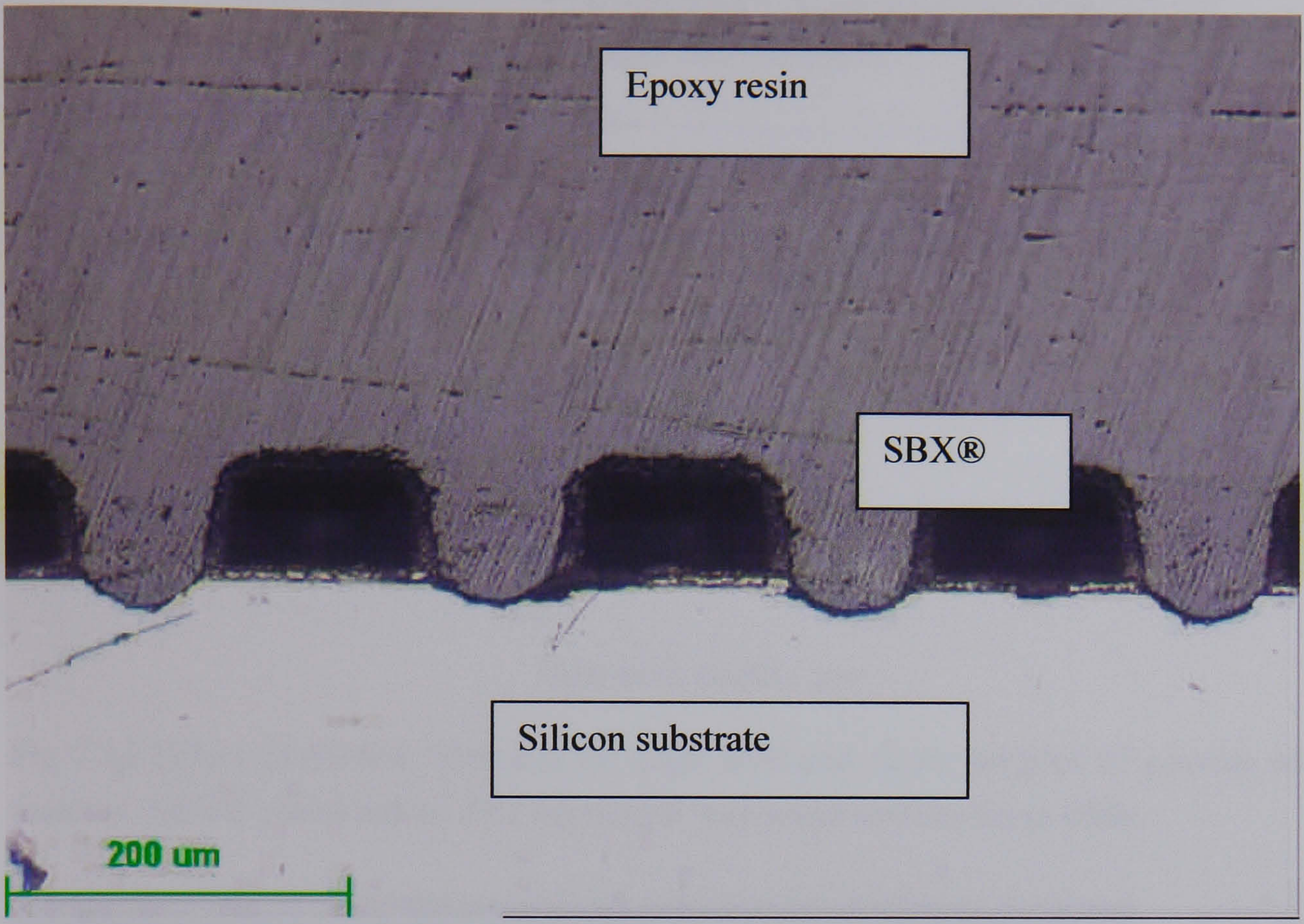

Fig 7.11 Optical micrograph of a polished cross section of (100 μm) cavities cut into a PZT-thick-film on silicon through powder blasting. The film has a photoresist coating of 50 μm thick SBX®.

The cross sections were measured for edge shift; it was found that a positive and negative edge shift occurred in films of 50 μm and 25 μm respectively (Fig 7.12). Minimum edge shift was calculated at 35 μm thickness of SBX® photoresist. Cavity depth was found to depend on the width of the feature, this was in line with the literature [125]. However, the thickness of the masking layer was found to be a more significant factor in determining the depth of the etched cavity at constant time and pressure.

SBX® was developed with tap water from the mains supply; however, water pressure was not sufficient to resolve features. However, developing SBX® with a high pressure water supply, served to fully resolve pattern features yielding line widths < 50 μm, see Fig 7.13 (overleaf), indicating that the residue had resulted from inefficient development. Powder blasted features that had been cut into PZT/Pt/Ti/Si using the mask design, enabling fully resolved features to be achieved. Features were resolved with minimum line widths and edge shifts.

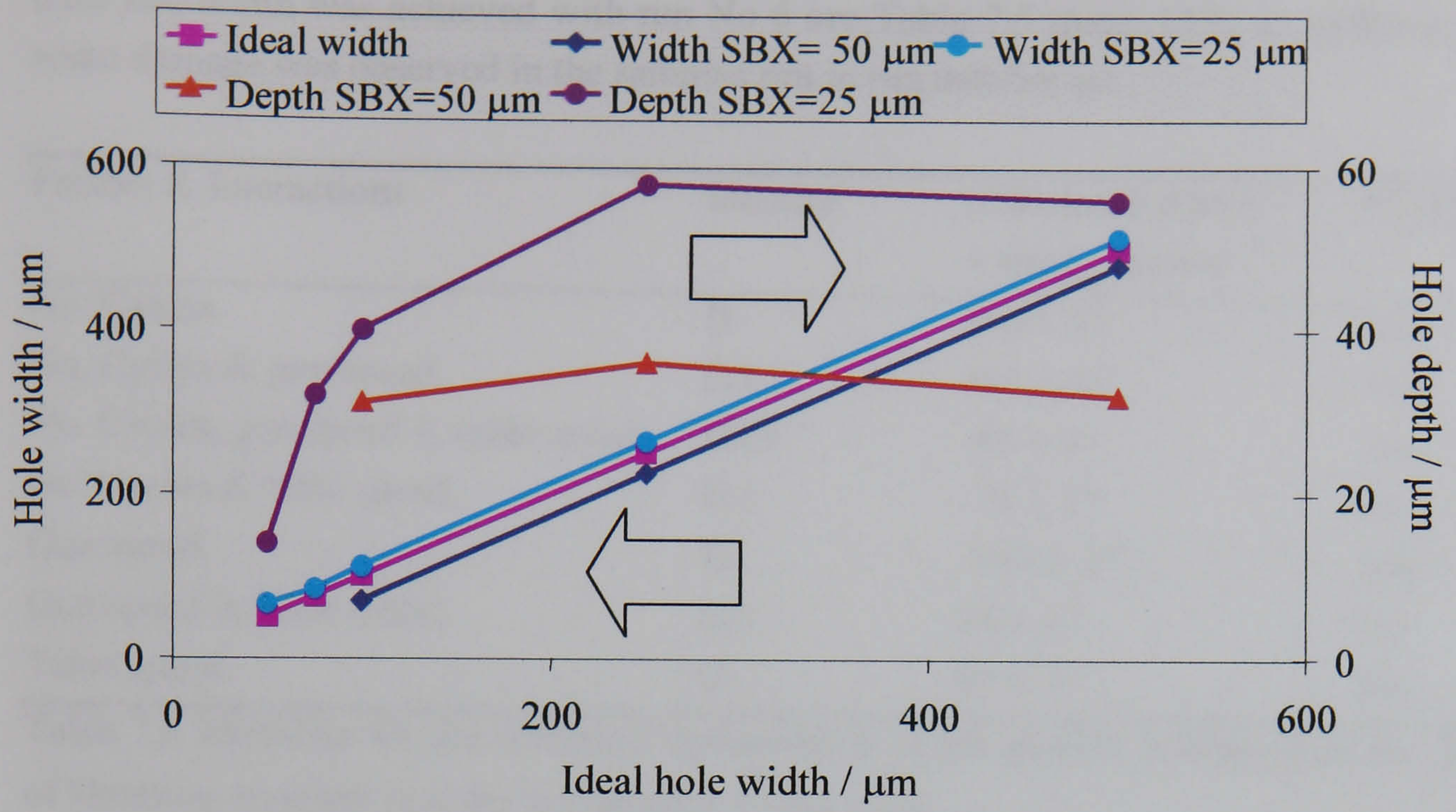

Fig 7.12 Effect of SBX® thickness on edge shift and depth profiles of powder blasted features. SBX® patterned on PZT on silicon was employed for these trials.

Fig 7.13 SBX® photo-patterned feature of the form: Photoresist/Au/Cr/PZT/Pt/Ti/SiO_2/Si. The resist was 35 μm thick. The feature has been resolved after automated development with a high-pressure-water-supply.

7.3.1.2 Machining

As $\Re \propto \frac{1}{l}$, the simplest means of extracting interactions from line widths was to calculate the identities for line widths and then reverse the sign of the identity (Table 7.6 overleaf).

Best line width was achieved with run No 6 see Table 7.5 (page 123). In addition, least resist damage was observed in the samples run in run number six.

Factors & Interactions	Identity	Calculated effects ± standard error	Significant
No. Cycles.	I1	295 ± 47	Yes
No. Cycles & gun speed.	I12	115 ± 47	Yes
No. Cycles, gun speed & table speed.	I123	-95 ± 47	Yes
No. Cycles & table speed.	I13	-75 ± 47	No
Gun speed.	I2	-245 ± 47	Yes
Gun speed & table speed.	I23	45 ± 47	No
Table speed.	I3	65 ± 47	No

Table 7.6 Identities for the statistical optimisation of the powder blasting process. Signs of identities reversed in order to represent $\Re$ and not l.

For single factor interactions, the results (in Table 7.6) show that the greater the number of cycles the better the resolution. Reducing the gun speed was also found to have a significant effect in improving resolution.

$$\Re \propto N_c \qquad (7.11)$$

$$\Re \propto \frac{1}{g_s}$$

The number of cycles, N_c, was related to the gun speed g_s by equation (7.12), where L_t and t_{run} are the track length and run time respectively. The resolution $\Re$ was found to depend upon the total time that the sample was powder blasted for, see equation (7.12).

$$t_{run} = \frac{2.L_T.N_c}{g_s} \qquad (7.12)$$

A Negative effect represents a reciprocal relationship between the effect or interaction and the response, see equation (7.13). Conversely, a positive effect represents a proportional relationship between the factor and the response.

$$I_{12} = I_1 * -I_2 \qquad (7.13)$$

$$(\pm 12) = (+1) * (-2)$$

$$(+1) = N_c ; (-2) = \frac{1}{g_s}$$

In the case of the two-factor interaction (12), there will be two conditions that effect resolution (see equation (7.14)). The sign of the interaction (12) determines the effect on the response.

$$(+12) = \left(\frac{N_c}{g_s}\right) \propto \Re \qquad (7.14)$$
$$(-12) = \left(\frac{N_c}{g_s}\right) \propto \frac{1}{\Re}$$

As a positive value for (12) was returned, in Table 7.6, it may be concluded that resolution is proportional to t_{run} (see equation (7.15)).

$$\Re \propto t_{run} = (+12) \qquad (7.15)$$

Table speed did not significantly effect the resolution. Table speed ω (angular velocity taken in the anti-clockwise direction) may be represented as: $\omega = 2\pi f$, where f is the frequency. Frequency, in this case, measures the number of times a second that a sample fixed to the table moves through the centre of the powder flux. The position of the fixed sample on the rotating table may be expressed as a sine wave with respect to the centre of the powder flux. The period of a full rotation, τ_{rot}, may be represented as $\tau_{rot} = {}^{2.\pi}\!/_{\omega}$. For simplicity, the flux is assumed stationary. The flux will project a static spot onto the rotating table. The spot will have a radius, r_{spot}, and its centre will be a length a_{spot} from the tables axis of rotation. The position that the sample enters the flux can be expressed in terms of a phase angle ϕ (see equation (7.16)).

$$\phi = \cot\left(\frac{r_{spot}}{a_{spot}}\right) \qquad (7.16)$$

Phase angle may be used to determine the period that the sample spends in the flux per rotation τ_{spot}, equation (7.17).

$$\tau_{spot} = \frac{2.\cot\left({}^{r_{spot}}\!/_{a_{spot}}\right)}{\omega} \qquad (7.17)$$

The period that the sample spends outside the flux can be defined as τ_{out}:

$$\tau_{out} = \frac{2.\left[\pi - \cot\left({}^{r_{spot}}\!/_{a_{spot}}\right)\right]}{\omega} \qquad (7.18)$$

As there was no significant effect observed for table speed ω, and as the angle ϕ was an experimental constant: it followed that $\Re$ was independent of τ_{spot} and τ_{out}.

It may be shown that, the identity, (-123) corresponds to $t_{tot}.\omega$ (($(12)=t_{tot}$ and $(3)=\omega$), or the total number of revolutions, revs, see equations (7.19) to (7.21). It should be noted that both, the identities, (12) and (3) were positive in Table 7.6. Therefore the period that a sample spent in the flux was not significant, but the number of times that the sample passed through the flux was.

$$(\pm 123) = (+12) * (+3) \qquad (7.19)$$
$$(+12) = t_{run}; (+3) = \omega$$

$$(+123) = t_{run}.\omega \propto \Re \qquad (7.20)$$
$$(-123) = t_{run}.\omega \propto \frac{1}{\Re}$$

$$\Re \propto \frac{1}{\omega.t_{run}} \propto \frac{1}{revs} \qquad (7.21)$$

Slikkerveer et al have studied the powder blasting erosion mechanisms of elastomeric [126] and brittle materials [109]. The effect of the angle of the gun θ_{gun} with respect to the sample was studied. The erosion rates of elastomeric and brittle materials were found to be greatest at oblique (15 °) and normal (90 °) angles respectively. Therefore, it is most likely that SBX®, an elastomer, will be eroded at low values of θ_{gun} and that $\Re \propto 1/\theta_{gun}$. Erosion rate, Er, is the ratio of weight of material removed from a sample (m_0-m_t) per weight of impacting powder particles (m_{powder}), see equation (7.22) [126].

$$Er = \frac{m_o - m_t}{m_{powder}} \qquad (7.22)$$

In the case of a sample fixed to a rotating table relative to a static gun, θ_{gun} will fluctuate with the table rotation (Fig 7.14). There will be a value of θ_{gun} at which maximum erosion of the elastic material occurs: $\theta_{elastic}$. The elastic erosion rate $Er_{elastic}$ will be proportional to the number of times the sample passes through $\theta_{elastic}$; this occurs twice a revolution, see equation (7.23).

$$Er_{elastic} \propto 2.revs.\theta_{elastic} \qquad (7.23)$$

The erosion of the elastomer or the SBX® will have a damaging effect on the resolution of the resist; this can be shown in equation (7.24).

$$\Re \propto \frac{1}{Er_{elastic}} \tag{7.24}$$

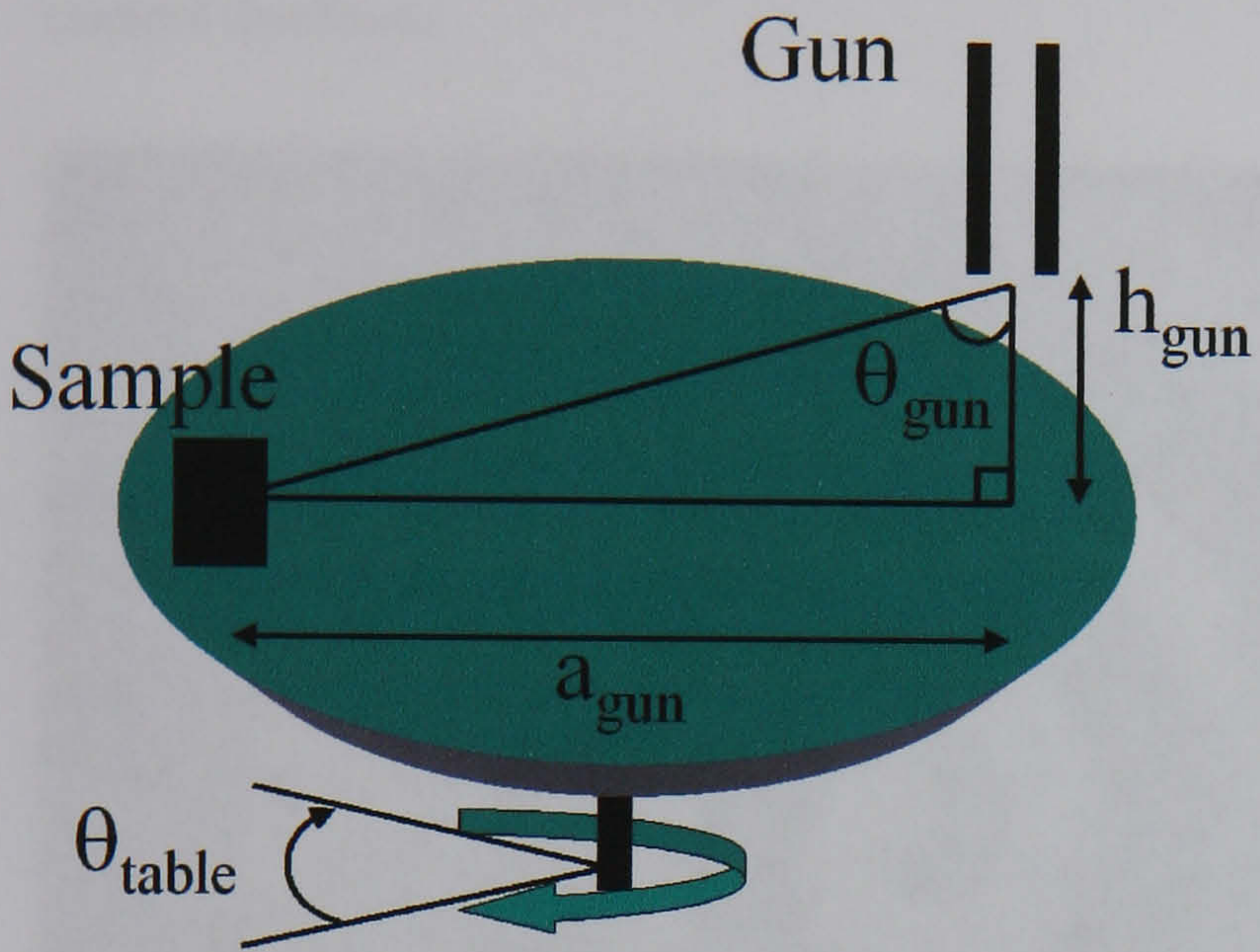

Fig 7.14 Rotating table with respect to a fixed gun. A sample is fixed to the table, and rotates with respect to the gun.

Substitution of equation (7.23) into equation (7.24) yields equation (7.25). Thus, resolution is lost because of accumulated damage to the elastic masking material. Equation (7.25) is similar to equation (7.21), but explains the loss of resolution in terms of damage accumulated to the SBX® mask.

$$\Re \propto \frac{1}{2.revs.\theta_{elastic}} \tag{7.25}$$

There is significant turbulence in the blast cabinet during powder blasting because of the inefficient flow of exhaust compressed air. Both used powder particles and debris are excited into a dust cloud. A consequence of this cloud is that there may be any number of random particle impacts on the sample surface. There are also a random number of particle-particle impacts. Powder particles in the flux would have a mean free path and the effect of the flux would decline as $\theta_{table} \to 180^\circ$, as the position of the sample moves to a maximum distance from the gun. It is anticipated that the angle $\theta_{elastic}$ occurs at θ_{table} values closer to ϕ and that $Er_{elastic}$ is reduced consequently.

7.3.1.3 Device Wafers

Fully resolved devices were cut into the PZT on Silicon, see Fig 7.15 and Fig 7.16. Cavities were cut with line widths down to 80 μm: the minimum line width for features on the device mask. Powder blasting was run for N_c=14 and an etch-depth of 40 μm was achieved. The etch-depth was consistent across the wafer. Cavity widths ≤80 μm were cut to a maximum depth of 35 μm. However, cavity widths >80 μm were cut to a maximum depth of 40 μm. All devices were cut to the required depth of 20-30 μm below the Si substrate surface: so that when actuators are released the mechanical support has the correct thickness.

Fig 7.15 A 2mm diameter spiral actuator

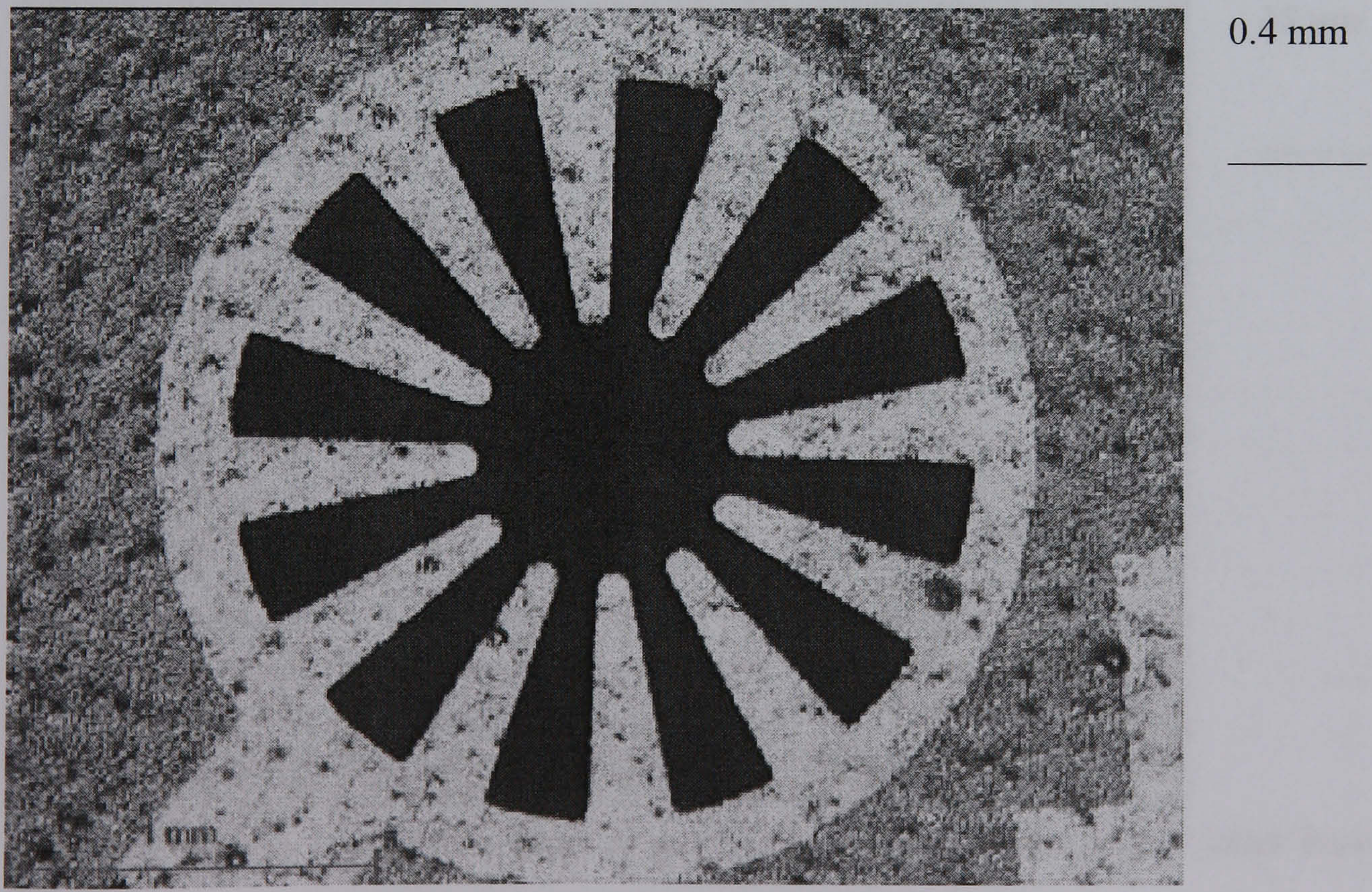

Fig 7.16 2mm diameter spoke actuators

The roughness of a powder blasted edge is shown in plan and cross section in Fig 7.18 and Fig 7.19 respectively. Fig 7.19 was photographed at 30 ° normal to obtain the sidewall (see also Fig 7.17). The cut edge, shown in Fig 7.18, is straight with a deviation of ≤5 μm and the face has an angle that is near vertical. A higher magnification picture of the face of the cut edge is shown in Fig 7.20. As there is no grain pull out, this would indicate that intra-grain cleavage has occurred during powder blasting. The Al_2O_3 particles appear to cut straight through the PZT of the thick film.

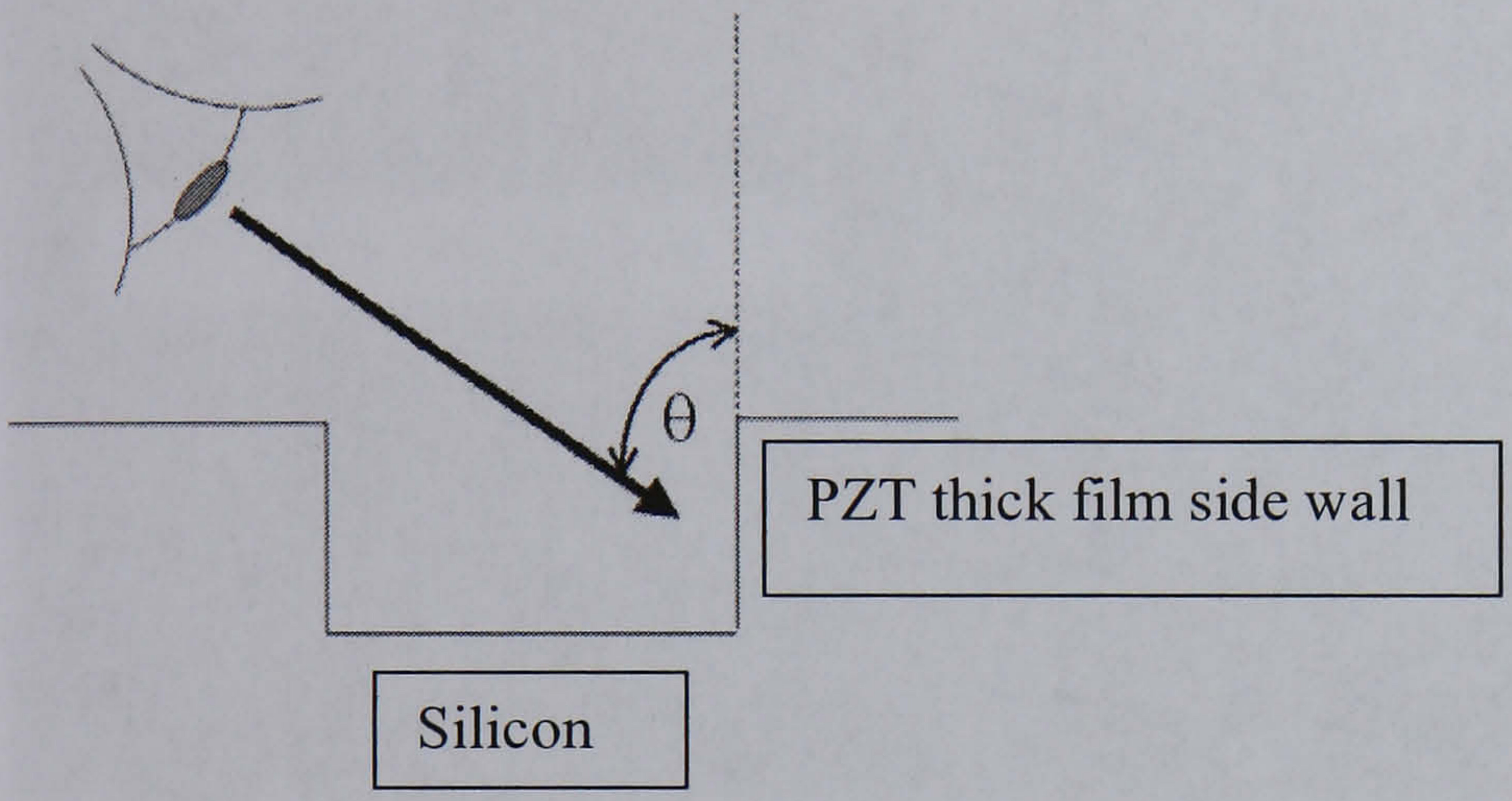

Fig 7.17 Observation angle for SEM analysis of powder blasted PZT thick films. The angle of observation θ is 30 °. The diagram shows a cross section of a cavity created through powder blasting. SEM analysis is conducted on the side wall of the eroded cavity.

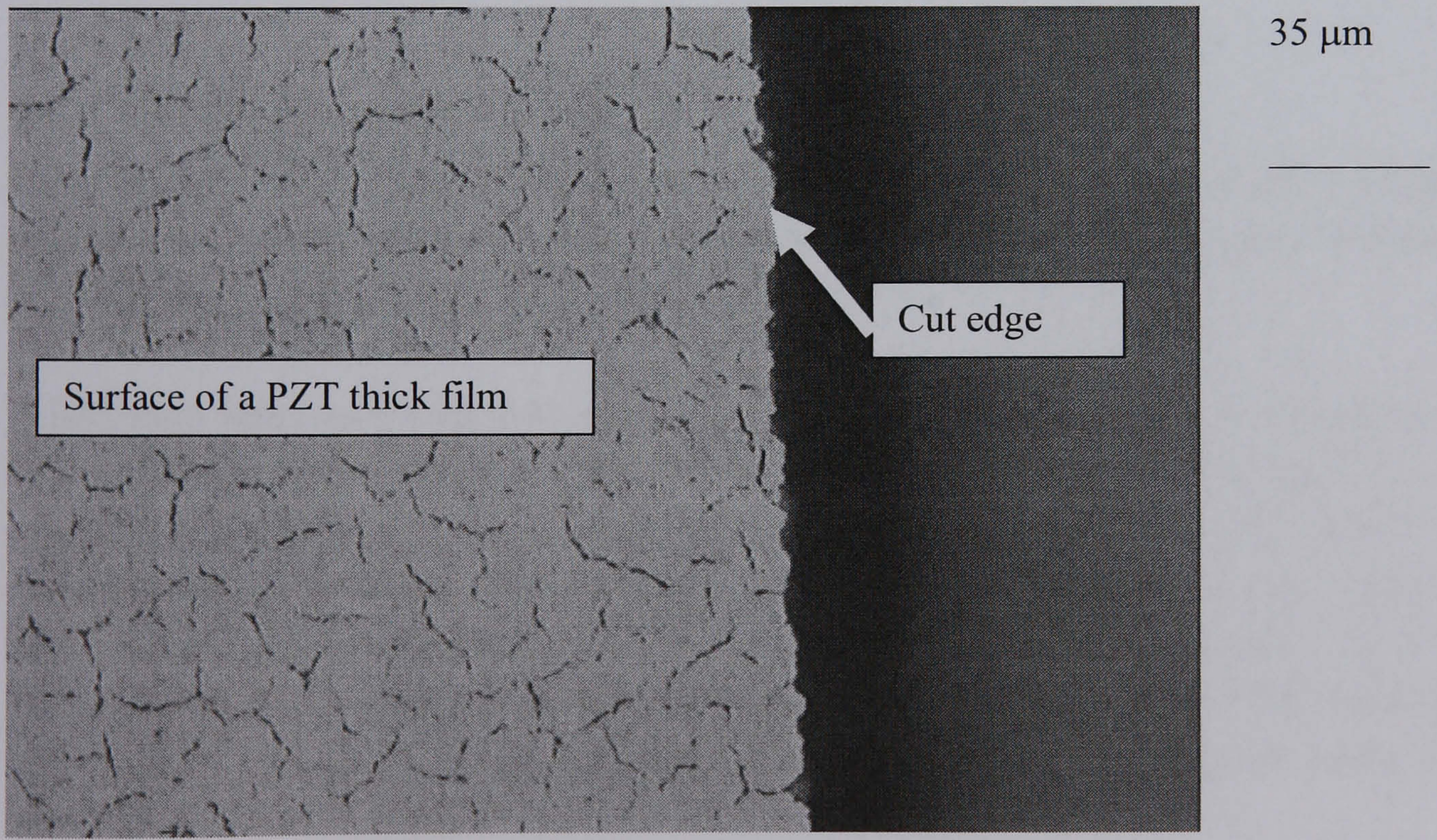

Fig 7.18 *Plan view* of a cut edge of a PZT thick film. Photographed after Powder Blasting

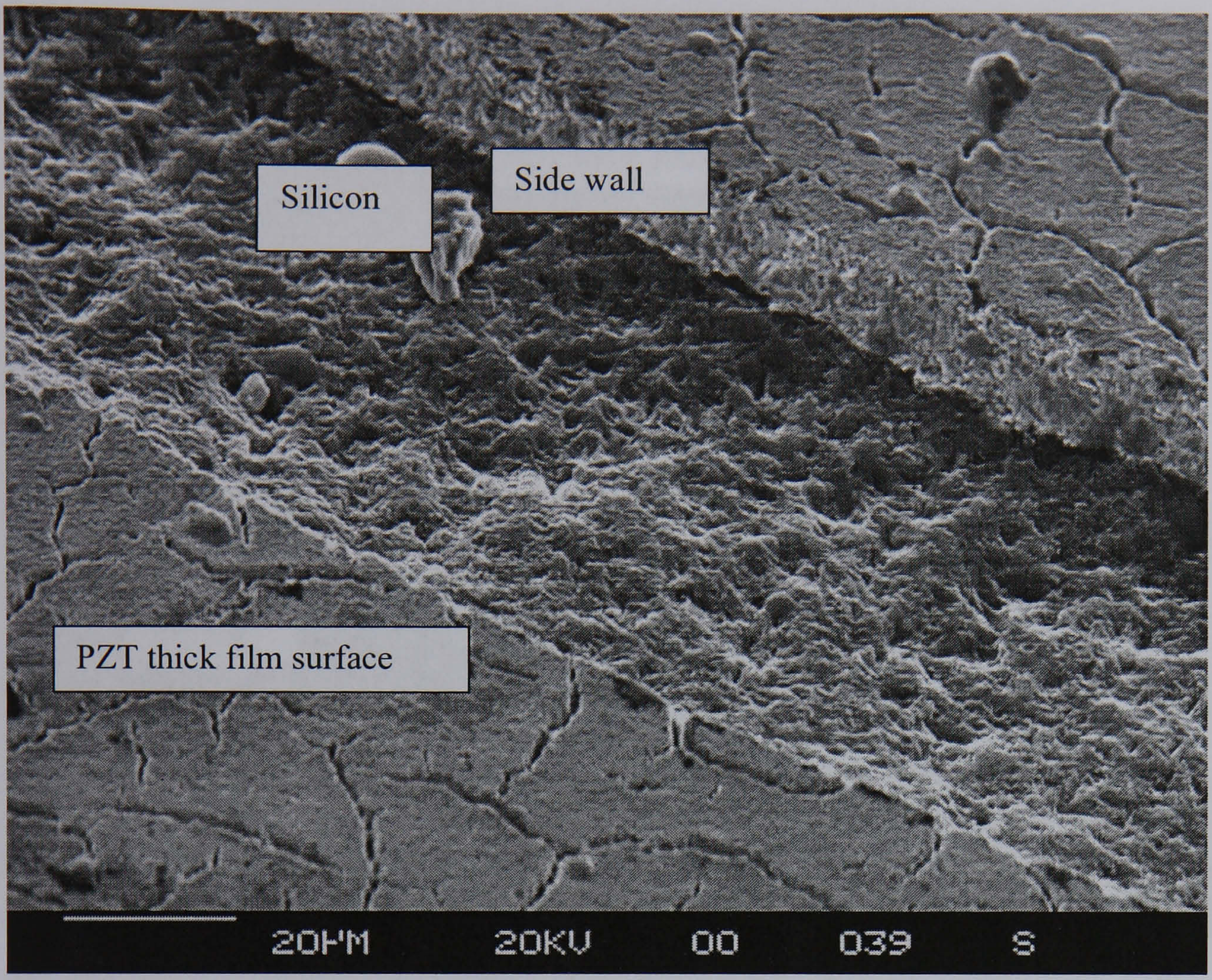

Fig 7.19 Powder blasted trench. The diagram shows a trench cut into a PZT thick film on a platinised silicon support. The picture is taken at a 30 ° angle, relative to the normal, in order to observe the cut sidewall (see also Fig 7.17).

7.3.2 Wet Chemical Etching Of PZT

Resist etching rate and the resist thickness were measured as 4.25 nm/min and 1.86 μm respectively. The thickness of the photoresist was considered to give adequate protection given the low etch rate in the etching solution.

A PZT thick film was etched to reveal a clean back electrode after 14 minutes of exposure to the etching solution (see Fig 7.22). The photoresist was intact after etching with no evidence of pin holing. However, a precipitate, here referred to as A1, was observed to form only on the Pt surface. The precipitate A1 formed only after samples were exposed to the etching solution for longer than 30 minutes. EDX analysis indicated that A1 was $PbCl_x$ (see Fig 7.21); however, the detector was equipped with a beryllium filter reducing sensitivity to low atomic weight elements. Consequently, the EDX detector could not detect the presence of O or F.

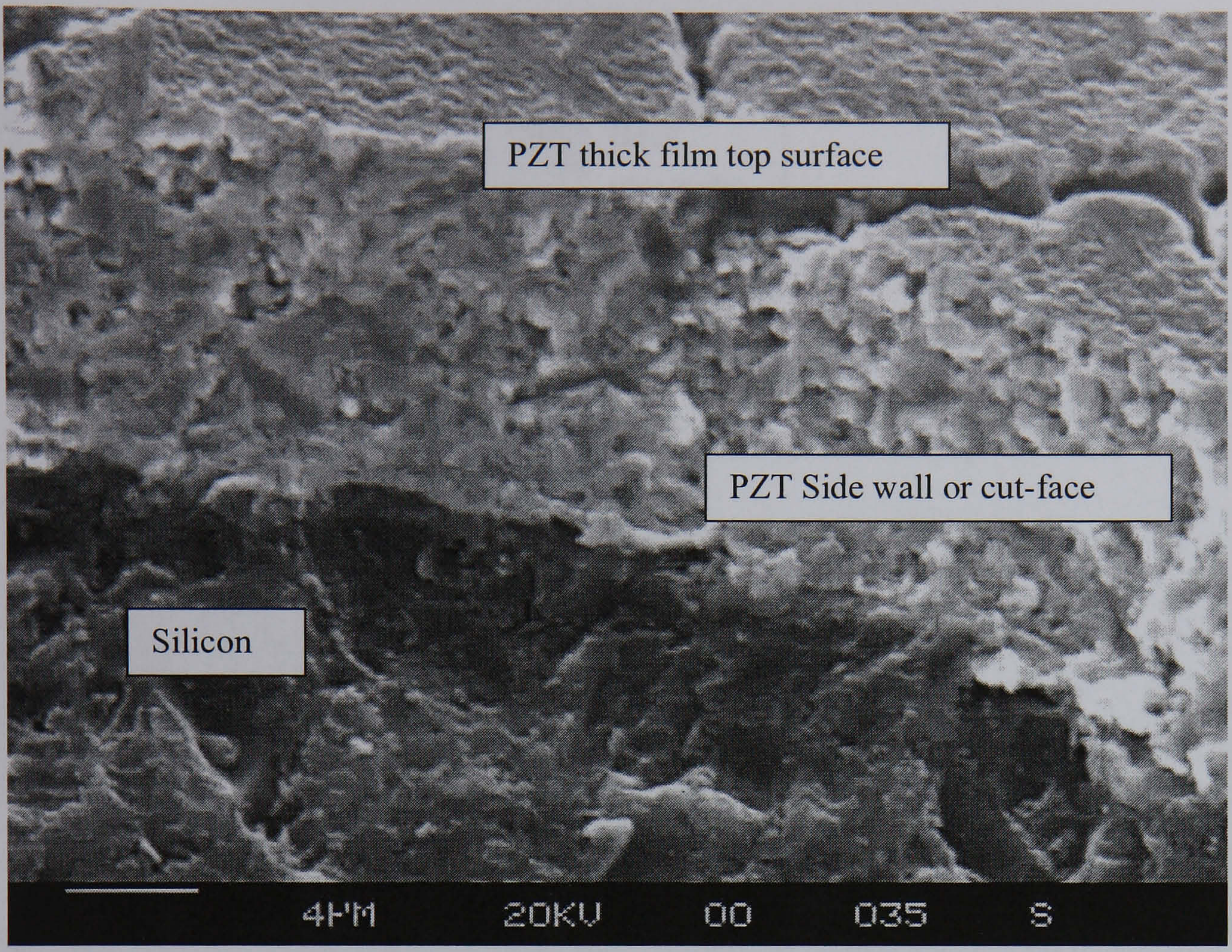

Fig 7.20 SEM micrograph of a powder blasted thick film. The micrograph shows the cut-face of the PZT thick film. The picture was taken at a 30 ° angle, relative to the normal, to observe the cut sidewall (see also Fig 7.17).

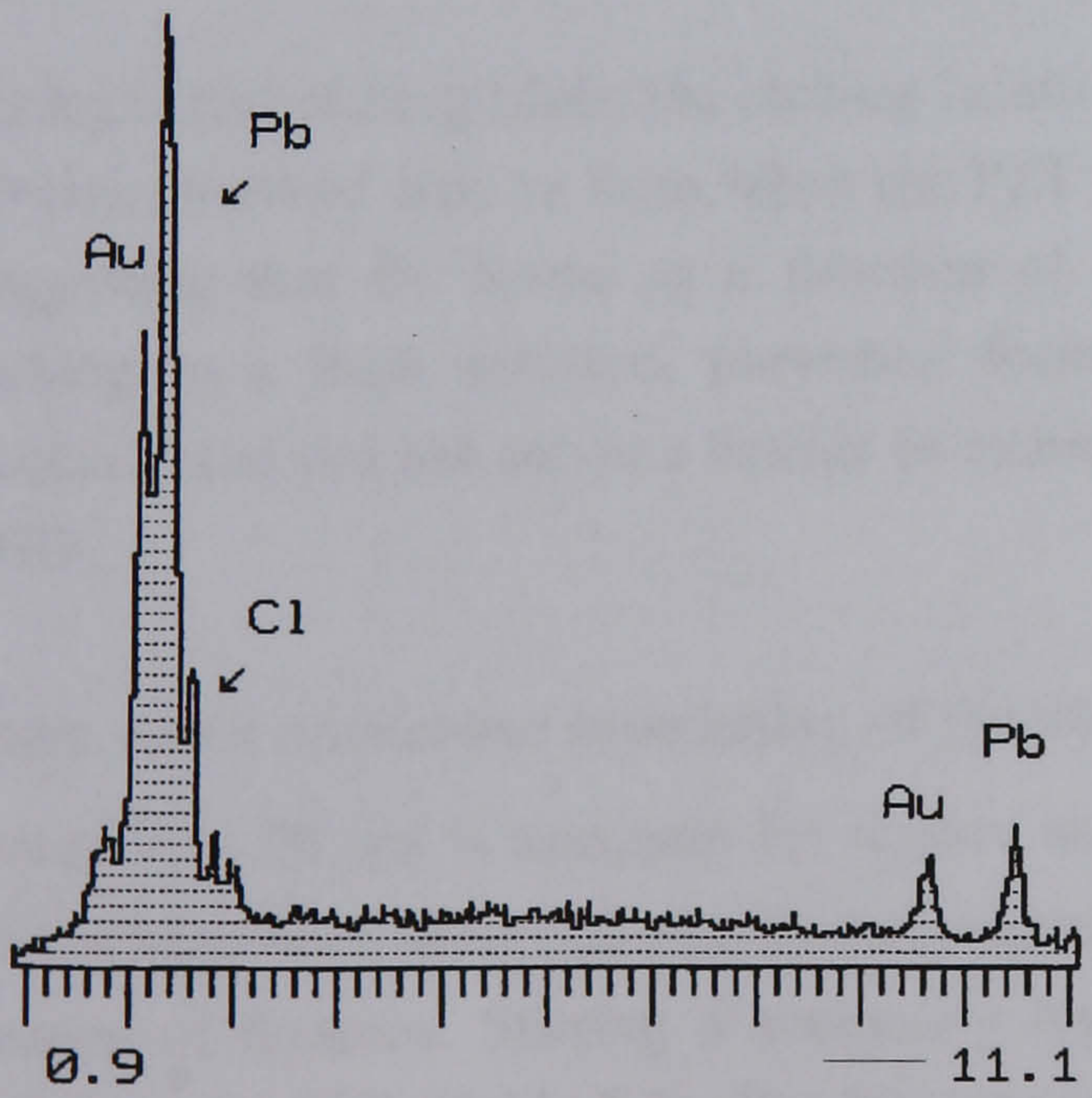

Fig 7.21 EDX spectrum of the residue that was observed to form on the back electrode after 35 minutes of etching

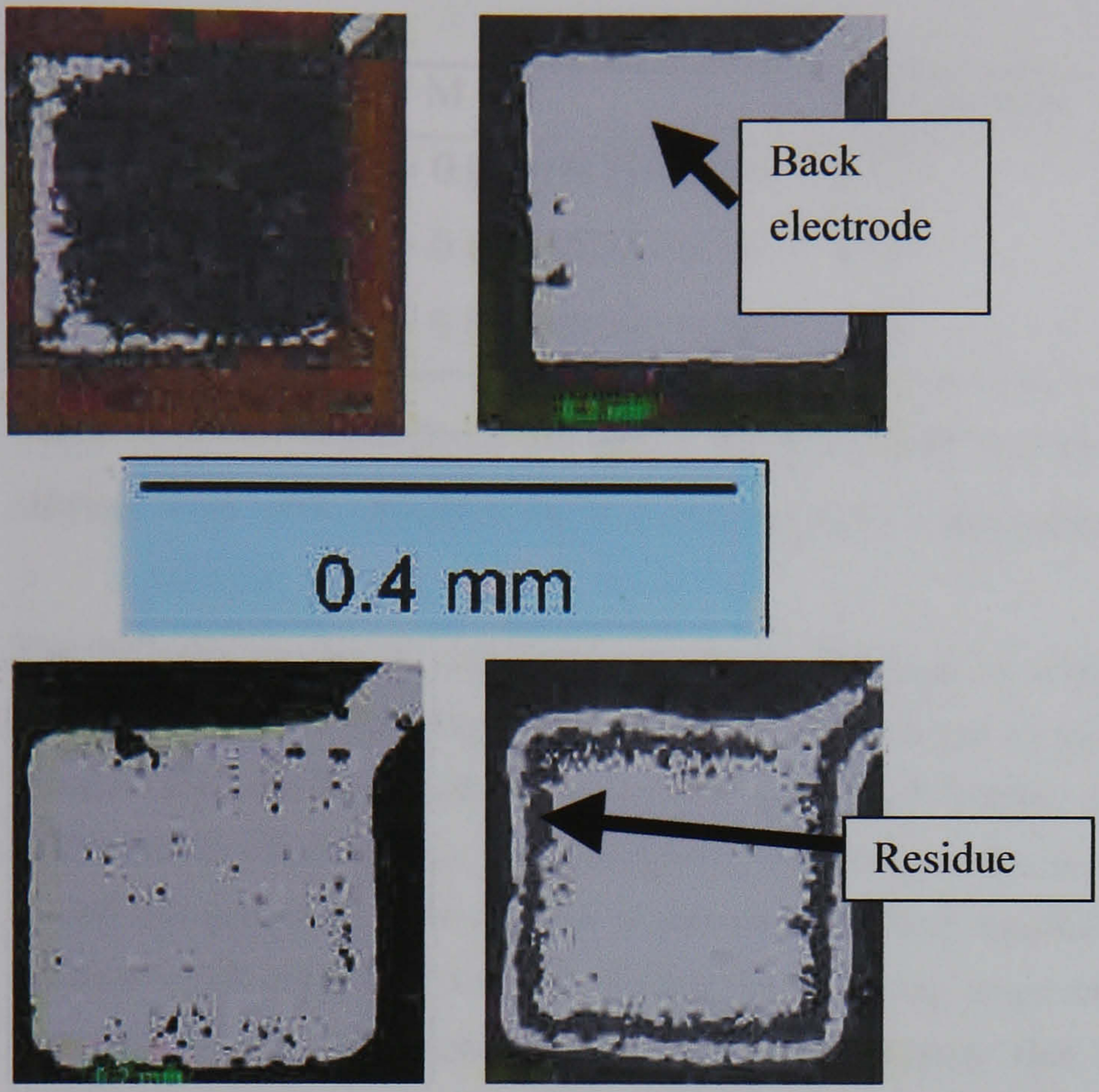

Fig 7.22 Plan view of etched features in PZT. Samples etched for 5 (*top left*), 14 (*top right*), 30 (*bottom left*) and 45 (*bottom right*) minutes

Another, precipitate, B1, was observed to form only on the exposed PZT during the wet etching of PZT thick films. B1 acted as a barrier layer preventing further etching of the PZT, and was observed to form within a few minutes of starting the etch.

During initial etching trials, the etching solution was frequently re-cycled. The precipitate B1 was observed only to form when the PZT was etched in a re-cycled etching solution. Suggesting that B1 forms as a function of Pb concentration in the etching solution. Etching in a fresh solution, prevented formation of B1. A1 only formed on the Pt electrode and did not act as a barrier to etching. Further, B1, was found to be soluble in HNO_3.

There was a one-to-one broadening of the etched feature such that $Er_d \approx Er_l$. A lateral spread of ≤ 20 μm is adequate for feature sizes of 500 x 500 μm for electrical contact. Masks have been designed with feature separations >> 20 μm, obviating etching induced overlap of features. Stirring dramatically improved Er_d and γ without resulting in pin holing of the PZT (Table 7.7). The increase in the etch rate with stirring suggests that the kinetics of the etching reaction are diffusion controlled. Lowering of the etch concentration resulted in an increase in undercut. The sputtered Cr/Au electrode must cover the sidewalls to ensure electrical contact between the surface electrode pads and the back Pt electrode. As sputtering is a line-of-sight process a value of $\alpha_{PZT} < 90°$ (~70-80°) is desirable for electrical contact between surface electrode pads and the back electrode.

	Conc. / M	Er_d / μm/min	γ / %	α / °
Not stirred	$[HF]=0.08;[HCl]=0.16$	0.77	50	N/A
Stirred	$[HF]=0.08;[HCl]=0.16$	2.16	71	73
Stirred	$[HF]=0.06;[HCl]=0.12$	1.91	69	75

Table 7.7 The dependence of Er_d, γ an α on both etching solution concentration and stirring. This table concerns the wet etching of PZT thick films.

The Pt back electrode sustained significant damage in samples that were etched for 45 minutes and more (see Fig 7.23). The Pt was observed to peel away from the substrate in places. The exposed substrate surface indicated bubble formation beneath the back electrode. In other words, there had been a chemical reaction at the interface between the Pt and the substrate. It is unclear if this reaction had resulted from the etching process or because of an interface reaction during the sintering stage of PZT thick film preparation. However, it will be argued in the discussion chapter that the bubbling arises from an interface reaction between Pb and the underlying substrate during sintering. This conclusion is based on experimental data presented elsewhere in this thesis (see also Fig 8.6 of section 8.3.1 of chapter 8).

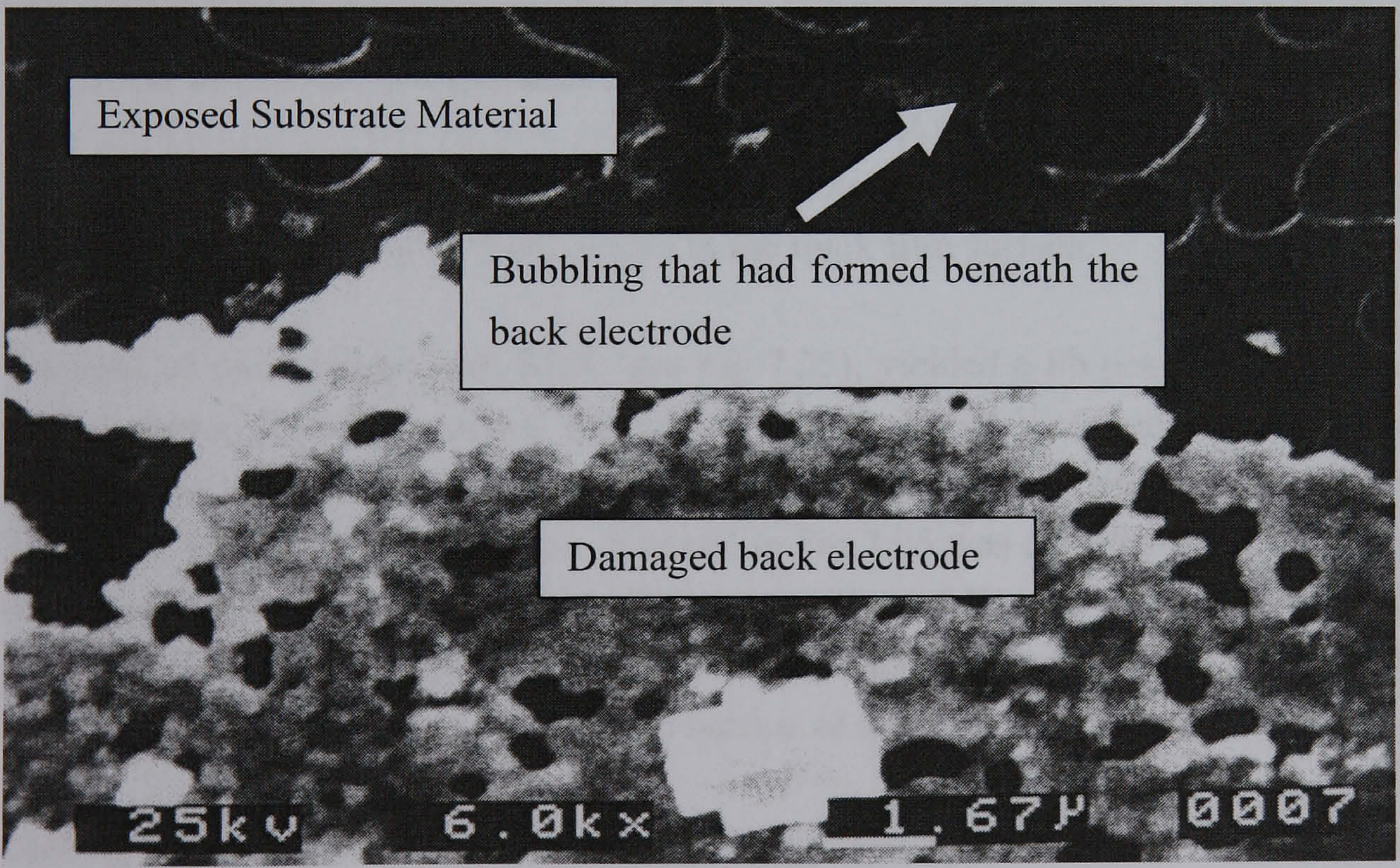

Fig 7.23 SEM Micrograph of the Pt electrode after 45 minutes exposure to the etching solution. The image shows that the Pt has sustained substantial damage and has peeled away from the substrate in places. The image shows the presence of bubbles that have formed beneath the back electrode.

After wet etching, the photoresist was stripped to reveal the un-etched surface of the PZT. A SEM micrograph can be seen in Fig 7.24 of the un-etched surface adjacent to an etched feature. In the micrograph, crystals were observed to have formed through cracks in the film surface. The crystalline material is labelled as C1.

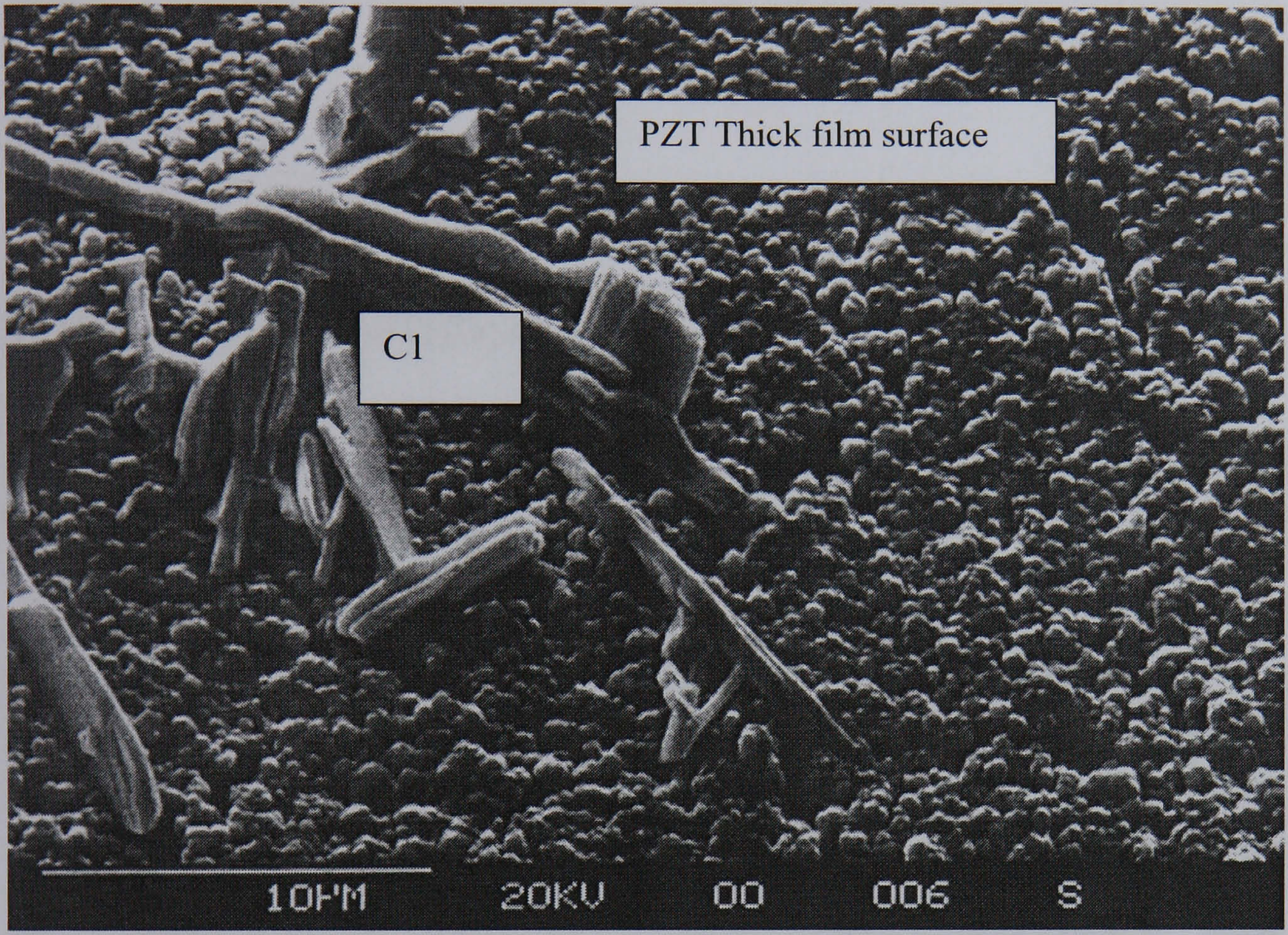

Fig 7.24 PZT thick film surface, adjacent to a wet etched feature. The micrograph was taken after wet etching, and the removal of photoresist. The image shows a crystalline material, C1, pushing up through cracks in the thick film surface.

Analysis of the crystals, with EDX (see Fig 7.25), yielded a Pb peak. However, as EDX cannot detect O or H analysis of PbO or PbOH would yield only a Pb signal. The precipitation of pure metallic lead from the etching solution was considered unlikely. Therefore, the Pb peak which was observed in Fig 7.25 was considered to correspond to a lead based material and not to lead. The composition of C1 was thought to be either PbO or $Pb(OH)_2$ that had formed through depletion of the PZT material thick film. This last point will be discussed in the discussion section at the end of this thesis.

Etching of the PZT thick film resulted in roughened side walls (see Fig 7.26). The side wall picture was observed by tilting the SEM sample to 30 ° (see also Fig 7.17 above). The PZ26 powder has a grain size of 0.6 μm. The roughening of the side walls shown in Fig 7.26 is ascribed to grain pullout from the PZT thick film. Additional evidence for grain pull out was the observation of powder grains in the beaker after etching. Etching, therefore, does not occur through the grain, but at the grain boundaries, freeing powder particles from the PZT thick film.

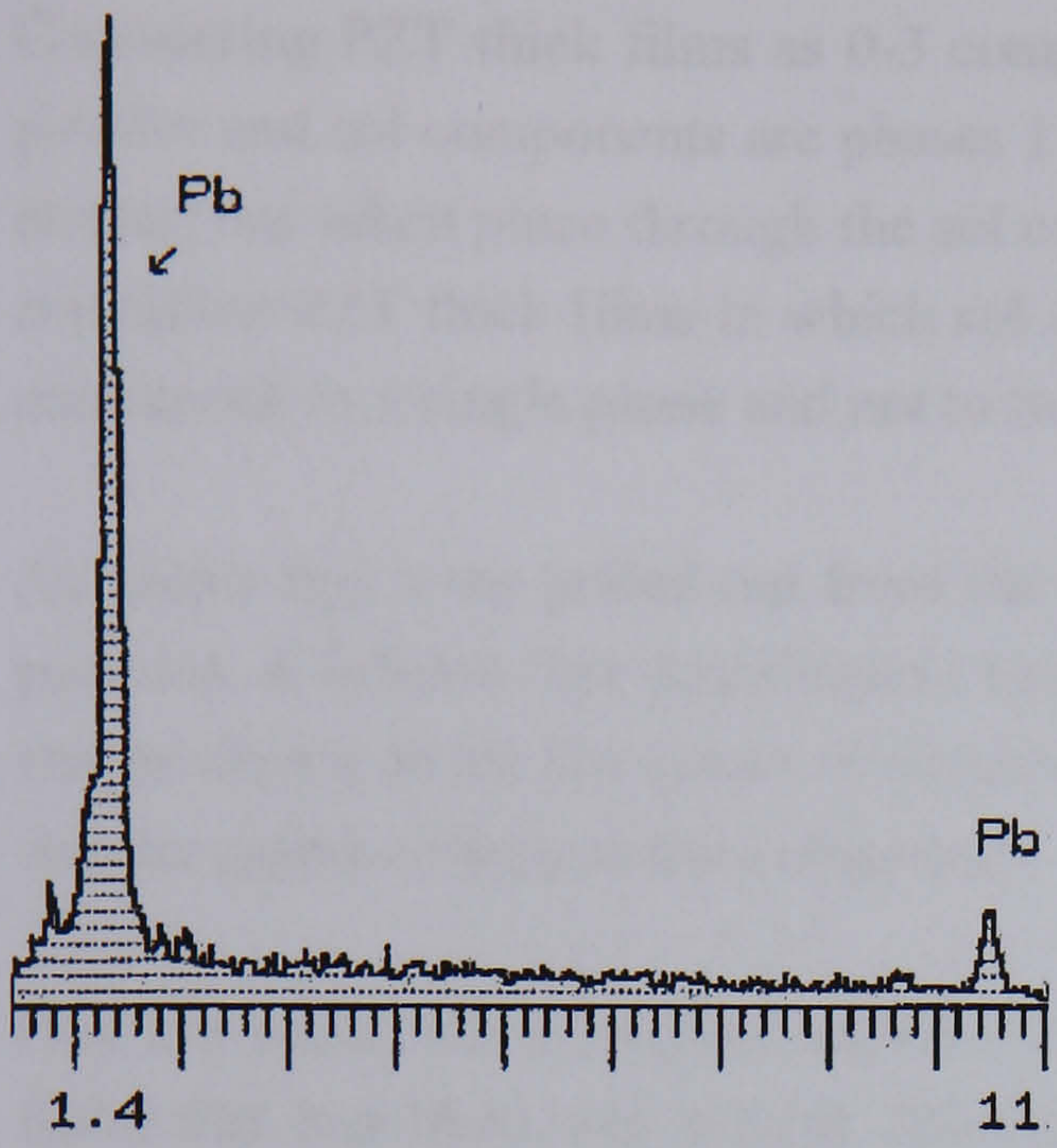

Fig 7.25 EDX spectrum of the precipitated crystalline material observed on the surface of the PZT after 14 minutes of etching. The precipitate was shown in Fig 7.24 above.

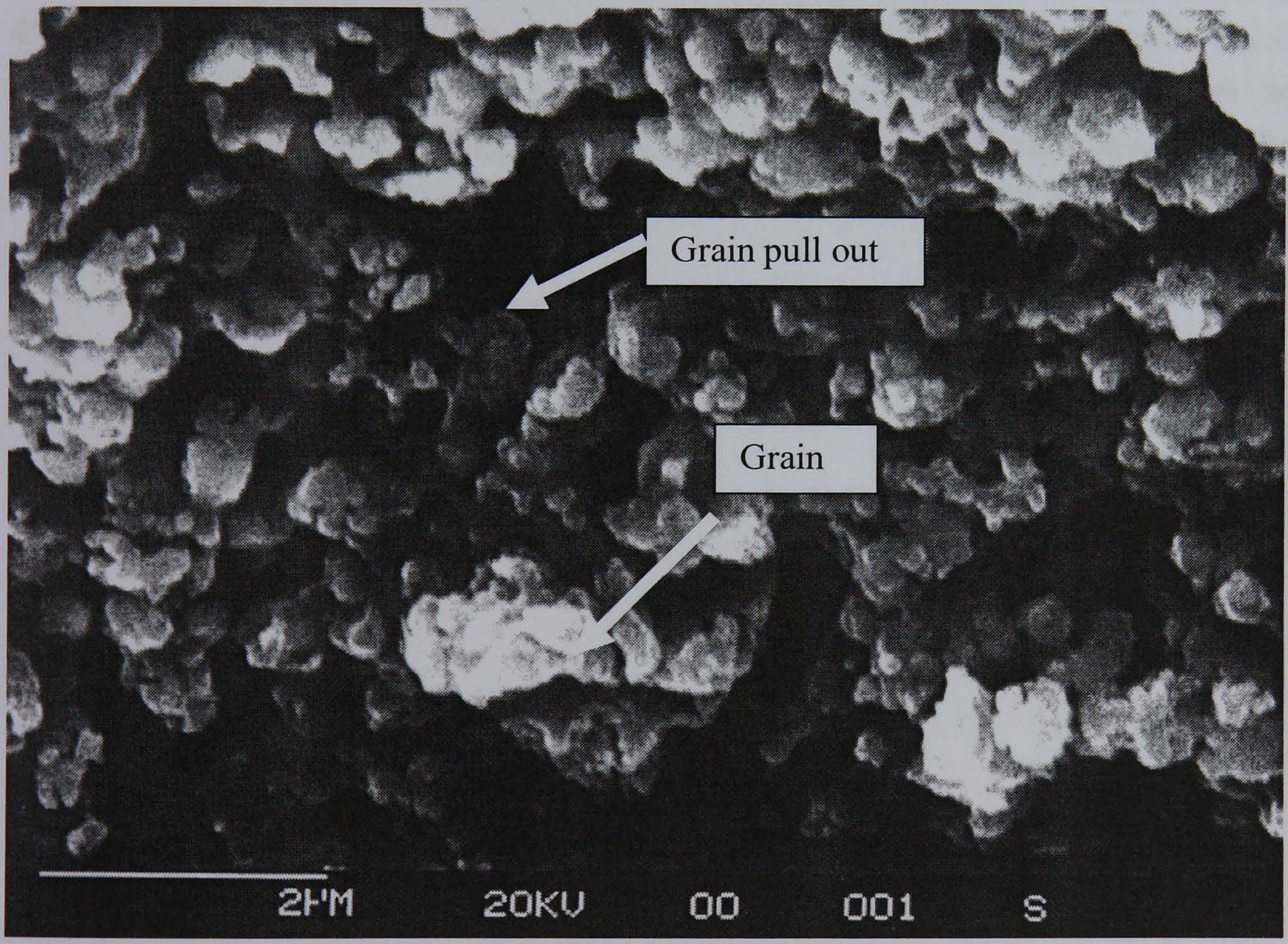

Fig 7.26 SEM micrograph of the sidewall of the etched cavity. The cavity having been etched in a PZT thick film. The picture is taken at a 30 ° angle, relative to the normal, in order to observe the cut sidewall (see also Fig 7.17). The image shows grain-pull-out from the PZT.

Considering PZT thick films as 0-3 composites (see Fig 1.11 of chapter 1) in which the powder and sol components are phases 1 and 2 respectively. It is reasonable to think that etching has taken place through the sol component of the PZT thick film. However, fully crystalline PZT thick films in which sol and powder phases are compositionally identical correspond to a single phase and not to two.

As grains that were pulled out from the ceramic had a similar size to the PZ26 powder particles, it follows that densification between powder particles is small. No conclusions can be drawn about the extent of densification between the grains of the sol component and the grains of the powder component.

One last point, the crystalline material C1 was only found on the surface of PZT thick films that had been wet etched; this material was only found adjacent to wet etched features. The material C1 could have a composition similar to that of PbO. In which case it would be reasonable to think that C1 was the same as the second phase; the second phase was seen in the XRD spectrum of Ar-sintered PZT thick films in chapter 6 (see Fig 6.22 and Fig 6.23). In other words C1 formed during sintering and not during wet etching. However, were this the case then C1 should have been found on the surface of non-wet-etched PZT thick films, and C1 should also have been found away from wet etched features in other wet-etched-films. Therefore C1 forms during wet etching and not during sintering; C1 should not be confused with the second phase found by XRD.

8 Process Integration

8.1 Introduction

This chapter takes the processes for fabricating and patterning PZT thick films discussed in chapters 6 and 7 respectively and integrates them into the process route, discussed in section 5.2 of chapter 5. Here anisotropic wet etching of the silicon support is investigated and assessed. A Cr layer for the back face of the wafer to protect the back face against staining during PZT thick film fabrication is studied. This chapter concerns the integration of processes for the fabrication of devices. Most of the experimental work here is experimental development; consequently, an experimental section is included in this chapter as opposed to being included in the experimental chapter (chapter 4). At the end of this chapter a revised process route is presented. This route represents the final processing route that will be employed in the fabrication of the actuators to be discussed in the following chapter.

8.2 Experimental

8.2.1 Cantilever Release

A reflux set up was used to anisotropically wet etch Si; the set up was as follows: a 1 L round bottomed flask, a Liebzig condenser, heating mantle (Electromantal MA) and a temperature controller (Cole & Parmer Digi-Sence®). Refluxing was done at 60 °C in 20% KOH.

Samples were supported on a glass slide, with black wax, with the PZT coated face to the glass (see Fig 8.1). The PZT face of the thick film was placed in contact with the glass slide. The slide was heated on a hot plate to 80 °C, and black wax was melted about the border of the of the sample securing it to the slide. A PTFE support held the slide and sample vertically in the round-bottomed flask.

Samples were etched for 1-hour periods before removing from the etching set up to renew the wax. The Si face, exposed for etching, was masked with Si_3N_4 deposited and patterned at QUB Belfast. The nitride was deposited through LPCVD (low-pressure chemical vapour deposition) to a thickness of 200 nm (at 720 °C). It should be noted that the nitride was coated onto both faces of the wafer, and that Ti/Pt electrodes were sputtered onto the Si_3N_4/Si surface. A PZT thick film of the form $[4(C^{200,450}+4S^{200,450})]^{710}{}_{Air}$ was prepared onto the platinised wafer through the standard route. Subsequently, the wafer was diced into 2 x 2 cm pieces before mounting on glass and etching. It should be noted that no barrier layer was deposited onto the substrate before back electrode and thick film deposition.

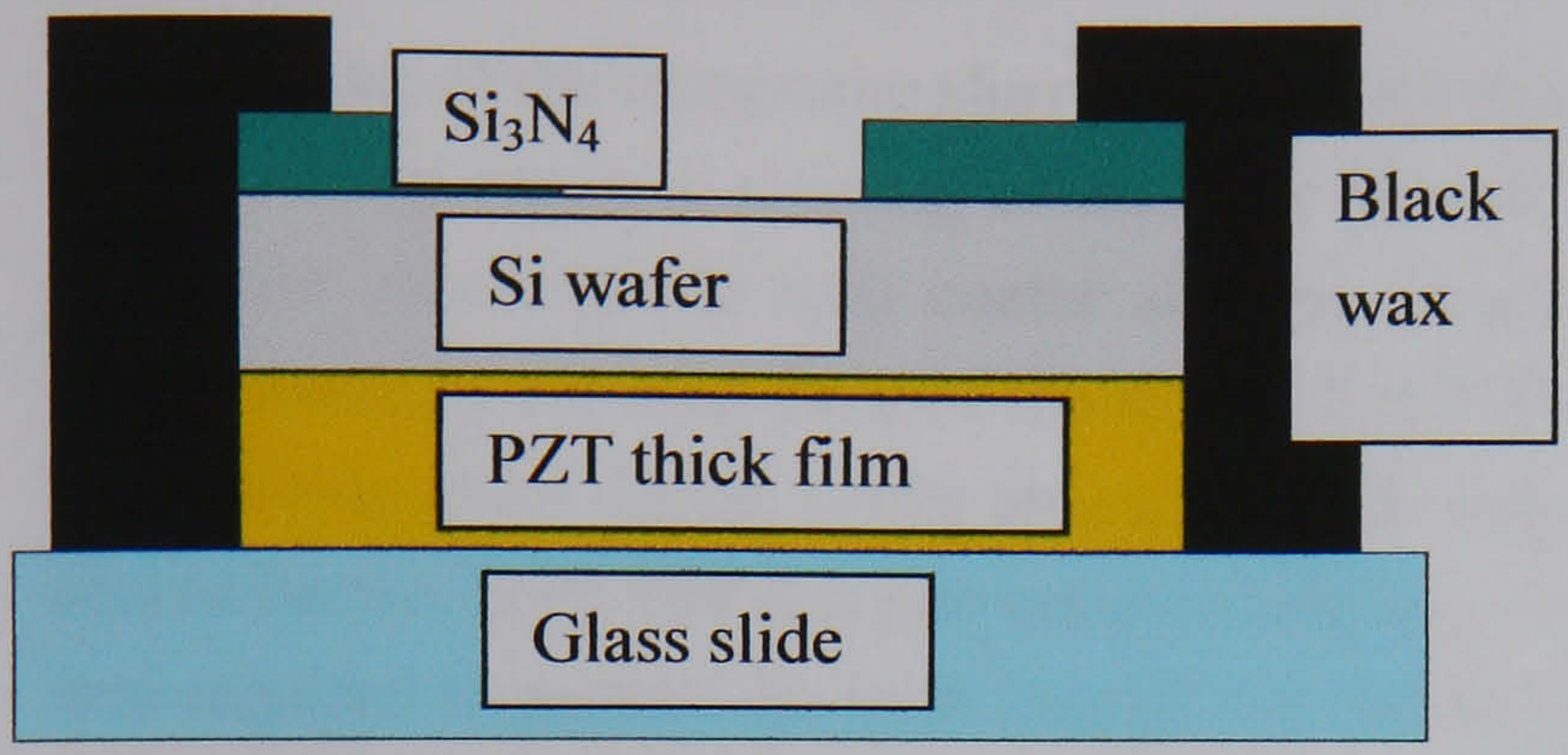

Fig 8.1 Sample mounting for anisotropic wet etching of Si.

It was found that etching of PZT thick films on $Si/Si_3N_4/Ti/Pt/PZT$ substrates resulted in the separation of the thick film from the substrate. More specifically, the back electrode was separated from the substrate (see Fig 8.2). Consequently, EDX was used to analyse the de-laminated surfaces of both PZT and substrate.

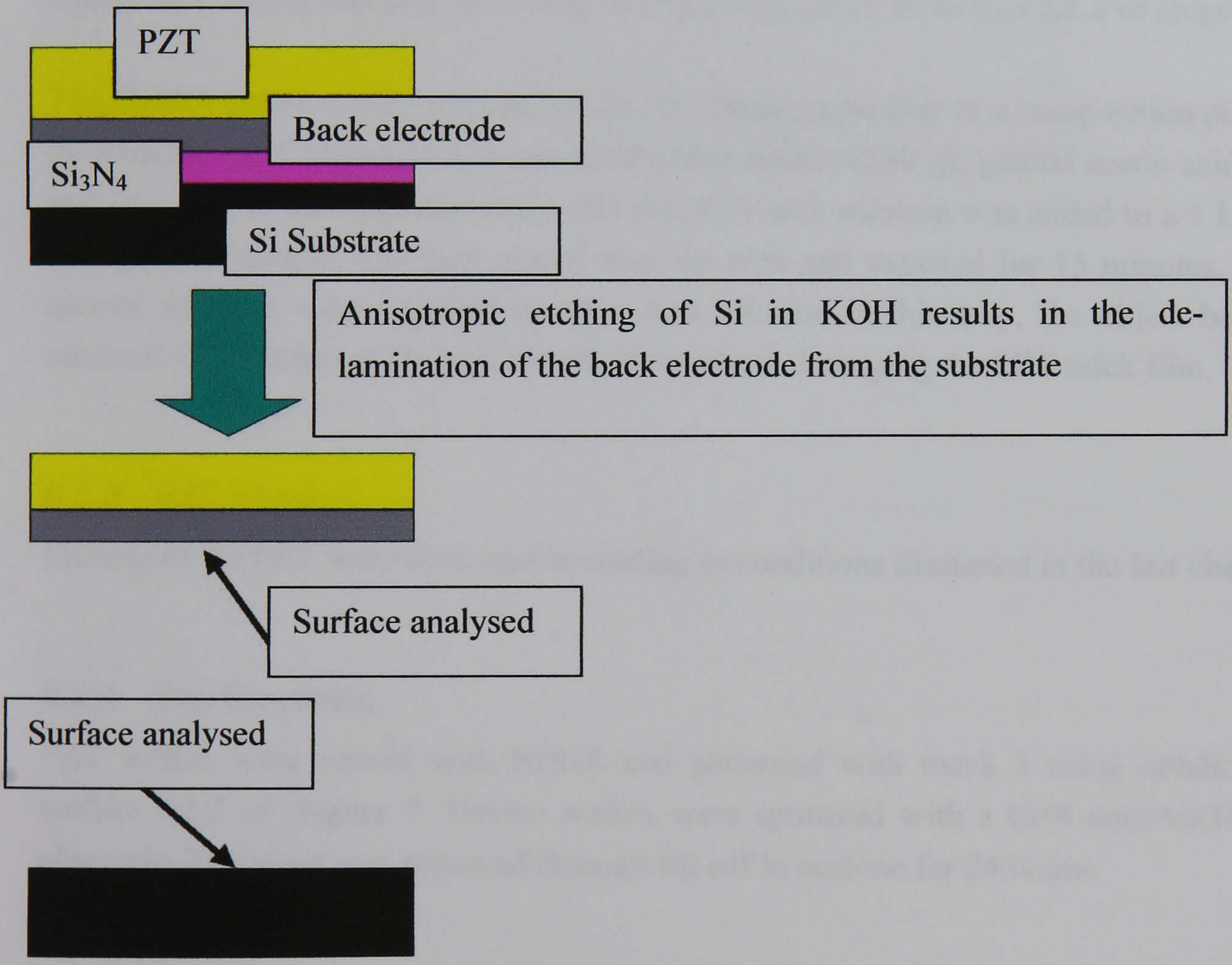

Fig 8.2 Anisotropic etching of Si substrates in KOH results in the de-lamination of the PZT thick film and back electrode from the substrate. Both cleaved electrode and cleaved substrate surfaces were analysed by SEM and EDX.

8.2.2 Back Face Protection

Spin coating of the composite slurry during PZT thick film deposition onto the top face of the wafer can result in staining of the back face of the wafer. The slurry accumulates on the wafer chuck of the spin coater and the accumulated slurry is transferred from the wafer chuck to the back face of the wafer. The PZT sol component of the slurry forms a lead silicate glass during wafer annealing with either Si_3N_4 or Si. The lead silicate glass acts as barrier layer that can prevent even etching of back face features. A protection layer was required to protect the back face of the device wafer during thick film deposition and to remove staining through lift-off of the protection layer and the unwanted PZT. It was decided that a thin Cr layer might serve this function and this was investigated.

A Si_3N_4 coated Si wafer was sputter coated on one face with Cr (300 nm) before deposition of a PZT thick film ($[4(C^{200,450}+4S^{200,450})]^{710}{}_{Air}$) on the other face. The wafer was quartered before sintering two of the quarters under air at 710 °C (for 30 min) in the RTA. The PZT coated faces of two quarters of the wafer, one sintered and one not, were coated in S1818 photoresist according to conditions given in section 7.2.2 of chapter 7.

The Cr etch solution was prepared by Dr. Q. Zhang according to a composition published by Roachwood Chemicals: Cerium ammonium nitrate (200 g), glacial acetic acid (35 g) and DI water (1 L). Approximately 200 ml of Cr etch solution was added to a 1 L plastic beaker. The sample was then placed into the etch and exposed for 15 minutes. All the quarter sections were exposed to a Cr etch solution in this way, the object being the removal of the staining through lift off, but without damaging the PZT thick film.

8.2.3 PZT Etching

Etching of the PZT was conducted according to conditions discussed in the last chapter.

8.2.4 Top Electrode

PZT wafers were coated with S1818 and patterned with mask 3 using conditions in section 7.2.2 of chapter 7. Device wafers were sputtered with a Cr(8 nm)/Au(100 nm) electrode. The resist was removed through lift off in acetone for 24 hours.

8.3 Results

8.3.1 Cantilever Release

The SEM micrograph of the cleaved surface of the Si substrate showed light and dark regions indicating that there were two different compositions present on this surface (see

Fig 8.3). EDX was employed to analyse the light and dark regions respectively to give spectra 1 and 2 in Fig 8.3.

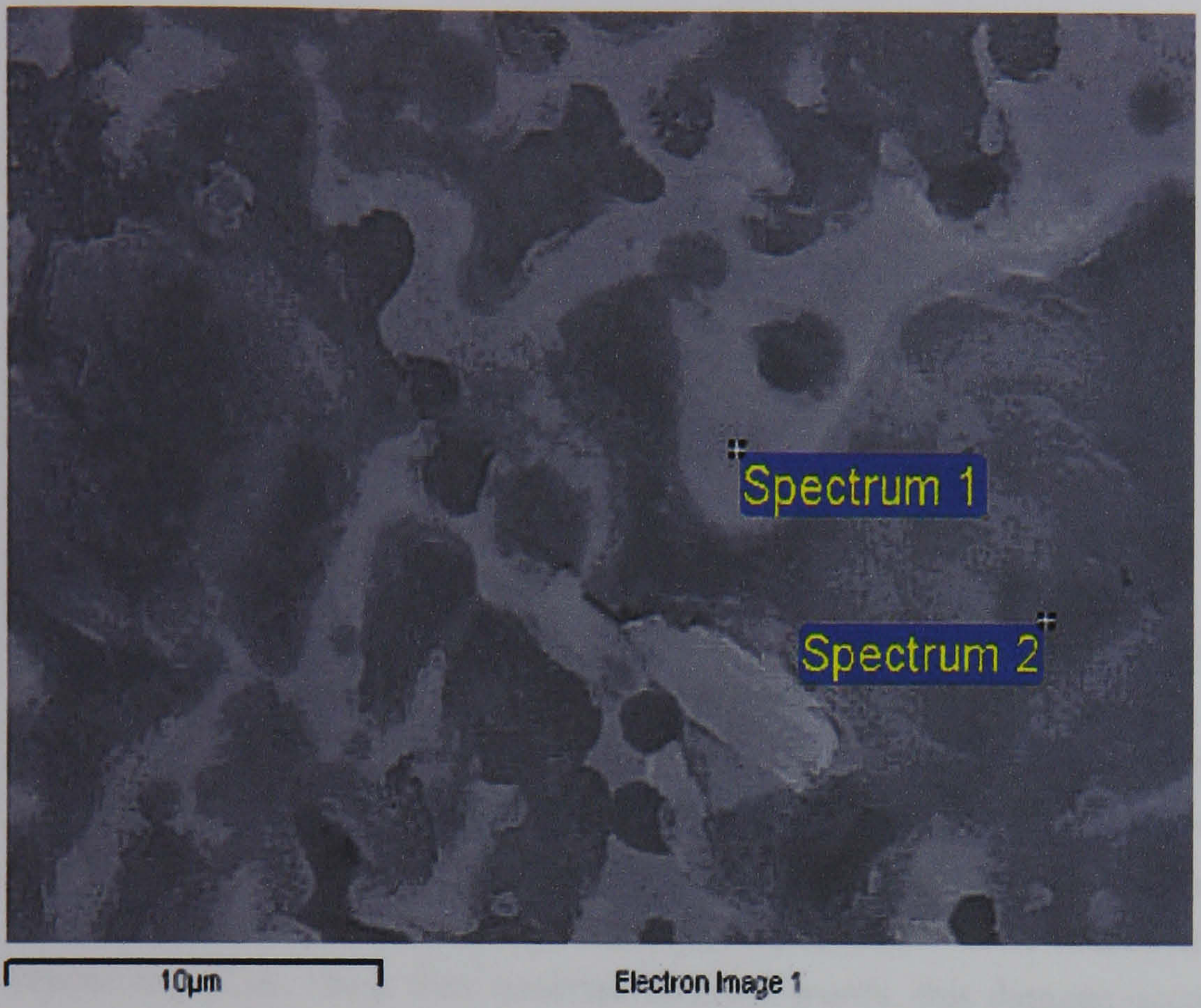

Fig 8.3 SFEG micrograph of the Si substrate cleaved from the PZT thick film interface. The micrograph shows light and dark regions on the Si. Spectrum 1 and 2 denote the sites of composition analysis for the light and dark regions respectively.

The elemental analysis of both spectrum 1 and 2 are summarised in Table 8.1. The greater proportion of Si in spectrum 2, as compared to spectrum 1, suggests that the dark region is closer in composition to the substrate. Spectrum 1 indicates a higher concentration of Pb. The only source of lead was the PZT. Pb is expected to decline in concentration the further the analysis moves away from the PZT; for example the deeper the analysis were conducted into the Si substrate, moving away from the thick film, the lower the expected Pb concentration. The data indicates that Spectrum 2 is the substrate and that spectrum 1 is an intermediary layer between the back electrode and the substrate. It should be noted that the presence of K arises from the use of KOH as the etch; therefore, K is not an important element in understanding the composition of the PZT-electrode/substrate interface. The absence of N in Table 8.1 is unusual as PZT thick films and electrodes were prepared on Si_3N_4 surfaces. This will be discussed in detail in the Discussion section below (see chapter 10).

Element	Spectrum 1 (light region)		Spectrum 2 (dark region)	
	Weight %	Atomic %	Weight %	Atomic %
C	n.d.	n.d.	16.34	29.56
O	25.12	53.21	16.18	21.96
Si	22.69	27.38	58.45	45.21
K	15.47	13.41	5.16	2.87
Pb	36.71	6.00	3.86	0.40

Table 8.1 Composition analysis by EDX of the cleaved surface of the Si substrate. It should be noted that spectrum 1 and 2 correspond to sites shown in Fig 8.3 where analysis was conducted. Not detected is noted n.d.

The back surface of the cleaved electrode is shown in Fig 8.4; this image, an optical micrograph, was obtained using the clean room microscope. Unfortunately, this microscope was not equipped with a calibrated scale, and therefore there is no scale available for this image. There are small black spots characteristic of pitting in the metal. There are also broad depressions that are characteristic of bubbling beneath the surface of the metal. It is unlikely that the bubbling took place because of the anisotropic wet etching of Si; therefore, this damage appears to have been caused during the thermal processing of the thick film material. In other words, this damage occurred during either sintering or the intermittent thermal treatments during PZT thick film deposition.

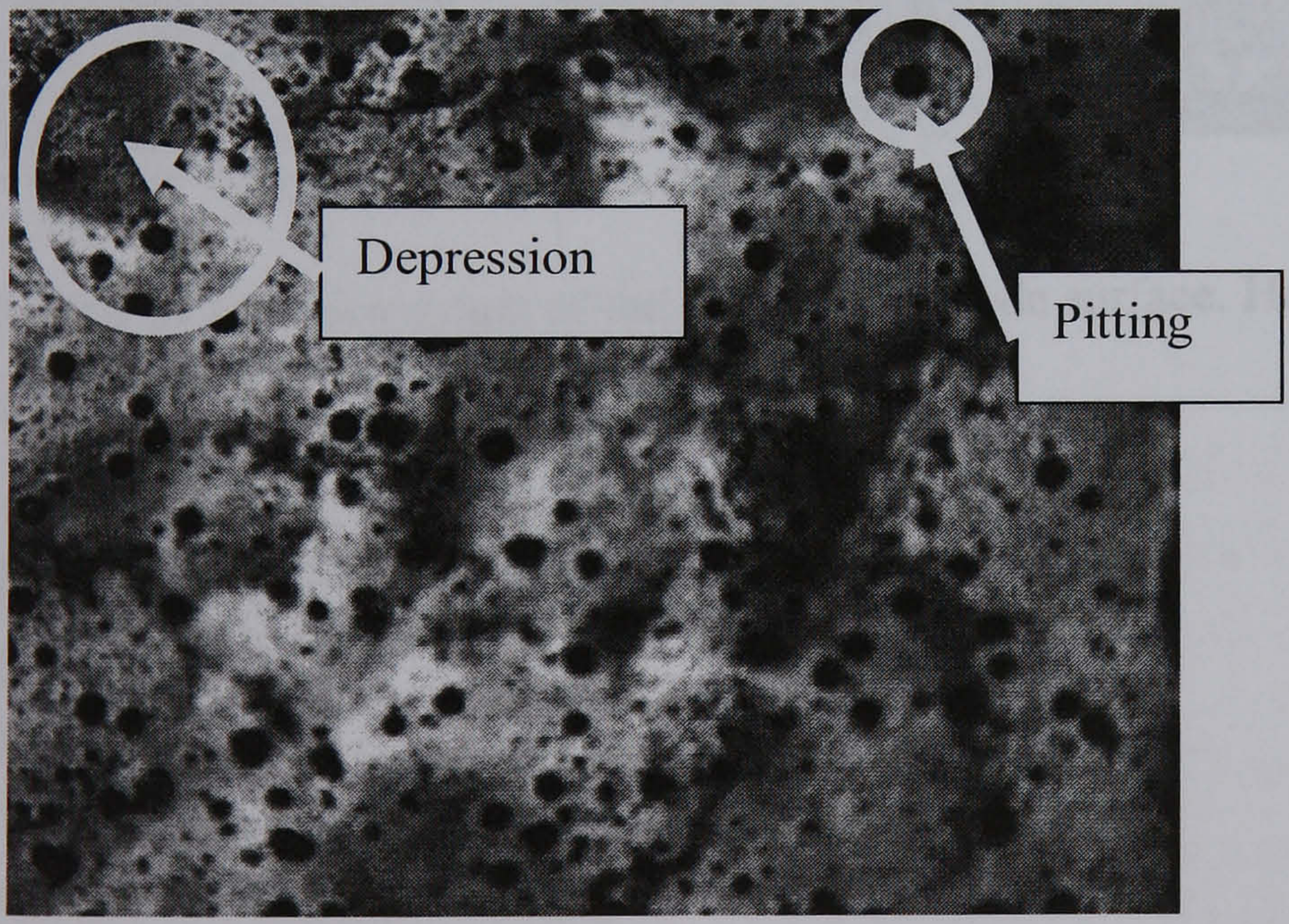

Fig 8.4 Optical Micrograph of the 'cleaved' electrode surface. The image was obtained using the a Reichert-Jung, Polyvar-Met Microscope at 50 x magnification. The image shows pitting characteristic of bubbling beneath the electrode surface.

The cleaved surface of the back electrode was also analysed by SFEG and EDX. A micrograph of the cleaved electrode is shown in Fig 8.5. There appears to be no evidence of variation in composition across the surface of the metal. Composition analysis of the back electrode is shown in Table 8.2. As expected there is a high proportion of both Pb and Pt present in this layer. Other metals were also observed at this interface. A note of caution, EDX will detect about 1 μm in depth below the surface that is analysed. As the thickness of the sputtered Pt electrode was only 200 nm, the values detected by EDX will arise partly because of the PZT thick film that sits above the back electrode.

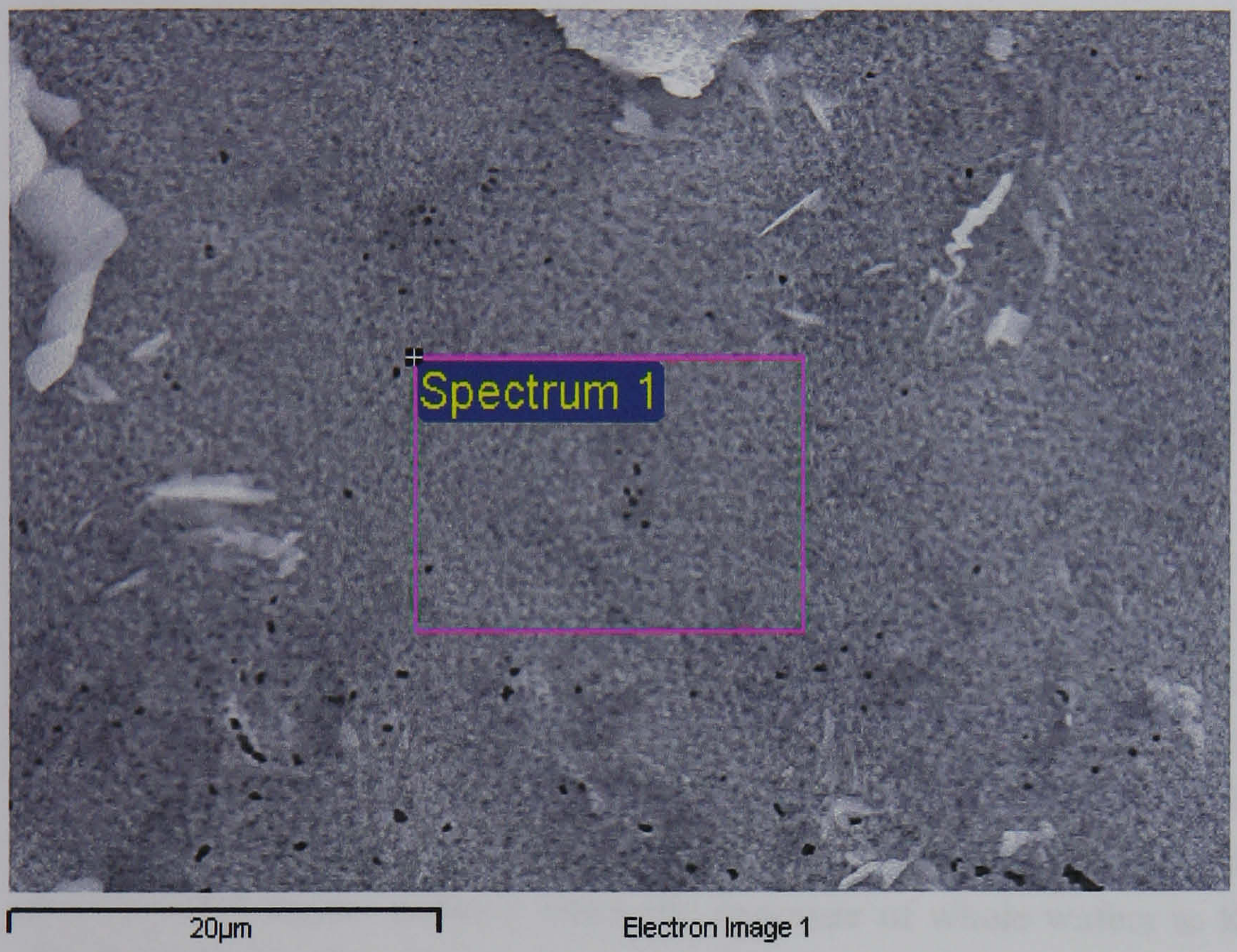

Fig 8.5 SFEG micrograph of the cleaved electrode surface. Here spectrum 1 was obtained in the pink rectangle.

Element	Weight %	Atomic %
O	3.00	23.43
K	2.07	6.61
Ti	2.95	7.68
Cu	2.23	4.38
Nb	1.85	2.48
Pt	66.08	42.28
Pb	21.83	13.15

Table 8.2 Composition analysis by EDX of spectrum 1 of the cleaved back electrode layer (site shown in Fig 8.5)

The absence of Pt and presence of Pb in the composition data in Table 8.1 shows that Pb from the thick film has passed through the Pt electrode. Further that the Pt has not passed into the underlying Si substrate. The existence of lead rich regions on the cleaved Si substrate surface suggests a lead rich layer intermediate between the Si and the electrode. Data from Table 8.1 and Table 8.2 were plotted in Fig 8.6; three compositionally differing layers were indicated. Further, the decline in Pb concentration coupled with the intermediate concentration of the light region implies that the light region lies between the substrate and the electrode. The relative intensities of Pb, Si and O in the intermediary layer corresponds to $PbSiO_3$: indicating that lead silicate glass forms between the electrode and substrate. The lead silicate is most likely to have formed during the thermal processing of the PZT thick film.

Wet etching of $Si/Si_3N_4Ti/Pt/PZT$ films resulted in the complete separation of the PZT thick film from the substrate, after 3 hours of etching. The de-lamination took place in an intermediary layer between the back electrode and the substrate. The higher proportion of K detected in the intermediate layer (see Table 8.1) indicates that the KOH attacked the $PbSiO_3$.

Sealing wafer pieces to glass supports with wax did not stop the etching solution from attacking the sample. Etching whole wafers would require that the entire surface and rim of the wafer to be sealed by wax to protect the intermediate layer from KOH. Therefore, PZT thick films on Si substrates, when anisotropically etched, are inherently open to delamination. For a Si wafer to be etched to the desired depth would require exposure times in the order of 8-12 hours. Successful etching, i.e. without film substrate separation, is considered highly unlikely when the exposure of whole wafers to KOH is conducted for 8-12 hours. For these reasons, the process (as discussed in section 5.2.1) was considered inherently flawed. A revised process using DRIE (deep reactive ion etching) to release the actuators will be presented at the end of this chapter. The use of DRIE (process 2) to etch the Si substrate removes the requirement for the samples to be exposed to KOH, and therefore also removes the risk of de-lamination of the PZT thick film from the substrate layer.

The existence of a TiO_2 barrier layer is expected to prevent diffusion of Pb from the film into the substrate. The barrier layer system may prevent the formation of the intermediate layer and prevent separation of the PZT thick film from the substrate during anisotropic etching. Anisotropic etching of Si wafers, with PZT thick films on TiO_2 barrier layers has not been attempted; hence, process 1 might actually work, yet process 2 has been selected for practicality, see section 8.3.5.

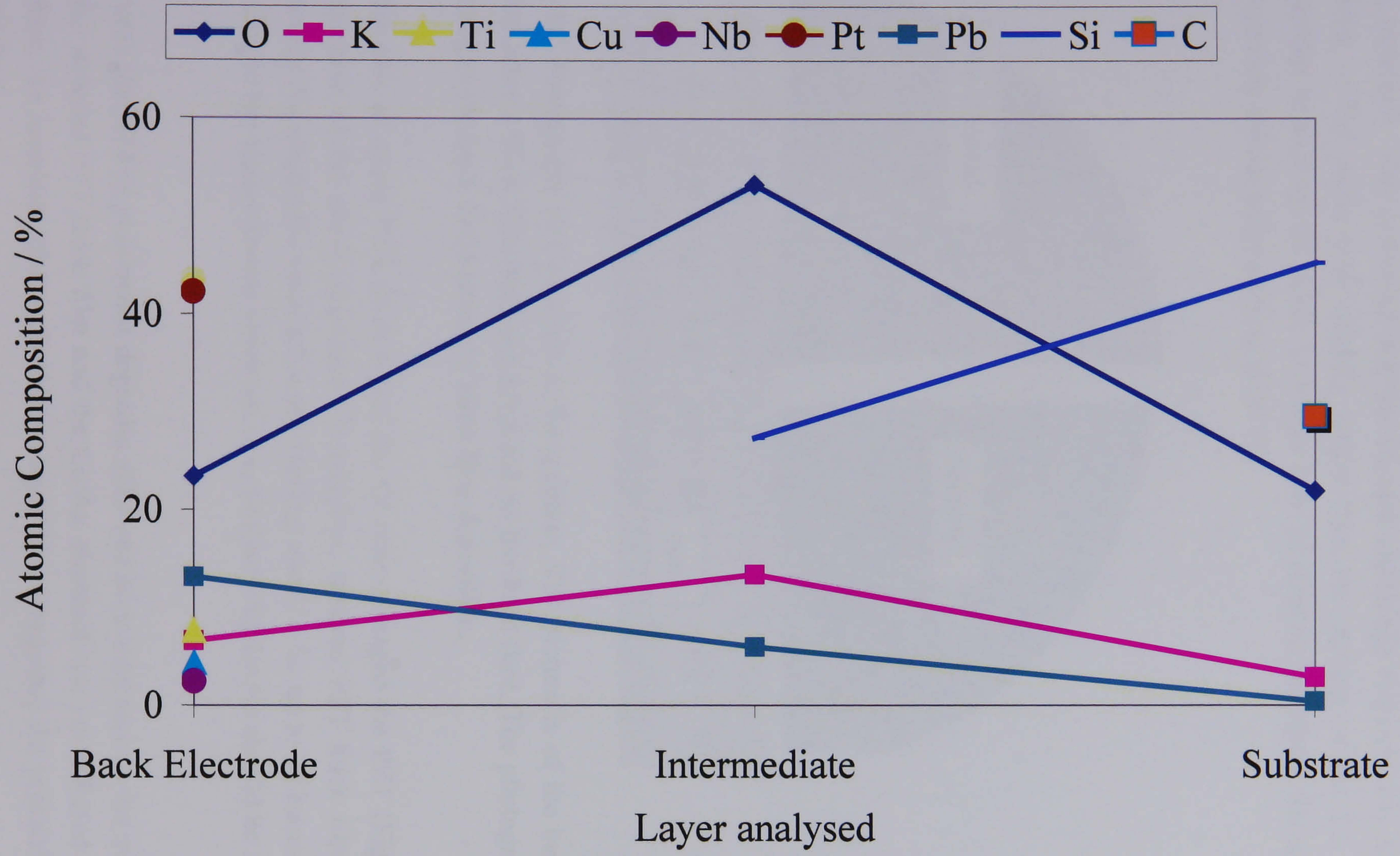

Fig 8.6 Composition analyses in cleaved layers of PZT/Pt/Ti/TiO_2/Si film. KOH was used to Cleave sample electrode from Si. Analysis indicated the presence of $PbSiO_3$ interface.

8.3.2 Back Face Protection

The Cr coating remained intact after deposition of the PZT thick film (see Fig 8.7). Full oxidation of the sintered Cr surface resulted in a slight change in coloration. Cr stripping, from the back face of the wafer yielded a clean silicon surface for all samples (see Fig 8.8, overleaf). This indicated that the Cr etch efficiently removes Cr. As expected, the etching of the oxide took slightly longer than the etching of the Cr. There was no advantage in etching the oxide for longer than 15 minutes; however, the removal of oxide was greatly enhanced by etching at 40 °C.

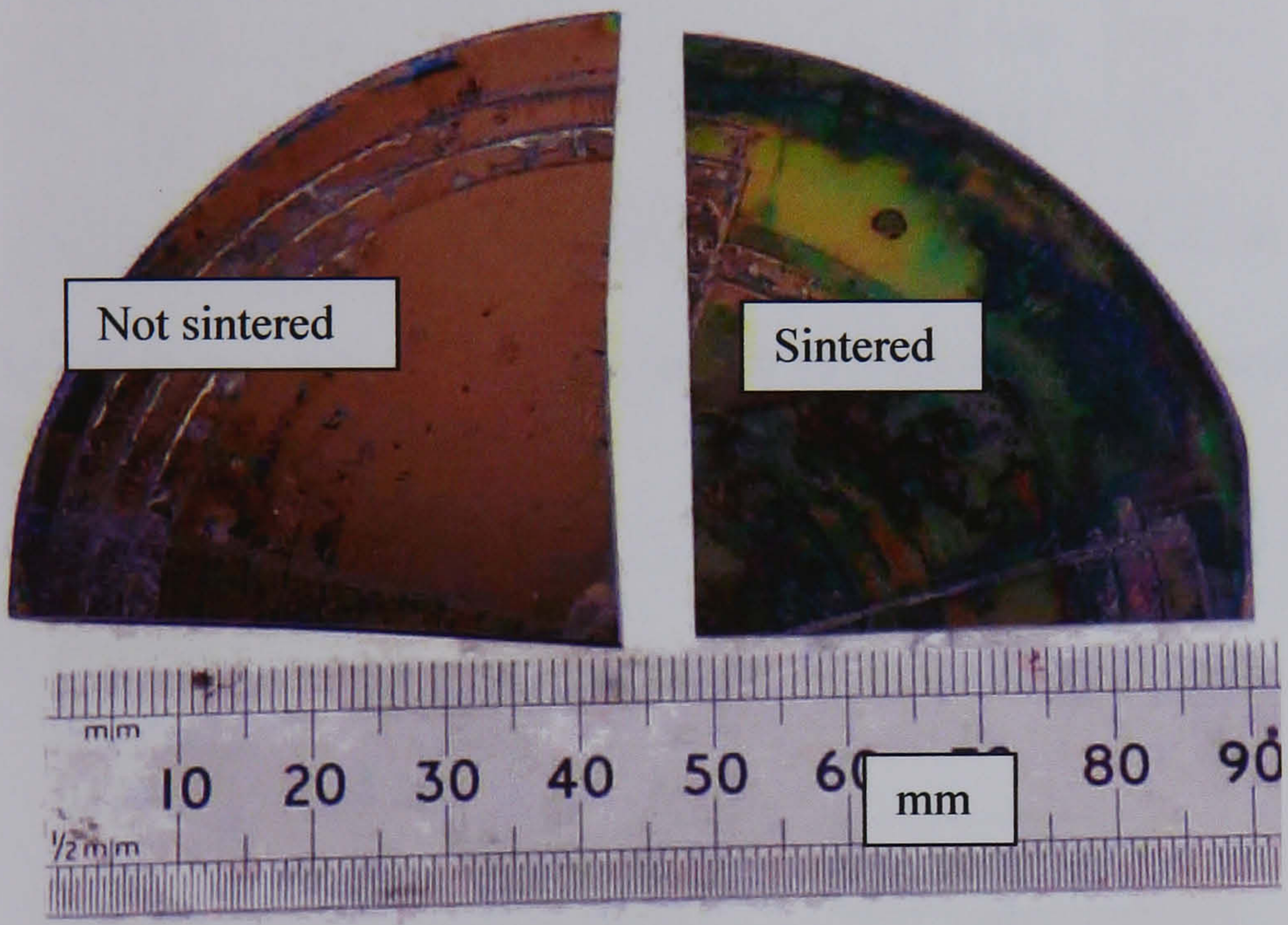

Fig 8.7 Photograph of Cr-coated wafer quarters. The picture is of the back face of the wafers after a thick film has been prepared on the front face. The photograph shows the staining of the back face caused by thick film deposition.

In the case of green PZT thick films, the Cr etch damaged the PZT (Fig 8.9, overleaf) irrespective of the resist protection. In addition, sintered PZT thick films with sputter coated Cr/Au electrodes were left in the etching solution for up to 24 hours: no damage to the film or the electrode was observed. It is unclear why Cr/Au should be stable to the Cr etch.

It seems that S1818 photoresist degrades after one hour exposure to the etching solution. As the sintered PZT thick film and the Cu/Au electrode are not effected by the etching solution, we conclude that a photoresist layer is not required for protection of the PZT coated face.

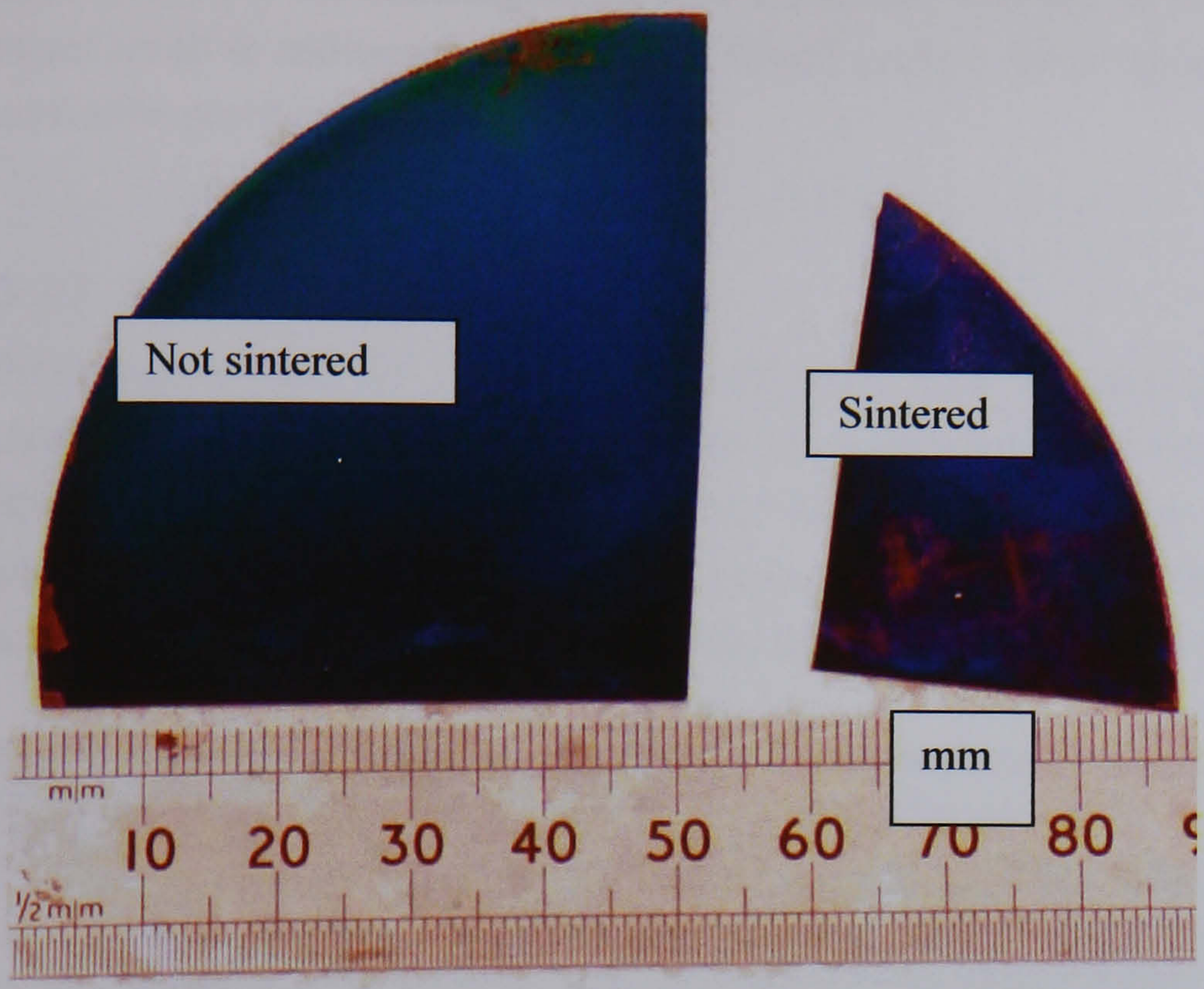

Fig 8.8 Photograph of the Back face of PZT-coated wafer-quarters. Photograph taken after the Cr was stripped.

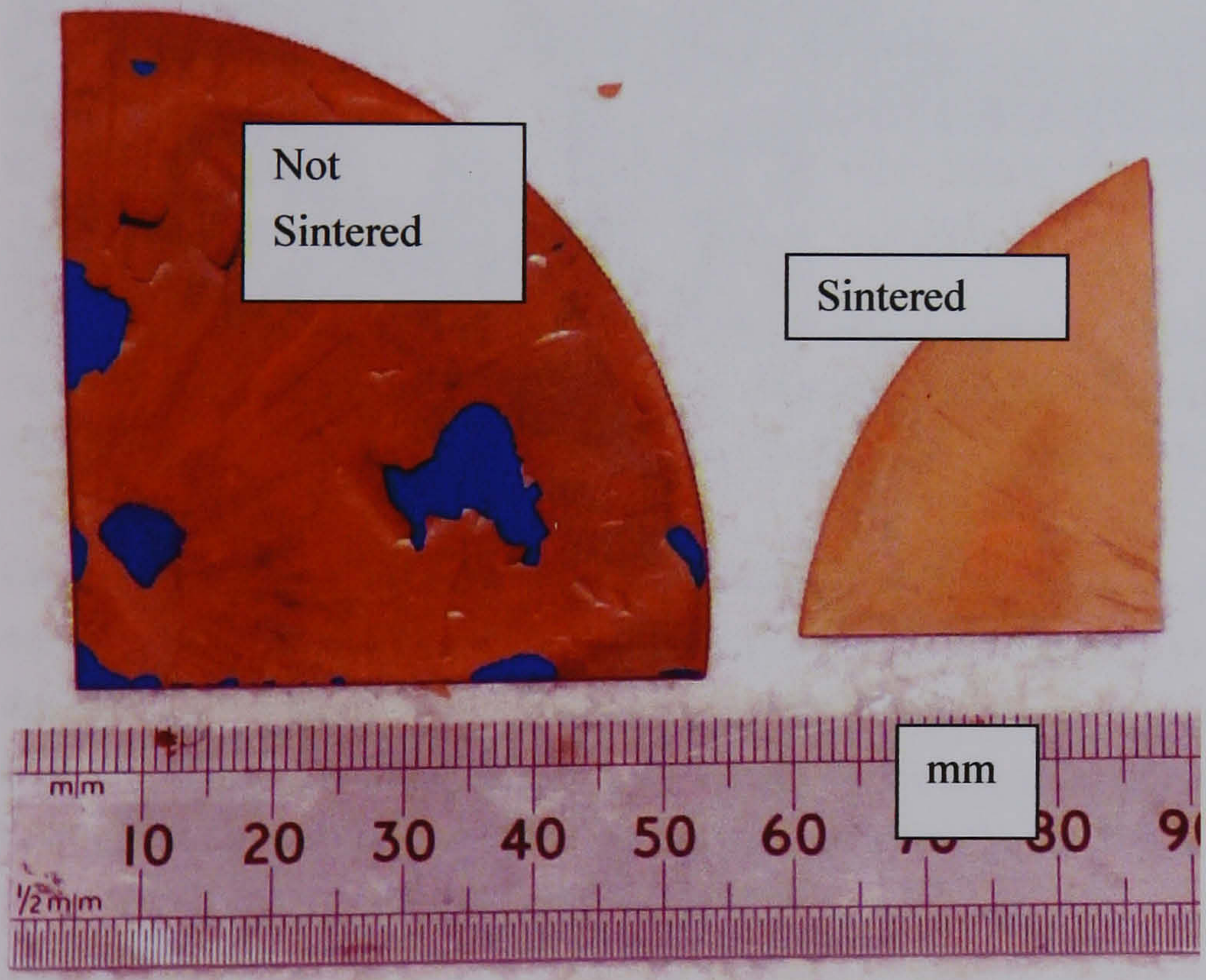

Fig 8.9 Photograph of the PZT-coated surface after Cr removal. The photograph is of wafer quarters.

The Cr layer was judged a success in protecting the back face of the wafer against staining. It was decided, because of the damage to green PZT, to await removal of this layer until after the sintering of the PZT thick film. Further, as the powder blasting stage might result in additional scratching of device wafers, the Cr layer was to be left in place until after powder blasting.

8.3.3 PZT Etching

Pin-holing of the PZT thick film was observed after wet etching. As noted in the last chapter, the S1818 photoresist was stable to etching solution. Asperities in the PZT thick films were detected with diameters and heights of ~100 µm. The fracturing of the asperities was consistent with that of glass chips (see Fig 8.10 below). It is considered most likely that the asperities puncture the resist giving rise to the pin holing observed.

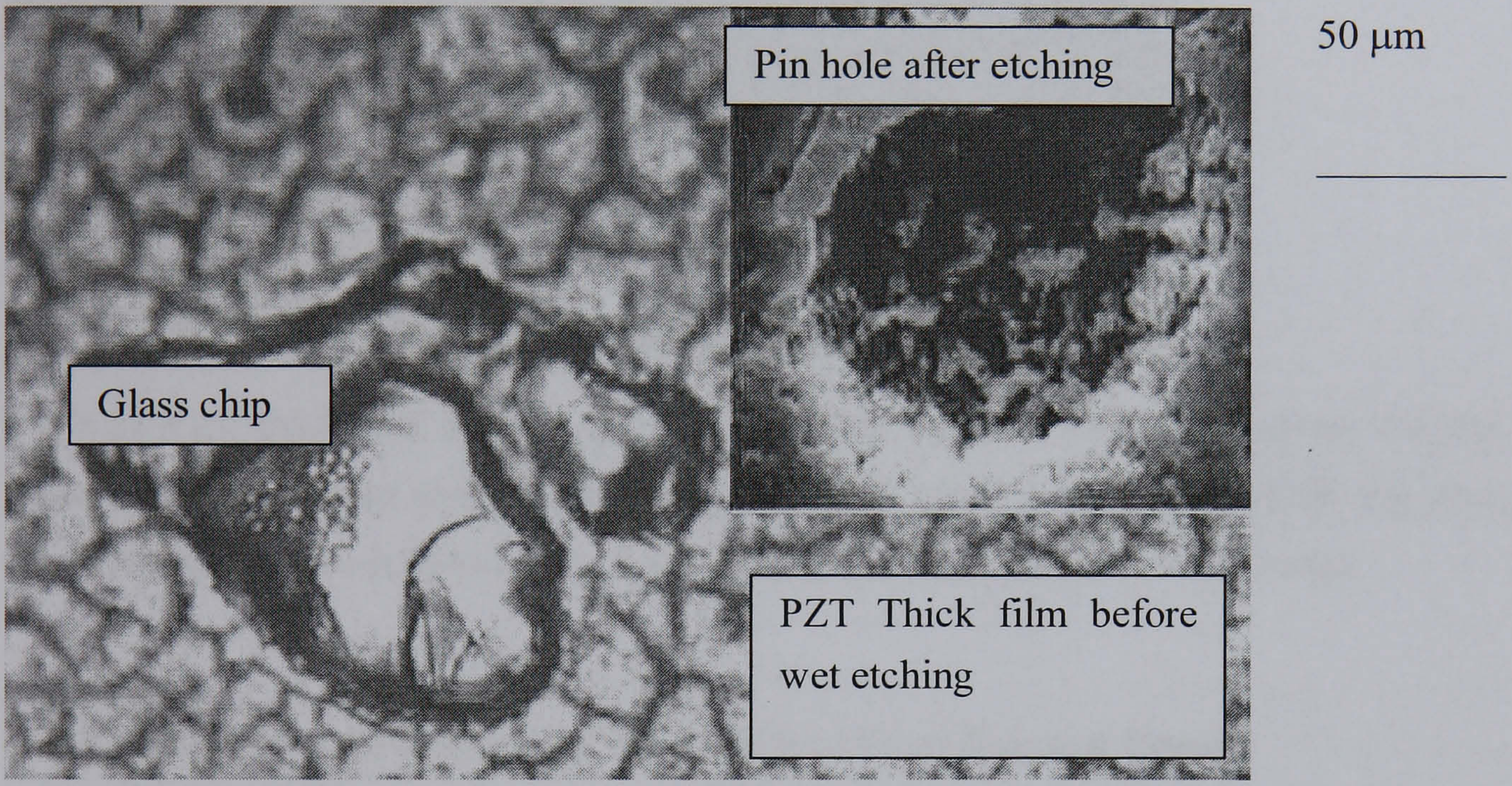

Fig 8.10 Optical micrograph of a glass chip embedded in the surface of a PZT thick film. Also shown (*inset in the top right corner*) a pin-hole in the PZT thick film after etching

Composite slurries were prepared through the ball milling of ceramic powders in the metal organic sol. The continued mechanical action of the pellets hitting the sidewalls of the glass jar must result in some chipping of the glass. Glass contamination of the composite slurry is anticipated as the cause of the asperities. It was decided, due to pin holing, not to wet-etch the PZT when preparing device wafers. Instead, the wet etching was to be delayed until the pin-holing had been resolved.

8.3.4 Top Electrode

A continuous surface electrode was formed on the surface of the PZT after lift off in acetone. However, even after 24 hours in the acetone some residual photoresist remained (see Fig 8.11). It was unclear why this should be the case; nevertheless, for the fabrication of working devices the residual photoresist was not considered to be too much of a problem and it was decided to proceed with this process.

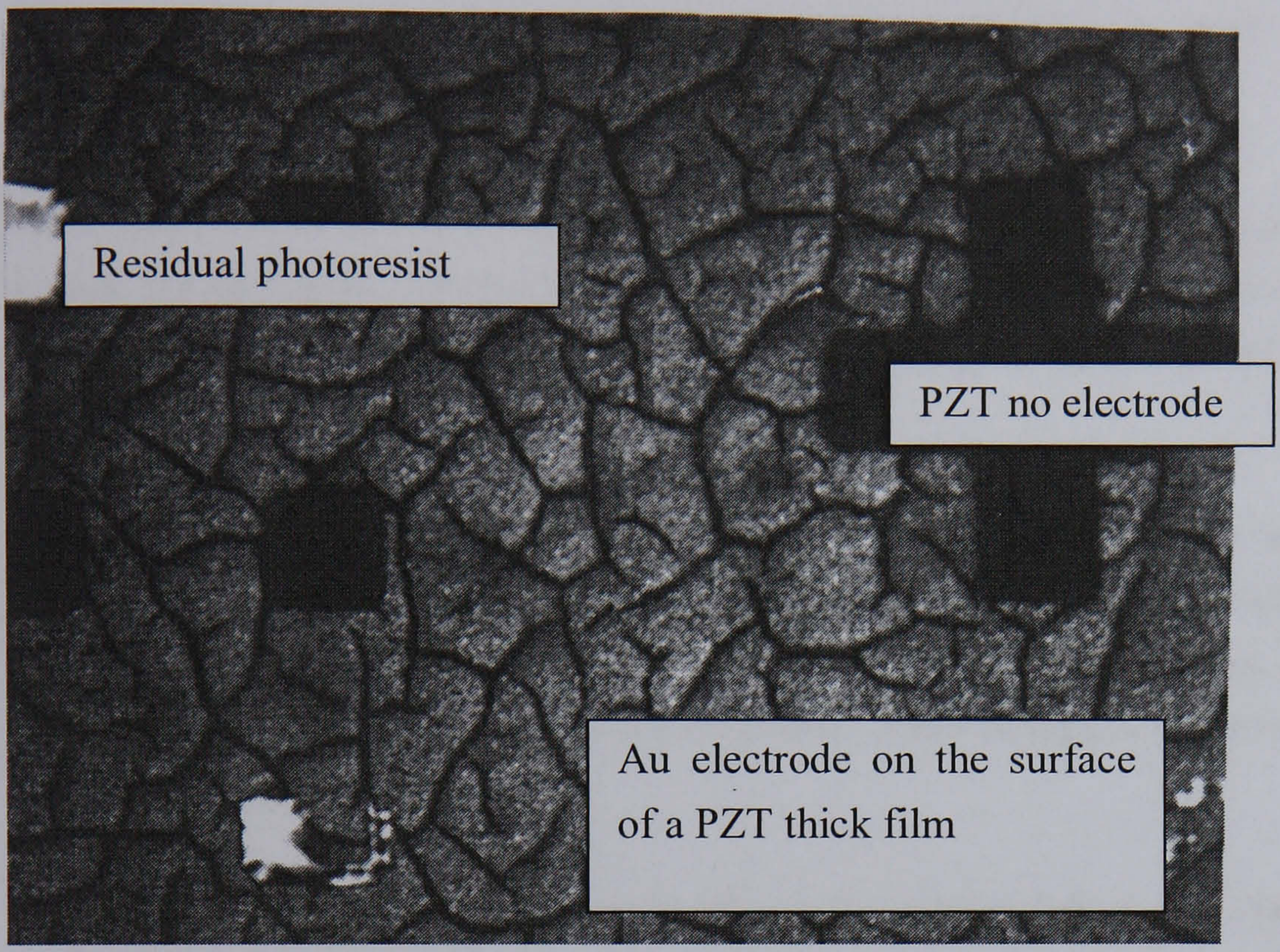

Fig 8.11 PZT thick film surface with electrode after lift off. The image shows residual photoresist attached to areas of the thick film. The image was obtained with the clean room microscope; consequently, no calibrated scale was available for this image.

8.3.5 Process 2: Si-DRIE. The Revised And Final Process Design

In order to eliminate interface damage from anisotropic wet etching, it was decided to release the actuators with DRIE (deep reactive ion etching). Therefore Process 1, see chapter 5 section 5.2.1, required modification based on the conclusions from this and earlier chapters.

The silicon-nitride-coating was incorporated as a barrier layer to selectively protect the silicon substrate from KOH; the elimination of anisotropic etching, therefore, rendered the silicon nitride redundant; if DRIE were used to release the actuators there would be no need for a silicon-nitride-coating. Consequently, a new process incorporating DRIE was proposed, see Fig 8.12 and Table 8.3. The new process was based on the use of Si and not Si_3N_4 wafers; further, as YSZ proved the better barrier layer for this substrate-system, the new process incorporates YSZ as the preferred barrier layer system. In the revised process it was proposed that YSZ should be deposited by EB-PVD onto a buried oxide/plane wafer as a diffusion barrier.

The back electrode was to be deposited through sputter deposition of Ti/Pt onto the YSZ. A Cr layer was then to be sputtered onto the back face of the wafer to protect the wafer from staining and scratching, step 5. The PZT thick film was to be deposited through the standard route, step 7. After sintering of the PZT thick film, the PZT was to be corona poled to align the domains within the ferroelectric.

S1818 photoresist was to be applied to the back face of the wafer and patterned with mask 1, step 11. In step 12, Cr was to be evaporated onto the back face of the wafer. In step 13 lift off in acetone was to be used to yield Cr alignment marks for subsequent back to front alignment.

Mask 2 was to be used in step 15 to photo-pattern the PZT thick film before wet etching. The PZT was to be wet etched using a dilute solution of $HF_{(aq)}$ and $HCl_{(aq)}$. The wet etching process was discussed in chapter 7 above. The object of this step was to make vias for electrical contact to the back electrode. After etching the photoresist was then to be stripped with acetone.

The next stage in processing was to deposit a surface electrode. The PZT is photo-patterned with S1818 using mask 3, step 19. Subsequently, a Cr layer (8 nm) was to be sputtered as an adhesion layer for Au (100 nm), which was also to be sputtered. Because the lift off process takes a long time, the wafer was to be left to stand in acetone overnight.

The SBX® photoresist was then to be applied (step 23), and photo-patterned using mask 4 yielding an anti abrasive coating. In step 24, the device wafer was to be powder blasted and the SBX® removed with stencil remover. After powder blasting, the PZT was to be protected with a layer of photoresist and the Cr was to be removed with a commercial Cr etch.

AZ52142 (Clariant) is a photoresist for DRIE applications. It is applied through spin coating; however, it was only to be applied here after the Cr layer has been etched and the wafer cleaned in step 17. The photoresist was to be patterned through front to back alignment with the top electrode. The device wafer was to be secured to a Si support wafer with vacuum grease. Deep-reactive-ion-etching, of the back face, of the device wafer was then to be commenced. The wafer was to be etched to the buried oxide layer where a lower etch rate ensures that there is an even etching of devices across the wafer. The wafer may then be sawn on the support wafer before release in acetone. This will yield a set of device chips that can be mounted on a PCB.

Step		Description
Starting material		Buried Oxide wafer see Table 5.5
1.	Clean	Standard clean see experimental chapter
2.	YSZ	EB-PVD deposition of YSZ (1 μm) diffusion barrier at 700 °C
3.	Clean	
4.	Metal	Sputtering of Ti (8 nm) and Pt (200 nm) back electrode
5.	Metal	Sputtering of Cr on to back face(300 nm)
6.	Clean	
7.	PZT	Deposit PZT thick film with intermittent thermal cycling up to 450 °C for 15 s
8.	Sintering	Sinter the PZT at 710 °C for 30 min in air
9.	Poling	Corona pole the PZT at 115 °C 10 kV for 10 min
10.	Clean	
11.	Photolithography	Mask 1 (back face alignment)
12.	Metal	Sputtering of Cr onto back face (300 nm)
13.	Lift off	Lift off Cr to yield alignment marks
14.	Clean	
15.	Photolithography	Mask 2 wet etch of PZT
16.	Etch	Etch PZT, to open paths for electrical contact, with dilute $HF(aq)_{(aq)}$ and $HCl_{(aq)}$
17.	Strip	Strip photoresist
18.	Clean	
19.	Photolithography	Mask 3 top electrode
20.	Metal	Sputter deposition of Cr (8 nm) and Au (100 nm) top electrode
21.	Lift off	Lift off photoresist with acetone over night.
22.	Clean	
23.	Photolithography	Mask 4 Device set for powder blasting. At RAL
24.	Powder Blasting	Powder blasting of device structures with Alumna-Powder (15 μm), at 80 psi, to a depth of 50 μm.
25.	Strip	Remove SBX with Stencil remover
26.	Clean	Remove powder with air wash before removing to the clean room for standard clean
27.	Photolithography	Protect PZT
28.	Etch	Remove Cr from the back face
29.	Strip	Strip photoresist
30.	Clean	
31.	Photolithography	Mask 1 back face pattern
32.	Mount	Support wafer for DRIE with vacuum grease

33.	Etch	DRIE through wafer to release cantilevers
34.	Sawing	Sawing of structure into chip set
35.	Release	Release chips from grease with acetone
36.	Plasma ash	Clean up surface of devices
37.	Mount	Mount chips on PCB

Table 8.3 The revised and final processing route. This route allows for the fabrication of spiral-piezoelectric-actuators. The actuators incorporate a PZT thick film as the active material. The actuators are released through Si-DRIE.

Process 2: Si-DRIE

Process Step

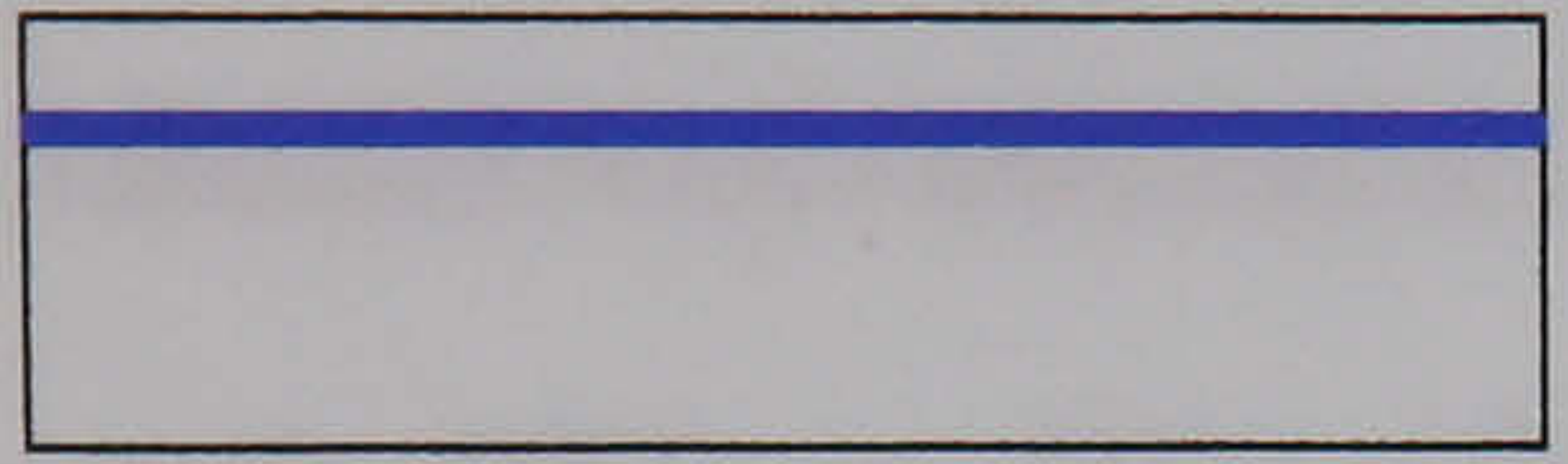

Buried Oxide wafer

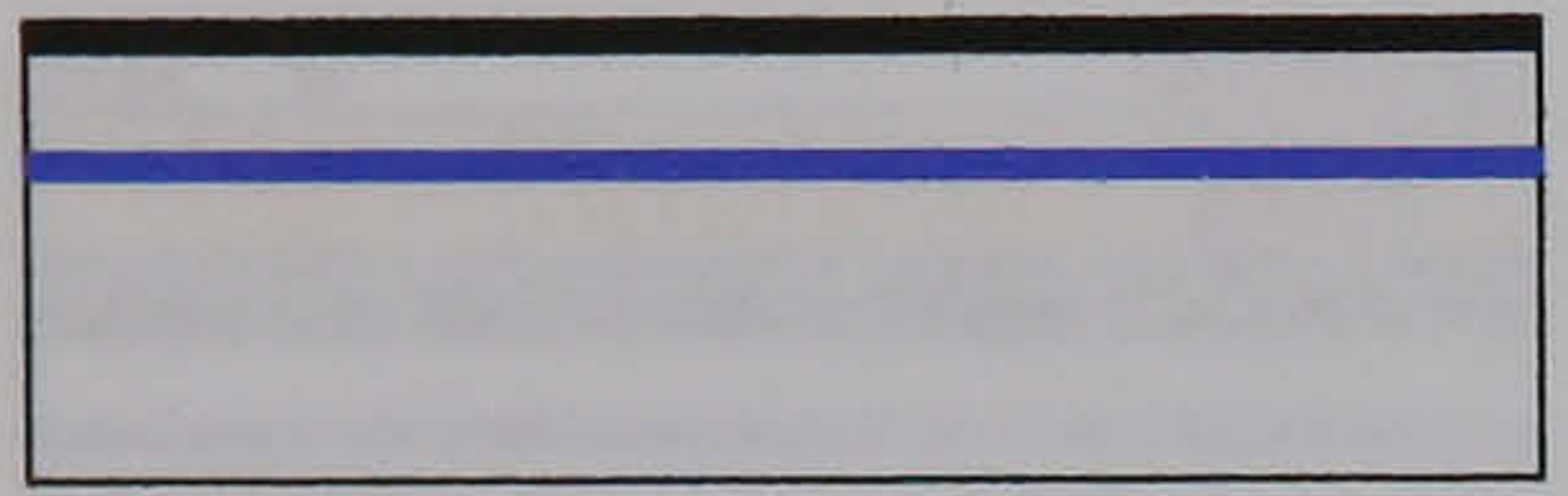

EB-PVD deposition of a YSZ diffusion barrier layer at 700 °C

4

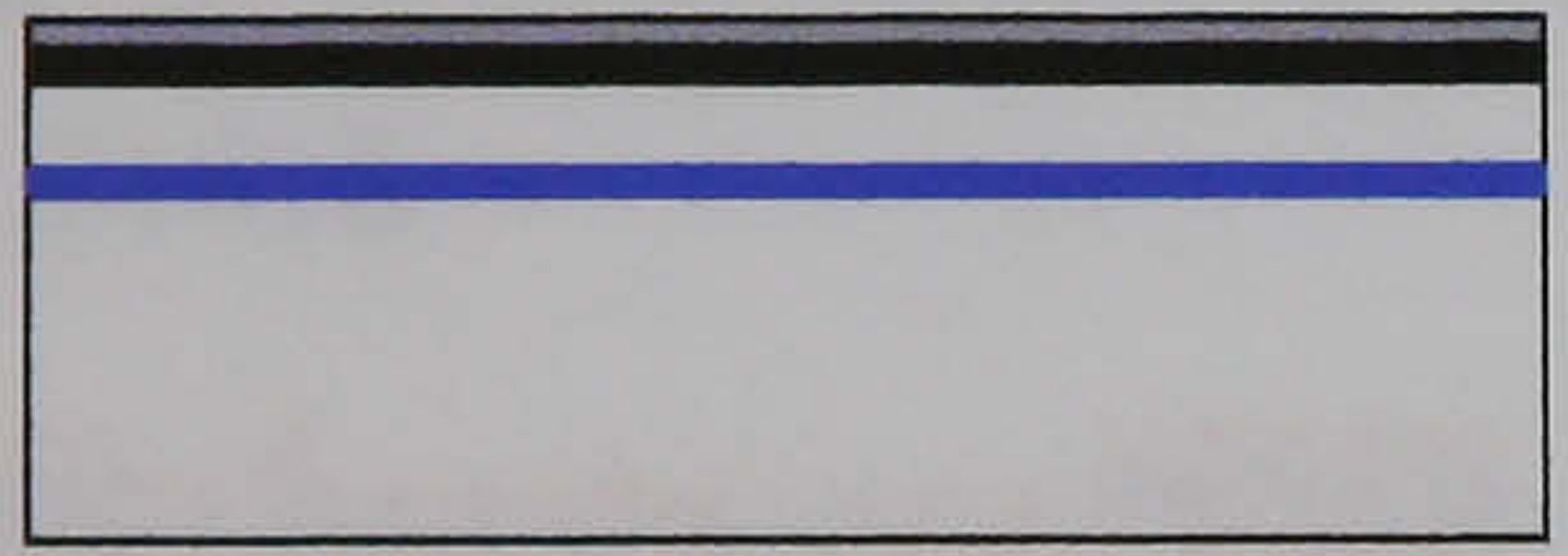

Sputter deposition of Ti/ Pt back electrode

5

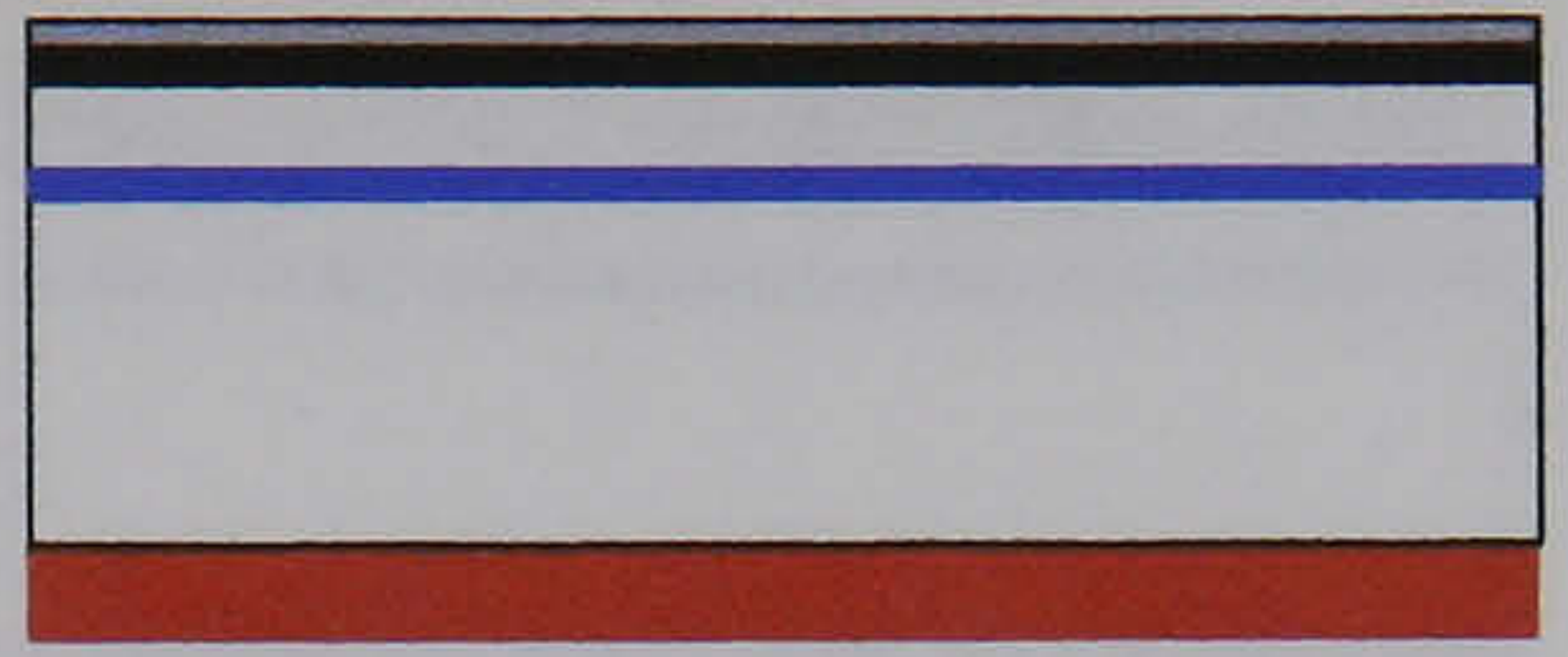

Sputter deposition of Cr onto the back face of the wafer to protect from scratching and staining

7

Deposition, sintering and corona poling of the PZT thick film.

11

Mask 1: Photo-patterning of the back face with S1818

12

Sputter deposition of Cr alignment marks

13

Lift off photoresist with acetone

15

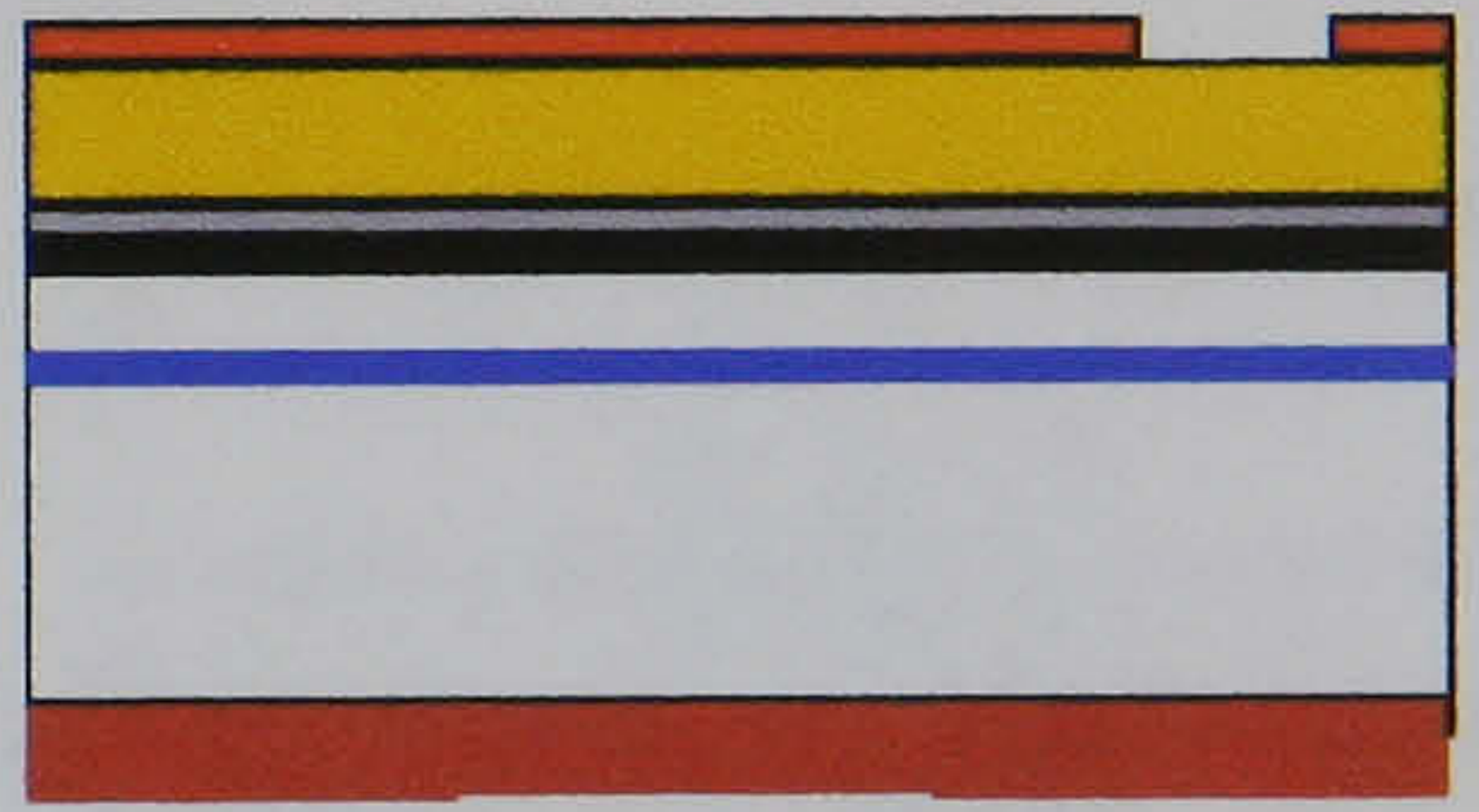

Mask 2 Photo-patterning of the PZT with S1818

16

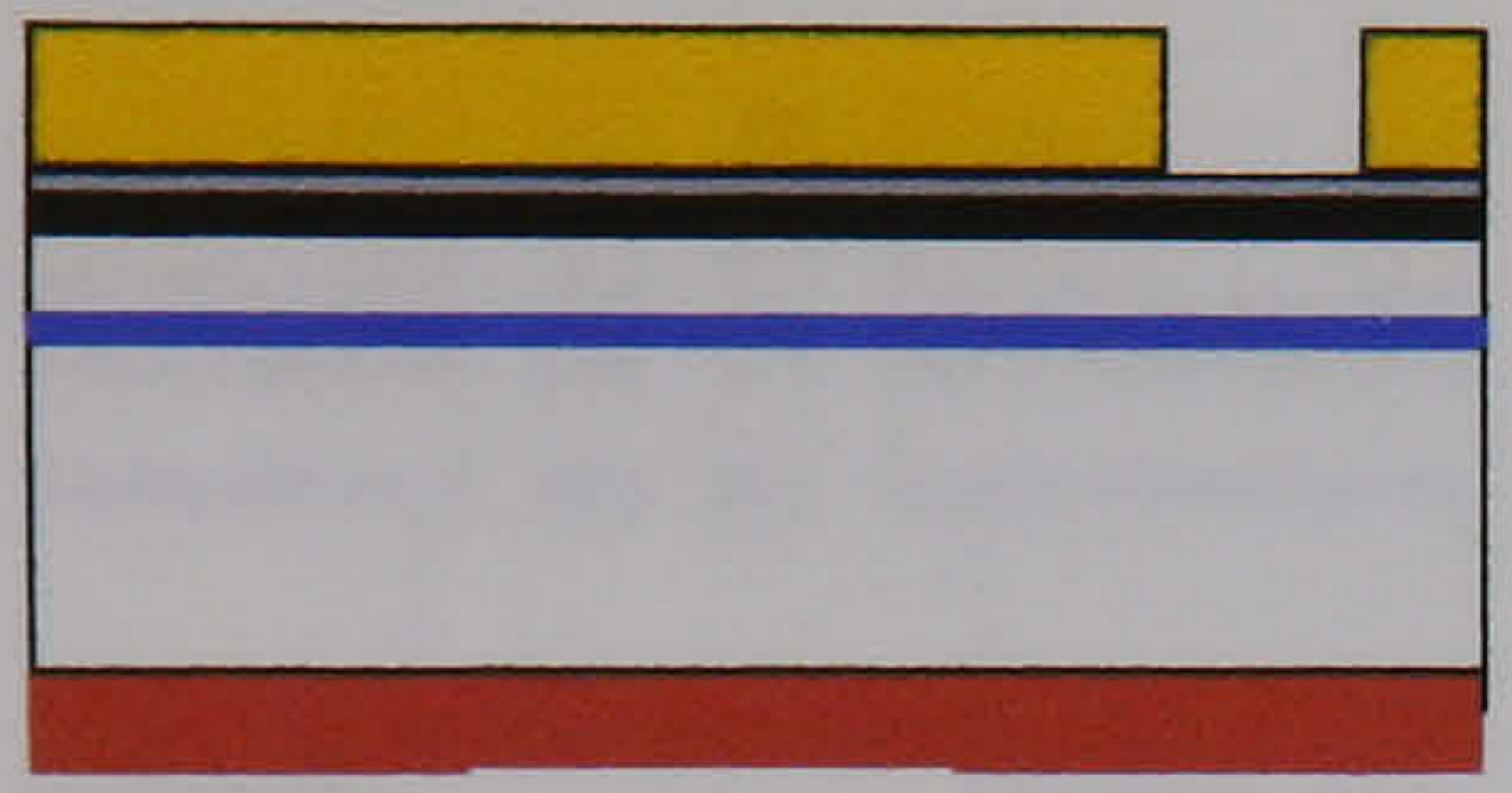

Wet etch PZT in HF(aq)/H_2O & Strip S1818 with Acetone

19

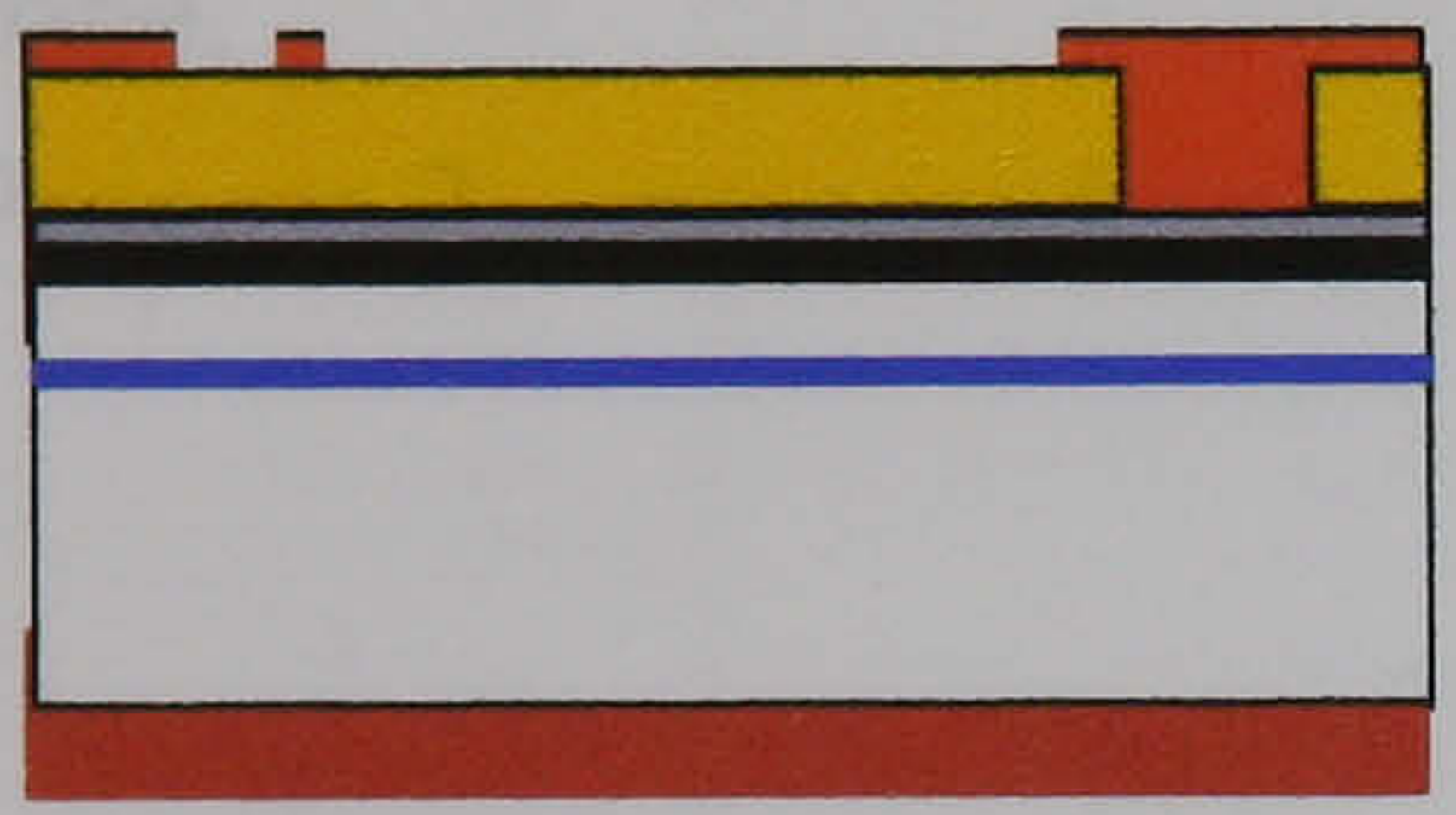

Mask 3: Photo-patterning of PZT with S1818

20

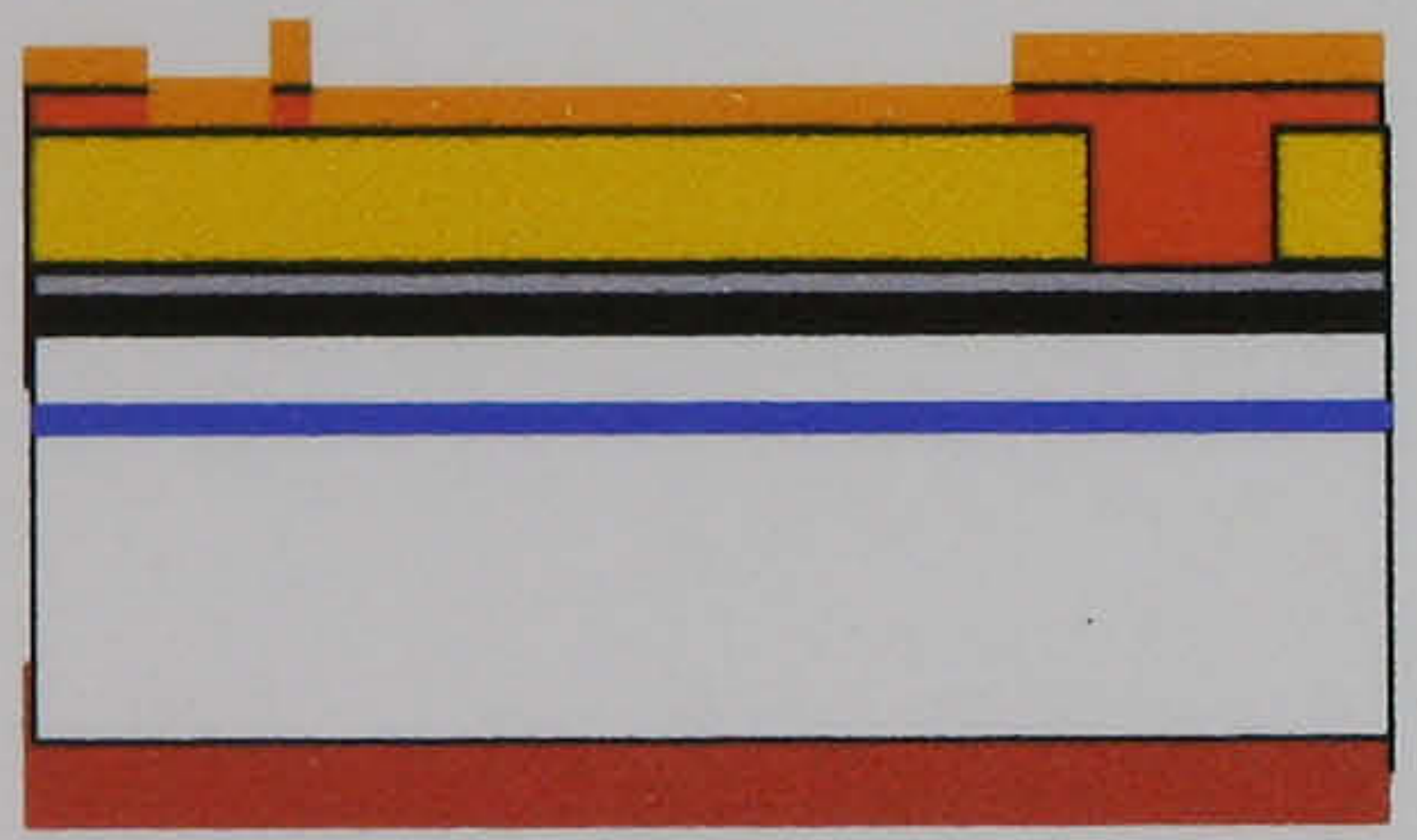

Sputter deposition of Au/Cr top electrode

21

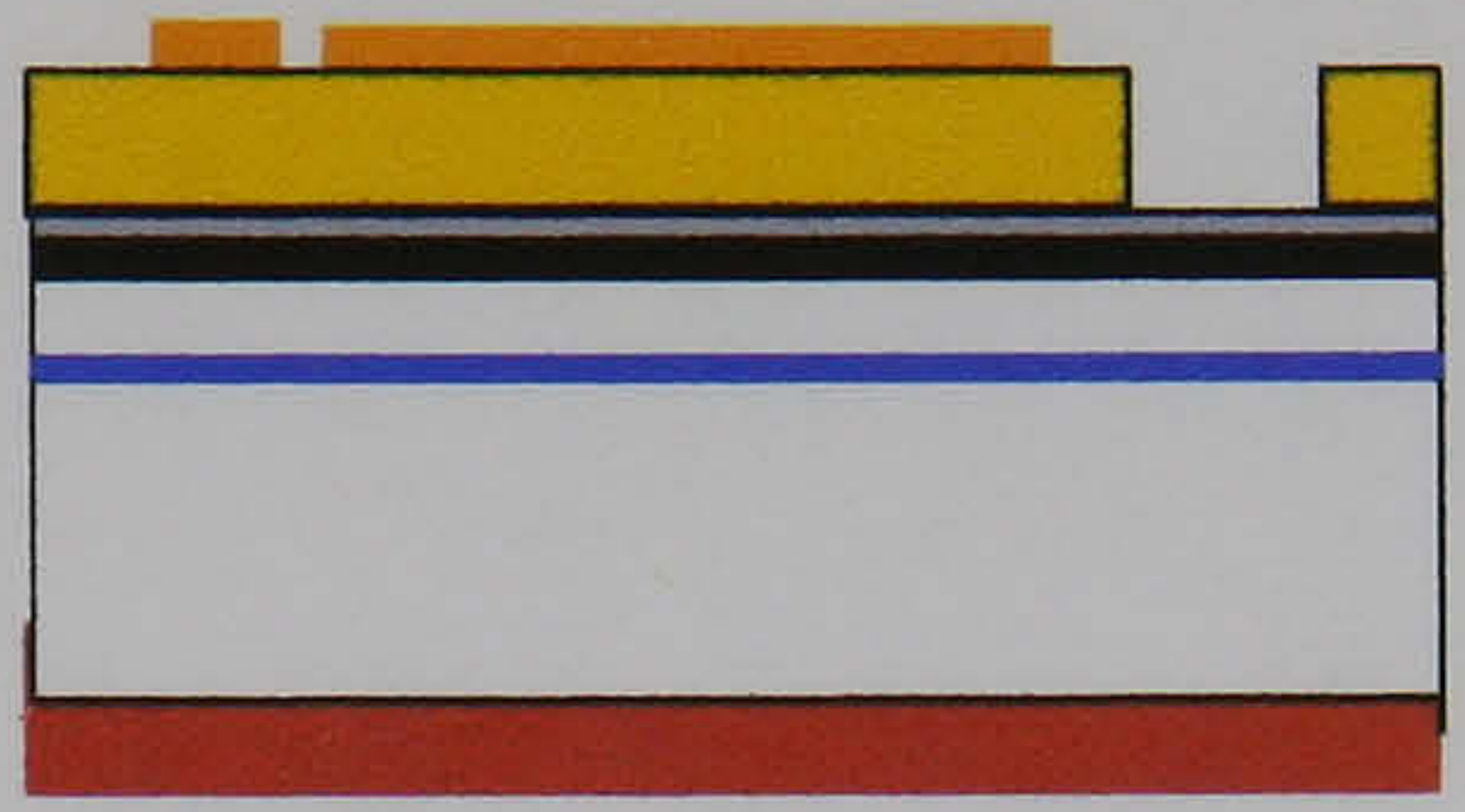

Lift off photoresist with acetone over night.

23

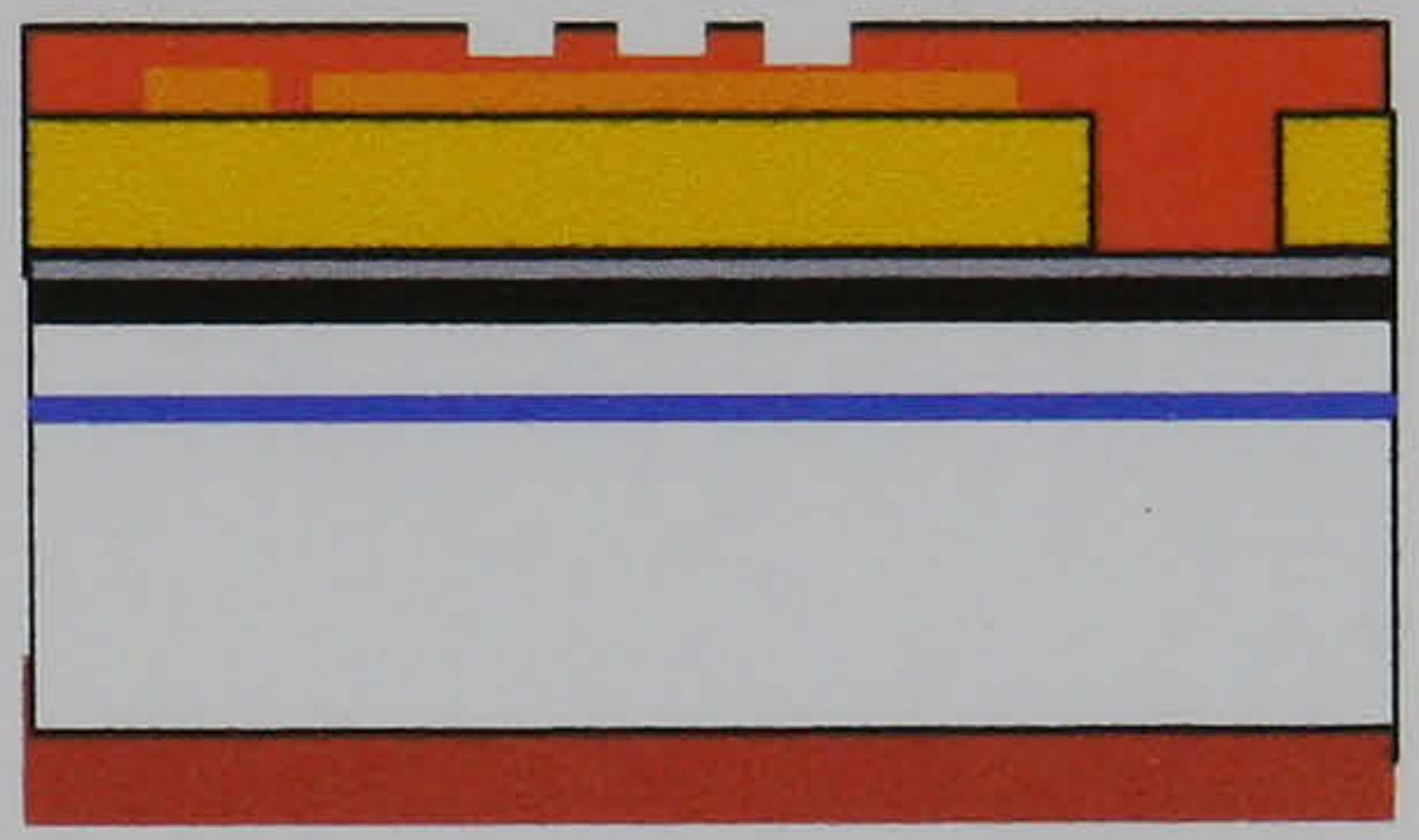

Photo-patterning of SBX

24

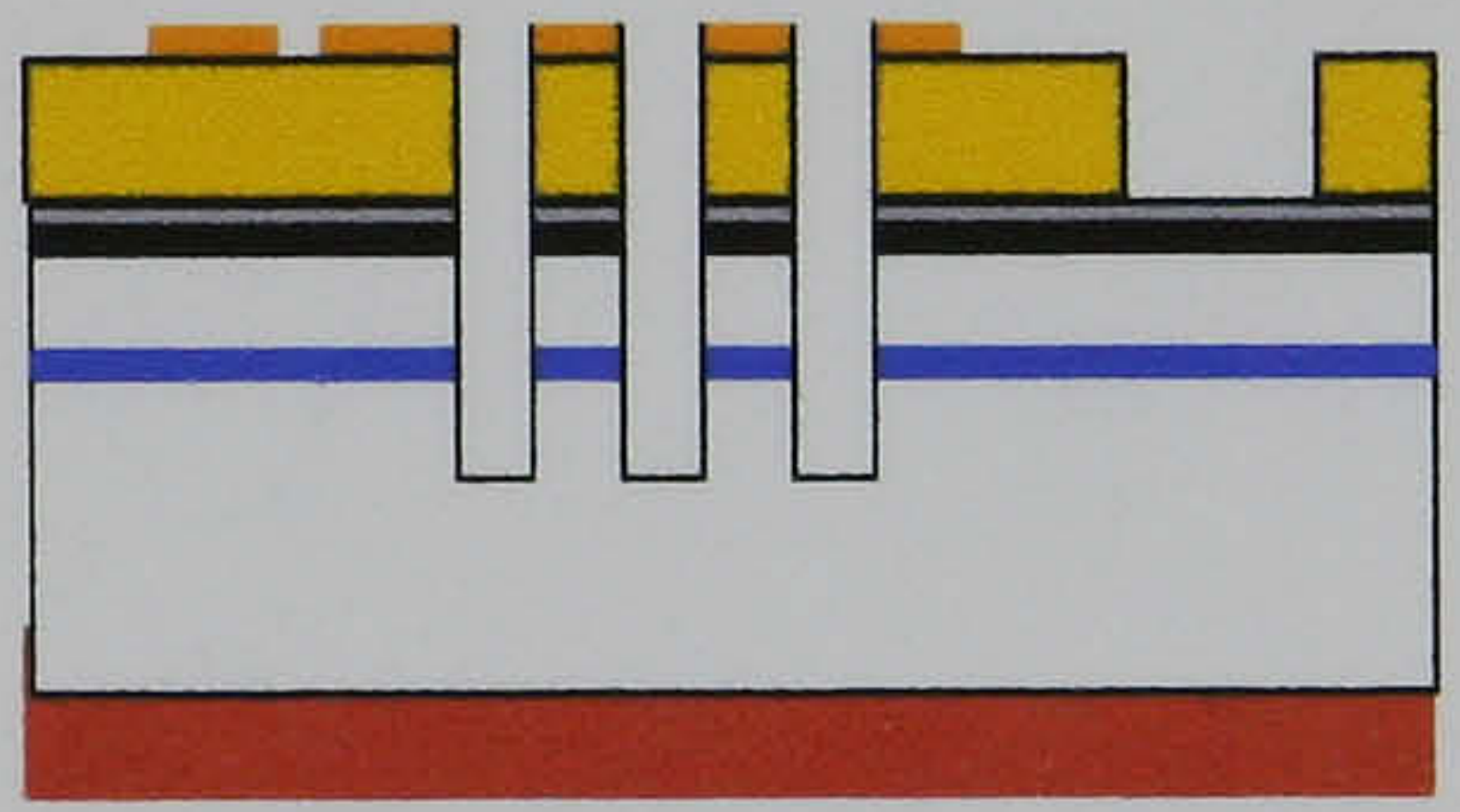

Powder blasting of device structures & Stripping of SBX

28

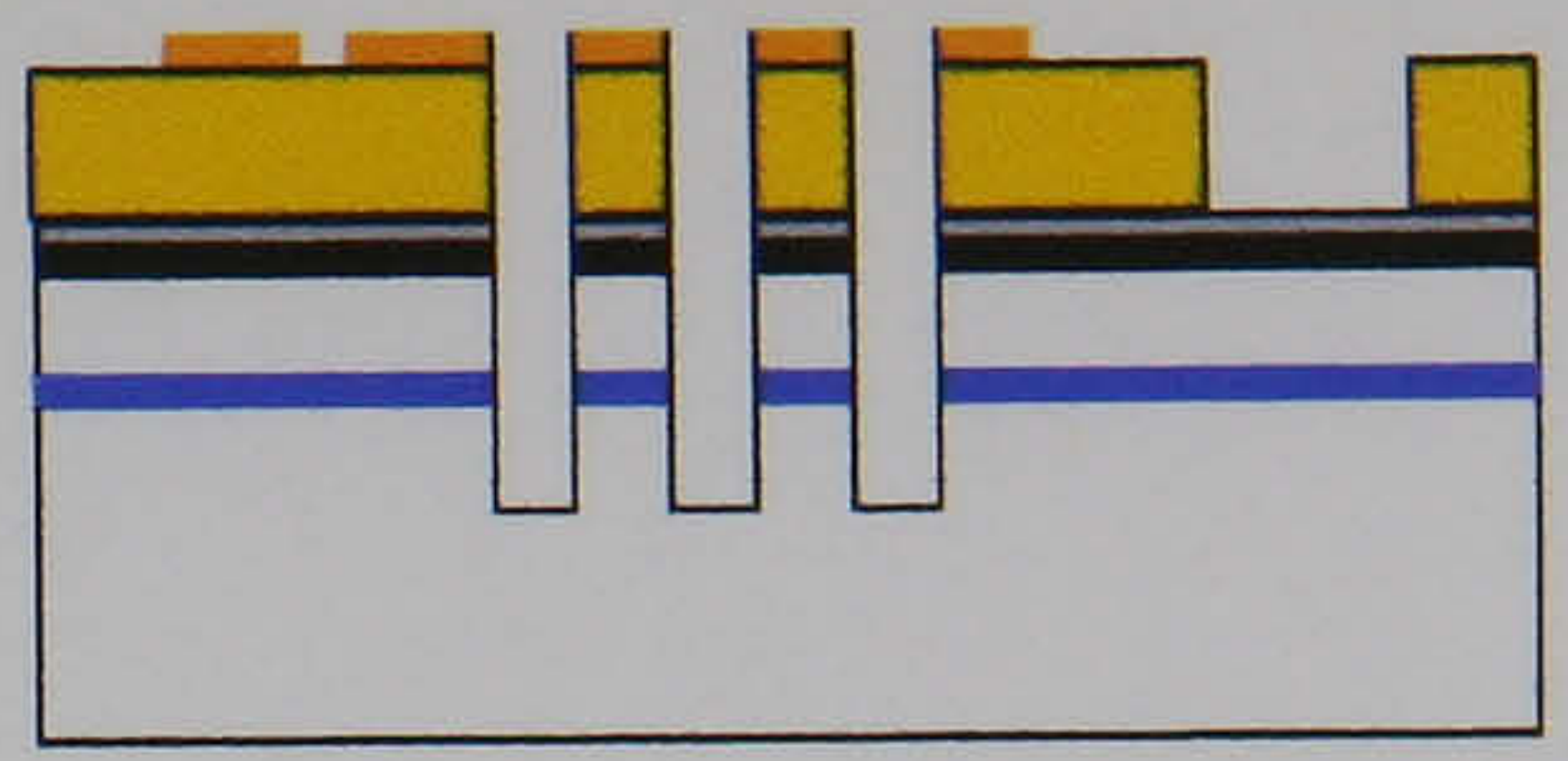

Stripping of Cr with Cr etch

31

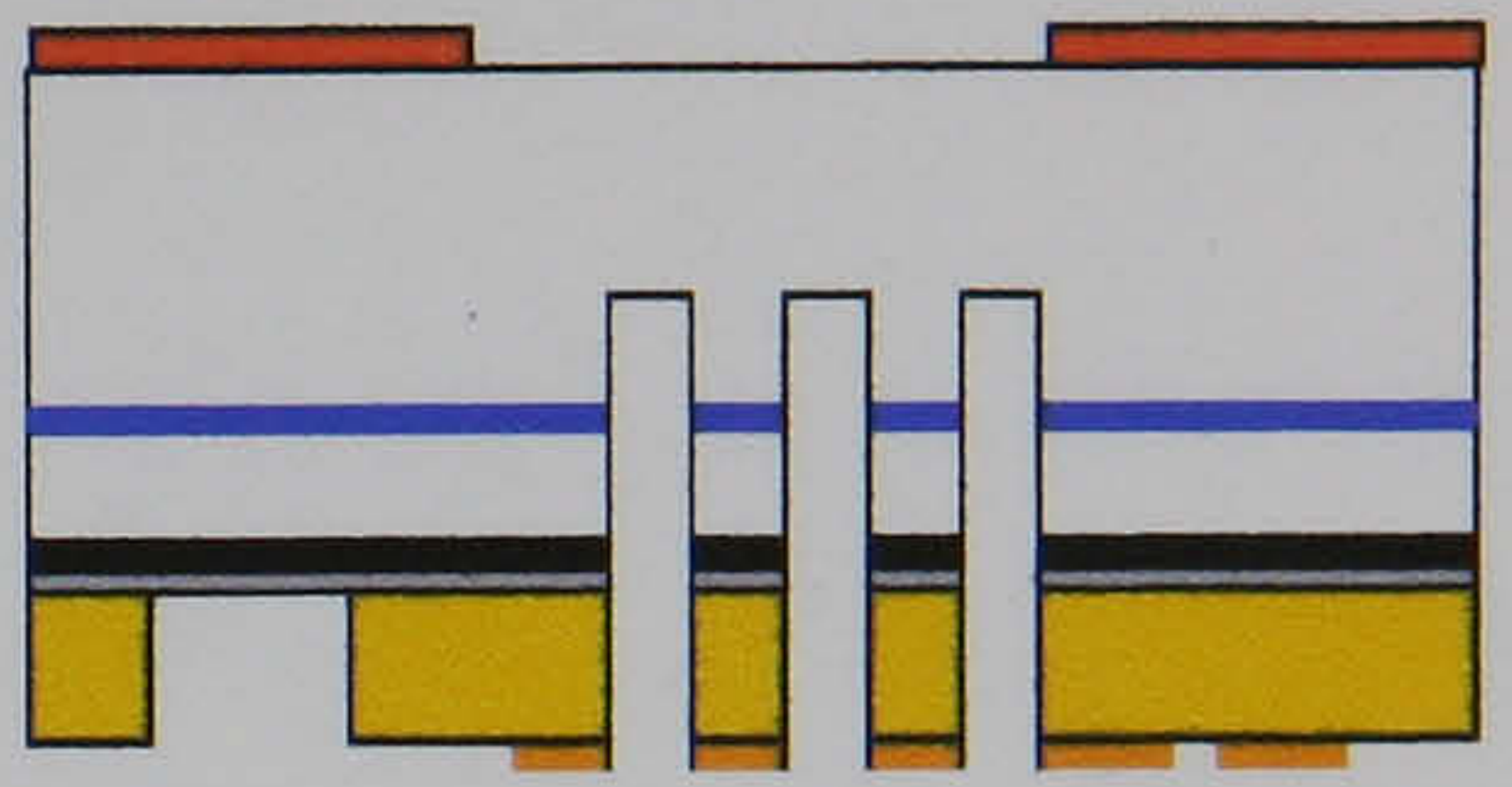

Mask 1: Photo-patterning of AZ52142

32

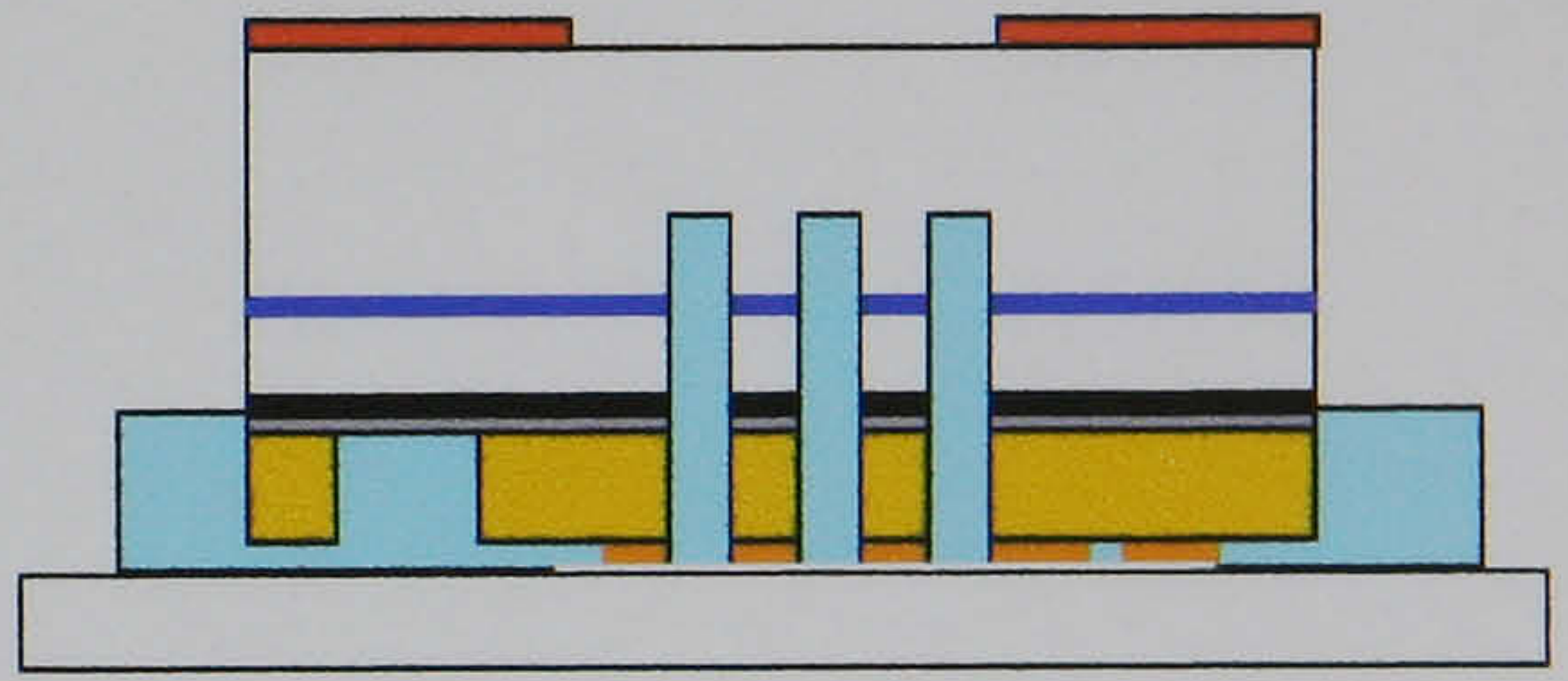

Vacuum greasing of device wafer to a support wafer & DRIE to release cantilever structures

33

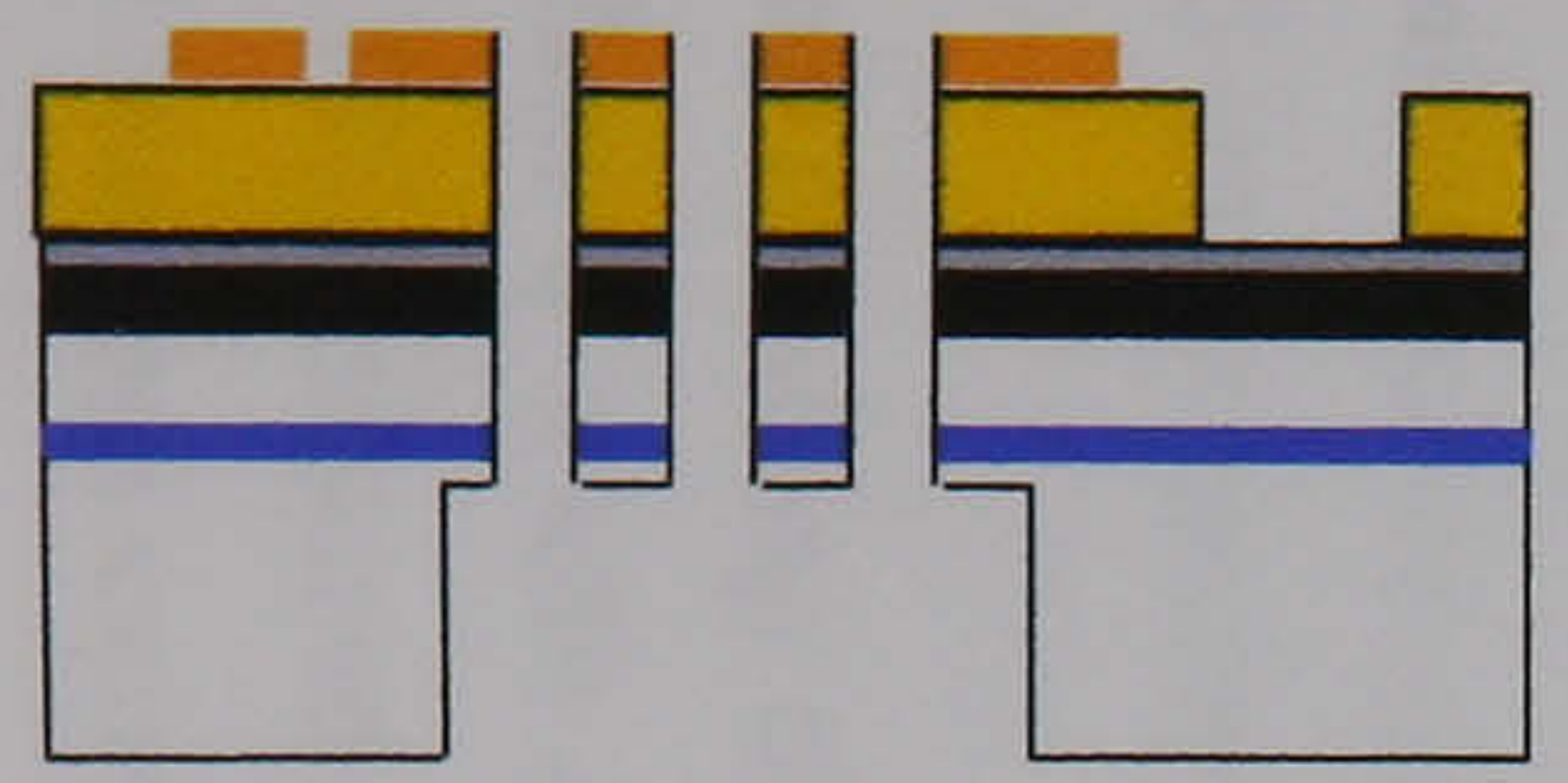

Dicing of wafer into chip set & release from the support wafer with acetone.

Fig 8.12 Process 2 – process flow

9 Device Fabrication & Analysis

9.1 Introduction

The object of this chapter is to discuss the issues arising from the combination of the different processing steps, the fabrication of the actuators and their experimental assessment. Two device wafers, rh100 and rh200, were prepared on Si <100> substrates with YSZ diffusion barriers and PZT thick films. In other words, rh100 and rh200 were prepared according to the modified process 2, which was discussed in section 8.3.5 of chapter 8 above. Following air sintering of these wafers, the thick films were corona poled. The next stage in the process was to etch the PZT; however, this was not done for the device wafers as will be discussed below. An electrode layer of Cr/Au was applied to the surface of the PZT thick film and patterned through lift off. In the last chapter, the device wafers were powders blasted in order to cut device structures into the PZT and Si substrate. Admittance analysis of an actuator was used to obtain piezoelectric resonances for structural information. Finally, a FE model of a piezoelectric spiral actuator is included in order to interpret experimental data

9.2 Finite Element Analysis Model Development

9.2.1 Model Specification

A 3D-spiral actuator was designed in Ansys® in order to model the effect of spiral geometry on deflection and resonant frequency. The computer code for the FE model of the piezoelectric actuator is reproduced in APPENDIX VI. The geometry was constructed through plotting two parallel paths of keypoints on a spiral path. The paths were segmented into areas and the areas extruded along the z-direction to achieve a cantilever of the given substrate thickness (25.8 μm). The surface area of the spiral beam was selected and extruded into another area to give the thickness of the piezoelectric layer 10 μm (Fig 9.1). A static electric field (1.50 x 10^6 v/m) was applied between both faces (top and bottom) of the piezoelectric layer. Deflections were determined through static displacements and resonant frequencies through modal analysis. The spiral geometry was specified in computer code to enable the model to be re-run, should the dimensions of the spiral need to be changed. The same dimensions of thickness for substrate and piezoelectric layers were used in analytical and FE linear unimorph cantilevers.

Mapped meshing of the spiral beam ensured an even distribution of elements. The spiral beam had a width of 166.67 μm, and it was meshed with five elements along the beam width. This ensured an element size of 33.3 μm x 33.3 μm x 10 μm; the element aspect ratio of 10:1 was not exceeded.

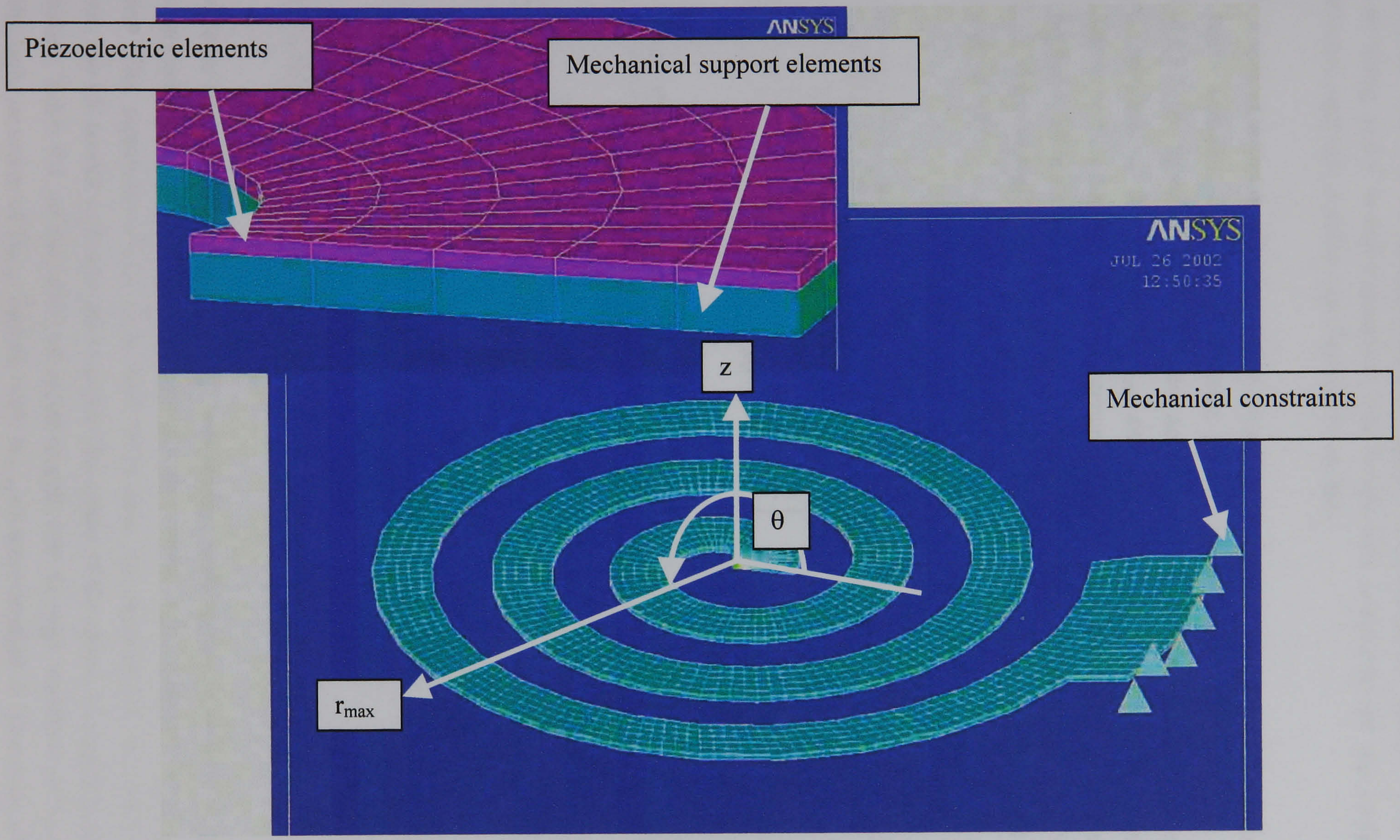

Fig 9.1 Spiral actuator image generated by the FE model. An active piezoelectric layer (PZT) was supported on a Si substrate (*inset*). The actuator was clamped at the arm where the mechanical constraints allow no motion (at the arm) in r, θ or along z.

Motorola 3203HD is a PZT ceramic for which there is a complete set of published elastic constants [124] (see APPENDIX IV). Consequently, Motorola 3203HD was selected as the piezoelectric material for comparison between FE and analytical models. The PZT was taken as being poled in the z-direction. The z-axis was normal to the top surface of the piezoelectric, and this was the case for all FE models.

A FE model of a linear actuator was devised for comparison with the Cross model of a linear beam actuator. The computer code for the linear beam FE actuator is given in APPENDIX VII. Spiral and linear beam actuators of equivalent length were compared, through alteration of the variables N_{turns} and D_{max}. For analytical models of equivalent length linear beam actuators, data was generated using equations (5.20), (5.21) and (5.22) from chapter 5. In order to aid the reader these equations are repeated below as (9.1), (9.2) and (9.3). They represent the fundamental resonant frequency, tip deflection and blocking force respectively.

$$f_{spiral} = \frac{14.08.h}{\pi^2.\left(D_{\max} + \frac{1}{2}\left((w_{spiral} + w_{void}).(N_{turns} - 1).N_{turns}\right)\right)^2} \tag{9.1}$$

$$\times \sqrt{\left(\frac{Y_p}{3.\rho_p}\right) \times \left(\frac{A^2.B^4 + 2.A.\left(2.B + 3.B^2 + 2.B^3\right) + 1}{(1 + B.C).(A.B + 1).(1 + B)^2}\right)}$$

$$\delta_{spiral} = \frac{3d_{31}E_3\pi^2\left(D_{\max} + \frac{1}{2}\left((w_{spiral} + w_{void}).(N_{turns} - 1).N_{turns}\right)\right)^2}{32h_m} \tag{9.2}$$

$$\times \left(\frac{2.A.B.(1 + B)^2}{A^2.B^4 + 2.A.\left(2.B + 3.B^2 + 2.B^3\right) + 1}\right)$$

$$F_{spiral} = \frac{3d_{31}E_3 w_{spiral} h^2 Y_p}{8\pi^2\left(D_{\max} + \frac{1}{2}\left((w_{spiral} + w_{void}).(N_{turns} - 1).N_{turns}\right)\right)} \tag{9.3}$$

$$\times \left(\frac{2.A.B}{(A.B + 1).(1 + B)}\right)$$

The effect of both D_{max} and N_{turns} on L_{spiral} was studied with respect to deflection, frequency and generated forces. Of particular interest was the effect of the shape of the spiral on the outcome. The equations (9.1), (9.2) and (9.3) take no account of the spiral's shape; however, the FE model will take into account the shape of the spiral. Essentially, there were two studies, Table 9.1, of the effect of spiral length: one through variation of N_{turns} and the other through variation of D_{max}. Spirals with N_{turns}=3 were studied at diameters of (D_{max} =) 2, 4 and 8 mm, and spirals of 8mm diameter, were prepared with N_{turns}=1,2...5. It should be noted that throughout these studies w_{spiral} was kept constant. It can be shown that w_{void} was a dependent variable

	Variables held constant	Variable changed
Study 1	(N_{turns}=3), (w_{spiral}=166.7 μm)	D_{max}=2,4 and 8mm
Study 2	(D_{max}=8 mm), (w_{spiral}=166.7 μm)	N_{turns}=1,2….5

Table 9.1 FE study of geometric variables

Displacement of the spiral actuator in a static field was modelled with static analysis. Modal analysis was employed to analyse the mode shapes of the spiral as a function of frequency.

9.2.2 Force Estimation

The Force frequency ratio F/f gives a straight line when plotted against cantilever length. As long as the spiral has the same width, materials properties and thickness as the linear cantilever from which F/f was determined, then the blocking force of the spiral F_s can be estimated:

$$F_s = \frac{L_s}{L} \times \frac{F}{f} \times f_s \tag{9.4}$$

Spiral geometry can be generated in FE and then modal analysis will yield the first resonant mode f_s for the structure. It is assumed, of course, that the force frequency relation will be linear for spiral actuators; there is no means of knowing that this is true. Caution is advised in interpreting blocking forces calculated for spiral actuators in this way!

9.3 Results

9.3.1 Actuator Release

DRIE was used to release actuators on wafer number rh100, see Fig 9.2 to Fig 9.8. However, it was not possible to resolve any devices from wafer number rh200 as the wafer split during processing. The wafer may have been weakened either because of thermal cycling during the PZT thick film deposition or radial crack formation during powder blasting. Crack formation was considered less likely: wafers were securely clamped during blasting and every effort was made to damp out vibrations.

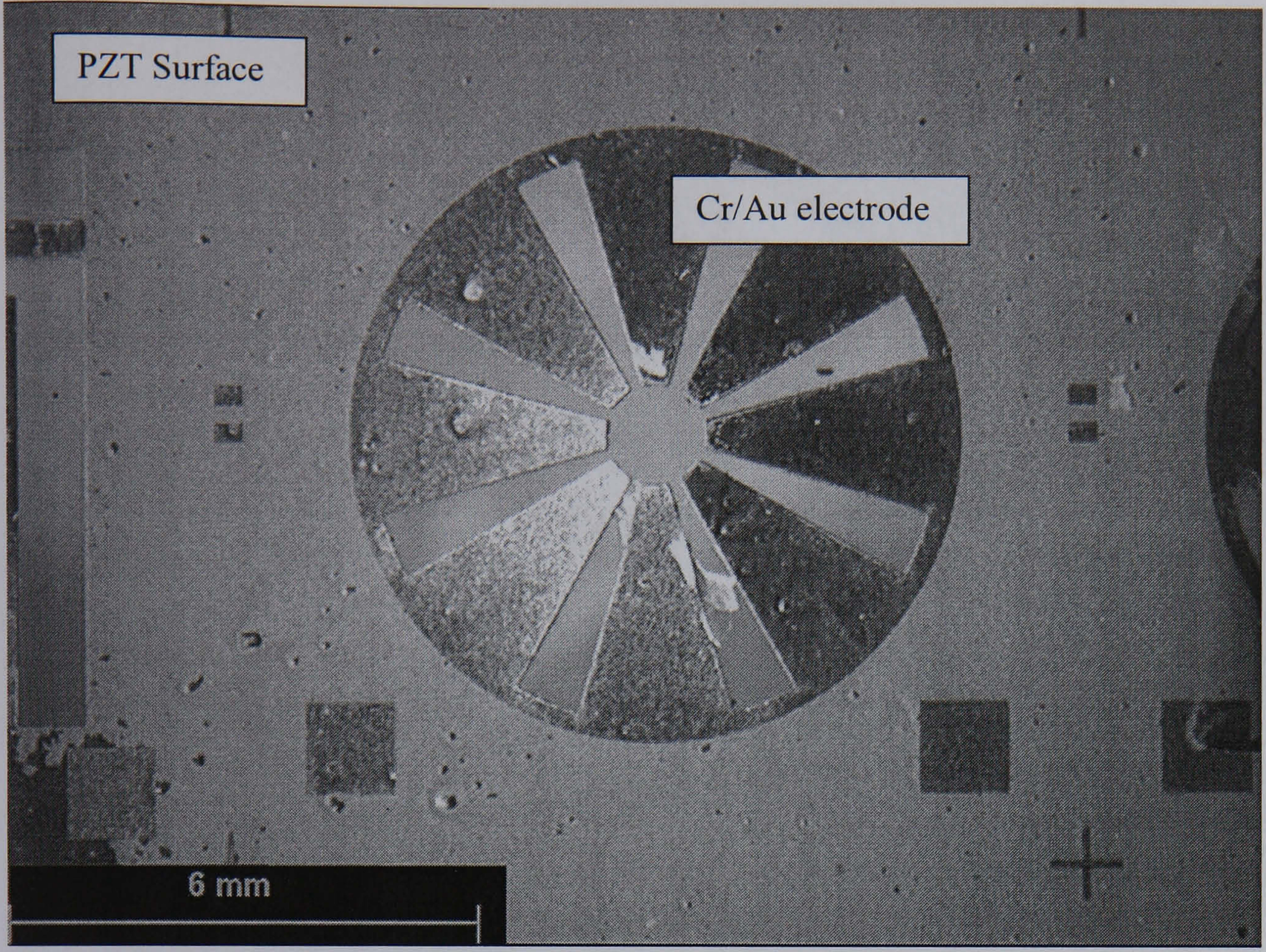

Fig 9.2 Released spoke actuator sp5.

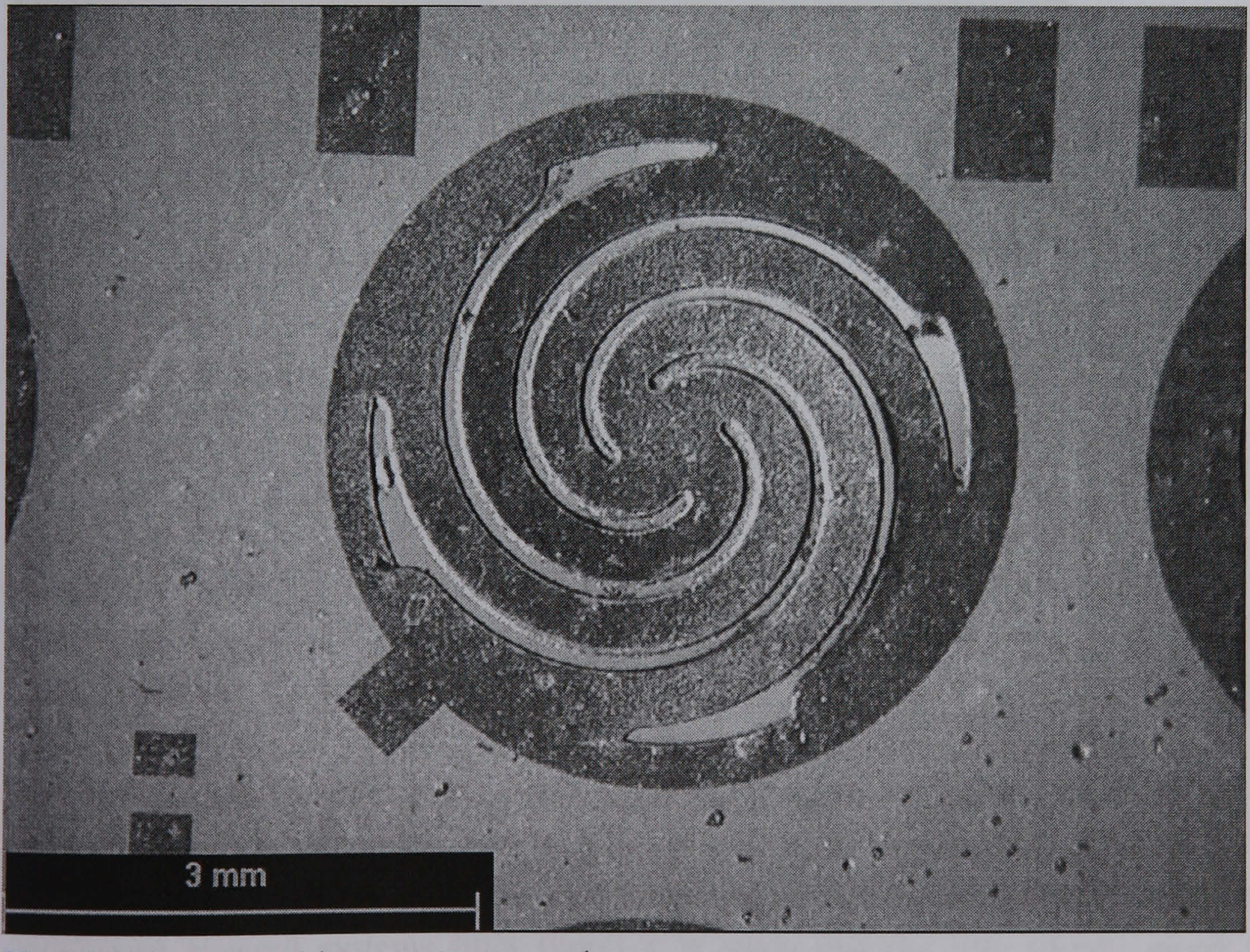

Fig 9.3 Released multi-arm actuator ma4

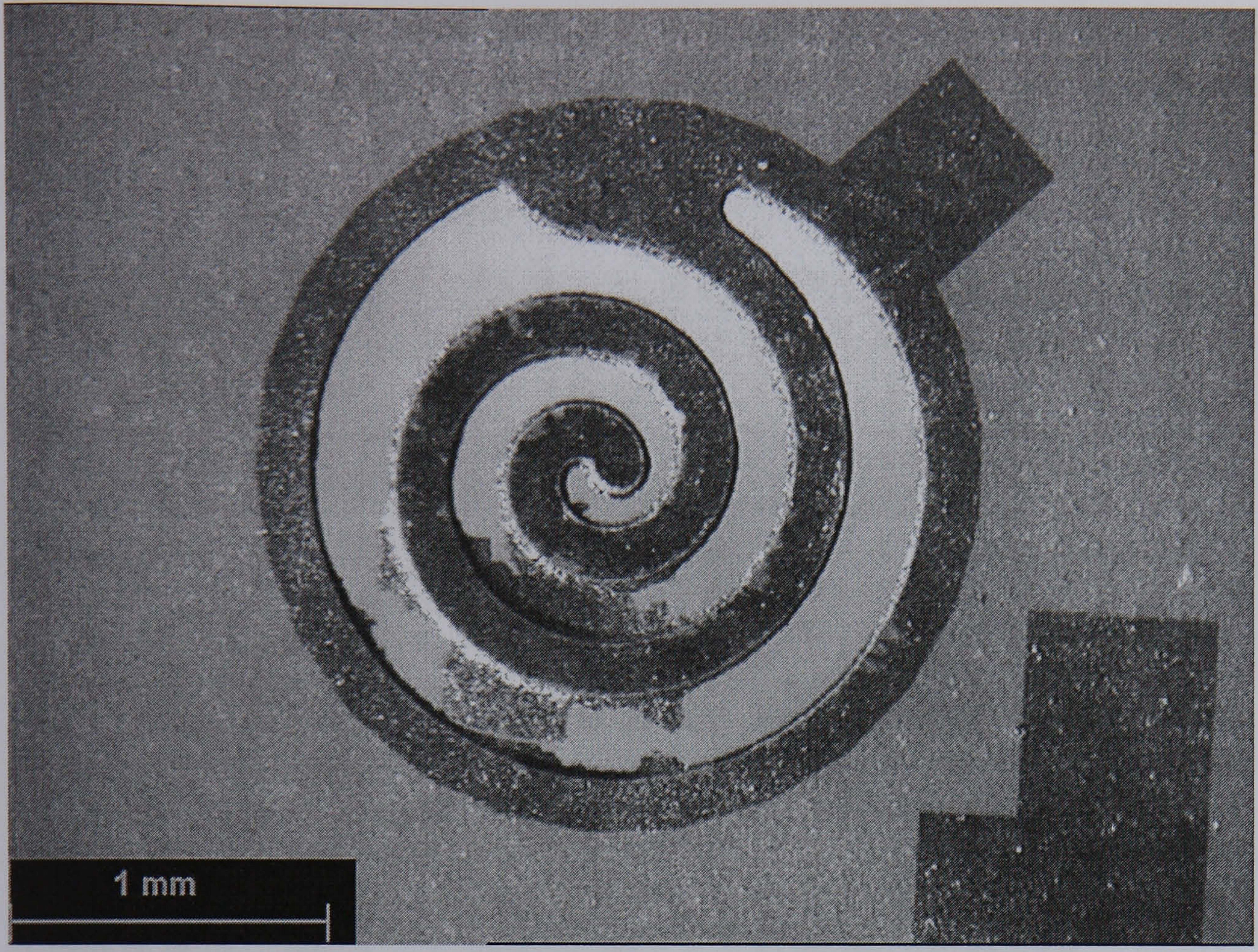

Fig 9.4 Released spiral actuator s5

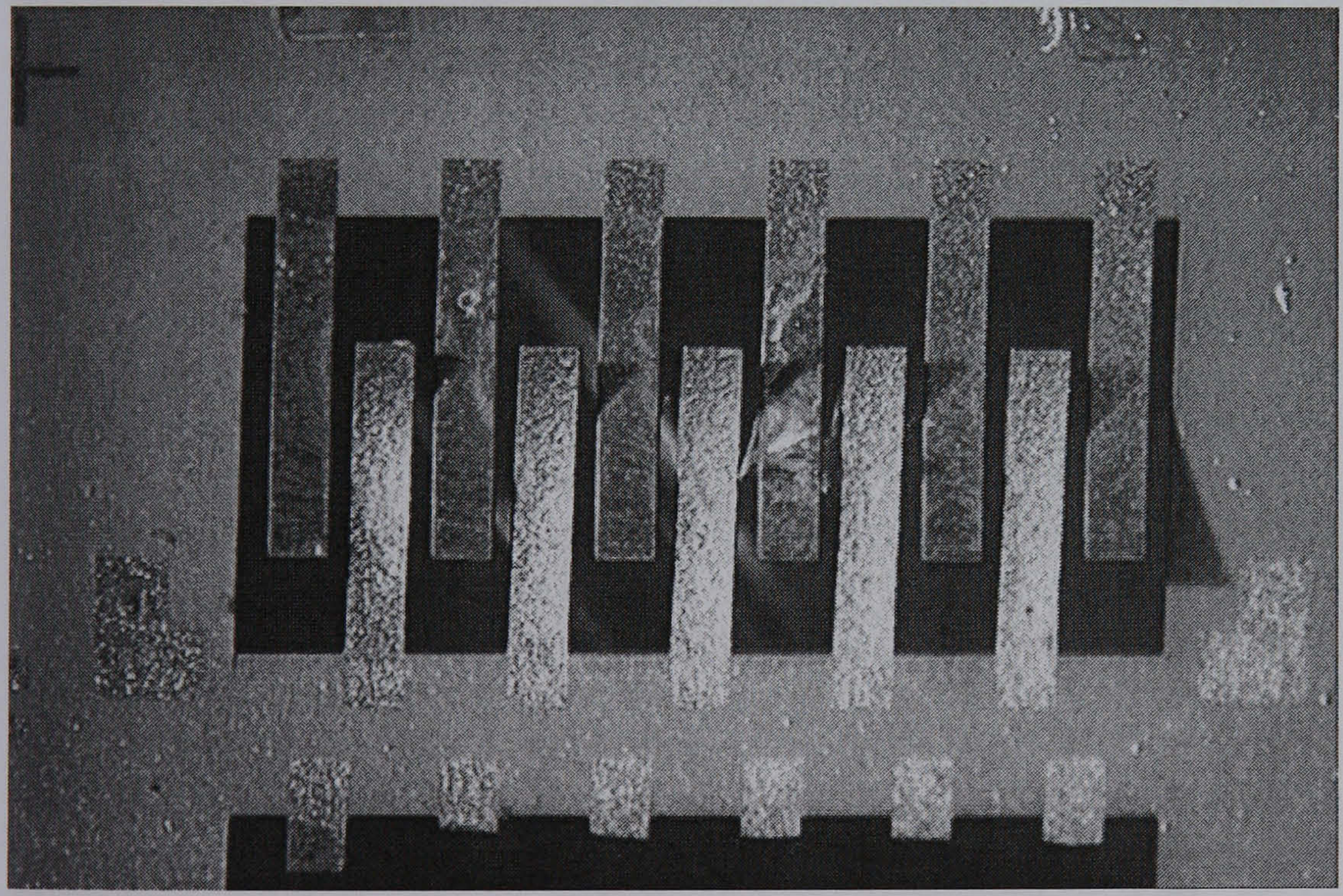

2.0 mm

Fig 9.5 Released array of linear actuators.

On their release, the actuators were observed to deform out of the plane of the wafer indicating that the actuators were pre-stressed. The actuators were observed to curve upwards indicating that the PZT thick film exerted a tensile stress on the cantilever. In constrained sintered systems (thin films) it is taken that the film shrinks along the z-direction; however, only shrinkage in the x-y plane would account for the presence of tensile stress regions in the thick films. The back face of the actuators shown in Fig 9.6

were deliberately bent out of the plane to show actuator thickness and the smooth surface of the released actuators. It was noted that some of the actuators broke away during deep reactive ion etching. It was speculated, that the internal stress, in the actuators, accounted for this.

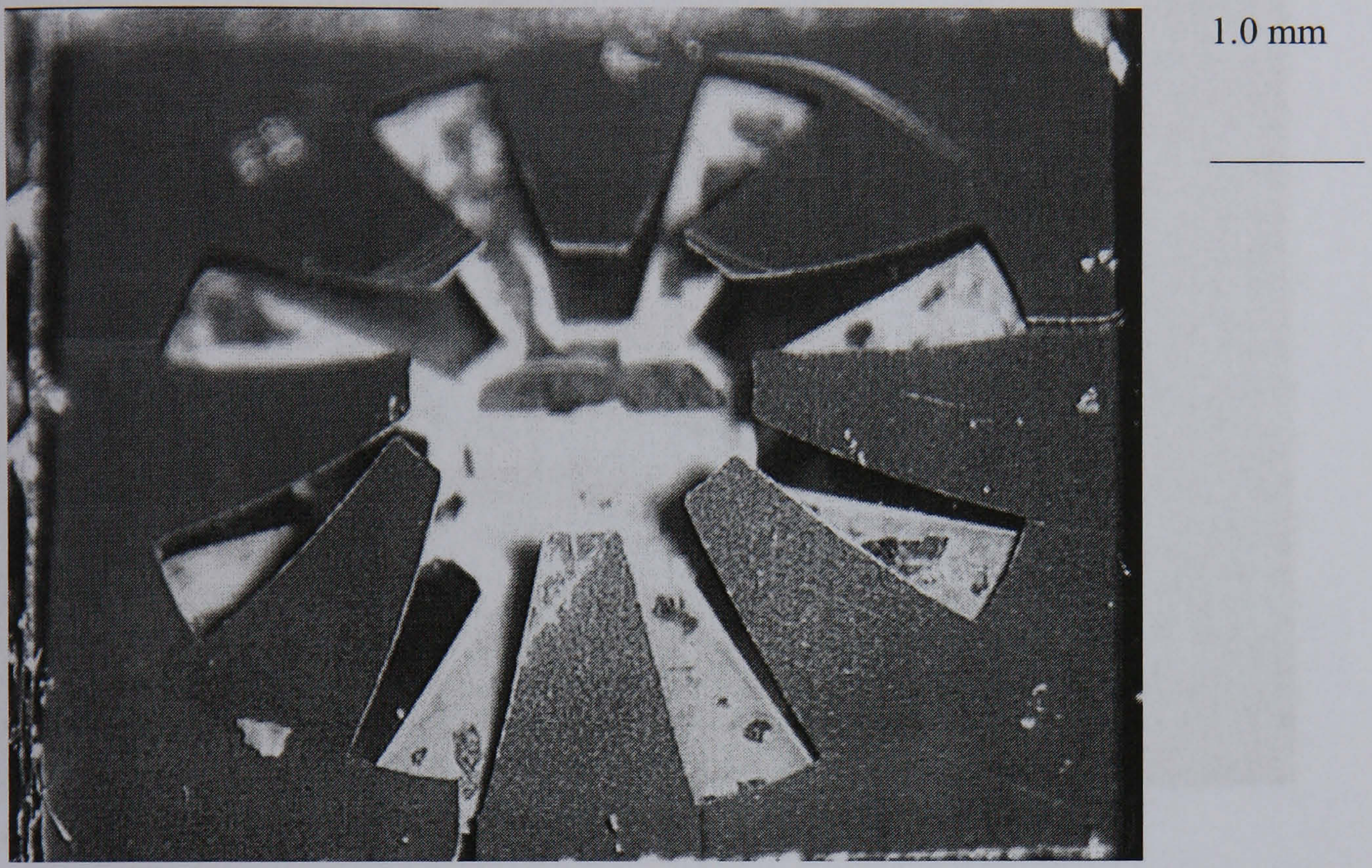

Fig 9.6 Under-side of released spoke actuators sp9.

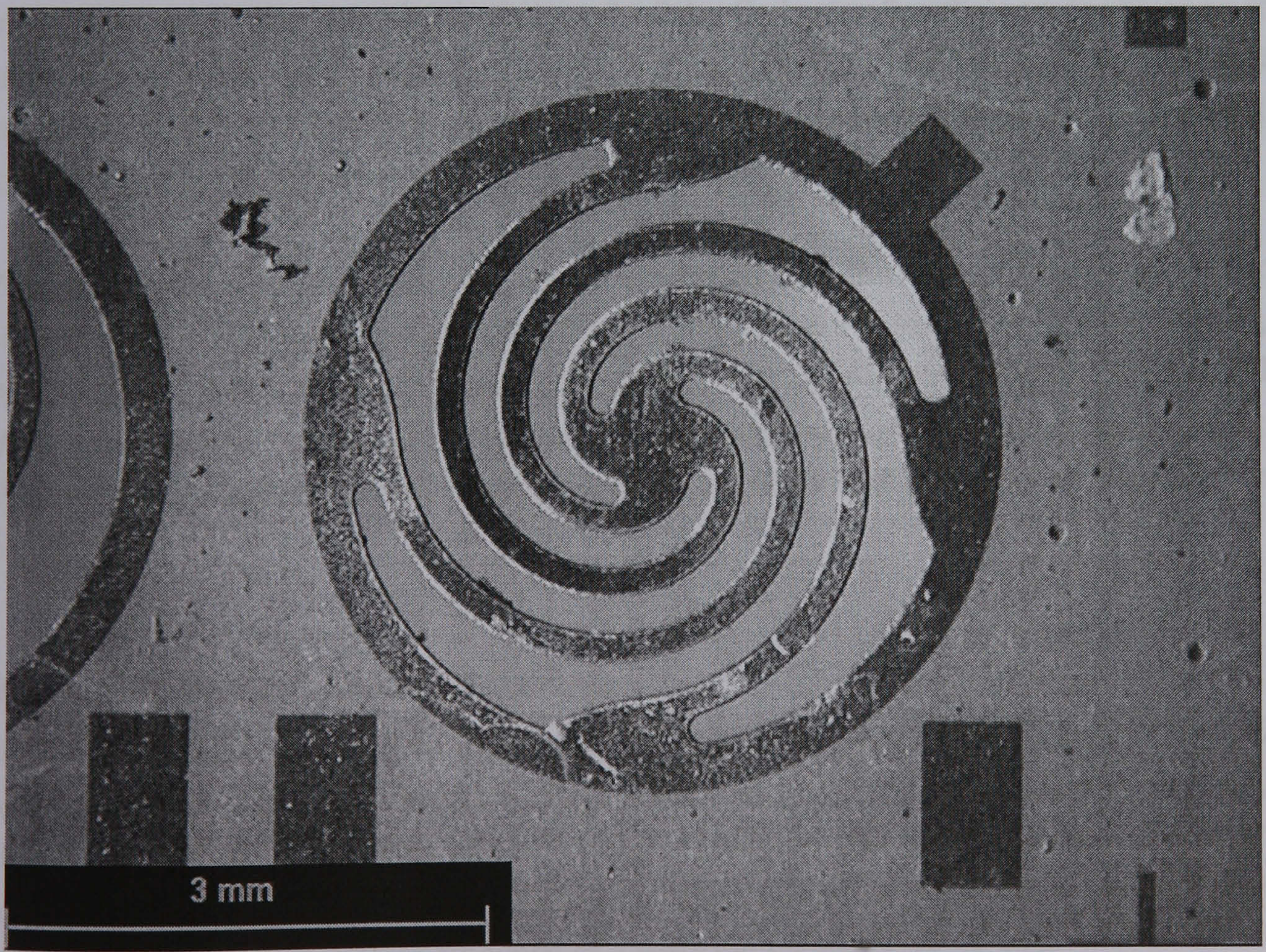

Fig 9.7 Released multi-arm actuator ma 3.

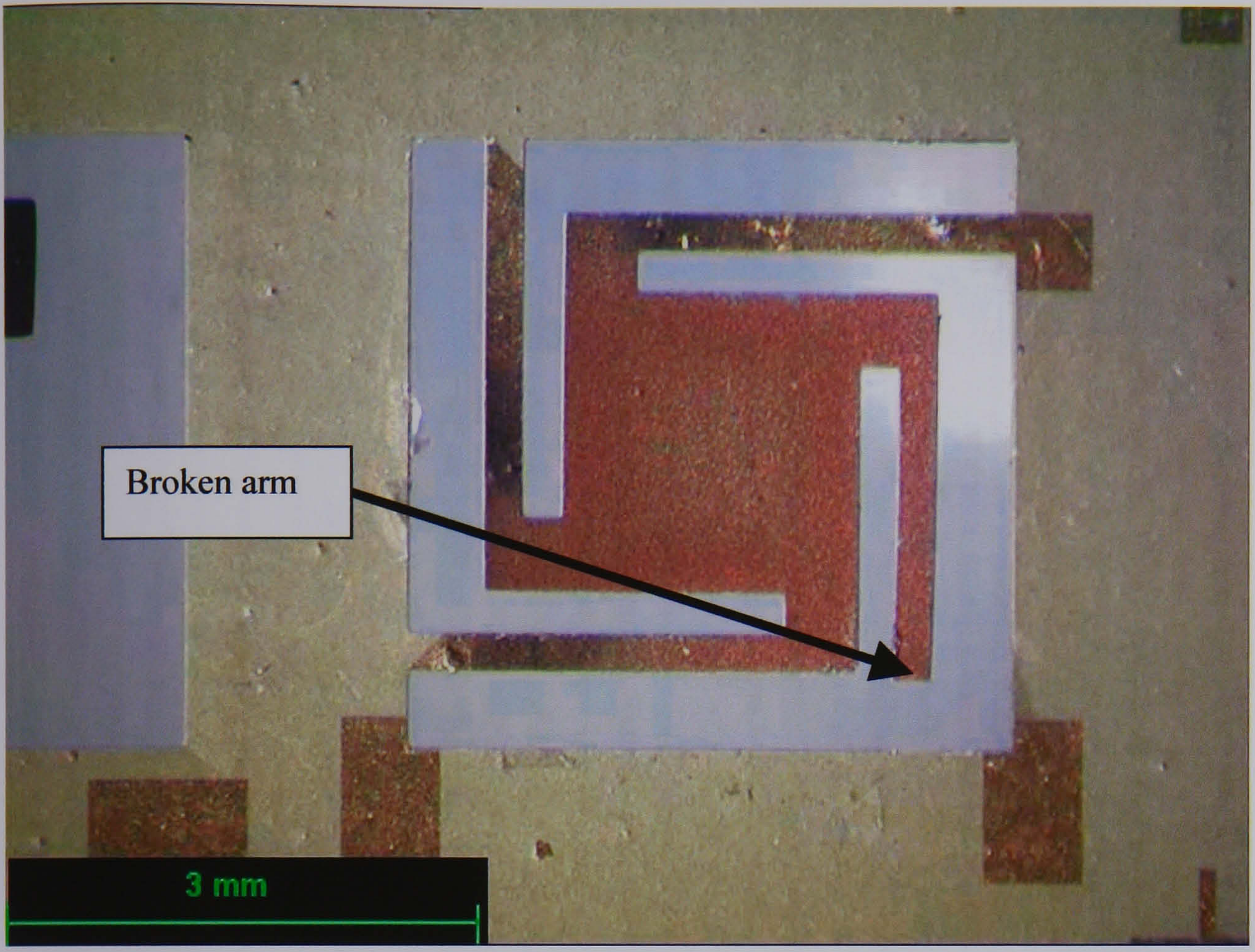

Fig 9.8 Released swastika device. Device broken in processing.

Wafers rh100 and rh200 were prepared with a Cr layer to eliminate back-face staining during PZT thick film deposition. Removal of the Cr layer after the powder blasting stage of processing yielded a clean Si face. There was no damage to either the PZT or the surface electrode. The Cr was left in place until the DRIE stage of processing: preventing scratching of the back face of the wafer.

Pre-stressing of actuators from the lateral contraction of the thick film, during sintering, caused many of the actuators to fail. Many of the actuators simply broke away during the release stage. Some actuators remained attached, but they were damaged. An example is shown in Fig 9.8. A change in colour was observed in highly stressed devices. Fig 9.8 shows that the surface electrode was changed from gold to red. It is unclear why this should be the case.

9.3.2 Admittance Analysis Of Devices

It proved difficult to obtain data from the fabricated devices. In the end, the only reliable spectrum that could be obtained was for a multi-arm device. The device that was used for the measurement is shown in Fig 9.7 above. However, this spectrum, shown in Fig 9.9, clearly showed resonance modes; it should be noted that these modes were very weak. None the less, this spectrum is clear evidence of a working piezoelectric device.

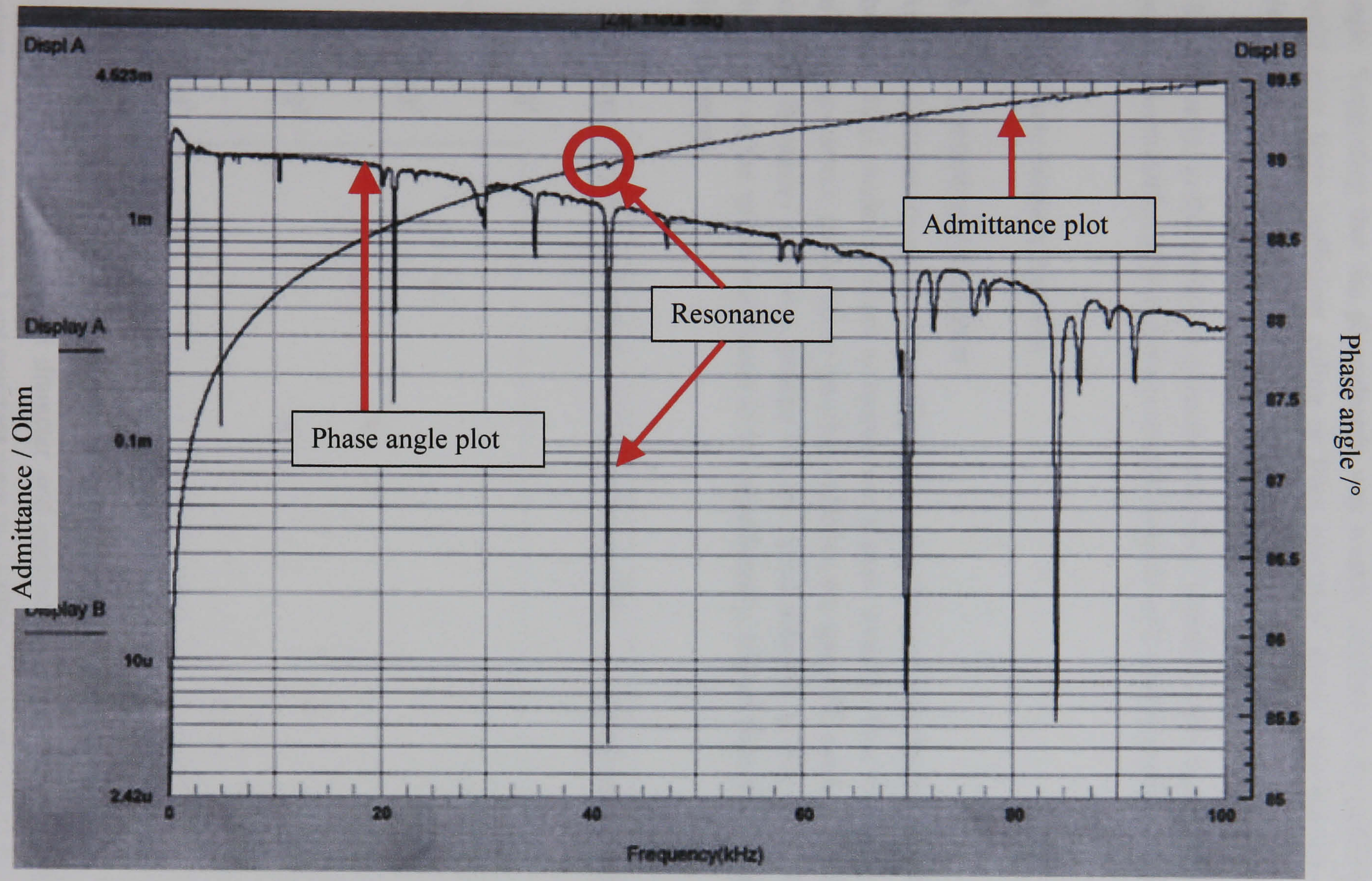

Fig 9.9 Admittance and phase angle scan of a multi-arm device, where $N_{arm}=4$, $w_{spiral}=166.7$ µm, $D_{max}=4$ mm and $N_{turns}=1$. The admittance scale is in Ohm's where u= micro (x 10^{-6}) and m = milli (x 10^{-3}). The scan was measured by Dr. S.A. Wilson.

A spectrum for a multi-arm device is shown in Fig 9.9, above. Weak piezoelectric resonant frequencies can be seen at 40.5, 70 and 83 kHz. The responses observed in the admittance plot were much weaker than the corresponding peaks in the plot of phase angle. Suggesting that the piezoelectric was weakly coupled to the applied field. This could arise from inefficient poling or from electrical shorts between top and bottom electrodes, or from mechanical damping of the actuator.

Unfortunately, in the modal frequencies that were identified, the signal was too weak to permit determination of the effective electromechanical coupling coefficient, $k_{(eff)}$.

9.3.3 *Finite Element Analysis*

9.3.3.1 Frequency Analysis

Actuator frequencies are plotted in Fig 9.10; it may be seen that the frequencies of FE and the analytical model of linear actuators correspond exactly. This indicates that the FE model was correct, and as far as possible validates the spiral FE model. The first mode of resonant frequency was also plotted for the spiral actuator in Fig 9.10. The resonant frequency of the spiral was found to be, significantly, higher than that of an equivalent linear actuator.

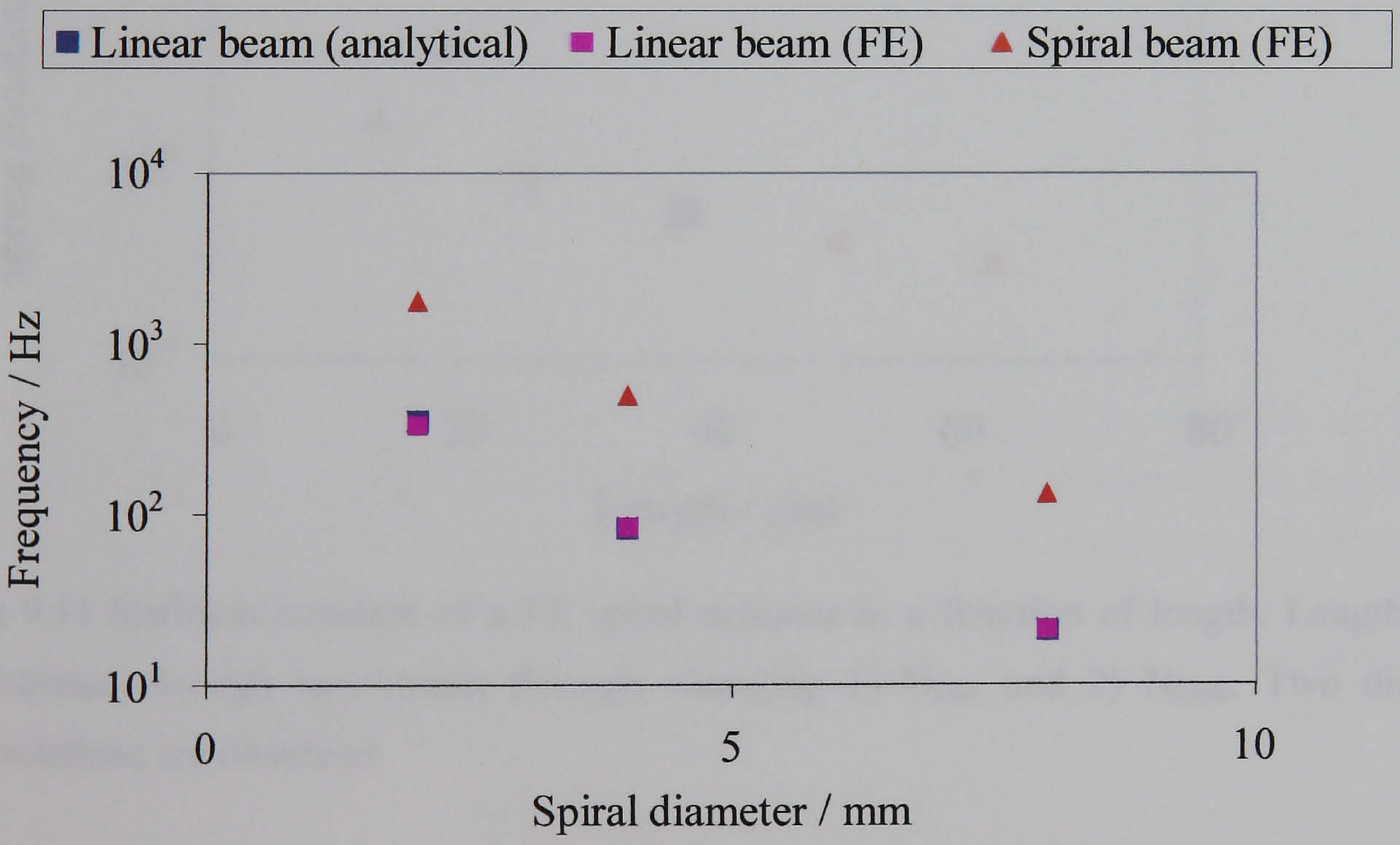

Fig 9.10 Frequency vs. spiral diameter and equivalent length in the case of linear actuators. The parameters kept constant were w_{spiral} (166.7 μm) and N_{turns} (3).

Equation (5.20) of section 5.1.2.3 (or equation (9.1) at the start of this chapter) gives the structural resonant frequencies for a linear unimorph cantilever of equivalent length to a spiral. As frequencies of equivalent length analytical and FE models correspond exactly, it follows that the first mode observed in all FE models was a structural mode. Consequently, the spiral spring constant K_s may be determined using Hooke's law, equation (9.5), where m_a is the mass of the spiral and f_s the first mode of frequency calculated from FE.

$$K_s = m_a(2\pi f_s)^2 \tag{9.5}$$

It should be noted that the subscript s denotes that the quantity was calculated from the FE model of the spiral actuator, and that the subscript spiral denotes calculation from the analytical model of the equivalent-linear-unimorph-actuator.

In the case of a linear beam, $K \propto 1/L$; however, this relationship does not hold for spiral beams. In the case of spirals when K_s was plotted as a function of L_s two distinct sample populations were observed (see Fig 9.11).

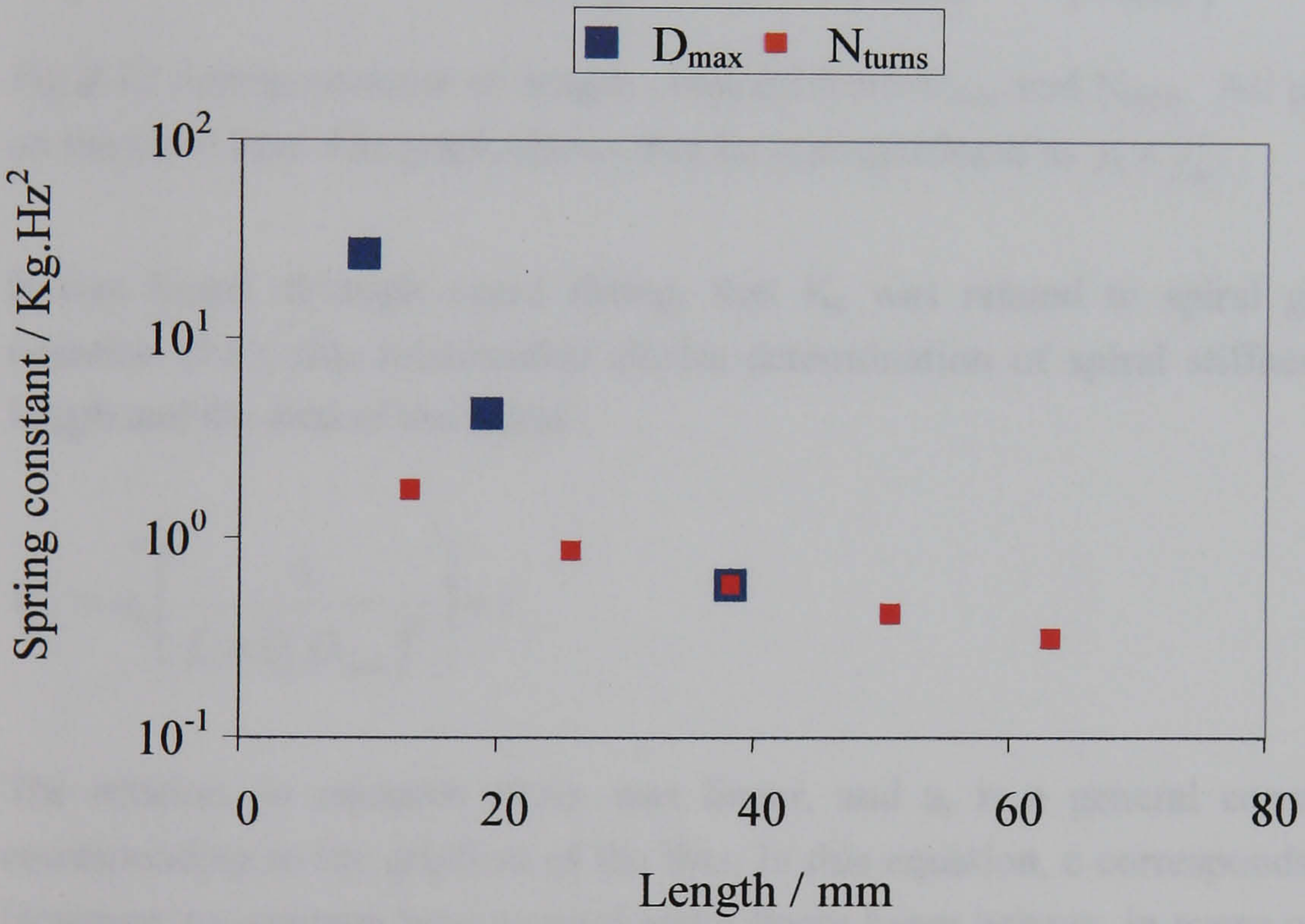

Fig 9.11 Stiffness constant of a FE spiral actuator as a function of length. Length was calculated through two routes through changing 1) D_{max} and 2) N_{turns}. Two distinct populations are observed.

These populations correspond to length as a function of D_{max} and N_{turns}. If K_s were simply a function of L_s then one would expect all points to lie on the same line. The existence of two distinct sample populations, both giving rise to differences in length, suggests that a factor other than length was contributing to K_s. The most logical explanation for this was that the shape of the spiral in some way contributes to the stiffness of the beam. However, plotting data for K_s against $1/(L_s\pi(\frac{1}{2}D_{\max})^2)$ yielded a straight line on which all data points lay (see Fig 9.12).

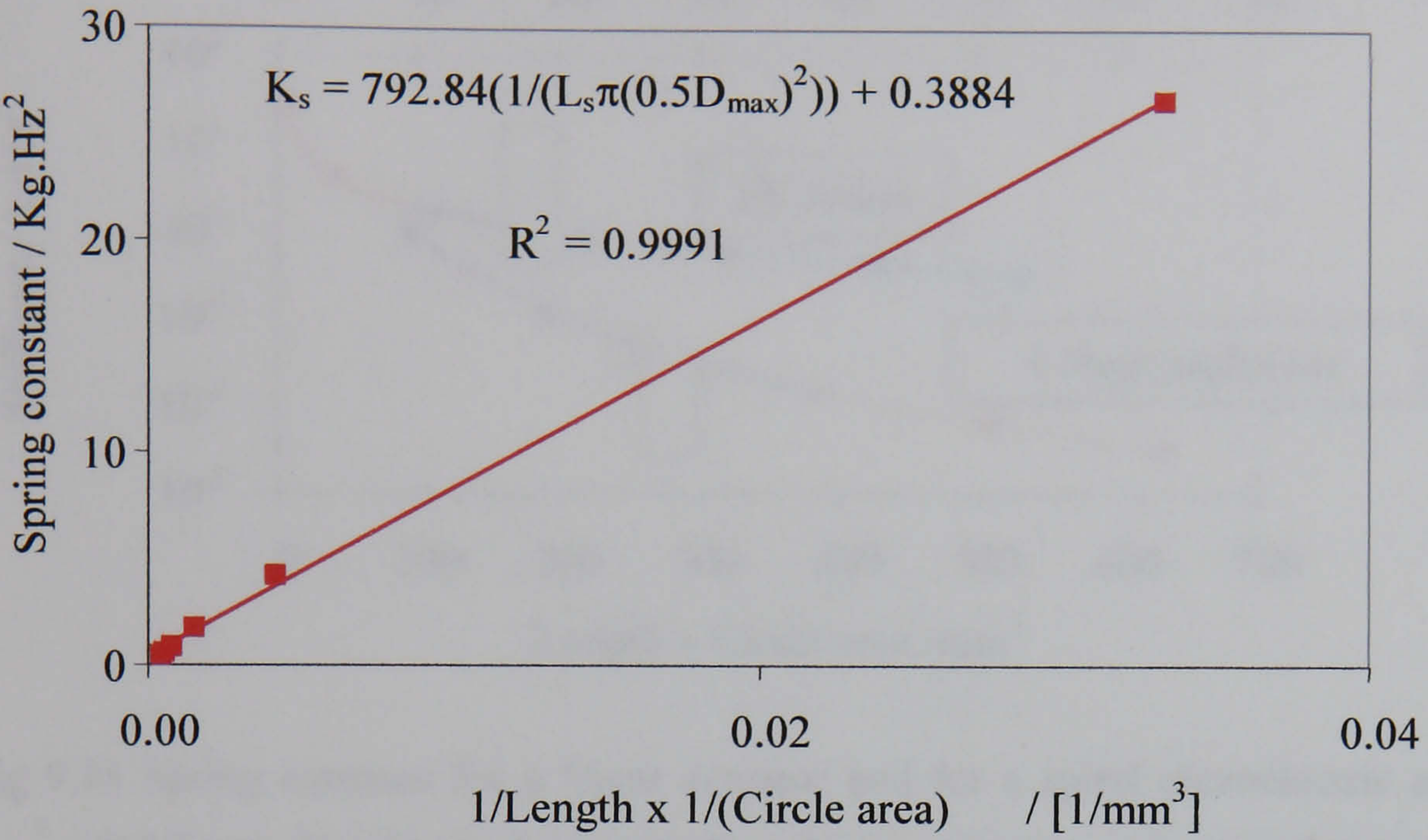

Fig 9.12 Spring constant of length obtained from D_{max} and $N_{turns.}$ All points are plotted on the same line. The graph shows that K_s is proportional to $\frac{1}{L} \times \frac{1}{\pi r^2}$.

It was found, through curve fitting, that K_s was related to spiral geometry through equation (9.6); this relationship allows determination of spiral stiffness from both the length and the area of the spiral.

$$K_s = a_s\left(\frac{1}{L_s\pi.\left(\frac{1}{2}D_{\max}\right)^2}\right) + c \qquad (9.6)$$

The relation, in equation (9.6), was linear, and a_s is a general constant in this case corresponding to the gradient of the line. In this equation, c corresponds to the intercept. However, to compare how a spiral and a linear beam behave, in terms of spring constant as a function of shape, it was necessary to plot values for K_s and K_{spiral} on a log scale (see Fig 9.13, overleaf). The spiral was much stiffer than the linear actuator. Further, K_s and K_{spiral} exhibit an inverse relation ship to D_{max}.

9.3.3.2 Cantilever Deflection

Good agreement was found between FE and analytical models for the out of plane deflection of the linear cantilever (Fig 9.14, overleaf) with respect to spiral diameter. The out of plane deflection of the spiral actuator was significantly lower than that of an equivalent linear actuator because of the greater spiral stiffness.

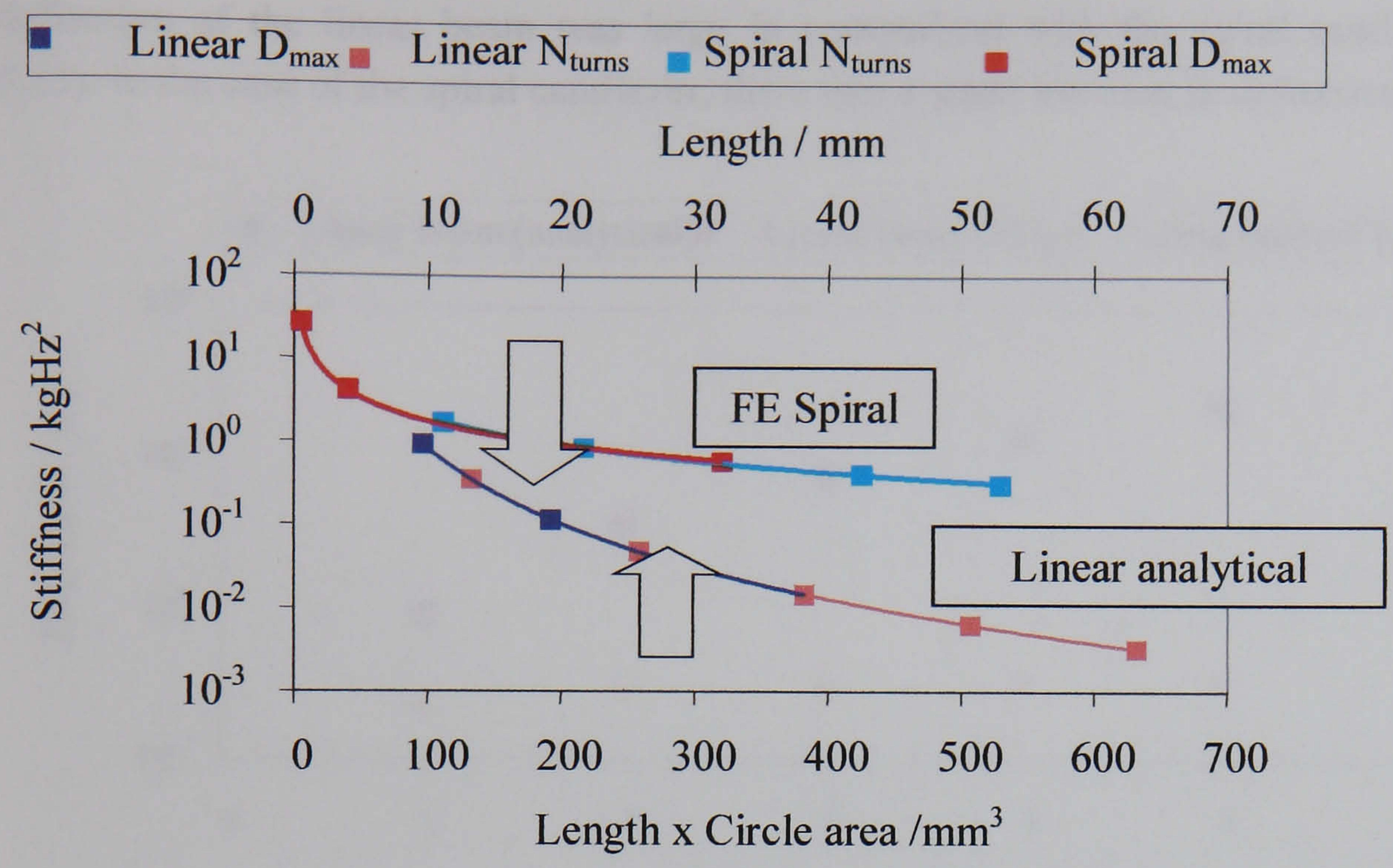

Fig 9.13 Spring constant for a linear actuator and for a spiral piezoelectric actuator of w_{spiral}=166.7 μm. The figure shows that for a linear actuator, where length was calculated from N_{turns} and D_{max}, all points lie on the same line. The figure shows that for a spiral beam all points lie on the same path only if K_s was plotted as a function of length x area.

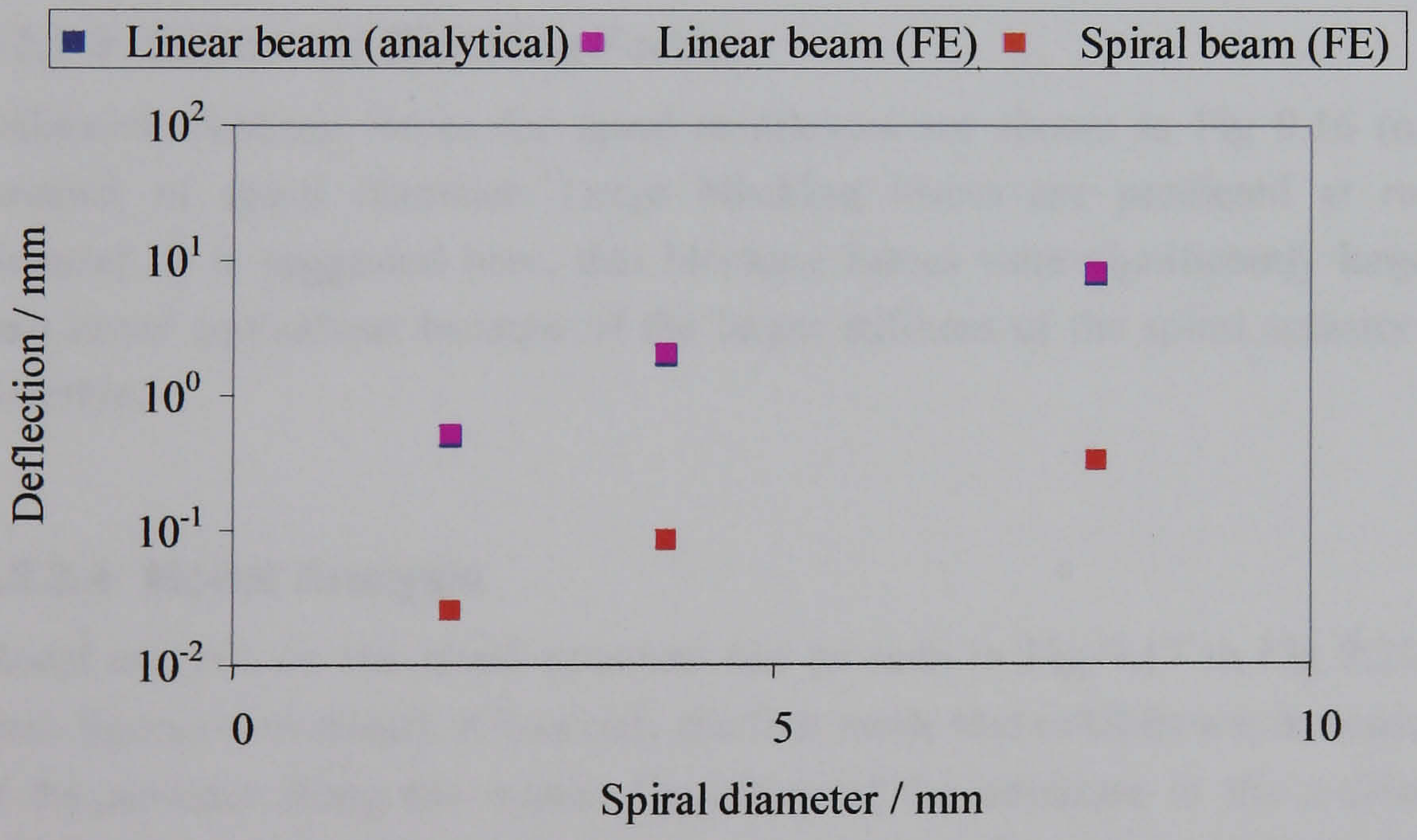

Fig 9.14 Deflection vs. spiral diameter and equivalent length in the case of linear actuators. The variables kept constant were w_{spiral} = 166.7 μm and N_{turns}=3. The diameter, D_{max}, was varied through 2 to 8 mm.

The spiral diameter was fixed and the number of spiral turns increased from 1 to 5. As the number of spiral turns was increased the equivalent length of the cantilever (linear or spiral) also increased and the stiffness of the cantilever decreased. Accordingly, the deflection of the linear beam was large in comparison with the spiral cantilever (Fig 9.15). In the case of the spiral cantilever, there was a small increase in deflection.

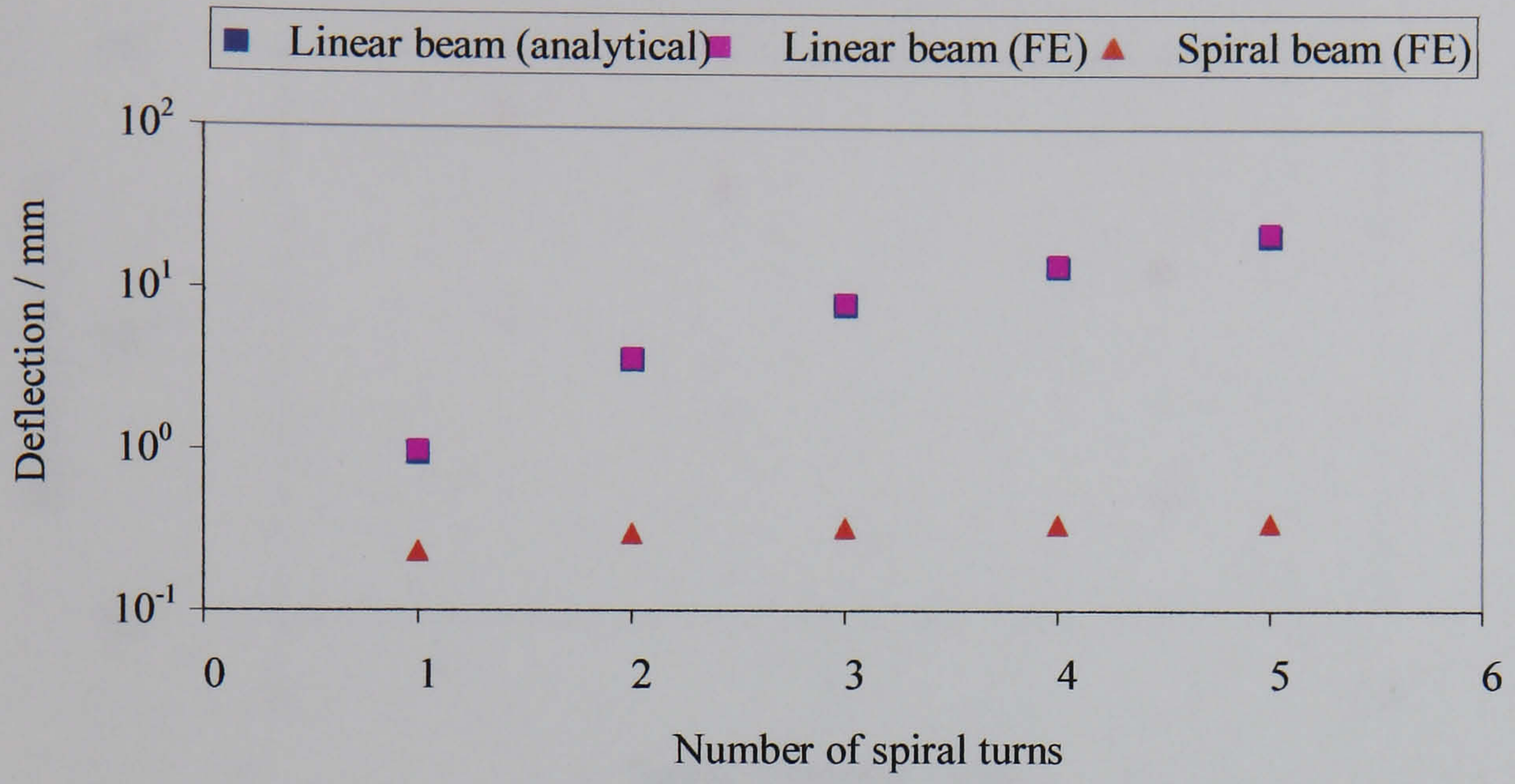

Fig 9.15 Deflection as a function of the number of spiral turns and equivalent length (in the case of a linear actuator). The Spiral had the following dimensions: D_{max} = 8 mm, w_{spiral} = 166.7 μm and N_{turns} was varied through 1 to 5.

9.3.3.3 Estimated Blocking Forces

Estimated blocking forces for spiral cantilevers are shown in Fig 9.16 (overleaf) as a function of spiral diameter. Large blocking forces are predicted at reduced spiral diameter. It is suggested here, that blocking forces were significantly larger for spirals than linear equivalents because of the larger stiffness of the spiral actuator along the z-direction.

9.3.3.4 Modal Analysis

Modal analysis on the spiral structure can be seen in Fig 9.17 to Fig 9.21 (the first of these figures is overleaf). It was only the first mode that exhibits a symmetrical deflection of the actuator along the z-axis. Operation of the structure in the z-direction can be achieved by driving the structure at the first mode of resonance. The inner coils of the spiral demonstrate the least movement under the excitation. In the case of a spiral beam of N_{turns} the radius at each turn will be $r_{N'_{turns}}$, and this parameter was defined in equation (9.7).

$$r_{N'_{turns}} = \left(w_{spiral} + w_{void}\right)N'_{turns} \tag{9.7}$$

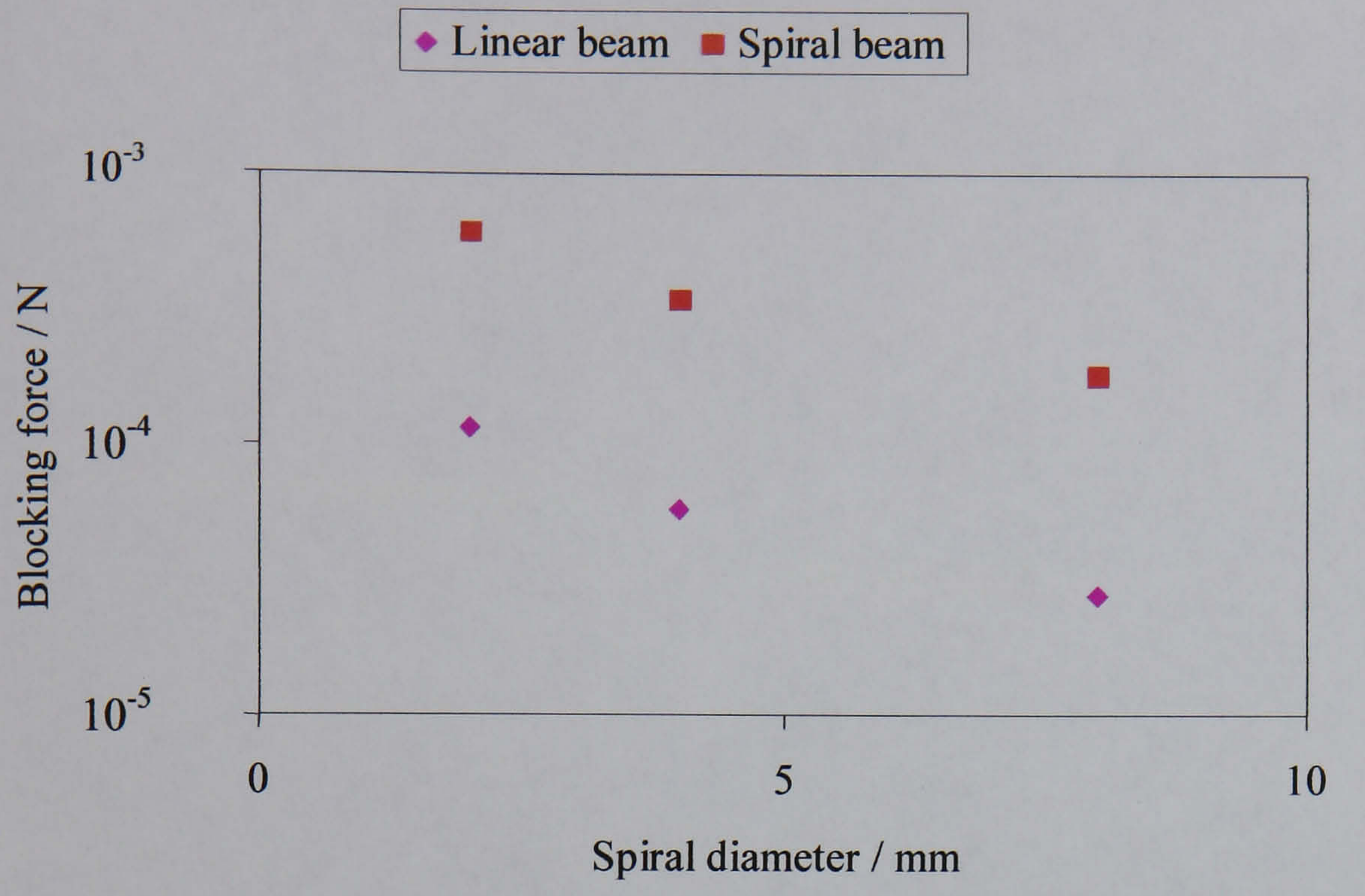

Fig 9.16 Estimated blocking force as a function of spiral diameter. The dimensions that were kept constant were w_{spiral} = 166.7 μm and N_{turns} = 3. The diameter D_{max} was varied between 2 and 8 mm.

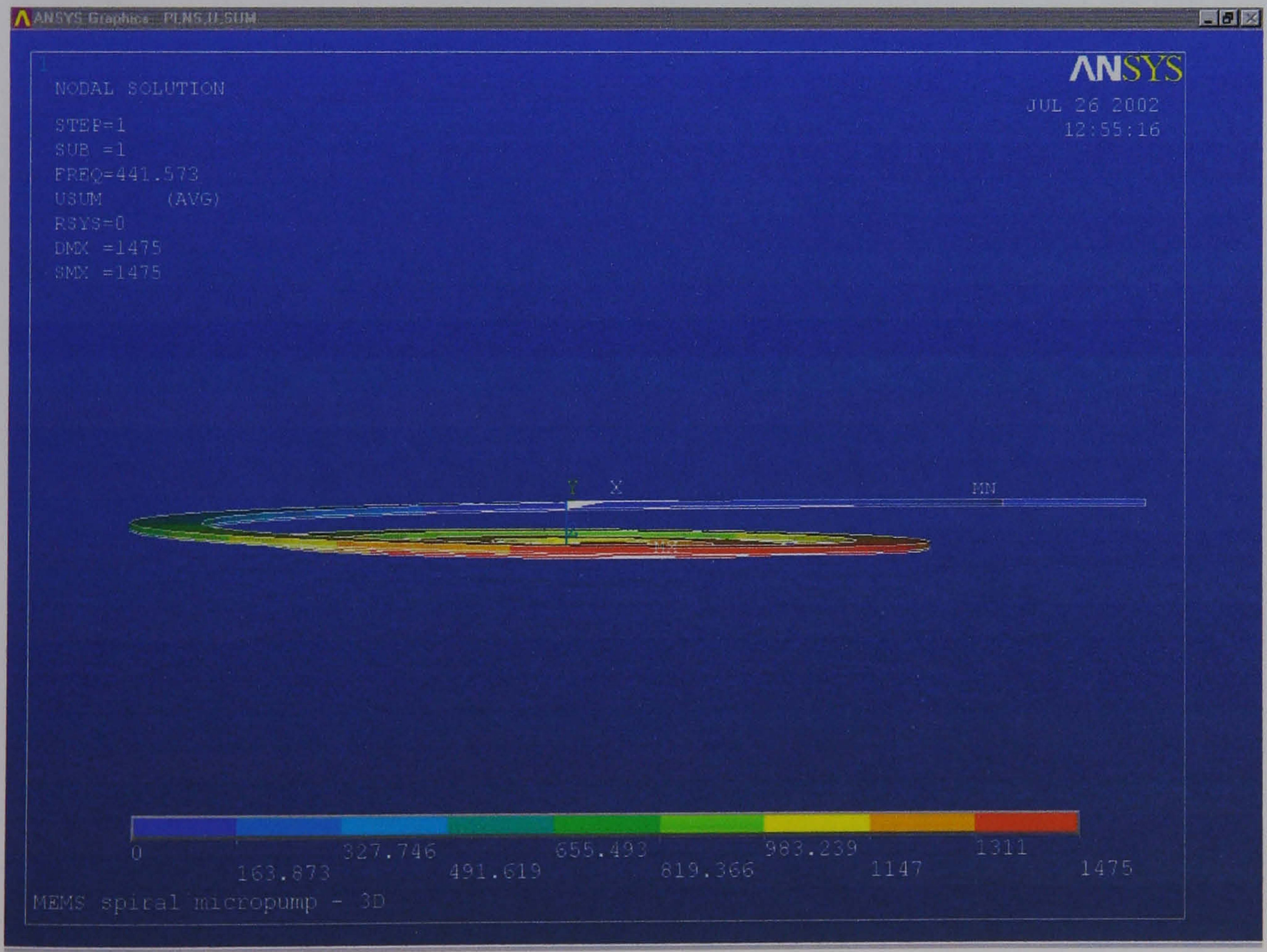

```
NODAL SOLUTION

STEP=1
SUB =1
FREQ=441.573
USUM       (AVG)
RSYS=0
DMX =1475
SMX =1475
```

Fig 9.17 Spiral actuator 1st modal frequency.

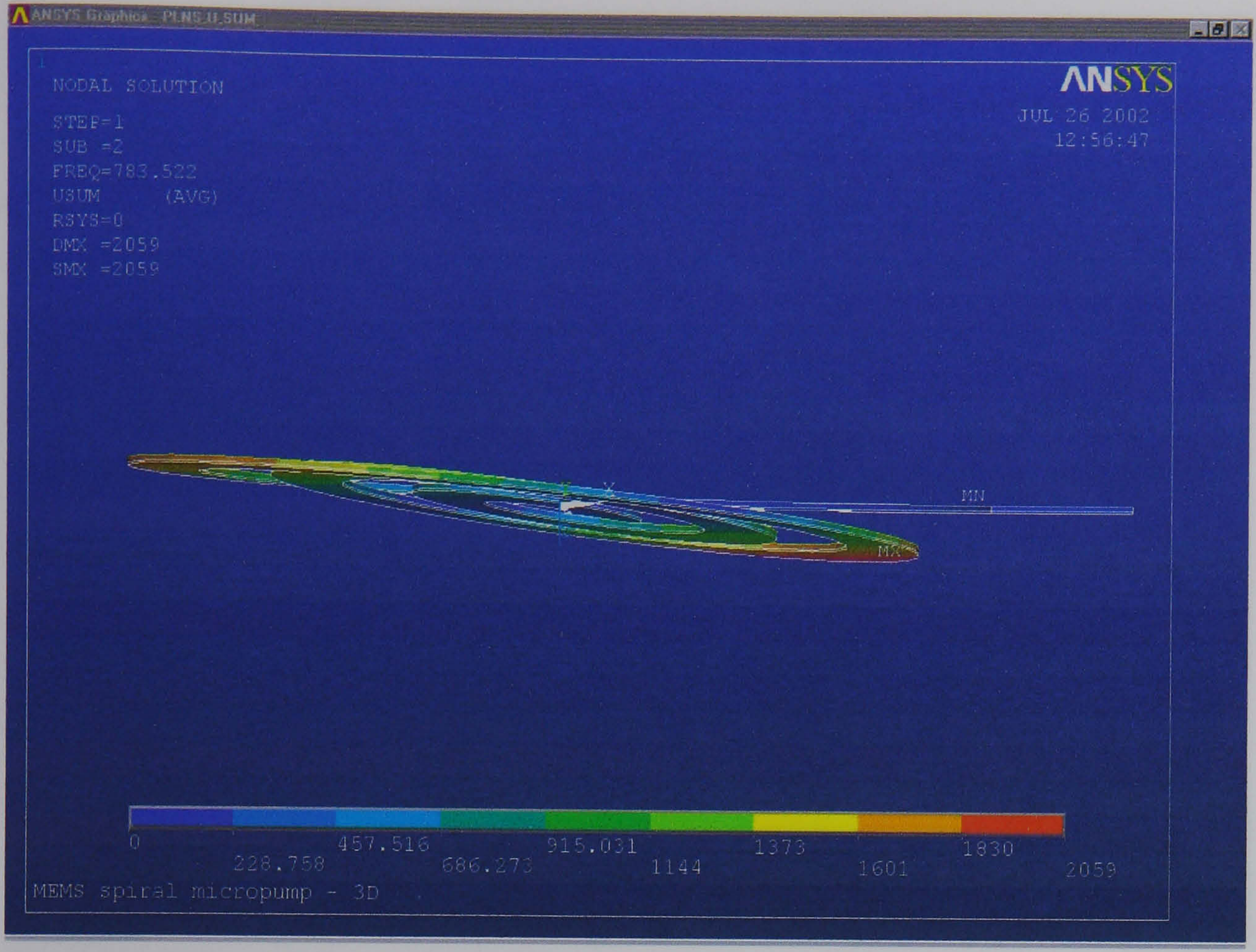

```
NODAL SOLUTION

STEP=1
SUB =2
FREQ=783.522
USUM      (AVG)
RSYS=0
DMX =2059
SMX =2059
```

Fig 9.18 Spiral actuator 2nd modal frequency

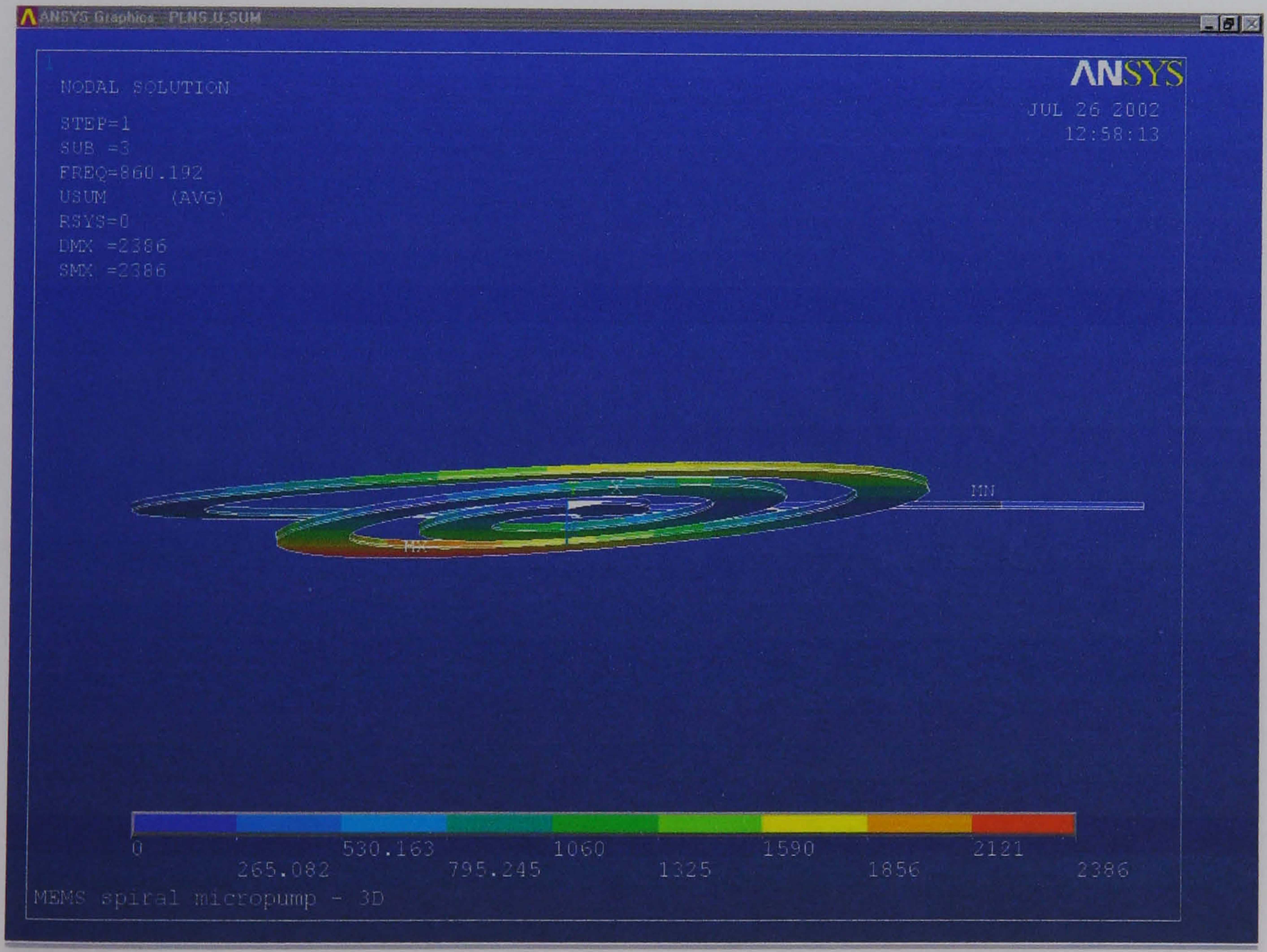

```
NODAL SOLUTION

STEP=1
SUB =3
FREQ=860.192
USUM      (AVG)
RSYS=0
DMX =2386
SMX =2386
```

Fig 9.19 Spiral actuator 3rd modal frequency.

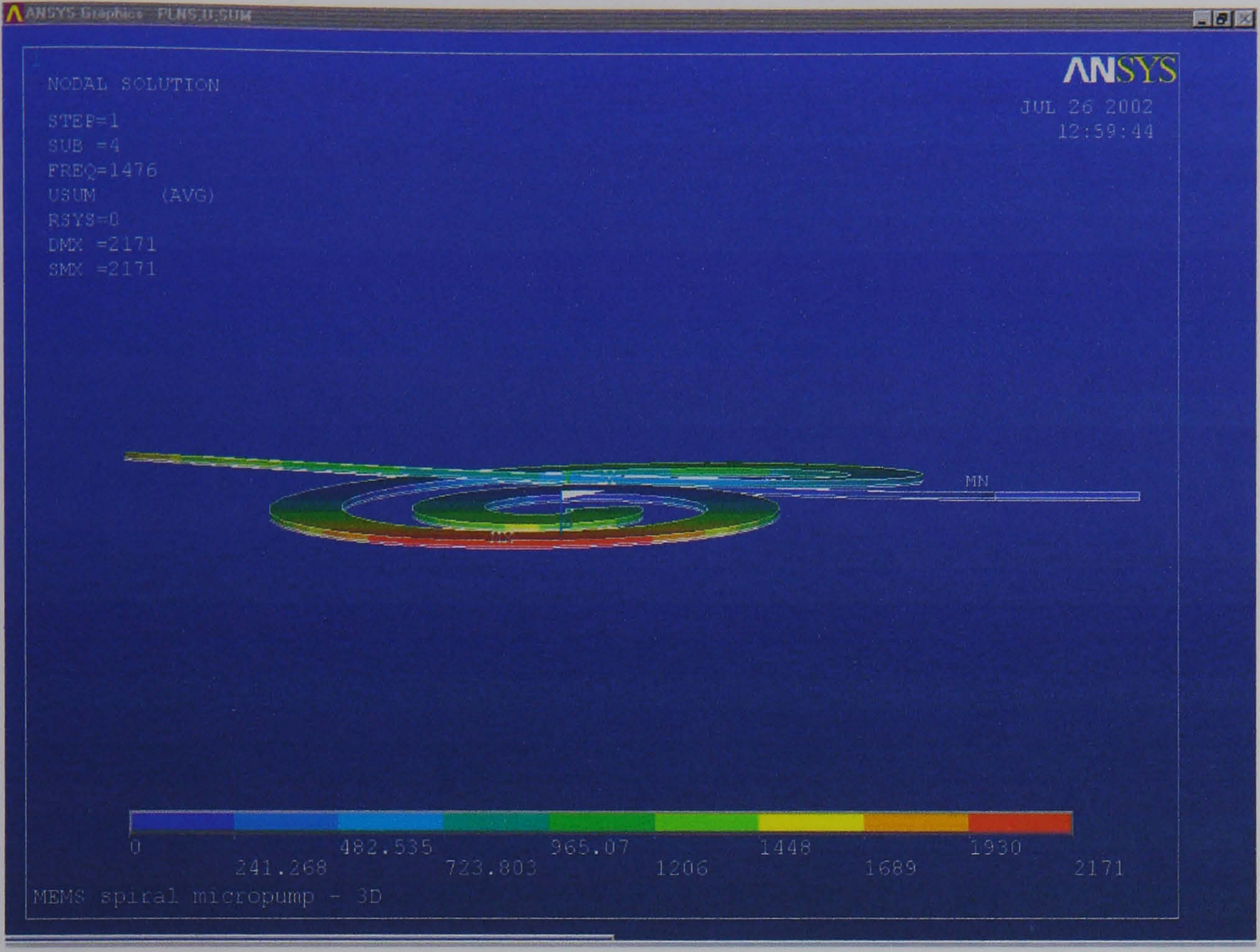

```
NODAL SOLUTION

STEP=1
SUB =4
FREQ=1476
USUM      (AVG)
RSYS=0
DMX =2171
SMX =2171
```

```
JUL 26 2002
12:59:44
```

```
MEMS spiral micropump - 3D
```

Fig 9.20 Spiral actuator 4th modal frequency

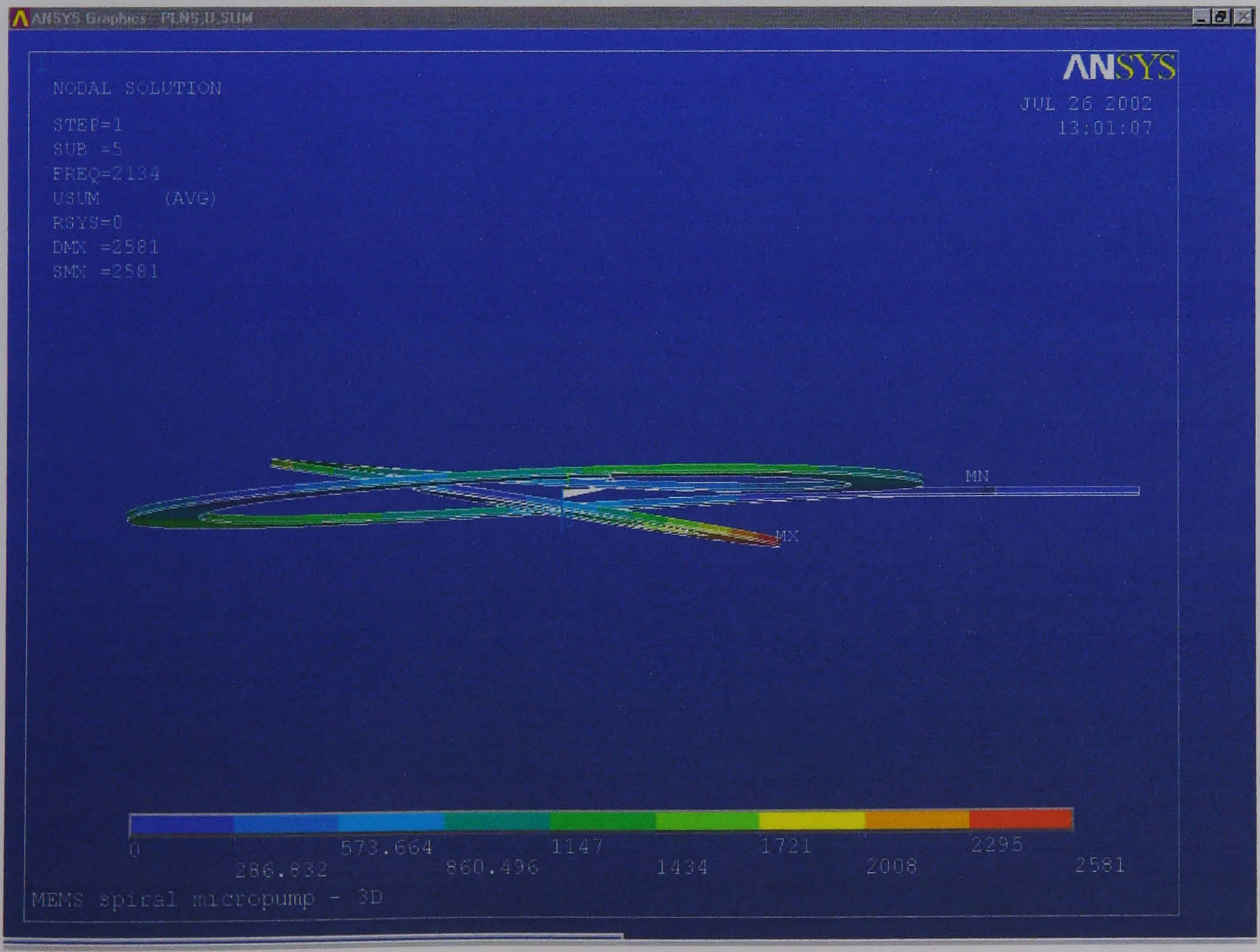

```
NODAL SOLUTION

STEP=1
SUB =5
FREQ=2134
USUM      (AVG)
RSYS=0
DMX =2581
SMX =2581
```

```
JUL 26 2002
13:01:07
```

```
MEMS spiral micropump - 3D
```

Fig 9.21 Spiral actuator 5th modal frequency.

The parameter N'_{turns} denotes an integer value, i.e. a whole rotation or whole number of rotations through 360 °; where N'_{turns} is any integer value up to N_{turns}. N'_{turns} will start at the origin of the spiral and increase in value toward the terminus.

$$N'_{turns} = 0,1,2....N_{turns} \qquad (9.8)$$

Then, it follows that, for each rotation of the spiral, moving outward from the centre, the area of the spiral will increase according to equation (9.9).

$$\frac{1}{\pi.r_1^2} > \frac{1}{\pi.r_2^2} > \frac{1}{\pi.r_{N^1_{turns}}^2} \qquad (9.9)$$

The spring constant K_N will change with each rotation in proportion to the radius (see equation (9.10)).

$$K_{N^1_{turns}} \propto \frac{1}{\pi.r_{N^1_{turns}}^2} \qquad (9.10)$$

The inner coils of the spiral will exhibit the greatest stiffness and resistance to deflection:

$$\therefore K_1 > K_2 > ..K_{N^1_{turns}} \qquad (9.11)$$

The effect of the thickness of the mechanical support was investigated (see Fig 9.22). It can be seen that as B (thickness ratio h_m/h_p) is increased that the modal frequency was increased. Further, at higher modes (9 or 10 and possibly above) the increase in frequency with B becomes huge. Mode 9 at B=25 corresponds to a tangential deflection. Modes 8 and 10 at B=25 correspond to out of plane flapping similar to that observed in Fig 9.21. Mode 8 at B=15 corresponds to a flapping action. Modes 9 and 10 at B= 2.5 correspond to flapping. All other mode shapes remain constant irrespective of substrate thickness. In all cases of B that were considered, the fundamental mode, as shown in Fig 9.17, always remained the same.

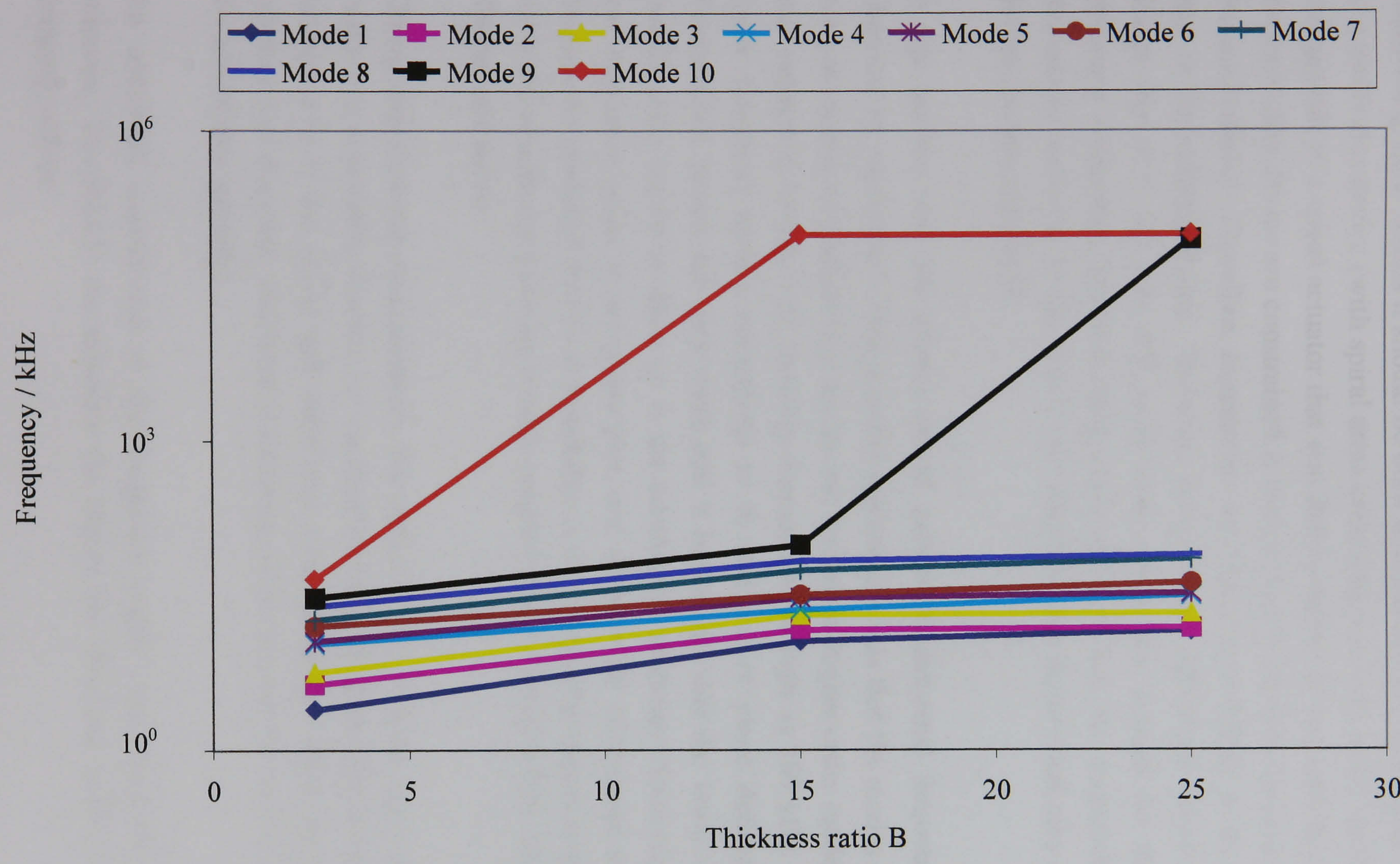

Fig 9.22 Modal frequencies, as a function of the thickness ratio B, for a spiral actuator. All data calculated by FE for an actuator of $N_{turns}=2$, $D_{max}=2$ mm and $w_{spiral} = 166.7$ µm

9.3.4 Comparison Of FE With Experimental Data From The Admittance Spectrum

This subsection compares the frequencies calculated by FE (see Fig 9.10) with the admittance spectrum discussed earlier (see Fig 9.9 and section 9.3.2 above). In interpreting these results it should be born in mind that the admittance curve corresponds to a multi-arm device (with spiral arms constrained at both ends), and that the FE model corresponds to a spiral actuator that was free to deflect at one end. Because the spirals of the multi-arm device are constrained at both ends it is likely to be structurally stiffer than the spiral device. Therefore, frequencies are likely to be higher in the experimental plot than in the calculated data. However, such was the difference between experiment and theory that it is felt that this point alone might not account for the difference. The structural difference between these two devices will be considered further in the discussion; however, in the rest of this chapter other factors that may have a bearing on the results are considered.

It was unclear why FE spirals should exhibit fundamental frequencies $\frac{1}{10}$ of those observed by experiment. One possible explanation was that the modes seen in Fig 9.9 do not correspond to fundamental modes but instead to higher order modes. This possibility was supported by Fig 9.22 showing frequencies as high as 100 kHz. These higher and lower frequency modes correspond to in and out of plane deflections respectively. Piezoelectric modes are very weak and it is possible that the lower order modes were insufficiently strong to show up in the admittance spectrum. However, there were some low frequency peaks in the phase plot, and these might correspond to the lower modal frequencies modelled by FE. A possibility is that peaks that appear in the phase angle but not in the admittance plots are weakly coupled modes that have been damped out by some mechanical means.

During experimental measurements, the surface of the actuator was surrounded by an air cushion. It is possible, that the air 'cushion' acted to mechanically damp modes. The large surface area of the spiral and multi-arm actuators makes these devices susceptible to squeeze film damping. Mechanical damping could account for weak and absent modes in the admittance spectrum.

An additional contribution to the frequency could come from the thickness of the substrate. The thicker the substrate the higher the observed frequency and mechanical damping will be.

In Fig 9.22 the fundamental frequency was shifted from 2.5 kHz to 15 kHz; corresponding to an increase in substrate thickness from 25 to 250 μm. An increase in the thickness of the mechanical support is unlikely, by itself, to account for the higher frequencies observed. Higher frequency modes are more likely to account for the anomaly between experiment and theory.

Another explanation might lie in differences between materials properties of Motorola HD3203 (used in the modelling of actuators) and the PZ26 material used in the fabrication of the actuators. The frequency is proportional to A. As Motorola HD3203 is a slightly softer material than PZ26 its A value will be higher; therefore, frequencies calculated using Motorola HD3203 should be lower than those calculated with PZ26. If, however, PZ26 was used to fabricate actuators and Motorola HD3203 was used to model the same devices (as was the case) then experimentally observed frequencies would be expected to be higher than those obtained from theory. Indeed this was the case; however, the difference between calculated frequencies for each material is<1 kHz, and this was too small to account for the observed differences in frequencies.

It seems most likely that the higher frequencies seen in Fig 9.9 were due to higher frequency modes, and lower modes were damped out. The cause of the damping seems less clear; it could be either squeeze film damping or in part due the thickness of the mechanical support. A further possibility is inefficient poling of the piezoceramic. Certainly, the effects arising from the use of different materials, between experiment and model, can be eliminated as a cause of any ambiguity. The existence of phase peaks at around 4 kHz corresponds quite nicely with calculated modes from FE, and confirms that the actuators are piezoelectrically active.

9.4 Acknowledgement

The author particularly wishes to acknowledge the help and assistance given by Mr. J. Southin. Who assisted in the writing of computer code; this code was used for the generation of the spiral shape in Ansys®.

10 Discussion

10.1 Introduction

In this section, material from each of the results chapters is brought together and discussed with reference to the literature review. PZT etching in dilute HF(aq) is discussed first followed by a discussion of powder blasting. A discussion of electrical and piezoelectric properties of PZT thick films and how these properties are effected by po_2 during sintering is next. There is also a discussion of the effects of po_2 on the stability of the back electrode. Process integration and device fabrication is discussed next. The final section of this chapter is the discussion of FE spiral and fabricated devices; this section discusses the FE modelling of spiral and other devices in the light of literature and materials properties.

10.2 PZT Etching

In section 7.3.2 of chapter 7, two precipitates, labelled as A1 and B1, were observed to form in the wet etching of PZT. A1 and B1 formed on the exposed back electrode and exposed PZT surfaces respectively. Bernstien and Miller [127] have observed the formation of a white precipitate on the surface of the PZT during wet etching. The precipitate was difficult to remove and they have speculated on its composition: PbF_2, $PbCl_2$ or $Pb(OH)_2$. Please note that B1 was also a white precipitate that proved difficult to remove from the PZT surface. The precipitate A1 was not white, and it formed only on the Pt surface and not on the PZT surface.

Bernstein and Miller [127] used an etching solution based on $HCl_{(AQ)}$ and $HF_{(AQ)}$; this solution incorporated HNO_3, HCOOH and NH_4Cl to dissolve PbF_2, $Pb(OH)_2$ and $PbCl_2$ salts respectively. The difficulty in incorporating HNO_3 and HCl into an effective etching solution to remove PZT from a back electrode, is the stability of the back electrode to the etching solution: Pt reacts with aqua regia [107] (3:1 HCl:HNO_3). The etching solution, used in chapter 7 above, contained only $HF_{(AQ)}$ and $HCl_{(AQ)}$ and none of the other ingredients used in the literature [127] to dissolve precipitates. Therefore, precipitation of PbF_2, $PbCl_2$ and $Pb(OH)_2$ was expected in samples etched in this project. The precipitate, B1, was found to be highly soluble in HNO_3, suggesting that B1 is PbF_2 and not $PbCl_2$.

The formation of crystalline material, C1, through the cracks in the film shown in Fig 7.24 was considered to be either PbO or $Pb(OH)_2$ in chapter 7 above. However, EDX would no more detect the difference between PbO and Pb than the difference between PbO and $Pb(OH)_2$. Definitive identification of C1 has not been possible. The formation of C1 through the cracks in the PZT indicates that it has resulted from the depletion of the PZT material and not as a precipitation product of the etching solution. It will be argued, below, that C1 is PbO that has been depleted from the PZT.

The EDX analysis of the precipitated material, A1, indicated that it was composed of $PbCl_x$. Therefore, it is suggested here that A1, B1 and C1 were $PbCl_2$, PbF_2 and PbO respectively.

The reactive chemistries of F^- and Cl^- ions on pure PZT has been explored concerning reactive ion etching of pure PZT in a CF_2Cl_2 plasma [103]. The thermodynamic stability of plasma products is in descending order: $TiF_4 > ZrF_4 >> PbF_x$, where x=2 or 4. Therefore, F^- is consumed by Ti^{4+} and Zr^{4+} in preference to Pb^{x+}; consequently, when PZT is etched in CF_2Cl_2 plasmas the F^-, F^- and Cl^- ions consume Ti^{IV}, Zr^{IV} and $Pb^{II \text{ or } IV}$ respectively [103]. The proportion of compounds formed in the plasma are given in decreasing order in equation (10.1) [103].

$$
\begin{aligned}
&[TiF_4] >> [TiF_3Cl] > [TiF_2Cl_2] > [TiFCl_3] > [TiCl_4] \\
&[ZrF_4] >> [ZrF_3Cl] > [ZrF_2Cl_2] > [ZrFCl_3] > [ZrCl_4] \\
&\{[PbCl_2] \approx [PbCl_4]\} > \{[PbF_2] \approx [PbF_4]\}
\end{aligned}
\tag{10.1}
$$

Taken from Mace et al [103]

RIE plasmas, in which the reactive components are Cl^- and F^-, give an indication of halide reactivity with PZT when PZT is etched with a RIE plasma. Chemically, the main difference between RIE and wet etching is that in aqueous media the fluorinated salt is hydrolysed. Pure PZT has been considered [103] equivalent to $PbO\text{-}(1\text{-}y)TiO_2\text{-}(y)ZrO_2$ where y+(1-y) = 1. In a plasma, gas phase reactions occur with Ti and Zr components of PZT before the depletion of Pb from PbO component [103]. However, in the liquid phase, TiF_4 is readily dissolved in $HF_{(AQ)}$ to yield $TiF_6^{2-}{}_{(AQ)}$ [128] (see equation (10.2)).

$$TiF_{4(AQ)} + 2HF_{(AQ)} + 2H_2O \longleftrightarrow TiF_{6(AQ)}^{2-} + 2H_3O^+{}_{(AQ)} \tag{10.2}$$

Zr, whilst belonging to the same group as Ti, can exhibit a range of fluorinated ions in aqueous solution: $ZrF_6^{2-}; ZrF_7^{3-}; Zr_2F_{12}^{4-}; ZrF_8^{4-}; Zr_2F_{14}^{6-}$ [129]; it is assumed here, for simplicity, that only ZrF_6^{2-} forms during etching.

$$ZrF_{4(AQ)} + 2HF_{(AQ)} + 2H_2O \longleftrightarrow ZrF_{6(AQ)}^{2-} + 2H_3O^+{}_{(AQ)} \tag{10.3}$$

Both PbF_2 and $PbCl_2$ are sparingly soluble in aqueous media [129]. PbF_4 and $PbCl_4$ form PbF_6^{2-} or $PbCl_6^{2-}$ respectively on dissolution in aqueous media. Oxidation of Pb^{II} to Pb^{IV} is essential for the formation of the hexfluoro-Pb ion and its solvation. Precipitation of $PbCl_x$ implies $PbCl_2$, as this salt is sparingly soluble in solution. Therefore, another component to the reaction is the reduction of Pb^{IV} to Pb^{II}. The precipitation of a lead halide, from the hexfluoro ion, is represented in equation (10.4), where X^- can be either F^- or Cl^-.

$$Pb^{IV}X^{2-}_{6(AQ)} + 2e^-_{(AQ)} \longleftrightarrow Pb^{II}X_{2(s)} \downarrow +4X^-{}_{(AQ)} \tag{10.4}$$

Depletion of the ZrO_2 and TiO_2 components of PZT through reaction would leave PbO. It seems most likely that PbO is precipitated from depleted PZT, accounting for the lead signal in the EDX spectra (see Fig 7.25). The presence of PbO indicates that ZrO_2 and TiO_2 are attacked preferentially in the liquid phase. In other words, PbO remains after other components of the PZT have been removed. Cracks that have developed in the PZT thick film surface due to sintering stresses form channels for the depleted PbO to leech to the surface of the film. A possible reaction scheme is proposed in equations (10.5) and (10.6).

$$\begin{aligned} &\{Pb^{II}O-(1-y)[TiO_2]-(y)[ZrO_2]\}_{(s)} + 6F^-_{(AQ)} + 4H^+_{(AQ)} \longleftrightarrow \\ &PbO_{(s)} + (1-y)[Ti(OH_2)_2F_6]^{2-}_{(AQ)} + (y)[Zr(OH_2)_2F_6]^{2-}_{(AQ)} \end{aligned} \tag{10.5}$$

Reaction (10.5) proceeds through formation of bis-aquo-hexfluoro anions. Subsequent elimination of the aqua ligands, as water, yields the solvated metal-hexfluoro anions (see reaction (10.6)).

$$\begin{aligned} &(1-y)[Ti(OH_2)_2F_6]^{2-}_{(AQ)} + (y)[Zr(OH_2)_2F_6]^{2-}_{(AQ)} \xleftrightarrow{-2H_2O} \\ &(1-y)[TiF_6]^{2-}{}_{(AQ)} + (y)[ZrF_6]^{2-}{}_{(AQ)} \end{aligned} \tag{10.6}$$

Simplification of equations (10.5) and (10.6) yields equation (10.7).

$$\begin{aligned} &\{PbO-(1-y)[TiO_2]-(y)[ZrO_2]\}_{(s)} + 6F^-_{(AQ)} + 4H^+_{(AQ)} \xleftrightarrow{-2H_2O} \\ &PbO_{(s)} + (1-y)[TiF_6]^{2-}{}_{(AQ)} + (y)[ZrF_6]^{2-}{}_{(AQ)} \end{aligned} \tag{10.7}$$

Lead is soluble in solution as the hexfluoro anion, and solvation follows equation (10.8).

$$Pb^{II}O_{(s)} + 6F^-_{(AQ)} + 2H^+_{(AQ)} \xleftrightarrow{-H_2O} [Pb^{IV}F_6]^{2-}_{(AQ)} + 2e^-_{(AQ)} \tag{10.8}$$

Displacement of F^- from the coordination sphere by Cl^- and the reduction of Pb^{IV} results in the precipitation of the $PbCl_2$ salt: reaction (10.9) is proposed.

$$[Pb^{IV}F_6]^{2-}_{(AQ)} + 2.Cl^-_{(AQ)} + 2e^-_{(AQ)} \xleftrightarrow{-6F_{(AQ)}} Pb^{II}Cl_{2(s)} \downarrow \tag{10.9}$$

Simplification of equations (10.8) and (10.9) yields equation (10.10).

$$Pb^{II}O_{(s)} + 2.Cl^-_{(AQ)} + 2H^+_{(AQ)} \overset{-H_2O}{\longleftrightarrow} Pb^{II}Cl_{2(s)} \downarrow \tag{10.10}$$

The following equation is proposed for the precipitation of PbF_2.

$$\left[Pb^{IV}F_6\right]^{2-}_{(AQ)} + 2e^-_{(AQ)} \overset{-4F^-_{(AQ)}}{\longleftrightarrow} Pb^{II}F_{2(s)} \downarrow \tag{10.11}$$

Simplification of equations (10.8) and (10.11) yields equation (10.12).

$$Pb^{II}O_{(s)} + 2F^-_{(AQ)} + 2H^+_{(AQ)} \overset{-H_2O}{\longleftrightarrow} Pb^{II}F_{2(s)} \downarrow \tag{10.12}$$

Combining equations for the depletion of PbO from PZT (equation (10.7)), the solvation of PbO (equation (10.8)), the precipitation of PbF_2 (equation (10.11)) and the precipitation of $PbCl_2$ (equation (10.9)) equation (10.13) is obtained.

$$\begin{array}{l}
\{PbO-(1-y)[TiO_2]-(y)[ZrO_2]\}_{(s)} + 6F^-_{(AQ)} + 4H^+_{(AQ)} \overset{-2H_2O}{\longleftrightarrow} \\
PbO_{(s)} + (1-y)[TiF_6]^{2-}{}_{(AQ)} + (y)[ZrF_6]^{2-}{}_{(AQ)} + 6F^-_{(AQ)} + 2H^+_{(AQ)} \overset{-H_2O}{\longleftrightarrow} \\
\left[Pb^{IV}F_6\right]^{2-}_{(AQ)} \quad + 2e^-_{(AQ)} + 2.Cl^-_{(AQ)} \quad \longleftrightarrow \quad Pb^{II}F_{2(s)} \downarrow + 2Cl^-_{(AQ)} + 4F^-_{(AQ)} \\
\qquad\qquad\qquad\qquad \uparrow \\
\qquad\qquad\qquad\qquad \downarrow \\
\qquad\qquad Pb^{II}Cl_{2(s)} \downarrow + 6F^-_{(AQ)}
\end{array} \tag{10.13}$$

The reaction shown in equation (10.13) proceeds through: the depletion of PbO from PZT with the solvation of Ti and Zr hexfluoro anions; the solvation and oxidation of Pb to form the hexfluoro species in solution; and the reductive precipitation equilibrium of Pb salts. In equation (10.13) it is assumed that Ti and Zr hexfluoro anions are stable and remain soluble in solution throughout the etching process. Further, the Pb species were precipitated in preference to Ti and Zr salts; the lower polarity of Pb species rendering them less soluble in solution.

The principal evidence for the depletion of PbO from PZT arises from the observation of material C1, and its analysis by EDX. It should be noted that C1 formed beneath the photoresist during etching, and C1 is therefore considered not to have formed through precipitation.

The material A1 was observed to form irrespective of the number of times that the etching solution had been used. B1, however, was only observed to precipitate when PZT was etched in solutions that had been used repeatedly. It was speculated, in chapter 7, that

B1 formation was a consequence of lead concentration in solution. It is suggested here, that as components of the PZT are built up in solution, that there is an equilibrium for the $F_{(AQ)}^-$ ligand between Zr and Ti components on the one hand, and Pb components on the other (see equation (10.14)).

$$\begin{array}{ccc} (1-y)[TiF_6]^{2-}{}_{(AQ)} + (y)[ZrF_6]^{2-}{}_{(AQ)} & \longleftrightarrow & [Pb^{IV}F_6]^{2-}_{(AQ)} + xF^-_{(AQ)} + 2e^-_{(AQ)} \\ & & \uparrow \\ & & \downarrow \\ & & Pb^{II}F_{2(s)} \downarrow \end{array} \tag{10.14}$$

In equation (10.14), there exists a competition for the F^- ligand between Pb and other components of etched species. Generally, the equilibrium favours the left-hand side of this equation. However, if the concentration of etched components is increased, because of repeatedly re-cycling the same solution, the competition for the F^- anion will also increase. A lead salt will be precipitated when the concentrations of Ti and Zr hexfluoro anions are high because the $Pb^{IV}F_6^{2-}$ anion loses F^- to the left hand side of equation (10.13), and to minimise this effect the system responds by reducing the amount of lead through the precipitation of the lead salt (PbF_2).

Wet etching of bulk PZT ceramic, by Trolier et al [130], resulted in the collection of a fine powder at the bottom of the etching container: after etching. Etching was conducted in concentrated $HCl_{(AQ)}$. This powder was analysed by XRD [130], and was shown to be pure PZT. Further, it was argued [130] that the etch: "Works by dissolving the material around the grains, freeing, rather than etching through the grain."

The implication being that the powder is composed of grains that have been freed during etching.

By comparison, in this work, grain pull out was observed in PZT thick films (see Fig 7.26). Cavities observed in the etched film were approximately 0.6 μm in diameter; this is the same as the particle size of Ferroperm PZ26 powder. In line with the observations of Trolier et al [130] powder was observed to collect in the beaker after etching of samples prepared in this project; supporting the conclusion that etching has taken place around and not through the grain. It was concluded that the grains that were pulled out of the film were from the powder component of the composite-slurry, and that these had been freed by the etch.

It was argued, in chapter 7 section 7.3.2, that the metalorganic sol had uniformly coated individual powder particles. As the powder particles had been held in place by the sol-component of the slurry it was concluded that the etch had attacked the sol-component of the thick film. It was also stated, in chapter 6, that the sintering of these films had resulted in compositionally identical sol and powder phases. The evidence for this arises in the XRD spectrum of Ar sintered PZT thick films in chapter 6 section 6.2.1 (see Fig 6.22). It should be noted that thick films used in the etching experiments were sintered under an Ar atmosphere. This spectrum shows a single-PZT phase with some PbO present as a second phase. In the literature review it was mentioned that Cu concentrated at the grain boundaries of PZT samples [42]; these samples had been prepared from PZ26 powder and had been sintered at 710 °C with the PbO-Cu_2O additive [42]. The implication of this was that the sintering-aid or some of its components were concentrating at the grain boundaries of the PZT. During preparation of the slurry the chemical composition of the sol was matched to the chemical composition of the powder. Therefore, the PZT of the sol and the powder must be identical in composition; however, the PZT-grain-boundaries of the sol and powder components of the thick-films must be compositionally-different from the PZT. The PZT can be regarded as a phase connected in three directions about isolated pores, but this phase can be further divided into isolated PZT grains surrounded in three directions by an interconnected grain boundary phase. This grain boundary phase will contain the second phase discussed above. This assumes that the second phase is uniformly distributed between the grains of both the sol and powder phases.

As the etching solution attacked the grain boundaries of the thick film it follows that the etching solution must be attacking the second phase. It is tempting to think that it was the second phase that was attacked and not the sol-derived-component of the thick film; however, were it only the second-phase that was attacked, or dissolved, then the sol-derived-component would remain intact, and there would be some residue of the sol-component remaining after etching. This evidence of this residue would be present either on the sidewall of the etched-feature after etching or at the bottom of the beaker after etching. Fig 7.26 shows no evidence of a residual-sol-component, hence, there was no evidence of residue on the sidewall of the etched feature. The only residue remaining in the beaker after-etching were powder particles dislodged from the thick film. Therefore the sol-component of the etched-thick-film must have been dissolved by the etching solution. In conclusion, the etching solution reacts with both the sol-component of the thick film and the second-phase.

All wet chemical etching of PZT seems to result in the dissolution of the grain boundary and the roughening of sidewalls. Roughening of the sidewalls of etched PZT features has been observed in bulk ceramics patterned with both laser assisted KOH etching [101] and concentrated HCl etching [130,131]. Roughening of etched sidewalls has also been observed in sol-gel PZT thin [107] and thick [127] films where the etching solution in both cases was a dilute mixture of HF(AQ) and HCl(AQ).

10.3 Powder Blasting

A unique aspect of this project was the development of a means for the patterning of conformal and dense PZT thick films. In particular the photo-patterning of elastomeric resists allowed line widths to be achieved down to 50 μm after powder blasting. A critical factor in the resolution of device shapes was the use of high-pressure water to wash residue from channels in the SBX. Optimum photoresist thickness was 35 μm, this was sufficient for pressures used during development of the resist (80 psi).

The development of powder blasting, and the optimisation of process conditions, was helped through a statistical model in which the effects of machining were studied with regard to the degradation of cut features. It was found that resolution declined with the number of sample revolutions.

In the literature [109,126] it had been argued that erosion of elastomeric and brittle materials was highest at oblique and normal angles respectively, where angle refers to the angle between the sample and the blast nozzle. In this project, samples were mounted on a rotating table within a blast-cabinet, see Fig 7.4. As the samples were rotated, θ_{gun} oscillated between oblique and normal angles (see Fig 7.14). Based on the literature and the findings discussed in the preceding paragraph it was proposed that damage accumulated to the resist as the sample passed through the elastic angle $\theta_{elastic.}$ Further, that the time that the sample spent in the flux was not significant in the accumulation of damage to the resist.

In the lost mould process [86-88], see chapter 2, a slurry of ceramic powder and organic binder was poured into a mould; subsequently, the mould was lost in a burnout stage. This process was used for fabricating 3D shapes from ceramic and is not, by design, well suited to the preparation of films. In principle, a 0-3 slurry of powder and sol could be used in place of the conventional slurry. Three dimensional device shapes, with circular or rounded features, could be fabricated in this way. Mechanical support layers and piezoelectric layers could be built up in this way. However, there are at least two draw backs to this approach: firstly, the formation of a lip due to surface tension forces, at the mould slurry interface, and second, surface roughness.

Direct write processes [90,91] were discussed in chapter 2. The gelation of the sol component of the PZT thick film would make it particularly suitable for use in a direct write process. The slurry freezes in place on contact with air, thus retaining the shape of the deposited layer. This is akin to the use of a thermo-set plastic in the fused deposition technique [91]. The absence of a thermo set plastic in deposited composites means that there is no need for a burn out step and that final sintered articles will possess a higher density. If this approach were to be tested, then the viscosity of the slurry would need to be increased. Perhaps some pre-hydrolysis of the sol component could be employed to aid viscosity. A problem of using slurries in direct write processes would be the clogging of the pen nib. The desired device shapes could, easily be written by pen onto the required substrate surface

In consideration of the use of direct write and lost mould processes in place of PZT thick films patterned through powder blasting, patterned features with the lost mould process should achieve sufficiently high resolution. The precision that the pen can place the composite 'ink', onto the substrate is the limiting factor as far as direct write processes are concerned. Powder blasting, as demonstrates here, allows precise patterning of any shape in the two dimensional plane. It is considered that powder blasting is superior to direct write processes as a tool for actuator manufacture in that the resolution is limited by the line width achieved in the masking material employed.

Ultrasonic cutting of PZT bulk ceramic [93,94] is limited to the cutting of straight shapes into the ceramic. As the actuators that were designed in chapter 5 had rounded corners and curved beams, none of them could have been fabricated through ultrasonic cutting of thick film PZT.

Jet machining [87] was also discussed in the literature section. In principle, this technique is applicable to green PZT thick films. The physical toughness of the green thick film is uncertain. In the literature, thick films were prepared through the tape casting of PZT powder in an organic vehicle before jet machining. In the case of PZT thick films prepared from 0-3 composite slurries, the sol component will have 'gelled' before sintering; consequently, the PZT film is a brittle glass-like material. The hydrolysed sol has formed a glass-like inorganic-polymer. It seems unlikely that even a high-pressure stream of air will dislodge media from the film.

In the case of tape cast media discussed in the literature [87], the powder particles of the film were held together by an organic binder. The solvent was used to dissolve this binder and hence loosen the powder particles, [87]. Jet machining as a process may also be applicable to green screen-printed thick films where an organic binder is also employed. However, the glass like nature of the polymerised-sol of the thick film will not be loosened in this way; hence, the PZT will not be dissolved by the action of a solvent: even under high pressure and even when green.

Powder blasting has yielded devices of 2-4 mm dimensions with line widths down to 50 µm. Device shapes have been cut through mechanically hard, and chemically inert, PZT. Device shapes with rounded corners and smooth edges have been fabricated. The advantage of powder blasting over jet machining is the ability to cut through mechanically hard and brittle materials such as dense PZT thick films. The process also yields circular features unachievable with ultrasonic cutting. In further work, composite

PZT thick films may be prepared on other substrate materials such as steel or graphite. Powder blasting as a tool may also be employed for the pattering of these films on these substrate materials.

10.4 Electrical & Piezoelectric Properties

10.4.1 Electrical Conductivity & XRD Spectra of PZT Thick Films.

The porosity of 0-3 connected (closed) pores was discussed in chapter 1, and Banno [14] has stated that tanδ does not depend on the density of phase 2 where phases 1 and 2 are as-described by the cubes model. Therefore the increase in tanδ that was observed with sintering temperature, under Ar, must be due to a change in the composition of the thick film, and not because of a decline in film density. There are two possibilities for the observed increase in electrical conductivity of Ar sintered films: 1) extrinsic doping and 2) a change in composition at the grain boundary.

As noted, in the literature [73], intrinsic electrical conductivity of PZT films sintered under atmospheres of high and low po_2 were expected to be high and low respectively. This was due to the formation of cation-vacancies caused by low po_2. The vacancies induce the formation of holes, and these holes act as positive charge carriers. However, PZT thick films, fabricated in our laboratory, sintered at high-po_2 showed lower electrical-conductivity than films sintered at low-po_2 (see Fig 6.2 and Fig 6.3 in chapter 6). Therefore an effect other than that of intrinsic-electrical-conduction must be found to account for the fact that Ar-sintered PZT thick films exhibit greater conductivity than air sintered PZT thick films.

Experimental XRD analysis of PZT thick films, presented in section 6.2.1 (see Fig 6.22 and Fig 6.24), showed these films to be perovskite. However, in the literature section (chapter 2) ref. [42], PZ26 ceramic pellets sintered with the PbO-Cu_2O additive were discussed; subsequent EDX analysis detected Cu at the PZT grain boundary. The preparative route employed in the experimental samples prepared in this project was identical to that used in the literature [42]. Cu_2O + PbO forms only 5 wt % of the slurry composition, and of this 5 wt %, Cu_2O and PbO form 20% and 80 % respectively. Therefore the presence of Cu within the thick film will only be at trace levels. It should be born in mind that XRD is very poor at detecting trace levels; therefore it is unlikely that XRD will detect Cu.

10.4.1.1 Phase Diagrams Of Pb And Cu Oxide Systems And The Role Of A Second Phase

CuO forms from the oxidation of Cu_2O, see Fig 10.1 and Fig 10.2; these phase diagrams will be used in the consideration of the effects of sintering at high po_2 (under air). In other words it is assumed that Cu_2O is rapidly oxidised to CuO under an air-atmosphere. The Cu_2O-PbO eutectic temperature (1026 °C) in Fig 10.2 is not to be confused with the Cu_2O-PbO eutectic temperature (680 °C) given in Fig 10.3. The Cu_2O-PbO eutectic occurs at 1026 °C (in Fig 10.2) because of the high temperature reduction of CuO to Cu_2O; whereas Cu_2O-PbO eutectic (in Fig 10.3) occurs at 680 °C because Cu_2O is the starting material and has already been formed.

It should be noted that CuO is reduced to Cu_2O at $T \leq 1026$ °C see Fig 10.2. Fig 10.1 to Fig 10.3 shows that as p_{O_2} is increased, the melting point of the eutectic temperature is increased. In the case of sintering at lower p_{O_2} (Ar atmosphere) Fig 10.3 is used in place of Fig 10.2.

10.4.1.1.1 Ar-Sintered PZT Thick Films

In chapter 6 the second phase, in Ar-sintered PZT, was identified as a mixture of litharge and massicot. The appearance of PbO under reducing conditions and its disappearance under oxidising conditions needs to be explained.

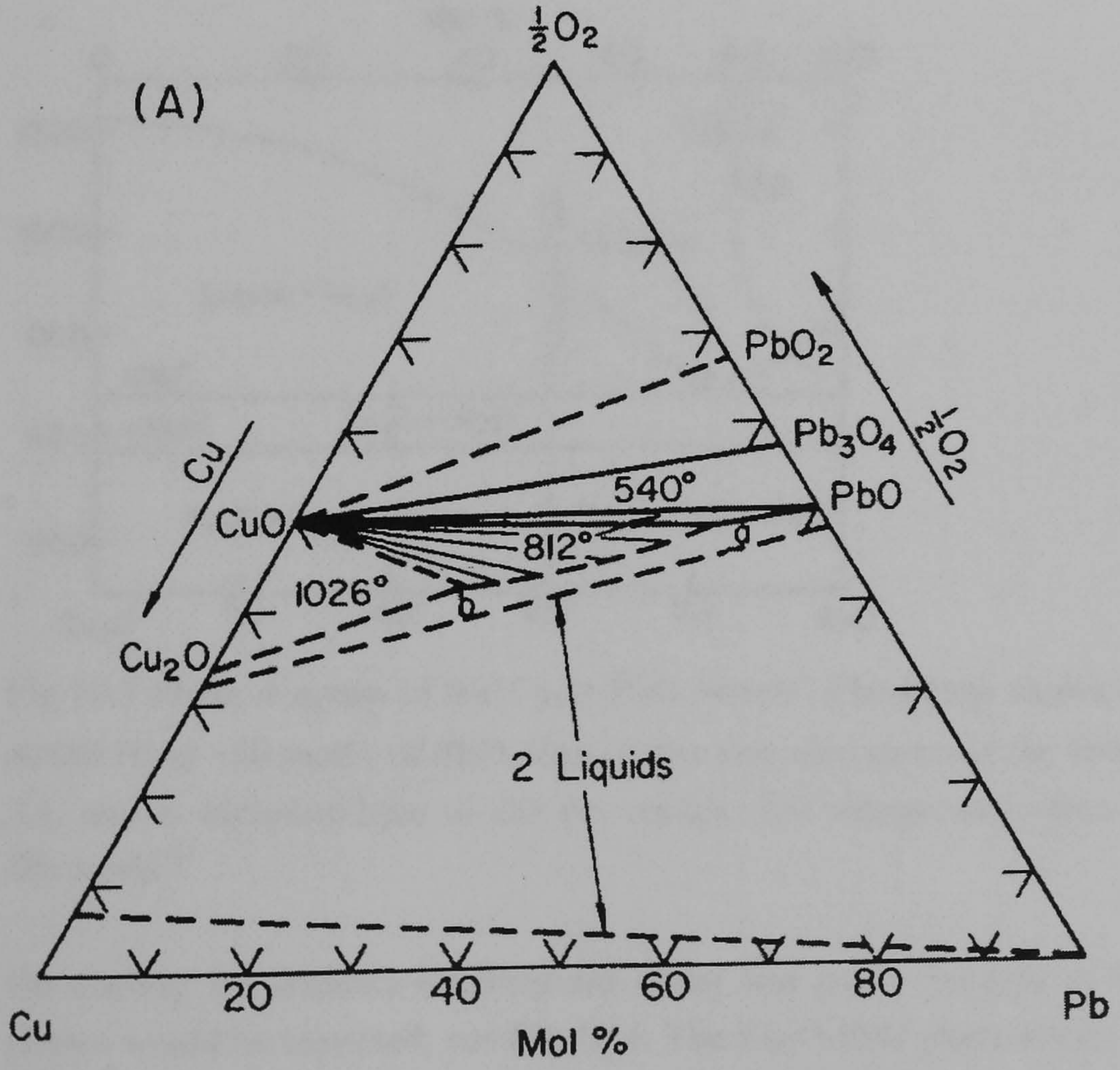

Fig 10.1 The Cu-Pb-O ternary phase diagram. The image was taken from Levin et al [132]

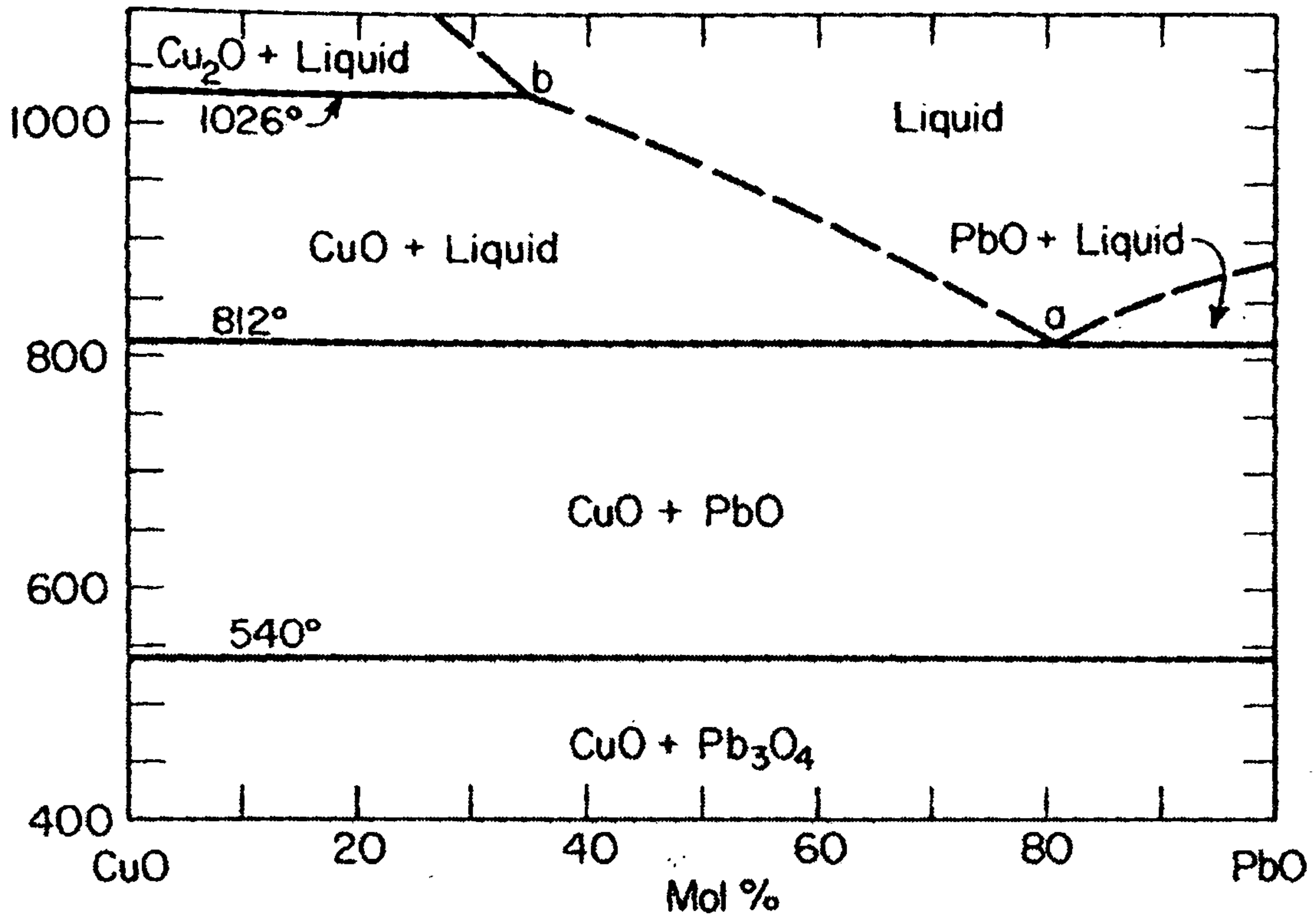

Fig 10.2 The CuO-PbO phase diagram where temperature is plotted against mol%. The image was taken from Levin et al [132]

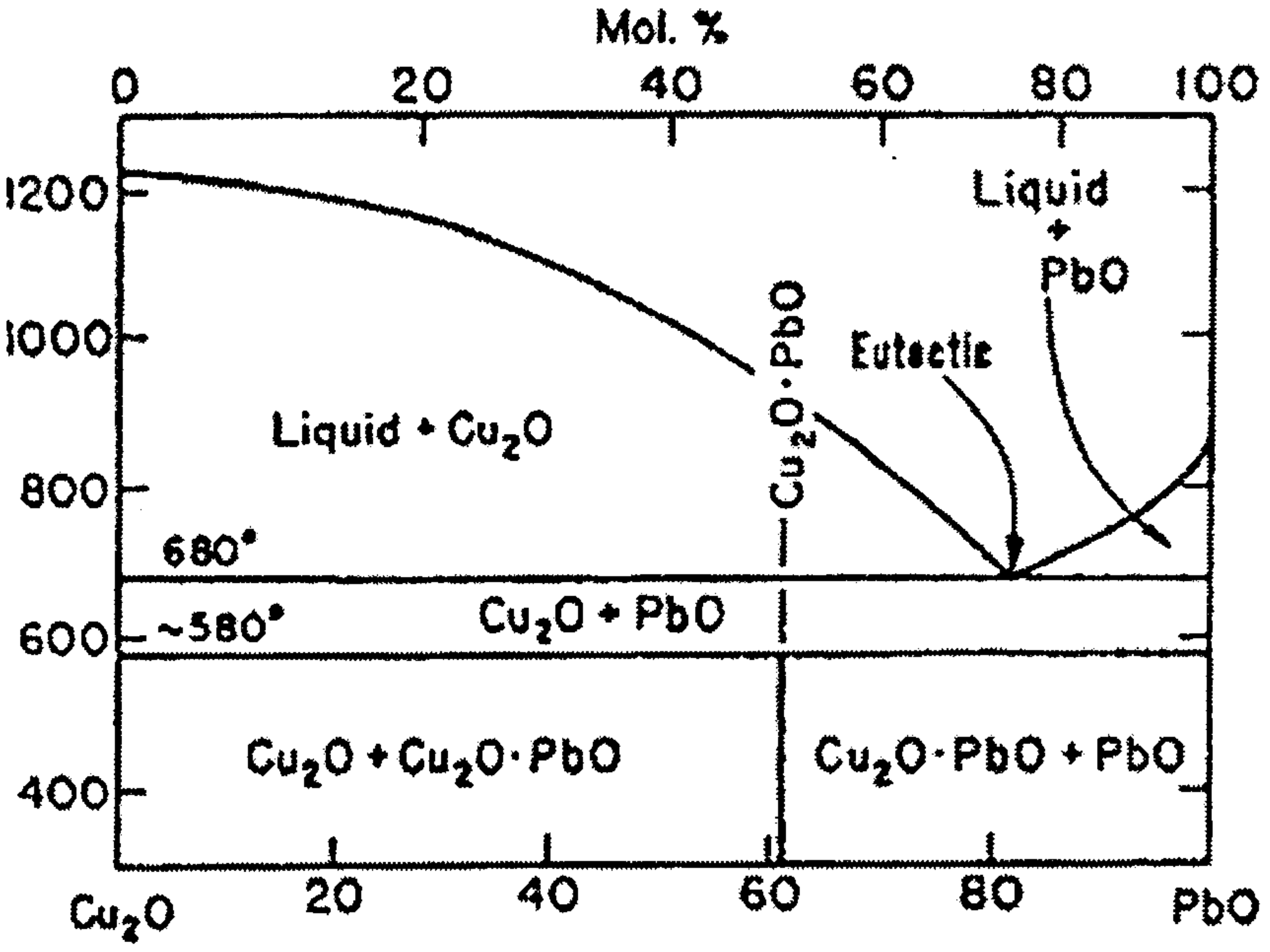

Fig 10.3 Phase diagram of the Cu_2O-PbO system. The image shows that a eutectic forms at 680 °C at ~80 mol% of PbO. This image was also given in the literature chapter as Fig 2.4, and is included here to aid the reader. The image was taken from Gebhardt and Obrowski [41]

On cooling the eutectic-sintering-aid under low-po_2 a mixture of Cu_2O.PbO and PbO phases would be expected, see Fig 10.3. The Cu_2O.PbO phase forms from the solid-state-diffusion of the solid mixture of Cu_2O and PbO on cooling through the solidus at 580 °C. Diffusion controlled processes occur relatively slowly, and under the conditions of rapid cooling the Cu_2O.PbO phase may not have time to form. This means that after sintering that Cu_2O and PbO would remain. Therefore even in much reduced conditions a PbO peak would be expected in the XRD spectrum. However, Cu_2O constitutes only 20 mol%

of the PbO, and it is unlikely that this would show up in the XRD spectrum of Ar-sintered thick films.

10.4.1.1.2 Air-Sintered PZT Thick Films

Under conditions of high po_2 (air sintering) no second phase was observed by XRD. According to Fig 10.2, the liquidus condition (812 °C) is not reached in films sintered at 710 °C with CuO and PbO. However, the starting materials in PZT thick films that were prepared in this project were Cu_2O and PbO; consequently, the Cu_2O has first to oxidise, to form CuO. The Cu_2O component might form a liquid with the PbO first, then oxidise and solidify at the sintering temperature (710 °C). That would explain why it was not effective as a sintering aid under oxidising conditions. SEM-fracture-cross-sections of air-sintered PZT thick films, fired at 710 °C, can be seen in Fig 6.13 to Fig 6.15; air-sintered thick films fired at 710 °C appear less dense than Ar-sintered films at the same temperature. However, the presence of PbO was still expected in the XRD spectrum of films sintered at high po_2. Therefore another reason must be found for the absence of PbO in the air-sintered PZT samples.

It should be noted that the detection limit for XRD is ~5%; therefore the absence of PbO peaks in the XRD spectrums of air-sintered PZT thick films could be attributed to a lower concentration of PbO in the thick film. However, the PbO signal has been attributed to the PbO component of the eutectic sintering aid, and it should be remembered that the levels of sintering aid used in the preparation of the Ar-sintered thick films were the same as the air-sintered thick films. Therefore the absence of a PbO signal suggests that some of the PbO component of the sintering aid has been 'lost' from the thick film. Of course some PbO is lost when PZT is sintered at high po_2 but this loss is from the PZT and not from any additional sintering aid that might have been added before sintering began. It can therefore be concluded that PbO loss from the air sintered thick films must occur by some other mechanism not already considered.

Only a perovskite phase was detected in the XRD spectrum of air-sintered-films. As noted above there may have been another phase present, but this would have been <5 %. With regard to the missing PbO the only explanation that can be offered for its' absence from the spectrum was that Pb, from the PbO, was still present in the thick film but in a perovskite phase. In other words Pb and Cu ions from the eutectic sintering aid had doped on the A and B lattice sites of PZT. Therefore it was not possible to resolve the presence of the sintering aid components of air-sintered PZT thick films by XRD as these components had become part of the PZT material. Presumably the doping of Pb and Cu ions from the eutectic sintering aid into the PZT lattice will create a material similar to the PZT-PCN material that was discussed in the literature section.

As the sintering aid was uniformly dispersed in the sol this phase will form at the grain boundaries of the PZ26-powder. The formation of a Cu rich phase similar to PZT-PCN at the PZT grain boundaries was anticipated; this was supported by the work of Corker et al [42] in which it was claimed that Cu was detected by EDX at the PZT grain boundary.

The role of Cu as an acceptor doping ion is discussed in section 10.4.1.2 and this is discussed in terms of the PZT-PCN system. Further, the chemistry of both PZT-PCN and PZT-PCN+0.5 mol% Mn^{4+} is discussed in greater detail. Of particular interest was the fact that Mn displaced Cu under oxidising conditions.

The PbO second phase showed up only in infiltrated-PZT-thick-films. Presumably, non-infiltrated thick films have some degree of open porosity; hence higher PbO was present in non-infiltrated-films even if they were sintered under Ar. The fact that the PCN type phase did not form at very low po_2 means that it cannot form in infiltrated-PZT-thick-films where the infiltrated-sol acts to block the diffusion of oxygen thereby lowering po_2. This explains why non-infiltrated-films exhibited no second phase [39,44] (see Fig 10.3).

10.4.1.2 Oxygen Partial Pressure

As reported in the literature [73], hole formation was the major cause of conductivity in undoped-PZT. Hole formation occurred under normal sintering conditions, and it was accelerated as po_2 was increased. Hole formation can be represented using the Kröger-Vink notation where V is a vacancy and h is a hole, see equation (10.15).

$$V_A \longleftrightarrow V_A^{||} + 2h^{\bullet} \qquad (10.15)$$

In equation (10.15) the subscripts A and B correspond to A and B lattice sites in the perovskite structure (see Fig 1.8 chapter 1). The superscripts | and • correspond to effective negative and positive charge respectively.

Higher electrical conductivity was found in films that were sintered under low po_2 (see Fig 6.3 of chapter 6); this was contrary to the literature [73] where sintering with a higher oxygen partial pressure yielded higher electrical conduction in PZT due to hole-formation.

Any increase in po_2 shifts the equilibrium position of equation (10.15) to the right. This is because Pb was volatilised as PbO under oxidising conditions; the loss of Pb^{2+} as PbO from the host material resulted in the formation of $V_A^{||}$ (more specifically $V_{Pb}^{||}$). The effect of the Ti or Zr ions is neglected because the volatility of Pb>>Ti or Zr; consequently, both Ti and Zr will interact with the atmosphere to a much lesser extent. Therefore higher po_2 increases the conductivity of undoped PZT ceramics, this was noted in the literature

[73]. Oxygen loss caused by sintering in atmospheres with reduced po_2 generates $V_O^{\bullet\bullet}$, and these vacancies act as electron donors, see equation (10.16).

$$V_O \longleftrightarrow V_O^{\bullet\bullet} + 2e^- \qquad (10.16)$$

Initially, these donors compensate for the acceptors caused by $V_A^{||}$ and the conductivity is reduced. However, when the amount of donors exceeds the amount of acceptors, then the conductivity starts to increase.

The conductivity of PZT thick films made in this work was complicated by the doping ions employed: Sb^{5+}, Nb^{5+} and Mn^{3+}. The general composition of undoped PZT at the morphotrophic phase boundary is $Pb(Ti_{0.53}Zr_{0.47})O_3$. Assuming doping on the B-site, where Ti was displaced, the composition of PZT prepared in this project was $Pb(Ti_{0.47}Mn_{0.02}Nb_{0.02}Sb_{0.02}Zr_{0.47})O_3$. This composition was used for all PZT thick films irrespective of the sintering atmosphere. In this composition there was a 2:1 ratio of donor to acceptor ions. Donor doped PZT systems exhibit higher resistivity than acceptor doped systems, when sintered under high po_2. Therefore, air-sintered PZT thick films prepared in this work might be expected to demonstrate higher electrical resistivity than undoped PZT. It should be noted that these films were sintered under reduced temperatures, relative to conventional ceramics, using a eutectic sintering aid. The eutectic-sintering-aid introduces a second liquid phase at the PZT-grain-boundaries, during sintering.

The effect of the second phase on the grain-boundary composition and on the electrical conductivity of the thick films was unclear. Of particular interest is the role of Cu^{2+} and its effect as a possible doping ion. Because Cu_2O is rapidly oxidised to CuO Cu^{2+} is considered the most likely doping ion to dope at the B-lattice site. If this is the case then Cu will act as a strong acceptor, see equation (10.17).

$$Cu^{2+} \longleftrightarrow Cu_B^{||} + 2h^{\bullet} \qquad (10.17)$$

Electrons generated under reducing conditions in equation (10.16) will be neutralised by the presence of $h^{\bullet}$ from equation (10.17). Therefore if Cu dopes it will act to moderate electrical conductivity at low po_2.

In consideration of the effect of possible Cu doping at high po_2, and in consideration of the role of Mn. The best system to compare thick films prepared in this project is the PZT-PCN system, and this was discussed in the literature chapter [71]. It was noted in the literature chapter that in air sintered PZT-PCN+0.5 mol% Mn that Cu was precipitated as CuO [71]. Equation (10.18) shows the displacement of Cu^{2+} by Mn^{4+} in the PCN system.

$$Mn^{4+} + Cu_B^{||} + 2h^{\bullet} \longleftrightarrow Mn_B + Cu^{2+} + 2e^{-} + 2h^{\bullet} \qquad (10.18)$$

It can be seen that substitution of Mn^{4} for Cu^{+} that the number of electrons and hole carriers cancel yielding equation (10.19)

$$Mn^{4+} + Cu_B^{||} + 2h^{\bullet} \longleftrightarrow Mn_B + Cu^{2+} \qquad (10.19)$$

This explains why Cu^{2+} doped PZT was resistive when sintered under high po_2; there should have be an increase in $[h^{\bullet}]$ and hence in electrical conductivity at ambient temperatures. However, it is suggested, here, that Cu^{2+} precipitated at the grain boundary of the PZT, and that this was oxidised to CuO. Indeed CuO would be expected to form under an oxidising atmosphere, see Fig 10.2. The evidence for this oxidation was in the resistivity of air-sintered PZT: if metallic Cu was present at grain boundaries then these films would be highly conductive. Therefore in the case of Mn doped PZT conductivity due to hole formation will be neutralised, and the resistivity of the PZT will be increased at ambient temperatures.

However, as noted in the literature chapter Mn^{4+} was reduced to $Mn^{3\text{ or }2+}$ during the sintering of Mn doped PZT-PCN samples. This resulted in the formation of oxygen vacancies to maintain electrical neutrality. Indeed PZT-PCN+0.5 mol% Mn samples were found to be more conductive than PZT-PCN, in the temperature range 25 °C to 700 °C [71]; this was ascribed to ionic conductivity and the formation of $V_O^{\bullet\bullet}$ [71]. To represent this process equation (10.20) is proposed.

$$Mn_B \longleftrightarrow Mn_B^{|} + \tfrac{1}{2}V_O^{\bullet\bullet} \longleftrightarrow Mn_B^{||} + V_O^{\bullet\bullet} \qquad (10.20)$$

However, films prepared in the current work were prepared from Mn_2O_3 and not MnO_2. Therefore Mn will be in the +3 and not +4 oxidation-state; consequently, equations (10.19) and (10.20) can be re-written as equations (10.21) and (10.22) respectively.

$$Mn^{3+} + Cu_B^{||} + 2h^{\bullet} \longleftrightarrow Mn_B^{|} + Cu^{2+} + h^{\bullet} \qquad (10.21)$$

$$Mn_B^{|} \longleftrightarrow Mn_B^{||} + \tfrac{1}{2}V_O^{\bullet\bullet} \qquad (10.22)$$

It should be noted that this increase in ionic conductivity will not occur at ambient temperatures and is therefore not relevant to the current work.

10.4.2 Electrode Substrate Interface

The cleaved interface between the Si substrate and The PZT thick film, discussed in chapter 8, yielded valuable information about the composition of the interface. Compositional analysis was conducted on the cleaved layers (Fig 8.6). Pt was found not to diffuse into the underlying Si. An O rich layer was found between the Si substrate and the back electrode. This layer also contained Pb, showing that Pb had diffused through the back electrode. This conclusion was supported by the literature [48] (see also Fig 2.11 in the literature review section) where a PZT thin film was fabricated on a $Si/SiO_2/Ti/Pt$ substrate, and Pb was observed to have diffused through the Pt electrode into the substrate.

Bubbling was observed at the interface between the substrate and the back electrode, and it was observed to have taken place on the substrate surface. This bubbling effect was observed in samples where the interface had been exposed through etching of the silicon substrate (Fig 8.3 and Fig 8.4) and the etching of the PZT thick film (Fig 7.23). It should be noted that bubbling beneath the back electrode has also been observed in the literature [46] (see Fig 2.10), where PZT thick films were screen-printed onto Si substrates. All thick films that exhibited the bubbling effect were sintered before analysis. The composition analysis, shown in Fig 8.6, indicated that there was a lead rich region on the surface of the cleaved silicon referred to as spectrum 1. Spectrum 1 corresponds to the area around the bubbles in Fig 8.3. Based on the results, both from our experiments and the literature, it was concluded that bubbling arose from the diffusion of Pb into the substrate: during sintering and not from KOH or HF etching solutions. The existence of bubbles beneath the back electrode is considered reproducible, given that bubbling has been observed in Fig 2.10, Fig 7.23, Fig 8.3 and Fig 8.4. This validates the conclusions based on Fig 8.6 of chapter 8.

In both Fig 2.11 and Fig 8.6 the Pt from the back electrode did not diffuse into the underlying substrate. Pb probably diffused from the sintering aid in the PZT thick film. In other words, PbO was reduced to atomic lead before diffusing through the back electrode into the substrate. As noted in the Literature Chapter, the reduction of PbO was likely to have taken place according to equation (2.5). Subsequently, the Pb was oxidised to yield the lead silicate glass (see equations (10.23) and (10.24)) detected in the substrate, see Fig 8.6.

$$Pb + \tfrac{1}{2}O_2 \rightarrow PbO \qquad (10.23)$$

$$PbO(l) + SiO_2(s) \rightarrow PbSiO_3(s) \qquad (10.24)$$

The proportions of Pb, Si and O, presented in Fig 8.6, indicate the presence of a lead silicate glass. Some free energies of formation (ΔG_f) for lead silicate glasses ($PbSiO_3$) are listed in Table 10.1, and it was found that $PbSiO_3$ was most likely compound to form from $PbO+SiO_2+0.5O_2$ because this reaction has the most –ve ΔG_f value. Free energies of formation for SiO_2 from Si + O_2 and Si_3N_4 +O_2 are also included in the table. It should be noted, that SiO_2 must exist before $PbSiO_3$ formation can take place; therefore ΔG_f values for SiO_2 are expected to be more –ve than for $PbSiO_3$. In addition the reduction of PbO by Si is also considered. Although its ΔG_f is not as –ve as that of $PbSiO_3$ formation under oxidising conditions, and is considered less likely to form. Finally, $PbSiO_3$ forms at 550°C [133] in oxidising conditions, well below the sintering temperatures employed in the current work.

Reactants	Products	ΔG_f^{θ} / k.J/mol	ΔG_f^{E} / k.J/mol
PbO + SiO_2	$PbSiO_3$	-23.51	-20.89
2PbO + SiO_2	Pb_2SiO_4	-26.15	-31.35
PbO + SiO+0.5O_2	$PbSiO_3$	-747.89	-658.85
O_2 + Si	SiO_2	-850.73	-950.73
0.33Si_3N_4 + O_2	SiO_2 + (2/3)N_2	-636.51	-668.88
2PbO+Si	2Pb+SiO_2	-474.93	-381.56

Table 10.1 Free energies of formation of selected reactions under standard conditions (superscript) θ and at the sintering temperature (superscript) E. Data compiled from [134]

The Si layer, analysed in Fig 8.6, had no trace of N, which was surprising, given that there was a Si_3N_4 layer in this sample prior to back face etching with KOH. Molten PbO in an air atmosphere fluxes with Si_3N_4 [70]. The surface of the nitride consists of a thin silica layer formed by contact with air, see equation (10.25). The silica is dense and once formed prevents further silica formation by blocking the diffusion of oxygen.

$$\tfrac{1}{3}Si_3N_4(s) + O_2(g) \rightarrow SiO_2(s) + \tfrac{2}{3}N_2(g)\uparrow \qquad (10.25)$$

Silica consumes the nitride according to equation (10.25). The air atmosphere will then reform a new silica layer that will be rapidly consumed by the PbO according to equation (10.24). In this way, a thin nitride layer may be consumed rapidly; equations (10.24) and (10.25) may be combined into equation (10.26).

$$PbO(l) + \tfrac{1}{3}Si_3N_4(s) + O_2(g) \rightarrow PbSiO_3(s) + \tfrac{2}{3}N_2(g)\uparrow \qquad (10.26)$$

Experimentally, it would prove difficult to detect the evolution of $N_2(g)$ during sintering. Thick films on Ti/Pt/Si substrates, sintered under air are also likely to form the $PbSiO_3$ according to equation (10.24). SiO_2 forms from the reaction of Si with atmospheric O_2, (equation (10.27)).

$$Si(s) + O_2(g) \rightarrow SiO_2(s) \tag{10.27}$$

Formation of lead silicate glass on Si will then proceed under an oxidising atmosphere in the presence of Pb. Concerning the separation of the electrode from the substrate, the bubbling in the electrode surface (see Fig 8.6 chapter 8) is similar to that seen in the literature for screen-printed PZT thick films on silicon (see Fig 2.10 chapter 2). This supports the view that Pb diffusion saturates the electrode layer and then continues into the underlying substrate. After re-oxidation of the metastable phase, oxygen diffuses through the back electrode to react with Si and Pb present.

It should be noted that the intermetallic was observed to form in Ar sintered films even at temperatures as low as 710 °C, when the pores of the ceramic had been sealed with sol (see chapter 2). Intermetallic formation was acute in films where there had been no intermittent pyrolysis of sol layers, and where the sol had formed glassy layers between the composite slurry layers [43]. The increased carbon content of these films, due to the absence of pyrolysis, is considered to have aided the formation of the metastable phase. In the literature, intermetallic formation proceeded through the formation of Pt_3Pb and then PtPb [43], see equation (2.7); it was proposed that this proceeded through the reduction of PbO from the sintering aid by residual C in the thick film equation (2.6). Combining equations (2.6) and (2.7) to yield equation (10.28).

$$\begin{aligned} &PbO(l) + C(s) + 3Pt(s) \rightarrow Pt_3Pb(s) + CO(g)\uparrow + 2PbO(l) + 2C(s) \\ &\rightarrow 3PtPb(s) + 2CO(g)\uparrow \end{aligned} \tag{10.28}$$

The intermetallic seems to form at low oxygen partial pressures. However, lead silicate glass can only form from the product of lead oxide and silica, not from atomic Pb. The intermetallic can only form from atomic Pb and atomic Pt. The most likely explanation is that the reaction has six stages:

1) Residual C reduces the PbO component of the sintering aid to Pb. This stage takes place in the thick film.
2) Diffusion of atomic Pb into the Pt electrode.
3) Pt_3Pb formation
4) PtPb forms with continued diffusion of Pb into the Pt back electrode
5) Excess Pb diffuses through the back electrode
6) Pb and Si are oxidised, at a later point in the annealing process, yielding the Pt electrode and $PbSiO_3$ glass

In the case of a PZT thick film on a Pt/Ti/SiO_2/Si substrate equation (10.28) maybe combined with equations (10.24) and (10.27) to yield equation (10.29).

$$\begin{aligned}&PbO(l)+C(s)+3Pt(s)\rightarrow\\&Pt_3Pb(s)+CO(g)\uparrow+2PbO(l)+2C(s)\rightarrow\\&3PtPb(s)+2CO(g)\uparrow+PbO(l)+Si(s)+O_2(g)\rightarrow\\&PbSiO_3(s)\end{aligned}\tag{10.29}$$

The same approach to that used to derive equation (10.29), may be carried out for the PZT/Pt/Ti/Si_3N_4 system to yield equation (10.30).

$$\begin{aligned}&PbO(l)+C(s)+3Pt(s)\rightarrow\\&Pt_3Pb(s)+CO(g)\uparrow+2PbO(l)+2C(s)\rightarrow\\&3PtPb(s)+2CO(g)\uparrow+PbO(l)+\tfrac{1}{3}Si_3N_4(s)+O_2(g)\rightarrow\\&PbSiO_3(s)+\tfrac{2}{3}N_2(g)\uparrow\end{aligned}\tag{10.30}$$

Equations (10.29) and (10.30) may be simplified to equations (10.31) and (10.32) respectively.

$$\begin{aligned}&4PbO(l)+3C(s)+3Pt(s)+Si(s)+O_2(g)\rightarrow\\&3PtPb(s)+PbSiO_3(s)+3CO(g)\uparrow\end{aligned}\tag{10.31}$$

$$\begin{aligned}&4PbO(l)+3C(s)+3Pt(s)+\tfrac{1}{3}Si_3N_4(s)+O_2(g)\rightarrow\\&3PtPb(s)+PbSiO_3(s)+\tfrac{2}{3}N_2(g)\uparrow+3CO(g)\uparrow\end{aligned}\tag{10.32}$$

The Pt_3Pb intermetallic will be solid up to 915 °C. The solubility of platinum intermetallics in a lead-oxide-silica eutectic-solution is unknown. The intermetallic phase forms islands of PtPb surrounded by Pt_3Pb (see Fig 2.9) [43].

It should be noted that the minimum eutectic temperature of the Cu_2O-SiO_2 system is 1060 °C [70]. It is, therefore, unlikely that Cu_2O would dissolve in the silica even under oxidising conditions. Copper did not diffuse into the underlying substrate, see Fig 8.6. In addition, earlier work on PZT thick films [43] has also indicated that Cu is present near the electrode.

The lead silicate glass could form between electrode and substrate under conditions of higher oxygen partial pressure e.g. when sintered under air. Brooks et al [52] have observed the formation of a $PtPb_x$ intermetallic phase under an Ar atmosphere at 460 °C, in sol-gel derived PZT thin films on Pt/Ti/SiO_2/Si substrates. The intermetallic was completely re-oxidised to Pt + PbO in an O_2 atmosphere at the same temperature. Thus, it was unlikely that an intermetallic phase would be observed in PZT thick films sintered under an air atmosphere where oxygen partial pressure was higher. However, there was no reason why the lead silicate glass should not form under an oxidising atmosphere, without the intermetallic. Indeed the intermetallic could form initially under low oxygen partial pressure and then reform the Pt as oxygen diffuses to the electrode interface. The products of this reaction being the formation of additional lead silicate glass, see equations (10.33) and (10.34).

$$\begin{gathered}4PbO(l)+3C(s)+3Pt(s)+Si(s)+O_2(g)\rightarrow\\ 3PtPb(s)+PbSiO_3(s)+3CO(g)\uparrow+\tfrac{9}{2}O_2(g)+3Si(s)\rightarrow\\ 3Pt(s)+4PbSiO_3(s)\end{gathered}\tag{10.33}$$

$$\begin{gathered}4PbO(l)+3C(s)+3Pt(s)+\tfrac{1}{3}Si_3N_4(s)+O_2(g)\rightarrow\\ 3PtPb(s)+PbSiO_3(s)+\tfrac{2}{3}N_2(g)\uparrow+3CO(g)\uparrow+\tfrac{9}{2}O_2(g)+3Si(s)\rightarrow\\ 3Pt(s)+4PbSiO_3(s)\end{gathered}\tag{10.34}$$

The porosity of Pt with respect to Pb was discussed in the literature section. The reader is referred to Fig 2.11 in which a lead rich layer was observed to have diffused from a PZT thin film through a Pt layer [48]. In Fig 2.11 the Pt layer did not appear swollen or to have de-laminated from the substrate; this may have been expected if the intermetallic layer were present in the electrode after the film had been sintered. It should be noted that the intermetallic is a metastable phase that forms only under conditions of low po_2, and that as po_2 is increased the intermetallic disappears with the formation of PbO and the reformation of the Pt. In the case of thin films it is considered [45] that the intermetallic first forms in the electrode and is later re-oxidised yielding the Pt electrode; the PbO that is generated from this re-oxidation is thought to diffuse back into the PZT thin film [45]. The intermetallic is thought to form in the initial stages of firing [45] when there is a low po_2 at the electrode-film interface; however, as firing continues the po_2 at the film electrode interface increases and the intermetallic is re-oxidised. This suggests that the Pt electrode, in Fig 2.11, had reformed from re-oxidation and that the electrode was intact. It is unclear if the Pb layer in the SiO_2 layer, of Fig 2.11, had been oxidised to PbO, although the film adhesion seems good.

To summarise sections 8.3.1 (chapter 8) and 10.4.2 (chapter 10); lead, silicon and oxygen have been detected in levels that correspond to lead silicate glass at the electrode substrate interface. Diffusion of Pb into the Pt yields the $PtPb_x$ inter-metallic phase as discussed in the literature [43]. When the Pt layer is saturated with Pb, it appears that Pb diffuses into the underlying substrate. The intermetallic layer is then re-oxidised to Pt. Pb in the substrate is oxidised to PbO which can flux with any SiO_2 or Si_3N_4 that is present. Fluxing occurs due to the formation of a eutectic PbO-SiO_2 solution at 720 °C [70]. An air atmosphere will oxidise the surface of the Si or Si_3N_4; any PbO present will consume the SiO_2.

It seems likely that sintering stresses within the PZT thick film cause the electrode to de-laminate from the substrate. This, it would appear, is the most likely explanation for electrode de-lamination discussed above and shown in Fig 6.7 to Fig 6.12 and Fig 6.19 to Fig 6.20, see chapter 6. The process is assisted by the diffusion of Pb from the thick film into the underlying substrate see Fig 6.37 in chapter 6.

During sintering, the PZT thick film will be under a tensile stress. The presence of a liquid beneath the electrode may act as a lubricant. The electrode was partially mobile under these conditions; de-lamination may have occurred through blistering at points, and the elimination of Pb diffusion by the incorporation of a diffusion barrier coating was considered essential to prevent the PZT thick film delaminating.

Swelling of the back electrode was observed in the ion milled sample (Fig 6.33 chapter 6) (PZT/Pt/Ti/Si_3N_4) and in samples sintered under Ar at higher temperatures (in Fig 6.7 to Fig 6.12 chapter 6). Swelling of the back electrode has also been observed in the literature (see Fig 2.9 chapter 2 [43], and Fig 2.10 chapter 2 [46]). The swelling of the electrode was attributed to the formation of a lead intermetallic with the Pt of the electrode. Sintering under an Ar atmosphere is likely to have resulted in a low interfacial oxygen partial-pressure. Glass-like layers that formed from infiltration in Fig 2.9 (chapter 2) were anticipated to have further inhibited oxygen diffusion to the interface. Presumably, the low oxygen-partial-pressures that have resulted from sintering under Ar, with $m>3$, were considered to have prevented the reformation of the Pt electrode. The Pt back electrode reformed through intermetallic re-oxidation. In air sintered films the oxygen partial pressure was sufficient for the re-oxidation of the Pt electrode. Therefore, the intermetallic phase was observed only in films sintered under Ar atmospheres. It is considered that infiltrated films, where $m=1$, were sufficiently porous for O_2 to re-oxidise the electrode (see Fig 2.8 of chapter 2).

10.4.3 Electrical Properties

The progressive destruction of the back electrode with sintering temperature makes charge-carrier injection from the metal electrode to the PZT harder; thus, despite the increase in film density a decline in dielectric constant was actually observed.

A second phase forms within PZT thick films, as noted in section 10.4.1.1 above. It seems unlikely that this second-phase is electrically conductive, the composition being that of PbO. Electrical conductivity seems to arise as a consequence of the role of oxygen vacancies acting as electron donors at reduced po_2. This conductivity was moderated by Cu, which seems to dope at the grain boundaries of the PZT grains. Porosity as well as grain boundary composition contributes to a decline in the dielectric constant of Ar-sintered films when the sintering temperature was increased.

10.5 Process Integration & Device Fabrication

During the sintering of PZT thick films, Pb was found to diffuse toward the substrate. The addition of a YSZ diffusion barrier minimised Pb diffusion. The Si-DRIE route proved the most successful fabrication route stabilising PZT thick films. The TiO_2 barrier layer system was found to be better than YSZ on Si_3N_4 coated substrates. Both barrier layer systems worked well, yet the adhesion of the PZT thick film was better in the case of the YSZ barrier. It is considered most likely that the damage caused to the PZT thick film during anisotropic etching of Si results from the attack of KOH on the interfacial glass. As the lead silicate glass is thought to form from the diffusion of Pb during sintering, the addition of an effective barrier layer such as TiO_2 is thought to prevent its formation. It should be noted that Si etching of PZT/Pt/Ti/TiO_2/Si_3N_4/Si films with KOH has not to date been attempted and it is only likely, and not certain, that the KOH-Si_3N_4 process will work.

Air, as compared to Ar, sintering of thick films yielded denser structures, but with greater damage observed to the back electrode. However, introduction of the barrier layers has meant that PZT thick films can be sintered under an air atmosphere without damage being incurred to the electrode. The improved densification of PZT thick films is anticipated, therefore, to improve electrical and piezoelectric properties. Although piezoelectric and electrical properties have not been measured for PZT thick films fabricated onto barrier layer materials.

Intra-granular cleavage, such as was observed in Fig 7.20 of chapter 7, indicates that the internal structure of the PZT grains was dense. Therefore, porosity in the PZT thick films fabricated in this project appears to occur only at the grain boundaries.

The combination of processing steps yields conformal and dense PZT thick films. These films have a low surface roughness. The PZT can be etched to reveal the back electrode, or it can be blasted through to the underlying substrate. The combination of patterning route, allows any device shape to be cut into the plane of the PZT film. Indeed, a planar PZT film on any substrate material can be patterned in this way. The exception being highly elastic materials e.g. polymers. The introduction of DRIE to release the actuators permits thickness control of the actuator substrate if a buried oxide wafer was not used.

A unique aspect of this project was the integration of the 0-3 composite approach with silicon microfabrication technology. Any device can easily be released with controlled thickness of the device substrate. PZT films between 2 μm to 100 μm thick can be fabricated. This process relies on an original use of alignment marks using back-to-front alignment.

The densification of a 0-3 composite slurry PZT thick film during sintering introduces tensile stresses into the thick film. It should be noted that blistering was observed in films where substrate adhesion was undermined through PbO-SiO_2 fluxing. The addition of the barrier layer, YSZ or TiO_2 as the case may be, stabilises film-substrate adhesion and therefore eliminates blistering. However, the absence of blistering means that there is no mechanism for stress relief. PZT thick films stabilised with barrier layers are highly stressed. Air-sintered PZT thick films on Pt/Ti/YSZ/Si substrates are near fully dense with stable interfaces and will be highly stressed. Therefore, actuators fabricated from air sintered PZT thick films on Pt/Ti/YSZ/Si substrates will be pre-stressed and have stable interfaces between the piezoelectric and substrate layers, analogous to Rainbow-type actuators.

There may be technological advantages in the pre-stressing of actuators prepared through the 0-3 composite slurry route. As pre-stressed actuators have amplified deflections, actuators prepared through the 0-3 route may also exhibit higher than anticipated deflections. An interesting technological possibility is the combination of the higher structural stiffness of spiral actuators with the pre-stressing of the actuators. This could well result in spiral actuators with higher deflections than those calculated by FE.

10.6 FE Modelling of Spiral & Fabricated Devices

10.6.1 Frequency & Stiffness Of The Mechanical Support

Fundamental frequencies, calculated for spiral piezoelectric actuators, were significantly higher than for linear equivalent unimorph actuators (Fig 9.10 chapter 9). Fundamental modes were of the order of 4 kHz; however, experimental data suggested that the resonant frequencies were much higher at around 40 kHz (Fig 9.9 chapter 9). Piezoelectric spiral actuators, discussed in the literature (chapter 2), exhibited tangential deflections the order of 100 kHz (see Fig 2.16 *left*), where the tangential deflection was the fundamental mode. The literature [82] implies that the fundamental resonant mode of a spiral actuator was much higher even than those that were calculated by FE in section 9.3.3 of chapter 9.

Analytical equations [77,80] derived for straight piezoelectric unimorph actuators have shown that deflection, force and resonant frequency all depend on B, ρ_m and Y_m. For deflection at constant B, the thickness ratio h_m/h_p, materials with large ρ_m and Y_m, such as steel, exhibited the largest deflections [77,80]. For elastic materials where Y_m is low, (such as polyacrylate) a large value of B is required to reach δ_{max} [80]. Generated mechanical forces were found [80] to be strongly dependent on A, the elasticity ratio of Y_m/Y_p. However, calculated blocking forces were found to be independent of the density of the substrate. Material properties for a range of substrate materials are presented in APPENDIX III. As a substrate material, Si has a relatively low density and a comparatively high Young's Modulus. This means that as a substrate material, Si will be poor for tip deflection but should yield good mechanical forces.

The out-of-plane deflection amplification factor may be defined Γ_s for a unimorph spiral actuator. Γ_s is expressed as the ratio of the out-of-plane deflection of a spiral actuator, δ_s, to the tip-deflection of a straight unimorph actuator, $\delta_{straight}$ (see equation (10.35)).

$$\Gamma_s = \frac{\delta_s}{\delta_{straight}} \tag{10.35}$$

As Fig 9.14 (chapter 9) shows that $\delta_s < \delta_{straight}$ it follows that Γ_s will lie in the range $0 \leq 1$, and therefore $\Gamma_s \leq \Gamma$. Tangential amplification factors lie in the range $1 \leq \infty$. It should be noted that Γ was defined in the Literature chapter as the tangential deflection factor. Fig 9.14 suggests that the stiffness of the spiral beam opposes tip deflection. The maximum mechanical energy output, λ, (see APPENDIX III) is improved by an increase in A, an increase in the stiffness of the mechanical support. An increase in λ represents a greater conversion of the input mechanical energy into mechanical output energy, manifested as an increase in $\delta_{straight}$. One might expect an increase in λ to result from an increase in K_s for a spiral unimorph actuator, and thereby observe a larger value of Γ_s because of the spiral shape. This is, however, not the case. As λ should be aided by an increase in K_s then it is possible that this energy is converted into mechanical force instead of deflection.

The electrical energy converted into mechanical energy, for a particular piezoelectric material, can be expressed as the electromechanical coupling coefficient, k_{31}. Please note that the deflection of an actuator will be in proportion to k_{31}. However, the rigidity of the mechanical support may act to damp the deflection; therefore k_{31} represents only the efficiency between the applied electrical field and the mechanical output of the piezoelectric material, and not the overall efficiency of the actuator. The parameter λ takes into account the damping of the substrate material and the electromechanical coupling coefficient for a straight unimorph actuator.

Applying the findings of Steel at al [77], Wang, and Cross [80] to the current work, any increase in structural stiffness of a linear unimorph cantilever will result in improved mechanical forces. As FE modelling predicts a structurally stiffer support for a spiral geometry it follows that spiral actuators are likely to exhibit higher mechanical forces than linear unimorphs. Further, in the case of fabricated spirals, replacing the support material Si with one of higher Y_m and ρ_m, such as steel, is likely to maximise force from the spiral actuator. Linear unimorph cantilevers amplify deflection as a function of length.

However, for thin structures there is a substantial loss of stiffness as the beam length is increased. This leads to a decline in mechanical forces that can be generated. In the case of spiral actuators, the stiffness of the structure permits large actuator lengths to be contained compactly without the loss of stiffness.

10.6.2 PZT Thick Film-Substrate Interface & Hysteresis

In the case of PZT thick films fabricated through the composite-sol route, adhesion to metallic substrates can prove problematic. Metal surfaces are sometimes pre-treated with an acid to promote the presence of hydroxyl-groups before depositing the thick film. Adhesion is promoted through metal – oxide bonds in the as-deposited film. However, a thin oxide layer can create a thin resistive barrier between support and active piezoelectric layer. Inefficient charge transfer between back electrode and ceramic layer will reduce the observed ferroelectric properties in the thick film. Deposition of PZT thick films through the composite-sol route onto a steel substrate may appear advantageous from a mechanical point of view. However, the properties of the film-substrate interface materials may degrade the overall performance of the actuator. Therefore, steel may in fact be a poorer substrate material than platinised silicon.

Hysteresis in piezoelectric unimorph actuators acts in such a way as to reduce the fundamental frequency [83]. Experimental data, see Fig 9.9, demonstrated higher modal frequencies than those obtained from the FE model. Neither the FE model of the spiral nor the analytical models of unimorph cantilevers of equivalent length considered hysteresis. If hysteresis were responsible for the differences between experiment and theory, the reverse would be observed: theoretical frequencies would be higher than experimental ones. The admittance plot shown in Fig 9.9 (chapter 9) was obtained at low electric field (1 V); it should be noted that hysteresis effects only become apparent at high drive fields and that hysteresis is, for this reason, considered unlikely to account for the differences between experiment and theory.

As noted in section 9.3.4 of chapter 9, the experimental-data and FE-data were obtained from a multi-arm device and a single spiral model respectively. Each of the 4 spiral arms, of the multi-arm device, had the same dimensions as the single spiral of the FE model. Given that the spirals making up the multi-arm device were fixed at both ends and that the single spiral, in the FE model, was fixed only at one end it seems most likely that the multi-arm device was stiffer than the spiral. Therefore, it was anticipated that the multi-arm device would exhibit a higher value for the first mode of resonant frequency. However, such was the difference between the experimental and the theoretical data, that it was considered that this point alone was unlikely to account for the differences obtained. Consequently, it was proposed in chapter 9 that the higher experimental frequency was due to higher order modes, and that lower modes were damped out of the spectrum.

It is proposed here, that the higher experimental frequency arises as a combination of the structural stiffness of the multi-arm device and the damping of lower frequency modes. It is noted that this last statement is speculative, as there was no FE model of the multi-arm device with which to compare experiment with theory. The idea that the structural stiffness of the multi-arm was insufficient to account for differences in frequencies was also speculative; conversely, one might question the evidence to support the opposing view that the structure of the multi-arm device would be sufficiently stiff to account for the higher experimental frequency.

Materials properties of the piezoceramic and hysteresis effects have been discounted as the cause of differences between experimental and theoretical frequencies.

Crack free 0-3 PZT composite thick films have been processed on steel substrates [35] and Mumetal® [43]. If poor electrical and ferroelectric properties of films on metallic substrates can be overcome then the composite sol process is likely to lend itself well to the fabrication of THUNDER® type actuators. As far as the author is aware, THUNDER® type actuators have not been processed through this route.

An interesting idea for further development would be to coat both steel spring and aluminium plates with composite slurry and then bond the resulting structure with metalorganic sol: composite to composite face. This would allow thermal processing of THUNDER actuators at elevated temperatures thus increasing thermal mismatch and hence pre-stressing between the layers. Of course increasing pre-stressing is anticipated to increase strain amplification, and thereby deflection. The principal limitation on the temperature of processing existing devices is the temperature that polyimide can withstand before degrading. Therefore, a sol-powder process where adhesion between substrate and piezoelectric layer is a consequence of an interfacial chemical reaction will eliminate the requirement for polyimide glue to bond respective layers.

A further possibility is the fabrication of spiral-type THUNDER® actuators in which there is a combination of structural stiffness and thermal mismatch induced stresses leading to potentially higher deflection amplification. Such devices would be fabricated through spin casting of slurries onto thin metallic plates as substrates. The green thick film being powder blasted, and blasting continued until the metallic actuator had been fully released. The two faces of the spiral then bonded with a sol-gel as glue before sintering the structure.

10.6.3 Out Of Plane Deflection Compared With Tangentially Deflecting Devices

It is instructive to compare Fig 9.14 (chapter 9 experimental) with Fig 2.16 (chapter 2 literature). It may be deduced that radial amplification factors, Γ_{rad} i.e. the amplification factor for radial modes, are of a similar magnitude to, $\Gamma_{\text{out-of-plane}}$, the amplification factor for out of plane deflection (where $\Gamma_{\text{out-of-plane}} = \Gamma_s$). Amplification factors depend linearly on voltage V and length L_s. Irrespective of V or L_s, the parameters $\Gamma_{\text{out-of-plane}}$, Γ_{rad} and Γ_s will lie in the range $0 \leq 1$. Therefore it is reasonable to compare Fig 9.14 (chapter 9) with Fig 2.16 (chapter 2). It was noted in the literature section that radial and tangential deflections are broadly proportional to the d_{31}/d_{33} and d_{33}/d_{31} respectively.

Tangentially deflecting spirals of the type discussed in the Literature section and shown in Fig 2.13 have yielded deflections of 700 μm at resonance (see Fig 2.16 right). The cross-sectional area (or surface) normal to the line of deflection was small for these spirals. In the case of out-of-the-plane spiral actuators there was a large cross-sectional area (or surface) normal to the direction of deflection. The cross-sectional area that is normal to the line of deflection is the area that moves against atmospheric pressure; consequently, the larger the surface area that is normal to the line of deflection, the greater the mechanical damping: that the actuator experiences. The difference in the intensity of the deflections between tangentially deflecting spirals (in the literature) and out-of-the-plane spiral actuators (discussed in chapter 9 above) could be explained if the out-of-plane deflections were heavily air damped, due to the relatively large surface area of the spiral. The in-plane deflection being larger because the thinner dimension of the actuator (its thickness) experiences less resistance as it moves in the radial direction.

10.6.4 Comparison Of Analytical Models Of Straight Unimorph Actuators With The FE Models Of The Spiral Actuators

FE calculations of the spiral showed that the deflection of the inner coils of the spiral deflected less than the outer coils. As the curvature of the spiral increases toward the centre, it was suggested that the curvature of the spiral increased the resistance of the beam to deflection. This finding was in line with deflections observed by Mohammadi et al [82] in which a tangential deflecting spiral actuators exhibited less deflection of the inner coils. However, the curvature of the spiral was normal to the axis of deflection, for the spiral-type unimorph actuators modelled in this project. Out of plane deflection is thus reduced by spiral curvature. A conclusion of this is that the stiffness of the spiral in one direction affects the deflections possible in all others.

All the analytical models for unimorph and bimorph actuators, discussed in section 2.2 of the literature chapter, assume a straight beam with constant cross section. The beam is deformed out of the plane by an electric load, and the resulting forces and moments are determined (see also APPENDIX II). Deformation is assumed to occur only in two dimensions, x and y, along the centroidal axis. The width of the straight actuator is assumed to remain constant and not subject to a bending deformation; this assumption is sometimes referred to as a one-dimensional assumption. All points along the x direction of the centroidal axis have a constant stiffness.

In the case of a spiral unimorph actuator where the spiral is designed to deflect out-of-the-plane, the curvature is normal to the cross sectional length of the beam (see Fig 10.4). The centroidal axis of a spiral must have a spiral path. If we consider a cross sectional length of the spiral beam, of length rotated through ¼ of a turn ($\theta=\pi/2$), two points are selected from the cross sectional length, one at each end (see Fig 10.5). A circular path has a constant curvature but in the case of a spiral path its curvature is constantly changing. Therefore the curvature of the spiral path at point 1 (of Fig 10.5) will be less than the curvature at point 2 (of Fig 10.5). This spiral path changes its curvature between any two points, and by the arguments in section 9.3.3 above its stiffness. If an electric load deforms the spiral between these points, then the deformation will be non-uniform. The beam will be least deformed at the stiffest point: the point where the spiral path has the highest curvature normal to the cross sectional length. Therefore, forces and moments across the deformed cross section will be non-uniform.

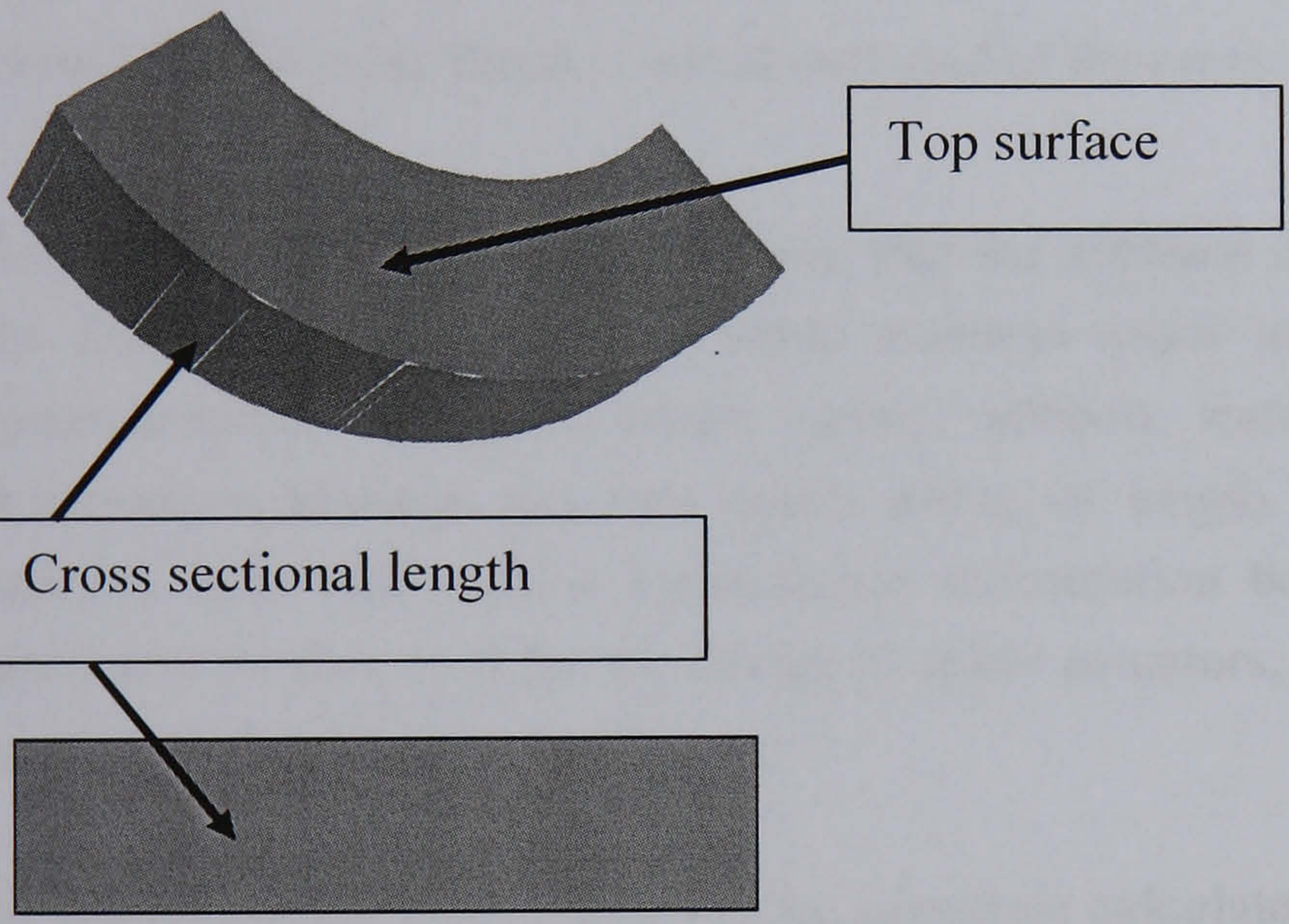

Fig 10.4 Top a ¼ turn ($\pi/2$) of a spiral beam the image is a 3D view of the beam section at an oblique angle. Bottom the cross section of this beam is seen as a 2D image viewed in cross section. The top surface of the beam section is curved and the curvature is normal to the cross sectional length.

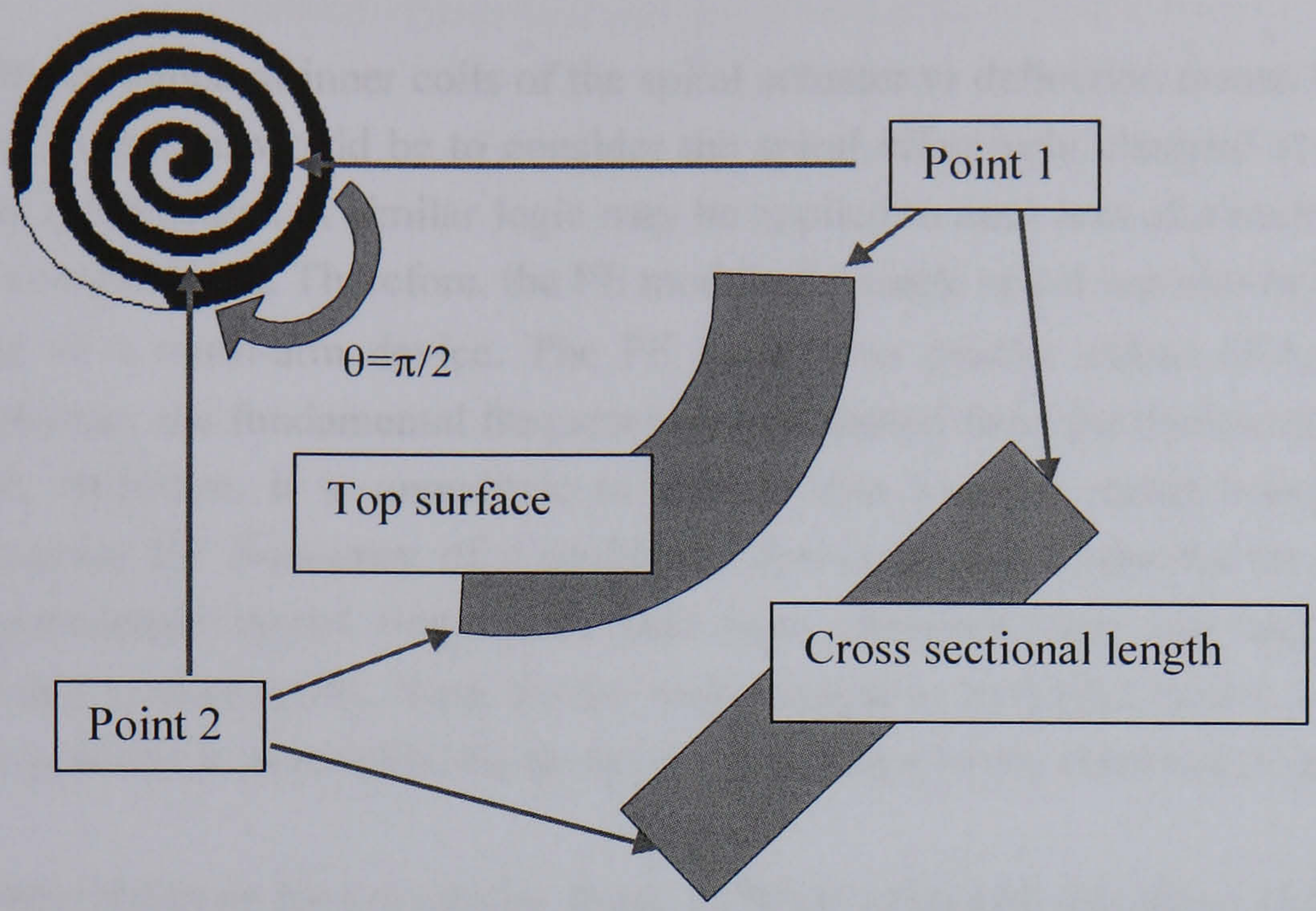

Fig 10.5 Selection of a ¼ turn (π/2) of a spiral beam. The image also shows the selection of two points on the beam – one at each end of the cross sectional length.

As straight unimorph models assume that the stiffness of two points along the length of the deformed beam will have equal stiffness under load, the beam will be deformed symmetrically. A spiral beam, under uniform load, cannot undergo symmetrical deformation between any two points along its length. Analytic models assume that a uniform load will yield a symmetrical deformation between two points. This is why analytical models used for the design of spiral actuators, in chapter 5 section 5.1.2, do not agree with calculations by FE.

To model a spiral beam, analytically, one must calculate the effect on bending forces and moments of the curvature of the beam along the centroid of the spiral, and this is not a trivial task.

10.6.5 Design Of Actuators Reviewed In The Light Of Findings From FE Modelling

In the case of spirals, δ_{spiral} will be much lower than anticipated from the adapted analytical models of chapter 5. On the other hand, f_{spiral} will be much higher. Mechanical forces and pressures are likely to be larger. These differences arise because of the increase in curvature of the beam from the outer circumference toward the origin. Analytical models for multi-arm devices were developed from analytical models of straight unimorph beams. Multi-arm devices have curved spiral beams, and, therefore, similar differences are expected between FE and analytical models for spirals and multi-arm devices respectively. It should be noted that there was no FE model of the multi-arm device; consequently, the statement in the last sentence is unverifiable.

The resistance of inner coils of the spiral actuator to deflection means that an appropriate approximation would be to consider the spiral effectively clamped at both the armature and at the origin. A similar logic may be applied to each arm of a multi-arm device: each is a single spiral. Therefore, the FE model of a single spiral can also be applied to a single arm of a multi-arm device. The FE model can predict values of δ_s, δ_{ma}, F_{ma} and F_s. However, the fundamental frequencies are obtained from the device structure as a whole, and, therefore, it is unrealistic to assume that a single spiral beam could accurately represent the frequency of a multi-arm device. It was suggested in chapter 9 that the experimental modal frequencies that were observed were too high for fundamental modes. Consequently, these modes were thought to be higher modes. It is, unfortunately, not possible to determine the modes corresponding to the observed frequencies.

Spoke actuators have a similar shape to linear unimorph actuators. An elementary model of a spoke actuator has been made and some data is presented in Table 10.2. Data shows that the spoke device has the same order of magnitude of frequency as the linear unimorph of equivalent length.

D_{max} / mm	D_c / mm	L_{spoke} / mm	N_{spoke}	w_{spoke} / µm	Linear actuator (FE) / Hz	Spoke actuator (FE) / Hz
2	0.67	0.67	4	847	68174	97085
3	0.67	1.17	8	444	22332	34256
4	0.67	1.67	12	260	10943	17546
8	0.67	3.67	4	2428	2261	4071
8	1.33	3.33	8	1307	2736	4389

Table 10.1 Comparison of frequencies of spokes between FE spoke devices and Linear unimorph equivalent spokes.

Re-design of devices is a possible option for further work. The redundancy of the inner coils means that these coils could be removed, thus maximising deflection of these devices.

10.6.6 Modelling Aims & Objectives

The principal objective was to generate a FE model for a unimorph spiral actuator, and this objective has been successfully met. The effect of the shape of the spiral has been understood through comparison with straight unimorph actuators of the same length. Unfortunately, it proved difficult to obtain good empirical results, and consequently, only limited conclusions could be drawn by comparison with FE models. The poor deflection of the spiral actuator means that the device is unlikely to achieve good stroke length in any pumping device. Therefore, the spiral actuator is not a good candidate for micro-pumping applications. Previous work [82] had indicated that the curvature of piezoelectric-spiral-actuators acts to inhibit tangential and radial deflections; however, it was not clear until this work that spiral curvature normal to the axis of deflection would also inhibit deflection.

The maximum deflection that can be achieved with a multi-arm device will be the maximum deflection of one of its spiral arms. It follows that stroke length in these devices will be inhibited for the same reasons as with spirals. Therefore, multi-arm devices are likely to make poor candidates for micro-pumping applications.

11 Concluding Remarks

11.1 Introduction

This section is subdivided into sections giving the different contributions to knowledge that were made during this project. Each subsection begins with a single paragraph that gives a little background information on the work prior to the work in this thesis. The purpose of this is to allow the reader to interpret the different contributions to knowledge, claimed in this work, against the knowledge that was available before this work was undertaken. This background information is very limited and the reader is referred to the literature review and the discussion for more details.

11.2 Sintering Aid/Electrical Conductivity Of PZT Thick Films

11.2.1 Background

PZT thick films, like thin films, are constrained systems; however, in the case of composite thick films the added powder introduces additional variables: a separate powder phase, greater porosity, and an additional sintering aid. Therefore resolving the effects of sintering conditions becomes more complicated as these systems are more complex. It should be noted that bulk ceramics are not necessarily constrained systems, and that screen-printed thick films do not contain a reactive sol component.

11.2.2 Present Work

In the current work, films that had both been Ar-sintered and infiltrated with sol exhibited a second phase. This second phase was identified as PbO and was observed to form only at low-po_2. The second phase was identified as a mixture of litharge and massicot.

This PbO phase seems to form instead of $PbO.Cu_2O$ + PbO; a $Cu_2O.PbO$ + PbO phase normally forms when molten PbO+Cu_2O is cooled through the 580 °C-solidus of the PbO-Cu_2O phase-diagram. The $PbO.Cu_2O$ + PbO phase is normally expected to form by solid state diffusion under low-po_2. However, based on the XRD spectrum of Ar-sintered thick films it was argued that solid PbO and Cu_2O formed instead. It was speculated that cooling occurred too rapidly for solid-state diffusion to take place; thus accounting for the presence of the PbO signal in the XRD spectrum of films that were sintered at low-po_2.

Pb and Cu were considered to dope on A and B lattice sites (of PZT) respectively, and this was why there was no PbO signal in the XRD spectrum of air-sintered PZT thick-films. As the second phase was resistive then any increase in electrical conductivity, of

Ar-sintered PZT, must have another explanation; presumably this increase must occur within the grain boundaries of the PZT.

It was mentioned in the literature review that firing PZT ceramics under atmospheres of low po_2 generates $V_O^{\bullet\bullet}$, and that these vacancies will act as electron donors. These donor electrons cancel positive holes generated by cationic vacancies, that have arisen by Pb volatilisation, during firing. In the case of PZT thick films that were prepared in this work it was speculated that when $[V_O^{\bullet\bullet}]<[V_{Pb}^{||}]$, $[V_O^{\bullet\bullet}]\approx[V_{Pb}^{||}]$ and $[V_O^{\bullet\bullet}]>[V_{Pb}^{||}]$ that the films were conductive, resistive and conductive respectively. It was further suggested that in very reducing conditions ($[V_O^{\bullet\bullet}]>>[V_{Pb}^{||}]$) there will be a large increase in electrical conductivity. Ar-sintered films fired at 900 °C were highly conductive (ρ_v = 7.60 to 17.43 M.Ohm.cm), and it was argued that firing under this atmosphere had given rise to the condition where $[V_O^{\bullet\bullet}]>>[V_{Pb}^{||}]$. Further, air-sintered thick films fired at 900 °C were highly resistive (ρ_v = 7170.77 to 18151.42 M.Ohm.cm), and it was speculated that firing under this atmosphere had given rise to the condition where $[V_O^{\bullet\bullet}]\approx[V_{Pb}^{||}]$.

It was proposed that the electrical conductivity of Ar-sintered-PZT was moderated by Cu. It was considered likely, by comparison with the Mn doped PZT-PCN system, that Mn displaced Cu^{2+} from the B-site. The major contribution of this part of the project was the resolution of the effect of these variables, i.e. oxygen partial-pressure and the PbO-Cu_2O additive, on the electrical conductivity of PZT thick-films.

11.3 Substrate, Electrode & Film Interfaces

11.3.1 Background

In the case of PZT thin films the thickness of the film can reduce oxygen partial pressure at the film-electrode interface, and this can aid intermetallic formation. The thickness of thin films also retards the re-oxidation of the intermetallic to Pt. However, sol-gel thin films do not contain a powder component, and hence porosity is not as significant as is the case in PZT thick films. Porosity is important as it can affect oxygen partial-pressure at the interface between the film and the electrode or at the interface between the electrode and the substrate.

11.3.2 Present Work

In the work discussed in this thesis it was found that Pb diffused into the both the electrode and the substrate. Bubbling was found on the surface of the silicon where the PZT-thick-film had been cleaved. It was proposed that the bubbling was accounted for by the presence of a lead-silicate glass. The formation of the lead-silicate-glass was linked with the de-lamination of the film and electrode from the substrate. The intermetallic and the lead silicate glass can both form depending on po_2, temperature, film thickness and the extent of infiltration.

In the case of composite thick films, porosity exists within the film. This can result in open channels within the film, thereby increasing oxygen partial pressure at the film-electrode interface and aiding the re-oxidation of the metastable phase. The infiltration of PZT thick-films with sol can reduce the porosity of the thick-film, and infiltration can prevent the re-oxidation of the intermetallic through the reduction of oxygen partial-pressure at the film-electrode-interface. A six-stage mechanism was proposed to account for the simultaneous formation of the intermetallic and the lead-silicate-glass:

Step 1	Residual C in the thick film reduces PbO to Pb
Step 2	Pb diffuses into the Pt back electrode
Step 3	Pt_3Pb formation in the intermetallic
Step 4	PtPb forms
Step 5	On saturation of the intermetallic layer Pb continues to diffuse into the underlying Si substrate
Step 6	At some later point when oxygen partial pressure has risen Pb is oxidised to PbO and Si to SiO_2 and these components can flux to form $PbSiO_3$

Therefore Pb diffusion was damaging to the ferroelectric and electric properties of the thick films, and needed to be eliminated. It was found that the best barrier layer system was YSZ on silicon, and that this worked well in preventing the diffusion of Pb from the thick film. YSZ was found to be a better diffusion barrier layer system than TiO_2 for PZT thick films on Si.

11.4 Thick Film Device Processing

11.4.1 Background

Devices of the type discussed in this thesis made with PZT thick films have not been discussed elsewhere. These devices and their fabrication route are original aspects of the current work.

There has been some earlier work on the wet etching of PZT materials, but not on the wet etching of PZT thick films. There has also been some work on the powder blasting of glass materials but not PZT. However, in this work PZT thick film materials were both wet-etched and powder-blasted for the first time. Earlier work on wet chemical etching of PZT had shown that powder particles were freed form bulk ceramics by an attack at the grain boundary.

11.4.2 Present Work

The development of a novel processing route for the fabrication of any 2D-device shape in the plane of the wafer was undertaken in the current work. The process also contains a means of controlling the thickness of the supporting actuator. Back face wafer staining by the sol component of the PZT thick film was eliminated by the addition of a Cr barrier layer. Si was considered the better substrate as this allowed both DRIE release of the actuators and the sintering of PZT thick films under an air atmosphere. Air sintering of PZT on Si was only permissible when used in conjunction with the YSZ barrier system. The fabrication of devices has been a major contribution of this project, for example the integration of powder blasting with thick film processing technology. This is important as PZT is both chemically-inert and mechanically-hard; consequently, PZT is a difficult material to machine or to pattern.

11.4.2.1 Wet Chemical Etching of PZT

In this work, for the first time, composite PZT thick films were wet etched in HF/HCl. The etching was optimised to achieve minimum line widths and under cut by controlling concentration, temperature and etching time. Optimum etch rates were achieved at 2.16 μm/min, with stirring.

The etching solution attacks the second phase located at the grain-boundaries of the PZT. The etching solution also attacks the sol-derived component of the PZT. The roughening of the sidewalls, of etched features, has resulted from the freeing of the powder component of the PZT thick film. This occurred partly because of an attack of the second-phase at the PZT grain boundary, and partly due to a chemical attack on the sol component of the thick film.

Wet etching of PZT resulted in the precipitation of PbF_2, PbO and $PbCl_2$. PbF_2 precipitated onto the etched-PZT-surface. PbO was found to form in cracks in the PZT-surface, but it only formed on the protected surface of the PZT. $PbCl_2$ was detected on the Pt-surface, where the PZT thick film had been etched back to the bare metal.

It was proposed that the chemical reaction, associated with wet etching, proceeds through the depletion of the Zr and Ti components of the PZT before reaction with PbO. PbF_2 salts precipitate from the solution because of competition with Zr and Ti components for F^- ion in solution.

11.4.2.2 Powder Blasting

Powder blasting results in the intra-granular cleavage of PZT grains. The statistical model of variables concluded that the resolution of the photoresist and hence the resolution of the final feature was inversely proportional to revs x $\theta_{elastic}$. Flux time was found not to be significant in further reducing the resolution of etched features.

Jet-machining was considered not to be appropriate for the machining of devices that were to be made with these materials. This was because the glass like nature of the composite thick film was brittle, and this was the case even before the film had been sintered. Therefore the best means of machining brittle PZT and cutting any device shape was powder blasting.

11.5 Device Design, Modelling, Fabrication And Testing

11.5.1 Background

Straight piezoelectric unimorphs had been modelled before, and there were analytical equations in the literature to describe how these devices worked. Earlier work on piezoelectric spirals had concentrated on the development of tangential deflecting devices. These devices had been fabricated through a fused deposition technique. These spirals were modelled through FE.

11.5.2 Present Work

In this project knowledge was advanced through the design of a novel spiral actuator that was designed to deflect out of the plane. Other devices proposed were multi-arms and spokes. Existing equations for straight-piezoelectric-unimorphs were modified so that spiral actuators had the correct length. These adapted models were extended to a range of other devices.

This work has furthered the understanding of this type of device through FE modelling. It was found that as the curvature of the beam increases toward the centre of the spiral that the curvature restricts the out-of-plane deflection of the beam. FE models showed that the mechanical stiffness of the spiral-beam was increased with the curvature of the beam; consequently, the inner coils exhibit virtually no deflection and appear to be redundant.

FE modelling also showed that the straight-unimorph-models did not accurately predict deflection or the first mode of resonant frequency. For example consider the case of a spiral actuator of dimensions: N_{turns}=3, w_{spiral}=166.7 μm and D_{max}=2 mm. In this case the FE spiral model generated a first resonant frequency of 1760 kHz. The FE and analytical models of straight unimorphs (of equivalent length to the spiral already mentioned) generated values of 350.5 kHz and 330.4 kHz respectively. With regard to deflection the values generated were: 0.496 mm (analytical model of straight unimorph), 0.514 mm (FE straight unimorph) and 0.026 mm (FE spiral unimorph). These differences between straight and spiral models arose because straight models did not take account of the increase in stiffness with the curvature of the spiral beam.

Spiral actuators allow large lengths to be contained compactly without the loss of mechanical stiffness. The structural stiffness of the spiral may aid an improvement in mechanical force output. As λ will be aided by an increase in K_s it follows that for spirals where K_s is large, that λ will also be large. If spiral actuators have small Γ_s values it may be the case that energy is not manifested as deflection but as mechanical force instead.

The stiffness of the spiral actuator in one direction affects the stiffness of the structure in all others. In other words for two points on the cross section of a beam the stiffness of one point will be lesser or greater than the other.

A multi-arm device was shown to be piezoelectrically active with an impedance scan. This devise exhibited resonant frequencies at 42, 70 and 85 kHz. The observed modes were very weak, and it was considered that air-damping had reduced the intensity of the observed modes.

12 Further Work

In this section further work is discussed; this, further work, has arisen from the experimental work, the modelling work and conclusions reached in the discussion chapter. This section concerns work that will complete the work in this project and also considers new directions arising from the present work.

Redesign of back face features is necessary for wire bonding to devices, in particular circular holes for DRIE etching. Further, the inclusion of dice marks in the mask set will provide an easy route for the dicing of chips through DRIE release. Release of devices through DRIE as opposed to sawing will eliminate vibration and thereby damage to fragile mechanical structures.

Finite element modelling of spirals needs to be advanced. In particular a harmonic analysis to assess spiral performance in a cyclic field which would be the operating condition for such a device. Further, resolution of the differences between FE models and impedance spectra are required. Spoke and multi-arm actuators are also deserving of a fuller investigation by FEA in which it is envisaged that structural considerations will be taken into account.

A comprehensive experimental analysis of fabricated devices is also required including, experimental means for determining force, frequency and displacement are required as a function of both static and cyclic fields. Structural analysis on all fabricated devices through impedance analysis needs to be completed.

From a materials perspective, a range of substrate materials could be explored concerning the fabrication of these actuators through powder blasting. For example, graphite could be employed where the cantilever was released through RIE in an oxygen-rich plasma. Alternatively, the growth of graphite on silicon and deposition onto this as a barrier system: the cantilever is released through the processes discussed in chapter 3 followed by RIE of the graphite layer. The use of graphite is interesting in that it might allow fabrication of micro-RAINBOW actuators where the large length of the actuator and increased structural stiffness are combined with pre-stressing of piezoelectric and substrate layers.

PZT thick films have been fabricated onto sheet-steel-substrates [35]: this would constitute an alternative substrate material. However, the author is aware of no means of releasing or controlling the cantilever thickness. If a steel substrate were used, powder blasting could be used to cut device structures into the metal.

A further project would incorporate a polymeric membrane into the actuator design for applications such as micropumps.

APPENDICIES

APPENDIX I Ferroelectric properties

	Materials properties			
Crystal system	Piezoelectric	Pyroelectric	Electrooptic	Enantiomorphous
Triclinic	1	1	1	1
Monoclinic	2, m	2, m	2, m	2
Orthorhombic	222, mm2	mm2	222, mm2	222
Tetragonal	4, $\bar{4}$, 422, 4mm, $\bar{4}$2m,	4, 4mm	4, $\bar{4}$, 422, $\bar{4}$2m	4, 422
Trigonal	3, 32, 3m	3, 3m	3, 32,	3, 32
Hexagonal	6,622, 6mm, $\bar{6}$m2	6, 6mm	6, 622	6, 622
Cubic	23, $\bar{4}$3m	none	23, 432	23, 432

∞ Point groups that can have non-zero values of the gyration tensor are defined as optically active. However, for uniaxial materials only those point groups that allow enantiomorphism can exhibit optical rotation of polarised light propagating along the optical axis.

Table A1 Symmetries giving rise to physical properties observed in Ferroelectric materials. Taken from IEEE standards on Piezoelectricity [7].

APPENDIX II Cross model of a Unimorph actuator

Frequency Determination

In the case of a unimorph piezoelectric actuator composed of two materials, a piezoelectric and mechanical support, each material will have a different Young's modulus. The transform cross section method proportions the width, w, of the layers of the beam by the ratio of the Young's modulus of the layers; consequently, the beam is defined by effectively one Young's modulus. The flexural rigidity and position of the centroidal axis can then be obtained for the transformed beam. The cross method uses the transformed cross section method to locate the centroidal axis, y_c, in the unimorph actuator, where y_c is measured from the base of the actuator.

$$y_c = \frac{1}{2}\frac{Ah_m^2 + 2h_m h_p + h_p^2}{Ah_m + h_p} \qquad \text{A 1}$$

As before $A = Y_p/Y_m$ where Y_p and Y_m are the Young's modulus for the piezoelectric layer and mechanical support respectively. The thickness of the actuator is $h=h_p+h_m$ where h_m and h_p are the thickness of the mechanical support and the piezoelectric layer respectively. There is also a thickness ratio B where $B=h_m/h_p$.

Once the centroidal axis has been located, the area-moment-of-inertia, I_c, can be determined using parallel axis theorem. This is calculated for each layer as a moment of inertia plus a term relative to the centroidal axis. Further, I_c can be expressed in terms of A and B (see equation A 2).

$$\begin{aligned} I_c &= \frac{Awh_m^3}{12} + \frac{wh_p^3}{12} + \frac{wh_m h_p y_c}{2} \\ &= \frac{wh_p^2}{12} \times \left[\frac{A^2B^4 + 2A(2B+3B^2+2B^3)+1}{AB+1}\right] \end{aligned} \qquad \text{A 2}$$

The flexural rigidity Y_pI_c is used to determine the resonant mode of frequency,

$$f_j = \frac{\varsigma_j^2}{2\pi L^2}\left(\frac{Y_pI_c}{m_a}\right)^{\frac{1}{2}} \qquad \text{A 3}$$

where f_j and ζ_j denote the frequency and eigenvalue of mode j. For the first mode of frequency (j=1) the eigenvalue is 1.875. This equation applies for a straight unimorph actuator of length L. The mass of the actuator m_a may be calculated from the densities of the mechanical support ρ_m and the piezoelectric layer ρ_p. It should be noted that there is also a density ratio C_ρ, this corresponds to $C_\rho=\rho_m/\rho_p$.

$$m_a = w(\rho_p h_p + \rho_m h_m) \qquad \text{A 4}$$

Substituting equations A 4 and A 2, into equation A 3 and rearranging yields equation A 5.

$$f = \frac{3.52h}{2\pi L^2} \times \sqrt{\left(\frac{Y_p}{3\rho_p}\right) \times \left[\frac{A^2B^4 + 2A(2B + 3B^2 + 2B^3) + 1}{(AB+1)(1+BC_\rho)(1+B)^2}\right]} \qquad \text{A 5}$$

This equation shows a separate non dimensional term. Allowing for comparison between actuators on mechanical-supports made of differing-materials.

Deflection Determination

The unimorph cantilever is unsymmetrical, and can produce both pure extensional and pure bending deformation; these, deformations, are denoted by the subscripts ext and ben respectively. The internal force arising from bending and extensional deformation is denoted F_{tot} and is the sum of internal forces.

$$F_{tot} = F_{ext} + F_{ben} \qquad \text{A 6}$$

Bending moments arising from extensional and pure bending deformation are denoted as M_{tot}

$$M_{tot} = M_{ext} + M_{ben} \qquad \text{A 7}$$

The tensor form of the converse piezoelectric effect is given in equation A 8.

$$S_{ij} = s^E_{ijkl}\sigma_{kl} + d_{kij}E_k \qquad \text{A 8}$$
$$i,j,k,l = 1,2,3$$

Here, S_{ij}, σ_{kl}, d_{kij} and E_k correspond to strain, stress, piezoelectric modulus and electric field. The elastic compliance at constant electric field is noted as s^E_{ijkl}. If an electric field is applied across the top and bottom surfaces of the piezoelectric plate of a straight unimorph piezoelectric actuator, then the expansion or contraction in length will produce a mechanical bending deformation. It is assumed that perfect bonding exists between the mechanical support and the ceramic plate. Because all surfaces are free and no forces, other than those from the electric field, are present, the stress components,

$\sigma_2=\sigma_3=\sigma_4=\sigma_5=\sigma_6$, are all-equal to zero. However, because the plate expands or contracts along the length of the actuator, the stress component in this direction is non zero ($\sigma_1\neq 0$). As the actuator can deform in all directions the strain components, S_1, S_2, S_3, S_4, S_5 and S_6, are all non zero. Using the reduced suffix notation, discussed in the introduction chapter, equation A 8 reduces to equation A 9.

$$\begin{aligned} S_1 &= s_{11}^E\sigma_1 + s_{12}^E\sigma_2 + s_{13}^E\sigma_3 + \ldots. + d_{31}E_3 \\ &= s_{11}^E\sigma_1 + d_{31}E_3 \end{aligned} \qquad \text{A 9}$$

Rearrangement of equation A 9 yields equation A 10, where $Y_p=1/s^E_{11}$. This equation represents stress in the piezoelectric plate of the unimorph.

$$\sigma_1 = \frac{S_1}{s_{11}^E} - \frac{d_{31}E_3}{s_{11}^E} = Y_p(S_1 - d_{31}E_3) \qquad \text{A 10}$$

The stress in the mechanical support, of the unimorph, involves no piezoelectric term and is purely a product of the elastic modulus and the internal strain (see equation A 11).

$$\sigma_1 = \frac{S_1}{s_{11}^E} = Y_m S_1 \qquad \text{A 11}$$

Extensional Deformation

The force due to extensional deformation with respect to the distance from the mid plane (see figure below), can be related to stress in the unimorph through equation A 12

$$dF_{ext} = \sigma_1 w dy \qquad \text{A 12}$$

Substituting equations A 10 and A 11 into A 12 the following integral equation can be set up to obtain F_{ext}. The stress term for the piezoelectric layer is integrated across the thickness of the plate (h=0 to h_p). The stress term for the mechanical support layer is integrated across the thickness of the mechanical support (h=0 to h_m). It should be noted that F_{ext} is obtained as the sum of integrated stresses in the piezoelectric and mechanical support layers.

$$F_{ext} = \int \sigma_1 w dy = \int_{h_p} \left(Y_p S_1 + Y_p d_{31} E_3\right) w dy + \int_{h_m} \left(Y_m S_1\right) w dy \qquad \text{A 13}$$

At the mid plane of the actuator, where y=0 (see Fig A1), the uniform strain component for S_1 will be S_0. Substituting S_0 for S_1 in equation A 13 and integrating: yields equation A 14.

$$F_{ext} = (Y_p h_p + Y_m h_m) w S_0 + (Y_p d_{31} E_3) w h_p \qquad \text{A 14}$$

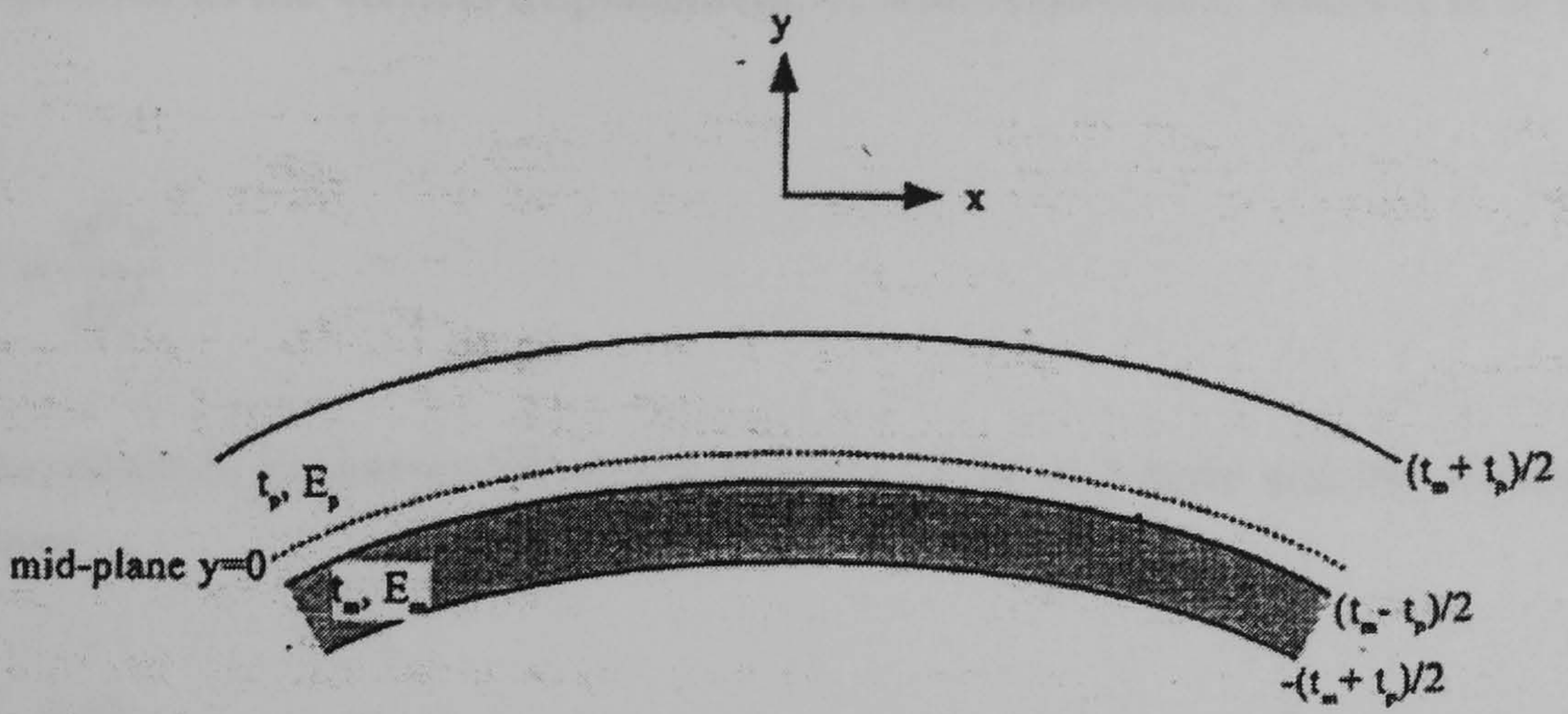

Fig A 1 Bending deformation of a unimorph actuator under an electric field. Image taken from Cross and Wang [80]. The parameters t_m, t_p, E_m, E_p, in the Figure, correspond to the respective parameters h_m, h_p, Y_m and Y_p, in the text.

The bending moment due to extensional force M_{ext} can be expressed, as in equation A 12, as equation A 15,

$$dM_{ext} = \sigma_1 wydy \qquad \text{A 15}$$

where y is with respect to the mid plane.

M_{ext} can be obtained through setting up an integral, in which stresses arising in the piezoelectric layer are integrated over the thickness of the piezoelectric layer as a function of distance from the mid plane. An additional term is added for moments arising from stresses in the mechanical support. Stresses in the mechanical support are integrated over-the-range of y as a distance from y=0 (see Figure above).

$$M_{ext} = \int \sigma_1 wydy = \int_{(h_m-h_p)/2}^{(h_m+h_p)/2} (Y_p S_1 + Y_p d_{31} E_3) wydy + \int_{-(h_m+h_p)/2}^{(h_m-h_p)/2} (Y_m S_1) wydy \qquad \text{A 16}$$

Integrating equation A 16 and substituting S_0 for S_1 yields equation A 17

$$M_{ext} = \frac{1}{2}(Y_p h_p h_m - Y_m h_m h_p) w S_0 + \frac{1}{2}(Y_p d_{31} E_3) w h_p h_m \qquad \text{A 17}$$

Pure Bending Deformation

In the case of pure bending deformation, the curvature of the driven actuator, κ, can be expressed as the vertical displacement, v, with respect to x, where x is as defined in Fig A 1.

$$\kappa = \frac{d^2 v}{dx^2} \qquad \text{A 18}$$

The strain S_1 is obtained from the product of the curvature and the distance from the mid plane.

$$S_1 = \kappa y \qquad \text{A 19}$$

Substituting equation A 19 into equations A 10 and A 11, to obtain values of σ_1 for pure bending. As before the integrals are set up to obtain F_{ben} as the sum of bending forces in the piezoelectric and mechanical support layers respectively.

$$F_{ben} = \int \sigma_1 w dy = \int_{(h_m-h_p)/2}^{(h_m+h_p)/2} (Y_p \kappa y) w dy + \int_{(h_m+h_p)/2}^{(h_m-h_p)/2} (Y_m \kappa y) w dy \qquad \text{A 20}$$

Integrating equation A 20 yields the following expression.

$$F_{ben} = \frac{1}{2}(Y_p - Y_m) w \kappa h_p h_m \qquad \text{A 21}$$

A similar approach, to that used in equation A 16, is used to obtain the pure bending moment (see equations A 22 and A 23).

$$M_{ben} = \int \sigma_1 w y dy = \int_{(h_m-h_p)/2}^{(h_m+h_p)/2} (Y_p \kappa y) w y dy + \int_{(h_m+h_p)/2}^{(h_m-h_p)/2} (Y_m \kappa y) w y dy \qquad \text{A 22}$$

$$M_{ben} = \left[Y_p \left(\frac{h_p h_m^2}{4} + \frac{h_p^3}{12} \right) + Y_m \left(\frac{h_m h_p^2}{4} + \frac{h_m^3}{12} \right) \right] w \kappa \qquad \text{A 23}$$

Determination Of Deflection From Pure Bending And Extensional Deformation Equations

The combination of equations for F_{ext}, M_{ext}, F_{ben} and M_{ben} yields A 24.

$$F_{tot} = F_{ext} + F_{ben} = \upsilon S_o + \nu\kappa + \varpi \qquad \text{A 24}$$
$$M_{tot} = M_{ext} + M_{ben} = \nu S_0 + o\kappa + \vartheta$$

The coefficients of the parameters introduced in equation A 24 may be extracted from equations A 14, A 17, A 21 and A 23 to yield equation A 25.

$$\upsilon = \left(Y_p h_p + Y_m h_m\right) \qquad \text{A 25}$$
$$\nu = \frac{1}{2}\left(Y_p - Y_m\right) h_p h_m w$$
$$o = \left[Y_p\left(\frac{h_p h_m^2}{4} + \frac{h_p^3}{12}\right) + Y_m\left(\frac{h_m h_p^2}{4} + \frac{h_m^3}{12}\right)\right] w$$
$$\varpi = \left(Y_p d_{31} E_3\right) w h_p$$
$$\vartheta = \frac{1}{2}\left(Y_p d_{31} E_3\right) w h_p h_m$$

When no external force is applied to the unimorph actuator $F_{tot}=0$ and $M_{tot}=0$ and equation A 24 can be solved for curvature. The solution can be expressed in a non-dimensional form

$$\kappa = \frac{\upsilon\vartheta - \nu\varpi}{\nu^2 - \upsilon o} \qquad \text{A 26}$$
$$= \frac{d_{31}E_3}{h_p} \times \left[\frac{6AB(1+B)}{A^2B^4 + 2A(2B + 3B^2 + 2B^3) + 1}\right]$$

Integration of equation A 18 yields an expression for the displacement, v, of the actuator at x.

$$v = \frac{\kappa x^2}{2} \qquad \text{A 27}$$

The tip deflection may be determined, from equation A 27, by setting x = L. It follows that when x = L that v=δ where δ is the tip deflection of the cantilever. The deflection, δ, of the actuator can be expressed as a function of the curvature. Further, deflection can be expressed in a non-dimensional form.

$$\delta = \frac{\kappa L^2}{2} = \frac{3L^2 d_{31} E_3}{2h} \times \left[\frac{2AB(1+B)^2}{A^2B^4 + 2A(2B + 3B^2 + 2B^3) + 1} \right]$$ A 28

Blocking Force Determination

The blocking force F that a unimorph actuator generates may be determined from the deflection of the cantilever and the flexural rigidity of the beam.

$$F = \frac{3Y_p I_c \delta}{L^3} = \frac{3Y_p I_c \kappa}{2L}$$ A 29

Substitution of equations A 27 and A 2 into equation A 29 yields, after some rearrangement, equation A 30

$$F = \frac{3wh^2 Y_p}{8L} \left[\frac{2AB}{(AB+1)(1+B)} \right]$$ A 30

APPENDIX III Mechanical Energy Output From Unimorph Actuators on Different Substrates.

The maximum mechanical output energy, λ, expresses the percentage of the input electrical energy that is converted into mechanical output: for unimorph actuators [83]. Maximum electrical energy output is related to the elastic ratio A and the electromechanical coupling factor, k_{31}, through equation A 31 [83].

$$\lambda = \frac{9k_{31}^2(A+\sqrt{A})}{32A+64\sqrt{A}+32-k_{31}^2(9A+17\sqrt{A}+8)} \qquad \text{A 31}$$

The calculated value of λ therefore depends on the elastic properties of the mechanical support and the piezoceramic. Elastic properties of a range of support materials are given in Table A2.

Support Material	Steel	Silicon	Aluminium	Acrylic
Density / kg/m^3	7700	2330	2992	1185
Young's' Modulus /GPa	195.0	156.0	65.0	3.1

Table A2 Mechanical properties of support layers

Mechanical and piezoelectric properties of a range of piezoceramics are given in Table A3.

Piezoelectric Material	PZT 5A	PZT 5H	HD3203	PZ26	PZT 4
Electromechanical coupling factor k_{31}	-0.33	-0.33	-0.34	-0.39	-0.44
Young's' Modulus /GPa	61.0	62.0	62.0	76.9	82.0

Table A3 Materials properties of different PZT Materials

The electromechanical coupling coefficient k_{31} is a materials property that measures coupling between electric field and mechanical output. The mechanical output of a unimorph actuator depends on the thickness ratio B and on the elastic ratio A. Therefore λ will depend on the coupling between the electrical field and piezoceramic the thickness ratio B and A.

Based on data in Table A2 and Table A3 it can be seen that the stiffer the support the greater the value of λ (see Table A4). Further, the more compliant the piezoceramic the greater the value of λ. Silicon makes quite a good support material although results for PZ26 are disappointing particularly when compared with Motorola HD3203.

Support	Steel		Silicon		Aluminium		Acrylic	
Piezoceramic	A	λ / %	A	λ / %	A	λ / %	A	λ / %
PZ26	2.54	1.931	2.03	1.848	0.85	1.513	0.04	0.534
PZT 4	2.38	1.929	1.90	1.845	0.79	1.501	0.04	0.522
PZT 5A	3.20	2.122	2.56	2.034	1.07	1.671	0.05	0.597
PZT 5H	3.15	2.575	2.52	2.451	1.05	1.955	0.05	0.634
HD3203	3.15	3.109	2.52	2.943	1.05	2.293	0.05	0.682

Table A4 Maximum mechanical energy outputs for a range of PZT materials on a range of substrates.

APPENDIX IV Materials Constants For Motorola HD3203

Symbol	Unit	Motorola HD 3203	Mechanical support (Si)
$\varepsilon_{11}=\varepsilon_{22}$	pF	$2420\times\varepsilon_0$	
ε_{33}	pF	$3330\times\varepsilon_0$	
d_{31}	10^{-10} C/N	-295	
e_{31}	C/m^2	-48.00	
e_{33}	C/m^2	-31.38	
$e_{15}=e_{24}$	C/m^2	14.29	
ρ	kg/m^3	7850	2330
c_{11}^E	GPa	139.7	
c_{12}^E	GPa	88.7	
c_{13}^E	GPa	99.7	
c_{33}^E	GPa	140.0	
c_{44}^E	GPa	25.1	
$c_{66}=c_{55}^E$	GPa	25.5	
Y_{11}^E	GPa	64.1	156.0

Table 5 Materials Properties for z-poled PZT (Motorola 3203 HD). Taken from Sherrit et al [124]. The table contains data that was used in the modelling of the actuators, and also gives the properties of the mechanical support that was used.

APPENDIX V Materials Constants For Ferroperm PZ-Series

Symbol	Unit	Pz24	Pz26	Pz27	Pz28	Pz29
ε_{33}	10^3	0.43	1.33	1.80	0.99	2.87
tan δ		0.002	0.003	0.017	0.004	0.016
$T_C >$	°C	330	330	350	330	235
k_{31}		0.292	0.327	0.327	0.332	0.370
k_{33}		0.659	0.684	0.699	0.687	0.752
k_{15}		0.327	0.553	0.609	0.631	0.671
d_{31}	10^{-10} C/N	-0.58	-1.28	-1.70	-1.14	-2.43
d_{33}	10^{-10} C/N	1.49	3.28	4.25	2.75	5.74
d_{15}	10^{-10} C/N	1.51	3.27	5.06	4.03	7.24
e_{31}	C/m^2	-1.45	-2.80	-3.09	-3.60	-5.06
e_{33}	C/m^2	9.9	14.7	16.0	12.4	21.2
e_{15}	C/m^2	6.55	9.86	11.64	10.67	13.40
ρ	kg/m^3	7700	7700	7700	7700	7460
c_{11}^E	GPa	162.00	168.00	147.00	152.00	134.00
c_{12}^E	GPa	88.40	110.00	105.00	90.50	89.70
c_{13}^E	GPa	87.50	99.90	93.70	87.40	85.70
c_{33}^E	GPa	134.00	123.00	113.00	118.00	109.00
$c_{44}^E = c_{55}^E$	GPa	43.50	30.10	23.00	26.50	18.50
c_{66}	GPa	36.80	28.80	21.20	30.70	22.00
Y_{11}^E	GPa	95.60	76.90	59.00	79.40	58.80

Table 6 Material properties for a range of piezoelectric materials from Ferroperm S/A[135]

APPENDIX VI Finite Element Code For The Piezoelectric Spiral Actuator

```
FINISH
/OUTPUT,out
/CLEAR
/OUTPUT,TERM
/FILENAME,pump300
/TITLE,MEMS 3D spiral unimorph
!/STITLE,1,Richard Haigh attempt 1.inp
/PLOPTS,LOGO,ON

! general parameters
            width                       =166.67e-6
            thick                       =25.8e-6
            thick_c                     =10e-6
            revs                        =5
            beams                       =2
            in_rad                      =width
            steps                       =(30*revs)
            radius                      =4e-3
            q                           =(83.33e-6)/width


!/TLABEL,-1,-.85,Silicon thickness = %thick%
!/TLABEL,-2,-.86,PZT thickness   = %height_c%
! solution parameters

            voltage                           =15
            silicon                           =1
            ceramic                           =2
            area                              =1
            f_min                             =10000
            f_max                             =30000
            deltaf                            =10000
            eps_0                             =8.854E-12
            *AFUN,RAD pi                      =ACOS(-1)
            *AFUN,DEG xi                      =0.005

! material properties Motorola HD3203
! index is based on IEEE notation poled in z direction
! * ceramic *
```

```
      dens_c            =7850
      eps11_c           =2420*eps_0
      eps33_c           =3330*eps_0
      e31_c             =-48.00
      e33_c             =-31.38
      e15_c             =14.29
      e24_c             =e15_c
      c11_c             =139.7E9
      c12_c             =88.7E9
      c13_c             =99.7E9
      c33_c             =140.0E9
      c44_c             =25.1E9

! * silicon *

          dens_s            =2330
          young_s           =155.8e9
          poiss_s           =0.2152
          shear_s           =64.1e9

! *** element declaration ***

       /PREP7

   ET,ceramic,SOLID5



   KEYOPT,ceramic,1,3
   KEYOPT,ceramic,3,0
   KEYOPT,ceramic,5,2

   ET,silicon,SOLID45

   KEYOPT,silicon,1,0
   KEYOPT,silicon,2,0
   KEYOPT,silicon,4,0
   KEYOPT,silicon,5,2
   KEYOPT,silicon,6,3
   KEYOPT,silicon,9,0


       FINISH
```

```
! *** material declaration SI units ***
        ! *** material declaration ***
        ! * ceramic material *
/PREP7
EMUNIT,EPZRO,ceramic
         MP,DENS,ceramic,dens_c
         MP,PERX,ceramic,eps11_c
         MP,PERY,ceramic,eps33_c
         MP,PERZ,ceramic,eps11_c

         TB,PIEZ,ceramic
         TBDATA,3,e31_c
         TBDATA,6,e31_c
         TBDATA,9,e33_c
         TBDATA,14,e24_c
         TBDATA,16,e24_c

         TB,ANEL,ceramic
         TBDATA,1,c11_c
         TBDATA,2,c12_c
         TBDATA,3,c13_c
         TBDATA,7,c11_c
         TBDATA,8,c13_c
         TBDATA,12,c33_c
         TBDATA,16,c44_c
         TBDATA,19,c44_c
         TBDATA,21,c44_c

        ! * silicon *

         MP,DENS,silicon,dens_s
         MP,EX,silicon,young_s
         MP,EY,silicon,young_s
         MP,EZ,silicon,young_s
         MP,NUXY,silicon,poiss_s
         MP,NUYZ,silicon,poiss_s
         MP,NUXZ,silicon,poiss_s
         MP,GXY,silicon,shear_s
         MP,GYZ,silicon,shear_s
         MP,GXZ,silicon,shear_s
```

```
        FINISH

!geometry and meshing

        /PREP7
        STAT
        KEYPTS
! define geometry
! plot spiral keypoints

CSYS,1
        r                       =0
        theta           =0
        *DO,i,1,steps,1
!Do-loop to plot a spiral path of keypoints
          theta=(i)*(360*revs/steps)
          r=theta*radius/(360*revs)
          K,i,r,theta,0
        *ENDDO

        CSYS,0
        K,,100,0,0
        K,,0,100,0
        CSYS,1

!set of Origins along bb
!to displace a set of kps relative to master set
        *DO,i,1,steps,1
        theta   =(i-2)*((360+(360*revs/steps))*revs/steps)
                r       =theta*radius/(360*revs)
                CSKP,10+i,1,i,steps+1,steps+2,,,
                K,,width,theta,0
                CSDELE,10+i,steps+10,1
        *ENDDO

!attach unit areas to kps
        *DO,i,1,steps-1,1
        A,i,i+1,i+steps+3,i+steps+2
        *ENDDO

!define geometry for arm
        CSYS,0
```

```
CSKP,14,0,2*steps-1,steps+1,steps+2,,,
K,999,width,0,0
CSKP,11,0,2*steps,steps+1,steps+2,,,
K,1000,width,0,0
CSKP,12,0,2*steps+1,steps+1,steps+2,,,
K,1001,width,0,0
CSKP,13,0,2*steps+2,steps+1,steps+2,,,
K,1002,width,0,0


      A,2*steps-1,2*steps,1000,999
      A,2*steps,2*steps+1,1001,1000
      A,2*steps+1,2*steps+2,1002,1001

      CSYS,0
      ASEL,ALL
      VEXT,ALL,,,0,0,thick,,,,
      VSEL,S,LOC,Z,0,thick
      VATT,silicon,,silicon
      ASEL,S,LOC,Z,(999/1000)*thick,(1001/1000)*thick
      VEXT,ALL,,,,,thick_c
      VSEL,S,LOC,Z,(999/1000)*thick,(1001/1000)*(thick+thick_c)
      VATT,ceramic,,ceramic

      CSYS,1
      VSEL,S,LOC,Z,-10,thick+thick_c+10,,1
      VSEL,R,LOC,X,0,10+radius+(2*width),,
      NUMMRG,KP,thick_c/1000,thick_c/1000
      NUMMRG,NODE,thick_c/1000,thick_c/1000
      NUMMRG,ELEM,thick_c/1000,thick_c/1000
      NUMMRG,KP,thick_c/1000,thick_c/1000
      ALLS

      ESIZE,width*q,,
      MSHAPE,0,3D
      MSHKEY,1
      VSEL,S,LOC,Z,0,thick+thick_c,,1
      VMESH,ALL

! Apply loads
FINISH
! *** boundary conditions ***
```

```
/PREP7
CSYS,1
        ASEL,S,LOC,X,radius+width,radius+2*width,,,,
        DA,ALL,UX,0
        DA,ALL,UY,0
        DA,ALL,UZ,0
        CSYS,0
        ASEL,S,LOC,Z,(999/1000)*(thick+thick_c),(1001/1000)*(thick+thick_c)
        ESEL,R,TYPE,,ceramic
        NSLE,S
        *GET,top_y,NODE,,MXLOC,Z
        *GET,bot_y,NODE,,MNLOC,Z
        NSEL,R,LOC,Z,top_y
        *GET,node_s,NODE,,NUM,MIN
        CM,signal,NODE
        CP,NEXT,VOLT,ALL
        ASEL,S,LOC,Z,(999/1000)*(thick),(1001/1000)*(thick)
        ESEL,R,TYPE,,ceramic
        NSLE,S
        NSEL,R,LOC,Z,bot_y
        *GET,node_m,NODE,,NUM,MIN
        CM,mass,NODE
        CP,NEXT,VOLT,ALL
        NALL
        D,node_m,VOLT,0
        D,node_s,VOLT,voltage
        ESEL,S,TYPE,,ceramic
        NSLE,S
        *GET,max_x,NODE,,MXLOC,X
        NSEL,R,LOC,Z,top_y
        NSEL,R,LOC,X,max_x
        *GET,upper,NODE,,NUM,MIN
        ESEL,S,TYPE,,ceramic
        NSLE,S
        NSEL,R,LOC,Z,bot_y
        NSEL,R,LOC,X,max_x
        *GET,lower,NODE,,NUM,MIN
        ALLS
        FINISH
        ALLS

! *** MODAL analysis ***
```

```
/SOLU
        ANTYPE,2
        MODOPT,LANB,10
        EQSLV,JCG
        MXPAND,,,,YES,,
        LUMPM,OFF
        PSTRES,0
        MODOPT,LANB,10,0,0, ,OFF, ,2
        ALLS
SOLVE
FINISH
/eof
```

APPENDIX VII Finite Element Code For The Straight Unimorph Piezoelectric Actuator

```
FINISH
/OUTPUT,out
/CLEAR
/OUTPUT,TERM
/FILENAME,pump300
/TITLE,MEMS 3D linear unimorph
!/STITLE,1,Richard Haigh attempt 1.inp
/PLOPTS,LOGO,ON
!/TLABEL,-1,-.85,Silicon thickness = %thick%
!/TLABEL,-2,-.86,PZT thickness   = %height_c%
! solution parameters
                    voltage                             =15
                    silicon                             =1
                    ceramic                             =2
                    area                                =1
                    f_min                               =10000
                    f_max                               =30000
                    deltaf                              =10000
                    eps_0                               =8.854E-12
                    *AFUN,RAD pi                        =ACOS(-1)
                    *AFUN,DEG xi                        =0.005

! material properties Motorola HD3203
! index is based on IEEE notation poled in z direction
! * ceramic *

       dens_c            =7850
       eps11_c           =2420*eps_0
       eps33_c           =3330*eps_0
       e31_c             =-48.00
       e33_c             =-31.38
       e15_c             =14.29
       e24_c             =e15_c
       c11_c             =139.7E9
       c12_c             =88.7E9
       c13_c             =99.7E9
       c33_c             =140.0E9
       c44_c             =25.1E9

! * silicon *
```

```
        dens_s          =2330
        young_s         =155.8e9
        poiss_s         =0.2152
        shear_s         =64.1e9

! *** element declaration ***
      /PREP7
   ET,ceramic,SOLID5



   KEYOPT,ceramic,1,3
   KEYOPT,ceramic,3,0
   KEYOPT,ceramic,5,2

   ET,silicon,SOLID45

   KEYOPT,silicon,1,0
   KEYOPT,silicon,2,0
   KEYOPT,silicon,4,0
   KEYOPT,silicon,5,2
   KEYOPT,silicon,6,3
   KEYOPT,silicon,9,0


      FINISH
! *** material declaration SI units ***
! *** material declaration ***
! * ceramic material *
/PREP7
EMUNIT,EPZRO,ceramic
       MP,DENS,ceramic,dens_c
       MP,PERX,ceramic,eps11_c
       MP,PERY,ceramic,eps33_c
       MP,PERZ,ceramic,eps11_c

       TB,PIEZ,ceramic
       TBDATA,3,e31_c
       TBDATA,6,e31_c
       TBDATA,9,e33_c
       TBDATA,14,e24_c
       TBDATA,16,e24_c
```

```
  TB,ANEL,ceramic
  TBDATA,1,c11_c
  TBDATA,2,c12_c
  TBDATA,3,c13_c
  TBDATA,7,c11_c
  TBDATA,8,c13_c
  TBDATA,12,c33_c
  TBDATA,16,c44_c
  TBDATA,19,c44_c
  TBDATA,21,c44_c

 ! * silicon *

  MP,DENS,silicon,dens_s
  MP,EX,silicon,young_s
  MP,EY,silicon,young_s
  MP,EZ,silicon,young_s
  MP,NUXY,silicon,poiss_s
  MP,NUYZ,silicon,poiss_s
  MP,NUXZ,silicon,poiss_s
  MP,GXY,silicon,shear_s
  MP,GYZ,silicon,shear_s
  MP,GXZ,silicon,shear_s

 FINISH


!geometry and meshing
        /PREP7
STAT
KEYPTS

 CSYS,0
        BLOCK,0,length,0,width,0,thick,
        VSEL,S,LOC,Z,0,thick
        VATT,silicon,,silicon
        ASEL,S,LOC,Z,(999/1000)*thick,(1001/1000)*thick,,0
        VEXT,ALL,,,,,thick_c
        VSEL,S,LOC,Z,thick,(thick+thick_c),,0
        VATT,ceramic,,ceramic
        CSYS,1
```

```
        VSEL,S,LOC,Z,-10,thick+thick_c+10,,1
        VSEL,R,LOC,X,0,10+radius+(2*width),,
        NUMMRG,KP,thick_c/1000,thick_c/1000
        NUMMRG,NODE,thick_c/1000,thick_c/1000
        NUMMRG,ELEM,thick_c/1000,thick_c/1000
        NUMMRG,KP,thick_c/1000,thick_c/1000
        ALLS
        ESIZE,width*q,,
        MSHAPE,0,3D
        MSHKEY,1
        VSEL,S,LOC,Z,0,thick+thick_c,,1
        VMESH,ALL

FINISH

! *** boundary conditions ***
/PREP7
CSYS,0
ASEL,S,AREA,,5,11,1,,,
        ASEL,U,AREA,,6,10,1,,,
        DA,ALL,UX,0
        DA,ALL,UY,0
        DA,ALL,UZ,0
        CSYS,0
        ASEL,S,LOC,Z,(999/1000)*(thick+thick_c),(1001/1000)*(thick+thick_c)
        ESEL,R,TYPE,,ceramic
        NSLE,S
        *GET,top_y,NODE,,MXLOC,Z
        *GET,bot_y,NODE,,MNLOC,Z
        NSEL,R,LOC,Z,top_y
        *GET,node_s,NODE,,NUM,MIN
        CM,signal,NODE
        CP,NEXT,VOLT,ALL
        ASEL,S,LOC,Z,(999/1000)*(thick),(1001/1000)*(thick)
        ESEL,R,TYPE,,ceramic          NSLE,S
        NSEL,R,LOC,Z,bot_y
        *GET,node_m,NODE,,NUM,MIN
        CM,mass,NODE
        CP,NEXT,VOLT,ALL
        NALL
        D,node_m,VOLT,0
        D,node_s,VOLT,voltage
```

```
        ESEL,S,TYPE,,ceramic
        NSLE,S
        *GET,max_x,NODE,,MXLOC,X
        NSEL,R,LOC,Z,top_y
        NSEL,R,LOC,X,max_x
        *GET,upper,NODE,,NUM,MIN
        ESEL,S,TYPE,,ceramic
        NSLE,S
        NSEL,R,LOC,Z,bot_y
        NSEL,R,LOC,X,max_x
        *GET,lower,NODE,,NUM,MIN
        ALLS
        FINISH
        ALLS
! *** MODAL analysis ***
/SOLU
        ANTYPE,2
        MODOPT,LANB,10
        EQSLV,JCG
        MXPAND,,,,YES,,
        LUMPM,OFF
        PSTRES,0
        MODOPT,LANB,10,0,0, ,OFF, ,2
        ALLS
SOLVE
FINISH
/eof
```

APPENDIX VIII Finite Element Code For The Spoke actuator

```
FINISH
/OUTPUT,out
/CLEAR
/OUTPUT,TERM
/FILENAME,pump300
/TITLE,MEMS spoke - 3D
!/STITLE,1,Richard Haigh attempt 1.inp
/PLOPTS,LOGO,ON


! solution parameters

                voltage             =15
                silicon             =1
                ceramic             =2
                eps_0               =8.854E-12
                *AFUN,RAD
                pi                  =ACOS(-1)
                *AFUN,DEG
                xi                  =0.005

! general parameters

                thick                =25.8e-6
                thick_c              =10e-6
                in_dia               =1.33e-3
                beta                 =10.58
                radius               =4e-3
                q                    =83.33e-6/in_dia


! material properties Motorola HD3203
! index is based on IEEE notation poled in z direction
! * ceramic *

        dens_c              =7850
        eps11_c             =2420*eps_0
        eps33_c             =3330*eps_0
        e31_c               =-48.00
        e33_c               =-31.38
```

```
        e15_c                =14.29
        e24_c                =e15_c
        c11_c                =139.7E9
        c12_c                =88.7E9
        c13_c                =99.7E9
        c33_c                =140.0E9
        c44_c                =25.1E9

! * silicon *

            dens_s               =2330
            young_s              =155.8e9
            poiss_s              =0.2152
            shear_s              =64.1e9

! *** element declaration ***
         /PREP7
    ET,ceramic,SOLID5



    KEYOPT,ceramic,1,3
    KEYOPT,ceramic,3,0
    KEYOPT,ceramic,5,2

    ET,silicon,SOLID45

    KEYOPT,silicon,1,0
    KEYOPT,silicon,2,0
    KEYOPT,silicon,4,0
    KEYOPT,silicon,5,2
    KEYOPT,silicon,6,3
    KEYOPT,silicon,9,0


         FINISH
```

```
! *** material declaration SI units ***
! *** material declaration ***
! * ceramic material *
/PREP7
EMUNIT,EPZRO,ceramic
          MP,DENS,ceramic,dens_c
          MP,PERX,ceramic,eps11_c
          MP,PERY,ceramic,eps33_c
          MP,PERZ,ceramic,eps11_c

          TB,PIEZ,ceramic
          TBDATA,3,e31_c
          TBDATA,6,e31_c
          TBDATA,9,e33_c
          TBDATA,14,e24_c
          TBDATA,16,e24_c

          TB,ANEL,ceramic
          TBDATA,1,c11_c
          TBDATA,2,c12_c
          TBDATA,3,c13_c
          TBDATA,7,c11_c
          TBDATA,8,c13_c
          TBDATA,12,c33_c
          TBDATA,16,c44_c
          TBDATA,19,c44_c
          TBDATA,21,c44_c
         ! * silicon *
          MP,DENS,silicon,dens_s
          MP,EX,silicon,young_s
          MP,EY,silicon,young_s
          MP,EZ,silicon,young_s
          MP,NUXY,silicon,poiss_s
          MP,NUYZ,silicon,poiss_s
          MP,NUXZ,silicon,poiss_s
          MP,GXY,silicon,shear_s
          MP,GYZ,silicon,shear_s
          MP,GXZ,silicon,shear_s

         FINISH
```

```
!geometry and meshing

        /PREP7
        CYL4,0,0,in_dia/2,beta,radius,,thick
        VEXT,2,,,0,0,thick_c,,,,

! * groups volumes into components *

        VSEL,S,LOC,Z,thick,thick+thick_c
        CM,ceramic,VOLU
        VSEL,S,LOC,Z,0,thick
        CM,silicon,VOLU

! * defines material attributes to components *

        CMSEL,S,ceramic
        VATT,ceramic,,ceramic
        CMSEL,S,silicon
        VATT,silicon,,silicon

        CSYS,1
        VSEL,S,LOC,Z,-10,thick+thick_c+10,,1
        VSEL,R,LOC,X,0,10+radius+(2*in_dia),,
        NUMMRG,KP,thick_c/1000,thick_c/1000
        NUMMRG,NODE,thick_c/1000,thick_c/1000
        NUMMRG,ELEM,thick_c/1000,thick_c/1000
        NUMMRG,KP,thick_c/1000,thick_c/1000
        ALLS

        ESIZE,in_dia*q,,                    !max 1 division along shortest line
        MSHAPE,0,3D                         !hex in 3d
        MSHKEY,1                            !mapped meshing
        VSEL,S,LOC,Z,0,thick+thick_c,,1
        VMESH,ALL

        ! Apply loads
        ASEL,S,AREA,,3,3,,,,
        ASEL,A,AREA,,8,8,,,,
        DA,ALL,ALL,1
```

```
ASEL,S,LOC,Z,(999/1000)*(thick+thick_c),(1001/1000)*(thick+thick_c)
ESEL,R,TYPE,,ceramic
NSLE,S
*GET,top_y,NODE,,MXLOC,Z                !from point on top surface
*GET,bot_y,NODE,,MNLOC,Z
NSEL,R,LOC,Z,top_y
*GET,node_s,NODE,,NUM,MIN
CM,signal,NODE                          !assign name of signal to nodes
CP,NEXT,VOLT,ALL
ASEL,S,LOC,Z,(999/1000)*(thick),(1001/1000)*(thick)
ESEL,R,TYPE,,ceramic               !electric field through ceramic to base
NSLE,S
NSEL,R,LOC,Z,bot_y
*GET,node_m,NODE,,NUM,MIN
CM,mass,NODE
CP,NEXT,VOLT,ALL                        !apply voltage DOF

NALL
D,node_m,VOLT,0
D,node_s,VOLT,voltage

ESEL,S,TYPE,,ceramic
NSLE,S
*GET,max_x,NODE,,MXLOC,X
NSEL,R,LOC,Z,top_y
NSEL,R,LOC,X,max_x
*GET,upper,NODE,,NUM,MIN

ESEL,S,TYPE,,ceramic
NSLE,S
NSEL,R,LOC,Z,bot_y
NSEL,R,LOC,X,max_x
*GET,lower,NODE,,NUM,MIN

ALLS
FINISH
ALLS
```

```
! *** MODAL analysis ***
        /SOLU
        ANTYPE,2
        !*
        MODOPT,LANB,5
        EQSLV,JCG                   ! SPAR
        MXPAND,,,,YES,,
        LUMPM,OFF
        PSTRES,0
        !*
        MODOPT,LANB,5,0,, ,OFF, ,2
        !ALPHAD,alpha
        !BETAD,beta
        !DMPRAT,xi
        ALLS
SOLVE
FINISH
/eof
```

References

(1) Whatmore, R. W. In *Fundamentals of Ceramics Engineering*; Vincenzini, P., Ed.; Elsevier Applied Science: London, 1991.

(2) Herbert, J. M. *Ferroelectric Transducers and Sensors*; Gordon & Breach Science Publishers Ltd., 1997.

(3) Jaffe, B.; Cook, W. R.; Jaffe, H. *Piezoelectric Ceramics*; Academic Press Inc., 1971.

(4) Moulson, A. J.; Herbert, J. M. *Electroceramics - Materials Properties and Applications*; Gordon & Breach Science Publishers Ltd., 1990.

(5) Xu, Y. *Ferroelectric Materials and Their Applications*; Elsevier Science Publishers B.V., 1991.

(6) Kingery, W. D.; Birnie, D. P.; Chiang, Y. M. *Physical Ceramics - Principles for ceramic science and engineering*; John Wiley & Sons Inc., 1997.

(7) IEEE In *Key Papers in Physics: Piezoelectricity*; Zwick-Rosen, C., Hiremath, B. V., Newnham, R. E., Eds.; American Institute of Physics: New York, 1992.

(8) Nye, J. F. *Physical Properties of Crystals - Their Representation by Tensors & Matrices*; 1 ed.; Oxford University Press, 1957.

(9) Lee, S. S.; White, R. M. *Sensors and Actuators, Part A Physical* **1996**, *52*, 41-5.

(10) Ferrari, V.; Marioli, D.; Taroni, A.; Ranucci, E. *Sensors and Actuators, Part B Chemical* **2000**, *68*, 81-7.

(11) Piekarski, B.; Dubey, M.; Devoe, D.; Zakar, E.; Zeto, R.; Conrad, J.; Piekarz, R.; Ervin, J. D. *Integrated Ferroelectrics* **1999**, *24*, 147-54.

(12) Morten, B.; De Cicco, G.; Prudenziati, M. *Sensors and Actuators, Part A Physical* **1993**, *37-38*, 337-42.

(13) Koch, M.; Harris, N.; Evans, A.; White, N. M.; Brunnschweiler, A. *Sensors and Actuators, Part A Physical* **1998**, *70*, 98-103.

(14) Bar Cohen, Y.; Chang, Z. Proceedings of SPIE's 7th, Annual International Symposium on Smart Structures and Materials, Newport, California, U.S.A., 2000; p Paper No. 3992-103.

(15) Prudenziati, M. *Thick Film Sensors*; Elsevier Science B.V.: Amsterdam, The Netherlands, 1994.

(16) Birnie, D. P. University of Arizona web site: http://www.mse.arizona.edu/faculty/birnie/Coatings/SpinCoat.htm, Accessed 2000.

(17) Skinner, D. P.; Newnham, R. E.; Cross, L. E. *Matter Research Bulletin* **1978**, *13*, 525-36.

(18) Cross, L. E. *Materials Chemistry and Physics* **1996**, *43*, 108-15.

(19) Barrow, D. A.; Petroff, T. E.; Tandon, R. P.; Sayer, M. *Journal of Applied Physics* **1997**, *81*, 876-81.

(20) Banno, H. *American Ceramic Society Bulletin* **1987**, *66*, 1332-7.

(21) Lee, S. S.; White, R. M. *Sensors and Actuators, Part A Physical* **1998**, *71*, 153-7.

(22) Yang, Z.; Matsumoto, S.; Goto, H.; Matsumoto, M.; Maeda, R. *Sensors and Actuators, Part A Physical* **2001**, *93*, 266-72.

(23) Ohuchi, H.; Nakano, K.; Endoh, H.; Uchino, K. *Ferroelectrics* **1986**, *68*, 257-64.

(24) Bar Cohen, Y.; Chang, Z. Proceedings of SPIE's 8th, Annual International Symposium on Smart Structures and Materials, Newport, California, U.S.A., 2001; 4327-52.

(25) Chen, B.; Cheeseman, B. A.; Safari, A.; Danforth, S. C.; Chou, T. W. *IEEE Transactions on Ultrasonics Ferroelectrics and Frequency Control* **2002**, *49*, 319-26.

(26) Tomikawa, Y.; Masamura, K.; Sugawara, S.; Konno, M. *Ferroelectrics* **1986**, *68*, 235-48.

(27) Ogawa, T.; Ando, A.; Wakino, K. *Ferroelectrics* **1986**, *68*, 249-46.

(28) Lappalainen, J.; Johannes, F.; Moilanen, H.; Leppavuori, S. *Sensors and Actuators, Part A Physical* **1995**, *46-47*, 104-9.

(29) Luginbuhl, P.; Racine, G. A.; Lerch, P.; Romanowicz, B.; Brooks, K. G.; de Rooij, N. F.; Renaud, P.; Setter, N. *Sensors and Actuators, Part A Physical* **1996**, *54*, 530-5.

(30) Cattan, E.; Haccart, T.; Velu, G.; Remiens, D.; Bergaud, C.; Nicu, L. *Sensors and Actuators, Part A Physical* **1999**, *74*, 60-4.

(31) Wang, Q. M.; Xu, B.; Zhang, Q.; Liu, R. H.; Cross, L. E. *Journal of Applied Physics* **1999**, *86*, 3352-60.

(32) Haertling, G. H. *American Ceramic Society Bulletin* **1994**, *73*, 93-6.

(33) Li, X.; Shih, W. Y.; Aksay, I. A.; Shih, W. H. *Journal of the American Ceramic Society* **1999**, *82*, 1733-40.

(34) Hellbaum, R. F.; Bryant, R. G.; Fox, R. L. In *United States Patent No. 5,632,841* United States of America, 1997.

(35) Barrow, D. A.; Petroff, T. E.; Sayer, M. In *United States Patent No. 5,585,136* United States of America, 1996.

(36) Sayer, M.; Wu, Z.; Yi, G. *Journal of Applied Physics* **1988**, *64*, 2717-24.

(37) Barrow, D. A.; Petroff, T. E.; Sayer, M. *Surface Coatings Technology* **1995**, *76-77*, 113-8.

(38) Wang, Z.; Zhao, C.; Zhu, W.; Tan, O. K.; Liu, W.; Yao, X. *Materials Chemistry and Physics* **2002**, *75*, 71-75.

(39) Corker, D. L.; Zhang, Q.; Whatmore, R. W.; Perin, C. *Journal of the European Ceramic Society* **2002**, *22*, 383-90.

(40) Gurkovich, S. R.; Blum, J. B. *Ferroelectrics* **1985**, *62*, 189-94.

(41) Gebhardt, E.; Obrowski, W. *Zeitschrift für Metallkunde* **1954**, *45*, 332-9.

(42) Corker, D. L.; Whatmore, R. W.; Ringgaard, E.; Wolny, W. W. *Journal of the European Ceramic Society* **2000**, *20*, 2039-45.

(43) Haigh, R. D. MSc. Thesis, Cranfield University, 2000.

(44) Perin, C. MSc. Thesis, Cranfield University, 1999.

(45) Wilson, R. Ph.D. Thesis, Cranfield University, 2001.

(46) Beeby, S. P.; Blackburn, A.; White, N. M. *Journal of Micromechanics and Microengineering* **1999**, *9*, 218-29.

(47) Glynne-Jones, P.; Beeby, S. P.; Dargie, P.; Papakostas, T.; White, N. M. *Measurement Science & Technology* **2000**, *11*, 526-31.

(48) Wang, Z. J.; Chu, J. R.; Maeda, R.; Kokawa, H. *Thin Solid Films* **2002**, *416*, 66-71.

(49) Maas, R.; Koch, M.; Harris, N. R.; White, N. M.; Evens, A. G. R. *Materials Letters* **1997**, *31*, 109-12.

(50) Chen, I. W.; Chen, S. Y. *Ferroelectrics* **1994**, *152*, 25-30.

(51) Chen, I. W.; Chen, S. Y. *Journal of the American Ceramic Society* **1994**, *77*, 2332-6.

(52) Brooks, K. G.; Reaney, I. M.; Klissurska, R. D.; Huang, Y.; Bursill, L.; Setter, N. *Journal of Materials Research* **1994**, *9*, 2540-53.

(53) Huang, Z.; Zhang, Q.; Whatmore, R. W. *Journal of Materials Science Letters* **1998**, *17*, 1157-59.

(54) Chen, S. Y.; Chen, I. W. *Journal of the American Ceramic Society* **1998**, *81*, 97-105.

(55) Kim, J. D.; Hana, S.; Kawagoe, S.; Sasaki, K.; Hata, T. *Thin Solid Films* **2001**, *385*, 293-7.

(56) Horita, S.; Naruse, T.; Watanabe, A.; Masuda, A.; Kawada, T.; Abe, Y. *Applied Surface Science* **1997**, *117/118*, 429-33.

(57) Kim, S. H.; Kim, C. E.; Oh, Y. J. *Thin Solid Films* **1997**, *305*, 321-6.

(58) Klissurska, R. D.; Maeder, T.; Brooks, K. G.; Setter, N. *Microelectronic Engineering* **1995**, *29*, 297-300.

(59) Velu, G.; Remiens, D. *Journal of the European Ceramic Society* **1999**, *19*, 2005-13.

(60) Treichel, O.; Kirchhoff, V. *Surface and Coatings Technology* **2000**, *123*, 268-72.

(61) Tong, H. D.; Zwijze, R. A. F.; Berenschot, J. W.; Wiegerink, R. J.; Krijnen, G. J. M.; Elwenspoek, M. Proceedings of the SeSens Workshop, 2001; p 697-702.

(62) Nicholls, J. R.; Lawson, K. J.; Johnstone, B.; Rickerby, D. S. *Surface and Coatings Technology* **2002**, *151-152*, 383-91.

(63) Wellman, R. G.; Nicholls, J. R. *Wear* **2000**, *242*, 89-96.

(64) Hartmanova, M.; Thurzo, I.; Jergel, M.; Bartos, J.; Kadlec, F.; Zelezny, V.; Tunega, D.; Kundracik, F.; Chromik, S.; Brunel, M. *Journal of Materials Science* **1998**, *33*, 969-75.

(65) Cheon, C. I.; Lee, Y. B.; Kim, S. J.; Bang, K. S.; Kim, J. C.; Lee, H. G. *Transactions on Electrical and Electronic Materials* **2003**, *4*, 20-3.

(66) Chromik, S.; Wuyts, B.; Vavra I; Rosova, F.; Hanik, S.; Benacka, S.; Bruynseraede, Y. *Physica C* **1994**, *226*, 153-8.

(67) Myoren, H.; Nishiyama, Y.; Fukumoto, H.; Nasu, H.; Osaka, Y. *Japanese Journal of Applied Physics* **1989**, *28*, 351-5.

(68) Myoren, H.; Nishimoto, Y.; Miyamoto, N.; Kai, Y.; Yamanaka, Y.; Osaka, Y.; Nishiyama, F. *Japanese Journal of Applied Physics* **1990**, *29*, 955-7.

(69) Harada, K.; Nakanishi, H.; Itozaki, H.; Yazu, S. *Japanese Journal of Applied Physics* **1991**, *30*, 934-8.

(70) Lay, L. A. *Corrosion Resistance of Technical Ceramics*; HMSO: London, 1983.

(71) Pelaiz Barranco, A.; Calderon Pinar, F.; Perez Martinez; Torres Garcia, E. *Journal of the European Ceramic Society* **2001**, *21*, 523-29.

(72) Torres Garcia, E.; Pelaiz Barranco, A.; Vazquez, C.; Calderon Pinar, F.; Perez Martinez, O. *Thermochimica Acta* **2001**, *372*, 39-44.

(73) Gerson, R.; Jaffe, H. *Journal of Physical Chemistry of Solids* **1963**, *24*, 979-84.

(74) *Ceramic Dielectrics & Capacitors*; 1st ed.; Herbert, J. M., Ed.; Gordon & Breach Science Publishers: Reading, 1997; Vol. 6.

(75) Smits, J.; Dalke, S. I.; Cooney, T. K. *Sensors and Actuators, Part A Physical* **1991**, *28*, 41-61.

(76) Germano *IEEE Transactions on Audio & Electronics* **1971**, *19*, 6-12.

(77) Steel, H., Harper *Journal of Physics, Part D Applied Physics* **1978**, *11*, 979-89.

(78) Smits, J.; Choi, W. S. *IEEE Transactions on Ultrasonics Ferroelectrics and Frequency Control* **1991**, *38*, 256-70.

(79) Weinberg, M. S. *Journal of Microelectromechanical Systems* **1999**, *8*, 529-33.

(80) Wang, Q. M.; Cross, L. E. *Ferroelectrics* **1998**, *215*, 187-13.

(81) Berlincourt, D.; Kruger, H. H. A. *Journal of Applied Physics* **1959**, *30*, 1804-10.

(82) Mohammadi, F.; Kholkin, A. L.; Jadidian, B.; Safari, A. *Applied Physics Letters* **1999**, *75*, 2488-90.

(83) Wang, Q. M.; Du, X. H.; Xu, B.; Cross, L. E. *IEEE Transactions on Ultrasonics, Ferroelectrics, and Frequency Control* **1999**, *46*, 638-46.

(84) White, N. M.; Koch, M.; Harris, N.; Maas, R.; Evans, A. G. R.; Brunnschweiler, A. *Measurement, Science and Technology* **1997**, *8*, 49-57.

(85) Weihua, Z.; Gaoyang, Z.; Zhiming, C. *Materials Science and Engineering* **2003**, B99, 168-72.

(86) Su, B.; Pearse, D. H.; Button, T. W. *Journal of the European Ceramic Society* **2001**, *21*, 2005-9.

(87) Lubitz, K.; Wolff, A.; Preu, G. *Ferroelectrics* **1992**, *133*, 21-6.

(88) Safari, A.; Janas, V. F.; Panda, R. *Proceedings of The SPIE - International Society for Optical Engineering* **1996**, *2721*, 251-62.

(89) Janas, V. F.; Safari, A. *Journal of the American Ceramic Society* **1995**, *78*, 2945-55.

(90) King, B. H.; Dimos, D.; Yang, P.; Morissette, S. L. *Journal of Electroceramics* **1999**, *3*, 173-78.

(91) Allahverdi, M.; Danforth, S. C.; Jafari, M.; Safari, A. *Journal of the European Ceramic Society* **2001**, *21*, 1485-90.

(92) Jiang, X. N.; Sun, C.; Zhang, X.; Xu, B.; Ye, Y. H. *Sensors and Actuators, Part A Physical* **2000**, *87*, 72-7.

(93) Savakus, H. P.; Klicker, K. A.; Newnham, R. E. *Materials Research Bulletin* **1981**, *16*, 677-80.

(94) Ohara, Y.; Miyayama, M.; Koumoto, K.; Yanagida, H. *Journal of Material Science Letters* **1993**, *12*, 1279-82.

(95) Lukacs, M.; Sayer, M.; Foster, S. *Integrated Ferroelectrics* **1999**, *24*, 95-106.

(96) Eyett, M.; Bauerle, D.; Wersing, W.; Thomann, H. *Journal of Applied Physics* **1987**, *62*, 1511-4.

(97) Lee, Y. C.; Kuo, S. H. *Sensors and Actuators, Part A Physical* **2001**, *93*, 57-62.

(98) Ohara, Y.; Miyayama, M.; Koumoto, K.; Yanagida, H *Sensors and Actuators, Part A Physical* **1994**, *40*, 187-90.

(99) Knowles, M.; Webb, C. *Physics World* **1995**, 41-4.

(100) Kruusing, A. *Optics and Lasers in Engineering* **2004**, *41*, 329-52.

(101) Shiosaki, T.; Masuda, H.; Adachi, M.; Kawabata, A. Proceedings of the 6th, Meeting on Ferroelectrics and Their Applications, Kyoto, Japan, 1987; 159-61.

(102) Suchaneck, G.; Tews, R.; Gerlach, G. *Surface and Coatings Technology* **1999**, *116-119*, 456-460.

(103) Mace, H.; Achard, H.; Peccoud, L. *Microelectronic Engineering* **1995**, *29*, 45-48.

(104) Tang, T. A.; Chen, Z.; Li, N.; Zou, S. X. *Ferroelectrics* **1999**, *232*, 927-932.

(105) Oh, S.; Park, H. B.; Joo, S. H.; Oh, S. J.; Yoo, M. H.; Kim, B. H.; Lee, J. H.; Yoo, C. Y.; Lee, S. I.; Lee, M. Y. *Journal of the Korean Physical Society* **1998**, *32*, 1649-51.

(106) Wang, S. A.; Li, X. H.; Wakabayashi, K.; Esashi, M. *Journal of the American Ceramic Society* **1999**, *82*, 1339-41.

(107) Liu, W.; KO, J.; Zhu, W. *Journal of Material Science Letters* **2000**, *19*, 2263-5.

(108) Belloy, E.; Sayah, A.; Gijs, M. *Sensors and Actuators, Part A Physical* **2000**, *86*, 231-37.

(109) Slikkerveer, P. J.; Bouten, P. C. P.; Haas, F. *Sensors and Actuators, Part A Physical* **2000**, *85*, 296-303.

(110) Lighthart, H. J.; Slikkerveer, P. J.; In't-Veld, F. H.; Swinkels, P. H. W.; Zonneveld, M. H. *Philips Journal of Research* **1996**, *50*, 475-99.

(111) Belloy, E.; Thurre, S.; Walckiers, E.; Sayah, A.; Gijs, M. A. M *Sensors and Actuators, Part A Physical* **2000**, *84*, 330-37.

(112) Bouten, P. C. P.; Scholten, H. F.; Pourreuix, C. *Wear* **1999**, *233-35*, 512-22.

(113) Schasfoort, R.; Duijn, R. G.; Schlautmann, S.; Frank, H.; Billiet, H.; Dedem, G.; Berg, A. Micro Tool Analysis Systems 2000, 2000; p 391-94.

(114) Matthee, T.; Wecker, J.; Behner, H.; Friedel, G. *Journal of Applied Physics Letters* **1992**, *61*, 1240-2.

(115) *Rough Surfaces*; 1st ed.; Thomas, T. R., Ed.; Longman Group Ltd.: London & New York, 1982.

(116) Singh, J.; Chandra, S.; Chand, A. *Sensors and Actuators, Part A Physical* **1999**, *77*, 133-8

(117) Beeby, S. P.; Grabham, N. J.; White, N. M. *Sensors and Actuators, Part A Physical* **2001**, *92*, 168-74.

(118) Piekarski, B.; DeVoe, D.; Dubey, M.; Kaul, A. R.; Conrad, J. *Sensors and Actuators, Part A Physical* **2001**, *91*, 313-20.

(119) Beeby, S. P.; White, N. M. *Sensors and Actuators, Part A Physical* **2001**, *88*, 189-97.

(120) Dorey, R.; Haigh, R. D.; Stringfellow, S. B.; Whatmore, R. W. *British Ceramic Transactions* **2002**, *101*, 146-8.

(121) Wensink, H.; Jansen, H. V.; Berenschot, J. W.; Elwenspoek, M. C. *Journal of Micromechanics and Microengineering* **2000**, *10*, 175-80.

(122) *Handbook of Microlithography, Micromachining and Microfabrication*; Rai-Choudhury, P., Ed.; SPIE Optical Engineering Press and The Institution of Electrical Engineers: Washington and London, 1997; Vol. 1-Microlithography.

(123) Box, G. E.; Hunter, G. H.; Hunter, J. S. *Statistics for Experimenters. An Introduction to Design, Data Analysis and Model Building*; John Wiley & Sons.: New York, 1978.

(124) Sherrit, S.; Widerick, H. D.; Mukherjee, B. K. Proceedings of the SPIE, Medical Imaging Conference, Newport Beach, C.A., USA, 1997.

(125) Wensink, H.; Elwenspoek, M. *Sensors and Actuators, Part A Physical* **2002**, *102*, 157-64.

(126) Slikkerveer, P. J.; van Dongen, P.; Touwslager, F. *Wear* **1999**, *236*, 189-98.

(127) Miller, R. A.; Bernstein, J. J. *Integrated Ferroelectrics* **2000**, *29*, 225-31.

(128) Nicholls, D. *Complexes And First Row Transition Elements*; The Macmillan Press Ltd.: London, 1995.

(129) Cotton, F. A.; Wilkinson, G. *Advanced Inorganic Chemistry*; 5th ed.; John Wiley & Sons: New York, 1988.

(130) Trolier, S. E.; Xu, C.; Newnham, R. E. *IEEE Transactions on Ultrasonics, Ferroelectrics, and Frequency Control* **1988**, *35*, 839-42.

(131) Trolier, S. E.; Geist, C.; Safari, A.; Newnham, R. E.; Xu, Q. C. Proceedings of the 6th, IEEE International Symposium on Applications of Ferroelectrics, Bethlehem, PA, USA, 1986; 707-10.

(132) *Phase Diagrams for Ceramists - 1975 Supplement*; Levin, E. M.; McMurdie, H. F., Eds.; The American Ceramic Society: Columbus, Ohio, USA, 1975; Vol. 3.

(133) Simeonova, J. M.; Dimitriev, Y. B.; Dimitrov, V. V. *Dokladi Na Bolgarskata Akademiya Na Naukite* **1980**, *33*, 765-67.

(134) *CRC Handbook of Chemistry & Physics*; 69th ed.; Weast, R. C.; Astle, M. J.; Beyer, W. H., Eds.; Chemical Rubber Publishing Co., 1988.

(135) Ferroperm (S/A); Ferroperm web site: http://www.ferroperm-piezo.com/hoejre-forside.html, Accessed 2004.